Sedimentary iron and trace metal cycling in oxygen minimum zones: Implications for marine productivity and redox evolution

Habilitationsschrift
vorgelegt an der Mathematisch-Naturwissenschaftlichen
Fakultät der Christian-Albrechts-Universität zu Kiel

Dr. Florian Scholz

Kiel, 2018

Abstract

Because of anthropogenic global warming, the world ocean is currently losing oxygen. This trend called ocean deoxygenation is particularly pronounced in low-latitude upwelling-related oxygen minimum zones (OMZs). In these areas, the temperature-related oxygen drawdown is additionally modulated by biogeochemical feedback mechanisms between sedimentary iron and phosphorus release, water column nitrogen cycling and primary productivity. Similar feedbacks were likely active during past periods of global warming and ocean deoxygenation. However, their integrated role in amplifying or mitigating climate change-driven ocean anoxia has not been evaluated in a systematic fashion. Moreover, many studies on past (de)oxygenation events emphasize anoxic-sulfidic (i.e., euxinic) basins such as the Black Sea rather than upwelling-related OMZs as modern analogue systems.

This habilitation thesis consists of nine published stand-alone articles dealing with the biogeochemical cycling of iron and other redox-sensitive metals (and their isotopes) in the sediments and water columns of modern and ancient OMZs. The findings of these independent chapters are summarized and synthesized in a review article entitled “Identifying oxygen minimum-type biogeochemical cycling in Earth history using inorganic geochemical proxies”. The goal of this synthesis chapter is to provide a general framework of paleo-redox proxies that can be used to identify OMZ-type biogeochemical cycling and the associated biogeochemical feedbacks in the geological record.

Nitrate-reducing (i.e., nitrogenous) conditions in the water column and iron-reducing (i.e., ferruginous) to sulfidic conditions in the surface sediment are identified as key-features of anoxic OMZs in the modern ocean. Because of the elevated iron solubility under anoxic conditions in OMZs, sedimentary Fe can be mobilized into the water column and redistributed across the continental margin. By using a generalized model of sedimentary iron release and trapping, it is demonstrated that the extent of iron mobilization and transport in modern OMZs is comparable to that inferred for the euxinic Black Sea and ferruginous water columns in Earth history. Based on this result, it is suggested that many sedimentary iron enrichments in the geological record are broadly consistent with OMZ-type biogeochemical cycling, especially if enhanced chemical weathering and reactive iron supply to the ocean during past periods of global warming are taken into account. Future studies on paleo-(de)oxygenation events with a combined focus on iron, sulfur and nitrogen cycling may reveal that nitrogenous OMZs were an important feature of the ocean through Earth’s history.

Kurzfassung

Die globale Erwärmung führt derzeit zu abnehmenden Sauerstoffkonzentrationen im Weltozean. Besonders ausgeprägt ist die Sauerstoffabreicherung in den auftriebsbedingten Sauerstoffminimumzonen der niederen Breiten. In diesen Ozeanregionen beeinflussen zudem biogeochemische Rückkopplungen zwischen der sedimentären Nährstofffreisetzung (z.B. Eisen und Phosphor), dem Stickstoffkreislauf in der Wassersäule und der Primärproduktion die Entwicklung der Sauerstoffkonzentrationen. Es ist anzunehmen, dass ähnliche Rückkopplungsmechanismen während anoxischer Ereignisse in der Erdgeschichte existierten. Inwiefern biogeochemische Rückkopplungen die durch Klimaveränderungen hervorgerufene Sauerstoffarmut im Ozean verstärkt oder abgeschwächt haben ist bisher jedoch nur unzureichend erforscht. Dies ist insbesondere der Fall, da viele Studien, die sich mit anoxischen Ereignissen in der Erdgeschichte befassen, nicht Sauerstoffminimumzonen sondern anoxische und sulfidische (euxinische) Becken wie das Schwarze Meer als heutiges Modellsystem nutzen.

Diese Habilitationsschrift besteht aus neun publizierten wissenschaftlichen Artikeln, die sich mit den biogeochemischen Kreisläufen des Eisens und anderer redox-sensitiver Metalle (und deren Isotope) in den Sedimenten und Wassersäulen von heutigen und vergangenen Sauerstoffminimumzonen beschäftigen. Die Erkenntnisse dieser unabhängigen Kapitel sind in einem vorangestellten Aufsatz zusammengefasst und synthetisiert. Hauptziel dieser Synthese ist die Entwicklung einer Systematik von Paläoumweltindikatoren, die zur Erkennung von Sauerstoffminimumzonen und den zugehörigen biogeochemischen Rückkopplungen in sedimentären Archiven genutzt werden kann.

Nitratreduzierende Bedingungen in der Wassersäule (engl. Nitrogenous) und eisenreduzierende (engl. Ferruginous) bzw. sulfidische Bedingungen im Oberflächensediment werden dabei als typische Merkmale anoxischer Sauerstoffminimumzonen im heutigen Ozean identifiziert. Aufgrund der erhöhten Eisenlöslichkeit unter sauerstofffreien Bedingungen kann sedimentäres Eisen in die Wassersäule mobilisiert und entlang des Kontinentalrands umgelagert werden. Mithilfe eines generalisierten Modells der sedimentären Eisenfreisetzung und -ablagerung wird gezeigt, dass die Effektivität der Eisenmobilisierung und des Eisentransports ähnlich stark ausgeprägt ist wie im euxinischen Schwarzen Meer sowie in mutmaßlich eisenreichen Wassersäulen in früheren Ozeanen. Basierend auf den Erkenntnissen wird postuliert, dass viele sedimentäre Eisenanreicherungen in geologischen Archiven mit einem Ablagerungsmilieu ähnlich dem in heutigen Sauerstoffminimumzonen erklärt werden können. Dies gilt insbesondere wenn eine Intensivierung der Verwitterung an Land während Perioden globaler Erwärmung, mit der Folge eines verstärkten Eintrags von reaktiven Eisenmineralen in den Ozean, in

Betracht gezogen wird. Zukünftige Studien über anoxische Ereignisse in der Erdgeschichte, die sowohl den Eisen- und Schwefelkreislauf als auch den Stickstoffkreislauf berücksichtigen, werden möglicherweise beweisen, dass die für Sauerstoffminimumzonen typischen Redoxverhältnisse auch in früheren Ozeanen verbreitet waren.

Introduction and synthesis chapter

Identifying oxygen minimum zone-type biogeochemical cycling in Earth history using inorganic geochemical proxies

1. Introduction

The currently observed trend of ocean deoxygenation poses a severe threat to marine ecosystems (Diaz, 2001; Diaz and Rosenberg, 2008). Moreover, ocean anoxia is regarded as one the main causes for extinction events in Earth history (Meyer and Kump, 2008). As a consequence, there is a growing and converging interest in the biogeochemistry of oxygen-deficient ocean regions across different scientific communities.

A recent global compilation of dissolved oxygen data suggests that the ocean has lost 2 % of its oxygen content over the last few decades (Schmidtko et al., 2017). An important part of this trend is related to anthropogenic global warming which increases ocean stratification and reduces ventilation by impeding deep convection of oxygenated surface water. In addition, the solubility of oxygen in seawater decreases with increasing temperature (Benson and Krause, 1980; Mataer and Hirst, 2003; Keeling et al., 2011). Changes in land use have led to enhanced nutrient inputs to the coastal ocean, which has resulted in increased primary production, carbon export and respiratory oxygen consumption in subsurface waters (Rabalais et al., 2010; Howarth et al., 2011). Hotspots of ocean deoxygenation are the tropical oxygen minimum zones (OMZs) (Fig. 1) where upwelling of nutrient-rich water generates an environment with high primary production and naturally low to zero oxygen concentrations in the subsurface (~100 – 900 m water depth). Human-induced global environmental change causes an additional oxygen drawdown and spatial expansion of these tropical OMZs (Stramma et al., 2008). In addition to physical mechanisms and external nutrient inputs, the intensity and spatial extent of OMZs is regulated by internal

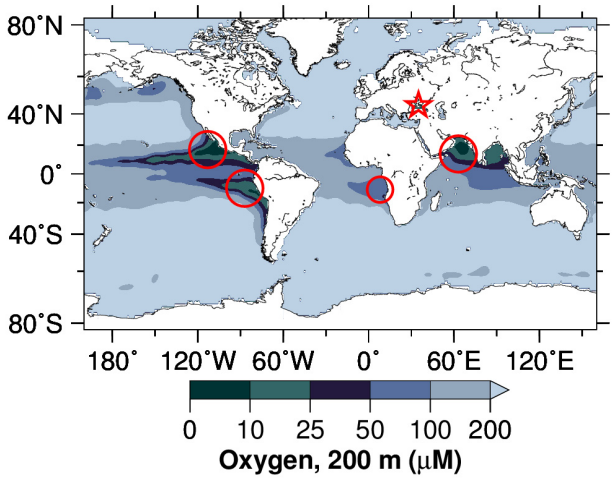

Fig. 1. *Global map showing the distribution of oxygen in the ocean at 200 m water depth (data from NOAA World Ocean Atlas). Major OMZs that are mentioned in this article are depicted by red circles. The red star indicates the location of the semi-restricted and euxinic Black Sea.*

biogeochemical feedback mechanisms. Upon oxygen depletion, fixed nitrogen loss through denitrification reduces the nitrate concentration in upwelling water masses thus imposing a negative feedback on primary production, carbon export and oxygen consumption (Canfield et al., 2006). In contrast, enhanced recycling of phosphorus and iron from anoxic sediments are a positive feedback for primary production (Ingall and Jahnke, 1994; Van Capellen and Ingall, 1994; Wallmann, 2003; Scholz et al., 2014a). Whether OMZ intensity will be amplified or mitigated by these feedback mechanisms in the future depends on complex interactions between the marine biogeochemical cycles of nitrogen, phosphorus, iron and sulfur and is a matter of ongoing debate (e.g., Canfield et al., 2006; Ulloa et al., 2012; Landolfi et al., 2013).

Since many biotic crises in Earth's history were associated with ocean anoxia (Meyer and Kump, 2008), paleoceanographers, geobiologists and other scientists working on paleo-environmental perturbations have a long-standing interest in ocean deoxygenation. Traditionally, semi-restricted basins with anoxic and sulfidic (commonly referred to as euxinic) conditions in the deep water such as the Black Sea were considered to be the best modern analogue environments for ocean anoxia in the geological past (e.g., Lyons et al., 2009). However, oxygen drawdown and euxinia in these silled basins is related to freshwater input and sluggish circulation, which results in an excessively long deep water residence time compared to open-marine environments. The comparability of anoxic continental margin settings in the geological past with modern euxinic basins is therefore limited, especially if causal connections between biogeochemical feedbacks and anoxia are to be established. As a consequence, there is a growing interest in OMZs as potential analogue environments for biogeochemical cycling within the context of open-marine anoxia in Earth history (e.g., Zhang et al., 2016; Hammarlund et al., 2017; Guilbaud et al., 2018). Recent studies hypothesized that OMZ-type redox structures have existed at least since the Mesoproterozoic (1400 Ma ago) (Zhang et al., 2016).

The goal of this review is to synthesize recent research findings on biogeochemical processes in the water column and sediments of OMZs, and how these become registered in sedimentary archives. Much of this synthesis will be based on understanding biogeochemical cycling and the development of paleo-redox proxy signatures in the Peruvian OMZ (Fig. 2) and the euxinic Black Sea (Fig. 3). These two anoxic marine environments are considered to be type localities for upwelling-related and silled basin-type anoxia. Moreover, they are comparably well-studied using state-of-the-art paleo-redox proxies that are commonly applied in studies on biogeochemical cycling in pre-Cenozoic Earth history (i.e., iron speciation, redox-sensitive trace metals). Other pronounced OMZs (northeast equatorial Pacific, Arabian Sea, Benguela upwelling) will also be considered provided that pertinent data are available. Euxinic

basins with less restricted deep water compared to the Black Sea (e.g., Baltic Sea Deeps, Cariaco Basin) are considered to be intermediate systems that share characteristics with both open-marine OMZs and the Black Sea (e.g., Algeo and Lyons, 2006; Scholz et al., 2013). For sake of clarity, I will not explicitly refer to these intermediate environments in this article.

Many biogeochemical processes that produce a specific sedimentary fingerprint are relevant for biogeochemical (de)oxygenation feedbacks (e.g., denitrification, sedimentary phosphorus and iron release). As a consequence, the sedimentary fingerprints presented in this review cannot only be used to identify OMZ-type biogeochemical cycling in the geological record but also to evaluate whether the intensity and expansion of paleo-OMZs was amplified or mitigated by biogeochemical feedback mechanisms. Finally, I will identify open questions and future challenges in reconciling observations in modern OMZ-type environments and the paleo-record.

2. Biogeochemical cycling in modern OMZs

2.1. The influence of ocean circulation on water mass age and oxygen consumption

Tropical OMZs are laterally fed with central and intermediate water masses that are subducted into the ocean interior at higher latitudes (Sloyan and Rintouil, 2001; Karstensen et al., 2008). Along the flow path of these water masses within the thermocline, degradation of downward sinking organic material drives oxygen consumption and release of remineralized nutrients. Wind-driven upwelling of the oxygen-depleted and nutrient-rich water at the eastern ocean boundaries results in high rates of primary and export production as well as further oxygen drawdown in the subsurface. The overall extent of oxygen depletion in eastern boundary OMZs is controlled by the rate of primary production and respiration, both locally and along the flow path, as well as the rate of central and intermediate water formation (Karstensen et al., 2008). The latter is a function of upwelling intensity and climatic conditions in the source regions (Talley, 1993; Karstensen et al., 2008). Water masses within the eastern equatorial Pacific OMZ off Peru have spent approximately 100 to 200 years within the ocean interior (Brandt et al., 2015). During this time, respiratory oxygen consumption has led to a very low or zero oxygen concentration. In comparison, deep water residence time in the Black Sea is considerably longer (literature data range from several hundred to several thousand years) (Murray et al., 1991; Özsoy and Ünlüata, 1997; Algeo and Lyons, 2006), which implies that deep water anoxia can be maintained despite a much lower primary productivity in surface waters (~130 g C m^{-2} yr^{-1}) (Grégoire and Beckers, 2004) compared to the Peruvian upwelling region (~1300 g C m^{-2} yr^{-1}) (Pennington et al., 2006). The Black Sea is characterized by density

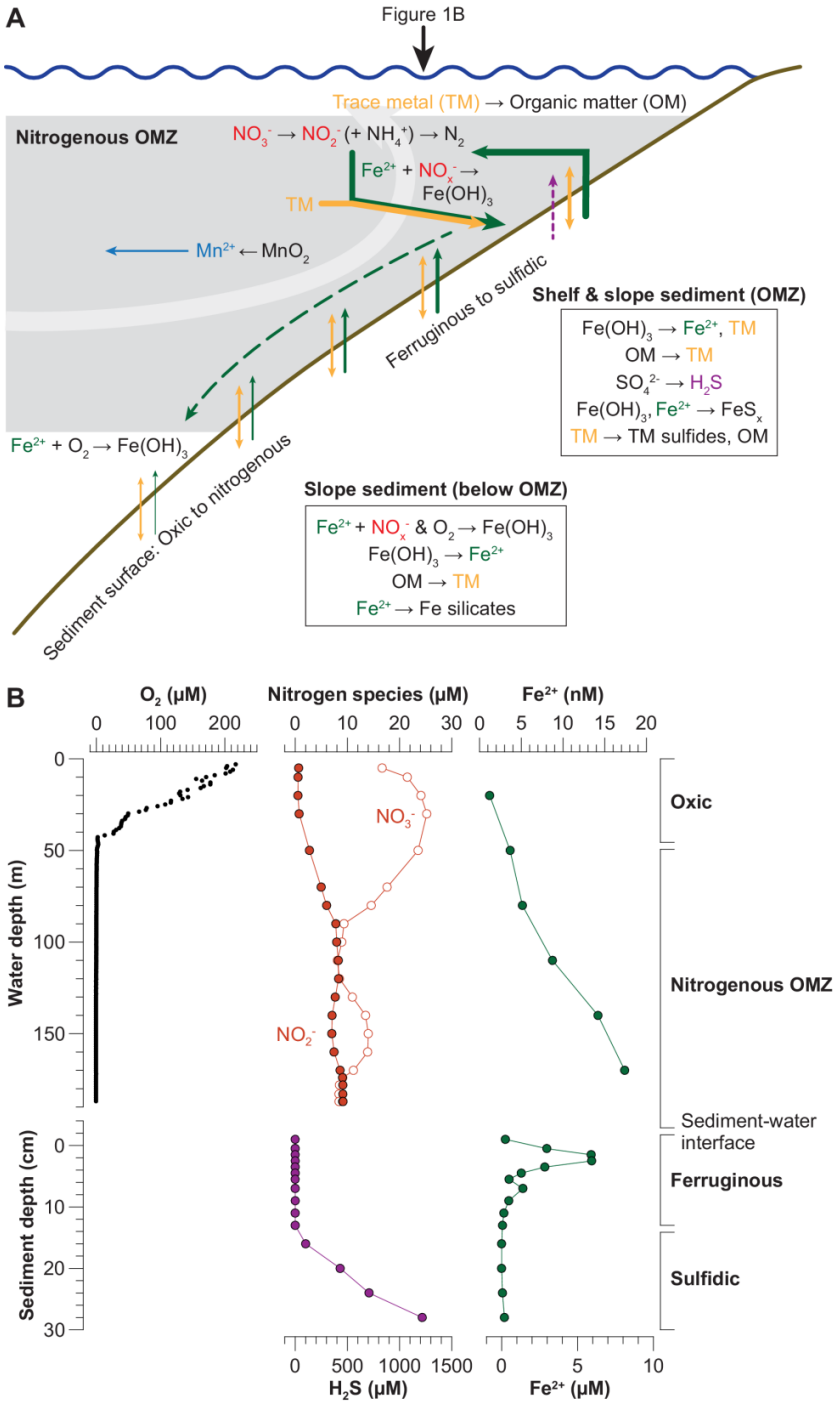

Fig. 2. *Biogeochemical cycling in the water column and sediments of oxygen minimum zones:* ***(A)*** *Schematic sketch illustrating element fluxes (arrows, colors are indicative for elements or species) and turnover. The size and direction of arrows is indicative of the flux magnitude and direction relative to the sediment-water interface or geometry of the continental margin. Note that only processes that are relevant for the discussion of proxy signatures are considered. Trace metal cycling is presented in a generalized fashion to provide an overview about relevant processes.* ***(B)*** *Examples for water column and pore water profiles of major redox species in the Peruvian OMZ (Scholz et al., 2011, 2016).*

stratification and an estuarine circulation pattern related to a positive freshwater balance where continental run-off and precipitation exceed evaporation. Since the basin's sill at the Bosporus straits is located above the layer with the highest density gradient (pycnocline), deep water exchange is highly restricted. Moreover, the stable density stratification limits upward mixing of nutrient-replete deep waters into the photic zone. Therefore, biogeochemical feedbacks, which may modulate the intensity and expansion of open-marine OMZs, are less likely to establish in the Black Sea or other semi-restricted euxinic basins.

2.2. Water column biogeochemistry and benthic-pelagic coupling

2.2.1. Nitrogen and manganese

The most pronounced OMZs of the modern ocean are located in the northeast and southeast equatorial Pacific, the Arabian Sea and the Benguela upwelling system off the coast of Namibia (Fig. 1) (Paulmier and Ruiz-Pino, 2009). In these ocean regions, oxygen has been drawn down to very low levels and organic carbon degradation in the OMZ is mediated by reduction of nitrate (NO_3^-) to nitrite (NO_2^-) and gaseous nitrogen compounds (N_2O, N_2) (Fig. 2A) (Gruber and Sarmiento, 1997; Lam and Kuypers, 2011). In addition to this heterotrophic pathway called denitrification, NO_2^- is also reduced to N_2 by the chemolithoautotrophic anammox process (anaerobe ammonia oxidation) (Daalsgaard et al., 2003; Kuypers et al., 2005; Hammersley et al., 2007). Oxygen measurement with highly sensitive electrochemical sensors in the core of the Peruvian and Chilean OMZs suggest that denitrification is only possible at oxygen concentration below ~50 nM (Thamdrup et al., 2012). Since N_2 is unavailable to non-nitrogen fixing primary producers, denitrification and anammox represent the ultimate sink for bioavailable (fixed) nitrogen in the ocean (Gruber, 2008). As a result of partial denitrification and as a biogeochemical signature of nitrate-reducing or 'nitrogenous' conditions, NO_2^- accumulates in the water column of (essentially) anoxic OMZs (Fig. 2B).

Bacterial reduction of manganese (Mn) oxide minerals, the pathway following denitrification in the natural succession of organic carbon degradation processes, also takes place in the water column of anoxic OMZs (Fig. 2). From a water column perspective, it is generally difficult to differentiate in situ Mn oxide reduction and dissolution in the lower water column from sedimentary sources (Hawco et al., 2016). However, surface sediments in anoxic OMZs are strongly depleted in Mn relative to the lithogenic background (Böning et al., 2004; Brumsack, 2006) suggesting that much of the Mn loss must take place prior to deposition. Consistent with this notion, pore water Mn concentrations and dissolved Mn fluxes across the sediment-water interface in OMZs are too low as to account for the extent of sedimentary Mn

depletion (Scholz et al., 2011) and water column observations (Johnson et al., 1992, 1996). Much of the Mn that is reductively dissolved in the water column is efficiently transported offshore within the OMZ (Klinkhammer and Bender, 1980; Lewis and Luther, 2000) and contributes to Mn accumulation in the deep-ocean (Koschinsky and Halbach, 1995; Klinkhammer et al., 2009).

2.2.2. Iron and sulfur

Surface sediments in OMZs are characterized by maxima in pore water Fe^{2+} at or very close to the sediment water interface (Fig. 2B) (Van der Weijden, 1999; Severmann et al., 2010; Noffke et all., 2012). The dissolved Fe^{2+} in the ferruginous pore water is derived from the reductive dissolution of Fe (oxyhydr)oxide minerals by dissimilatory Fe reduction and abiotic Fe reduction with hydrogen sulfide (H_2S) (Canfield, 1989). Due to the absence of oxygen in the bottom water and surface sediment, pore water Fe^{2+} can be transported across the sediment-water interface by molecular diffusion without being re-oxidized and -precipitated (Fig. 2). The benthic Fe efflux generally increases with decreasing bottom water oxygen concentration and increasing organic carbon rain rate (McManus et al., 1997; Elrod et al., 2004; Severmann et al., 2010; Noffke et al., 2012), because these parameters control the extent of Fe re-oxidation and the intensity of anaerobic microbial metabolism (actual release of Fe from organic material is negligible) (Dale et al., 2015). Due to this general relationship, benthic Fe fluxes tend to decrease from the productive shelf and upper slope in an offshore direction and towards greater water depth (Fig. 2A) (Noffke et al., 2012; Scholz et al., 2016). Due to sedimentary Fe release, OMZ waters are characterized by elevated concentrations of dissolved Fe^{2+} (tens of nM) compared to well-oxygenated coastal water (Fig. 2B) (e.g., Landing and Bruland, 1987; Bruland et al., 2005; Vedamati et al., 2014). In contrast to Mn, however, only a small portion of the reduced Fe is stabilized and transported offshore within the OMZ. This iron is presumably in colloidal form and bound to organic ligands, which allows it to be transported over longer distances (Lohan and Bruland, 2008; Kondo and Moffet, 2015). The remaining Fe is re-precipitated and -deposited close to the sedimentary source. Re-oxidation and scavenging of sediment-derived Fe^{2+} in the anoxic OMZ off Peru has been attributed to nitrate-dependent Fe oxidation (Scholz et al., 2016; Heller et al., 2017). In this process, dissolved Fe^{2+} is oxidized with NO_3^- as the terminal electron acceptor, either coupled to the microbial reduction of NO_3^- (Straub et al., 1996; Raiswell and Canfield, 2012) or to an abiotic reduction of NO_2^- catalyzed by the reactive surfaces of Fe (oxyhydr)oxide minerals (Picardal, 2012; Klüglein and Kappler, 2013). As evidenced by high sedimentary Fe fluxes and elevated Fe concentrations in the nitrogenous bottom water of OMZs, nitrate-dependent Fe oxidation (and any other Fe scavenging process in OMZs) is relatively inefficient in demobilizing sediment-derived Fe compared to re-oxidation with oxygen. Therefore, reducible Fe can be continuously cycled between the surface

sediment and overlying water through oxidation, deposition and dissolution until a fraction of it is retained in the sediment and buried (Fig. 2A) (Scholz et al., 2014b; Scholz et al., 2016). Sedimentary Fe enrichments in the oxic-anoxic transition area at the lower boundary of the Peruvian OMZ indicate that much of the Fe released from shelf and slope sediments eventually accumulates further downslope where oxygen and nitrate penetrate into the sediment thus preventing further Fe release (Fig. 2A) (Scholz et al., 2014b, c).

Iron (oxyhydr)oxides minerals scavenge phosphate (PO_4^{3-}) and other particle-reactive compounds (e.g., trace metals) in the water column. Therefore, reductive Fe dissolution and release from OMZ sediments is generally accompanied by PO_4^{3-} release (McManus et al., 1997; Noffke et al., 2012). Sedimentary Fe and PO_4^{3-} release (phosphorus is released from both Fe (oxyhydr)oxides and organic material) support primary productivity in upwelling regions (Johnson et al., 1999; Bruland et al., 2005) and are major sources of dissolved Fe and PO_4^{3-} to the global ocean (Wallmann et al., 2010; Dale et al., 2015).

Bacterial sulfate reduction is the dominant pathway of organic matter degradation in OMZ sediments (Thamdrup and Canfield, 1996; Bohlen et al., 2011). Since any H_2S produced immediately reacts with dissolved Fe and reactive Fe (oxyhydr)oxide minerals, H_2S does not accumulate in the pore water before these highly reactive Fe phases (i.e., highly reactive towards H_2S) have been completely converted to pyrite (FeS_2) or metastable sulfide minerals (Canfield, 1989; Canfield et al., 1992). In addition, H_2S concentrations in surface sediments of OMZs are kept at a low level by sulfide-oxidizing, nitrate-reducing bacteria such as *Thioploca* and *Thiomargarita* (Ferdelman et al., 1997; Schulz et al., 1999). Some of these microorganisms form filaments that are used to actively transport NO_3^- into the sediment for H_2S oxidation (Fossing et al., 1995).

A number of studies have reported plumes of H_2S (up to a few tens of µM) in the water column of the Peruvian and Namibian OMZs (Schunck et al., 2013; Brüchert et al., 2003). On the Peruvian continental margin, sulfidic events coincided with high productivity and water column stagnation following the main upwelling season. Under such conditions, NO_3^- and NO_2^- which normally oxidize H_2S in the surface sediment become depleted in the bottom water so that H_2S can escape into the water column (Fig. 2A, Fig. 4) (Sommer et al., 2016). Because of the high solubility of Fe^{2+} in weakly sulfidic water (Rickard, 2006), sulfidic events in the Peruvian OMZ are accompanied by exceptionally high dissolved Fe^{2+} concentrations in the water column (up to hundreds of nM) (Fig. 4) (Scholz et al., 2016). Chemolithoautotrophic sulfide oxidation with NO_3^- or other nitrogen compounds (Schunck et al., 2013) and nitrate-dependent Fe oxidation (Scholz et al., 2016) likely remove dissolved H_2S and Fe^{2+} at the boundaries of the plume.

2.2.3. Trace metals

The goal of this section is to provide a general overview about different modes of trace metal delivery and fixation in OMZ sediments. Therefore, I will focus on metals that are well-characterized using data for sediments, pore waters and particulate matter. For detailed reviews of trace metal cycling in the context of ocean anoxia the reader is referred to Brumsack (2006) and Tribovillard et al. (2006).

Arguably the best studied and most frequently used trace metals in the context of ocean anoxia and paleo-redox conditions are vanadium (V), molybdenum (Mo) and uranium (U). These metals have a long residence time (several tens to hundreds thousands of years) and largely uniform concentration in open-ocean seawater (V is somewhat depleted in the surface ocean) but are generally enriched in anoxic sediments (Tribovillard et al., 2006). Traditionally, it was argued that V, Mo and U accumulate in OMZ sediments by downward diffusion from the bottom water (Böning et al., 2004; Brumsack, 2006). Such a scenario of trace metal accumulation requires a downward directed concentration gradient from the bottom water to the sediment depth of metal removal. This type of pore water profile is common for U but rather atypical for V and Mo (Barnes and Cochran, 1990; Klinkhammer and Palmer, 1991; Zheng et al., 2000; McManus et al., 2005; Morford et al., 2005; Scholz et al., 2011). In agreement with this observation, solid phase mass accumulation rates of U are broadly consistent with benthic fluxes (Klinkhammer and Palmer, 1991; McManus et al., 2005). By contrast, sedimentary mass accumulation rates of V and Mo in anoxic OMZs (Böning et al., 2004; Scholz et al., 2011) are generally higher than expected based on estimates of downward diffusion from the bottom water (Scholz et al., 2017). This observation implies that sedimentary V and Mo enrichments require a solid carrier phase that delivers these elements to the seafloor. Consistent with this notion, many pore water profiles of V and Mo in OMZs are characterized by surficial maxima indicating that V and Mo are released from solid carriers during early diagenesis (Zheng et al., 2000; Scholz et al., 2011). Release of V and Mo into the pore water drives an upward directed diffusive flux across the sediment-water interface as well as a downward directed flux into the zone of metal removal (Scholz et al., 2017). Shallow V and Mo peaks in the pore water often coincide with the accumulation of dissolved Fe (and sometimes Mn) suggesting that Fe (oxyhydr)oxides adsorb particle-reactive metals in the water column and “shuttle” them to the sediment surface (Shaw et al., 1990; Zhang et al., 2000; Scholz et al., 2011). Such a scenario is supported by laboratory experiments (Chan and Riley, 1966a, b) and water column observations showing that V and Mo are associated with Fe-rich particles in the anoxic and nitrogenous water column of the Peruvian OMZ (Scholz et al., 2017; Ho et al. in press). Downward sinking organic material is likely to be another important carrier phase for V, Mo and U (Fig. 2A) (e.g., Nameroff et al., 2002; Zheng et al. 2002;

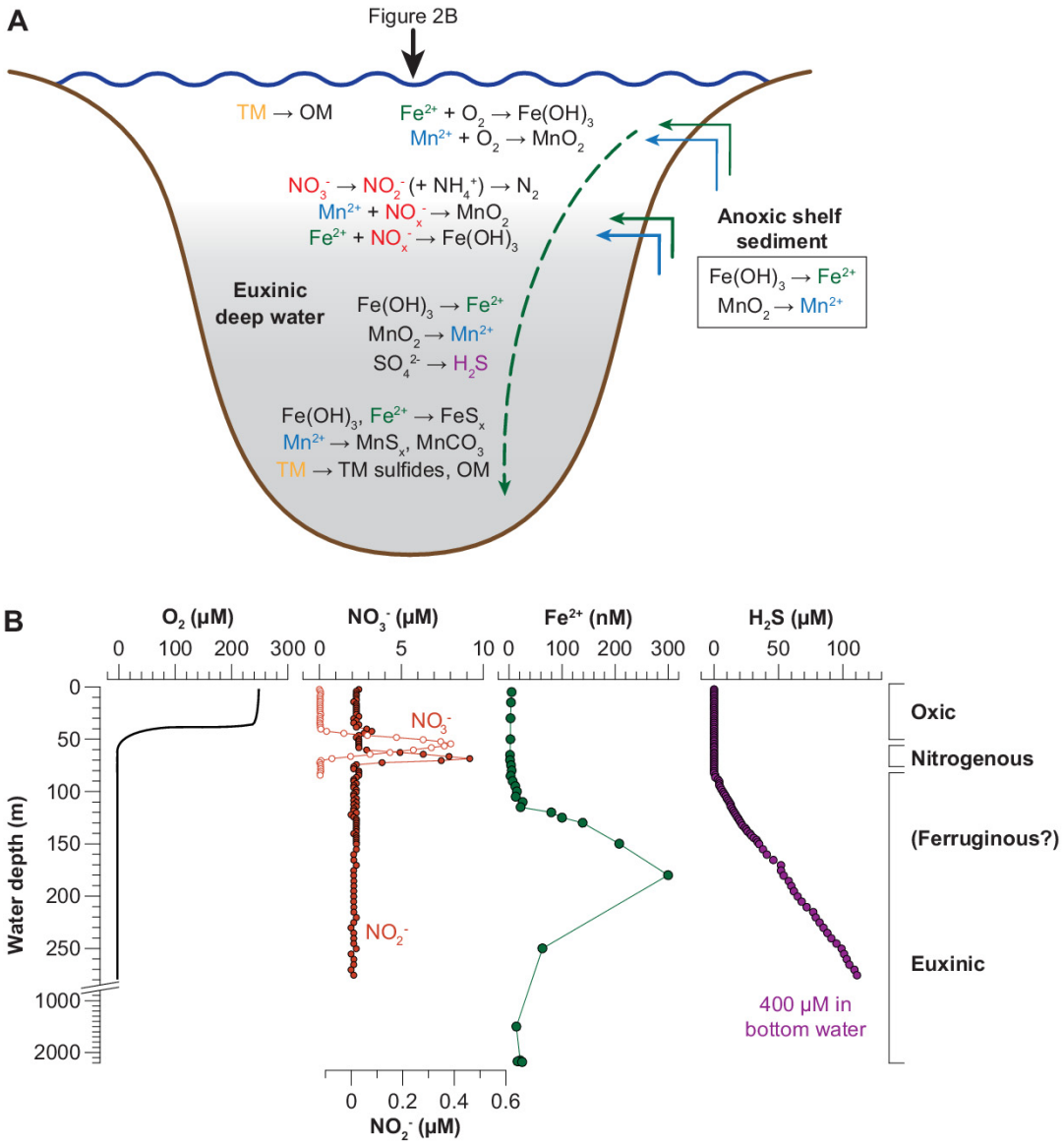

Fig. 3. *Biogeochemical cycling in the water column of the euxinic Black Sea:* ***(A)*** *Schematic sketch illustrating element fluxes and turnover. See Fig. 2A for details.* ***(B)*** *Examples for water column profiles of major redox species in the Black Sea (Friederich et al., 1990; Lewis and Landing., 1991).*

Ohnemus et al., 2017, Ho et al., 2018). However, it is not known how much of the metals bound to organic material is actively incorporated by organisms and how much is passively scavenged in the anoxic water column.

The efficiency of the removal mechanism from pore water determines the magnitude of diffusive delivery (U) and the extent to which metals delivered by solid carriers are retained and buried or lost to the water column by diffusion across the sediment-water interface (V and Mo). The removal of U from

pore water is mediated by reduction of U(VI) to U(IV) and precipitation of U(IV) oxides or adsorption to reactive surfaces (Tribovillard et al., 2006). Since U reduction can be mediated by Fe-reducing bacteria (Lovley et al., 1991), diffusive U accumulation in the sediment is favored in depositional settings where Fe reduction takes place close to the sediment surface (McManus et al., 2005). The mechanism(s) leading to V precipitation in anoxic sediments are not well characterized. It is generally believed that V reduction (V(V) to V(IV) to V(III)) and removal is induced under anoxic (i.e., ferruginous) but not necessarily sulfidic conditions in the pore water (Emerson and Huested, 1991; Wehrli and Stumm, 1989; Wanty and Goldhaber, 1992; Tribovillard et al., 2006). In contrast, Mo removal from pore water into sulfurized organic molecules and pyrite or other Fe sulfide compounds requires the presence of dissolved H_2S (Helz et al., 1996; Erickson and Helz, 2000; Tribovillard et al., 2004; Vorlicek et al., in press).

2.3. Comparison to biogeochemical cycling in the euxinic Black Sea

All of the biogeochemical processes taking place in the water column and sediments of OMZs (Fig. 2) are observed in the euxinic Black Sea as well (Fig. 3). However, the location (e.g., sediment and pore water versus water column) and water depth where they take place is different, which has important implications for the dynamics of nutrient turnover, primary production and respiratory oxygen consumption.

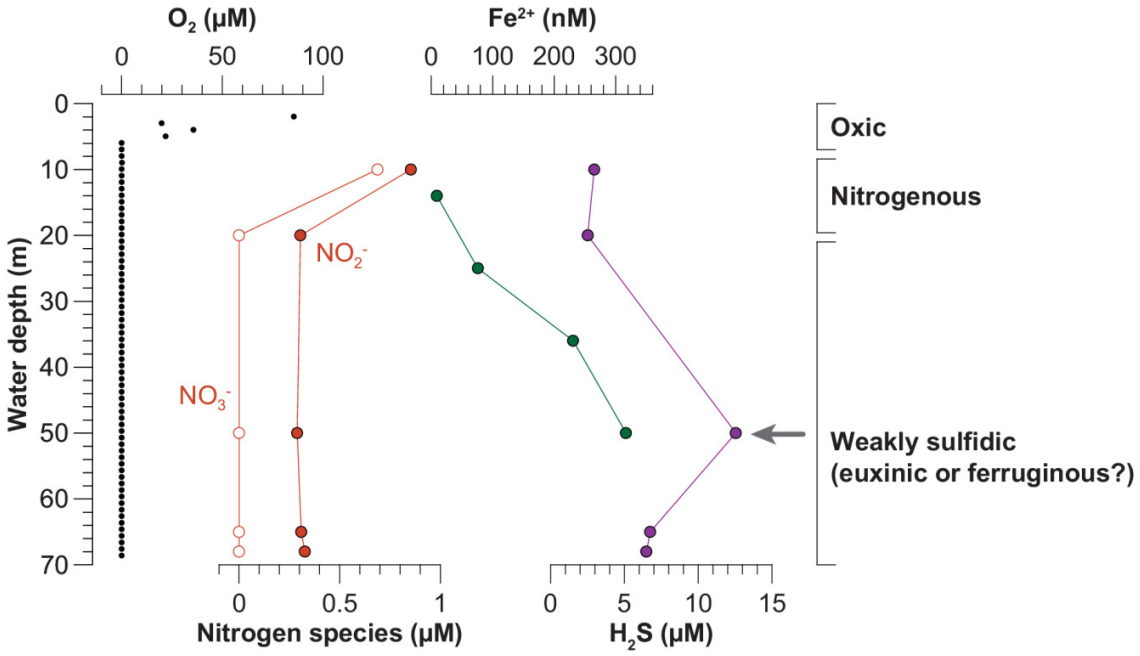

Fig. 4. *Examples for water column profiles of major redox species in the Peruvian OMZ during a sulfidic event in the water column (Scholz et al., 2016). The maxima in H_2S and Fe^{2+} (depth depicted by horizontal arrow) were formed by lateral transport of water masses from shallower areas.*

In the Black Sea, oxygen is depleted within the uppermost 70 m and the nitrogenous zone is located between ~70 and 100 m water depth (Fig. 3B) (Friederich et al., 1990; Kuypers et al., 2003). Below the depth of NO_3^- and NO_2^- depletion, organic carbon degradation is chiefly mediated by bacterial sulfate reduction and H_2S concentrations increase up to about 400 µM within the deep water. Elevated Fe^{2+} concentrations up to 300 nM (i.e., comparable to those in the sulfidic plumes in the Peruvian OMZ) (Fig. 2B) are observed within the weakly sulfidic layer between ~100 and 200 m water depth (Fig. 3B). Below this depth, dissolved Fe concentrations are capped by the solubility of Fe sulfide minerals such as mackinawite (FeS) and greigite (Fe_3S_4) (Lewis and Landing, 1991).

Similar to sediments in OMZs, anoxic shelf sediments in the Black Sea release Fe to the water column (Wijsman et al., 2001). Most of this sediment-derived Fe is re-precipitated in the oxic bottom water, but a small part is transported offshore, presumably in colloidal form or stabilized by organic ligands (Raiswell and Canfield, 2012). Once trapped within the anoxic deep water, shelf-derived Fe cannot escape to shallower areas anymore since the basin is capped by nitrogenous and oxic water masses which efficiently oxidize any Fe that is transported in a vertical direction by diffusion or advection (Fig. 3). In fact, water column profiles of Fe^{2+}, $NO_3^-$and NO_2^- suggest that much of the Fe trapping could be mediated by nitrate-dependent Fe oxidation (Scholz et al., 2016) rather than oxidation with oxygen (Fig. 3B). Due to the oxidative barrier overlying the Black Sea deep water, concentrations of Fe and Mn (and also PO_4^{3-}) (Dellwig et al., 2010) rise to appreciable levels until the solubility products of authigenic minerals are exceeded. An important implication of this trapping mechanism is that, in contrast to upwelling-related OMZs, nutrients are retained in the deep water and/or buried in the basin sediments rather than recycled and transported into the photic zone by coastal upwelling. Therefore, primary productivity in the pelagic Black Sea is controlled by external nutrient inputs from rivers and shelf sources (Grégoire and Beckers, 2004) whereas in OMZs upwelling of thermocline water (Pennington et al., 2006) and redox-dependent nutrient recycling from anoxic shelf sediments supply most of the nutrients to the productive surface ocean (Johnson et al., 1999; Bruland et al., 2005; Dale et al., 2017). Due to the proximity and mutual dependency of sedimentary nutrient sources and sinks, primary productivity and respiration, the intensity and expansion of OMZs can be amplified or mitigated by benthic-pelagic feedback mechanisms.

2.4. Amplification or mitigation of anoxia by benthic-pelagic feedbacks

According to conventional theory, the extent of reducing conditions in OMZs is bounded by a negative feedback within the nitrogen cycle (Canfield, 2006; Ulloa et al., 2012). Once oxygen is depleted, denitrification and anammox within the nitrogenous zone decrease the size of the bioavailable NO_3^- pool.

Importantly, however, most of the OMZs in the modern ocean are located in high-nutrient-low-chlorophyll (HNLC) regions (eastern equatorial Pacific, Benguela upwelling) which implies that primary productivity and, by inference, respiratory oxygen consumption is limited by Fe rather than NO_3^- (Hutchins and Bruland, 1998; Johnson et al., 1999). Given the well-established relationship between

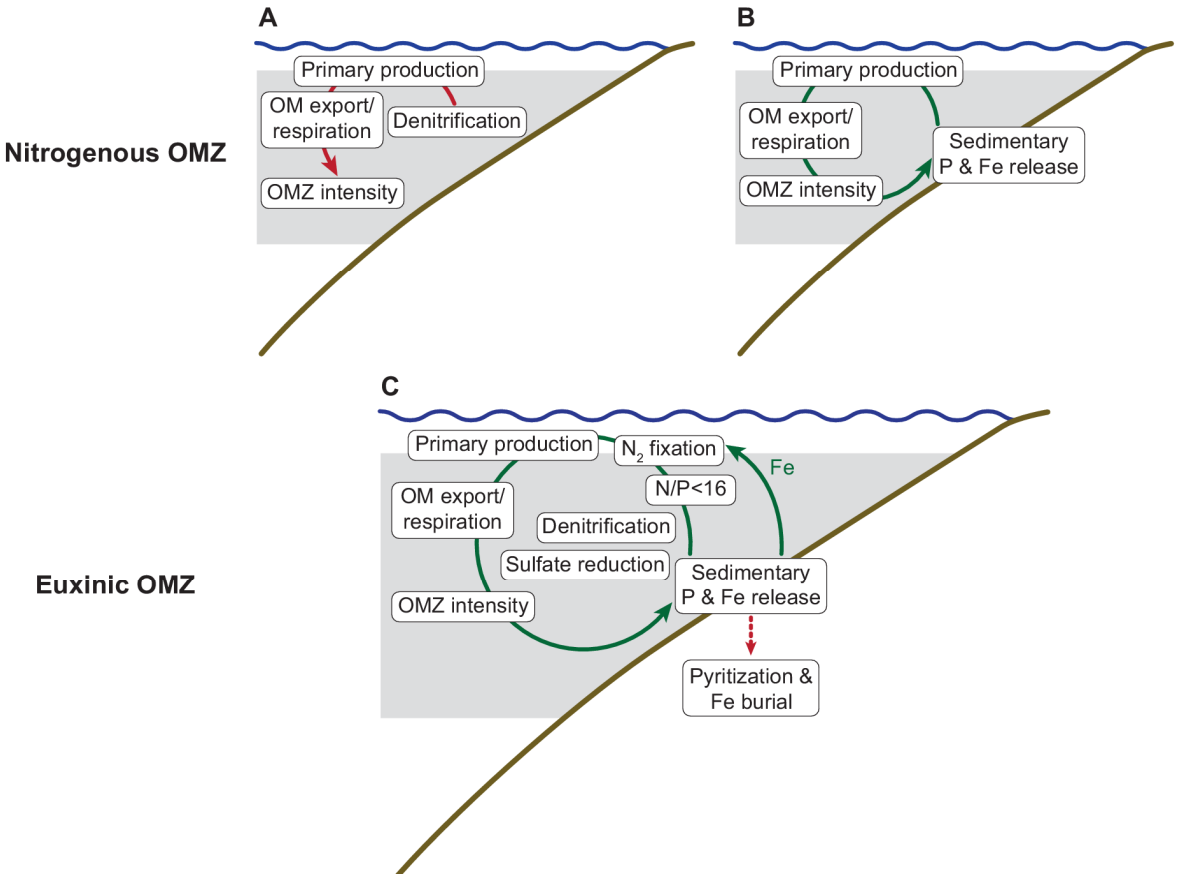

Fig. 5. *Biogeochemical feedbacks which can amplify (green arrows) or mitigate (red arrows) OMZ intensity.* ***(A)*** *Negative feedback for OMZ intensity through denitrification (Canfield, 2006).* ***(B)*** *Positive feedback for OMZ intensity through sedimentary Fe and PO_4^{3-} release (Ingall and Jahnke, 1994; Van Capellen and Ingall, 1994; Scholz et al., 2014a).* ***(C)*** *Cancelation of the negative feedback in (A) by nitrogen fixation (Canfield, 2006). Nitrogen-fixing organisms are favored by low nitrogen to phosphorus ratios and high Fe supply related to sedimentary PO_4^{3-} and Fe release. The feedback in (C) could transfer an OMZ from a nitrogenous to a euxinic mean redox state.*

bottom water oxygen concentration and sedimentary Fe release (Severmann et al., 2010; Dale et al., 2015), ocean deoxygenation could lead to an increase in Fe supply to the surface ocean in these regions. This would lead to an increase in primary and export production and could therefore cause OMZ intensification in a positive feedback loop (Fig. 5B) (Scholz et al., 2014a). In a related fashion, PO_4^{3-} release from anoxic sediments is thought to amplify marine productivity and ocean anoxia on geological timescales, e.g., during oceanic anoxic events (Ingall and Jahnke, 1994; Van Capellen and Ingall, 1994; Wallmann, 2003).

A dynamic interplay of the feedback connections described above could have a strong impact on nutrient and redox cycling in OMZs. Modelling studies suggest that any negative feedback between primary production and denitrification in OMZs (Figure 4A) can be overcome if the bioavailable NO_3^- pool in the photic zone is continuously replenished by nitrogen fixation (Canfield, 2006). Under such circumstances, sulfate reduction can become the dominant organic matter respiration pathway and H_2S can accumulate in the water column (Fig. 5C). Theoretically, nitrogen fixation in OMZs is favored by dissolved nitrogen to PO_4^{3-} ratios below that of non-nitrogen-fixing phytoplankton (N/P < 16) (Redfield, 1963; Tyrell, 1999; Gruber, 2008) related to denitrification and sedimentary phosphorus release. Moreover, sedimentary Fe release can satisfy the tremendous Fe demand of nitrogen-fixing organisms (Fig. 5C) (Falkowski, 1997; Moore and Doney, 2007). Such a scenario is in line with findings in the Peruvian OMZ where short-lived events of NO_3^- and NO_2^- depletion and weakly sulfidic conditions in the water column (Fig. 4) were shown to coincide with intense nitrogen fixation (Löscher et al., 2014) enabled by Fe and PO_4^{3-} release from the anoxic shelf sediments (Noffke et al., 2012). Whether such feedbacks between the nitrogen, phosphorus and Fe cycles could drive OMZs into permanently euxinic conditions has yet to be evaluated. It has been hypothesized that substantial accumulation of H_2S in the bottom water and surface sediment causes a shutdown of sedimentary Fe release at a certain point, because most of the Fe is converted to pyrite and buried in the sediment (Fig. 5C) (Scholz et al., 2014a). In other words, pyrite formation could turn the OMZ sediments from a net source to a net sink for Fe thus cancelling the feedback between sedimentary Fe release and biological productivity.

Given the strongly differing residence times of nitrogen, Fe and phosphorus in the ocean (fixed nitrogen: ~10^3 years; Fe: ~10^2 years; PO_4^{3-}: ~10^4 years) (Gruber, 2008; Wallmann, 2010; Boyd and Ellwood, 2010), feedback connections among their biogeochemical cycles are likely to unfold on longer timescales. Biogeochemical modeling in the context of past oceanic anoxic events can be a powerful tool to evaluate the role of benthic-pelagic feedbacks in modulating OMZ expansion and intensity. However, for ground truthing purposes any paleo-modeling needs to be informed by paleo-proxy records. The following

discussion of proxy signatures of OMZ-type biogeochemical cycling is meant to provide a framework for the reconstruction of biogeochemical feedbacks in OMZ-like paleo-settings.

3. Sedimentary fingerprint of OMZ-type biogeochemical cycling

3.1. Iron-based paleo-proxies

Enrichments of reactive Fe in marine sediment and sedimentary rocks are generally regarded as a paleo-indicator for anoxic conditions in the water column at the time of deposition. This rationale is related to observations in the modern Black Sea (Fig. 6B) where sediments are characterized by highly reactive Fe (Fe_{HR}) to total Fe ratios (Fe_{HR}/Fe_T) > 0.38, which is used as a threshold to indicate anoxia (Raiswell and Canfield, 1998; Poulton and Canfield, 2011). These enrichments, along with elevated Fe to aluminum (Al) ratios relative to the lithogenic background, are generated by Fe release from shelf sediments and Fe trapping in the euxinic basin, a mechanism referred to as "shelf-to-basin Fe shuttle" (Raiswell and Anderson, 2005; Lyons and Severmann, 2006). Due to sulfidic conditions within the water column and sediments, most of the reactive Fe supplied from the surrounding shelf areas is converted to pyrite. Therefore, a high proportion of pyrite Fe (Fe_{py}) within the Fe_{HR} pool is considered to be a paleo-indicator for euxinic conditions (Fe_{py}/Fe_{HR} > 0.8 is used as a threshold for euxinia) (Raiswell et al., 1997; Poulton and Canfield, 2011). Highly reactive Fe (sum of Fe (oxyhydr)oxide, Fe carbonate and pyrite) is recovered from bulk sediment by wet chemical extraction techniques (Canfield et al., 1986; Poulton and Canfield, 2005). These observations are the framework upon which a triad of Fe-based paleo proxies (Fe_{HR}/Fe_T, Fe_T/Al, Fe_{py}/Fe_{HR}) is widely used to track anoxia in the geological record, including in open-marine settings. However, I suggest here that the interpretation of these proxies in open-marine settings will differ because of differences in the geological and biogeochemical factors that underpin Fe mobilization and deposition.

3.1.1. Observations in modern OMZs

In the context of OMZs, associating anoxia with sedimentary Fe enrichments is problematic. Surface sediments in OMZs are ferruginous which implies that reactive Fe can be mobilized and transported across the sediment-water interface (see Section 2.2.2.). Provided that bottom currents transport the dissolved Fe away from the source area, one would expect the remaining sediment to be become depleted rather than enriched in highly reactive Fe. By contrast, re-deposition of the transported Fe at another location, e.g., due to re-oxidation with NO_3^-, NO_2^- or oxygen in the water column, and retention as pyrite in the sediment would generate an enrichment of highly reactive Fe in the sink area. Depending on the size and distance between source and sink areas and the transport capacity for Fe within the OMZ

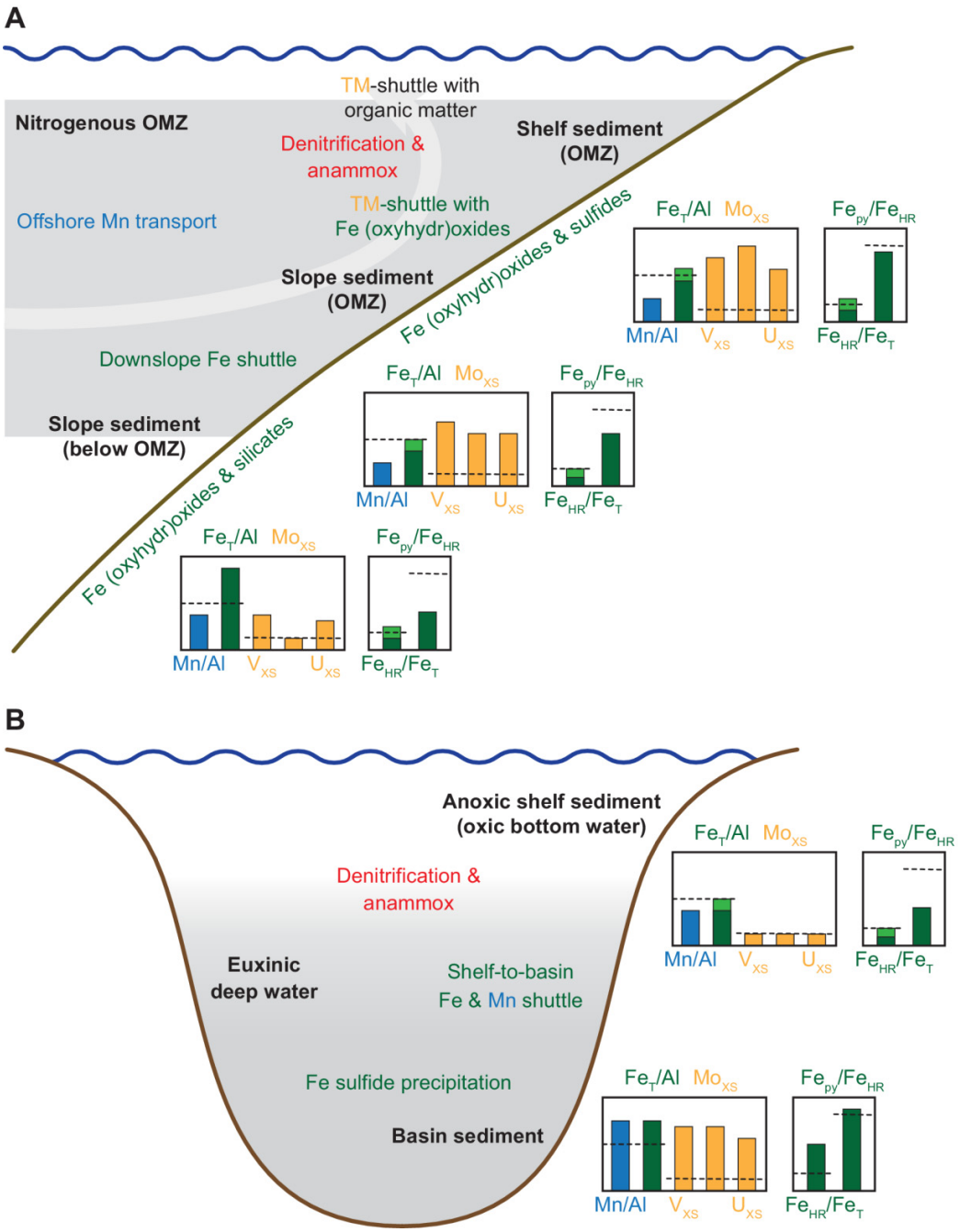

***Fig. 6**. Schematic comparison of trace metal- and iron-based paleo-redox proxy signatures in **(A)** the Peruvian OMZ and **(B)** the euxinic Black Sea (after Böning et al. (2004); Brumsack (2006); Lyons and Severmann (2006); Raiswell and Canfield (1998); Scholz et al. (2011, 2014a, b); Wijsman et al., (2001)). The principle processes leading to the formation of proxy signatures are indicated as well (see Fig. 2 and Fig. 3 for details). Horizontal dashed lines in the Mn/Al and Fe_T/Al diagrams depict the composition of lithogenic material. Horizontal dashed lines in the Fe_{HR}/Fe_T and Fe_{py}/Fe_{HR} diagrams depict threshold values for anoxic and euxinic conditions, respectively (Raiswell and Canfield et al., 1998; Poulton and Canfield, 2011).*

waters, Fe redistribution across the continental margin would yield a complex pattern of sedimentary Fe enrichments and depletions. Consistent with this scenario, shelf sediments within the Peruvian OMZ are slightly enriched in reactive Fe whereas slope sediment within the OMZ are depleted in highly reactive Fe compared to continental margin sediments with oxic bottom water (Fig. 6A) (Scholz et al., 2014b, c). Due to intense sulfate reduction within the sediment, pyrite is the principle burial phase for reactive Fe throughout the Peruvian OMZ (Suits and Arthur, 2000; Scholz et al., 2014a). Slope sediments underlying the lower boundary of the OMZ are characterized by elevated Fe_T/Al, which has been attributed to a net supply of highly reactive Fe from further upslope. Because slope sediments below the Peruvian OMZ are non-sulfidic (Scholz et al., 2011) much of the reactive Fe (oxyhydr)oxide delivered is converted to authigenic silicate minerals (e.g., glauconite), consisting of both ferrous and ferric Fe, during early diagenesis (Suits and Arthur, 2000; Böning et al., 2004; Scholz et al., 2014c). As silicate Fe is not dissolved by conventional chemical extraction techniques for the recovery of highly reactive Fe (e.g., Poulton and Canfield, 2005), sediments below the OMZ display highly elevated Fe_T/Al ratios but inconspicuous Fe_{HR}/Fe_T ratios (Scholz et al., 2014c). Authigenic glauconite has been observed at the boundaries of other OMZs (Mullins et al., 1985) and, interestingly, the conditions leading to the precipitation of this mineral are similar to those leading to the formation of greenalite (Harder, 1980; Tosca et al., 2016), the predominant Fe silicate mineral in Precambrian banded iron formations (Bekker et al, 2010).

3.1.2. Theoretical framework for the interpretation of iron-based paleo-proxies in the context of OMZs

The distributions of highly reactive Fe phases in modern OMZs are rather complex compared to euxinic basins where the source and sink areas are clearly separated from each other (Raiswell and Anderson, 2005; Scholz et al., 2014b). To interpret long-term proxy records of Fe_{HR}/Fe_T or Fe_T/Al at a single location within or adjacent to an OMZ, a systematic framework of how geological factors (sedimentation rate, continental margin geometry relative to the water column redox structure) control the extent of sedimentary Fe enrichment or depletion is required.

In Fig. 7A and Fig. 7B, indices for sedimentary Fe enrichment and anoxia (Fe_T/Al, Fe_{HR}/Fe_T) are plotted against benthic Fe effluxes and authigenic (i.e., non-lithogenic) Fe rain rates. At higher background sedimentation of terrigenous Fe and Al, Fe release or trapping has a smaller impact on Fe_T/Al or Fe_{HR}/Fe_T than in a scenario where little terrigenous material is delivered (Raiswell and Anderson, 2005). To account for this effect, I computed scenarios of reactive Fe release or trapping with different sediment mass accumulation rates (MARs) (Fig. 7). The benthic Fe effluxes and MARs applied in these calculationsver the typical range of values observed in the modern ocean (Burdige, 2007; Dale et al., 2015). As no literature data for authigenic Fe rain rates are available, the range of published benthic Fe

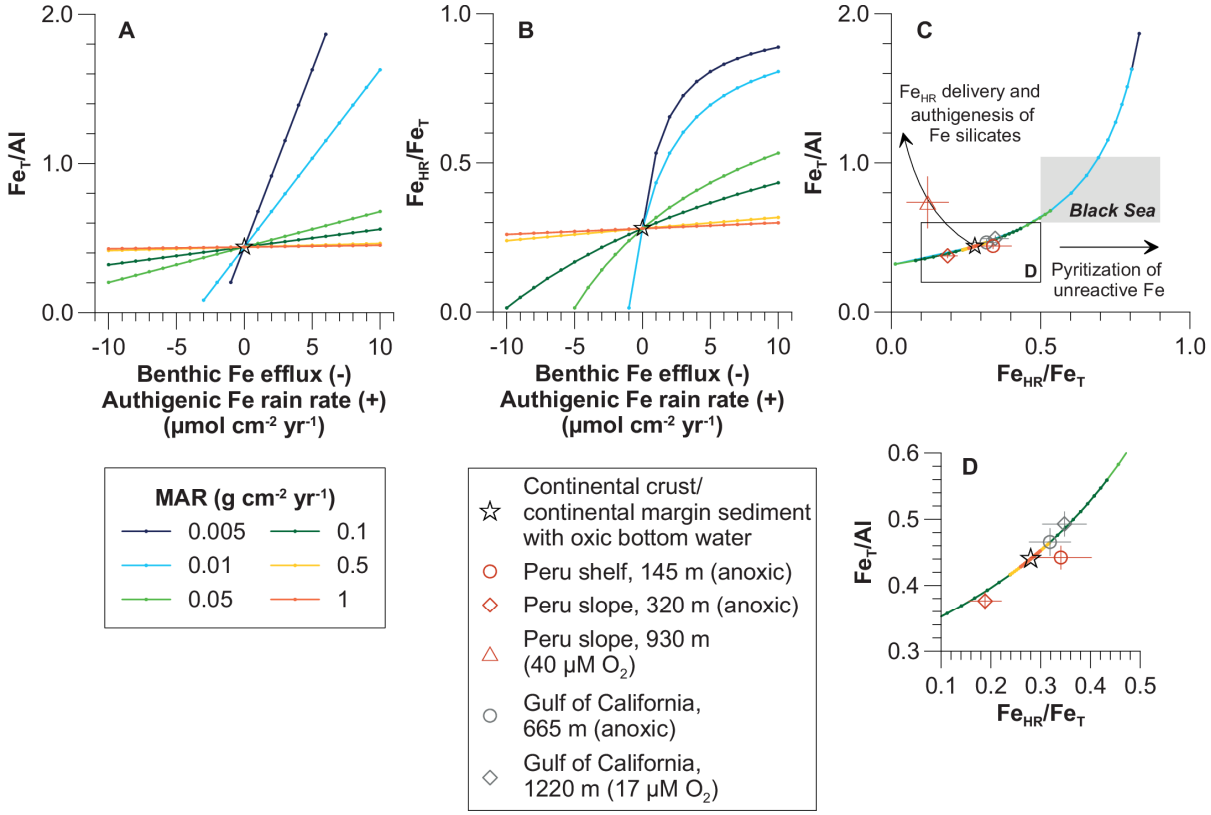

Fig 7. *Theoretical framework for the interpretation of sedimentary Fe enrichment and depletion:* ***(A)*** *Fe_T/Al as a function of benthic Fe efflux (negative sign on x-axis), authigenic Fe rain rate (positive sign on x-axis) and sediment mass accumulation rate (MAR) (colored lines); the black star depicts the Fe_T/Al of the average upper continental crust (McLennan, 2001).* ***(B)*** *Fe_{HR}/Fe_T as a function of benthic Fe efflux, authigenic Fe rain rate and MAR; the black star depicts the average Fe_{HR}/Fe_T of continental margin sediments with oxic bottom water (Poulton and Raiswell, 2002).* ***(C)*** *Relationships shown in (A) and (B) in a cross plot of Fe_T/Al versus Fe_{HR}/Fe_T; symbols depict the average Fe_T/Al ± SD and Fe_{HR}/Fe_T ± SD of sediment cores from the OMZs off the coast of Peru (Scholz et al., 2014b, c) and in the Gulf of California (F. Scholz, unpublished data). The range of Fe_T/Al and Fe_{HR}/Fe_T observed in pelagic Black Sea sediments is shown for comparison (Raiswell and Canfield, 1998; Lyons and Severmann, 2006). The trend depicting delivery of Fe_{HR} and authigenesis of Fe silicate minerals was calculated by using a 1:9 ratio between newly delivered and pre-existing Fe_{HR} that is incorporated into silicate minerals.* ***(D)*** *Close-up of (C) showing OMZ sediments in greater detail. See Supplementary Information for further details about the underlying calculations.*

effluxes was adopted for this parameter as well (with reverse sign). The validity of this approach is demonstrated by the values of Fe_T/Al and Fe_{HR}/Fe_T obtained in the different scenarios of reactive Fe trapping, which are consistent with published data for modern euxinic basins and paleo-records (e.g., Raiswell and Canfield, 1998; Lyons and Severmann, 2006; Poulton et al., 2010). The starting value for each scenario of reactive Fe release or trapping is the Fe_T/Al of the average upper continental crust (McLennan, 2001) and the Fe_{HR}/Fe_T of continental margin sediments with oxic bottom water (Poulton

and Raiswell, 2002). All scenarios as well as Fe_T/Al and Fe_{HR}/Fe_T data for sediments from the Peruvian continental margin, the Gulf of California and the Black Sea are plotted in a diagram of Fe_T/Al versus Fe_{HR}/Fe_T in Fig. 7C (a close-up highlighting OMZ data is shown in Fig. 7D).

The generalized modeling scenarios reveal that reactive Fe release and trapping theoretically results in Fe_T/Al and Fe_{HR}/Fe_T values that lie on one single trend line (Fig. 7C). The mass accumulation of terrigenous sediment determines the extent of deviation from the starting value at a given authigenic Fe rain rate or benthic Fe efflux. Most of the data plotted in Fig. 7C and Fig. 7D plot along this trend line, which corroborates that redistribution of reactive Fe is responsible for the observed variability. Slope sediments in the Peruvian OMZ are characterized by lower Fe_T/Al and Fe_{HR}/Fe_T compared to the starting value (Fig. 7C and D). Typical MARs on the Peruvian slope are of the order of 0.01 - 0.05 g cm^{-2} yr^{-1} (Scholz et al., 2011). To generate the observed deviation in Fe_T/Al and Fe_{HR}/Fe_T from the starting value at this MAR, a benthic efflux of ~1 µmol cm^{-2} yr^{-1} is required. This estimate is in good agreement with the range of benthic Fe fluxes observed in the same area (0.3 - 3.2 µmol cm^{-2} yr^{-1}) (Noffke et al., 2012) suggesting that, indeed, sedimentary Fe release has caused the observed depletion in reactive Fe (Scholz et al., 2014b). Deviations from the trend line in Fig. 7C towards higher Fe_{HR}/Fe_T can be generated by pyritization of unreactive Fe, e.g., due to a long-term exposure of clay minerals to H_2S (Raiswell and Canfield, 1996). Conversely, delivery of reactive Fe and precipitation of authigenic Fe silicate minerals would generate a shift towards lower Fe_{HR}/Fe_T and higher Fe_T/Al. Consistent with this scenario, sediments below the Peruvian OMZ, which have been shown to be enriched in Fe silicate minerals, plot on the corresponding trend line (Fig. 7C) (Scholz et al, 2014c).

In general, elevated Fe_T/Al and $Fe_{HR}/Fe_T > 0.38$ require either a high authigenic Fe rain rate or a low rate of terrigenous background sedimentation (Fig. 7). Taking the threshold for anoxia as a reference value, the modest deviations in Fe_{HR}/Fe_T observed in the OMZs off Peru and in the Gulf of California (Fig. 7C) would not be indicative of anoxic conditions in the bottom water. Importantly, however, these continental margin environments are characterized by a one to two order of magnitude higher MAR (Calvert et al., 1966; Scholz et al., 2011) compared to the pelagic Black Sea (MAR: <0.005 g cm^{-2} yr^{-1}) (Brumsack, 1989; Calvert et al., 1991). Taking this difference in MAR into account reveals that sediments in these systems receive a similar supply of authigenic Fe as pelagic Black Sea sediments (compare dark blue and greenish lines in Fig. 7A and Fig. 7B). Applying one single threshold of Fe_{HR}/Fe_T for anoxia in a broad range of depositional environments seems questionable in this context.

On open-marine continental margins, the balance between reactive Fe source and sink areas likely depends on a combination of biogeochemical and sedimentological factors. The OMZ in the Gulf of

California is located between 400 and 800 m water depth (Campbell and Gieskes, 1984). Due to the sheltered character and semi-restricted bathymetry of the Gulf of California, Fe released from shelf and upper slope sediments can be transported downslope and accumulate within and below the OMZ. By contrast, the Peru OMZ is located at shallower depth (below 50-100 m water depth) and sedimentary Fe release takes place in a dynamic shelf environment where strong bottom currents can transport sediment-derived solutes in an alongshore direction (Suess et al., 1987). Local enrichments in reactive Fe are likely to form in organic carbon depocenters (Reimers and Suess, 1983) where shallow pyrite formation (Scholz et al, 2014a) is supported by intense bacterial sulfate reduction in the surface sediment (Bohlen et al., 2011). Sediments on the upper slope within the Peruvian OMZ are frequently re-suspended by internal waves (Mosch et al., 2012), which causes comparably low net sedimentation rates (Scholz et al, 2011) and creates a favorable environment for sedimentary Fe depletion. Downward focusing of sediment-derived Fe from the upper slope into the oxic sink area with less dynamic sediment transport regime causes Fe accumulation in a relatively confined area close to the lower boundary of the OMZ (Scholz et al., 2014b).

Considering the small scale variability in sedimentological factors on the Peruvian continental margin, a laterally consistent enrichment in reactive Fe like in the Black Sea is unlikely to evolve. By contrast, in a less dynamic environment such as the Gulf of California continental slope, widespread Fe enrichments may develop, provided that background sedimentation does not overwhelm the authigenic Fe rain rate. In both OMZs, spatial (modern surface sediments) or temporal (in a paleo-record) variability in Fe_T/Al and Fe_{HR}/Fe_T along the trend lines in Fig. 7C (toward both higher and lower values) is indicative of enhanced Fe mobility in the surface sediment and bottom water. Provided that Fe transport in the water column takes place within reach of the photic zone (e.g., through upwelling like in the Peruvian OMZ), the mobilized Fe can support biological productivity in the surface ocean.

3.2. Trace metal-based paleo-proxies

Metals respond in a systematic fashion to the redox gradients observed in the water column and surface sediments of OMZs (Fig. 6A) (Nameroff et al., 2002; Böning et al., 2004, 2005; Scholz et al., 2011). Because of reductive Mn dissolution and offshore transport in the water column, OMZ sediments are commonly depleted in Mn relative to lithogenic material (Böning et al., 2004, 2005; Borchers et al., 2005). By contrast, in euxinic basins Mn supplied from the surrounding shelf areas is trapped within the basin (Fig. 6B) (Brumsack, 2006; Lyons and Severmann, 2006; Scholz et al., 2013). Sedimentary Mn depletion is not limited to the area where the OMZ impinges the seafloor but extents further downslope into areas with well-oxygenated bottom water (Böning et al., 2004, 2005; Scholz et al., 2011). Therefore,

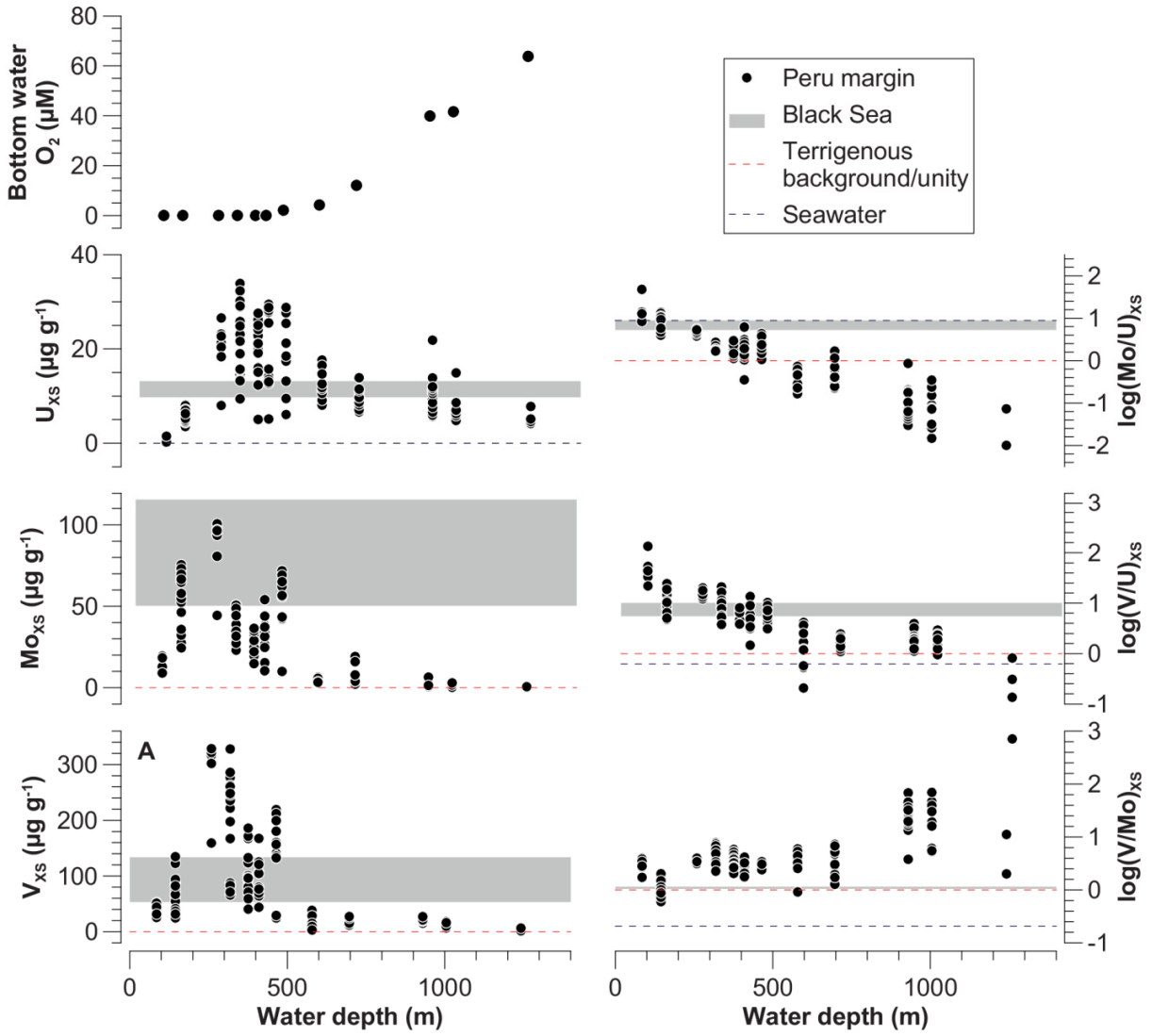

Fig. 8. *Lateral distribution of bottom water oxygen concentrations, sedimentary trace metal enrichments (expresses as excess metal (Me) concentrations relative to the metal to Al ratio of the upper continental crust (McLennan, 2001): $Me_{XS} = (Me)_{sample} - (Me/Al)_{crust} \cdot (Al)_{sample}$) and logarithmic trace metal ratios ($log(Me/Me)_{XS}$) across the Peruvian continental margin at 11 °S (data from Scholz et al. (2011)). Element concentration ratios are presented as logarithmic ratios to avoid asymmetry effects. The logarithmic trace metal ratio in seawater and composition of Holocene Black Sea sediments (range between the average of Unit 1 and Unit 2 sediments) (Brumsack, 2006) are shown for comparison.*

Mn depletion relative to crustal material is generally indicative of the presence of an open-marine OMZ in the overlying water column (Table 1).

The behavior of many other metals that have been used as a paleo-redox proxy is tied to the redox state of the bottom water and surface sediment (Fig. 6A, Fig. 8). On the Peruvian continental margin, U is the first element to become enriched in the sediment as the oxygen concentrations in the bottom water

Table 1. *Biogeochemical conditions and processes in OMZs and associated paleo-redox proxies.*

Biogeochemical conditions and processes	Paleo-redox proxy
Redox conditions (see Fig. 8 for details)	
Anoxic water column (open-marine)	Mn/Al < UCC[1]
Oxic surface sediment	$(Mo/U)_{XS}$ < UCC
Ferruginous surface sediment	UCC ≤ $(Mo/U)_{XS}$ < seawater
Sulfidic surface sediment	$(Mo/U)_{XS}$ ≥ seawater
Iron cycle	
Reactive Fe release or trapping , Fe mobility in surface sediment and bottom water (see trend lines in Fig. 6)	$Fe_{HR}/Fe_{T,}$ Fe_T/Al
Pyritization, Fe trapping, retention and burial	Fe_{py}/Fe_{HR}
Phosphorous cycle	
P release	C/P (relative to phytoplankton)
P burial	P/Al, phosphorous speciation
Nitrogen cycle (water column)	
Denitrification, anammox, nitrogen fixation	$\delta^{15}N$, biomarker

[1]UCC: Upper continental crust (McLennan, 2001).

decrease (Fig. 8). This trend can be explained by U reduction and fixation under ferruginous conditions in the surface sediment. As the bottom water and surface sediments become more reducing, V and Mo accumulation outpace U accumulation. Sedimentary Mo enrichments reach comparable values to Black Sea sediments (Fig. 8) on the shallow shelf where H_2S is detectable shortly below the sediment-water interface (Böning et al., 2004; Scholz et al., 2011). Based on this pattern, Scholz et al. (2004a) suggested that ratios of excess Mo to U (see caption of Fig. 8 for a definition of excess metal concentrations) can be used in conjunction with Fe speciation data to reconstruct whether surface sediments were oxic, ferruginous or sulfidic at the time of deposition (Table 1, Fig. 8). Differentiating between ferruginous and sulfidic conditions in surface sediment is important for assessing whether conditions were conducive to sedimentary Fe release or Fe trapping, retention and burial as pyrite (Scholz et al., 2014a).

Sedimentary Molybdenum concentrations above 25 µg g^{-1} have been suggested to be generally indicative for euxinic conditions (Scott and Lyons, 2012; Dahl et al, 2013). Sediments in the OMZs off Peru and Namibia clearly exceed this threshold (Fig. 7) (Böning et al., 2004; Borchers et al., 2005; Scholz et al., 2011) which has tentatively been attributed to the occurrence of sulfidic events and Mo scavenging from the sulfidic water column (Dahl et al., 2013). However, on the Peruvian continental margin, particulate Mo concentrations within sulfidic water masses are low compared to those in nitrogenous and oxic water massed (Scholz et al., 2017). Based on this observation, Scholz et al. (2017) hypothesized that Mo accumulation in shelf sediments is accelerated by Mo delivery with Fe

(oxhydr)oxides that precipitate in the water column through nitrate-dependent Fe oxidation. Further research on the distribution, isotope composition and speciation of particulate metals in OMZs will help to better characterize the mode of trace metal scavenging under anoxic conditions.

Recently, Zhang et al. (2016) introduced V depletion relative to terrigenous material as an indicator for weakly oxic conditions in the bottom water at the boundaries of OMZs. This notion was based on observations in the northeast equatorial Pacific off Mexico where sediments below the OMZ seem to be slightly depleted in V but enriched in Mo relative to lithogenic material (Nameroff et al., 2002). Zhang et al. (2016) attributed this observation to V release from Mn oxide minerals under anoxic but non-sulfidic conditions in the surface sediment underlying weakly oxic bottom water. The mechanism of Mo fixation under Mn-reducing and non-sulfidic conditions was not specified by Zhang et al. (2016). In general, the deviations in V concentration from lithogenic material reported by Nameroff et al. (2002) are small. Moreover, V concentrations in lithogenic material are generally high (almost two orders of magnitude higher than Mo) but can vary considerably as a function of provenance and lithology (McLennan, 2001). As a consequence, small depletions of V relative to a high lithogenic background are associated with a large uncertainty.

Within the oxygen gradient at the lower boundary of the Peruvian OMZ, ratios of excess V to Mo clearly exceed the V/Mo of the upper continental crust, which implies that under weakly oxic conditions V is more efficiently delivered and/or retained than Mo. This observation is in conflict with the proxy rationale outlined by Zhang et al. (2016) but consistent with the general notion that V can accumulate under anoxic and non-sulfidic conditions whereas Mo accumulation requires the availability of free H_2S (Tribovillard et al., 2006). On the Peruvian continental margin excess V/Mo ratios decrease throughout the redox-gradient in the bottom water and approach the V/Mo of the upper continental crust in sulfidic shelf sediments (Fig. 8). According to this pattern, V/Mo could be applied along with Mo/U to trace the transition from ferruginous to sulfidic conditions in the surface sediment (Table 1).

Excess V concentrations in the Peruvian OMZ are generally high compared to Black Sea sediments (Fig. 8). This trend could be related to V delivery by Fe (oxyhydr)oxides (Scholz et al. (2017) and/or organic particles originating from the photic zone or the OMZ itself (Ho et al., 2018, in press). Ohnemus et al. (2017) demonstrated that heterotrophic (presumably denitrifying) microbial communities in the Peruvian OMZ are particularly enriched in V and other transition metals compared to phototrophic organism at the sea surface. Other nutrient-type trace metals that are poorly soluble under sulfidic conditions (e.g., cadmium (Cd)) are generally enriched in the sediments of productive upwelling areas compared to sediments in euxinic basins (Brumsack, 2006). This trend is even more pronounced when

nutrient-type trace metals are normalized to Mo. Sweere et al. (2016) demonstrated that ratios of Cd to Mo increase from values close to seawater (Cd/Mo = 0.007) in restricted basins to values similar to phytoplankton (Cd/Mo = 2) (Brumsack, 1986) in open-marine upwelling regions. Future work comparing the speciation and isotope composition of metals in particulate matter and sediments of OMZs may help to identify the specific sedimentary fingerprint of different biological communities (with different enzymes and thus metal quota) and metabolisms in the overlying water column.

3.3. Tool box for the identification of benthic-pelagic feedbacks in the geological record

Proxy signatures for redox conditions and sedimentary Fe release and trapping (Fe_T/Al, Fe_{HR}/Fe_T, $(Mo/U)_{XS}$) (Table 1) can be combined with paleo-indicators for sedimentary phosphorus and water column nitrogen cycling to identify OMZ-type biogeochemical cycling and the associated interplay of benthic-pelagic feedbacks (Fig. 5) in the geological record.

Phosphorus is preferentially remineralized from organic material relative to carbon under anoxic conditions in the bottom water (Ingall and Jahnke, 1994, 1997; Wallmann et al., 2010). Therefore, sedimentary PO_4^{3-} release in anoxic ocean regions generates elevated sedimentary carbon to phosphorus ratios (Ingall and Van Cappellen, 1990; Algeo and Ingall, 2007) compared to the average composition of phytoplankton (C/P > 106) (Redfield, 1963). This signature can be used to identify sedimentary phosphorus release in the geological record (Table 1) (März et al., 2008; Mort et al., 2008; Poulton et al., 2015). Conversely, the extent of phosphorus burial with organic material, Fe (oxyhydr)oxides or biogenic and authigenic phosphorus minerals (carbonate fluorapatite, CFA) can be evaluated by a combination of elevated phosphorus to Al ratios (P/Al) and sedimentary phosphorus speciation (e.g., Schenau and De Lange, 2001; Mort et al., 2008; März et al., 2008; Poulton et al., 2015) (Table 1). In modern OMZs enhanced sedimentary P/Al ratios are often observed in slope sediments where low to zero net sedimentation rates and strong bottom currents favor the accumulation of CFA nodules and crusts (Glenn and Arthur, 1988). In this case, elevated P/Al and CFA concentrations are not indicative of enhanced phosphorus burial on a continental margin scale but rather for sediment reorganization and CFA built-up in a confined area.

Nitrogen cycling in the water column (i.e., nitrogen loss under nitrogenous versus nitrogen fixation under euxinic conditions) can be reconstructed by the aid of nitrogen isotopes (Table 1). Denitrification and anammox in the nitrogenous water column leaves the remaining NO_3^- enriched in the heavy nitrogen isotope (^{15}N). If the remaining NO_3^- is incorporated into phytoplankton biomass and subsequently preserved in the sediments, water column nitrogen loss can be identified in the

sedimentary record by elevated $\delta^{15}N$ values relative to atmospheric nitrogen ($\delta^{15}N_{sediment} > 0$ ‰) (Altabet et al., 1995; Ganeshram et al., 2000; Galbraith et al., 2004). Quantitative denitrification, which is a prerequisite for the onset of bacterial sulfate reduction and euxinic conditions in an OMZ, would cancel out any isotope fractionation associated with partial nitrogen loss (Boyle et al., 2013). Under such circumstances, the sedimentary $\delta^{15}N$ approaches the nitrogen isotope composition of nitrogen-fixing microorganisms ($\delta^{15}N_{sediment} \leq 0$ ‰) (see, e.g., Higgins et al. (2012) and Ader et al., (2016) for further details, including the role of ammonia). Importantly, nitrogen isotope ratios have to be interpreted on a relative scale as the regional $\delta^{15}N$ is superimposed by the global secular $\delta^{15}N$ trend (Algeo et al, 2014). For instance, during Cretaceous oceanic anoxic events, partial water column denitrification likely generated a lower $\delta^{15}N_{sediment}$ compared to the present-day, since the $\delta^{15}N$ of the global NO_3^- pool was shifted to a lower value. Additional information on nitrogen cycle processes can be derived from diagnostic biomarkers (Kuypers et al., 2002; Bauersachs et al., 2010).

4. Nitrogenous, ferruginous or euxinic conditions in Phanerozoic OMZs?

In studies on biogeochemical cycling in pre-Cenozoic Earth history, ocean anoxia is typically associated with euxinia or ferruginous conditions whereas nitrogenous conditions, the predominant expression of anoxia in the modern ocean, are neglected. The definition of euxinic conditions is based on the presence of dissolved H_2S in the water column (Meyer and Kump, 2008; Lyons et al., 2009). In contrast, ferruginous conditions are solely defined based on a proxy signature that is thought to indicate anoxia ($Fe_{HR}/Fe_T > 0.38$) but non-sulfidic conditions ($Fe_{py}/Fe_{HR} < 0.8$) in the water column (Poulton and Canfield, 2011).

The concept of an anoxic and ferruginous ocean was originally assigned to the Archean era. Prior to the onset of oxic weathering of sulfide minerals on land the ocean was poor in sulfate. Under these circumstances, H_2S produced by complete sulfate reduction could be quantitatively titrated by Fe supplied by hydrothermal venting and, subsequently, dissolved Fe could rise to appreciable levels (Holland, 1984; Canfield, 1998; Poulton and Canfield, 2011). Greatly enhanced Fe mobility and transport in a ferruginous ocean in the Archean is manifested in the widespread deposition of banded iron formations (Bekker et al., 2010).

More recently, the proxy signature of ferruginous conditions has been reported for a number of Phanerozoic sections where quantitative sulfate consumption is in many cases inconsistent with the sulfur isotope record (März et al., 2008; Dickson et al., 2014; Lenniger et al., 2014; Poulton et al., 2015; Clarkson et al., 2016). In a scenario where dissolved sulfate has been quantitatively reduced to hydrogen

sulfide, the $\delta^{34}S$ of sedimentary pyrite is expected to reflect the sulfur isotope composition of contemporary seawater (e.g., as constrained from sulfate-containing evaporite samples) (Canfield and Raiswell, 1999). Conversely, if pyrite-sulfur is characterized by an isotopic offset from contemporary seawater (i.e., $\delta^{34}S_{pyrite} < \delta^{34}S_{seawater}$), sulfate reduction must be incomplete and ferruginous conditions cannot be attributed to quantitative sulfate depletion. In these cases, ferruginous conditions are thought to be a redox state intermediate between nitrogenous and euxinic, where dissolved Fe^{2+} is the dominant redox species in the water column (Poulton and Canfield, 2011). In the modern ocean such an intermediate stage of ferruginous conditions does not exist in the water column but only in the sediment pore water (Fig 1B). In fact, the highest Fe concentrations observed in the water column of the Black Sea and the Peruvian margin (during sulfidic events) coincide with even higher H_2S concentrations (300 nM Fe^{2+} versus 10 to 50 µM H_2S)(Fig. 3B and 3). In the Black Sea water column, solid Fe (oxyhydr)oxides are several orders of magnitude less abundant and have a shorter residence time compared to dissolved sulfate (Lewis and Landing, 1991). Therefore, Fe reduction in particles cannot outpace H_2S generation by bacterial sulfate reduction. Instead, a rapid switch from nitrogenous to weakly sulfidic conditions takes place with no Fe-rich and NO_3^-/NO_2^--depleted and non-sulfidic stage in between. On the Peruvian margin, Fe^{2+} and H_2S are jointly released from the sediment into the water column upon NO_3^- and NO_2^- depletion (Scholz et al., 2016; Sommer et al., 2016). Here, the lack of a ferruginous intermediate stage prior to the onset of sulfidic conditions is likely related to the high solubility of reduced Fe in sulfidic waters (Rickard, 2006). However, as demonstrated in Section 3.1. Fe transport in the water column and redistribution of sedimentary reactive Fe does not require a water column where Fe^{2+} dominates over NO_3^-, NO_2^- and H_2S. Even under the nitrogenous to weakly sulfidic conditions prevailing in modern OMZs, sediment-derived Fe can be transported, which is demonstrated by significant sedimentary Fe enrichments in the Gulf of California and on the Peruvian margin. In fact, recalculating the Fe_T/Al and Fe_{HR}/Fe_T observed in these settings for a lower MAR of terrigenous material (like in the pelagic Black Sea) yields a proxy signature that is indicative of ferruginous conditions (Fig. 9A).

According to Poulton and Canfield (2011), ferruginous anoxia dominates over euxinia during times of enhanced reactive Fe supply to the ocean, e.g., due to enhanced chemical weathering under conditions of elevated atmospheric CO_2 and warmer climate. Under such circumstances, an excess of highly reactive Fe over sulfate is thought to facilitate the onset of euxinic conditions. In this context, it is worth noting that sedimentary H_2S release on the Peruvian shelf can occur despite the presence of unsulfidized Fe (oxhydr)oxide in the surface sediment (Scholz et al., 2016). The theoretical effect of enhanced terrigenous Fe supply to continental margin sediments on sedimentary Fe redistribution can be evaluated in Fig. 9B. More intense weathering of silicate minerals to Fe (oxyhydr)oxides, e.g., through expansion of tropical laterite soils, would shift Fe_{HR}/Fe_T to higher values and thus the relationship between Fe_T/Al and Fe_{HR}/Fe_T parallel to the x-axis. In contrast, more intense weathering of Fe-rich rock

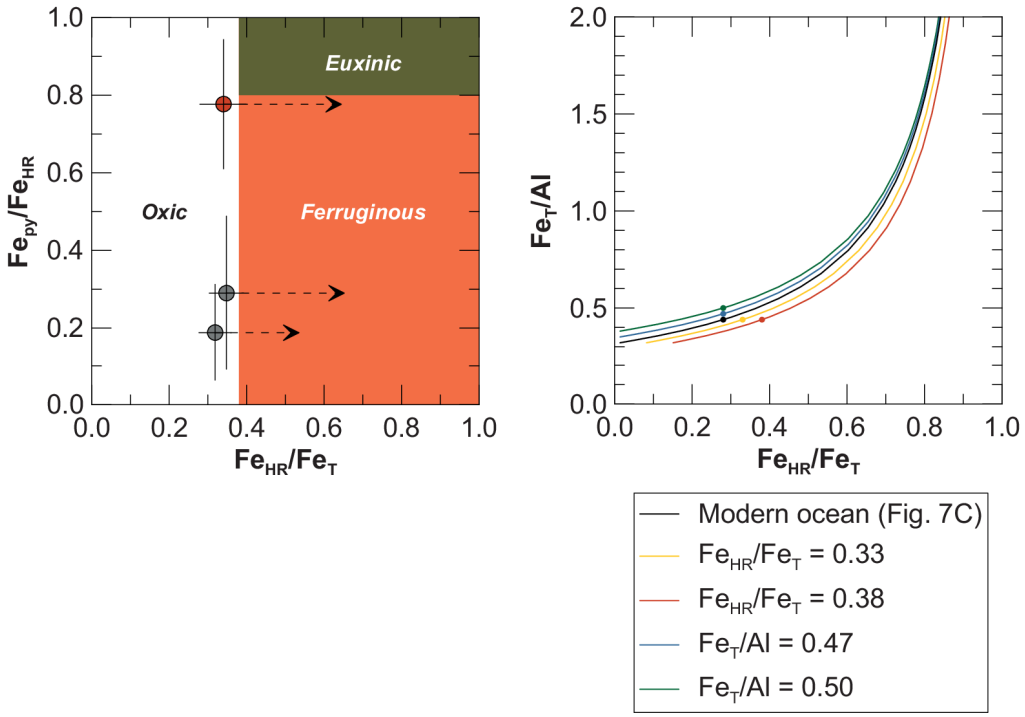

Fig. 9. (A) *Cross plot of Fe_{py}/Fe_{HR} versus Fe_{HR}/Fe_T with fields for oxic, ferruginous and euxinic proxy signatures (Poulton and Canfield, 2011). Symbols depict the average $Fe_{py}/Fe_{HR} \pm$ SD and $Fe_{HR}/Fe_T \pm$ SD of sediment cores from the Peruvian continental margin (Scholz et al., 2014c) and the Gulf of California (F. Scholz, unpublished data). Only sediment cores with elevated Fe_{HR}/Fe_T relative to sediments with oxic bottom water are shown (see Fig. 7C). The arrows were calculated under the assumption that the sediment cores had a one order of magnitude lower sediment mass accumulation rate (i.e., approximately similar to the Black Sea) but the same authigenic Fe rain rate (Fig. 7B). The high SD of Fe_{py}/Fe_{HR} is related to the downcore increase in pyritization because of increasing H_2S concentrations in the pore water (Scholz et al., 2014c).* ***(B)*** *Cross plot of Fe_T/Al versus Fe_{HR}/Fe_T illustrating scenarios of sedimentary Fe release and trapping for situations with a higher terrigenous Fe_{HR}/Fe_T or Fe_T/Al. See Supplementary Information for further details about the underlying calculations.*

types (e.g., more mafic than felsic igneous rocks) (Nockolds, 1954) in the hinterland would yield a higher Fe_T/Al and, thus, shift the relationship parallel to the y-axis. Both of these trends facilitate the generation of a ferruginous proxy signature at a given MAR and authigenic Fe rain rate (Fig. 9B), regardless of whether the redox state in the water column is nitrogenous, euxinic or ferruginous. Based on this reasoning, I propose that the ferruginous proxy signature is generally consistent with Fe cycling in a nitrogenous to weakly sulfidic water column like in a modern OMZ.

5. Summary and future directions

Anoxic OMZs in the modern ocean are characterized by nitrogenous conditions in the water column and ferruginous to sulfidic conditions in the surface sediment. A combination of Fe- and trace metal-based paleo-proxies can be used to identify this redox structure and the associated biogeochemical processes and feedback mechanisms in sedimentary archives. A generalized model of sedimentary Fe release and trapping was used to demonstrate that the extent of Fe mobilization and transport in modern OMZs can be comparable to that inferred for the euxinic Black Sea and ferruginous water columns in Earth history. Based on this finding it is argued that the ferruginous proxy signature is broadly consistent with Fe cycling in a nitrogenous OMZ, especially if enhanced chemical weathering and reactive Fe input to the ocean during past periods of global warming are taken into account. Variability in Fe_T/Al and Fe_{HR}/Fe_T along specific trend lines is proposed as a paleo-indicator for sedimentary Fe release and trapping on a regional scale. The enhanced Fe mobility in surface sediments and bottom waters implied by reactive Fe depletion or enrichment in paleo-records may have amplified primary production and nitrogen fixation thus contributing to the occurrence of euxinic conditions along productive continental margins in Earth history (e.g., Grice et al., 2005; Owens et al., 2013). As a summary of this review article, I propose a proxy-based scheme for the distinction between restricted basin-type and open-marine, upwelling-related anoxic settings with nitrogenous, euxinic or ferruginous conditions in the water column (Fig. 10).

Most studies on biogeochemical cycling in pre-Cenozoic Earth history focus on proxies for Fe and sulfur cycling to differentiate between euxinic and ferruginous anoxia. Adding proxies for nitrogen cycling to this routine may provide new insights into how nitrogen cycling processes (denitrification) affected Fe mobility during past periods of ocean anoxia (e.g., Michiels et al., 2017). More work on sedimentary Fe speciation and redistribution in modern OMZs is required to better characterize controlling factors and the extent of Fe release, transport and trapping along productive continental margins. For instance, chemical weathering in tropical river catchments, intense terrigenous input by large streams and an extended shelf width on passive continental margins are factors that are likely to affect the extent of sedimentary Fe redistribution in OMZs. Many of the biogeochemical processes described in this article

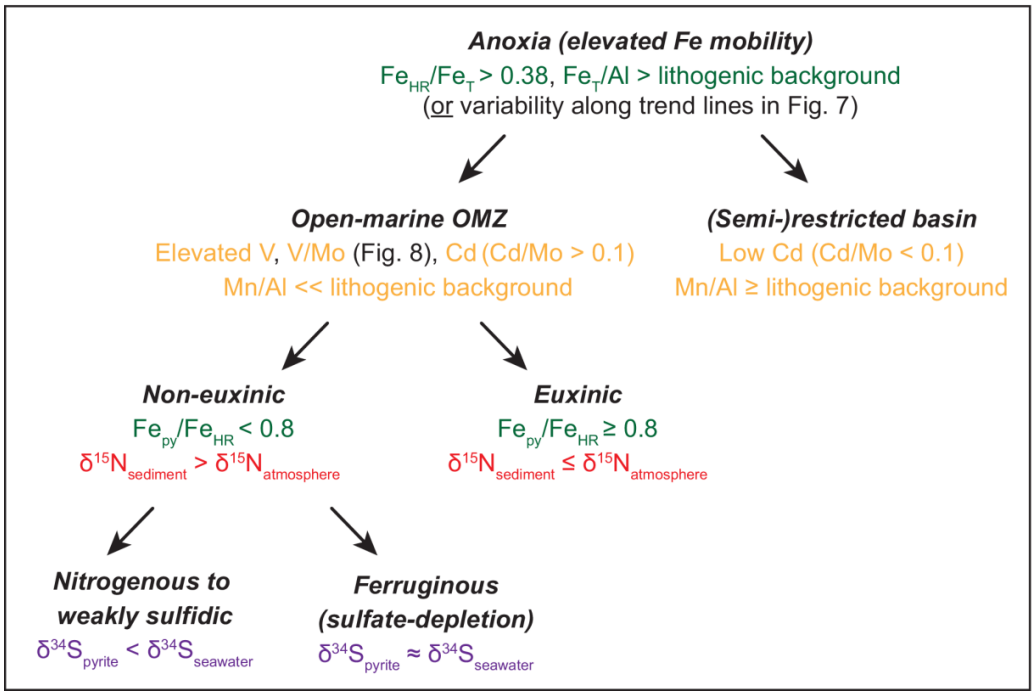

Fig. 10. *Proxy-based scheme for the identification of different types of anoxic settings in the geological record (restricted basin-type versus upwelling-related/open-marine with nitrogenous, euxinic or ferruginous conditions in the water column). The threshold values of Cd/Mo are from Sweere et al. (2016). Regional nitrogen isotope variability has to be interpreted relative to the global secular $\delta^{15}N$ trend (see Section 3.3 for further information).*

have been shown to affect the isotope composition of metals (e.g., vanadium, chromium, iron, molybdenum, thallium, uranium) (Teng et al., 2017). However, with the exception of Fe and Mo (e.g., Poulson et al., 2006; Poulson-Brucker et al., 2009; Severmann et al., 2006, 2010; Scholz et al., 2014a, b, 2017), none of these promising isotope geochemical tools has been studied in a systematic fashion in OMZs (i.e., across the entire bottom water redox-gradient, ideally including not only sediments but also pore waters and particles). Comparing sedimentary trace metal ratios and metal isotope values with trace metal quota and isotope compositions of different biological communities could help to identify specific metabolisms that are associated with nitrogenous or euxinic OMZs in the geological record. More research on the distribution, isotope composition and/or speciation (dissolved, particles, sediment) of metals that accumulate under anoxic but non-sulfidic conditions (e.g., rhenium, chromium, vanadium) can provide valuable insights into the specific sedimentary fingerprint of redox gradients at the boundaries of OMZs. Combining such novel tools with well-established geochemical proxies in both modern and ancient anoxic settings will help to better constrain the role and abundance of OMZ-type biogeochemical cycling throughout Earth history.

Acknowledgements

I would like to thank Klaus Wallmann and Jim McManus for providing comments on an earlier version of this article as well as for arousing my interest in the role of sediments in ocean biogeochemical dynamics. Furthermore, I would like to thank Andy Dale, Don Canfield, Simon Poulton, Emma Hammarlund, Andreas Kappler, Jim Moffett and all members of my research group for helpful discussions over the past years. This work was supported by the German Research Foundation (DFG) through my Emmy Noether Research Group (ICONOX - Iron Cycling in Marine Sediments and the Nutrient and Oxygen Balance of the Ocean) and Collaborative Research Centre 754 (Climate-Biogeochemistry Interactions in the Tropical Ocean).

References

Ader, M., Thomazo, C., Sansjofre, P., Busigny, V., Papineau, D., Laffont, R., Cartigny, P. and Halverson, G.P. (2016) Interpretation of the nitrogen isotopic composition of Precambrian sedimentary rocks: Assumptions and perspectives. Chemical Geology 429, 93-110.

Algeo, T.J. and Ingall, E. (2007) Sedimentary Corg:P ratios, paleocean ventilation, and Phanerozoic atmospheric pO_2. Palaeogeography, Palaeoclimatology, Palaeoecology 256, 130-155.

Algeo, T.J. and Lyons, T.W. (2006) Mo-total organic carbon covariation in modern anoxic marine environments: Implications for analysis of paleoredox and paleohydrographic conditions. Paleoceanography 21, PA1016.

Algeo, T.J., Meyers, P.A., Robinson, R.S., Rowe, H. and Jiang, G.Q. (2014) Icehouse-greenhouse variations in marine denitrification. Biogeosciences 11, 1273-1295.

Altabet, M.A., Francois, R., Murray, D.W. and Prell, W.L. (1995) Climate-related variations in denitrification in the Arabian Sea from sediment 15N/14N ratios. Nature 373, 506.

Barnes, C.E. and Cochran, J.K. (1990) Uranium removal in oceanic sediments and the oceanic U balance. Earth and Planetary Science Letters 97, 94-101.

Bauersachs, T., Speelman, E.N., Hopmans, E.C., Reichart, G.-J., Schouten, S. and Damsté, J.S.S. (2010) Fossilized glycolipids reveal past oceanic N2 fixation by heterocystous cyanobacteria. Proceedings of the National Academy of Sciences 107, 19190-19194.

Bekker, A., Slack, J.F., Planavsky, N., Krapez, B., Hofmann, A., Konhauser, K.O. and Rouxel, O.J. (2010) Iron formation: The sedimentary product of a complex interplay among mantle, tectonic, oceanic, and biospheric processes. Economic Geology 105, 467-508.

Benson, B.B. and Krause Jr., D. (1980) The concentration and isotope fractionation of gases dissolved in freshwater in equilibrium with the atmosphere: 1. Oxygen. Limnology and Oceanography 25, 662-671.

Bohlen, L., Dale, A.W., Sommer, S., Mosch, T., Hensen, C., Noffke, A., Scholz, F. and Wallmann, K. (2011) Benthic nitrogen cycling traversing the Peruvian oxygen minimum zone. Geochimica et Cosmochimica Acta 75, 6094-6111.

Böning, P., Brumsack, H.J., Böttcher, M.E., Schnetger, B., Kriete, C., Kallmeyer, J. and Borchers, S.L. (2004) Geochemistry of Peruvian near-surface sediments. Geochimica Et Cosmochimica Acta 68, 4429-4451.

Böning, P., Cuypers, S., Grunwald, M., Schnetger, B. and Brumsack, H.J. (2005) Geochemical characteristics of Chilean upwelling sediments at ~ 36°S. Marine Geology 220, 1-21.

Borchers, S.L., Schnetger, B., Boning, P. and Brumsack, H.J. (2005) Geochemical signatures of the Namibian diatom belt: Perennial upwelling and intermittent anoxia. Geochemistry Geophysics Geosystems 6, Q06006, doi:10.1029/2004GC000886.

Boyd, P.W. and Ellwood, M.J. (2010) The biogeochemical cycle of iron in the ocean. Nature Geoscience 3, 675-682.

Boyle, R.A., Clark, J.R., Poulton, S.W., Shields-Zhou, G., Canfield, D.E. and Lenton, T.M. (2013) Nitrogen cycle feedbacks as a control on euxinia in the mid-Proterozoic ocean. Nature Communications 4, 1533.

Brandt, P., Bange, H.W., Banyte, D., Dengler, M., Didwischus, S.H., Fischer, T., Greatbatch, R.J., Hahn, J., Kanzow, T., Karstensen, J., Körtzinger, A., Krahmann, G., Schmidtko, S., Stramma, L., Tanhua, T. and Visbeck, M. (2015) On the role of circulation and mixing in the ventilation of oxygen minimum zones with a focus on the eastern tropical North Atlantic. Biogeosciences 12, 489-512.

Brüchert, V., Jørgensen, B.B., Neumann, K., Riechmann, D., Schlösser, M. and Schulz, H. (2003) Regulation of bacterial sulfate reduction and hydrogen sulfide fluxes in the central namibian coastal upwelling zone. Geochimica et Cosmochimica Acta 67, 4505-4518.

Bruland, K.W., Rue, E.L., Smith, G.J. and DiTullio, G.R. (2005) Iron, macronutrients and diatom blooms in the Peru upwelling regime: brown and blue waters of Peru. Marine Chemistry 93, 81-103.

Brumsack, H.-J. (1986) The inorganic geochemistry of Cretaceous black shales (DSDP Leg 41) in comparison to modern upwelling sediments from the Gulf of California. Geological Society, London, Special Publications 21, 447-462.

Brumsack, H.-J. (1989) Geochemistry of recent TOC-rich sediments from the Gulf of California and the Black Sea. International Journal of Earth Sciences 78, 851-882.

Brumsack, H.-J. (2006) The trace metal content of recent organic carbon-rich sediments: Implications for Cretaceous black shale formation. Palaeogeography, Palaeoclimatology, Palaeoecology 232, 344-361.

Burdige, D.J. (2007) Preservation of organic matter in marine sediments: Controls, mechanisms, and an imbalance in sediment organic carbon budgets? Chemical Reviews 107, 467-485.

Calvert, S.E. (1966) Accumulation of diatomaceous silica in the sediments of the Gulf of California. Geological Society of America Bulletin 77, 569-596.

Calvert, S.E., Karlin, R.E., Toolin, L.J., Donahue, D.J., Southon, J.R. and Vogel, J.S. (1991) Low organic carbon accumulation rates in Black Sea sediments. Nature 350, 692.

Campbell, A.C. and Gieskes, J.M. (1984) Water column anomalies associated with hydrothermal activity in the Guaymas Basin, Gulf of California. Earth and Planetary Science Letters 68, 57-72.

Canfield, D.E. (1989) Reactive iron in marine sediments. Geochimica et Cosmochimica Acta 53, 619-632.

Canfield, D.E. (1998) A new model for Proterozoic ocean chemistry. Nature 396, 450-453.

Canfield, D.E. (2006) Models of oxic respiration, denitrification and sulfate reduction in zones of coastal upwelling. Geochimica et Cosmochimica Acta 70, 5753-5765.

Canfield, D.E. and Raiswell, R. (1999) The evolution of the sulfur cycle. American Journal of Science 299, 697-723.

Canfield, D.E., Raiswell, R., Westrich, J.T., Reaves, C.M. and Berner, R.A. (1986) The use of chromium reduction in the analysis of reduced inorganic sulfur in sediments and shales. Chemical Geology 54, 149-155.

Canfield, D.E., Raiswell, R. and Bottrell, S.H. (1992) The reactivity of sedimentary iron minerals toward sulfide. American Journal of Science 292, 659-683.

Canfield, D.E. and Thamdrup, B. (2009) Towards a consistent classification scheme for geochemical environments, or, why we wish the term 'suboxic' would go away. Geobiology 7, 385-392.

Chan, K.M. and Riley, J.P. (1966) The determination of molybdenum in natural waters, silicates and biological materials. Analytica Chimica Acta 36, 220-229.

Chan, K.M. and Riley, J.P. (1966) The determination of vanadium in sea and natural waters,biological materials and silicate sediments and rocks. Analytica Chimica Acta 34, 337-345.

Clarkson, M.O., Wood, R.A., Poulton, S.W., Richoz, S., Newton, R.J., Kasemann, S.A., Bowyer, F. and Krystyn, L. (2016) Dynamic anoxic ferruginous conditions during the end-Permian mass extinction and recovery. Nature Communications 7.

Dahl, T.W., Ruhl, M., Hammarlund, E.U., Canfield, D.E., Rosing, M.T. and Bjerrum, C.J. (2013) Tracing euxinia by molybdenum concentrations in sediments using handheld X-ray fluorescence spectroscopy (HHXRF). Chemical Geology 360â€“361, 241-251.

Dale, A.W., Nickelsen, L., Scholz, F., Hensen, C., Oschlies, A. and Wallmann, K.C.G. (2015) A revised global estimate of dissolved iron fluxes from marine sediments. Global Biogeochemical Cycles 10.1002/2014GB005017.

Dale, A.W., Graco, M. and Wallmann, K. (2017) Strong and dynamic benthic-pelagic coupling and feedbacks in a coastal upwelling system (Peruvian shelf). Frontiers in Marine Science 4, doi: 10.3389/fmars.2017.00029.

Dalsgaard, T., Canfield, D.E., Petersen, J., Thamdrup, B. and Acuna-Gonzalez, J. (2003) N2 production by the anammox reaction in the anoxic water column of Golfo Dulce, Costa Rica. Nature 422, 606-608.

Dellwig, O., Leipe, T., März, C., Glockzin, M., Pollehne, F., Schnetger, B., Yakushev, E.V., Böttcher, M.E. and Brumsack, H.-J. (2010) A new particulate Mn-Fe-P-shuttle at the redoxcline of anoxic basins. Geochimica et Cosmochimica Acta 74, 7100-7115.

Diaz, R.J. (2001) Overview of hypoxia around the world. Journal of Environmental Quality 30, 275-281.

Diaz, R.J. and Rosenberg, R. (2008) Spreading dead zones and consequences for marine ecosystems. Science 321, 926-929.

Dickson, A.J., Rees-Owen, R.L., März, C., Coe, A.L., Cohen, A.S., Pancost, R.D., Taylor, K. and Shcherbinina, E. (2014) The spread of marine anoxia on the northern Tethys margin during the Paleocene-Eocene Thermal Maximum. Paleoceanography 29, 2014PA002629.

Elrod, V.A., Berelson, W.M., Coale, K.H. and Johnson, K.S. (2004) The flux of iron from continental shelf sediments: A missing source for global budgets. Geophys. Res. Lett. 31.

Emerson, S.R. and Huested, S.S. (1991) Ocean anoxia and the concentrations of molybdenum and vanadium in seawater. Marine Chemistry 34, 177-196.

Erickson, B.E. and Helz, G.R. (2000) Molybdenum(VI) speciation in sulfidic waters:: Stability and lability of thiomolybdates. Geochimica et Cosmochimica Acta 64, 1149-1158.

Falkowski, P.G. (1997) Evolution of the nitrogen cycle and its influence on the biological sequestration of CO2 in the ocean. Nature 387, 272-275.

Ferdelman, T.G., Lee, C., Pantoja, S., Harder, J., Bebout, B.M. and Fossing, H. (1997) Sulfate reduction and methanogenesis in a Thioploca-dominated sediment off the coast of Chile. Geochimica et Cosmochimica Acta 61, 3065-3079.

Fossing, H., Gallardo, V.A., Jørgensen, B.B., Hüttel, M., Nielsen, L.P., Schulz, H., Canfield, D.E., Forster, S., Glud, R.N., Gundersen, J.K., Küver, J., Ramsing, N.B., Teske, A., Thamdrup, B. and Ulloa, O. (1995) Concentration and transport of nitrate by the mat-forming sulphur bacterium Thioploca. Nature 374, 713.

Friederich, G.E., Codispoti, L.A. and Sakamoto, C.M. (1990) Bottle and pumpcast data from the 1988 Black Sea expedition, Monterey Bay Aquarium Research Institute Technical Report No. 90-3.

Galbraith, E.D., Kienast, M., Pedersen, T.F. and Calvert, S.E. (2004) Glacial-interglacial modulation of the marine nitrogen cycle by high-latitude O2 supply to the global thermocline. Paleoceanography 19, PA4007.

Ganeshram, R.S., Pedersen, T.F., Calvert, S.E., McNeill, G.W. and Fontugne, M.R. (2000) Glacial-interglacial variability in denitrification in the world's oceans: Causes and consequences. Paleoceanography 15, 361-376.

Glenn, C.R. and Arthur, M.A. (1988) Petrology and major element geochemistry of Peru margin phosphorites and associated diagenetic minerals: Authigenesis in modern organic-rich sediments. Marine Geology 80, 231-267.

Grégoire, M. and Beckers, J.M. (2004) Modeling the nitrogen fluxes in the Black Sea using a 3D coupledhydrodynamical-biogeochemical model: Transport versus biogeochemicalprocesses, exchanges across the shelf break and comparison of the shelf and deep sea ecodynamics. Biogeosciences 1, 33-61.

Grice, K., Cao, C., Love, G.D., Böttcher, M.E., Twitchett, R.J., Grosjean, E., Summons, R.E., Turgeon, S.C., Dunning, W. and Jin, Y. (2005) Photic zone euxinia during the Permian-Triassic superanoxic event. Science 307, 706-709.

Gruber, N. (2008) The marine nitrogen cycle: Overview and challenges, in: Capone, D.G., Bronk, D.A., Mulholland, M.R., Carpenter, E.J. (Eds.), Nitrogen in the marine environment. Academic Press, pp. 1-50.

Gruber, N. and Sarmiento, J.L. (1997) Global patterns of marine nitrogen fixation and denitrification. Global Biogeochemical Cycles 11, 235-266.

Guilbaud, R., Slater, B.J., Poulton, S.W., Harvey, T.H.P., Brocks, J.J., Nettersheim, B.J. and Butterfield, N.J. (2018) Oxygen minimum zones in the early Cambrian ocean. Geochemical Perspectives Letters 6, 33-38.

Hamersley, M.R., Lavik, G., Woebken, D., Rattray, J.E., Lam, P., Hopmans, E.C., Damste, J.S.S., Kruger, S., Graco, M., Gutierrez, D. and Kuypers, M.M.M. (2007) Anaerobic ammonium oxidation in the Peruvian oxygen minimum zone. Limnol. Oceanogr. 52, 923-933.

Hammarlund, E.U., Gaines, R.R., Prokopenko, M.G., Qi, C., Hou, X.-G. and Canfield, D.E. (2017) Early Cambrian oxygen minimum zone-like conditions at Chengjiang. Earth and Planetary Science Letters 475, 160-168.

Harder, H. (1980) Syntheses of glauconite at surface temperatures. Clays and Clay Minerals 28, 217-222.

Hawco, N.J., Ohnemus, D.C., Resing, J.A., Twining, B.S. and Saito, M.A. (2016) A dissolved cobalt plume in the oxygen minimum zone of the eastern tropical South Pacific. Biogeosciences 13, 5697-5717.

Heller, M.I., Lam, P.J., Moffett, J.W., Till, C.P., Lee, J.-M., Toner, B.M. and Marcus, M.A. (2017) Accumulation of Fe oxyhydroxides in the Peruvian oxygen deficient zone implies non-oxygen dependent Fe oxidation. Geochimica et Cosmochimica Acta 211, 174-193.

Helz, G.R., Miller, C.V., Charnock, J.M., Mosselmans, J.F.W., Pattrick, R.A.D., Garner, C.D. and Vaughan, D.J. (1996) Mechanism of molybdenum removal from the sea and its concentration in black shales: EXAFS evidence. Geochimica et Cosmochimica Acta 60, 3631-3642.

Higgins, M.B., Robinson, R.S., Husson, J.M., Carter, S.J. and Pearson, A. (2012) Dominant eukaryotic export production during ocean anoxic events reflects the importance of recycled NH4+. Proceedings of the National Academy of Sciences 109, 2269-2274.

Ho, P., Lee, J.-M., Heller, M.I., Lam, P.J. and Shiller, A.M. (2018) The distribution of dissolved and particulate Mo and V along the U.S. GEOTRACES East Pacific Zonal Transect (GP16): The roles of oxides and biogenic particles in their distributions in the oxygen deficient zone and the hydrothermal plume. Marine Chemistry, 201, 242-255.

Holland, H. D. (1984). The chemical evolution of the atmosphere and oceans. Princeton University Press, Princeton.

Howarth, R., Chan, F., Conley, D.J., Garnier, J., Doney, S.C., Marino, R. and Billen, G. (2011) Coupled biogeochemical cycles: Eutrophication and hypoxia in temperate estuaries and coastal marine ecosystems. Frontiers in Ecology and the Environment 9, 18-26.

Hutchins, D.A. and Bruland, K.W. (1998) Iron-limited diatom growth and Si:N uptake ratios in a coastal upwelling regime. Nature 393, 561-564.

Ingall, E. and Jahnke, R. (1994) Evidence for enhanced phosphorus regeneration from marine sediments overlain by oxygen depleted waters. Geochimica et Cosmochimica Acta 58, 2571-2575.

Ingall, E. and Jahnke, R. (1997) Influence of water-column anoxia on the elemental fractionation of carbon and phosphorus during sediment diagenesis. Marine Geology 139, 219-229.

Ingall, E.D. and Van Cappellen, P. (1990) Relation between sedimentation rate and burial of organic phosphorus and organic carbon in marine sediments. Geochimica et Cosmochimica Acta 54, 373-386.

Johnson, K.S., Berelson, W.M., Coale, K.H., Coley, T.L., Elrod, V.A., Fairey, W.R., Iams, H.D., Kilgore, T.E. and Nowicki, J.L. (1992) Manganese Flux from Continental-Margin Sediments in a Transect through the Oxygen Minimum. Science 257, 1242-1245.

Johnson, K.S., Chavez, F.P. and Friederich, G.E. (1999) Continental-shelf sediment as a primary source of iron for coastal phytoplankton. Nature 398, 697-700.

Johnson, K.S., Coale, K.H., Berelson, W.M. and Michael Gordon, R. (1996) On the formation of the manganese maximum in the oxygen minimum. Geochimica et Cosmochimica Acta 60, 1291-1299.

Karstensen, J., Stramma, L. and Visbeck, M. (2008) Oxygen minimum zones in the eastern tropical Atlantic and Pacific oceans. Progress in Oceanography 77, 331-350.

Keeling, R.F., Körtzinger, A. and Gruber, N. (2011) Ocean deoxygenation in a warming world. Annual Review of Marine Science 2, 199-229.

Klinkhammer, G.P. and Bender, M.L. (1980) The distribution of manganese in the Pacific Ocean. Earth and Planetary Science Letters 46, 361-384.

Klinkhammer, G.P. and Palmer, M.R. (1991) Uranium in the oceans - Where it goes and why. Geochimica et Cosmochimica Acta 55, 1799-1806.

Klinkhammer, G.P., Mix, A.C. and Haley, B.A. (2009) Increased dissolved terrestrial input to the coastal ocean during the last deglaciation. Geochemistry Geophysics Geosystems 10, Q03009, doi:03010.01029/02008GC002219.

Klueglein, N. and Kappler, A. (2013) Abiotic oxidation of Fe(II) by reactive nitrogen species in cultures of the nitrate-reducing Fe(II) oxidizer Acidovorax sp. BoFeN1 – questioning the existence of enzymatic Fe(II) oxidation. Geobiology 11, 180-190.

Kondo, Y. and Moffett, J.W. (2015) Iron redox cycling and subsurface offshore transport in the eastern tropical South Pacific oxygen minimum zone. Marine Chemistry 168, 95-103.

Koschinsky, A. and Halbach, P. (1995) Sequential leaching of marine ferromanganese precipitates: Genetic implications. Geochimica et Cosmochimica Acta 59, 5113-5132.

Kuypers, M.M.M., Lavik, G., Woebken, D., Schmid, M., Fuchs, B.M., Amann, R., JÃ¸rgensen, B.B. and Jetten, M.S.M. (2005) Massive nitrogen loss from the Benguela upwelling system through anaerobic ammonium oxidation. Proceedings of the National Academy of Sciences of the United States of America 102, 6478-6483.

Kuypers, M.M.M., Pancost, R.D., Nijenhuis, I.A. and Sinninghe Damsté, J.S.C. (2002) Enhanced productivity led to increased organic carbon burial in the euxinic North Atlantic basin during the late Cenomanian oceanic anoxic event. Paleoceanography 17, 3-1-3-13.

Kuypers, M.M.M., Sliekers, A.O., Lavik, G., Schmid, M., Jorgensen, B.B., Kuenen, J.G., Sinninghe Damsté, J.S., Strous, M. and Jetten, M.S.M. (2003) Anaerobic ammonium oxidation by anammox bacteria in the Black Sea. Nature 422, 608.

Lam, P. and Kuypers, M.M.M. (2011) Microbial nitrogen cycling processes in oxygen minimum zones. Annual Review of Marine Science 3, 317-345.

Landing, W.M. and Bruland, K.W. (1987) The contrasting biogeochemistry of iron and manganese in the Pacific Ocean. Geochimica et Cosmochimica Acta 51, 29-43.

Landolfi, A., Dietze, H., Koeve, W. and Oschlies, A. (2013) Overlooked runaway feedback in the marine nitrogen cycle: The vicious cycle. Biogeosciences 10, 1351-1363.

Lenniger, M., Nøhr-Hansen, H., Hills, L.V. and Bjerrum, C.J. (2014) Arctic black shale formation during Cretaceous Oceanic Anoxic Event 2. Geology 42, 799-802.

Lewis, B.L. and Landing, W.M. (1991) The biogeochemistry of manganese and iron in the Black Sea. Deep Sea Research Part A. Oceanographic Research Papers 38, Supplement 2, S773-S803.

Lewis, B.L. and Luther III, G.W. (2000) Processes controlling the distribution and cycling of manganese in the oxygen minimum zone of the Arabian Sea. Deep Sea Research 47, 1541-1561.

Loescher, C.R., Groskopf, T., Desai, F.D., Gill, D., Schunck, H., Croot, P.L., Schlosser, C., Neulinger, S.C., Pinnow, N., Lavik, G., Kuypers, M.M.M., LaRoche, J. and Schmitz, R.A. (2014) Facets of diazotrophy in the oxygen minimum zone waters off Peru. ISME J.

Lohan, M.C. and Bruland, K.W. (2008) Elevated Fe(II) and dissolved Fe in hypoxic shelf waters off Oregon and Washington: An enhanced source of iron to coastal upwelling regimes. Environ. Sci. Technol. 42, 6462-6468.

Lovley, D.R., Phillips, E.J.P., Gorby, Y.A. and Landa, E.R. (1991) Microbial reduction of uranium. Nature 350, 413-416.

Lyons, T.W., Anbar, A.D., Severmann, S., Scott, C. and Gill, B.C. (2009) Tracking euxinia in the ancient ocean: A multiproxy perspective and Proterozoic case study. Annu. Rev. Earth Planet. Sci. 37, 507-534.

Lyons, T.W. and Severmann, S. (2006) A critical look at iron paleoredox proxies: New insights from modern euxinic marine basins. Geochimica et Cosmochimica Acta 70, 5698-5722.

März, C., Poulton, S.W., Beckmann, B., Kuster, K., Wagner, T. and Kasten, S. (2008) Redox sensitivity of P cycling during marine black shale formation: Dynamics of sulfidic and anoxic, non-sulfidic bottom waters. Geochimica et Cosmochimica Acta 72, 3703-3717.

Matear, R.J. and Hirst, A.C.C. (2003) Long-term changes in dissolved oxygen concentrations in the ocean caused by protracted global warming. Global Biogeochemical Cycles 17, n/a-n/a.

McLennan S. M. (2001) Relationships between the trace element composition of sedimentary rocks and upper continental crust. Geochemistry Geophysics Geosystems 2, paper number 2000GC000109.

McManus, J., Berelson, W.M., Coale, K.H., Johnson, K.S. and Kilgore, T.E. (1997) Phosphorus regeneration in continental margin sediments. Geochimica et Cosmochimica Acta 61, 2891-2907.

McManus, J., Berelson, W.M., Klinkhammer, G.P., Hammond, D.E. and Holm, C. (2005) Authigenic uranium: relationship to oxygen penetration depth and organic carbon rain. Geochimica Et Cosmochimica Acta 69, 95-108.

Meyer, K.M. and Kump, L.R. (2008) Oceanic euxinia in Earth history: Causes and consequences. Annu. Rev. Earth Planet. Sci. 36, 251-288.

Michiels, C.C., Darchambeau, F., Roland, F.A.E., Morana, C., Lliros, M., Garcia-Armisen, T., Thamdrup, B., Borges, A.V., Canfield, D.E., Servais, P., Descy, J.-P. and Crowe, S.A. (2017) Iron-dependent nitrogen cycling in a ferruginous lake and the nutrient status of Proterozoic oceans. Nature Geoscience 10, 217-221.

Moore, J.K. and Doney, S.C. (2007) Iron availability limits the ocean nitrogen inventory stabilizing feedbacks between marine denitrification and nitrogen fixation. Global Biogeochemical Cycles 21, GB2001, doi:2010.1029/2006GB002762.

Morford, J.L., Emerson, S.R., Breckel, E.J. and Kim, S.H. (2005) Diagenesis of oxyanions (V, U, Re, and Mo) in pore waters and sediments from a continental margin. Geochimica Et Cosmochimica Acta 69, 5021-5032.

Mort, H.P., Adatte, T., Keller, G., Bartels, D., Föllmi, K.B., Steinmann, P., Berner, Z. and Chellai, E.H. (2008) Organic carbon deposition and phosphorus accumulation during Oceanic Anoxic Event 2 in Tarfaya, Morocco. Cretaceous Research 29, 1008-1023.

Mosch, T., Sommer, S., Dengler, M., Noffke, A., Bohlen, L., Pfannkuche, O., Liebetrau, V. and Wallmann, K. (2012) Factors influencing the distribution of epibenthic megafauna across the Peruvian oxygen minimum zone. Deep Sea Research Part I: Oceanographic Research Papers 68, 123-135.

Mullins, H.T., Thompson, J.B., McDougall, K. and Vercoutere, T.L. (1985) Oxygen-minimum zone edge effects: Evidence from the central California coastal upwelling system. Geology 13, 491-494.

Murray, J.W., Top, Z. and Özsoy, E. (1991) Hydrographic properties and ventilation of the Black Sea. Deep Sea Research Part A. Oceanographic Research Papers 38, S663-S689.

Nameroff, T.J., Balistrieri, L.S. and Murray, J.W. (2002) Suboxic trace metal geochemistry in the Eastern Tropical North Pacific. Geochimica et Cosmochimica Acta 66, 1139-1158.

Nockolds, S.R. (1954) Average chemical composition of some igneous rocks. Geological Society of America Bulletin 65, 1007-1032.

Noffke, A., Hensen, C., Sommer, S., Scholz, F., Bohlen, L., Mosch, T., Graco, M. and Wallmann, K. (2012) Benthic iron and phosphorus fluxes across the Peruvian oxygen minimum zone. Limnol. Oceanogr. 57, 851-867.

Ohnemus, D.C., Rauschenberg, S., Cutter, G.A., Fitzsimmons, J.N., Sherrell, R.M. and Twining, B.S. (2017) Elevated trace metal content of prokaryotic communities associated with marine oxygen deficient zones. Limnology and Oceanography 62, 3-25.

Owens, J.D., Gill, B.C., Jenkyns, H.C., Bates, S.M., Severmann, S., Kuypers, M.M.M., Woodfine, R.G. and Lyons, T.W. (2013) Sulfur isotopes track the global extent and dynamics of euxinia during Cretaceous Oceanic Anoxic Event 2. Proceedings of the National Academy of Sciences 110, 18407-18412.

Özsoy, E. and Ünlüata, U. (1997) Oceanography of the Black Sea: A review of some recent results. Earth-Science Reviews 42, 231-272.

Paulmier, A. and Ruiz-Pino, D. (2009) Oxygen minimum zones (OMZs) in the modern ocean. Progress in Oceanography 80, 113-128.

Pennington, J.T., Mahoney, K.L., Kuwahara, V.S., Kolber, D.D., Calienes, R. and Chavez, F.P. (2006) Primary production in the eastern tropical Pacific: A review. Progress In Oceanography 69, 285-317.

Picardal, F. (2012) Abiotic and microbial interactions during anaerobic transformations of Fe(II) and NOx. Frontiers in Microbiology 3, doi: 10.3389/fmicb.2012.00112.

Poulson Brucker, R.L., McManus, J., Severmann, S. and Berelson, W.M. (2009) Molybdenum behavior during early diagenesis: Insights from Mo isotopes. Geochemistry Geophysics Geosystems 10.

Poulson, R.L., Siebert, C., McManus, J. and Berelson, W.M. (2006) Authigenic molybdenum isotope signatures in marine sediments. Geology 34, 617-620.

Poulton, S.W. and Canfield, D.E. (2005) Development of a sequential extraction procedure for iron: implications for iron partitioning in continentally derived particulates. Chemical Geology 214, 209-221.

Poulton, S.W. and Canfield, D.E. (2011) Ferruginous conditions: A dominant feature of the ocean through Earth's history. ELEMENTS 7, 107-112.

Poulton, S.W. and Raiswell, R. (2002) The low-temperature geochemical cycle of iron: From continental fluxes to marine sediment deposition. American Journal of Science 302, 774-805.

Poulton, S.W., Fralick, P.W. and Canfield, D.E. (2010) Spatial variability in oceanic redox structure 1.8 billion years ago. Nature Geoscience 3, 486-490.

Poulton, S.W., Henkel, S., März, C., Urquhart, H., Flögel, S., Kasten, S., Sinninghe Damsté, J.S. and Wagner, T. (2015) A continental-weathering control on orbitally driven redox-nutrient cycling during Cretaceous Oceanic Anoxic Event 2. Geology 43, 963-966.

Rabalais, N.N., Diaz, R.J., Levin, L.A., Turner, R.E., Gilbert, D. and Zhang, J. (2010) Dynamics and distribution of natural and human-caused hypoxia. Biogeosciences 7, 585-619.

Raiswell, R. and Canfield, D.E. (1996) Rates of reaction between silicate iron and dissolved sulfide in Peru margin sediments. Geochimica et Cosmochimica Acta 60, 2777-2787.

Raiswell, R. and Canfield, D.E. (1998) Sources of iron for pyrite formation in marine sediments. American Journal of Science 298, 219-245.

Raiswell, R. and Anderson, T.F. (2005) Reactive iron enrichment in sediments deposited beneath euxinic bottom waters: constraints on supply by shelf recycling. Geological Society, London, Special Publications 248, 179-194.

Raiswell, R., Buckley, F., Berner, R.A. and Anderson, T.F. (1988) Degree of pyritization of iron as a paleoenvironmental indicator of bottom-water oxygenation. Journal of Sedimentary Research 58, 812-819.

Raiswell, R. and Canfield, D.E. (2012) The iron biogeochemical cycle past and present. Geochemical Perspectives 1, 1-220.

Redfield, A.C., Ketchum, B.H. and Richards, F.A. (1963) The influence of organisms on the composition of sea-water, in: Hill, M.N. (Ed.), The Sea. Wiley-Interscience, New York, pp. 26-77.

Reimers, C.E. and Suess, E. (1983) Spatial and temporal patterns of organic matter accumulation on the Peru continental margin, in: Suess, E., Thiede, J. (Eds.), Coastal upwelling: Part B. Sedimentary record of ancient coastal upwelling. Plenum Press, New York, pp. 311-346.

Rickard, D. (2006) The solubility of FeS. Geochimica et Cosmochimica Acta 70, 5779-5789.

Schenau, S.J. and De Lange, G.J. (2001) Phosphorus regeneration vs. burial in sediments of the Arabian Sea. Marine Chemistry 75, 201-217.

Schmidtko, S., Stramma, L. and Visbeck, M. (2017) Decline in global oceanic oxygen content during the past five decades. Nature 542, 335-339.

Scholz, F., Hensen, C., Noffke, A., Rohde, A., Liebetrau, V. and Wallmann, K. (2011) Early diagenesis of redox-sensitive trace metals in the Peru upwelling area: response to ENSO-related oxygen fluctuations in the water column. Geochimica et Cosmochimica Acta 75, 7257-7276.

Scholz, F., McManus, J. and Sommer, S. (2013) The manganese and iron shuttle in a modern euxinic basin and implications for molybdenum cycling at euxinic ocean margins. Chemical Geology 355, 56-68.

Scholz, F., McManus, J., Mix, A.C., Hensen, C. and Schneider, R.R. (2014a) The impact of ocean deoxygenation on iron release from continental margin sediments. Nature Geoscience 7, 433-437.

Scholz, F., Severmann, S., McManus, J. and Hensen, C. (2014b) Beyond the Black Sea paradigm: The sedimentary fingerprint of an open-marine iron shuttle. Geochimica et Cosmochimica Acta 127, 368-380.

Scholz, F., Severmann, S., McManus, J., Noffke, A., Lomnitz, U. and Hensen, C. (2014c) On the isotope composition of reactive iron in marine sediments: Redox shuttle versus early diagenesis. Chemical Geology 389, 48-59.

Scholz, F., Löscher, C.R., Fiskal, A., Sommer, S., Hensen, C., Lomnitz, U., Wuttig, K., Göttlicher, J., Kossel, E., Steininger, R. and Canfield, D.E. (2016) Nitrate-dependent iron oxidation limits iron transport in anoxic ocean regions. Earth and Planetary Science Letters 454, 272-281.

Scholz, F., Siebert, C., Dale, A.W. and Frank, M. (2017) Intense molybdenum accumulation in sediments underneath a nitrogenous water column and implications for the reconstruction of paleo-redox conditions based on molybdenum isotopes. Geochimica et Cosmochimica Acta 213, 400-417.

Schulz, H.N., Brinkhoff, T., Ferdelman, T.G., Hernandez Mariné, M., Teske, A. and Jørgensen, B.B. (1999) Dense populations of a giant sulfur bacterium in Namibian shelf sediments. Science 284, 493-495.

Schunck, H., Lavik, G., Desai, D.K., Grosskopf, T., Kalvelage, T., Loescher, C.R., Paulmier, A., Contreras, S., Siegel, H., Holtappels, M., Rosenstiel, P., Schilhabel, M.B., Graco, M., Schmitz, R.A., Kuypers, M.M.M. and LaRoche, J. (2013) Giant hydrogen sulfide plume in the oxygen minimum zone off Peru supports chemolithoautotrophy. Plos One 8.

Scott, C. and Lyons, T.W. (2012) Contrasting molybdenum cycling and isotopic properties in euxinic versus non-euxinic sediments and sedimentary rocks: Refining the paleoproxies. Chemical Geology 324-325, 19-27.

Severmann, S., Johnson, C.M., Beard, B.L. and McManus, J. (2006) The effect of early diagenesis on the Fe isotope compositions of porewaters and authigenic minerals in continental margin sediments. Geochimica et Cosmochimica Acta 70, 2006-2022.

Severmann, S., McManus, J., Berelson, W.M. and Hammond, D.E. (2010) The continental shelf benthic iron flux and its isotope composition. Geochimica et Cosmochimica Acta 74, 3984-4004.

Shaw, T.J., Gieskes, J.M. and Jahnke, R.A. (1990) Early diagenesis in differing depositional environments: The response of transition metals in pore water. Geochimica et Cosmochimica Acta 54, 1233-1246.

Sloyan, B.M. and Rintoul, S.R. (2001) Circulation, renewal, and modification of Antarctic Mode and Intermediate Water. Journal of Physical Oceanography 31, 1005-1030.

Sommer, S., Gier, J., Treude, T., Lomnitz, U., Dengler, M., Cardich, J. and Dale, A.W. (2016) Depletion of oxygen, nitrate and nitrite in the Peruvian oxygen minimum zone cause an imbalance of benthic nitrogen fluxes. Deep Sea Research Part I: Oceanographic Research Papers 112, 113-122.

Stramma, L., Johnson, G.C., Sprintall, J. and Mohrholz, V. (2008) Expanding oxygen-minimum zones in the tropical oceans. Science 320, 655-658.

Straub, K.L., Benz, M., Schink, B. and Widdel, F. (1996) Anaerobic, nitrate-dependent microbial oxidation of ferrous iron. Applied and Environmental Microbiology 62, 1458-1460.

Suess, E., Kulm, L.D. and Killingley, J.S. (1987) Coastal upwelling and a history of organic-rich mudstone deposition off Peru, in: Brook, J., Fleet, A.J. (Eds.), Geological Society Special Publication, pp. 181-197.

Suits, N.S. and Arthur, M.A. (2000) Sulfur diagenesis and partitioning in Holocene Peru shelf and upper slope sediments. Chemical Geology 163, 219-234.

Sweere, T., van den Boorn, S., Dickson, A.J. and Reichart, G.-J. (2016) Definition of new trace-metal proxies for the controls on organic matter enrichment in marine sediments based on Mn, Co, Mo and Cd concentrations. Chemical Geology 441, 235-245.

Talley, L.D. (1993) Distribution and formation of North Pacific Intermediate Water. Journal of Physical Oceanography 23, 517-537.

Teng, F.-Z., Dauphas, N. and Watkins, J.M. (2017) Non-traditional stable isotopes: Retrospective and prospective. Reviews in Mineralogy and Geochemistry 82, 1-26.

Thamdrup, B. and Canfield, D.E. (1996) Pathways of carbon oxidation in continental margin sediments off central Chile. Limnol. Oceanogr. 41, 1629-1650.

Thamdrup, B., Dalsgaard, T. and Revsbech, N.P. (2012) Widespread functional anoxia in the oxygen minimum zone of the Eastern South Pacific. Deep Sea Research Part I: Oceanographic Research Papers 65, 36-45.

Tosca, N.J., Guggenheim, S. and Pufahl, P.K. (2016) An authigenic origin for Precambrian greenalite: Implications for iron formation and the chemistry of ancient seawater. Geological Society of America Bulletin 128, 511-530.

Tribovillard, N., Algeo, T.J., Lyons, T.W. and Riboulleau, A. (2006) Trace metals as paleoredox and paleoproductivity proxies: An update. Chemical Geology 232, 12-32.

Tribovillard, N., Riboulleau, A., Lyons, T.W. and Baudin, F. (2004) Enhanced trapping of molybdenum by sulfurized marine organic matter of marine origin in Mesozoic limestones and shales. Chemical Geology 213, 385-401.

Tyrrell, T. (1999) The relative influences of nitrogen and phosphorus on oceanic primary production. Nature 400, 525-531.

Ulloa, O., Canfield, D.E., DeLong, E.F., Letelier, R.M. and Stewart, F.J. (2012) Microbial oceanography of anoxic oxygen minimum zones. Proceedings of the National Academy of Sciences 109, 15996-16003.

Van Cappellen, P. and Ingall, E.D. (1994) Benthic phosphorus regeneration, net primary production, and ocean anoxia: A model of the coupled marine biogeochemical cycles of carbon and phosphorus. Paleoceanography 9, 677-692.

Van der Weijden, C.H., Reichart, G.J. and Visser, H.J. (1999) Enhanced preservation of organic matter in sediments deposited within the oxygen minimum zone in the northeastern Arabian Sea. Deep Sea Research Part 46, 807-830.

Vedamati, J., Goepfert, T. and Moffett, J.W. (2014) Iron speciation in the eastern tropical South Pacific oxygen minimum zone off Peru. Limnol. Oceanogr. 59, 1945-1957.

Vorlicek, T.P., Helz, G.R., Chappaz, A., Vue, P., Vezina, A. and Hunter, W. (2018) Molybdenum Burial Mechanism in Sulfidic Sediments: Iron-Sulfide Pathway. ACS Earth and Space Chemistry, in press.

Wallmann, K. (2003) Feedbacks between oceanic redox states and marine productivity: A model perspective focused on benthic phosphorus cycling. Global Biogeochemical Cycles 17, 1084.

Wallmann, K. (2010) Phosphorus imbalance in the global ocean? Global Biogeochemical Cycles 24, DOI: 10.1029/2009GB003643.

Wanty, R.B. and Goldhaber, M.B. (1992) Thermodynamics and kinetics of reactions involving vanadium in natural systems: Accumulation of vanadium in sedimentary rocks. Geochimica et Cosmochimica Acta 56, 1471-1483.

Wehrli, B. and Stumm, W. (1989) Vanadyl in natural waters: Adsorption and hydrolysis promote oxygenation. Geochimica et Cosmochimica Acta 53, 69-77.

Wijsman, J.W.M., Middelburg, J.J. and Heip, C.H.R. (2001) Reactive iron in Black Sea sediments: Implications for iron cycling. Marine Geology 172, 167-180.

Zhang, S., Wang, X., Wang, H., Bjerrum, C.J., Hammarlund, E.U., Costa, M.M., Connelly, J.N., Zhang, B., Su, J. and Canfield, D.E. (2016) Sufficient oxygen for animal respiration 1,400 million years ago. Proceedings of the National Academy of Sciences, doi.org/10.1073/pnas.1523449113.

Zheng, Y., Anderson, R.F., van Geen, A. and Kuwabara, J. (2000) Authigenic molybdenum formation in marine sediments: A link to pore water sulfide in the Santa Barbara Basin. Geochimica Et Cosmochimica Acta 64, 4165-4178.

Supplementary information

Generalized model for sedimentary iron release and trapping

The Fe_T/Al and Fe_{HR}/Fe_T after reactive Fe release or trapping were calculated with the following equations:

$$Fe_T/Al = \frac{MAR \cdot [Al] \cdot \left(\frac{Fe_T}{Al}\right)_{crust} + ((RR_{Fe}, F_{Fe}) \cdot M_{Fe})}{MAR \cdot [Al]}$$

$$Fe_{HR}/Fe_T = \frac{MAR \cdot [Al] \cdot \left(\frac{Fe_T}{Al}\right)_{crust} \cdot \left(\frac{Fe_{HR}}{Fe_T}\right)_{oxic} + ((RR_{Fe}, F_{Fe}) \cdot M_{Fe})}{MAR \cdot [Al] \cdot \left(\frac{Fe_T}{Al}\right)_{crust} + ((RR_{Fe}, F_{Fe}) \cdot M_{Fe})}$$

MAR: Sediment mass accumulation rate, in g cm^{-2} yr^{-1}.

[Al]: Aluminum concentration in the sediment, in mg g^{-1}. Scenarios of Fe loss or gain where calculated by assuming using a sedimentary Al concentration of 50 mg g^{-1} which is consistent with published data for sediments on the Peruvian margin, in the Gulf of California and the Black Sea (Scholz et al., 2011; Brumsack, 2006).

$(Fe/Al)_{crust}$: Fe_T/Al of the average upper continental crust, 0.44 (McLennan, 2001).

$(Fe_{HR}/Fe_T)_{oxic}$: Fe_{HR}/Fe_T of continental margin sediments with oxic bottom water, 0.28 ± 0.06 (Poulton and Raiswell, 2002).

RR_{Fe}: Authigenic Fe rain rate, in mmol cm^{-2} yr^{-1} (positive sign).

F_{Fe}: Benthic Fe efflux, in mmol cm^{-2} yr^{-1} (negative sign).

M_{Fe}: Molar mass of Fe, 55.845 mg $mmol^{-1}$.

Sediment geochemical data for sediments from the Gulf of California

Sediment cores were collected in the Gulf of California during RV Sonne cruise SO241 in June and July 2015. Pore water recovery and sediment subsampling was realized in a glove bag under anoxic conditions as explained in Scholz et al. (2011). Total iron (Fe) and aluminum (Al) concentrations were determined after total digestion by inductively coupled plasma optical emission spectroscopy (ICP-OES) (see Scholz et al. (2011) for details). Certified reference standards (SDO-1, USGS; MESS-3, Canadian Research Council) were digested and analyzed on a routine basis. The obtained values for Fe and Al were always within the certified ranges. A sequential sediment extraction for the recovery of highly reactive Fe phases was applied to the freeze-dried and ground sediment samples (Poulton

and Canfield, 2005). An in-house standard (OMZ-1) and the Certified Reference Material PACS-3 (Canadian Research Council) were extracted during each batch of sequential extractions. The results for the sum of highly reactive Fe without Fe bound to pyrite (Fe_{py}) were consistent with data generated at the University of Southern Denmark (SDU) for the same standard material (GEOMAR, OMZ-1: 0.47 $\pm$ 0.02 wt. %, n = 18, PACS-3: 1.25 $\pm$ 0.01, n = 7; SDU, OMZ-1: 0.44 $\pm$ 0.05 wt. %, n = 3, PACS-3: 1.26 $\pm$ 0.04, n = 12). The chromium reduction method was used for the determination of Fe_{py} (Canfield et al., 1986). The accuracy of the method was monitored by determining the pyrite content of mixtures between pure pyrite and quartz sand.

References

Brumsack H.-J. (2006) The trace metal content of recent organic carbon-rich sediments: Implications for Cretaceous black shale formation. Palaeogeography, Palaeoclimatology, Palaeoecology 232, 344-361.

Canfield D. E., Raiswell R., Westrich J. T., Reaves C. M., and Berner R. A. (1986) The use of chromium reduction in the analysis of reduced inorganic sulfur in sediments and shales. Chemical Geology 54, 149-155.

McLennan S. M. (2001) Relationships between the trace element composition of sedimentary rocks and upper continental crust. Geochemistry Geophysics Geosystems 2, paper number 2000GC000109.

Poulton S. W. and Raiswell R. (2002) The low-temperature geochemical cycle of iron: From continental fluxes to marine sediment deposition. American Journal of Science 302, 774-805.

Poulton S. W. and Canfield D. E. (2005) Development of a sequential extraction procedure for iron: implications for iron partitioning in continentally derived particulates. Chemical Geology 214, 209-221.

Scholz F., Hensen C., Noffke A., Rohde A., Liebetrau V., and Wallmann K. (2011) Early diagenesis of redox-sensitive trace metals in the Peru upwelling area: response to ENSO-related oxygen fluctuations in the water column. Geochimica et Cosmochimica Acta 75, 7257-7276.

Appendix: Published research articles

Early diagenesis of redox-sensitive trace metals in the Peru upwelling area: response to ENSO-related oxygen fluctuations in the water column
Florian Scholz, Christian Hensen, Anna Noffke, Anne Rohde, Volker Liebetrau, Klaus Wallmann
2011, Geochimica et Cosmochimica Acta 75, 7257-7276

Benthic iron and phosphorus fluxes across the Peruvian oxygen minimum zone
Anna Noffke, Christian Hensen, Stefan Sommer, Florian Scholz, Lisa Bohlen, Thomas Mosch, Michelle Graco, Klaus Wallmann
2012, Limnology and Oceanography 57, 851-867

The manganese and iron shuttle in a modern euxinic basin and implications for molybdenum cycling at euxinic ocean margins
Florian Scholz, James McManus, Stefan Sommer
2013, Chemical Geology 355, 56-68

Beyond the Black Sea paradigm: The sedimentary fingerprint of an open-marine iron shuttle
Florian Scholz, Silke Severmann, James McManus, Christian Hensen
2014a, Geochimica et Cosmochimica Acta 127, 368-380

On the isotope composition of reactive iron in marine sediments: Redox shuttle versus early diagenesis
Florian Scholz, Silke Severmann, James McManus, Anna Noffke, Ulrike Lomnitz
2014b, Chemical Geology 389, 48-59

The impact of ocean deoxygenation on iron release from continental margin sediments
Florian Scholz, James McManus, Alan C. Mix, Christian Hensen, Ralph R. Schneider
2014c, Nature Geoscience 7, 433-437

A revised global estimate of dissolved iron fluxes from marine sediments
Andrew W. Dale, Levin Nickelsen, Florian Scholz, Christian Hensen, Andreas Oschlies, Klaus Wallmann
2015, Global Biogeochemical Cycles, doi:10.1002/2014GB005017

Nitrate-dependent iron oxidation limits iron transport in anoxic ocean regions
Florian Scholz, Carolin R. Löscher, Annika Fiskal, Stefan Sommer, Christian Hensen, Ulrike Lomnitz, Kathrin Wuttig, Jörg Göttlicher, Ralph Steininger, Donald E. Canfield
2016, Earth and Planetary Science Letters 454, 272-281

Intense molybdenum accumulation in sediments underneath a nitrogenous water column and implications for the reconstruction of paleo-redox conditions based on molybdenum isotopes
Florian Scholz, Christopher Siebert, Andrew W. Dale, Martin Frank
2017, Geochimica et Cosmochimica Acta 213, 400-417

Contribution to research articles with multiple authors

Scholz et al. (2011): Sample collection at sea (50 %), geochemical analyses (60 %), data interpretation (100 %) and manuscript preparation (95 %).

Noffke et al. (2012): Sample collection at sea (30 %), geochemical analyses (20 %), data interpretation (40 %) and manuscript preparation (10 %).

Scholz et al. (2013): Geochemical analyses (80 %), data interpretation (100 %) and manuscript preparation (95 %).

Scholz et al. (2014a): Sample collection at sea (50 %), geochemical and isotopic analyses (70 %), data interpretation (100 %) and manuscript preparation (95 %).

Scholz et al. (2014b): Sample collection at sea (50 %), geochemical and isotopic analyses (70 %), data interpretation (100 %) and manuscript preparation (95 %).

Scholz et al. (2014c): Geochemical analyses (90 %), data interpretation (100 %) and manuscript preparation (95 %).

Dale et al. (2015): Data interpretation (30 %) and manuscript preparation (10 %).

Scholz et al. (2016): Geochemical analyses (60 %), data interpretation (80 %) and manuscript preparation (90 %).

Scholz et al. (2017): Sample collection at sea (50 %), geochemical analyses (50 %), data interpretation (90 %) and manuscript preparation (95 %).

Available online at www.sciencedirect.com

SciVerse ScienceDirect

Geochimica et Cosmochimica Acta 75 (2011) 7257–7276

Geochimica et Cosmochimica Acta

www.elsevier.com/locate/gca

Early diagenesis of redox-sensitive trace metals in the Peru upwelling area – response to ENSO-related oxygen fluctuations in the water column

Florian Scholz *, Christian Hensen, Anna Noffke, Anne Rohde, Volker Liebetrau, Klaus Wallmann

Leibniz Institute of Marine Sciences, IFM-GEOMAR, Marine Biogeochemistry, Wischhofstraße 1-3, D-24148 Kiel, Germany

Received 11 April 2011; accepted in revised form 2 August 2011; available online 9 August 2011

Abstract

Pore water and solid phase data for redox-sensitive metals (Mn, Fe, V, Mo and U) were collected on a transect across the Peru upwelling area (11°S) at water depths between 78 and 2025 m and bottom water oxygen concentrations ranging from ~0 to 93 μM. By comparing authigenic mass accumulation rates and diffusive benthic fluxes, we evaluate the respective mechanisms of trace metal accumulation, retention and remobilization across the oxygen minimum zone (OMZ) and with respect to oxygen fluctuations in the water column related to the El Niño Southern Oscillation (ENSO).

Sediments within the permanent OMZ are characterized by diffusive uptake and authigenic fixation of U, V and Mo as well as diffusive loss of Mn and Fe across the benthic boundary. Some of the dissolved Mn and Fe in the water column re-precipitate at the oxycline and shuttle particle-reactive trace metals to the sediment surface at the lower and upper boundary of the OMZ. At the lower boundary, pore waters are not sufficiently sulfidic as to enable an efficient authigenic V and Mo fixation. As a consequence, sediments below the OMZ are preferentially enriched in U which is delivered via both in situ precipitation and lateral supply of U-rich phosphorites from further upslope. Trace metal cycling on the Peruvian shelf is strongly affected by ENSO-related oxygen fluctuations in bottom water. During periods of shelf oxygenation, surface sediments receive particulate V and Mo with metal (oxyhydr)oxides that derive from both terrigenous sources and precipitation at the retreating oxycline. After the recurrence of anoxic conditions, metal (oxyhydr)oxides are reductively dissolved and the hereby liberated V and Mo are authigenically removed. This alternation between supply of particle-reactive trace metals during oxic periods and fixation during anoxic periods leads to a preferential accumulation of V and Mo compared to U on the Peruvian shelf. The decoupling of V, Mo and U accumulation is further accentuated by the varying susceptibility to re-oxidation of the different authigenic metal phases. While authigenic U and V are readily re-oxidized and recycled during periods of shelf oxygenation, the sequestration of Mo by authigenic pyrite is favored by the transient occurrence of oxidizing conditions.

Our findings reveal that redox-sensitive trace metals respond in specific manner to short-term oxygen fluctuations in the water column. The relative enrichment patterns identified might be useful for the reconstruction of past OMZ extension and large-scale redox oscillations in the geological record.

* Corresponding author. Tel.: +49 431 600 2562; fax: +49 431 6002928.

E-mail address: fscholz@ifm-geomar.de (F. Scholz).

0016-7037/$ - see front matter © 2011 Elsevier Ltd. All rights reserved.
doi:10.1016/j.gca.2011.08.007

1. INTRODUCTION

1.1. Scientific conception

It is generally accepted that the accumulation of redox-sensitive metals in marine sediments is primarily controlled by bottom water oxygen concentrations classifying the respective environment into oxic (>63 μM O_2), hypoxic (<63 μM O_2), anoxic (0 μM O_2) or anoxic-sulfidic (0 μM O_2, >0 μM H_2S) (classification after Middelburg and Levin, 2009). The fixation or liberation of metals is mostly due to the differing solubility of oxidized and reduced species. In other words, interaction between sediment pore waters and minerals is the ultimate reason for most trace metal enrichments or depletions with respect to the detrital background. Much of our knowledge on the behavior of redox-sensitive metals in oceanic pore waters has been deduced at oxic and hypoxic sites in the N Atlantic and N Pacific margins (e.g. Klinkhammer and Palmer, 1991; Shaw et al., 1994; Zheng et al., 2000; Chaillou et al., 2002; Zheng et al., 2002a; McManus et al., 2005; Morford et al., 2005) as well as in anoxic-sulfidic basins with restricted water column circulation such as the Cariaco Trench and the Black Sea (e.g. Anderson et al., 1989a,b; Barnes and Cochran, 1990; Emerson and Huested, 1991). To date, no systematic studies on the pore water chemistry of trace metals have been carried out in the pronounced eastern boundary oxygen minimum zones (OMZs) of the southern Pacific and Atlantic. This is a remarkable gap, considering that these regions strongly differ from the aforementioned systems regarding their water column circulation pattern and/or the extent of detrital input, primary productivity and oxygen depletion. The Peru upwelling system is of additional interest, since it is strongly affected by oceanographic large-scale perturbations related to the El Niño Southern Oscillation (ENSO). Understanding the influence of ENSO-related annual and interannual oscillations in bottom water redox conditions on trace metal cycling is not possible based on solid phase geochemical data alone, but necessitates a thorough examination of pore water profiles.

The trace metals studied here, V, Mo and U, are widely used as paleo-redox indicators (e.g. Brumsack, 2006; Tribovillard et al., 2006; Algeo and Tribovillard, 2009). A detailed understanding of how they respond to transient re-oxidation and redox oscillations is an important prerequisite to identify similar environmental conditions in the geological record. Moreover, climate change and anthropogenically induced eutrophication will lead to an increasing occurrence of seasonal or perennial shelf hypoxia in the coming decades (Diaz, 2001; Diaz and Rosenberg, 2008; Stramma et al., 2008). Trace element cycling in the dynamic Peruvian OMZ may therefore serve as a paradigm for future scenarios in which high-amplitude oxygen fluctuations such as those related to ENSO will occur more frequently.

In this article we discuss sediment and pore water data for V, Mo, U and related redox species (Mn, Fe, H_2S) that were collected on a transect across the Peruvian OMZ at 11°S. The comparison of authigenic mass accumulation rates and diffusive benthic fluxes enables a quantitative evaluation of the respective mechanisms of trace metal accumulation and retention or remobilization. Finally, we discuss implications for the use of U–Mo systematics as a paleo-proxy for oxygen fluctuations in bottom water and combine our results in a conceptual model, illustrating the lateral and temporal variability of V, Mo and U diagenesis across the Peru upwelling area.

1.2. Marine geochemistry of vanadium, molybdenum and uranium

The three trace metals studied here share many chemical characteristics giving rise to their joint enrichment in oxygen-deficient sediment facies. There are, however, subtle differences in their diagenetic behaviors that make this suite of elements particularly interesting for studies on redox oscillations. While Mo and U exhibit a conservative behavior in the ocean (residence time of Mo: ~800 kyr, U: ~400 kyr), a slight surface depletion is observed for V (residence time of V: ~50 kyr). In oxic seawater, their major dissolved species are oxyanions of V(V) (vanadate, HVO_4^{2-}), Mo(VI) (molybdate, MoO_4^{2-}) and U(VI) (uranyl carbonate, $UO_2(CO_3)_3^{4-}$) (Bruland and et al., 1983; Tribovillard et al., 2006).

Vanadate readily adsorbs to Mn and Fe (oxyhydr)oxides in the water column and molybdate is also well known for its strong affinity to particulate Mn (oxyhydr)oxides in oxic settings (Chan and Riley, 1966a,b; Shimmield and Price, 1986; Wehrli and Stumm, 1989; Barling and Anbar, 2004). Moreover, in a recent isotope geochemical study Goldberg et al. (2009) underscored the importance of Fe (oxyhydr)oxides as a solid carrier for Mo to the sediment surface. Upon reductive dissolution of Mn and Fe (oxyhydr)oxides in the surface sediment, V and Mo oxyanions are released into the pore water and either diffuse back into the water column or become trapped by authigenic phases within the sediments (Shaw et al., 1990; Emerson and Huested, 1991; Morford et al., 2005). In reducing (pore) waters V(V) is stepwise reduced to V(IV) and, if free H_2S is present, to V(III) (Wehrli and Stumm, 1989; Wanty and Goldhaber, 1992). Most of the reduced V species are prone to removal from the dissolved phase, through surface adsorption of vanadyl (VO^{2+}) or organic V(IV) complexes, formation of insoluble V(III) oxides or hydroxides and incorporation of V(III) in refractory organic compounds (e.g. porphyrins) or authigenic clay minerals (Breit and Wanty, 1991; Wanty and Goldhaber, 1992; Calvert and Pedersen, 1993). Molybdate undergoes successive sulfidation at H_2S concentrations above a critical threshold level (~0.1 μM; Zheng et al., 2000) leading to the formation of thiomolybdates ($MoO_xS_{4-x}^{2-}$, $1 < x < 4$) (Helz et al., 1996; Erickson and Helz, 2000). Because of the strong affinity of thiomolybdates to reactive surfaces, Mo is readily scavenged in anoxic-sulfidic environments by forming bonds with metal-rich particles (e.g. less reactive Fe oxides), Fe sulfides and sulfur-rich organic molecules (Huerta-Diaz and Morse, 1992; Helz et al., 1996; Bostick et al., 2003; Tribovillard et al., 2004; Vorlicek et al., 2004). If Mo (and presumably also V) is removed from pore water at or directly below the sediment surface, a direct diffusive flux across the benthic boundary may be established (Zheng et al., 2000).

Uranyl carbonate does not adsorb to Mn and Fe (oxy-hydr)oxides or any other inorganic particles in the water column. In reducing pore water, U(VI) is reduced to U(IV), a process that is typically observed in the Fe reduction zone (Barnes and Cochran, 1990, 1991; Klinkhammer and Palmer, 1991; Zheng et al., 2002a). Since U reduction does not occur in the water column of anoxic basins (Anderson et al., 1989a,b), it is believed to be catalyzed by reactive mineral surfaces and, most notably, enzymes produced by Fe and possibly sulfate reducing bacteria (Lovley et al., 1991; Lovley and Phillips, 1992; Lovley et al., 1993; Liger et al., 1999; Zheng et al., 2002a; Suzuki et al., 2005). Reduced U is removed from the pore water through adsorption or precipitation of U oxides (mainly uraninite, UO_2). The resulting concentration gradient promotes a downward diffusive flux of U across the benthic boundary. A variety of interlinked factors have been proposed to control the magnitude of this flux, including the bottom water oxygen concentration, the sinking rate of organic carbon and the combined rates of Fe and sulfate reduction (Zheng et al., 2002a; McManus et al., 2005, 2006; Morford et al., 2009a). It is generally agreed that most of the U in anoxic sediments is delivered by diffusion across the sediment–bottom water interface (McManus et al., 2005; Morford et al., 2009a). Notwithstanding, a few studies have revealed that a significant portion of the U buried in sediments beneath an anoxic water column may be delivered as bioauthigenic U (or particulate non-lithogenic U, PNU) which had originally formed in the photic zone (Anderson et al., 1989a; Zheng et al., 2002a,b). At oxic sites, this organically bound U is completely regenerated during its transit through the water column (Anderson, 1982). According to Zheng et al. (2002b), however, preservation of the bioauthigenic U may reach 100% if water column oxygen concentrations drop below 25 μM.

Once accumulated, trace metals may be re-mobilized if they become temporarily exposed to more oxidizing conditions, e.g. due to re-suspension and bioturbation or bioirrigation. Therefore, sediments underlying oxic bottom water retain only a small fraction of the originally delivered metals (Zheng et al., 2002a; Morford et al., 2009a,b). Because of their different sources (particulate versus diffusive) or diagenetic sinks (oxides, sulfides, association with organic molecules), V, Mo and U are anticipated to respond in different manner to lateral and temporal changes in bottom water oxygenation.

2. STUDY AREA

The coastal area off Peru (Fig. 1) is characterized by southeasterly alongshore winds driven by the Pacific Subtropical Anticyclone throughout most of the year. These atmospheric conditions promote strong offshore Ekman transport of surface waters within the Peru coastal current and upwelling of subsurface waters from the poleward flowing Peru undercurrent (Strub and Montecino, 1998). The upwelled water is oxygen-depleted and rich in nutrients thus enabling a high primary productivity in the photic zone (~3.6 g C m^{-2} d^{-1}; Pennington et al., 2006). Intense degradation of organic matter leads to a near-complete drawdown of dissolved oxygen in the water column. As a result, an OMZ is established above the Peruvian shelf and upper slope extending roughly from <100 to 700 m water depth (oxycline of 22 μM defined by Fuenzalida et al. (2009). While the lower boundary of the OMZ is relatively stable, the upper boundary underlies considerable fluctuations that are mainly tied to the passage of coastal trapped waves (Gutiérrez et al., 2008). These emerge from equatorial Kelvin waves in the equatorial East Pacific and occur more frequently during positive ENSO periods (Brink, 1982; Hormazabal et al., 2001; Pizarro et al., 2001). The propagation of coastal trapped waves is accompanied by a significant thermocline and oxycline deepening, shifting the upper boundary of the OMZ by 100 m water depth or more (Gutiérrez et al., 2008). Most intense oxygenation events have been observed during the El Niño periods of 1982/1983 and 1997/1998 during which the upper boundary of the OMZ deepened to almost 300 m (Levin et al., 2002; Fuenzalida et al., 2009). Seasonal fluctuations are of inferior importance although a maximum in wind speed and coastal upwelling has been reported for austral winter and spring (Scheidegger and Krissek, 1983; Strub and Montecino, 1998; Soto-Mardones et al., 2004).

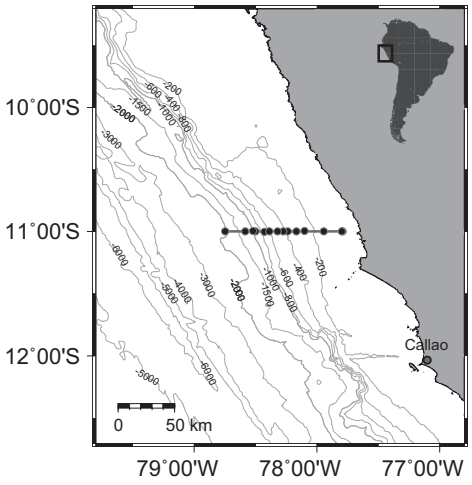

Fig. 1. Location map showing the Peruvian continental margin (bathymetric data from GEBCO 2008 data base). The sampling stations on the 11°S transect (horizontal line) are indicated by the black dots.

Offshore Peru between 10° and 14°S, upwelling-influenced sediments accumulate in a coastal mud lens extending from the depth of the wave base to 500 m water depth on the upper slope. The anomalously fine grained sediments in this area consist of a mixture of terrigenous matter with ~18 wt.% of biogenic silica and organic mater contents of up to 20 wt.% (Scheidegger and Krissek, 1983). Below the mud lens and up to a water depth of >1500 m, strong bottom currents cause reworking and winnowing of sediments leading to a much coarser grain size distribution and lower contents of organic carbon. Furthermore, the high energy regime prevailing mid-slope favors the formation and accumulation of phosphorite crusts and nodules (Reimers and Suess, 1983; Glenn and Arthur, 1988).

Table 1
Geographical coordinates, water depth and water column properties at the sampling stations. Bottom water (BW) temperatures and oxygen concentrations were derived from nearby CTD casts. Sediment data were collected for all MUCs. No pore water data for trace metals are available for MUC52, MUC26 and MUC27.

	Station	Device	Latitude S	Longitude W	Water depth (m)	BW temperature (°C)	BW O_2 (μM)
M77-1	543	MUC52	10°59.99'	77°47.40′	78	12.7	<LD
M77-1	568	BIGO-05	11°00.02′	77°47.72′	85	12.7	<LD
M77-1	470	MUC29	11°00.00′	77°56.61′	145	12.8	<LD
M77-2	016	BIGO-T	10°59.80′	78°05.91′	259	12.0	<LD
M77-1	449	MUC19	11°00.01′	78°09.97′	319	11.1	<LD
M77-1	481	MUC33	78°14.19′	11°00.00′	376	8.3	<LD
M77-1	519	MUC43	78°16.29′	11°00.01′	410	8.3	<LD
M77-1	455	MUC21	11°00.01′	78°19.24′	465	7.9	2.1
M77-1	487	MUC39	11°00.00′	78°23.17′	579	7.2	4.2
M77-1	459	MUC25	11°00.03′	78°25.60′	697	6.1	12.1
M77-1	445	MUC15	10°59.98′	78°30.02′	930	4.8	39.9
M77-1	549	MUC53	10°59.99′	78°31.27′	1005	4.7	41.6
M77-1	460	MUC26	11°00.01′	78°35.11′	1242	3.6	63.8
M77-1	462	MUC27	10°59.97′	78°44.76′	2025	2.3	93.4

<LD: Below limit of detection (~1.5–2.0 μM).

3. MATERIALS AND METHODS

3.1. Sampling and onboard analytics

Fourteen sediment cores were retrieved on a transect along 11°S during the M77-1 and M77-2 cruises of RV Meteor that took place from November 22nd to December 21st of 2008 (Fig. 1). The geographical position and water column properties of all sampling stations are summarized in Table 1. Hydrographic data and oxygen concentrations in the water column were obtained by deploying a CTD/rosette equipped with an oxygen sensor. Sediment samples were retrieved using a video-guided multiple corer (MUC) equipped with PVC liners with an inner diameter of 10 cm. After recovery, MUCs with an undisturbed sediment/bottom water interface were plugged and immediately carried into a cooling lab which was kept at in situ (i.e. seafloor) temperature. The bottom water was siphoned with a plastic tube and filtered through cellulose acetate syringe filters. Sediment subsampling was performed under inert atmosphere in an argon-flushed glove bag. The glove bag was filled and emptied repeatedly in order to remove any oxygen prior to sampling. The MUCs were cut into 1–5 cm thick slices with the highest resolution at the surface and the pore water was separated from the sediment by centrifuging for 20 min at 4500 rpm. The centrifuge vials were then transferred into a second glove bag where the supernatant water was filtered through cellulose acetate syringe filters. A small pore water aliquot was acidified in the glove bag with ascorbic acid for onboard Fe analyses. Concentrations of ferrous Fe and H_2S were determined shortly after pore water recovery by standard spectrophotometric techniques (Stookey, 1970; Grasshoff et al., 2002). Subsamples for metal analyses were stored in acid-cleaned LDPE vials and acidified with concentrated HNO_3 (supra pure). The residual sediments in centrifuge vials were frozen and stored for total digestions after the cruise. An additional sediment aliquot was taken from a parallel MUC and stored in air tight plastic cups for the determination of water content and porosity as well as for total organic carbon (TOC) and total sulfur (TS) analyses. Two of the sediment cores discussed in this article were obtained from benthic lander deployments (Biogeochemical Observatory – BIGO; Sommer et al., 2006). These cores were processed in the same way as described above for MUCs.

3.2. Chemical analyses

The TOC and TS content of freeze-dried and ground sediment samples was determined by flash combustion in a Carbo Erba Element Analyzer (NA1500) with an analytical precision of about 1% for replicate analyses. For total metal concentrations, 100 mg of freeze dried and ground sediment sample were digested in HF (40%, supra pure), HNO_3 (65%, supra pure) and $HClO_4$ (60%, p.a.). The accuracy of the digestion procedure was monitored by including method blanks and the reference standards SDO-1 (Devonian Ohio Shale, USGS; Govindaraju, 1994), MESS-3 (Marine Sediment Reference Material, Canadian Research Council) as well as the in-house standard OMZ-1. Average values of replicate digestions were generally well within the recommended ranges with relative standard deviations (RSD) being <1% for Al, Mn and Fe and <5% for V, Mo and U ($n = 9$).

The analysis of Mn, Fe and Al in digestion solutions was carried out using an inductively coupled plasma optical emission spectrometer (ICP-OES, VARIAN 720-ES). Trace metal concentrations (V, Mo and U) in digestion solutions as well as the metal concentration (Mn, Fe, V, Mo and U) of all bottom and pore water samples were measured by inductively coupled plasma mass spectrometry (ICP-MS, Agilent Technologies 7500 Series) in H_2 reaction (Fe) or He collision (other elements) mode. Samples were diluted 20-fold with 2% HNO_3 (sub-boiled, distilled) prior to analysis. Calibration standards for bottom and pore water analyses were prepared with an appropriate volume of artificial seawater in order to adjust them to the sample matrix. Samples and standards were spiked with an internal standard solution (Sc, Y and In) in order to correct for instrumental mass bias. Despite internal standardization, an instrumental drift was observed for U. Therefore, each block of four

Table 2
Accuracy values for replicate measurements of CASS-5 Nearshore Seawater Reference Material ($n = 87$). The measured values are average concentrations ± standard deviation (% RSD).

Element	Measured value (nM)	Certified value (nM)
Mn	47.0 ± 2.5 (5.4%)	47.7 ± 3.6
Fe	<LD	25.8 ± 2.0
V	24.3 ± 2.3 (9.3%)	25.9 ± 2.7
Mo	95.4 ± 1.5 (1.6%)	102[a]
U	12.1 ± 0.3 (2.3%)	12.6[a]

<LD: below limit of detection.
[a] Recommended value without certification.

samples was bracketed with a pair of an appropriate calibration standard and a certified reference standard (CASS-5, Nearshore Seawater; Canadian Research Council) was measured in the middle of each block. The drift was corrected for by calculating a drift factor from the change in U concentration measured for the calibration standard and the goodness of the correction was monitored by comparing the concentration measured for the reference standard with the certified value. Accuracies for replicate analyses of CASS-5 are summarized in Table 2. Our results for Mn and V are in good agreement with the certified ranges and precision values based on replicate measurement of CASS-5 and pore water samples are <10% RSD for all elements. CASS-5 is not certified for Mo and U but the deviation of our average values from the recommended values are <10% which is a typical uncertainty for trace metals in reference standards. Concentrations of Fe in CASS-5 are below the detection limit of our method. However, the ICP-MS results for total Fe are mostly in good agreement with the ferrous Fe data obtained onboard by spectrophotometry. Deviations >5% occur mainly at the OMZ boundaries and are therefore attributed to higher concentrations of ferric Fe. Diffusive benthic fluxes for Fe reported in later sections and all pore water Fe plots are based on the onboard Fe data.

3.3. Quantification of trace metal accumulation

Sediment mass accumulation rates (MARs; in $g\,cm^{-2}\,kyr^{-1}$) were calculated from sedimentation rate (SR; in $cm\,kyr^{-1}$), dry bulk density (ρ_{dry}; in $g\,cm^{-3}$) and the average porosity at the lower core end (ϕ_∞):

$$MAR = \rho_{dry}(1-\phi_\infty)SR$$

Sedimentation rates were obtained for selected cores by measuring gamma-ray excess ^{210}Pb activities and modeling the resulting profiles as described in Meysman et al. (2005). Porosity values were determined from the water loss after freeze drying and dry bulk density was approximated from TOC concentrations using an empirical relationship that is based on data for Peru upwelling sediments from Böning et al. (2004). Multiplying the MAR with the average authigenic metal concentration ($[Me]_{auth}$) yields the authigenic metal MAR. The authigenic metal concentration, which is defined as the difference between the total metal concentration ($[Me]_{tot}$) and the detrital background ($[Me]_{detr}$), was calculated as follows:

Table 3
Metal/Al ratios for average andesite in the Andean Arc and common reference materials.

Metal/Al	Andesite in the Andean Arc[a]	Post-Archean average shale[b]	Average upper continental crust[c]
Fe/Al	0.47	0.56	0.44
Mn/Al ($\times10^{-2}$)	1.23	0.95	0.75
V/Al ($\times10^{-3}$)	1.39	1.44	1.33
Mo/Al ($\times10^{-4}$)	0.26	0.15	0.19
U/Al ($\times10^{-4}$)	0.37	0.32	0.35

[a] GEOROC data base, Max-Planck Institute for Chemistry, Mainz, Germany (Sarbas and Nohl, 2009).
[b] Taylor and McLennan (1985).
[c] McLennan (2001).

$$[Me]_{auth} = [Me]_{tot} - \frac{[Me]_{detr}}{[Al]_{detr}}[Al]_{tot} \quad (1)$$

Böning et al. (2004) demonstrated that the chemical composition of andesite is an appropriate representation of the detrital background on the Peruvian margin. Average metal/Al ratios for andesite rocks in the Andean Arc were derived from the GEOROC data base of the Max-Planck Institute for Chemistry, Mainz, Germany (Sarbas and Nohl, 2009). A comparison between the ratios of andesite in the Andean Arc, Post-Archaean Australian average shale and average upper continental crust is provided in Table 3.

Diffusive fluxes of metals across the benthic boundary were calculated by Fick's first law of diffusion:

$$\text{Flux} = -\phi D_{sed}\frac{d[C]}{dx} \quad (2)$$

where $d[C]/dx$ denotes the concentration difference between the bottom water and the uppermost pore water sample divided by the depth of the uppermost pore water sample (0.5 cm). By definition, positive fluxes are directed into the sediment. Diffusion coefficients for metal ions in seawater (D_{sw}) were adjusted to in situ temperature and pressure using the Stokes–Einstein equation. Diffusion coefficients for sediments (D_{sed}) were calculated as:

$$D_{sed} = \frac{D_{sw}}{\theta^2} \quad (3)$$

and tortuosity (θ^2) was derived from porosity using the following relationship from Boudreau (1996):

$$\theta^2 = 1 - \ln(\phi^2) \quad (4)$$

Diffusion coefficients for Fe, Mn, Mo (MoO_4^{2-}) and U (UO_2^{2+}) under standard conditions were taken from Li and Gregory (1974), Morford et al. (2009a) pointed out that the D_{sw} of Mo would be more appropriate for calculating diffusive fluxes for $UO_2(CO_3)_3^{4-}$, the major U species in seawater. However, in order to ensure consistency with most other studies on the diagenetic behavior of U, we decided to adhere to the D_{sw} of UO_2^{2+}. Because of an apparent lack of a published D_{sw} for V, we adopted the one of Mo (MoO_4^{2-}) (cf. Emerson and Huested, 1991), which appears to be reasonable considering that oxyanions are the major V species in seawater (see Section 1.2).

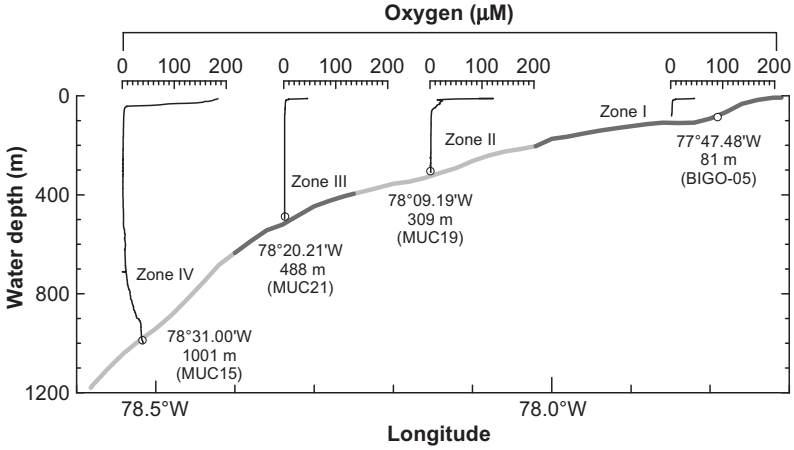

Fig. 2. Bathymetry (data from GEBCO 2008 database) and concentration-depth profiles for dissolved oxygen at selected CTD stations on the 11°S transect. The alternating shades of gray of the bathymetry represent zones I to IV in Fig. 3. Circles depict the exact location of the CTD casts. The sediment core closest to each station is given in parentheses.

4. RESULTS AND DISCUSSION

4.1. Sediment redox state and diagenetic zoning

At the time of sampling, the Peruvian margin was overlain by a pronounced OMZ with the core ($O_2 < 2$ µM) ranging roughly from 50 to 500 m water depth (Fig. 2). Pore water profiles of Mn, Fe, H_2S, U, V and Mo are shown in Fig. 3. The stations are ordered according to increasing water depth and combined in 4 subpanels based on similarities in the shape of their pore water profiles. These subpanels and the corresponding areas on the margin (i.e. water column and sediments) will be referred to as zone I (shallowest stations) to zone IV (stations below ~600 m water depth) in the following sections. Fig. 2 shows exemplary oxygen profiles in the water column for each of the four zones. The only zone where bottom water oxygen concentrations rose above a few µM during the sampling campaign is zone IV.

Highest dissolved Mn and Fe concentrations (up to 190 nM of Mn and 35 µM of Fe) are observed in zone I where pore water profiles of Mn and Fe display pronounced maxima close to the sediment/bottom water interface. Lower concentrations and less steep concentration-depth gradients prevail in zones II and III. In zone IV, the uppermost few cm of the sediments show again a surface maximum in Mn whereas the Fe concentrations drop to zero. Diffusive benthic fluxes for Mn, Fe, U, V and Mo are shown in Table 4 and plotted against water depth in Fig. 4. Highest flux values for both Mn and Fe are observed in the shallowest core in zone I (BIGO-05). The Mn fluxes decrease steadily with increasing water depth to values close to zero in MUC21 (465 m) and increase again below. The Fe fluxes are more randomly distributed in zones II and III and are zero in zone IV.

The Mn and Fe flux across the benthic boundary is driven by reductive dissolution of reactive Mn and Fe (oxyhydr)oxides in the surface sediments (Froelich et al., 1979; Burdige, 1993; Pakhomova et al., 2007). Notwithstanding, most of the Mn which is delivered to the OMZ is already reduced in the water column (cp. Böning et al., 2004). This is illustrated by low pore water Mn concentrations and diffusive fluxes compared to other continental margin settings (Figs. 3 and 4; cp. Pakhomova et al., 2007 and references therein), little downcore variability of Mn/Al in the sediments (see Supplementary EA-Table 1 in the Electronic Annex) and a strong depletion of Mn with respect to the detrital background in sediments on the entire continental margin (Fig. 5 and Böning et al., 2004). Some Fe reduction might occur in the water column as well. However, the benthic Fe fluxes reported here fall in the upper range of values reported for a wide range of environments (Severmann et al., 2010; Noffke et al., 2011), suggesting that the surface sediments are the principal locus of Fe reduction in the Peruvian OMZ. A similar conclusion has been drawn by Bruland et al. (2005) based on the distribution of dissolved ferrous Fe in the water column. The magnitude of the diffusive Fe flux across the sediment/bottom water interface is controlled by both the bottom water oxygen concentrations and the availability of reactive Fe (Pakhomova et al., 2007; Severmann et al., 2010). Assuming that the bottom water oxygen level remains favorable for the transfer of ferrous Fe across the benthic boundary for a prolonged period of time, the reactive Fe pool will become progressively depleted, unless it is replenished through detrital input. Such a scenario of reactive Fe depletion in sediments underlying a permanently anoxic but non-sulfidic water column is in agreement with Fe/Al ratios significantly below the detrital background in zones II and III (Fig. 5) and low concentrations of reactive Fe minerals in the central part of the OMZ reported by Suits and Arthur (2000). Apparently, detrital inputs from the continent are not sufficient to balance the reductive loss of Fe from sediments in this section of the Peruvian margin. Some of the released Fe seems to be laterally transported in the water column and re-oxidized and deposited at the oxycline in zone IV (~900–1100 m) where Fe/Al ratios increase above the detrital background (Fig. 5). Here, elevated bottom water oxygen levels (~40 µM, Table 2 and Fig. 2) prevent the Fe which is reduced in the sediments from being transported across the benthic boundary (Fig. 3). Therefore,

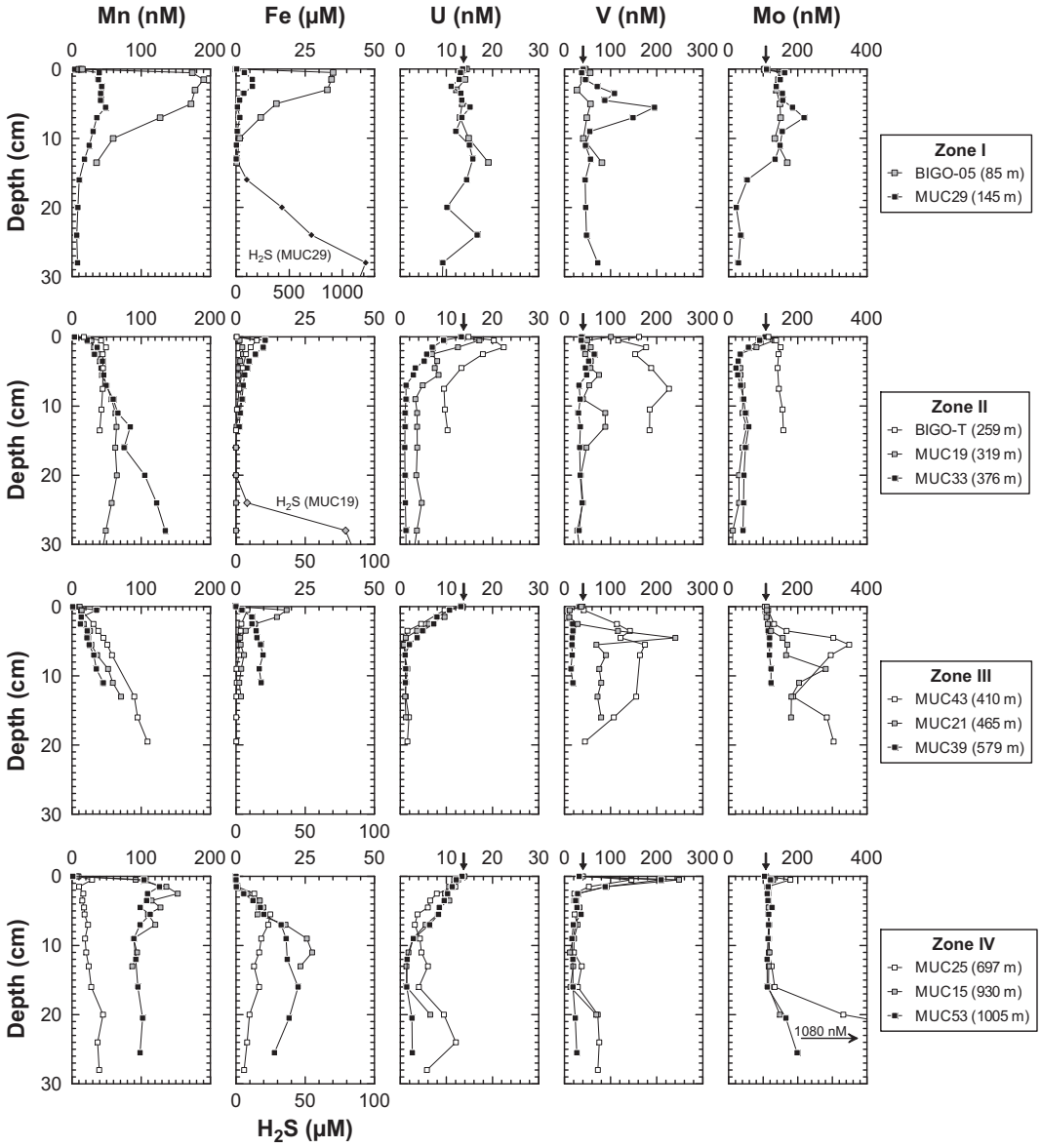

Fig. 3. Pore water profiles for Mn, Fe, H_2S, U, V and Mo. Concentrations of Fe and H_2S (diamonds) are shown in common diagrams. The only stations where H_2S concentrations were found to be above the detection limit of the method applied (~2 μM) are MUC29 and MUC19. The uppermost data point of each profile (depth of zero) represents bottom water concentrations. Arrows above upper *x*-axis indicate average seawater values ($[U]_{sw} = 13.7$ nM, $[V]_{sw} = 40.3$ nM, $[Mo]_{sw} = 108$ nM).

most of the delivered excess Fe may be retained in the sediments. A similar export mechanism of reactive Fe has been reported for sediments of the Arabian and Mexican upwelling areas where sedimentary Fe/Al ratios are significantly higher below than within the OMZ (Van der Weijden et al., 1999; Nameroff et al., 2002). In analogy to Fe, increasing pore water Mn concentrations (Fig. 3) and diffusive benthic fluxes (Fig. 4) below zone III could imply a relative enrichment of Mn at the sediment surface in zone IV. However, because of its shallower reduction zone and sluggish oxidation kinetics compared to Fe, most of the Mn which is liberated at the sediment surface may diffuse back into the water column. As a consequence of this shallow recycling, any delivery of 'excess' Mn in zone IV is not recorded in the Mn/Al ratios (Fig. 5).

The relatively high benthic Fe fluxes observed at the shallowest station (BIGO-05) may partly be due to an increased supply of detrital (oxyhydr)oxides from the continent (Suits and Arthur, 2000). Another portion of the pore water Fe at the shelf stations, however, has likely been delivered from zones II and III through lateral transport of dissolved Fe in the water column and re-oxidation and deposition at the upper oxycline during periods of shelf oxygenation. Upon the recurrence of anoxic conditions (like those prevailing during our sampling campaign), this pool of excess Fe is reduced and partly recycled into the water column, thus leading to particularly high benthic fluxes compared to stations in zones II and III. A similar alternation of particulate supply and reductive release may be anticipated for Mn which shows also higher pore

Table 4
Diffusive flux of Mn, Fe, U, V and Mo across the sediment/bottom water interface. Positive values denote a downward flux into the sediment.

Core	Water depth (m)	Diffusive benthic flux				
		Mn (nmol cm^{-2} yr^{-1})	Fe (μmol cm^{-2} yr^{-1})	U (nmol cm^{-2} yr^{-1})	V (nmol cm^{-2} yr^{-1})	Mo (nmol cm^{-2} yr^{-1})
BIGO-05	85	−40.6	−8.83	+0.13	−4.5	−16.7
MUC29	145	−9.3	−0.66	+0.08	+1.3	−19.7
BIGO-T	259	−6.5	−1.89	−0.90	+17.2	−8.3
MUC19	319	−5.7	−0.33	−0.64	+18.7	−8.6
MUC33	376	−4.0	−2.30	+0.53	+0.1	+4.9
MUC43	410	−2.2	−0.85	+0.52	−0.8	−2.9
MUC21	465	−0.5	−3.19	+0.31	+6.2	−0.1
MUC39	579	−6.9	−0.43	+0.30	+6.1	−1.3
MUC25	697	−3.1	0	+0.10	−24.1	−16.1
MUC15	930	−12.5	0	+0.20	−45.6	−4.6
MUC53	1005	−13.1	0	+0.10	−32.6	−3.2

water concentrations and diffusive benthic fluxes in zone I compared to zones II and III. As Mn/Al ratios in zone I are similarly low as in the other zones (Fig. 5), it is anticipated that accumulation of Mn during oxic periods and release during anoxic periods largely cancel out each other. In contrast, the Fe/Al ratios are equal to or slightly above the detrital background in zone I suggesting a more efficient trapping of the reactive Fe which is delivered from land and the OMZ during periods of shelf oxygenation. This is in agreement with results from Suits and Arthur (2000) who reported the highest degrees of pyritization (DOPs) and the highest pyrite concentrations on the entire Peruvian margin for sediments on the shelf.

The above discussion of Mn and Fe data reveals a complex interplay between reductive release, lateral transport, deposition and recycling across the margin. This framework of how redox gradients and oscillations affect metal cycling in the Peruvian OMZ will be revisited and substantiated in the following discussion of U, V and Mo data.

4.2. Controls on the benthic flux of trace metals

4.2.1. Uranium

Most sediment cores in zone II to zone IV show dissolved U concentrations decreasing downward from seawater-like values at the top to 1.0–3.0 nM at 5–10 cm below surface (Fig. 3). At greater sediment depth, U concentrations remain either constant or increase again in MUC15 and MUC53. In agreement with previous studies on anoxic marine sediments, the removal of U close to the sediment surface is attributed to reduction of U(VI) to U(IV) followed by precipitation of UO_2 or other authigenic U phases (e.g. Barnes and Cochran, 1990, 1991; Klinkhammer and Palmer, 1991). The resulting downward diffusive U flux increases between zone IV and zone II and reaches its highest value in MUC33 at 376 m (Table 4, Fig. 4). Previous studies in a broad range of oxic and hypoxic marine settings revealed striking relationships between authigenic U accumulation and the organic carbon rain and degradation rates as well as the oxygen penetration depth (Zheng et al., 2002a; McManus et al., 2005; Morford et al., 2009a). All of these parameters dictate the extent of reducing conditions in the surface sediments and, therefore, the activity of Fe and sulfate reducing bacteria, both of which are capable of mediating U reduction (Lovley et al., 1991; Lovley and Phillips, 1992; Zheng et al., 2002a). During our sampling campaign, the Peru margin was characterized by a continuous landward decrease in bottom water oxygen concentration (Table 1, Fig. 2) and increasing carbon rain and degradation rates as well as Fe and sulfate reduction rates towards the shore (Bohlen et al., 2011). Furthermore, U depletion occurred generally at or shortly below the depth of the highest Fe concentrations (Fig. 3). These observations support the general conception that authigenic U accumulation is controlled by the combined rates of Fe and sulfate reduction close to the sediment/bottom water interface (Zheng et al., 2002a; McManus et al., 2005).

At depths shallower than MUC33, surface sediments are still favorable for U reduction, which is demonstrated by maxima in dissolved Fe at 0.5 cm and bottom water oxygen concentrations close to zero. However, dissolved U concentrations above bottom water values at the sediment surface of MUC19 and particularly BIGO-T (Fig. 3) indicate a considerable diffusive U flux out of the sediments (Table 4, Fig. 4). Furthermore, pore water U profiles in zone I do not show any regular U depletion but scatter around bottom water values. Similar U profiles have been observed in bioturbated and/or bioirrigated sediments underlying oxic bottom water (Zheng et al., 2002a; Morford et al., 2009a,b) or in estuaries with seasonal oxygen fluctuations in the water column (Shaw et al., 1994). In such settings, authigenic U which had precipitated during more reducing periods undergoes transient re-oxidation and recycling through diffusion across the benthic boundary. Pore water U in zone I follows a highly transient zig–zag-pattern which may be ascribed to ENSO-related high amplitude changes between oxic and anoxic conditions. In contrast to that, the dissolved U distribution in MUC19 is much closer to steady state with respect to the present bottom water oxygen level (cf. MUC33). Accordingly, the continuous growth of the surficial U peak between >320 and ~250 m (MUC19, BIGO-T) and the absence of any pore water U depletion in zone I are attributed to the enhanced intensity, frequency and duration of oxygenation episodes with decreasing water depth (Gutiérrez et al., 2008).

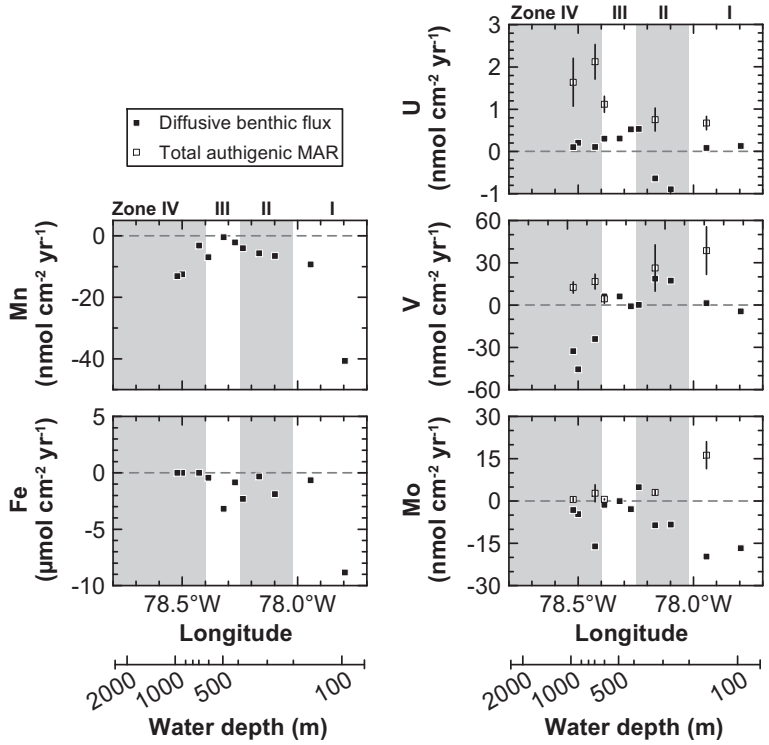

Fig. 4. Plots of diffusive benthic fluxes (Mn, Fe, V, Mo and U) for all cores where pore water data are available and authigenic MARs for selected cores (U, V and Mo) against longitude. An alternative scale bar translating longitude into water depth is shown as well. The exact values and error margins are listed in Tables 4 and 5. Positive diffusive fluxes are directed downward into the sediment. Horizontal dashed lines depict a diffusive flux or MAR of zero. The grayish and whitish arrays represent zones I to IV in Fig. 3.

Zheng et al. (2002a) reported a threshold oxygen level of 15 µM above which U remobilization may occur. However, Levin et al. (2002) pointed out that even during the intense El Niño event of 1997/1998 the bottom water oxygen concentration at the deepest station where U remobilization is observed (MUC19) did not rise above ~2.2 µM. Although the Peruvian margin experienced several positive ENSO periods in the years prior to our sampling campaign, there was no major El Niño event comparable to those of 1982/1983 and 1997/1998 (see Fig. A1 Appendix A for a time series of the Oceanic Niño Index, ONI). We therefore assume that even a minute increase in bottom water oxygen concentration (i.e. $\leqslant$2 µM), shifting the U(VI)/U(IV) boundary by a few cm, may be sufficient to cause shallow remobilization of authigenic U. The shift of the redox boundary is likely supported by reduced fluxes of particulate organic carbon from the overlying water column during positive ENSO periods (Gutiérrez et al., 2000). Another factor that potentially enhances U remobilization is the activity of bioturbating organisms. Levin et al. (2002) and Gutiérrez et al. (2008) demonstrated that bioturbating fauna rapidly inhabits the Peruvian shelf and upper slope sediments during oxygenation episodes and even persists for several months after anoxic conditions have reestablished.

4.2.2. Vanadium and molybdenum

It has been argued in previous studies that downward diffusion of V and Mo across the sediment/bottom water interface due to authigenic removal is the primary mechanism of V and Mo accumulation in sediments on the Peruvian margin and other upwelling areas (Zheng et al., 2000; Böning et al., 2004, 2009). A downward directed concentration gradient across the sediment surface requires a shallow authigenic V and Mo sink. This sink must be highly effective to prevent any excess V and Mo that is released from Mn and Fe (oxyhydr)oxides from accumulating in pore water. Otherwise a shallow peak will establish promoting both an upward directed diffusive flux across the benthic boundary and a downward flux towards the authigenic sink.

Most sediment cores in zones I to IV display dissolved V and Mo concentrations above local bottom water values in the uppermost section of the sediment column (~0–10 cm; Fig. 3). Some of these shallow peaks coincide with maxima in dissolved Mn and Fe suggesting a common supply or cycling of V and Mo with Mn and/or Fe. This is particularly the case in zone IV where both V and Mo display pronounced peaks in the Mn reduction zone (up to 248 nM of V and 179 nM of Mo). However, dissolution of Mn (oxyhydr)oxides alone is unlikely to account for the shallow V and Mo enrichment in pore water since diffusive benthic Mn fluxes range in the same order of magnitude as the diffusive V and Mo fluxes (Table 4, Fig. 4). For comparison, in other settings where release of V and Mo from Mn (oxyhydr)oxides has been postulated, dissolved Mn concentrations in pore water (and by inference the diffusive benthic fluxes) exceed those of V and Mo by several orders of magnitudes (Shaw et al., 1990; Morford et al., 2005).

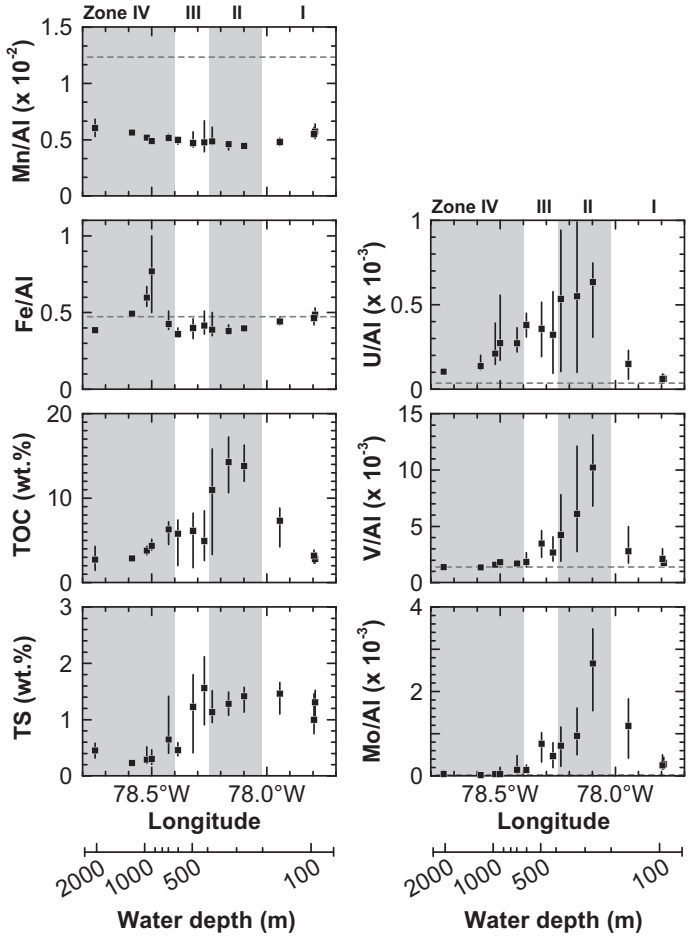

Fig. 5. Average Mn/Al, Fe/Al, TOC, TS, U/Al, V/Al and Mo/Al ratios for each core plotted against longitude. An alternative scale bar translating longitude into water depth is shown as well. Normalized metal concentrations are used to eliminate the effect of varying dilution with detrital material. Error bars span the range between the highest and lowest value of each core. Horizontal dashed lines depict the metal/Al ratio of the detrital background (andesite in the Andean Arc, see Table 2). The grayish and whitish arrays represent zone I to zone IV in Fig. 3. Solid phase geochemical data are summarized in Supplementary EA-Table 1 and EA-Table 2 in the Electronic Annex.

Surface sediments in zone IV receive high loads of reactive Fe that has been supplied from zones II and III through lateral transport within the anoxic water column and re-precipitation at the lower boundary of the OMZ (cf. Section 4.1). However, since the regeneration of V and Mo occurs at shallower sediment depth than Fe reduction, release during quantitative dissolution of Fe (oxyhydr)oxides cannot account for the surficial V and Mo peaks either. In fact, the coinciding zones of V, Mo and Fe removal at 2–3 cm do rather suggest that most of the V and some of the Mo released at the sediment surface is re-adsorbed to Fe (oxyhydr)oxides shortly below. Another possible explanation for the shallow V and Mo accumulation in pore waters of zone IV is release form fragile organic substances in the thin oxic surface layer (Brumsack and Gieskes, 1983; Audry et al., 2006). Neither of the above explanations can be verified based on our data. However, since both V and Mo are attracted by metallic surfaces under oxic conditions (e.g. Chan and Riley, 1966a,b; Barling and Anbar, 2004; Goldberg et al., 2009) and since they are both liberated concomitantly with Mn we anticipate that some kind of particulate shuttle is involved. Below the shallow peaks, the presence of dissolved Fe and seawater-like V and Mo concentrations indicate that H_2S concentrations in pore waters of zone IV are too low as to drive significant V reduction or Mo sulfidation. As a consequence, most of the liberated V and Mo is lost through diffusion across the benthic boundary (see negative benthic fluxes in Table 4 and Fig. 4). Again increasing concentrations below 15 cm indicate ongoing mobilization of V and Mo (and also U) below the depth of Mn and Fe recycling. This could be related to deep-reaching bioturbation and/or bioirrigation causing re-oxidation of authigenic metal phases that were precipitated during more reducing periods or at greater sediment depth (Morford et al., 2009b). This explanation is supported by findings of Levin et al. (2002) who reported a comparably high abundance of burrowing fauna below the permanent OMZ.

Pore water profiles in zone I and the shallowest core in zone II (BIGO-T) display somewhat erratic V and Mo peaks both within and below the Mn and Fe reduction zones. Release from either Mn or Fe (oxyhydr)oxides can-

not be distinguished at the given sampling resolution. However, the coincident Mn, Fe and Mo increase in the uppermost cm (Fig. 3) and the high upward diffusive Mn, Fe and Mo fluxes (Table 4, Fig. 4) in zone I suggest some Mo release from dissolving (oxyhydr)oxides. The lack of a significant benthic V flux might be related to shallow re-adsorption of V(IV) species that are known to form in manganous or ferruginous pore waters (e.g. Calvert and Pedersen, 1993). Below the Mn and Fe reduction zone and up to a depth of ~10 cm, pore water profiles of V and Mo display a similar zig–zag-pattern as the U profiles. These transient irregularities indicate that V and Mo are also affected by remobilization during periods of shelf oxygenation. The pore water Mo profile of MUC29 in zone I shows a steep decrease below 13 cm which is coincident with the accumulation of H_2S (Fig. 3). This is in excellent agreement with the general conception of Mo being scavenged from pore water at a critical threshold concentration of H_2S (Helz et al., 1996; Erickson and Helz, 2000; Zheng et al., 2000). Intense Mo authigenesis close to the sediment surface would theoretically support a downward diffusive Mo flux across the benthic boundary. However, because of the shallow accumulation of dissolved Mo from metal (oxyhydr)oxides and re-dissolved authigenic phases, the actual benthic flux in MUC29 is directed out of the sediment (Table 4 and Fig. 4).

At greater depth than BIGO-T, re-oxidation occurs less frequently, which should favor shallow Mo authigenesis and diffusive resupply from the bottom water. Both MUC19 and MUC33 in zone II display sharp concentration gradients at or shortly below the sediment surface and a Mo minimum at shallow depth (<30 nM at 3–5 cm; Fig. 3). We did not detect any shallow H_2S in MUC19 and MUC33. However, the threshold level for sulfidation of molybdate and Mo–Fe–S co-precipitation reported by Zheng et al. (2000) is clearly below the detection limit of our H_2S method (~2 μM). Therefore, active Mo authigenesis might have occurred at the time of sampling. Both MUC19 and MUC33 display TOC maxima at 3 to 7 cm depth (see Supplementary EA-Table 2 in the Electronic Annex) suggesting that hot spots of H_2S production are associated with organic-rich micro niches. MUC33 is the only core where a significant downward benthic Mo flux was observed in this study (Table 4). In this permanently anoxic area of the Peruvian margin, the development of a downward decreasing Mo gradient across the benthic boundary is likely favored by the continuous stripping of Mn and Fe in the water column and the surface sediments, respectively (see Section 4.1). Because of the strong Mn and Fe depletion arising from that (Fig. 5), sediment particles provide little adsorption sites for Mo which would then impede the downward benthic flux upon its release during early sediment diagenesis.

Pore water profiles of V and Mo in zone III are more heterogeneous and generally somewhat scattered. This is commonly observed in continental margin sediments (e.g. Shaw et al., 1990; Morford et al., 2005) and has been assigned to H_2S production in microenvironments (Zheng et al., 2000) and the contrasting solubility of V and Mo species in manganous or ferruginous versus sulfidic pore waters (Calvert and Pedersen, 1993; Algeo and Maynard, 2004). Furthermore, zone III is located at the transition between the permanently anoxic and the hypoxic section of the Peruvian margin (Table 1, Fig. 2). Although fluctuations in bottom water oxygenation are less frequent and vigorous here compared to zone I, non-steady state diagenesis might have contributed to the irregular shape of the pore water profiles. The negative excursions in the Mo profiles of zone III may indicate some Mo authigenesis in distinct depth intervals. However, Mo concentrations are always ⩾bottom water values suggesting that pore waters are generally not sulfidic enough as to support an appreciable downward benthic Mo flux. Authigenic removal of V(IV) may also take place under non-sulfidic conditions (e.g. Calvert and Pedersen, 1993), which could explain the downward benthic V flux in MUC21 and MUC39 (Table 4).

In summary, the pore water V and Mo data suggest that direct diffusive supply of V and particularly Mo is limited to sediments in a narrow depth range underlying the most persistent and pronounced OMZ (~ > 320–400 m). In the other areas, V and Mo are rather delivered with solid carriers such as detrital particles whose surfaces are coated with metallic (oxyhydr)oxides. Strictly speaking, this interpretation is only valid for the exact time of our sampling campaign. However, the sampling was conducted following a 1-year-lasting negative ENSO period (see Fig. A1 Appendix A) and during the season of most intense upwelling (e.g. Scheidegger and Krissek, 1983). It is unlikely, that conditions are much more favorable for diffusive V and Mo supply during other, presumably more oxic periods.

4.3. Long-term accumulation of trace metals

All of the three trace elements investigated show highest Al-normalized concentrations in zone II, coincident with the TOC maximum (Fig. 5). At greater water depth, V and Mo concentrations drop rapidly to the detrital background whereas U concentrations remain elevated on the entire continental margin. The opposite is observed on the shelf, where U and V concentrations drop abruptly at depth ⩽ BIGO-T whereas Mo concentrations decrease more gradually. These patterns are generally in good agreement with previously published data for the Peruvian upwelling area (Böning et al., 2004).

Table 5 shows a compilation SRs, MARs and authigenic metal MARs for selected cores (see Supplementary EA-Fig. 1 in the Electronic Annex for profiles of excess ^{210}Pb and model fits). Dividing the SRs by the length of the respective cores reveals that the study intervals cover a time span of approximately 300 (MUC29) to 1000 (MUC19) yr. A comparison of diffusive benthic U, V and Mo fluxes with authigenic MARs is provided in Fig. 4. The above defined depth range, encompassing the most persistent and pronounced OMZ (~ > 320–400 m or 78.15–78.25°W), is the only area where the diffusive supply of all trace metals investigated is broadly in agreement with their total authigenic MARs (extrapolating the authigenic MAR of MUC19 to the neighboring core MUC33). In the remaining areas, the lack of agreement between these two calculated

Table 5
Compilation of sedimentation rates (SR), mass accumulation rates (MARs) and authigenic metal MARs for selected cores. See Supplementary EA-Fig. 1 in the Electronic Annex for profiles of excess ^{210}Pb and model fits.

Core	Water depth (m)	SR (cm kyr^{-1})	ϕ_∞	ρ_{dry} (g cm^{-3})[b]	MAR (g cm^{-2} kyr^{-1})	Authigenic metal concentration[c]			Authigenic metal MAR		
						$[U]_{auth}$ (nmol g^{-1})	$[V]_{auth}$ (nmol g^{-1})	$[Mo]_{auth}$ (nmol g^{-1})	U (nmol cm^{-2} yr^{-1})	V (nmol cm^{-2} yr^{-1})	Mo (nmol cm^{-2} yr^{-1})
MUC29	145	160[a]			28[a]	23 ± 6	1275 ± 604	580 ± 170	0.65 ± 0.16	36 ± 17	16.2 ± 4.8
MUC19	319	50	0.89	1.54	8	89 ± 32	3033 ± 1937	363 ± 114	0.75 ± 0.27	26 ± 16	3.1 ± 1.0
MUC39	579	26	0.70	2.27	18	63 ± 11	170 ± 174	34 ± 9	1.11 ± 0.19	3.0 ± 3.1	0.60 ± 0.16
MUC25	697	81	0.70	2.18	53	39 ± 8	252 ± 101	51 ± 57	2.08 ± 0.41	13 ± 5	2.7 ± 3.0
MUC53	1005	58	0.63	2.38	51	31 ± 11	175 ± 77	7 ± 12	1.60 ± 0.56	9 ± 4	0.35 ± 0.61

[a] Approximate SR and MAR derived from Reimers and Suess (1983).
[b] Dry bulk density was estimated from TOC using an empirical relationship that is based on data for Peru upwelling sediments from Böning et al. (2004): $\rho_{dry} = -0.08[TOC] + 2.68$ ($R^2 = 0.70$, $n = 16$).
[c] Given as mean value ± SD.

parameters could reflect temporal variability in pore water chemistry. However, as ENSO conditions were negative during the 12 months preceding our sampling campaign, it may be anticipated that redox conditions on the Peruvian margin were rather favorable for diffusive V and Mo supply (see Fig. A1 Appendix A and previous section). This, along with the striking mismatch between the highest U MARs (zone IV) and the location of the permanent OMZ, suggests that mechanisms other than diffusion across the benthic boundary should be considered for trace metal supply and/or accumulation in the remaining areas.

4.3.1. Solid phase speciation of uranium

Authigenic U MARs in zone IV exceed the corresponding benthic fluxes by a factor of up to 20 and are higher than any of the benthic fluxes hitherto reported for anoxic marine sediments (up to 1.52 nmol cm^{-2} yr^{-1} in the California Borderland Basins; Zheng et al., 2002a). The only known additional source of authigenic U to marine sediments is particulate non-lithogenic U (PNU) in sinking organic matter (Anderson et al., 1989a; Zheng et al., 2002a,b). Preservation of PNU is favored by the persistent anoxia in the Peruvian OMZ (Zheng et al., 2002b). Moreover, the distribution of U/Al ratios and TOC concentrations across the margin is highly correlated (Fig. 5, $R^2 = 0.79$, $n = 148$) suggesting that organic matter plays more than an indirect role for the authigenic accumulation of U. The plausibility of PNU as an important U source to the sediment may be evaluated by comparing the U/TOC ratios of water column particulate matter and surface sediments. Unfortunately, we do not dispose of U/TOC ratios for particulate matter off Peru. Zheng et al. (2002) reported U/TOC ratios of 0.33–0.45 × 10^{-4} for water column particulate matter in the NE Pacific, offshore California. The U/TOC ratios of surface sediments in zone I (0.64–0.94 × 10^{-4}) are broadly in agreement with this range. Moreover, Hirose and Sugimura (1991) pointed out, that U/TOC ratios in sinking organic matter increase exponentially over more than one order of magnitude with increasing primary productivity. Considering the particularly high primary productivity in Peru coastal waters (Pennington et al., 2006), most of the U/TOC ratios in surface sediments (0.64–2.1 × 10^{-4}) are in agreement with a high contribution of PNU to the overall U supply. However PNU is unlikely the burial phase causing the difference between diffusive and total U accumulation in zones III and IV (Fig. 4). This is illustrated in Fig. 6, a plot of U/TOC ratios against sediment depth. The U/TOC ratios in zones I and II are either constant or increase in the top 10 cm to values of ~2.5 × 10^{-4}. This is in agreement with organic matter degradation as well as U reduction and precipitation from pore water. In contrast to that, U/TOC ratios in zone III are more heterogeneous with maximum values as high as 12 × 10^{-4} shortly below the sediment surface. These values are far too high as to be explained with PNU as the primary host phase. Consequently, some mechanism of diagenetic redistribution has to be considered. Because of strong bottom currents and the associated effects of reworking and winnowing, zone III reveals low net sedimentation rates (Table 5), which favors the formation and accumulation of phosphorite crusts

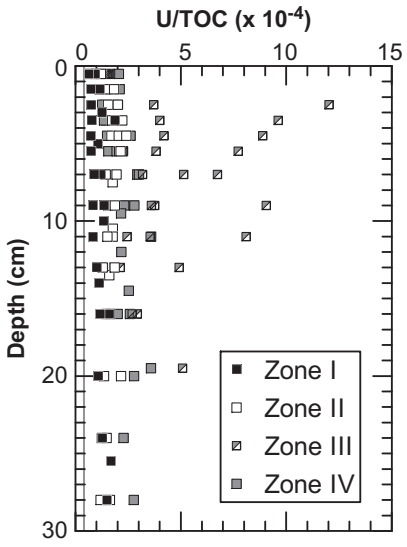

Fig. 6. Plot of U/TOC ratios versus sediment depth. The vertical gray line indicates the range of U/TOC ratios published for water column particulate matter in the NE Pacific, offshore California (Zheng et al., 2002b).

and nodules (Reimers and Suess, 1983; Glenn and Arthur, 1988). In agreement with this general observation, numerous macroscopic phosphorite concretions were recovered from the MUCs in zone III and previous studies revealed increasing P concentrations and P/C ratios across the Peruvian margin (Böning et al., 2004). Phosphorites are known to be enriched in U with respect to both the detrital background and the surrounding sediment matrix (Veeh et al., 1974; Jarvis et al., 1994) and Böning et al. (2004) reported a good correlation between U and P for a sediment core from the Peruvian slope (598 m water depth). Combining the average inorganic P concentration (i.e. corrected for the organic P content) of 1.9 wt.% reported for this core by Böning et al. (2004) with the range of U concentrations published by Arning et al. (2009) for phosphorite crusts from the Peruvian margin ($\sim$150–280 μg g^{-1} or U/P ratio of $\sim 0.9–1.7 \times 10^{-4}$) yields phosphorite-bound U concentrations of $\sim$17–32 μg U g^{-1} bulk sediment. This calculation further substantiates the assumption of Böning et al. (2004) that authigenic phosphorite is most likely an important host for U in Peru slope sediments (80–250% of the U MAR in zone III). Glenn and Arthur (1988) emphasized the role of lateral sediment transport and reorganization for the enrichment of phosphorites on the Peruvian slope. Sediment MARs increase below zone II (Table 5) leading to increasing authigenic U MARs (Fig. 4), despite a general decrease in U/Al (Fig. 5). It is therefore anticipated that much of the U buried in zones III and IV is of allochthonous origin, i.e. has originally accumulated further upslope. The ultimate origin of the phosphorite-bound U (dissolved U in pore water versus PNU) and the mode of incorporation (inorganic versus microbial mechanism) cannot be resolved based on our data. However, in consideration of the apparent imbalance between diffusive and total U supply in most areas on the Peruvian margin, at least some of the U buried is likely delivered as PNU or another, yet unidentified U phase.

4.3.2. V–Mo–U covariation in Peru upwelling sediments

The lowest authigenic MARs of V and Mo as well as the lowest V/Al and Mo/Al ratios are observed in zone IV and the deepest core in zone III (Figs. 4 and 5). This in agreement with the pore water data suggesting that redox conditions below the permanent OMZ are not reducing enough as to enable a downward benthic flux or an efficient authigenic removal of the V and Mo that is released from solid carriers. Lateral input of phosphorite-rich sediments from further upslope cannot compensate for that, since authigenic phosphorites do not sequester V or Mo to a significant extent (Jarvis et al., 1994). The small but still significant V MAR observed in zone IV might be related to lateral supply of some other authigenic V phase from further upslope or to re-adsorption of V(IV) to refractory Fe (oxyhydr)oxides. In sharp contrast to U, authigenic MARs of V and Mo are most pronounced in MUC29 in zone I where they exceed all of the benthic fluxes observed in this study. A similar mismatch between diffusive and total authigenic Mo supply has been postulated (though not proven based on pore water data) for weakly restricted basins with redox variations at short time scales (e.g. Saanich Inlet and Cariaco Basin) (Algeo and Lyons, 2006; Algeo and Tribovillard, 2009). In such settings, vertical fluctuations of the chemocline alternately promote (i) Mo scavenging by Mn and Fe (oxyhydr)oxides that precipitate in the water column during oxic periods and (ii) reductive recycling of the Mn and Fe at the sediment surface as well as sulfidation and fixation of the released Mo during anoxic periods (Berrang and Grill, 1974; Adelson et al., 2001; Algeo and Lyons, 2006). This particulate shuttle leads to an enhanced supply of particle-reactive elements as compared to those that are chiefly delivered by molecular diffusion (e.g. U) (Algeo and Tribovillard, 2009). On the Peruvian shelf, the continuous displacement of the upper boundary of the OMZ likely exerts a similar effect on Mo cycling. During periods of shelf oxygenation, surface sediments receive particulate Mo associated with terrigenous Mn and Fe (oxyhydr)oxides. This terrigenous supply is particularly pronounced during El Niño events, when otherwise arid coastal Peru receives heavy rainfall resulting in enhanced continental erosion and runoff (Wells, 1990). Moreover, additional (oxyhydr)oxides are likely supplied through reoxidation and precipitation of dissolved Mn and Fe at the retreating upper oxycline of the OMZ. After the recurrence of anoxic conditions, the (oxyhydr)oxides are reductively dissolved and recycled whereas the hereby liberated Mo is removed into authigenic phases. This scenario is in excellent agreement with the pore water Mo profile of MUC29, indicating both Mo release and authigenic removal, as well as the relatively high upward directed benthic fluxes of Mn and Fe in zone I compared to zones II and III. Moreover, a particulate shuttle, driven by ENSO-related fluctuations in bottom water oxygenation, is a viable explanation for the decoupling of U and Mo accumulation on the Peruvian shelf. However, the pore water profiles in zone I do not only indicate Mo release from metal (oxyhydr)oxides but also

Mo, V and U remobilization. Consequently, not only preferential supply but also preferential loss of specific elements has to be considered in this discussion.

Further insights into the different modes of trace metal supply versus remobilization may be obtained from cross plots of authigenic Mo versus authigenic V und U concentrations (Fig. 7). Concomitantly increasing authigenic V and Mo concentrations in zones IV and III (Fig. 7a) reflect the decreasing sediment redox potential determined by decreasing bottom water oxygen concentrations towards the core of the OMZ. MUC33 and MUC19 in zone II display a separate trend implying a relative increase in the efficiency of V accumulation. This is likely related to the abrupt TOC increase from ~5 to >10 wt.% at the transition between zones III and II (Fig. 5). Refractory organic matter is an important host phase for reduced V species (Breit and Wanty, 1991) and Algeo and Maynard (2004) reported a TOC threshold of ~7 wt.% beyond which they detected a significant increase in V accumulation in Pennsylvanian black shales. The V accumulation in zone II is likely favored by the ubiquity of refractory organic compounds providing binding sites for the reduced V in pore water. In contrast, Mo resides primarily in sulfidic phases in anoxic sediments (Huerta-Diaz and Morse, 1992; Algeo and Maynard, 2004; Tribovillard et al., 2004) and any influence of the TOC content would be rather indirect, i.e. by determining the intensity of sulfate reduction (McManus et al., 2006). The highest authigenic V and Mo concentrations are observed in BIGO-T, the shallowest core in zone II. Pore water profiles of this core indicate redox oscillations in the water column (Fig. 3) suggesting that a significant portion of the V and Mo has been shuttled by metal (oxyhydr)oxides. At the transition to zone I, however, authigenic V concentrations decrease abruptly whereas Mo concentrations in MUC29 are still higher than in most samples of zones II and III. This is unlikely due to preferential Mo supply with particulate matter, since V has a higher affinity to Mn and Fe (oxyhydr)oxides than Mo (Takematsu et al., 1985). Alternatively, reduced retention of authigenic V during oxygenation periods might be the reason for the decoupling. The major diagenetic sink of Mo is Fe sulfides (pyrite and structurally similar Mo–Fe–S phases) (Bostick et al., 2003; Vorlicek et al., 2004) whereas V does not enter sulfide minerals to a significant extent (Huerta-Diaz and Morse, 1992; Scholz and Neumann, 2007). Concentrations of TS in MUC29 are among the highest observed throughout this study. Moreover, TS is decoupled from TOC in zone I (Fig. 5), which clearly indicates enhanced preservation of sulfur with respect to organic carbon. As mentioned in Section 4.1, Suits and Arthur (2000) reported the highest pyrite concentrations and DOP values throughout the Peruvian margin (12.0–13.5°S) for sediments on the shelf. The high pyrite concentrations have been assigned to the enhanced availability of reactive Fe compounds. Furthermore, Suits and Arthur (2000) hypothesized that pyrite formation on the Peruvian shelf is particularly favored by ENSO-related redox oscillations. This is related to the enhanced formation of sulfur intermediates (S^0, $S_2O_3^{2-}$, S_n^{2-}) from H_2S under slightly oxidizing conditions, which in turn stimulates the conversion of Fe monosulfides (FeS) to pyrite via the polysulfide pathway (Schoonen and Barnes, 1991; Schoonen, 2004; Rickard and Morse, 2005). In addition, experimental work by Vorlicek et al. (2004) has revealed that polysulfides (S_n^{2-}) do also promote the conversion of $MoOS_3^{2-}$ to MoS_4^{2-}, which is the ultimate step for the long-term fixation of Mo onto authigenic pyrite. As a consequence, Mo accumulation and burial is rather favored than perturbed by transient oxygenation on the Peruvian shelf. In contrast to that, V(III) is readily oxidized to V(V) under oxic conditions leading to a destabilization of authigenic V oxides and hydroxides (Wehrli and Stumm, 1989). Another factor that potentially limits the accumulation of authigenic V on the shelf is the enhanced carbon turnover and reduced preservation of refractory organic compounds under increasingly oxic conditions (Sun et al., 1993, 2002). This assumption is corroborated by the combined observations of decreasing TOC concentrations (Fig. 5) but increasing organic matter degradation rates in the landward direction across the Peruvian shelf (Bohlen et al., in press).

The discriminating effect of redox oscillations on the long-term accumulation of different trace metals is most evident

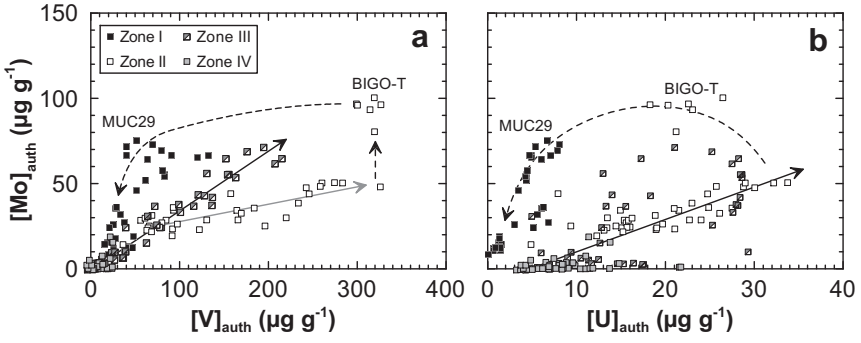

Fig. 7. Cross plot of (a) authigenic Mo concentration versus authigenic V concentration and (b) authigenic Mo concentration versus authigenic U concentration. Solid lines in (a) are linear regressions through samples in zones IV and III (black solid arrow; $R^2 = 0.95$, $n = 89$) and MUC33 and MUC19 in zone II (gray solid arrow; $R^2 = 0.72$, $n = 36$). The solid line in (b) is a linear regression though data of zones IV, III and MUC33 and MUC19 in zone II ($R^2 = 0.60$, $n = 125$). The dashed lines illustrate enhanced supply of Mo with metal (oxyhydr)oxides and remobilization of V and U in consequence of ENSO-related oxygenation events in BIGO-T and zone I. See text for further explanation.

in Fig. 7b, a cross plot of authigenic Mo versus authigenic U concentrations. Concomitantly increasing authigenic Mo and U concentrations between zone IV and MUC19 in zone II (Fig. 7b) are in agreement with the increasing diffusive benthic fluxes and reflect the decreasing benthic redox potential towards the central OMZ. At shallower depth, however, authigenic U concentrations decrease dramatically while Mo concentrations continue to increase. One reason for this decoupling is that U does not adsorb to (oxyhydr)oxides in the water column and therefore does not participate in the particulate shuttle (cp. Algeo and Tribovillard, 2009). Another reason, however, is most likely related to the strong susceptibility to re-oxidation of authigenic U. It was argued in Section 4.2.1 that pore water U profiles on the Peruvian shelf are strongly affected by remobilization. The re-oxidized and dissolved authigenic U in pore water induces an upward concentration gradient and thus impedes any additional U accumulation. Thus, the combined evidence of our pore water and sediment data strongly suggest that reduced uptake and preferential loss of U during oxygenation periods is of equal importance for the decoupling of U and Mo accumulation on the Peruvian shelf.

4.4. Implication for the use of U–Mo systematics as paleo-redox proxy

A number of studies have proposed to use Mo and U systematics to gain information about paleo-redox conditions (Algeo and Lyons, 2006; McManus et al., 2006; Algeo and Tribovillard, 2009). This approach is of great relevance for upwelling areas or other oxygen-deficient settings where recent studies have attempted to reconstruct past OMZ extension and/or ENSO variability (e.g. Nameroff et al., 2004; Gutiérrez et al., 2009; Díaz-Ochoa et al., 2011). McManus et al. (2006) derived an empirical relationship between sedimentary U/Mo ratios and oxygen concentrations in bottom water. Disregarding MUC27 at 2025 m water depth, U/Mo ratios decrease upslope across the Peruvian margin (Fig. 8) and broadly retrace the bottom water oxygen concentration at the time of sampling (Table 1). However, the corresponding correlation trend is quite different from the one presented by McManus et al. (2006)

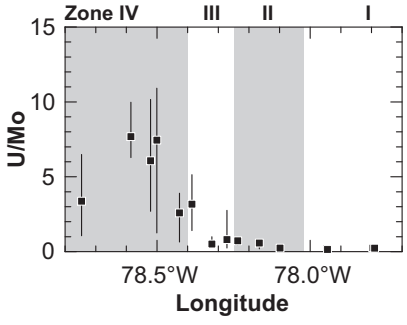

Fig. 8. Plot of U/Mo ratio versus longitude. Error bars span the range between the highest and lowest value of each core. The grayish and whitish arrays represent zone I to zone IV in Fig. 3.

(Fig. 9a) suggesting that any relationship to bottom water oxygen is of rather regional relevance. Major deviations from the trend by McManus et al. (2006) are observed in zone I where fluctuations in bottom water oxygenation enhance Mo accumulation (through particulate supply) and diminish U accumulation (through remobilization) thus pushing the U/Mo ratios to lower values. By contrast, comparably high U/Mo ratios in zones III and IV are attributed to the relative enrichment of U over Mo in authigenic phosphorites which are particularly abundant on the Peruvian slope. McManus et al. (2006) suggested that their empirical relationship is in fact due to increasing sulfate reduction rates and thus an increased availability of dissolved H_2S in pore water with decreasing oxygen concentrations in bottom water. This assumption is in agreement with our findings on U and Mo diagenesis in Peru upwelling sediments and further corroborated by the exponential relationship observed between U/Mo ratios and sediment TS (including MUC27, Fig. 9b). The non-linearity of this relationship is not surprising, given that U reduction is mediated by both Fe- and sulfate-reducing bacteria whereas authigenic Mo fixation requires the presence of H_2S. In light of these findings, U/Mo ratios in sediments or sedimentary rocks might be used to constrain whether shallow pore waters were ferruginous or (at least temporarily) sulfidic at the time of deposition. This could be also a promising approach to trace the past location of the lower boundary of the Peruvian OMZ where U/Mo ratios rapidly drop at the transition from zone IV to III (Fig. 8). However, as for the relationship between U/Mo and bottom water oxygen, variable processes of sediment redistribution on the slope may complicate the interpretation of paleo-records.

It is important to note that the use of U/Mo ratios obscures the decoupling of U with respect to Mo on the Peruvian shelf (Figs. 8 and 9), although this holds great potential for the reconstruction of past oxygen fluctuations in bottom water. Algeo and Tribovillard (2009) presented sedimentary U and Mo concentrations in cross plots of enrichment factors in order to illustrate multiple controls on U–Mo covariation in oxygen-deficient marine systems. They identified distinct arrays (dashed lines in Fig. 10) indicating (i) concomitantly increasing U and Mo accumulation with decreasing benthic redox potential in open-ocean upwelling areas and (ii) preferential accumulation of Mo over U in weakly restricted basins with a particulate shuttle in the water column. These U–Mo covariation patterns were then used to reconstruct depositional conditions in paleo-marine systems. Plotting our Mo and U data from the Peruvian margin in a cross plot of enrichment factors yields additional information on how bottom water oxygen fluctuations in open-ocean settings may affect U–Mo systematics. The trend line of shelf cores in Fig. 7b (curved arrow) appears as a straight line in Fig. 10 (linear regression through samples of zone I and BIGO-T). This line is almost identical to the trend of weakly restricted basins with a particulate shuttle in the water column of Algeo and Tribovillard (2009). We have identified a similar mechanism on the Peruvian margin. However, in contrast to restricted basins, where the chemocline fluctuates up and down, the OMZ boundaries move rather laterally across a flat shelf leading

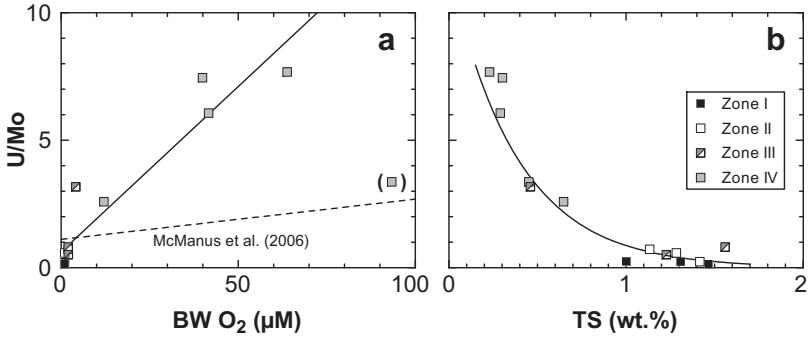

Fig. 9. Cross plots of average U/Mo ratios versus (a) bottom water (BW) oxygen concentration and (b) TS. See error bars in Figs. 5 and 8 for uncertainties. Solid black lines represent linear ($R^2 = 0.90$, $n = 13$) or exponential fits ($R^2 = 0.83$, $n = 14$) (MUC27 is shown in parentheses in (a) and has not been considered in the fit). The black dashed line in (a) represents the empirical relationship between U/Mo ratio and BW oxygen concentration in hypoxic marine settings by McManus et al. (2006).

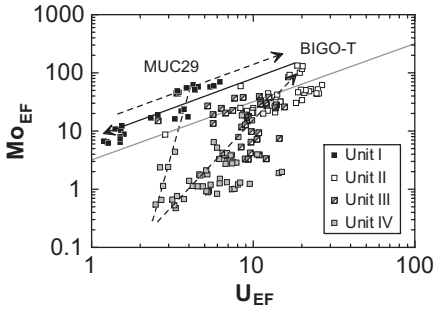

Fig. 10. Cross plot of Mo enrichment factors versus U enrichment factors. The metal enrichment factor is defined as $Me_{EF} = [Me]_{tot}/[Al]_{tot}/[Me]_{detr}/[Al]_{detr}$ where the index 'detr' refers to the detrital background (andesite in the Andean Arc, see Table 2). Note the logarithmic scale of both axes. The solid gray line depicts the relative proportion of Mo and U in seawater (weight ratio of $[Mo]_{sw}/[U]_{sw} = 3.2$). The dashed lines are adapted from Algeo and Tribovillard (2009) and illustrate a decreasing sediment redox potential in open marine systems (straight arrow) and enhanced Mo supply with metal (oxyhydr)oxides (i.e. a particulate shuttle) in weakly restricted basins (branched arrow). The solid black arrow is a linear regression through samples in zone I and BIGO-T in zone II ($R^2 = 0.82$, $n = 38$). See text for further explanation.

to a transition between areas where mostly oxic and others where mostly anoxic conditions in bottom water prevail. Although enhanced Mo supply with coated particulates is an important aspect of this environment, preferential loss of U during oxic periods is almost certainly of equal importance for the characteristic U–Mo pattern observed. Keeping that in mind, cross plots of Mo versus U like those in Figs. 7b and 10 could be of great use for the reconstruction of past OMZ variability and redox oscillations in ancient open-ocean environments in general.

5. SUMMARY AND CONCLUSIONS

We have investigated the spatial and temporal variability of trace metal diagenesis (U, V and Mo) across the Peru upwelling area. Our findings are summarized in a conceptual model consisting of two end member situations that correspond to negative (La Niña) and positive (El Niño) ENSO conditions (Fig. 11).

A: Within the permanent OMZ, U, V and Mo diffuse across the sediment/bottom water interface and precipitate in the zones of Fe and sulfate reduction. Since Mn reduction is largely completed in the water column, sediments receive little Mn-bound, particulate V and Mo. This favors the establishment of a downward directed benthic V and Mo flux. Because of the permanently anoxic but non-sulfidic conditions in the bottom water, surface sediments within the OMZ are subject to a continuous diffusive loss of Fe. Some of the dissolved Mn and Fe in the water column are re-precipitated at the oxyclines and deposited at the lower and upper boundary of the OMZ.

B: Sediments below the OMZ receive particulate V and Mo with metal (oxyhydr)oxides that have precipitated at the lower oxycline. This particulate V and Mo is released into the pore water upon Mn and Fe reduction. Since pore waters below the OMZ are generally not sufficiently sulfidic for an efficient authigenic removal, most of the liberated V and Mo is lost through upward diffusion across the benthic boundary. Intense U accumulation below the OMZ is attributed to both in situ reduction of U in the Fe reduction zone and lateral input of U-rich phosphorites from further upslope. The long term accumulation of V, Mo and U below the OMZ is diminished by the activity of bioturbating and bioirrigating organisms.

C: Sediments on the Peruvian shelf are strongly affected by ENSO-related oxygen fluctuations in bottom water. During positive ENSO periods, when bottom waters on the shelf are oxic, terrigenous Mn and Fe (oxyhydr)oxides as well as metal (oxyhydr)oxides that have precipitated at the retreating oxycline shuttle V and Mo to the sediment surface. After the recurrence of anoxic conditions, the Mn and Fe (oxyhydr)oxides are reductively recycled thus leading to high benthic Mn and Fe fluxes as compared to the

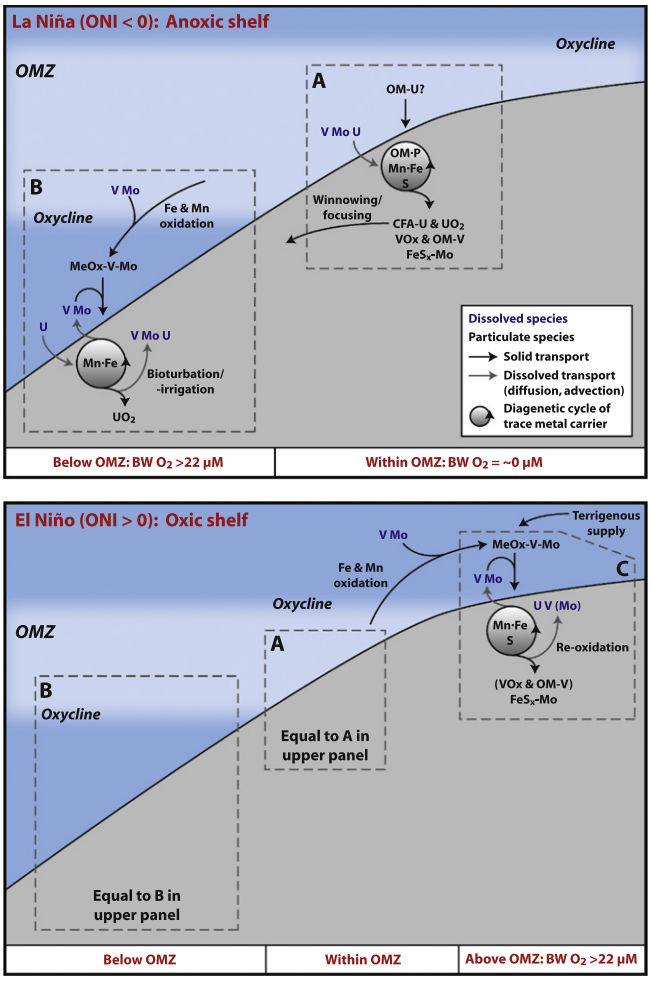

Fig. 11. Conceptual model for trace metal cycling across the Peruvian continental margin during two end member situations corresponding to negative (La Niña) and positive (El Niño) ENSO conditions. The abbreviations are as follows: MeOx = metal (oxyhydr)oxides, OM = organic matter, CFA = phosphorites (calcium fluoride apatite), VOx = V(III) oxides and hydroxides, FeS_x = Fe sulfides. See text for a detailed explanation of the biogeochemical processes in A, B and C.

permanent OMZ. Upon dissolution of the particulate carriers, the adsorbed V and Mo are released into the pore water and authigenically removed in the sulfate reduction zone. This alternation between supply of particle-reactive trace metals during oxic periods and authigenic fixation during anoxic periods leads to a preferential accumulation of V and Mo over U on the Peruvian shelf. The decoupling between V, Mo and U accumulation is further accentuated by the varying susceptibility to re-oxidation of the different authigenic metal phases. While authigenic V and U are readily re-oxidized and recycled during oxygenation periods, Mo accumulation with authigenic pyrite is favored by the occasional occurrence of slightly oxidizing conditions.

ENSO-related redox fluctuations in bottom water are likely to affect metal cycling along the entire SE Pacific ocean margin and similar phenomena might have occurred in ancient oceans through earth history. This study reveals that relative enrichments and/or depletions of redox-sensitive trace metals (most notably Mo and U) are sensitive to short-term fluctuations in bottom water oxygenation. The next step will be to apply this concept downcore in order to reconstruct past OMZ extension and variability as well as to identify large-scale redox fluctuations in the geological record.

ACKNOWLEDGMENTS

We are indebted to the IFM-GEOMAR technicians A. Bleyer, M. Dibbern, B. Domeyer, R. Ebbinghaus, A. Petersen and R. Surberg for their enthusiastic help and cooperation during the M77 cruises and the post-cruise work in Kiel. Furthermore, we would like to thank the officers and crew of RV Meteor for their commitment during the sampling campaign. Constructive and insightful comments from Thomas J. Algeo, Nicolas Tribovillard and one anonymous reviewer as well as from the associate editor, George R. Helz, are greatly appreciated. This work is a contribution of the Sonderforschungsbereich 754 "Climate-Biogeochemistry Interactions in the Tropical Ocean" (www.sfb754.de/en/) which is supported by the Deutsche Forschungsgemeinschaft.

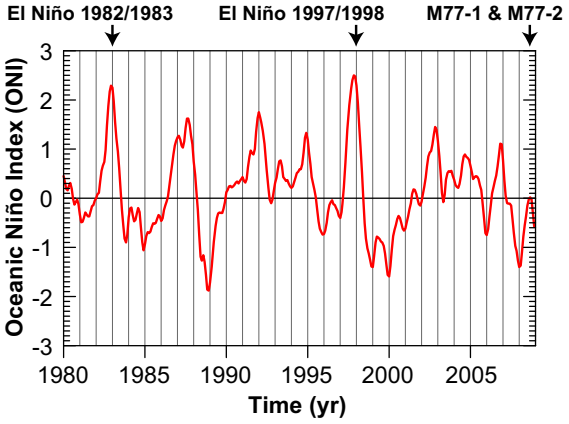

Fig. A1. Time series of the Oceanic Niño Index (ONI) between 1980 and 2008 (data from the U.S. National Oceanic and Atmospheric Administration, NOAA). The ONI is defined as the three monthly running mean of the sea surface temperature anomaly in the Niño 3.4 region (5°N–5°S, 120°–170°W). The strong El Niño events of 1982/1983 and 1997/1998 as well as the period of the research cruises M77-1 and M77-2 are indicated by vertical arrows. In general, positive ONI periods are associated with warmer temperatures and frequent shelf oxygenation whereas negative ONI periods are associated with lower temperatures and shelf anoxia.

APPENDIX A

APPENDIX B. SUPPLEMENTARY DATA

Supplementary data associated with this article can be found, in the online version, at doi:10.1016/j.gca.2011.08.007.

REFERENCES

Adelson J. M., Helz G. R. and Miller C. V. (2001) Reconstructing the rise of recent coastal anoxia; molybdenum in Chesapeake Bay sediments. *Geochim. Cosmochim. Acta* **65**, 237–252.

Algeo T. J. and Maynard J. B. (2004) Trace-element behavior and redox facies in core shales of Upper Pennsylvanian Kansas-type cyclothems. *Chem. Geol.* **206**, 289–318.

Algeo T. J. and Lyons T. W. (2006) Mo-total organic carbon covariation in modern anoxic marine environments: implications for analysis of paleoredox and paleohydrographic conditions. *Paleoceanography* **21**, PA1016. doi:10.1029/2004PA001112.

Algeo T. J. and Tribovillard N. (2009) Environmental analysis of paleoceanographic systems based on molybdenum–uranium covariation. *Chem. Geol.* **268**, 211–225.

Anderson R. F. (1982) Concentration, vertical flux, and remineralization of particulate uranium in seawater. *Geochim. Cosmochim. Acta* **46**, 1293–1299.

Anderson R. F., Lehuray A. P., Fleisher M. Q. and Murray J. W. (1989a) Uranium deposition in Saanich Inlet sediments, Vancouver Island. *Geochim. Cosmochim. Acta* **53**, 2205–2213.

Anderson R. F., Fleisher M. Q. and LeHuray A. P. (1989b) Concentration, oxidation state, and particulate flux of uranium in the Black Sea. *Geochim. Cosmochim. Acta* **53**, 2215–2224.

Arning E. T., Lückge A., Breuer C., Gussone N., Birgel D. and Peckmann J. (2009) Genesis of phosphorite crusts off Peru. *Mar. Geol.* **262**, 68–81.

Audry S., Blanc G., Schäfer J., Chaillou G. and Robert S. (2006) Early diagenesis of trace metals (Cd, Cu, Co, Ni, U, Mo, and V) in the freshwater reaches of a macrotidal estuary. *Geochim. Cosmochim. Acta* **70**, 2264–2282.

Barling J. and Anbar A. D. (2004) Molybdenum isotope fractionation during adsorption by manganese oxides. *Earth Planet. Sci. Lett.* **217**, 315–329.

Barnes C. E. and Cochran J. K. (1990) Uranium removal in oceanic sediments and the oceanic U balance. *Earth Planet. Sci. Lett.* **97**, 94–101.

Barnes C. E. and Cochran J. K. (1991) Geochemistry of uranium in Black Sea sediments. *Deep-Sea Res.* **38**, 1237–1254.

Berrang P. G. and Grill E. V. (1974) The effect of manganese oxide scavenging on molybdenum in Saanich Inlet, British Columbia. *Mar. Chem.* **2**, 125–148.

Bohlen L., Dale A. W., Sommer S., Mosch T., Hensen C., Noffke A., Scholz F. and Wallmann K. (2011) Benthic nitrogen cycling traversing the Peruvian oxygen minimum zone. *Geochim. Cosmochim. Acta.* **75**, 7257–7276.

Böning P., Brumsack H. J., Böttcher M. E., Schnetger B., Kriete C., Kallmeyer J. and Borchers S. L. (2004) Geochemistry of Peruvian near-surface sediments. *Geochim. Cosmochim. Acta* **68**, 4429–4451.

Böning P., Brumsack H. J., Schnetger B. and Grunwald M. (2009) Trace element signatures of Chilean upwelling sediments at 36 S. *Mar. Geol.* **259**, 112–121.

Bostick B. C., Fendorf S. and Helz G. R. (2003) Differential adsorption of molybdate and tetrathiomolybdate on pyrite (FeS_2). *Env. Sci. Technol.* **37**, 285–291.

Boudreau B. P. (1996) The diffusive tortuosity of fine-grained unlithified sediments. *Geochim. Cosmochim. Acta* **60**, 3139–3142.

Breit G. N. and Wanty R. B. (1991) Vanadium accumulation in carbonaceous rocks: a review of geochemical controls during deposition and diagenesis. *Chem. Geol.* **91**, 83–97.

Brink K. H. (1982) A Comparison of long coastal trapped wave theory with observations off Peru. *J. Phys. Oceanogr.* **12**, 897–913.

Bruland A. et al. (1983) Trace elements in seawater. In *Chemical oceanography*, vol. 8 (eds. J. P. Riley and R. Chester), pp. 157–220. Chemical oceanography. Academic Press, London.

Bruland K. W., Rue E. L., Smith G. J. and DiTullio G. R. (2005) Iron, macronutrients and diatom blooms in the Peru upwelling regime: brown and blue waters of Peru. *Mar. Chem.* **93**, 81–103.

Brumsack H. J. and Gieskes J. M. (1983) Interstitial water trace-metal chemistry of laminated sediments from the Gulf of California, Mexico. *Mar. Chem.* **14**, 89–106.

Brumsack H. J. (2006) The trace metal content of recent organic carbon-rich sediments: implications for Cretaceous black shale formation. *Paleogeogr. Palaeocl.* **232**, 344–361.

Burdige D. J. (1993) The biogeochemistry of manganese and iron reduction in marine-sediments. *Earth-Sci. Rev.* **35**, 249–284.

Calvert S. E. and Pedersen T. F. (1993) Geochemistry of recent oxic and anoxic marine sediments: implications for the geological record. *Mar. Geol.* **113**, 67–88.

Chaillou G., Anschutz P., Lavaux G., Schäfer J. and Blanc G. (2002) The distribution of Mo, U, and Cd in relation to major redox species in muddy sediments of the Bay of Biscay. *Mar. Chem.* **80**, 41–59.

Chan K. M. and Riley J. P. (1966a) The determination of molybdenum in natural waters, silicates and biological materials. *Anal. Chim. Acta* **36**, 220–229.

Chan K. M. and Riley J. P. (1966b) The determination of vanadium in sea and natural waters, biological materials and silicate sediments and rocks. *Anal. Chim. Acta* **34**, 337–345.

Díaz-Ochoa J. A., Pantoja S., De Lange G. J., Lange C. B., Sánchez G. E., Acuña V. R., Muñoz P. and Vargas G. (2011) Oxygenation variability in Mejillones Bay, off northern Chile, during the last two centuries. *Biogeosciences* **8**, 137–146.

Diaz R. J. (2001) Overview of Hypoxia around the World. *J. Environ. Qual.* **30**, 275–281.

Diaz R. J. and Rosenberg R. (2008) Spreading dead zones and consequences for marine ecosystems. *Science* **321**, 926–929.

Emerson S. R. and Huested S. S. (1991) Ocean anoxia and the concentrations of molybdenum and vanadium in seawater. *Mar. Chem.* **34**, 177–196.

Erickson B. E. and Helz G. R. (2000) Molybdenum(VI) speciation in sulfidic waters: stability and lability of thiomolybdates. *Geochim. Cosmochim. Acta* **64**, 1149–1158.

Froelich P. N., Klinkhammer G. P., Bender M. L., Luedtke N. A., Heath G. R., Cullen D., Dauphin P., Hammond D., Hartman B. and Maynard V. (1979) Early oxidation of organic matter in pelagic sediments of the eastern equatorial Atlantic: suboxic diagenesis. *Geochim. Cosmochim. Acta* **43**, 1075–1090.

Fuenzalida R., Schneider W., Garcés-Vargas J., Bravo L. and Lange C. (2009) Vertical and horizontal extension of the oxygen minimum zone in the eastern South Pacific Ocean. *Deep-Sea Res.* **56**, 992–1003.

Glenn C. R. and Arthur M. A. (1988) Petrology and major element geochemistry of Peru margin phosphorites and associated diagenetic minerals: authigenesis in modern organic-rich sediments. *Mar. Geol.* **80**, 231–267.

Goldberg T., Archer C., Vance D. and Poulton S. W. (2009) Mo isotope fractionation during adsorption to Fe (oxyhydr)oxides. *Geochim. Cosmochim. Acta* **73**, 6502–6516.

Govindaraju K. (1994) Compilation of working values and sample description for 383 geostandards. *Geostandard Newslett.* **18**, 1–158.

Grasshoff K., Erhardt M. and Kremling K. (2002) *Methods of Seawater Analysis*. Wiley-VCH, Weinheim.

Gutiérrez D., Gallardo V. A., Mayor S., Neira C., Vasquez C., Sellanes J., Rivas M., Soto A., Carrasco F. and Baltazar M. (2000) Effects of dissolved oxygen and fresh organic matter on the bioturbation potential of macrofauna in sublittoral sediments off Central Chile during the 1997/1998 El Niño. *Mar. Ecol.-Prog. Ser.* **202**, 81–99.

Gutiérrez D., Enríquez E., Purca S., Quipúzcoa L., Marquina R., Flores G. and Graco M. (2008) Oxygenation episodes on the continental shelf of central Peru: remote forcing and benthic ecosystem response. *Prog. Oceanogr.* **79**, 177–189.

Gutiérrez D., Sifeddine A., Field D. B., Ortlieb L., Vargas G., Chavez F. P., Velazco F., Ferreira V., Tapia P., Salvatteci R., Boucher H., Morales M. C., Valdes J., Reyss J. L., Campusano A., Boussafir M., Mandeng-Yogo M., Garcia M. and Baumgartner T. (2009) Rapid reorganization in ocean biogeochemistry off Peru towards the end of the Little Ice Age. *Biogeosciences* **6**, 835–848.

Helz G. R., Miller C. V., Charnock J. M., Mosselmans J. F. W., Pattrick R. A. D., Garner C. D. and Vaughan D. J. (1996) Mechanism of molybdenum removal from the sea and its concentration in black shales: EXAFS evidence. *Geochim. Cosmochim. Acta* **60**, 3631–3642.

Hirose K. and Sugimura Y. (1991) Chemical speciation of particulate uranium in seawater. *J. Radioanal. Nucl. Chem.* **149**, 83–96.

Hormazabal S., Shaffer G., Letelier J. and Ulloa O. (2001) Local and remote forcing of sea surface temperature in the coastal upwelling system off Chile. *J. Geophys. Res.* **106**, 16657–16671.

Huerta-Diaz M. A. and Morse J. W. (1992) Pyritization of trace metals in anoxic marine sediments. *Geochim. Cosmochim. Acta* **56**, 2681–2702.

Jarvis I., Burnett W. C., Nathan Y., Almbaydin F. S. M., Attia A. K. M., Castro L. N., Flicoteaux R., Hilmy M. E., Husain V., Qutawnah A. A., Serjani A. and Zanin Y. N. (1994) Phosphorite geochemistry – state of the art and environmental concerns. *Eclogae Geol. Helv.* **87**, 643–700.

Klinkhammer G. P. and Palmer M. R. (1991) Uranium in the oceans – where it goes and why. *Geochim. Cosmochim. Acta* **55**, 1799–1806.

Levin L., Gutiérrez D., Rathburn A., Neira C., Sellanes J., Muñoz P., Gallardo V. and Salamanca M. (2002) Benthic processes on the Peru margin: a transect across the oxygen minimum zone during the 1997–98 El Niño. *Prog. Oceanogr.* **53**, 1–27.

Li Y.-H. and Gregory S. (1974) Diffusion of ions in sea water and in deep-sea sediments. *Geochim. Cosmochim. Acta* **38**, 703–714.

Liger E., Charlet L. and Van Cappellen P. (1999) Surface catalysis of uranium(VI) reduction by iron(II). *Geochim. Cosmochim. Acta* **63**, 2939–2955.

Lovley D. R. and Phillips E. J. (1992) Reduction of uranium by *Desulfovibrio desulfuricans*. *Appl. Environ. Microbiol.* **58**, 850–856.

Lovley D. R., Phillips E. J. P., Gorby Y. A. and Landa E. R. (1991) Microbial reduction of uranium. *Nature* **350**, 413–416.

Lovley D. R., Roden E. E., Phillips E. J. P. and Woodward J. C. (1993) Enzymatic iron and uranium reduction by sulfate-reducing bacteria. *Mar. Geol.* **113**, 41–53.

McLennan S. M. (2001) Relationships between the trace element composition of sedimentary rocks and upper continental crust. *Geochem. Geophys. Geosyst.* 2, paper number 2000GC000109.

McManus J., Berelson W. M., Klinkhammer G. P., Hammond D. E. and Holm C. (2005) Authigenic uranium: relationship to oxygen penetration depth and organic carbon rain. *Geochim. Cosmochim. Acta* **69**, 95–108.

McManus J., Berelson W. M., Severmann S., Poulson R. L., Hammond D. E., Klinkhammer G. P. and Holm C. (2006) Molybdenum and uranium geochemistry in continental margin sediments: paleoproxy potential. *Geochim. Cosmochim. Acta* **70**, 4643–4662.

Meysman F. J. R., Boudreau B. P. and Middelburg J. J. (2005) Modeling reactive transport in sediments subject to bioturbation and compaction. *Geochim. Cosmochim. Acta* **69**, 3601–3617.

Middelburg J. J. and Levin L. A. (2009) Coastal hypoxia and sediment biogeochemistry. *Biogeosciences* **6**, 1273–1293.

Morford J. L., Emerson S. R., Breckel E. J. and Kim S. H. (2005) Diagenesis of oxyanions (V, U, Re, and Mo) in pore waters and sediments from a continental margin. *Geochim. Cosmochim. Acta* **69**, 5021–5032.

Morford J. L., Martin W. R. and Carney C. M. (2009a) Uranium diagenesis in sediments underlying bottom waters with high oxygen content. *Geochim. Cosmochim. Acta* **73**, 2920–2937.

Morford J. L., Martin W. R., François R. and Carney C. M. (2009b) A model for uranium, rhenium, and molybdenum diagenesis in marine sediments based on results from coastal locations. *Geochim. Cosmochim. Acta* **73**, 2938–2960.

Nameroff T. J., Balistrieri L. S. and Murray J. W. (2002) Suboxic trace metal geochemistry in the Eastern Tropical North Pacific. *Geochim. Cosmochim. Acta* **66**, 1139–1158.

Nameroff T. J., Calvert S. E. and Murray J. W. (2004) Glacial-interglacial variability in the Eastern Tropical North Pacific oxygen minimum zone recorded by redox-sensitive trace metals. *Paleoceanography* **19**, PA1010. doi:10.1029/2003PA000912.

Noffke A., Hensen C., Sommer S., Croot P., Scholz F., and Wallmann K. (2011) The benthic iron and phosphorus source across the Peruvian oxygen minimum zone. *ASLO 2011 – Aquatic Sciences Meeting*, Book of Abstracts, p. 183 (abstr.).

Pakhomova S. V., Hall P. O. J., Kononets M. Y., Rozanov A. G., Tengberg A. and Vershinin A. V. (2007) Fluxes of iron and manganese across the sediment–water interface under various redox conditions. *Mar. Chem.* **107**, 319–331.

Pennington J. T., Mahoney K. L., Kuwahara V. S., Kolber D. D., Calienes R. and Chavez F. P. (2006) Primary production in the eastern tropical Pacific: a review. *Prog. Oceanogr.* **69**, 285–317.

Pizarro O., Clarke A. J. and Van Gorder S. (2001) El Niño sea level and currents along the South American coast: comparison of observations with theory. *J. Phys. Oceanogr.* **31**, 1891–1903.

Reimers C. E. and Suess E. (1983) Spatial and temporal patterns of organic matter accumulation on the Peru continental margin. In *Coastal Upwelling: Part B. Sedimentary Record of Ancient Coastal Upwelling* (eds. E. Suess and J. Thiede). Plenum Press, New York, NY., pp. 311–346.

Rickard D. and Morse J. W. (2005) Acid volatile sulfide (AVS). *Mar. Chem.* **97**, 141–197.

Sarbas B. and Nohl U. (2009) The GEOROC database – a decade of "online geochemistry". *Geochim. Cosmochim. Acta* **73**, A1158.

Scheidegger K. F. and Krissek L. A. (1983) Zooplankton and nekton: natural barriers to the seaward transport of suspended terrigenous particles off Peru. In *Coastal Upwelling: Part A. Responses of the Sedimentary Regime to Present Coastal Upwelling* (eds. E. Suess and J. Thiede). Plenum Press, New York, NY., pp. 303–336.

Scholz F. and Neumann T. (2007) Trace element diagenesis in pyrite-rich sediments of the Achterwasser lagoon, SW Baltic Sea. *Mar. Chem.* **107**, 516–532.

Schoonen M. A. A. and Barnes H. L. (1991) Reactions forming pyrite and marcasite from solution: II. Via FeS precursors below 100 °C. *Geochim. Cosmochim. Acta* **55**, 1505–1514.

Schoonen M. A. A. (2004) Mechanisms of sedimentary pyrite formation. In *Sulfur biogeochemistry – past, present)* (eds. J. P. Amend, K. J. Edwards and T. W. Lyons). Geological Society of America Special Paper 379, Boulder, CO, pp. 117–134.

Severmann S., McManus J., Berelson W. M. and Hammond D. E. (2010) The continental shelf benthic iron flux and its isotope composition. *Geochim. Cosmochim. Acta* **74**, 3984–4004.

Shaw T. J., Gieskes J. M. and Jahnke R. A. (1990) Early diagenesis in differing depositional environments: the response of transition metals in pore water. *Geochim. Cosmochim. Acta* **54**, 1233–1246.

Shaw T. J., Sholkovitz E. R. and Klinkhammer G. (1994) Redox dynamics in the Chesapeake Bay: the effect on sediment/water uranium exchange. *Geochim. Cosmochim. Acta* **58**, 2985–2995.

Shimmield G. B. and Price N. B. (1986) The behavior of molybdenum and manganese during early sediment diagenesis – offshore Baja California, Mexico. *Mar. Chem.* **19**, 261–280.

Sommer S., Pfannkuche O., Linke P., Luff R., Greinert J., Drews M., Gubsch S., Pieper M., Poser M. and Viergutz T. (2006) Efficiency of the benthic filter: biological control of the emission of dissolved methane from sediments containing shallow gas hydrates at Hydrate Ridge. *Global Biogeochem. Cy.* **20**, GB2019. doi:10.1029/2004GB002389.

Soto-Mardones L., Parés-Sierra A. and Durazo R. (2004) Ekman modulation of the sea-surface temperature on the Eastern South Pacific. *Deep-Sea Res.* **51**, 551–561.

Stookey L. L. (1970) Ferrozine – a new spectrophotometric reagent for iron. *Anal. Chem.* **42**, 779–781.

Stramma L., Johnson G. C., Sprintall J. and Mohrholz V. (2008) Expanding oxygen-minimum zones in the tropical oceans. *Science* **320**, 655–658.

Strub P. T., Mesías J. M., Montecino V., Rutllant J., and Salinas S. (1998) Coastal ocean circulation off Western South America. In *The Sea* (eds. A. R. Robinson and K. H. Brink). John Wiley & Sons, New York, NY. pp. 273–313.

Suits N. S. and Arthur M. A. (2000) Sulfur diagenesis and partitioning in Holocene Peru shelf and upper slope sediments. *Chem. Geol.* **163**, 219–234.

Sun M.-Y., Lee C. and Aller R. C. (1993) Laboratory studies of oxic and anoxic degradation of chlorophyll-*a* in Long Island Sound sediments. *Geochim. Cosmochim. Acta* **57**, 147–157.

Sun M.-Y., Aller R. C., Lee C. and Wakeham S. G. (2002) Effects of oxygen and redox oscillation on degradation of cell-associated lipids in surficial marine sediments. *Geochim. Cosmochim. Acta* **66**, 2003–2012.

Suzuki Y., Kelly S. D., Kemner K. M. and Banfield J. F. (2005) Direct microbial reduction and subsequent preservation of uranium in natural near-surface sediment. *Appl. Environ. Microb.* **71**, 1790–1797.

Takematsu N., Sato Y. and Okabe S. (1985) The partition of vanadium and molybdenum between manganese oxides and seawater. *Geochim. Cosmochim. Acta* **49**, 2395–2399.

Taylor S. R. and McLennan S. M. (1985) *The continental crust: its composition and evolution*. Blackwell, Oxford.

Tribovillard N., Riboulleau A., Lyons T. and Baudin F. (2004) Enhanced trapping of molybdenum by sulfurized organic matter of marine origin in Mesozoic limestones and shales. *Chem. Geol.* **213**, 385–401.

Tribovillard N., Algeo T. J., Lyons T. and Riboulleau A. (2006) Trace metals as paleoredox and paleoproductivity proxies: an update. *Chem. Geol.* **232**, 12–32.

Van der Weijden C. H., Reichart G. J. and Visser H. J. (1999) Enhanced preservation of organic matter in sediments deposited within the oxygen minimum zone in the northeastern Arabian Sea. *Deep-Sea Res.* **46**, 807–830.

Veeh H. H., Calvert S. E. and Price N. B. (1974) Accumulation of uranium in sediments and phosphorites on the South West African shelf. *Mar. Chem.* **2**, 189–202.

Vorlicek T. P., Kahn M. D., Kasuya Y. and Helz G. R. (2004) Capture of molybdenum in pyrite-forming sediments: role of ligand-induced reduction by polysulfides. *Geochim. Cosmochim. Acta* **68**, 547–556.

Wanty R. B. and Goldhaber M. B. (1992) Thermodynamics and kinetics of reactions involving vanadium in natural systems: accumulation of vanadium in sedimentary rocks. *Geochim. Cosmochim. Acta* **56**, 1471–1483.

Wehrli B. and Stumm W. (1989) Vanadyl in natural waters: adsorption and hydrolysis promote oxygenation. *Geochim. Cosmochim. Acta* **53**, 69–77.

Wells L. E. (1990) Holocene history of the El Nino phenomenon as recorded in flood sediments of northern Peru. *Geology* **18**, 1134–1137.

Zheng Y., Anderson R. F., van Geen A. and Kuwabara J. (2000) Authigenic molybdenum formation in marine sediments: a link to pore water sulfide in the Santa Barbara Basin. *Geochim. Cosmochim. Acta* **64**, 4165–4178.

Zheng Y., Anderson R. F., Van Geen A. and Fleisher M. Q. (2002a) Remobilization of authigenic uranium in marine sediments by bioturbation. *Geochim. Cosmochim. Acta* **66**, 1759–1772.

Zheng Y., Anderson R. F., Van Geen A. and Fleisher M. Q. (2002b) Preservation of particulate non-lithogenic uranium in marine sediments. *Geochim. Cosmochim. Acta* **66**, 3085–3092.

Associate editor: George R. Helz

Limnol. Oceanogr., 57(3), 2012, 851–867

doi:10.4319/lo.2012.57.3.0851

Benthic iron and phosphorus fluxes across the Peruvian oxygen minimum zone

A. Noffke,[a,*] C. Hensen,[a] S. Sommer,[a] F. Scholz,[a] L. Bohlen,[a] T. Mosch,[a] M. Graco,[b] and K. Wallmann [a]

[a] Helmholtz-Zentrum für Ozeanforschung Kiel, Kiel, Germany
[b] Instituto del Mar del Perú, Callao, Peru

Abstract

Benthic fluxes of dissolved ferrous iron (Fe^{2+}) and phosphate (TPO_4) were quantified by in situ benthic chamber incubations and pore-water profiles along a depth transect (11°S, 80–1000 m) across the Peruvian oxygen minimum zone (OMZ). Bottom-water O_2 levels were < 2 μmol L^{-1} down to 500-m water depth, and increased to $\sim$ 40 μmol L^{-1} at 1000 m. Fe^{2+} fluxes were highest on the shallow shelf (maximum 316 mmol m^{-2} yr^{-1}), moderate (15.4 mmol m^{-2} yr^{-1}) between 250 m and 600 m, and negligible at deeper stations. In the persistent OMZ core, continuous reduction of Fe oxyhydroxides results in depletion of sedimentary Fe : Al ratios. TPO_4 fluxes were high (maximum 292 mmol m^{-2} yr^{-1}) throughout the shelf and the OMZ core in association with high organic carbon degradation rates. Ratios between organic carbon degradation and TPO_4 flux indicate excess release of P over C when compared to Redfield stoichiometry. Most likely, this is caused by preferential P release from organic matter, dissolution of fish debris, and/or P release from microbial mat communities, while Fe oxyhydroxides can only be inferred as a major P source on the shallow shelf. The benthic fluxes presented here are among the highest reported from similar, oxygen-depleted environments and highlight the importance of sediments underlying anoxic water bodies as nutrient sources to the ocean. The shelf is particularly important as the periodic passage of coastal trapped waves and associated bottom-water oxygenation events can be expected to induce a transient biogeochemical environment with highly variable release of Fe^{2+} and TPO_4.

Oxygen minimum zones (OMZ), water layers with oxygen concentrations < 20 μmol L^{-1}, are persistent hydrographic features in large parts of the ocean, in particular the eastern Pacific, the northern Indian Ocean, and the eastern Atlantic off southwest Africa (Helly and Levin 2004). One of the most extended and intense OMZs (dropping to oxygen concentrations close to anoxia in core regions; Stramma et al. 2008) is located in the eastern South Pacific, underneath the productive coastal waters of the Humboldt Current System. This OMZ stretches from 37°S, Chile, to the equatorial belt (0–5°S) and reaches its greatest extension off Peru between 5 and 13°S, with $>$ 600-m thickness to about 1000 km offshore (Fuenzalida et al. 2009).

The complex maintenance mechanisms and dynamics of OMZs still have not been sufficiently resolved. However, the principal factors leading to their formation are intense oxygen consumption in response to high surface productivity, sustained by high amounts of upwelled nutrients, and sluggish ventilation due to the hydrographic regime (Wyrtki 1962). Climate models predict an overall decline of dissolved oxygen in the ocean interior to emerge from global warming (Matear and Hirst 2003). For the tropical OMZs this decline was recently confirmed by 50-yr time series analyses of O_2 data (collected since 1960; Stramma et al. 2008).

In response to the expansion of the hypoxic water masses, major changes in nutrient cycling could occur and affect the marine carbon, nitrogen, phosphorus, and iron cycles via various feedback mechanisms. Thus, improving current knowledge on the key biogeochemical and physical processes governing today's OMZs by quantitative approaches remains critical to estimating the ocean's responses to global warming and becomes a future research challenge.

Oxygen depletion substantially affects the biogeochemical reactions of redox-sensitive elements. This in particular applies to iron (Fe) and phosphorus (P), whose individual cycles are strongly linked in the marine environment. A number of previous studies have resulted in the observation that under oxygen-deficient bottom-water conditions dissolved ferrous iron (Fe^{2+}) and phosphate (TPO_4) are preferentially released into the pore fluids and overlying bottom water (Sundby et al. 1986; Ingall and Jahnke 1997; McManus et al. 1997). Particulate ferric iron oxides and hydroxides (hereafter referred to as iron oxyhydroxides) scavenge phosphate, and oxygen deficiency promotes their reduction to soluble states by microbial induced dissolution and the concomitant liberation of metal-oxide-bound phosphate (Sundby et al. 1992). Phosphate release from iron oxyhydroxides may further be enhanced through reductive dissolution by hydrogen sulfide (Jensen et al. 1995). Furthermore, in addition to these metal oxide interactions, growing evidence has been presented that phosphate is preferentially regenerated from P-bearing organic matter (as compared to C) under hypoxic and anoxic bottom-water conditions (Ingall et al. 1993).

Despite the obvious biogeochemical significance of organic rich sediments underlying productive upwelling systems for global element cycles and related feedbacks on ocean–climate interactions, relatively few systematic in situ studies on benthic nutrient turnover have been conducted to date. Phosphate fluxes derived from benthic chamber incubations are available for the continental margins off Washington State (Devol and Christensen 1993; Hartnett and Devol 2003), central California (Ingall and Jahnke

* Corresponding author: anoffke@geomar.de

1997; McManus et al. 1997; Berelson et al. 2003), and northwest Mexico (Hartnett and Devol 2003), as well as the California borderland basins (Ingall and Jahnke 1997; McManus et al. 1997; Hammond et al. 2004). Measurements in the Arabian Sea (Woulds et al. 2009) have recently complemented the existing data pool. With regard to iron, the knowledge on benthic release rates is even smaller. This can mainly be ascribed to the fact that generally aeolian dust deposition (Jickells et al. 2005) has been assumed to be the major supply pathway of iron to the open ocean, and it was only recently that the potential contribution of a sedimentary iron source has begun to be considered (Moore and Braucher 2008). Much of the work done in continental margin upwelling settings focused on iron inventories and turnover in the water column. However, a number of these studies highlight the role of sediments supplying iron to the water column by mechanisms of resuspension (Hutchins et al. 1998) and reductive mobilization (Johnson et al. 1999). Direct measurements with benthic chambers revealed that reductive mobilization can be significant in such sedimentary settings (McManus et al. 1997; Elrod et al. 2004; Severmann et al. 2010).

In this paper we report seabed fluxes of dissolved phosphate and iron for the OMZ off Peru. To our knowledge, this represents the first detailed investigation on benthic release of this redox-sensitive couple in the eastern South Pacific upwelling region. Benthic fluxes were derived from time series of in situ incubations with benthic landers and calculations from pore-water gradients. Sampling was conducted along a latitudinal transect (11°S) at water depths from 80 m to 1000 m, affected by regionally varying environmental influences (redox conditions, hydrodynamics and organic carbon availability). This enabled us to directly link magnitudes of nutrient release with potential controlling parameters.

Methods

Regional setting—The Peruvian coast is part of the most productive marine ecosystem in the world. High primary productivity of up to 3.6 g C m^{-2} d^{-1} (Pennington et al. 2006) is sustained by coastal upwelling that transports cold, oxygen-poor but nutrient-rich water to the well-mixed surface layer. Upwelling off Peru is perennial, favored by almost constant alongshore-oriented winds, which drive an offshore Ekman transport of surface waters (Strub et al. 1998). Upwelled waters are predominantly fed by Equatorial Subsurface Water, which is transported poleward with the Peru Chile Undercurrent (Strub et al. 1998). Intensity of the coastal upwelling changes seasonally due to varying wind strength with maximum wind speed and coastal upwelling occurring in austral winter and spring (Pennington et al. 2006). The OMZ that develops from intense degradation of organic matter and associated oxygen consumption extends roughly from $<$ 100 m to 700 m (oxycline of 22 μmol L^{-1} defined by Fuenzalida et al. 2009). Seasonal changes in upwelling intensity typically result in variable mixed surface layer depths of 10 m to 40 m (Bakun 1985). However, periodic oxygenation events of the bottom waters may reach down to about 100-m water depth as observed off Callao at 12°S (Gutiérrez et al. 2008). According to this study, the vertical position of the upper boundary of the OMZ (defined as the 22 μmol L^{-1} isopleth) fluctuated between 10-m to 90-m water depth (mean depth: 52 m) over a period of 13 yr (1992–2005). Such oxygenation events are strongly associated with the passage of coastal trapped waves that occur more frequently during positive El Niño Southern Oscillation (ENSO) periods (Gutiérrez et al. 2008) and are associated with a significant deepening of the thermo- and oxycline. Most intense oxygenation events have been reported for the strong El Niño periods in 1982–1983 and 1997–1998 during which the upper boundary of the OMZ deepened to almost 300 m (Levin et al. 2002; Fuenzalida et al. 2009).

Between 11–15°S, underneath the region of most intense primary productivity (Pennington et al. 2006), organic rich ($\gg$ 5 wt%), diatomaceous muds accumulate at water depths between 50 m and 500 m (Suess et al. 1987). A distinct feature of this region is a thick lens-shaped deposit that extends between 10.5°S and 13.6°S from outer shelf to upper slope depths (Krissek et al. 1980). Preservation and burial within this deposit is due to high bulk sedimentation rates, which are favored by reduced bottom velocities in the poleward directed undercurrent (Suess et al. 1987). At greater water depths, increasing fluctuations in the velocity and direction of bottom currents result in lower sedimentation rates (Reimers and Suess 1983), winnowing, and the accumulation of phosphorite crusts and nodules (Reimers and Suess 1983; Glenn and Arthur 1988).

Sediment sampling and in situ flux measurements—Sediment samples were taken during the R/V *Meteor* cruise M77-1/2 in October–December 2008, using a video-guided multiple corer (MUC) and two benthic landers (Biogeochemical Observatories — BIGO and BIGO-T) along a latitudinal depth transect at 11°S (Fig. 1; Table 1). Bottom-water O_2 levels of $<$ 2 μmol L^{-1} extended from $\sim$ 50-m to $\sim$ 500-m water depth (Fig. 2), hitherto referred to as OMZ. During the time of sampling, the shallow shelf Sta. 543 and Sta. 568, at 78-m and 85-m water depth, respectively, also displayed bottom-water O_2 levels $<$ 2 μmol L^{-1}. However, these sites might experience periodic oxygenation events similar to those observed at a 94-m-deep site off Callao (Gutiérrez et al. 2008). As with increasing water depth oxygenation events can be assumed to occur more rarely, we henceforth refer to the core of the OMZ as the depth range between 250 down to its lower boundary at $\sim$ 500 m.

Sediment cores (inner diameter: 10 cm) retrieved by MUC were immediately transferred into a cold room that was kept at in situ temperature (4°C). Core processing was performed within 1–2 h upon retrieval. Two parallel cores were processed for all MUC stations. The overlying bottom water was sampled and filtered through 0.2-μm cellulose acetate (CA) syringe filters, and the remaining water was siphoned off and discarded. The first one of the two parallel cores was vertically sectioned within a glove bag under an argon atmosphere. The sediments were transferred to 50-mL centrifuge tubes preflushed with argon, and pore water was separated using a refrigerated centrifuge for 20 min at 4500 revolutions per minute

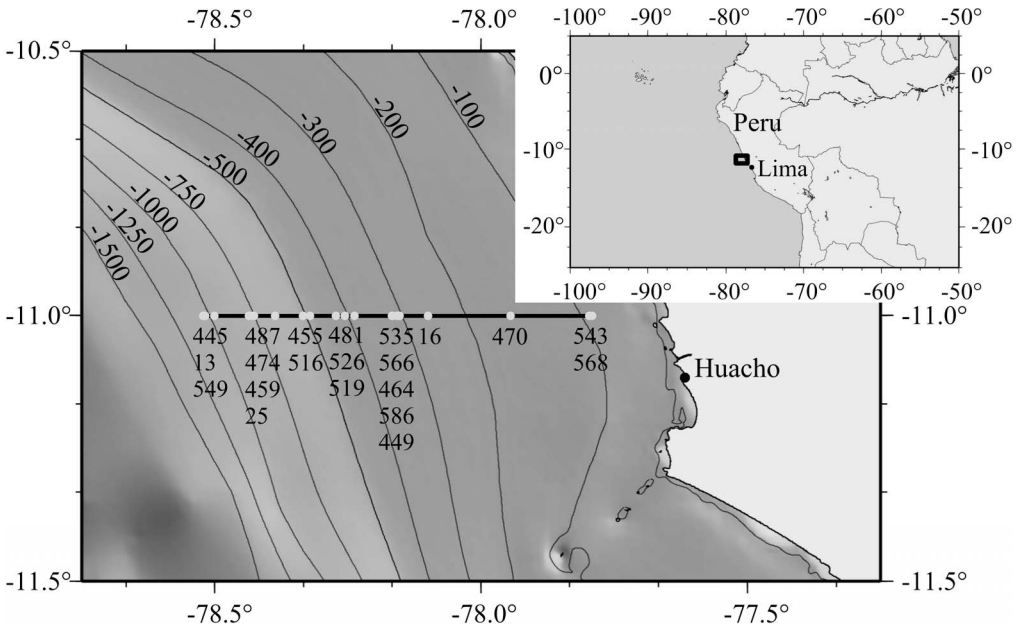

Fig. 1. Location map showing the Peruvian continental margin (bathymetry based on the Earth Topography Five Minute Grid [ETOPO5]). The sampling stations on the latitudinal transect at 11°S (horizontal line) are indicated by the gray dots. Where stations were close together, station names were listed in descending order in accordance with increasing water depth.

(rpm). Supernatant pore fluids were filtered under argon through 0.2-μm CA syringe filters. Centrifuge residuals were stored frozen for total sediment digestion and the extraction of highly reactive iron phases after the cruise. Pore water from the sediments retrieved at Sta. 543 and Sta. 516 was extracted using rhizons (Seeberg-Elverfeldt et al. 2005) instead of the glove bag method. Prior to deployment, the rhizons were preconditioned in an oxygen-free water bath. To ensure that the samples had not been in contact with air, the first 0.5 mL of extracted pore water were discarded. Pore waters from the other parallel core were extracted using a pore-water press (Teflon squeezers equipped with 0.2-μm CA filters), which was operated with argon at pressure gradually increasing to 2.5 bar. Additional samples for the determination of water content and porosity, as well as for total organic carbon (TOC) analyses, were taken from each depth interval, filled into preweighed plastic vials, and stored refrigerated for subsequent processing in the home laboratory. Squeeze cakes were also kept refrigerated until onshore preparation for x-ray fluorescence (XRF) analyses. Only the results from the glove bag extractions are presented in this study, if not otherwise indicated.

In situ benthic flux measurements were conducted using the biogeochemical observatories BIGO and BIGO-T (Sommer et al. 2009). BIGO contained two circular flux chambers (internal diameter 28.8 cm, area 651.4 cm^2). BIGO-T is similar to BIGO, but contained only one benthic chamber of the same size as those deployed in BIGO. An online video-controlled launching system allowed smooth placement of the observatories at selected sites on the seafloor. Two hours after the observatories were placed on the seafloor, the chamber(s) were slowly driven into the sediment ($\sim$ 30 cm h^{-1}). During this initial time period, the water inside the flux chamber was periodically replaced with ambient bottom water. After the chamber was fully driven into the sediment, the chamber water was again replaced with ambient bottom water to flush out solutes that might have been released from the sediment during chamber insertion. The water volume enclosed by the benthic chamber was in the range of 8.8 L to 18.5 L. To determine Fe^{2+} and TPO_4 fluxes, four sequential water samples were removed from the chamber with glass syringes (volume: $\sim$ 47 mL). The glass syringes were connected to the chamber using 1-m-long Vygon tubes with a dead volume of 6.9 mL. Prior to deployment, these tubes were filled with distilled water. In the case of the BIGO-T, the chamber was completely flushed with ambient seawater after half of the total deployment time, and a series of four water samples was taken before and after flushing, henceforth referred to as first incubation and second incubation, respectively. The flux measurements were conducted for different time periods in the range from 17.8 h to 23 h as defined from the time interval between the first and the last syringe water sampling. After recovery of the observatories, short cores (inner diameter: 10 cm) were retrieved from the incubated sediments and processed in the glove bag as described above for MUCs.

Chemical analyses—Onboard analytics: All shipboard analyses were performed shortly after pore-water extraction or recovery of benthic landers. Ammonium (NH_4^+), total dissolved sulfide (TH_2S), and total dissolved phosphate (TPO_4) analyses—in pore-water and incubated bottom-water samples—as well as dissolved ferrous iron (Fe^{2+}) analyses (in pore-water samples only) were realized onboard with a Hitachi U-2001 spectrophotometer, applying standard techniques (Grasshoff et al. 1999). Where

Table 1. Location, bottom-water oxygen concentration (BW O_2), and solid-phase geochemical data (TOC, TOC : P_{excess}, reactive Fe, and Fe : Al, each for 0–1 cm sediment depth) of the study sites during the R/V *Meteor* cruise M77/ 1-2. Further included are positions of CTD deployments for water column O_2 (representative profile shown in Fig. 2) and water column nutrients. Empty cells indicate that the parameter was not measured.

Station	Device	Cruise leg	Latitude (S)	Longitude (W)	Depth (m)	BW O_2 (μmol L^{-1})	TOC (wt%)	TOC : P_{excess}	Highly reactive Fe (wt%)	Fe : Al*
543	MUC 52	1	10°59.99′	77°47.40′	78	<2	3.50	181		0.46
568	BIGO 5	1	11°00.02′	77°47.72′	85	<2	3.76	297	0.36	0.44
470	MUC 29	1	11°00.02′	77°56.60′	145	<2	7.61	139	0.19	0.42
16	BIGO T	1	10°59.80′	78°05.91′	259	<2	13.54	171	0.12	0.41
535	BIGO T3	1	11°00.00′	78°09.12′	305	<2	15.18	140		
566	BIGO T4	1	11°00.00′	78°09.13′	309	<2	11.48			
464	BIGO 1	1	11°00.00′	78°09.92′	315	<2	15.45	134		
586	BIGO T5	1	11°00.00′	78°09.40′	316	<2	13.79	128		
449	MUC 19	1	11°00.01′	78°09.97′	319	<2	10.65	88	0.08	0.42
481	MUC 33	1	11°00.00′	78°14.19′	376	<2	10.86	58	0.09	0.38
526	BIGO 3	1	11°00.02′	78°15.27′	397	<2	14.75	95		
519	MUC 43	1	11°00.01′	78°16.29′	410	<2	8.50	43	0.07	0.36
455	MUC 21	1	11°00.00′	78°19.23′	466	<2	4.50	25	0.14	0.42
516	MUC 40	1	11°00.00′	78°20.00′	512	<2	6.07	3		0.42
487	MUC 39	1	11°00.02′	78°23.17′	579	4	6.48	26	0.12	0.37
474	BIGO 2	1	11°00.01′	78°25.55′	695	12	6.53	38		
459	MUC 25	1	11°00.03′	78°25.60′	697	12	6.72	53	0.32	0.48
25	BIGO	2	10°59.47′	78°26.10′	716	7	8.08	39		
445	MUC 15	1	11°00.00′	78°30.02′	928	39	5.15	20	0.26	0.87
13	BIGO	2	10°59.82′	78°31.05′	978	40	4.09	14		
549	MUC 53	1	10°59.81′	78°31.27′	1005	40	4.00	30	0.20	0.56
438	CTD-RO 16	1	11°00.69′	78°35.03′	1261					
463	CTD-RO 22	1	11°00.01′	78°44.86′	2031					

* From Scholz et al. 2011.

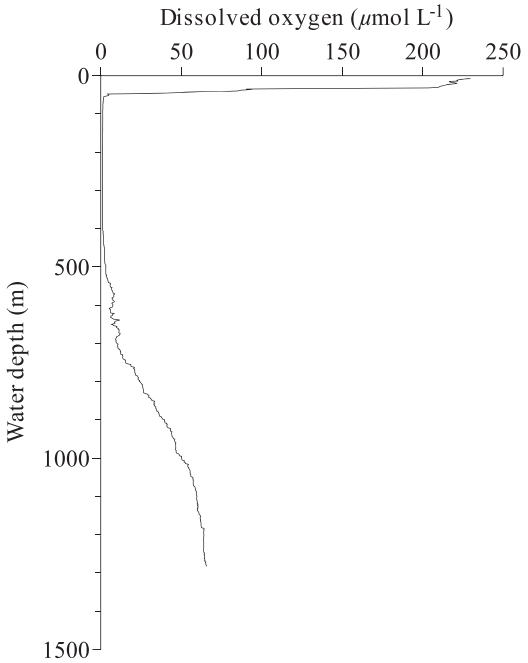

Fig. 2. Representative profile of dissolved oxygen (438 CTD-RO 16, position shown in Table 1) through the OMZ at 11°S during October–December 2008.

necessary, subsamples of pore water were diluted with oxygen-free artificial seawater prior to analysis. Ascorbic acid was added, still within the glove bag, to subsamples of pore and bottom waters for onboard Fe^{2+} analyses. Total alkalinity (TA) was determined by titration following the method of Ivanenkov and Lyakhin (1978). For selected cores, sulfate (SO_4^{2-}) was measured onboard by Ion Chromatography (716 IC-Compact, Metrohm). Sample aliquots for additional SO_4^{2-} analyses in the home laboratories were stored in plastic vials. Further information about the above-described analytical methods is available on the GEOMAR web site (www.geomar.de). For Fe analyses in the incubated bottom-water samples retrieved by benthic landers, aliquots were stored in acid-washed plastic vials and acidified with suprapure HNO_3. All sample aliquots were kept refrigerated until performance of analysis. Fe determinations were performed in the home laboratory by inductively coupled plasma mass spectrometry (ICP-MS Agilent 7500 series). Precision, determined by replicate analyses of calibration standards was $\leq 2\%$. We assume that all dissolved Fe released from the pore water is present as Fe^{2+}. Data on conductivity, temperature, depth (CTD) as well as oxygen bottom-water levels were taken from casts of a Sea-Bird Electronics, Inc., CTD system equipped with a water sampling rosette (RO), which were conducted nearby at each station investigated. During the CTD casts CTD-RO 16 and 22, water samples from Niskin bottles were spectrophotometrically analyzed for dissolved phosphate.

Solid phase analyses: Porosity was calculated from the weight loss of wet sediment during freeze-drying, assuming a dry solid density of 2 g cm^{-3} based on data published by Böning et al. (2004). Freeze-dried sediments were ground, pretreated with HCl to drive out carbonate carbon, and analyzed for TOC by flash combustion using a Carlo Erba Elemental Analyzer. Analytical precision for replicate samples was found to be 1%. The water content of centrifuge residuals was determined separately in order to recalculate the highly reactive Fe content for dry sediments.

Reactive Fe (term used in this article, which mainly combines Fe oxyhydroxides, Fe monosulfides (FeS), and Fe carbonates [Kostka and Luther 1994]) was extracted by adding 20 mL of cold 0.5 mol L^{-1} HCl to 0.5 g of wet sediment in 50-mL centrifuge tubes and shaking the samples for 1 h. The extracts were centrifuged, pipetted off, and filtered through 0.2-μm CA syringe filters. For total Fe determinations, 0.1-mL samples were added to 5 mL of a reducing ferrozine solution (1 g L^{-1} ferrozine in 50 mmol L^{-1} 4-(2-hydroxyethyl)-1-piperazineethanesulfonic acid [HEPES] buffer, pH 7, plus hydroxylammonium chloride [10 g L^{-1}]). After 20 min, Fe was measured at 562 nm using a Hitachi U-2001 spectrophotometer. Long-term precision of the in-house standard OMZ-1 was $< 5\%$ relative standard deviation.

Total concentrations of phosphorus and aluminum were analyzed by XRF spectrometry using a Philips PW 1480 spectrophotometer (equipped with a rhodium x-ray tube) on samples prepared as lithium tetraborate fused glass beads (ratio sample : flux 1 : 6). Loss on ignition was not determined for the samples, and P and Al contents were calculated from unnormalized oxides (P_2O_5, Al_2O_3). Average values of replicate analyses of different rock reference samples agreed well with the recommended values, and precision was better than 2% and 5% for P_2O_5 and Al_2O_3, respectively. Excess phosphorus (P_{excess}) was calculated as $P_{sample} - (P:Al_{andesite} \times Al_{sample})$ to remove the detrital P fraction according to Böning et al. (2004). The P : Al ratio for andesite was derived from Le Maitre (1976).

Flux calculations—Diffusive fluxes of Fe^{2+} and TPO_4 across the sediment–water interface (SWI) were calculated through application of Fick's first law of diffusion (Boudreau 1997).

$$J = -\Phi_0 D_s (dC/dz) \quad (1)$$

where Φ_0 is the porosity at the SWI (0–1 cm), D_s is the effective diffusion coefficient in the sediment at the SWI, and dC/dz is the pore-water gradient estimated from the concentration between the uppermost sediment interval (0–1 cm) and the bottom water. Bottom-water concentrations of TPO_4 were typically taken from measurements of Niskin bottle samples (463 CTD-RO 22, position shown in Table 1). In some cases, bottom-water concentrations of MUC samples seem to be artificially elevated because of sediment dispersal during sampling. However, the resulting difference in flux calculations is negligible. For each sampling site, molecular diffusion coefficients for ferrous iron (Fe^{2+}) and phosphate (HPO_4^-) in seawater corrected for in situ temperature (CTD measurements) were taken from Boudreau (1997) and further adjusted to in situ salinities and pressures by the Stokes Einstein relationship

(Li and Gregory 1974). The effective diffusion coefficient in the sediment was calculated from the adjusted molecular diffusion coefficient and tortuosity (derived by the empirical equation of Boudreau [1997]).

Solute concentrations obtained from the benthic chamber incubations were corrected for dilution with Milli-Q water originating from the water-filled Vygon tubing (V = 6.9 mL) connecting the individual syringes and the chamber. Benthic chamber fluxes were calculated from the slope determined by linear regression of the concentration versus the incubation time. During the deployments of BIGO 5 chamber 1 and 13 BIGO chamber 1 and chamber 2, the first data points were deviating from the subsequent ones. This might be due to a variety of reasons, such as contamination during subsampling onboard and laboratory handling, mixing of pore water into the enclosed water body when the benthic chamber was driven into the sediment, or failure of the water sampling system. In these cases, the first sample was excluded from the regression to calculate the respective fluxes. At the deeper, more-oxygenated stations below ~ 700-m water depth, it was not possible to measure a reliable flux of Fe^{2+} during the course of the benthic chamber incubations.

Results

Pore water—Pore-water profiles of Fe^{2+} and TPO_4 (from multicorer deployments) are shown in Fig. 3. Typically, distinct concentration maxima of Fe^{2+} were located close to the SWI in sediments overlain by the oxygen-depleted water body (< 2 μmol L^{-1}, Fig. 3). With increasing sediment depth, concentrations showed a strong decrease, and Fe^{2+} generally was no more detectable within 7 cm to 14 cm below the sediment surface. Highest concentrations of Fe^{2+} were measured in pore waters from the uppermost shelf station (543: 79.8 μmol L^{-1}, 1.5-cm depth) imposing a steep concentration gradient to the SWI. At stations underlying oxic bottom waters, the concentration peak shifted deeper into the sediment, and gradients between the uppermost sediment interval and the bottom water were very small or nonexistent. Similar to Fe^{2+}, highest TPO_4 concentrations typically occurred close to the sediment surface. Peaks generally shifted to greater sediment depth with increasing water depth. Except for the two shallowest stations, the concentrations decreased with increasing sediment depth below the maximum.

Profiles of some major pore-water constituents are exemplarily shown in Fig. 4 for three stations from the shallow shelf (Sta. 543), the OMZ core (Sta. 481), and below the OMZ (Sta. 549) to present trends across the transect and to provide the basis to relate TPO_4 and Fe^{2+} to the overall geochemistry of the setting (*see* General aspects of pore-water geochemistry). NH_4^+ and TA concentrations generally increased with sediment depth, reaching maximum values of 1.3 mmol L^{-1} and 13.7 meq L^{-1}, respectively, at shelf Sta. 543. Both NH_4^+ and TA markedly decreased with increasing water depth. SO_4^{2-} decreased only slightly with depth and at the shelf station, from 29.5 mmol L^{-1} to 23.5 mmol L^{-1} within 28-cm sediment depth, whereas no gradients were observed at the deeper stations. TH_2S was present only below 18 cm on the shelf, increasing to 760 μmol L^{-1} in the 26–30-cm interval; and it was undetectable over the sampled sediment length in the two other cores.

Benthic fluxes—The diffusive fluxes, as well as the chamber fluxes, of Fe^{2+} and TPO_4 are presented in Table 2 and illustrated in Figs. 5A and 6A, respectively, with positive fluxes being defined as from the sediment into the water column. The original data from the benthic chamber incubations can be provided from the authors on demand.

Total fluxes of dissolved Fe^{2+} and TPO_4 measured in benthic chambers were, in most cases, higher than the diffusive fluxes derived from pore-water gradients (Table 2). For sites located within the OMZ, ratios between fluxes measured by the chamber and diffusive fluxes average to 2.1 and 1.3 for Fe^{2+} and TPO_4, respectively. Limitations by depth resolution during pore-water sampling, leading to possible underestimation of the gradient's steepness, could have caused part of the discrepancy between the two methods. Furthermore, a significant fraction of the flux may have originated from the degradation of fresh organic matter (indicated by a thin fluffy layer covering numerous of the M77 cores) at the sediment–water interface that was not recorded in the pore-water profiles (Slomp et al. 1998). The contribution of biological pore-water irrigation to benthic chamber fluxes was probably negligible in the OMZ, due to its low significance in anoxic sediments, but may have been more important at the more-oxygenated stations. Consistently, diffusive phosphate fluxes displayed stronger deviations from chamber fluxes at deeper stations below the OMZ (range of ratios between chamber and diffusive fluxes: 3.3–8.6). On the shelf, benthic fluxes may have also been influenced by bioirrigation. Despite the strong oxygen deficiency, numerous small polychaetes were observed in sediment cores retrieved by the benthic chambers. This observation is in agreement with Levin et al. (2002) and Gutiérrez et al. (2008), who reported that bioturbating organisms rapidly invade the Peruvian shelf and upper slope during oxygenation events and may persist for several months after the recurrence of anoxic conditions.

Although these uncertainties are inherent to the pore-water–derived fluxes, these data reveal a spatial pattern across the transect similar to the benthic chamber fluxes. Hence the diffusive flux calculations provide reasonable approximations to total fluxes and can be used for a comparative study in the investigated area.

Solid phase data—Sediment geochemical data for reactive Fe, Fe : Al, TOC, and TOC : P_{excess} are provided in Table 1, Fig. 5 B,C (reactive Fe, Fe : Al), and Fig. 6 B,C (TOC, TOC : P_{excess}). Concentrations of reactive Fe were distinctively elevated at the shallow shelf stations, which are subjected to periodic oxygenation events (Gutiérrez et al. 2008), and below 600-m water depth, where O_2 levels increased (Fig. 5D). Concurrently with these increasing O_2 levels, Fe : Al ratios were above the average detrital background concentrations of 0.47 (Andean andesite;

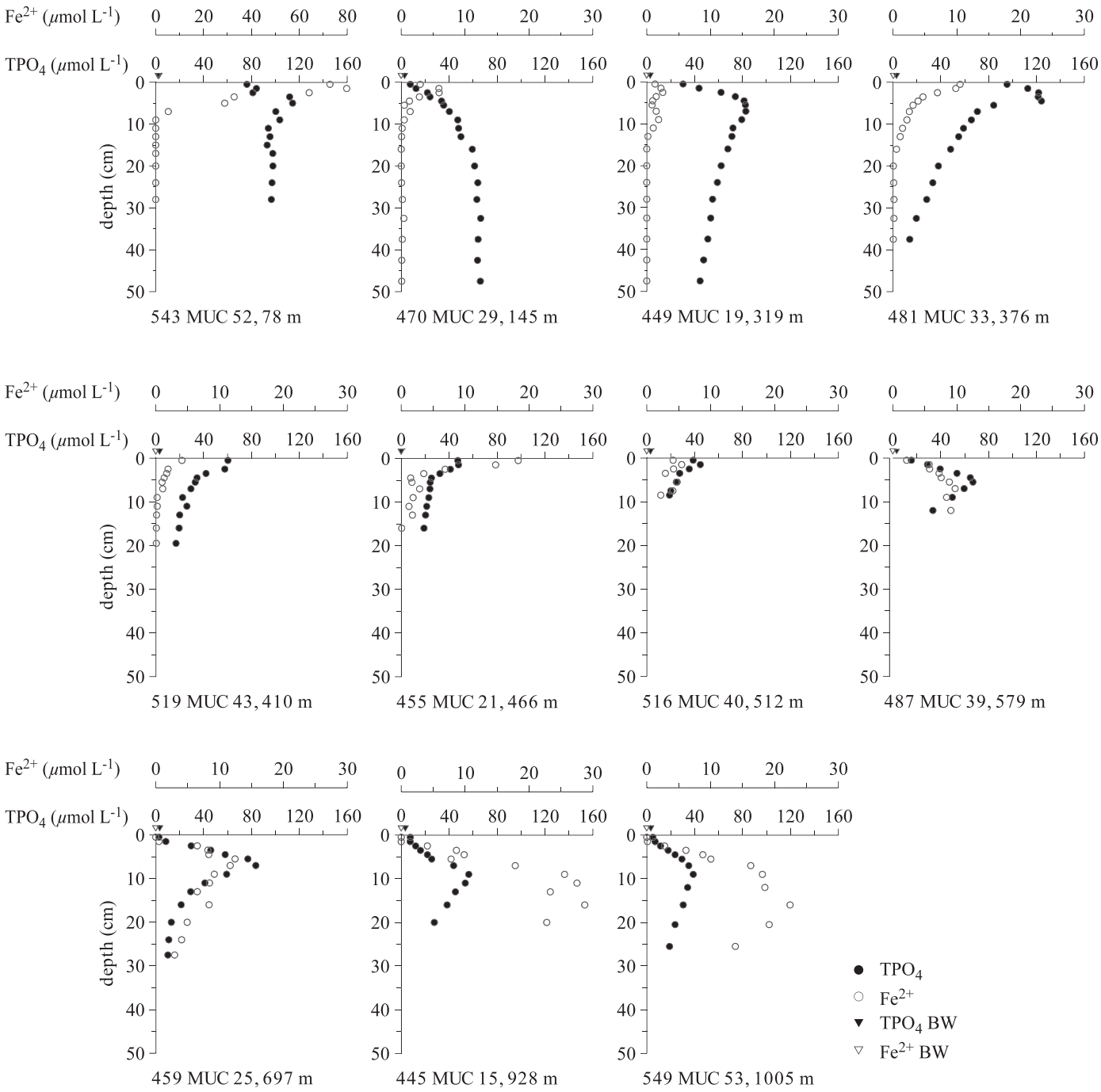

Fig. 3. Dissolved iron (Fe^{2+}, open circles) and phosphate (TPO_4, closed circles) pore-water profiles across the transect at 11°S. Sediments were retrieved using a multiple corer. Note: pore water at Sta. 543 and Sta. 516 was obtained by rhizon sampling. Triangles (open and closed for Fe^{2+} and TPO_4, respectively) indicate bottom-water concentrations, taken from CTD measurements for TPO_4.

Scholz et al. 2011). In contrast, at all shallower stations Fe : Al ratios were at and below the average (Fig. 5C). Measured TOC values were overall high, with a minimum concentration of 3.5 wt% on the shallow shelf and a maximum concentration of 15.5 wt% in the core of the OMZ (Fig. 6B). $TOC : P_{excess}$ ratios were elevated above Redfield ratio (106 : 1) at water depths ≤ 316 m; below 400 m, values were typically below 50 (Fig. 6C).

Discussion

General aspects of pore-water geochemistry—Peru margin sediments are characterized by significant organic matter degradation rates, which is demonstrated by the concurrent buildup of NH_4^+ and TA with sediment depth at all stations (Fig. 4). Pore-water gradients of NH_4^+ and TA reflect a decrease in organic matter degradation with

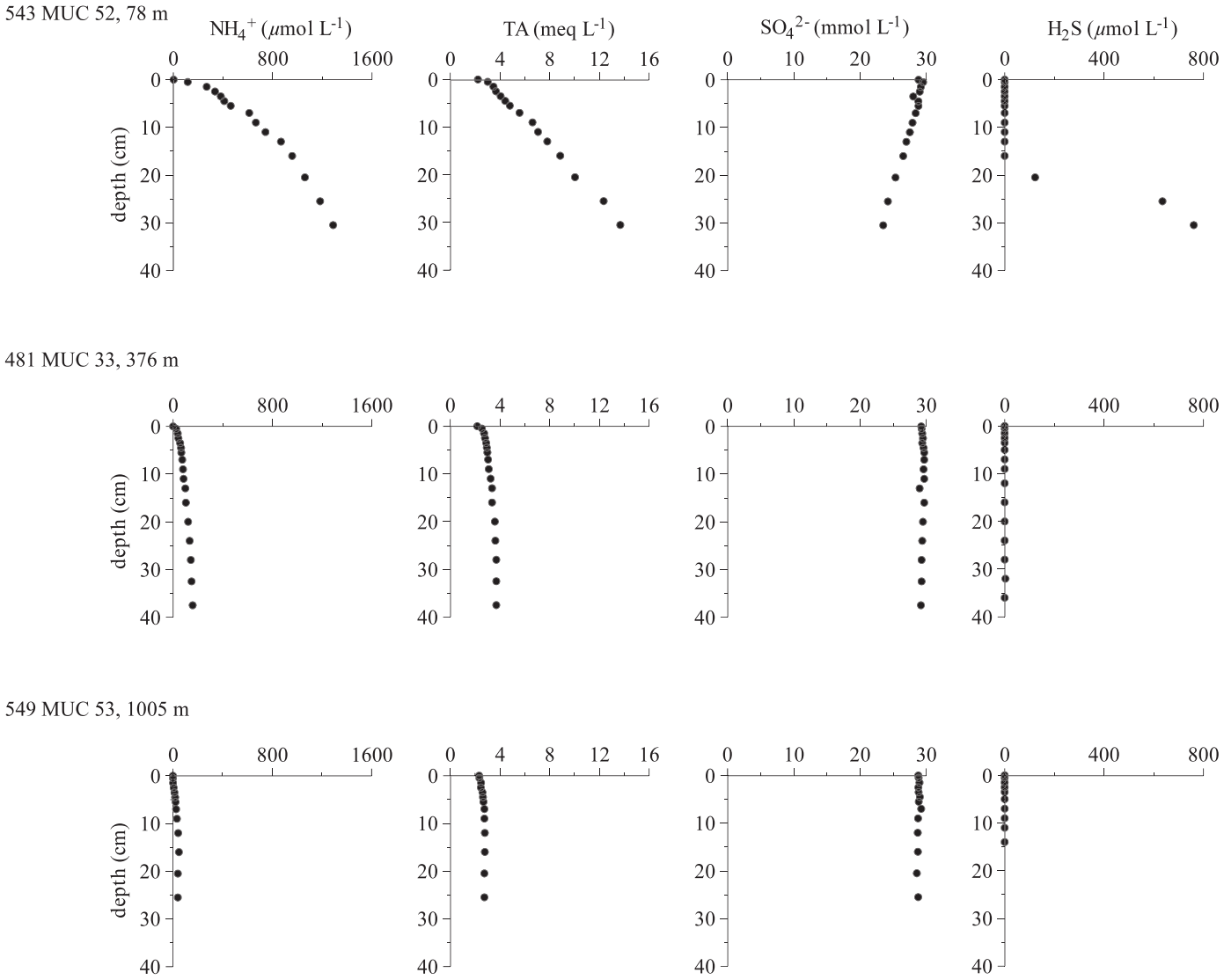

Fig. 4. Pore-water profiles of major pore-water constituents (NH_4^+, TA, SO_4^{2-}, and TH_2S) shown exemplarily for stations from the shallow shelf (Sta. 543), the OMZ core (Sta. 481), and below the OMZ (Sta. 549). The uppermost data point from each profile (depth of zero) represents the bottom-water concentration.

increasing water depth, which is generally consistent with the organic carbon oxidation rates of 8.2 mmol m^{-2} d^{-1} to 2.1 mmol m^{-2} d^{-1} derived from pore-water modeling that was conducted on selected stations from the same cruise (Bohlen et al. 2011). At the shelf (Sta. 543, Fig. 4), decreasing pore-water SO_4^{2-} concentrations and the presence of TH_2S below 20-cm sediment depth indicate intense sulfate reduction. In fact, pore-water modeling indicates that sulfate reduction at the shelf and upper slope contributes 80% to the entire organic carbon degradation (Bohlen et al. 2011). At the deeper stations (Sta. 481 and 549 in Fig. 4), no TH_2S was detected, which can be explained by complete precipitation of TH_2S as Fe sulfides or Fe^{2+} availability exceeding sulfide release from sulfate reduction. Under nearly anoxic conditions down to ~ 500-m water depth, reduction of Fe oxyhydroxides in the uppermost sediment horizon supports diffusion of Fe^{2+} into the bottom water (Table 2; Fig. 3). In this area near-surface TPO_4 and Fe^{2+} enrichments point towards P release during the reductive dissolution of Fe oxyhydroxides. However, only the pore-water profiles from sites at water depths > 400 m have mostly coincident concentration maxima indicative of the direct coupling of P and Fe cycles. Whereas, at shallower stations, maxima of both species are at slightly different vertical positions, suggesting other P sources and Fe precipitation (*see* Controls on benthic phosphate release). At the more-oxygenated stations below ~ 500-m water depth, the Fe diagenetic front is located deeper in the sediment. Here, pore-water profiles of Fe^{2+} indicate the precipitation of upward-diffusing Fe^{2+} into Fe oxyhydroxides within the thin oxic surface layer (Fig. 3). The concurrent decline of TPO_4 indicates that this TPO_4 is adsorbed or coprecipitated. Below the TPO_4 maxima, concentrations decrease to the base of the cores. Similar

Table 2. Chamber flux measurements and diffusive (pore-water–derived) fluxes of dissolved Fe^{2+} and TPO_4. Fluxes are given in mmol m^{-2} yr^{-1}. Averages are given for chamber fluxes and for diffusive fluxes from lander deployments with more than one sediment core recovered, where ± corresponds to the minimum and maximum fluxes; dashes indicate that at the station reliable chamber flux calculations were not possible because Fe^{2+} concentration changes with time did not exceed the analytical error. At the MUC stations chamber fluxes are not available because chambers were not deployed. Also included are flux ratios (chamber : diffusive) of Fe^{2+} and TPO_4, molar Fe : P pore-water concentration ratios (calculated for the Fe^{2+} peak position), and organic carbon oxidation rates (C_{ox}). C_{ox} was estimated by calculating HCO_3^- fluxes from TA gradients where bottom-water O_2 concentration was < 2 μmol L^{-1}, in order to provide for each diffusive TPO_4 flux an organic carbon oxidation rate (*see* text for further explanation).

Station	Device	Cruise leg	Depth (m)	Fe^{2+} flux chamber	Fe^{2+} flux diffusive	Ratio Fe^{2+} flux chamber : diffusive	TPO_4 flux chamber	TPO_4 flux diffusive	Ratio TPO_4 flux chamber : diffusive	Fe : TPO_4 pore water	C_{ox}
543	MUC 52	1	78		179.3			193.7		0.95	3274*
568	BIGO 5	1	85	316.1±33.6	88.3±0.9	3.6	169.9±15.9	75.8±10.2	2.2		2822±399
470	MUC 29	1	145		6.6			12.3		0.27	1220
16	BIGO T	1	259	—	18.9	—	211.4±4.3	148.3	1.4		3852
535	BIGO T3	1	305	3.8	6.8	0.56	209.2±14.2	151.1	1.4		888
566	BIGO T4	1	309	31.3	13.0	4	64.9±12.8	83.4	0.78		1244
464	BIGO 1	1	315	14.9	9.8±3.4	1.5	292.2±1.4	144.4±28.1	2		2634±729
586	BIGO T5	1	316	—	8.4	—	83.5±3.2	116.9	0.71		638
449	MUC 19	1	319		3.3			73.1		0.04	814
481	MUC 33	1	376		23.0			210.9		0.11	1374
526	BIGO 3	1	397	30±6.1	30.7	0.98	179.2±13.6	227.6	0.79		1442
519	MUC 43	1	410		8.5			123.1		0.07	518
455	MUC 21	1	466		31.9			79.9		0.39	216
516	MUC 40	1	512		7.8			69.7		0.12	425*
487	MUC 39	1	579		4.3			25.4		0.16	
474	BIGO 2	1	695	—	0.4± 0.4	—	20.5±6.1	2.9±1.2	7.1		
459	MUC 25	1	697		0.0			−1.0		0.16	
25	BIGO	2	716	—	0.0	—	18.2	5.5	3.3		
445	MUC 15	1	928		0.0			6.3		0.51	
13	BIGO	2	978	—	0.0	—	64.6±1.8	7.5	8.6		
549	MUC 53	1	1005		0.0			2.3		0.74	

* Obtained by pore-water squeezing.

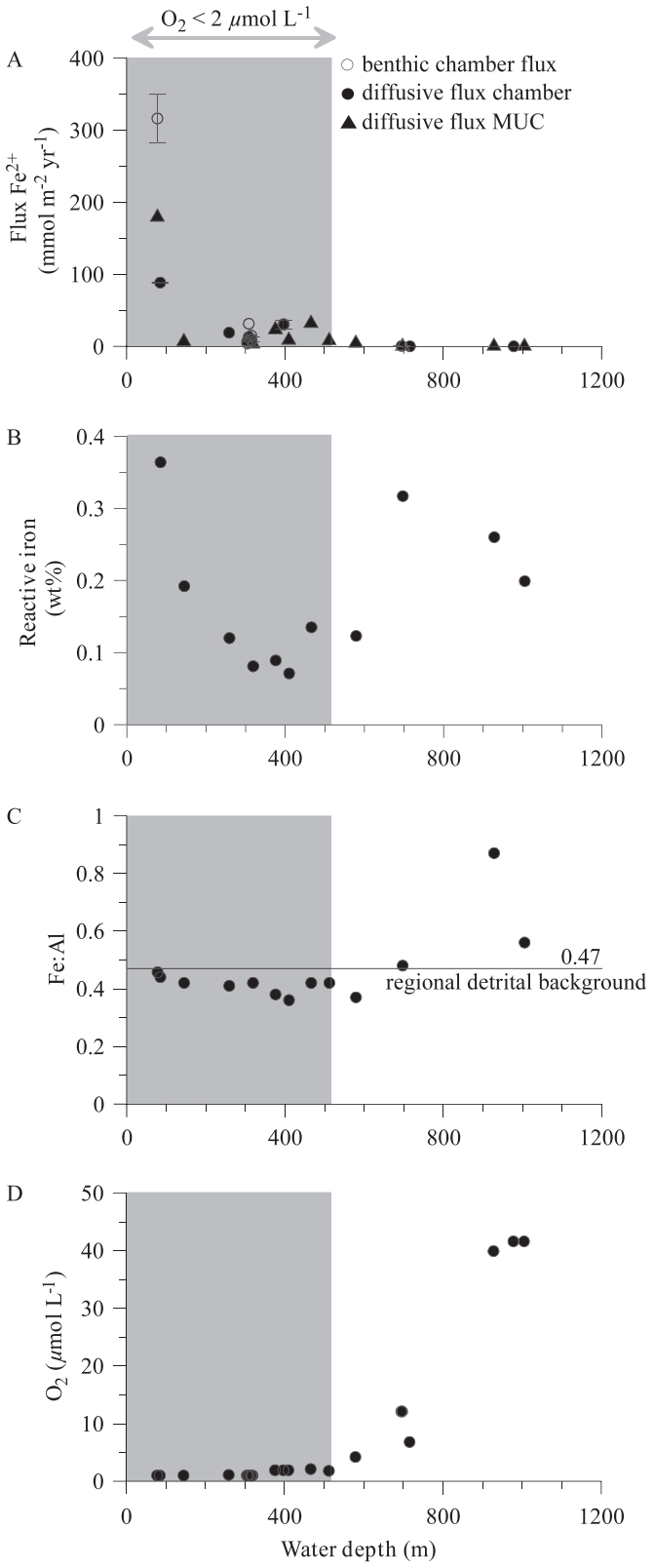

Fig. 5. Benthic Fe^{2+} fluxes and various parameters along the 11°S transect. (A) Fluxes of dissolved iron (Fe^{2+}; mmol m^{-2} yr^{-1}). Error bars correspond to minimum and maximum values of double measurements in lander deployments. (B) Reactive Fe contents (wt%) in surface sediments (0–1 cm). (C) Fe : Al ratios in surface sediments (0–1 cm; data from Scholz et al. 2011). Normalized Fe concentrations were used to eliminate the effect of varying dilution with detrital material. The black horizontal line depicts the Fe : Al ratio of the detrital background of 0.47 (andesite in the Andean Arc; Scholz et al. 2011). (D) Concentrations of dissolved O_2 in bottom waters. The gray array in each panel represents the OMZ where O_2 concentrations were < 2 µmol L^{-1}.

pore-water profiles of TPO_4 have previously been observed in the Peruvian (Froelich et al. 1988) as well as the Pakistan margin OMZ (Woulds et al. 2009) and have been attributed to carbonate fluorapatite precipitation.

Controls on benthic iron release—Dissolved Fe^{2+} fluxes across the sediment–water interface are controlled primarily by the bottom-water oxygen concentrations and the availability of reactive Fe (Pakhomova et al. 2007; Severmann et al. 2010). Under almost anoxic conditions (< 5 µmol O_2 L^{-1}; Table 1; Fig. 5D), elevated Fe^{2+} fluxes were observed down to ~ 600-m water depth. Below this depth, Fe^{2+} fluxes were negligible due to rising oxygen levels in the bottom water.

The highest Fe^{2+} fluxes measured on the shallow shelf at Sta. 543 and Sta. 568 (Table 2; Fig. 5A) coincide with the highest concentrations of reactive Fe (Fig. 5B), indicating high deposition rates of Fe oxyhydroxides. However, due to anoxic conditions right at the sediment surface, these become rapidly altered to Fe sulfides. Fe : Al ratios were close to the detrital background (Fig. 5C), which indicates that the reactive Fe is primarily supplied with Al and reflects a high input of detrital Fe oxyhydroxides from the continent. However, it is further plausible that part of the available Fe pool was deposited on the shelf during periods of bottom-water oxygenation, similar to those that were recorded during a long-term time series at a 94-m-deep site off Callao (Gutiérrez et al. 2008; M. Graco unpubl.). This time series revealed that, just prior to our research cruise, the shelf was oxygenated concurrent with a strong deepening of the oxycline (Fig. 7), reflecting the occurrence of a warming event along the Peruvian coast in association with Kelvin waves and the weakening of the coastal upwelling. During September 2008, the oceanographic conditions normalized and upwelling intensified. During such periods of shelf oxygenation, Fe^{2+} supplied from the deeper, permanent part of the OMZ may be reoxidized at the interface between anoxic and hypoxic water masses and be deposited on the seafloor. This mechanism has been suggested by Scholz et al. (2011), who showed that deposition and mobilization of trace metals on the Peruvian shelf is strongly affected by ENSO-related high amplitude oscillations of bottom-water oxygen concentrations (cf. Regional setting). During El Niño periods, surface sediments may also receive higher amounts of Fe oxyhydroxides from the continent because of heavy rainfall enhancing surface erosion and sediment discharge (Wells 1990). Dissolution of these Fe oxyhydroxides from either source induces increased Fe^{2+} fluxes when bottom-water conditions again turn anoxic, as was the case in September

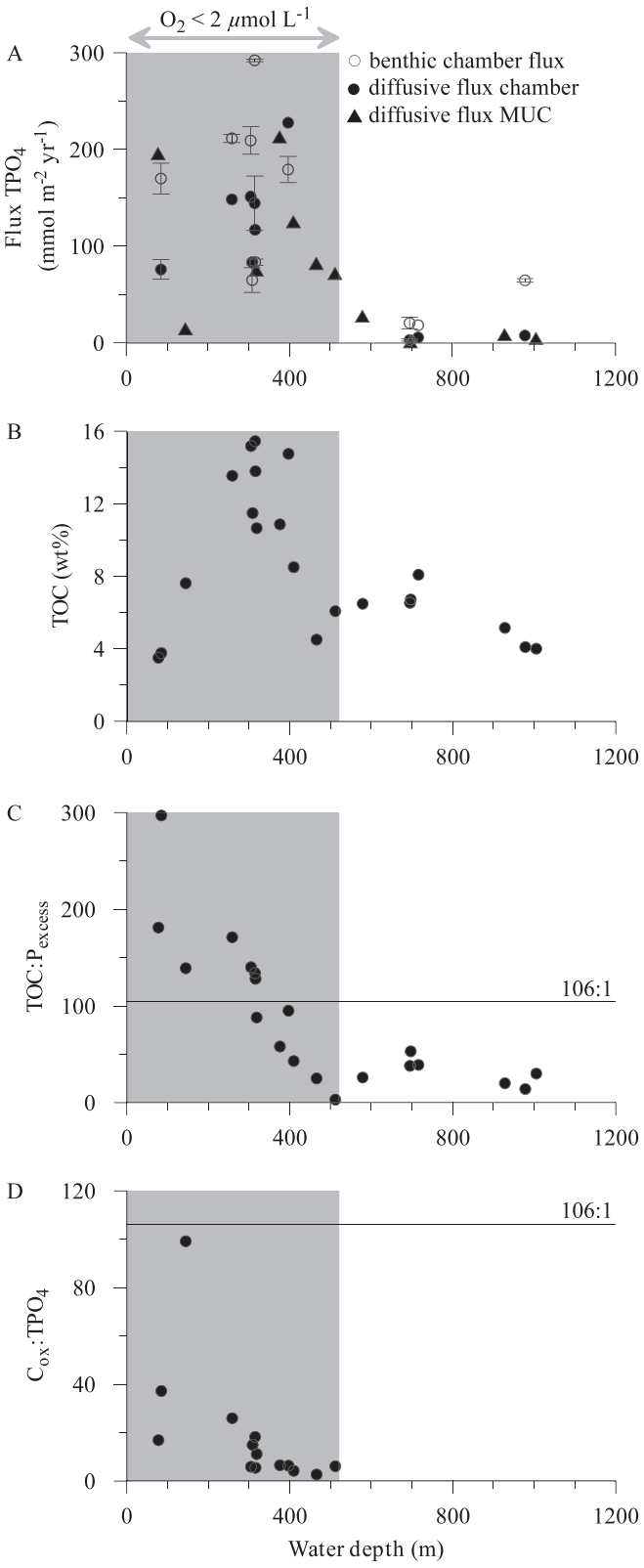

Fig. 6. Benthic TPO_4 fluxes and various parameters along the 11°S transect. (A) Fluxes of dissolved phosphate (TPO_4; mmol m^{-2} yr^{-1}). Error bars correspond to minimum and maximum values of double measurements in lander deployments. (B) TOC contents (wt%) in surface sediments (0–1 cm). (C) $TOC:P_{excess}$ ratios in surface sediments (0–1 cm). The black horizontal line depicts the TOC:P Redfield ratio of 106:1. (D) $C_{ox}:TPO_4$ flux ratios. The black horizontal line depicts the C:P Redfield ratio of 106:1. The gray array in each panel represents the OMZ where O_2 concentrations were < 2 µmol L^{-1}.

2008, about 1 month prior to the start of our research cruise at the end of October.

Intense sulfate reduction in the shelf sediments leads to the formation of Fe sulfides, which would be ultimately buried under permanently anoxic conditions. Under oxic bottom-water conditions, Fe sulfides may be recycled to the sediment surface by bioturbation and be reoxidized to Fe oxyhydroxides (Jørgensen and Nelson 2004). As mentioned in the Results section, there is a high potential for bioturbation at the shelf. However, the extent to which bioturbation affects the cycling of different Fe phases under oscillating oxic and anoxic bottom-water conditions and contributes to enhance overall Fe^{2+} flux on the shelf is not clear yet.

Within the core OMZ, Fe^{2+} fluxes were distinctly lower than at the 80-m stations, even though nearly anoxic bottom-water conditions (Table 1; Fig. 5A) provided suitable conditions for reductive Fe dissolution and release of Fe^{2+} across the benthic boundary. As oxygenation events can be assumed to occur more rarely down to these water depths, low bottom-water oxygen conditions in this region are supposed to be a persistent feature. Under such conditions, the reactive Fe pool will become progressively depleted over time. This is in agreement with the low reactive Fe concentrations as well as Fe:Al ratios significantly below the detrital background (Fig. 5B,C). Apparently, there is a strong imbalance between the reductive losses and the replenishment by detrital inputs from the continent in this region of the Peruvian margin.

Below about 700 m, increasing bottom-water oxygen concentrations (Table 1; Fig. 5D) cause the deepening of the redox front. Here, Fe^{2+} will be recycled within the sediment through reoxidation and reprecipitation in the surface layer (Fig. 3). Consequently, at these stations there was no flux of Fe^{2+} into the bottom water (Table 2; Fig. 5A). Both Fe:Al ratios and reactive Fe contents showed their maximum at ~ 900-m water depth (Fig. 5B,C) and showed decreasing values below. This strongly suggests that a large part of the Fe enrichment at the sediment surface derives from oxidative removal of Fe^{2+} that has been relocated from the core of the OMZ into the more-oxygenated deeper water layers. This is consistent with previous studies within the Arabian and Mexican OMZs that observed Fe enrichments linked to mechanisms of oxidative scavenging and OMZ relocation in sediments located below the OMZ (Van der Weijden et al. 1999; Nameroff et al. 2002).

Controls on benthic phosphate release—The distribution of TPO_4 fluxes along the transect (Fig. 6A) differs from that of Fe^{2+} (Fig. 5A), indicating different control mechanisms. While the release of Fe^{2+} from the seabed is largely

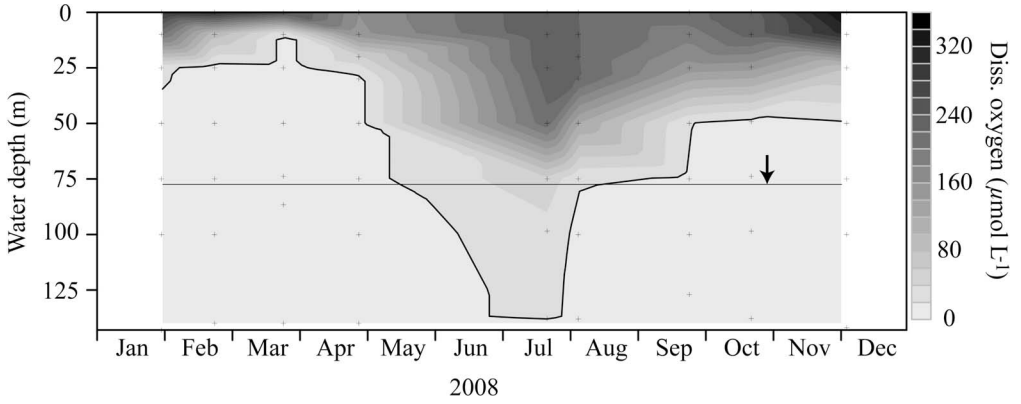

Fig. 7. Time-series of dissolved (diss.) oxygen (μmol L^{-1}) in 2008 off Callao (12°S). The gray horizontal line denotes the water depth of the shallowest station during the R/V *Meteor* cruise M77/1-2. The arrow denotes the start of this cruise. The black isoline corresponds to an oxygen concentration of 20 μmol L^{-1}.

determined by the availability of reactive iron that is reduced at the sediment surface, there are several sedimentary P sources that may contribute to the TPO_4 flux, comprising organic matter, iron bound P, and fish debris (Schenau and De Lange 2001).

With regard to P release driven by the reductive dissolution of Fe oxyhydroxides, the transect can be subdivided into distinct zones. At the sites shallower than 400-m water depth, noncoincident peaks of Fe^{2+} and TPO_4 indicate that TPO_4 liberation is at least partially decoupled from the reductive dissolution of Fe oxyhydroxides. In contrast, pore-water profiles of TPO_4 and Fe^{2+} from below 400-m water depth display similar trends, suggesting concurrent P release from the reductive dissolution of Fe oxyhydroxides. At all sites, the molar Fe : P ratios in the pore water at the peak position of Fe^{2+} ranged from 0.04 to 0.95 (Table 2), which is similar to Fe : P ratios measured in coastal sediments under anoxic conditions (Gunnars and Blomqvist 1997; Rozan et al. 2002; Lehtoranta and Heiskanen 2003). Such low Fe : P ratios indicate that, in addition to P release during reductive Fe dissolution, there was a further P source. If P release would be driven by the reductive Fe dissolution alone, one would expect Fe : P ratios in the range of 2 to 20 (Slomp et al. 1996; Gunnars and Blomqvist 1997; Anschutz et al. 1998). Another explanation for these low Fe : P ratios and the decoupling of pore-water TPO_4 and Fe^{2+} is the rapid formation of Fe sulfides (Rozan et al. 2002). For sites shallower than 400 m, sulfate reduction represents the major pathway of organic matter degradation (Bohlen et al. 2011), so that free dissolved Fe^{2+} can only exist in a narrow zone (< 10 cm) below the sediment surface.

At water depths between 250 m and 600 m (O_2 < 5 μmol L^{-1}), reactive Fe oxyhydroxides were almost absent (Fig. 5B); hence, Fe-bound P can obviously not serve as an important P source. At these sites, P release might be driven by organic matter degradation and dissolution of fish scales (*see* below). Only at the shallow shelf (Sta. 543), where the Fe : P ratio was close to unity, and at stations deeper than 600 m, Fe-bound P might be of some importance to the P cycle. On the shallow shelf, Fe oxyhydroxides are mainly supplied by the discharge of detrital sediments and reoxidation of dissolved Fe^{2+} when the shelf is oxygenated. Below 600-m water depth, Fe oxyhydroxides accumulate in the sediments, mainly due to the precipitation of dissolved Fe^{2+} at the lower oxycline (Scholz et al. 2011). However, at these stations both Fe and P are recycled within the sediment, resulting in low to zero fluxes.

In general, the deposition and degradation of organic matter in surface sediments underlying the OMZ is enhanced by enormous rates of surface-water productivity (Suess 1981). Consequently, organically bound P can be assumed as a major source contributing to the benthic TPO_4 flux. This is corroborated by the general agreement between TPO_4 fluxes (Fig. 6A) and the TOC content in surface sediments along the entire transect except the shallow shelf (Fig. 6B). Despite the lower TOC contents on the shelf, high organic carbon degradation rates of up to 8.2 mmol m^{-2} d^{-1} were calculated (Bohlen et al. 2011). Transient bottom-water oxygen levels are assumed to enhance organic matter degradation in sediments, leading to comparatively low TOC contents (Aller 1994). Another explanation is that at this site the solid phase composition is likely altered due to higher detrital sediment input. Below 600-m water depth, TPO_4 fluxes decreased distinctively despite still relatively high levels of TOC contents. This is due to increasing bottom-water O_2 levels and decreasing carbon degradation rates (Bohlen et al. 2011). Typically, high TOC : P ratios are observed in oxygen-deficient environments, indicating the preferential release of P over C (Ingall et al. 1993). The $TOC : P_{excess}$ ratio shown in Fig. 6C is corrected for the detrital P fraction (Böning et al. 2004) and represents a measure for the total reactive P. Down to 300-m water depth, the $TOC : P_{excess}$ ratios in surface sediments were distinctively elevated above the Redfield ratio, which is in agreement with $TOC : P_{excess}$ ratios measured previously in the same area (Böning et al. 2004). At sites below 300-m water depth, the strong decrease of $TOC : P_{excess}$ ratios may indicate the formation of authigenic P-bearing minerals and the accumulation of fish debris. Particularly, between 300-m and 400-m water depth, where high TPO_4 fluxes correspond to low $TOC : P_{excess}$ ratios in the sediment, it is likely that P regeneration from organic matter is masked by the

formation of authigenic minerals. Phosphorus accumulation in the form of phosphorites is well known in the Peruvian OMZ (Glenn and Arthur 1988), and we also found numerous macroscopic phosphorite concretions in sediment cores retrieved from water depths between 300 m and 600 m.

In order to provide a first-order estimate on how the measured TPO_4 fluxes relate to available P sources in the sediment, we exemplarily calculated "theoretical" TPO_4 fluxes for the sites at 85-m and 309-m water depth that would result from organic matter degradation in surface sediments (assuming Redfield ratio) and Fe-bound P. TPO_4 fluxes related to the reduction of Fe oxyhydroxides (TPO_4–Fe) were calculated from benthic Fe^{2+} fluxes (Table 2) and the molar Fe : P ratio of Fe oxyhydroxides, which is typically about 10 (Slomp et al. 1996). P release from the breakdown of organic matter (TPO_4–C_{ox}) was derived by approximating organic carbon degradation (C_{ox}, Table 2) in surface sediments underneath a nearly anoxic water body ($O_2 < 2$ μmol L^{-1}) using TA pore-water gradients. C_{ox} can be calculated from TA gradients because HCO_3^- rather than CO_2 is produced in anoxic diagenetic pathways (Froelich et al. 1979). Under near-neutral conditions, HCO_3^- contributes more than 90% to TA, so that the TA gradient can be reasonably well applied to calculate a diffusive HCO_3^- flux and, hence, use it as a proxy for C_{ox}. In addition, the values presented in Table 2 are in good agreement with modeled values of C_{ox} (Bohlen et al. 2011). The combined average flux of TPO_4–C_{ox} and TPO_4–Fe at the shelf (78–85 m, $n = 2$) was 53.5 mmol m^{-2} yr^{-1} and in the core of the OMZ (305–319 m, $n = 5$) was 13.0 mmol m^{-2} yr^{-1}. We are aware that the P release calculated from the Fe^{2+} flux represents a minimum estimate because it does not account for Fe^{2+} that is precipitated as FeS. These fluxes are a factor of 3 and 12 lower than the measured fluxes, which is in agreement with low molar C_{ox} : TPO_4 ratios of benthic fluxes (Fig. 6D, calculated from C_{ox} and TPO_4, Table 2). These results highlight the preferential release of P over C with respect to the average composition of marine organic matter from OMZ sediments. At the 85-m station, some of the mismatch between theoretical and measured TPO_4 fluxes could be leveled out, if the Fe : P ratio of Fe oxyhydroxides was distinctively lower. However, at 309 m, and at similar sites with low Fe^{2+} but high TPO_4 fluxes, any change in the Fe : P ratio would not help to further resolve the mismatch.

Apart from the non-Redfield degradation of organic matter there are a few other processes that may explain the high TPO_4 fluxes. Fish scales are exceptionally abundant in sediments of the Peruvian OMZ (Suess 1981), hence their dissolution may represent an important source of pore-water TPO_4 (Suess 1981; Schenau and De Lange 2001). In addition, storage and release of P by microorganisms and protozoans under oscillating oxic and anoxic conditions has been supposed to contribute to the benthic TPO_4 flux (Sannigrahi and Ingall 2005). Sannigrahi and Ingall (2005) provided evidence for the accumulation of polyphosphates in oxic sediments, whereas in anoxic sediments polyphosphates were absent. This has been interpreted as release of P under anoxic conditions when these organisms degrade their intracellular polyphosphate storage that was built up under oxic conditions, to gain energy. Recently, transient uptake and release of P under oscillating redox conditions has been reported for the giant sulfide-oxidizing bacteria *Thiomargarita namibiensis* and members of the genus *Beggiatoa* (Schulz and Schulz 2005; Goldhammer et al. 2010; Brock and Schulz-Vogt 2011). Widespread occurrence of filamentous sulfur bacteria on the Peruvian shelf and upper slope was observed in sediment samples and in seafloor images acquired during the same cruise (T. Mosch unpubl.). In fact, sulfur bacteria of the genera *Beggiatoa* and *Thioploca* are very common in OMZ sediments of the Peruvian and Chilean continental shelf as well as in other OMZs worldwide (Gallardo 1977; Levin et al. 2002; Gutiérrez et al. 2008). Within the context of episodic oxygenation events that occur at the Peruvian shelf and upper slope (Gutiérrez et al. 2008), we suggest that *Beggiatoa* can probably enhance TPO_4 fluxes via the above-described P metabolism. Sulfur bacteria have been further suggested to be involved in the formation of apatite, which contributes to mitigate P release from the seabed (Schulz and Schulz 2005). During ^{33}P radiotracer experiments, Goldhammer et al. (2010) observed the greatest conversion rates of phosphate to apatite mediated by sulfur bacteria under anoxic conditions. Apatite formation is indicated by decreasing pore-water phosphate concentrations with sediment depth at all sites except for the shelf. Despite constant P concentrations with increasing sediment depth, apatite formation can also be assumed for the shelf since in the absence of precipitation P would accumulate in the pore water due to organic matter degradation and the associated P release. However, it can not be resolved if, and to what extent, release of P from microbes contributes to apatite formation.

In conclusion, the OMZ represents an important Fe^{2+} and TPO_4 source to the bottom water. The core of the OMZ ($\sim$ 250–500 m), with rather stable bottom-water O_2 levels close to anoxia, is characterized with persistent but comparatively low Fe^{2+} and high TPO_4 fluxes. This is in strong contrast to the shelf region, which is subjected to oscillating bottom-water O_2 conditions that trigger a complex biogeochemical reaction network of Fe, P, and S turnover, resulting in transient high Fe^{2+} and TPO_4 release under anoxia. This renders the shelf a sensitive region that provides limiting nutrients to the surface water, allowing extensive phytoplankton blooms to develop in the Peruvian upwelling system.

Global significance of benthic phosphorus and iron fluxes from OMZs—To evaluate the importance of TPO_4 and Fe^{2+} fluxes in the Peruvian OMZ from a more general perspective, we compiled a comparative data set from other coastal upwelling and OMZ regions (Fig. 8). Overall, TPO_4 fluxes measured in this study generally exceed those reported from other OMZs throughout the world. The global benthic TPO_4 flux from oxic shelf and slope sediments (> 20 μmol L^{-1} O_2) has recently been estimated as 75×10^{10} mol yr^{-1} for an area of 90×10^6 km^2 (Wallmann 2010), corresponding to an average TPO_4 flux of 8 mmol m^{-2} yr^{-1}. The average TPO_4 flux from the

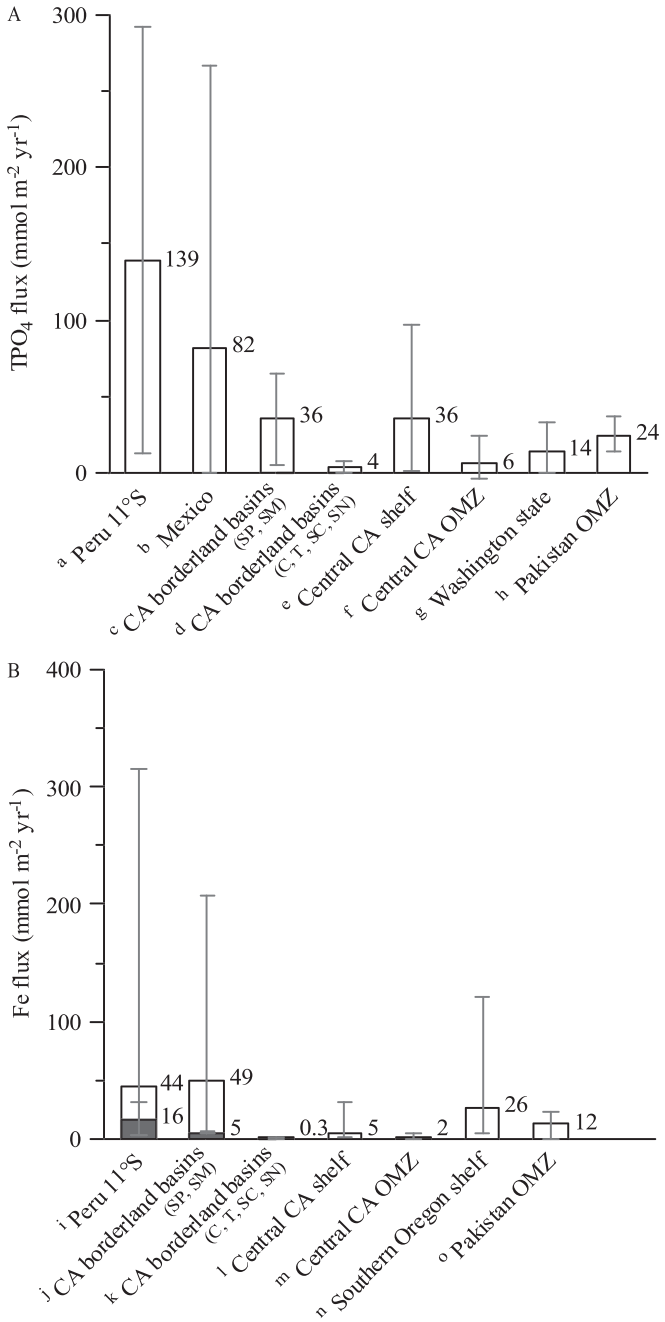

Fig. 8. Comparison of (A) phosphate (TPO_4) and (B) iron (Fe^{2+}) flux data from 11°S (total average of benthic chamber and diffusive fluxes for the OMZ ($O_2 < 2$ μmol L^{-1}, ~ 80–510-m water depth)) to data from other oxygen-deficient environments. Fluxes are given in mmol m^{-2} yr^{-1}. Values comprise single data points or total averages of all fluxes for any specific region. Fluxes shown by gray bars were calculated excluding high outlier Fe fluxes (*see* text for further explanation). (A) TPO_4 fluxes: [a]Peru 11°S; this study (water depth: 80–510 m, O_2: < 2 μmol L^{-1}), [b]Mexico; Hartnett and Devol 2003 (water depth: 100–1020 m, O_2: 0–6 μmol L^{-1}), [c]California borderland basins (SP = San Pedro basin, SM = Santa Monica basin); Berelson et al. 1987; Jahnke 1990; McManus et al. 1997; Hammond et al. 2004 (water depth: 900–910 m, O_2: 4–10 μmol L^{-1}), [d]California borderland basins (C = Catalina basin, T = Tanner basin, SC = San Clemente basin, SN = San Nicholas basin); Berelson et al. 1987; Bender et al. 1989; Ingall and Jahnke 1997; McManus et al. 1997; Hammond et al. 2004 (water depth: 1300–2070 m, O_2: 17–65 μmol L^{-1}), [e]Central California shelf; McManus et al. 1997; Berelson et al. 2003; Hammond et al. 2004 (water depth: 95–200 m, O_2: 64–185 μmol L^{-1}), [f]Central California OMZ; Reimers et al. 1992; McManus et al. 1997 (water depth: 530–1370 m, O_2: 16–65 μmol L^{-1}), [g]Washington State; Devol and Christensen 1993 (water depth: 40–630 m, O_2: 25–240 μmol L^{-1}), [h]Pakistan OMZ; Woulds et al. 2009 (water depth: 140–940 m, O_2: 1–3 μmol L^{-1}, post-monsoon). (B) Fe fluxes: [i]Peru 11°S; this study (water depth: 80–510 m, O_2: < 2 μmol L^{-1}), [j]California borderland basins (SP = San Pedro basin, SM = Santa Monica basin); McManus et al. 1997; Elrod et al. 2004; Severmann et al. 2010 (water depth: 880–910 m, O_2: 4–10 μmol L^{-1}), [k]California borderland basins (C = Catalina basin, T = Tanner basin, SC = San Clemente basin, SN = San Nicholas basin); McManus et al. 1997; Elrod et al. 2004 (water depth: 1300–2070 m, O_2: 17–65 μmol L^{-1}), [l]Central California shelf; McManus et al. 1997; Elrod et al. 2004; Severmann et al. 2010 (water depth: 95–200 m, O_2: 64–185 μmol L^{-1}), [m]Central California OMZ; McManus et al. 1997, Elrod et al. 2004 (water depth: 530–1370 m, O_2: 16–65 μmol L^{-1}), [n]Southern Oregon shelf; Severmann et al. 2010 (water depth: 90–190 m, O_2: 60–142 μmol L^{-1}), [o]Pakistan OMZ; Law et al. 2009 (water depth: 140–940 m, O_2: 1–3 μmol L^{-1}, post-monsoon).

Peruvian OMZ (< 2 μmol L^{-1} O_2) exceeds the average global flux from oxic shelf and slope environments by a factor of 17, which highlights the significance of anoxic sediments underlying the Peruvian and other OMZs as a major P source to the ocean.

Measurements of benthic Fe fluxes from continental shelf and slope sediments are only available from a very limited number of field studies. However, comparison with existing data reveals that fluxes presented in this study are among the highest recorded so far (Fig. 8). The highest total fluxes, associated with the highest variability, are observed on the shallow shelves, which typically experience the most intense environmental perturbations on various time scales. Including all stations of this study (Table 2), the resulting average flux in the Peruvian OMZ (< 2 μmol O_2 L^{-1}) is 44 mmol m^{-2} yr^{-1}, which is comparable to the average of 49 mmol m^{-2} yr^{-1} (white bars in Fig. 8) calculated for the California borderland basins (San Pedro and Santa Monica). Similar to the Peruvian shelf and upper slope, these basins are periodically ventilated (Berelson 1991), resulting in variable bottom-water oxygen concentrations and, hence, variable Fe fluxes (Severmann et al. 2010). The above average includes two high outlier fluxes (207 mmol m^{-2} yr^{-1}, San Pedro basin; 150 mmol m^{-2} yr^{-1}, Santa Monica basin; Severmann et al. 2010), measured when the basins were highly oxygen deficient (< 5 μmol O_2 L^{-1}). Fluxes measured when these sites were slightly more oxygenated (< 10 μmol O_2 L^{-1}, 5 mmol m^{-2} yr^{-1}) fall within the range of values measured in the Peruvian OMZ core at water depths > 85 m. Obviously, similar mechanisms of reoxidation during oxygenation periods and subsequent remobilization (resulting in highly elevated fluxes) during anoxic periods (*see* Controls on benthic iron release) are active in these settings. Exclusion of the highest

Fe fluxes measured at the Peruvian shelf stations (543, 568) and the outliers of the California borderland basins results in considerably lower average fluxes (gray bars in Fig. 8), which are comparable to those measured at river-dominated shelf sites (high reactive Fe input) from the Oregon and California margin (Severmann et al. 2010) or to those measured in the OMZ off Pakistan. Regardless of which data set is chosen, it is obvious that OMZs are major sources of dissolved Fe compared to normal marine environments. Based on an empirical relationship between Fe fluxes and organic carbon oxidation rates for settings > 20 μmol L^{-1} O_2, Elrod et al. (2004) estimated a dissolved Fe input of 8.9×10^{10} mol yr^{-1} for the global shelf area (3×10^7 km^2). This corresponds to an average Fe flux of 3 mmol m^{-2} yr^{-1}, which is obviously much lower than the average benthic Fe fluxes from sediments underlying oxygen-deficient waters and, hence, must be regarded as a minimum estimate.

An important pathway of Fe input to the surface ocean is atmospheric dust deposition. The following ''back-of-the-envelope'' calculation may illustrate how hotspots of benthic Fe mobilization compare to areas of high Fe input by dust deposition. One of the largest areas of atmospheric dust deposition is the tropical North Atlantic. Based on a composite map of dust delivery to the global oceans (Jickells et al. 2005), we calculated that the area of the North Atlantic hotspot (between 0–30°N) annually receives about 9.6×10^{10} kg dust, which translates into dissolved Fe fluxes of 3.4×10^7 kg yr^{-1} to 3.4×10^8 kg yr^{-1} that may become biologically available (assuming an Fe content of 3.5% in soil dust and an aerosol Fe solubility of 1–10% [Jickells and Spokes 2001]). Projecting the average Fe flux of 16–44 mmol m^{-2} yr^{-1} (Fig. 8) to a total area of the Peruvian OMZ ($O_2 < 0.5$ mL L^{-1} or 22 μmol L^{-1}) of 77,000 km^2 (Helly and Levin 2004) adds up to a total benthic flux of 6.9×10^7 kg yr^{-1} to 1.9×10^8 kg yr^{-1} and indicates that the source strengths of these completely different input mechanism are comparable in magnitude. However, at this time it is not clear if, and on which time scales, benthic Fe release may be considered as a potentially important source to the surface ocean. At least this could be significant in coastal upwelling systems with a low input of atmospheric dust, such as the Peruvian margin.

This study underlines the role of sediments underlying OMZs as important Fe^{2+} and TPO_4 sources to the bottom water, which provide important feedbacks that may affect surface-water primary productivity (Wallmann 2003) and, hence, accelerate the worldwide expansion of OMZs. Therefore, the investigation of benthic–pelagic coupling in oxygen-deficient waters along continental margins will require explicit consideration in the future.

Acknowledgments

We thank the captain and crew of the R/V *Meteor* for their effort and help during cruise M77/1-2, and A. Bleyer, B. Domeyer, M. Dibbern, R. Ebbinghaus, S. Kriwanek, D. Rau, and R. Surberg for help with biogeochemical analyses onboard and in the home laboratory. Furthermore, many thanks are due to B. Bannert, A. Petersen, and M. Türk for their technical assistance during benthic lander deployments; to P. Appel for management of XRF measurements; and, as well, to E. Piñero for her help with data treatment. We appreciate the editorial handling by Dr. Ronnie Glud and the constructive comments of three anonymous reviewers, which very much helped to improve the manuscript. This is a contribution of the Sonderforschungsbereich 754 ''Climate—Biogeochemistry in the tropical oceans,'' which is supported by the Deutsche Forschungsgemeinschaft.

References

Aller, R. C. 1994. Bioturbation and remineralization of sedimentary organic matter: effects of redox oscillation. Chem. Geol. **144:** 331–345, doi:10.1016/0009-2541(94)90062-0

Anschutz, P., S. Zhong, and B. Sundby. 1998. Burial efficiency of phosphorus and the geochemistry of iron in continental margin sediments. Limnol. Oceanogr. **43:** 53–64, doi:10.4319/lo.1998.43.1.0053

Bakun, A. 1985. Comparative studies and the recruitment problem: Searching for generalizations. CalCOFI Rep. **26:** 30–40.

Bender, M., R. Jahnke, R. Weiss, W. Martin, D. T. Heggie, J. Orchardo, and T. Sowers. 1989. Organic carbon oxidation and benthic nitrogen and silica dynamics in San Clemente Basin, a continental borderland site. Geochim. Cosmochim. Acta **53:** 685–697, doi:10.1016/0016-7037(89)90011-2

Berelson, W., and others. 2003. A time series of benthic flux measurements from Monterey Bay, CA. Cont. Shelf Res. **23:** 457–481, doi:10.1016/S0278-4343(03)00009-8

Berelson, W. M. 1991. The flushing of two deep-sea basins, southern California borderland. Limnol. Oceanogr. **36:** 1150–1166, doi:10.4319/lo.1991.36.6.1150

———, D. E. Hammond, and K. S. Johnson. 1987. Benthic fluxes and the cycling of biogenic silica and carbon in two southern California borderland basins. Geochim. Cosmochim. Acta **51:** 1354–1363, doi:10.1016/0016-7037(87)90320-6

Bohlen, L., and others. 2011. Benthic nitrogen cycling traversing the Peruvian oxygen minimum zone. Geochim. Cosmochim. Acta **75:** 6094–6111, doi:10.1016/j.gca.2011.08.010

Böning, P., H.-J. Brumsack, M. E. Böttcher, B. Schnetger, C. Kriete, J. Kallmeyer, and S. L. Borchers. 2004. Geochemistry of Peruvian near-surface sediments. Geochim. Cosmochim. Acta **68:** 4429–4451, doi:10.1016/j.gca.2004.04.027

Boudreau, B. P. 1997. Diagenetic models and their implementation. Springer.

Brock, J., and H. N. Schulz-Vogt. 2011. Sulfide induces phosphate release from polyphosphate in cultures of a marine *Beggiatoa* strain. ISME J. **5:** 497–506, doi:10.1038/ismej.2010.135

Devol, A. H., and J. P. Christensen. 1993. Benthic fluxes and nitrogen cycling in sediments of the continental margin of the eastern North Pacific. J. Mar. Res. **51:** 345–372, doi:10.1357/0022240933223765

Elrod, V. A., W. M. Berelson, K. H. Coale, and K. S. Johnson. 2004. The flux of iron from continental shelf sediments: A missing source for global budgets. Geophys. Res. Lett. **31:** L12307, doi:10.1029/2004GL020216

Froelich, P. N., G. P. Klinkhammer, M. L. Bender, N. A. Luedtke, G. R. Heath, D. Cullen, and P. Dauphin. 1979. Early oxidation of organic matter in pelagic sediments of the eastern equatorial Atlantic: Suboxic diagenesis. Geochim. Cosmochim. Acta **43:** 1075–1090, doi:10.1016/0016-7037(79)90095-4

———, and others. 1988. Early diagenesis of organic matter in Peru continental margin sediments: Phosphorite precipitation. Mar. Geol. **80:** 309–343, doi:10.1016/0025-3227(88)90095-3

Fuenzalida, R., W. Schneider, J. Garcés-Vargas, L. Bravo, and C. Lange. 2009. Vertical and horizontal extension of the oxygen minimum zone in the eastern South Pacific Ocean. Deep-Sea Res. II **56:** 992–1003, doi:10.1016/j.dsr2.2008.11.001

Gallardo, V. A. 1977. Large benthic microbial communities in sulfide biota under Peru-Chile subsurface countercurrent. Nature **268:** 331–332, doi:10.1038/268331a0

Glenn, C. R., and M. A. Arthur. 1988. Petrology and major element geochemistry of Peru margin phosphorites and associated diagenetic minerals: Authigenesis in modern organic-rich sediments. Mar. Geol. **80:** 231–267, doi:10.1016/0025-3227(88)90092-8

Goldhammer, T., V. Brüchert, T. G. Ferdelman, and M. Zabel. 2010. Microbial sequestration of phosphorus in anoxic upwelling sediments. Nat. Geosci. **3:** 557–561, doi:10.1038/ngeo913

Grasshoff, K., M. Erhardt, and K. Kremling. 1999. Methods of seawater analysis, 3rd ed. Wiley-VCH.

Gunnars, A., and S. Blomqvist. 1997. Phosphate exchange across the sediment-water interface when shifting from anoxic to oxic conditions—an experimental comparison of freshwater and brackish-marine systems. Biogeochemistry **37:** 203–226, doi:10.1023/A:1005744610602

Gutiérrez, D., E. Enríquez, S. Purca, L. Quipúzcoa, R. Marquina, G. Flores, and M. Graco. 2008. Oygenation episodes on the continental shelf of central Peru: Remote forcing and benthic ecosystem response. Prog. Oceanogr. **79**, 177–189, doi:10.1016/j.pocean.2008.10.025

Hammond, D. E., K. M. Cummins, J. McManus, W. M. Berelson, G. Smith, and F. Spagnoli. 2004. Methods for measuring benthic nutrient flux on the California margin: Comparing shipboard core incubations to in situ lander results. Limnol. Oceanogr.: Methods **2:** 146–159, doi:10.4319/lom.2004.2.146

Hartnett, H. E., and A. H. Devol. 2003. Role of a strong oxygen-deficient zone in the preservation and degradation of organic matter: A carbon budget for the continental margins of northwest Mexico and Washington State. Geochim. Cosmochim. Acta **67:** 247–264, doi:10.1016/S0016-7037(02)01076-1

Helly, J. J., and L. A. Levin. 2004. Global distribution of naturally occurring marine hypoxia on continental margins. Deep-Sea Res. I **51:** 1159–1168, doi:10.1016/j.dsr.2004.03.009

Hutchins, D. A., G. R. DiTullio, Y. Zhang, and K. W. Bruland. 1998. An iron limitation mosaic in the California upwelling regime. Limnol. Oceanogr. **43:** 1037–1045, doi:10.4319/lo.1998.43.6.1037

Ingall, E., and R. Jahnke. 1997. Influence of water column anoxia on the elemental fractionation of carbon and phosphorus during sediment diagenesis. Mar. Geol. **139:** 219–229, doi:10.1016/S0025-3227(96)00112-0

Ingall, E. D., R. M. Bustin, and P. Van Cappellen. 1993. Influence of water column anoxia on the burial and preservation of carbon and phosphorus in marine shales. Geochim. Cosmochim. Acta **57:** 303–316, doi:10.1016/0016-7037(93)90433-W

Ivanenkov, V. N., and Y. I. Lyakhin. 1978. Determination of total alkalinity in seawater, p. 110–114. *In* O. K. Bordovsky and V. N. Ivanenkov [eds.], Methods of hydrochemical investigations in the ocean. Nauka.

Jahnke, R. A. 1990. Early diagenesis and recycling of biogenic debris at the seafloor, Santa Monica Basin, California. J. Mar. Res. **48:** 413–436, doi:10.1357/002224090784988773

Jensen, H. S., P. B. Mortensen, F. Ø. Andersen, E. Rasmussen, and A. Jensen. 1995. Phosphorus cycling in a coastal marine sediment, Aarhus Bay, Denmark. Limnol. Oceanogr. **40:** 908–917, doi:10.4319/lo.1995.40.5.0908

Jickells, T. D., and L. J. Spokes. 2001. Atmospheric iron inputs to the oceans, p. 85–121. *In* D. R. Turner and K. A. Hunter [eds.], The biogeochemistry of iron in seawater. Wiley.

———, and others. 2005. Global iron connections between desert dust, ocean biogeochemistry, and climate. Science **308:** 67–71, doi:10.1126/science.1105959

Johnson, K. S., F. P. Chavez, and G. E. Friedrich. 1999. Continental shelf sediment as a primary source of iron for coastal phytoplankton. Nature **398:** 697–700, doi:10.1038/19511

Jørgensen, B. B., and D. C. Nelson. 2004. Sulfide oxidation in marine sediments: Geochemistry meets microbiology. Geol. Soc. Am. Spec. Pap. **379:** 63–81. doi:10.1130/0-8137-2379-5.63

Kostka, J. E., and G. W. Luther, III. 1994. Partitioning and speciation of solid phase iron in saltmarsh sediments. Geochim. Cosmochim. Acta **58:** 1701–1710, doi:10.1016/0016-7037(94)90531-2

Krissek, L. A., K. F. Scheidegger, and L. D. Kulm. 1980. Surface sediments of the Peru-Chile continental margin and the Nazca Plate. Geol. Soc. Am. Bull. **91:** 321–331, doi:10.1130/0016-7606(1980)91

Law, G. T. W., T. M. Shimmield, G. B. Shimmield, G. L. Cowie, E. R. Breuer, and S. M. Harvey. 2009. Manganese, iron and sulphur cycling on the Pakistan margin. Deep-Sea Res. II **56:** 305–323, doi:10.1016/j.dsr2.2008.06.011

Lehtoranta, J., and A.-S. Heiskanen. 2003. Dissolved iron : phosphate ratio as an indicator of phosphate release to oxic water of the inner and outer coastal Baltic Sea. Hydrobiologia **492:** 69–84, doi:10.1023/A:1024822013580

Le Maitre, R. W. 1976. The chemical variability of some common igneous rocks. J. Petrol. **17:** 589–637. doi:10.1093/petrology/17.4.589

Levin, L., and others. 2002. Benthic processes on the Peru margin: A transect across the oxygen minimum zone during the 1997–98 El Niño. Prog. Oceanogr. **53:** 1–27, doi:10.1016/S0079-6611(02)00022-8

Li, Y.-H., and S. Gregory. 1974. Diffusion of ions in sea water and in deep-sea sediment. Geochim. Cosmochim. Acta **38:** 703–714, doi:10.1016/0016-7037(74)90145-8

Matear, R. J., and A. C. Hirst. 2003. Long-term changes in dissolved oxygen concentrations in the ocean caused by protracted global warming. Glob. Biogeochem. Cycles **17:** 1125, doi:10.1029/2002GB001997

McManus, J., W. M. Berelson, K. H. Coale, K. S. Johnson, and T. E. Kilgore. 1997. Phosphorus regeneration in continental margin sediments. Geochim. Cosmochim. Acta **61:** 2891–2907, doi:10.1016/S0016-7037(97)00138-5

Moore, J. K., and O. Braucher. 2008. Sedimentary and mineral dust sources of dissolved iron to the world ocean. Biogeosciences **5:** 631–656, doi:10.5194/bg-5-631-2008

Nameroff, T. J., L. S. Balistrieri, and J. W. Murray. 2002. Suboxic trace metal geochemistry in the eastern tropical North Pacific. Geochim. Cosmochim. Acta **66:** 1139–1158, doi:10.1016/S0016-7037(01)00843-2

Pakhomova, S. V., P. O. J. Hall, M. Y. Kononets, A. G. Rozanov, A. Tengberg, and A. V. Vershinin. 2007. Fluxes of iron and manganese across the sediment-water interface under various redox conditions. Mar. Chem. **107:** 319–331, doi:10.1016/j.marchem.2007.06.001

Pennington, J. T., K. L. Mahoney, V. S. Kuwahara, D. D. Kolber, R. Calienes, and F. P. Chavez. 2006. Primary production in the eastern tropical Pacific: A review. Prog. Oceanogr. **69:** 285–317, doi:10.1016/j.pocean.2006.03.012

Reimers, C. E., R. A. Jahnke, and D. C. McCorkle. 1992. Carbon fluxes and burial rates over the continental slope and rise off central California with implications for the global carbon cycle. Glob. Biogeochem. Cycles **6:** 199–224, doi:10.1029/92GB00105

———, and E. Suess. 1983. Spatial and temporal patterns of organic matter accumulation on the Peru continental margin, p. 311–337. *In* J. Thiede and E. Suess [eds.], Coastal upwelling: Its sediment record. Part B: Sedimentary records of ancient coastal upwelling. Plenum Press.

Rozan, T. F., and others. 2002. Iron-sulfur-phosphorus cycling in the sediments of a shallow coastal bay: Implications for sediment nutrient release and benthic macroalgal blooms. Limnol. Oceanogr. **47:** 1346–1354, doi:10.4319/lo.2002.47.5.1346

Sannigrahi, P., and E. Ingall. 2005. Polyphosphates as a source of enhanced P fluxes in marine sediments overlain by anoxic water: Evidence from ^{31}P NMR. Geochem. Trans. **6:** 52–59, doi:10.1186/1467-4866-6-52

Schenau, S. J., and G. J. De Lange. 2001. Phosphorus regeneration vs. burial in sediments of the Arabian Sea. Mar. Chem. **75:** 201–217, doi:10.1016/S0304-4203(01)00037-8

Scholz, F., C. Hensen, A. Noffke, A. Rohde, V. Liebetrau, and K. Wallmann. 2011. Early diagenesis of redox-sensitive trace metals in the Peruvian upwelling area-response to ENSO-related oxygen fluctuations in the water column. Geochim. Cosmochim. Acta **75:** 7257–7276, doi:10.1016/j.gca.2011.08.007

Schulz, H. N., and H. D. Schulz. 2005. Large sulfur bacteria and the formation of phosphorite. Science **21:** 416–418, doi:10.1126/science.1103096

Seeberg-Elverfeldt, J., M. Schlüter, T. Feseker, and M. Kölling. 2005. Rhizon sampling of porewaters near the sediment-water interface of aquatic systems. Limnol. Oceanogr.: Methods **3:** 361–371, doi:10.4319/lom.2005.3.361

Severmann, S., J. McManus, W. M. Berelson, and D. E. Hammond. 2010. The continental shelf benthic iron flux and its isotope composition. Geochim. Cosmochim. Acta **74:** 3984–4004, doi:10.1016/j.gca.2010.04.022

Slomp, C. P., J. F. P. Malschaert, and W. Van Raaphorst. 1998. The role of adsorption in sediment-water exchange of phosphate in North Sea continental margin sediments. Limnol. Oceanogr. **43:** 832–846, doi:10.4319/lo.1998.43.5.0832

———, S. J. Van der Gaast, and W. Van Raaphorst. 1996. Phosphorus binding by poorly crystalline iron oxides in North Sea sediments. Mar. Chem. **52:** 55–73, doi:10.1016/0304-4203(95)00078-X

Sommer, S., and others. 2009. Seabed methane emissions and the habitat of frenulate tube worms on the Captain Arutyunov mud volcano (Gulf of Cadiz). Mar. Ecol. Prog. Ser. **382:** 69–86, doi:10.3354/meps07956

Stramma, L., G. C. Johnson, J. Sprintall, and V. Mohrholz. 2008. Expanding oxygen-minimum zones in the tropical oceans. Science **320:** 655–658, doi:10.1126/science.1153847

Strub, P. T., J. M. Mesías, V. Montecino, R. Rutland, and S. Salinas. 1998. Coastal ocean circulation of western South America, p. 273–313. *In* A. R. Robinson and K. H. Brink [eds.], The sea, v. 11. Wiley.

Suess, E. 1981. Phosphate regeneration from sediments of the Peru continental margin by dissolution of fish debris. Geochim. Cosmochim. Acta **45:** 577–588, doi:10.1016/0016-7037(81)90191-5

———, L. D. Kulm, and J. S. Killingley. 1987. Coastal upwelling and a history of organic rich mudstone deposition off Peru. *In* J. Brooks and A. J. Fleet [eds.], Marine petroleum source rocks. Geol. Soc. Spec. Publ. **26:** 181–197.

Sundby, B., L. G. Anderson, P. O. J. Hall, A. Iverfeldt, M. M. Rutgers van der Loeff, and S. F. G. Westerlund. 1986. The effect of oxygen on release and uptake of cobalt, manganese, iron and phosphate at the sediment-water interface. Geochim. Cosmochim. Acta **50:** 1281–1288, doi:10.1016/0016-7037(86)90411-4

———, C. Gobeil, N. Silverberg, and A. Mucci. 1992. The phosphorus cycle in coastal marine sediments. Limnol. Oceanogr. **37:** 1129–1145, doi:10.4319/lo.1992.37.6.1129

Van der Weijden, C. H., G. J. Reichart, and H. J. Visser. 1999. Enhanced preservation of organic matter in sediments deposited within the oxygen minimum zone in the northeastern Arabian Sea. Deep-Sea Res. I **46:** 807–830, doi:10.1016/S0967-0637(98)00093-4

Wallmann, K. 2003. Feedbacks between oceanic redox states and marine productivity: A model perspective focused on benthic phosphorus cycling. Glob. Biogeochem. Cycles **17:** 1084, doi:10.1029/2002GB001968

———. 2010. Phosphorus imbalance in the global ocean? Glob. Biogeochem. Cycles **24:** GB4030, doi:10.1029/2009GB003643

Wells, L. E. 1990. Holocene history of the El Niño phenomenon as recorded in flood sediments of northern coastal Peru. Geology **18:** 1134–1137, doi:10.1130/0091-7613(1990)018

Woulds, C., M. C. Schwartz, T. Brand, G. L. Cowie, G. Law, and S. R. Mowbray. 2009. Porewater nutrient concentrations and benthic nutrient fluxes across the Pakistan margin OMZ. Deep-Sea Res. II **56:** 333–346, doi:10.1016/j.dsr2.2008.05.034

Wyrtki, K. 1962. The oxygen minima in relation to ocean circulation. Deep-Sea Res. **9:** 11–23, doi:10-1016/0011-7471(62)90243-7

Associate editor: Ronnie Nøhr Glud

Received: 26 August 2011
Accepted: 29 January 2012
Amended: 27 February 2012

Chemical Geology 355 (2013) 56–68

Contents lists available at SciVerse ScienceDirect

Chemical Geology

journal homepage: www.elsevier.com/locate/chemgeo

The manganese and iron shuttle in a modern euxinic basin and implications for molybdenum cycling at euxinic ocean margins

Florian Scholz [a,*], James McManus [a], Stefan Sommer [b]

[a] College of Earth, Ocean, and Atmospheric Sciences (CEOAS), Oregon State University, 104 CEOAS Administration Building, Corvallis, OR 97331-5503, USA
[b] GEOMAR Helmholtz Centre for Ocean Research Kiel, Wischhofstraße 1-3, 24148 Kiel, Germany

ARTICLE INFO

Article history:
Received 7 March 2013
Received in revised form 3 July 2013
Accepted 8 July 2013
Available online 16 July 2013

Editor: David R. Hilton

Keywords:
Molybdenum
Manganese
Iron
Shuttle
Paleo-redox
Baltic Sea

ABSTRACT

A meaningful application of Mo as a paleo-redox proxy requires an understanding of Mo cycling in modern reducing environments. Stagnant euxinic basins such as the Black Sea are generally regarded as model systems for understanding euxinic systems during early Earth history. However, drawing direct parallels between the Black Sea and open-marine euxinic margins is somewhat complicated by differences in the seawater residence time between these two environments. We report sediment and pore water Mo, U, Mn and Fe data for a euxinic basin with a short seawater residence time; the weakly restricted Gotland Deep in the Baltic Sea. Here, prolonged periods of euxinia alternate with brief inflow events during which well-oxygenated, saline water penetrates into the basin. During these inflow events, dissolved Mn and Fe that has accumulated within the euxinic deep water can be oxidized and precipitated. Co-variations of Mo and U within the sediment suggest that these inflow and oxygenation events may favor Mo accumulation in the sediment through adsorption to freshly oxidized Mn and Fe solid phases. Once Mo is sequestered within the deeper euxinic water and sediments, Mo retention can be further facilitated by conversion to thiomolybdate species and interactions with organic matter and metal sulfides. By comparing our data with those from previous studies where a Mn and Fe "shuttle" for Mo has been demonstrated, we identify two prerequisites for the occurrence of this mechanism. First, there must be a water column oxic–anoxic redox-boundary; this provides a solubility contrast for Mn and Fe. Second, the residence time of seawater in the system has to be short (weeks to a few years). The latter criterion can be met through regular inflow in weakly restricted basins or upwelling in oxygen minimum zones at open-marine continental margins. Based on prior work, we suggest that similar conditions to those currently represented by the Gotland Deep may have prevailed at euxinic ocean margins during the Proterozoic. A boundary between euxinic and oxic water masses overlying the continental shelf may have resulted in accelerated Mo transport through the water column with Mn and Fe (oxyhydr)oxides. We propose that this mechanism, along with Mo isotope fractionation during adsorption, could contribute to the light Mo isotope composition observed in open-marine euxinic sediment facies of the Proterozoic.

1. Introduction

The bulk concentration and isotope composition of Mo in sediments or sedimentary rocks are commonly used proxies for characterizing the redox state of ancient marine systems. Their applications range from the detection of reducing conditions in the bottom water or sediment pore water (e.g., Zheng et al., 2000; McManus et al., 2006; Cartapanis et al., 2011) to the identification of sulfidic conditions within the water column (typically referred to as euxinia) on a global scale (Arnold et al., 2004; Scott et al., 2008; Kendall et al., 2009; Dahl et al., 2011). The ability of Mo to serve as a redox indicator is related to its contrasting behavior under oxic or non-sulfidic versus sulfidic conditions. In well oxygenated waters, like those prevailing throughout most of the contemporary ocean, Mo is present as molybdate (MoO_4^{2-}). Because Mo behaves conservatively under oxic conditions, its seawater concentration (~115 nM at S = 35) and oceanic residence time (~800 ka; Bruland, 1983) are high compared to other transition metals. In the presence of dissolved sulfide, MoO_4^{2-} is converted to thiomolybdate ($MoO_xS_{4-x}^{2-}$, $1 < x < 4$) (Helz et al., 1996; Erickson and Helz, 2000). Beyond a threshold H_2S_{aq} activity ($[H_2S]_{aq}$) of approximately 11 μM (at typical seawater pH) and provided that enough time is available to attain thermodynamic equilibrium, sulfidation may be complete (Helz et al., 1996). Owing to the proclivity of thiomolybdate species for reactive surfaces, Mo is readily scavenged from sulfidic waters by forming bonds to Fe sulfides and sulfur-rich organic molecules (Emerson and Huested, 1991; Huerta-Diaz and Morse, 1992; Zheng et al., 2000; Vorlicek and Helz, 2002; Bostick et al., 2003; Tribovillard et al., 2004; Vorlicek et al., 2004; Poulson Brucker et al., 2012). As a consequence of Mo removal under sulfidic conditions, the water column in isolated euxinic basins is often depleted in Mo relative to its salinity-normalized concentration (Algeo and Lyons, 2006; Nägler et

* Corresponding author. Tel.: +1 541 737 5224.
E-mail address: fscholz@coas.oregonstate.edu (F. Scholz).

0009-2541/$ – see front matter © 2013 Elsevier B.V. All rights reserved.
http://dx.doi.org/10.1016/j.chemgeo.2013.07.006

al., 2011). In a recent study, Helz et al. (2011) expanded the above concept of Mo removal from sulfidic water by emphasizing the role of pH in controlling the solubility of a nanoparticulate Fe–Mo–S mineral. According to this revised model, Mo concentrations in the water column reach a constant value once equilibrium with this nanoparticulate Fe–Mo–S mineral is attained (Helz et al., 2011).

The Mo isotope composition of modern seawater ($\delta^{98}Mo \approx 2.3‰$) is predominantly controlled by the input flux through river discharge and an isotopically light oxic sink associated with Mn-rich deposits in the deep-sea ($\delta^{98}Mo \approx -0.5‰$) (Barling et al., 2001; Siebert et al., 2003). Under persistently euxinic conditions, like those in the Black Sea below 400 m water depth, the sediment records the Mo isotope composition of seawater because Mo is quantitatively converted to MoS_4^{2-} and largely removed without fractionation from the dissolved phase (Arnold et al., 2004; Neubert et al., 2008). By analogy, if large parts of the ocean remained euxinic for a prolonged period of time (theoretically implying a global Mo drawdown without isotope fractionation) the isotope composition of seawater would reach a new steady state value that lies closer to the isotope value of the Mo input flux from rivers. Following this concept and assuming removal of Mo into the sediments without isotope fractionation, $\delta^{98}Mo$ values intermediate between seawater and river input in euxinic sediment facies of the Proterozoic have been interpreted as an indicator for more extended euxinia during this interval of Earth history (Arnold et al., 2004; Archer and Vance, 2008; Kendall et al., 2009; Dahl et al., 2011).

The reliability of Mo isotopes as a proxy for the extent of euxinia on a global scale is dependent upon two alternative fractionation mechanisms. If $[H_2S]_{aq}$ does not reach the threshold value required for complete sulfidation of molybdate (e.g., in weakly or intermittently euxinic basins), intermediate thiomolybdate species (i.e., $MoO_3S_1^{2-}$, $MoO_2S_2^{2-}$, $MoO_1S_3^{2-}$) may fractionate towards lighter values compared to the isotope composition of seawater (Tossell, 2005; Dahl et al., 2010; Nägler et al., 2011). Partial scavenging of intermediate thiomolybdate thus produces sedimentary $\delta^{98}Mo$ values intermediate between riverine input and contemporary seawater. An alternative mechanism for Mo removal is related to the affinity of molybdate for particulate Mn and Fe (oxyhydr)oxides. Laboratory experiments and field studies have both demonstrated that Mo adsorption to Mn and Fe (oxyhydr) oxides results in an isotope fractionation ($\Delta^{98}Mo_{seawater\text{-}adsorbed}$) of +2.8‰ for Mn (Siebert et al., 2003; Barling and Anbar, 2004; Wasylenki et al., 2008; Poulson Brucker et al., 2009) and +1.0 to +2.6‰ for Fe (Goldberg et al., 2009, 2012). Precipitation of Mn and Fe (oxyhydr)oxides at the interface between euxinic and oxic water masses may scavenge Mo that is then shuttled into the deep water or to the sediment surface (Berrang and Grill, 1974; Dellwig et al., 2010). Even though the final burial phase in the sediments after reductive re-dissolution of Mn and Fe might be similar to that of permanently euxinic basins, the Mn and Fe shuttle could potentially alter the Mo isotope composition of the deep water and sediment. Indeed, a number of studies have recognized that such a Mn and Fe shuttle enhances Mo accumulation in weakly restricted, euxinic basins (Algeo and Lyons, 2006; Algeo and Tribovillard, 2009). However, its quantitative contribution to the Mo burial flux and influence on the Mo isotope composition of the sediments has yet to be developed. Moreover, the actual transfer mechanism from the metastable Mn or Fe (oxyhydr)oxide carrier to the final Mo burial phase has not been addressed.

The two removal mechanisms outlined above are particularly important where water masses with contrasting redox conditions and spatially variable boundaries co-exist. Modern examples for this kind of environment are intermittently euxinic basins (e.g., Cariaco Basin, Saanich Inlet; Algeo and Tribovillard, 2009) or sediments underlying open-marine oxygen minimum zones at continental margins (e.g., off California and Peru; Zheng et al., 2000; Scholz et al., 2011). In these environments, dynamic redox interfaces between oxic and anoxic or euxinic conditions favor intense Mn and Fe redox cycling with potentially important implications for the vertical transport of Mo through the water column and its burial within the sediment. This same Mo shuttling could have operated in ancient oceans. For instance, a number of recent studies presented evidence for localized euxinic conditions at continental margins in the late Archean (Reinhard et al., 2009; Kendall et al., 2010) and the Proterozoic (e.g., Poulton et al., 2010; Li et al., 2010; Johnston et al., 2010; Poulton and Canfield, 2011).

The Gotland Deep in the Baltic Sea is a prime locality for investigating the behavior of Mo in a dynamic redox environment where both euxinic conditions and intense Mn and Fe redox cycling favor Mo accumulation in the sediment. Here, extended periods of euxinia are interrupted by inflow events during which saline and well-oxygenated water from the North Sea penetrates the basin (Matthäus et al., 2008). These inflow and oxygenation events are accompanied by a pulsed deposition of Mn (oxyhydr)oxides at the basin floor (Huckriede and Meischner, 1996; Neumann et al., 1997). In the present article, we combine new pore water and sediment data for Mo and ancillary parameters with data from previous studies to evaluate (1) the mechanism of Mo transfer from the water column to the sediment surface and into the final burial phase, (2) how the frequency of inflow events impact Mo burial and (3) how the Mn and Fe shuttle might affect the Mo isotope composition of sediments in dynamic euxinic environments.

2. Study area

The Baltic Sea (Fig. 1A) is one of the ocean's largest brackish water basins. The estuarine circulation pattern and semi-enclosed character of the Baltic Sea promote vertical stratification and oxygen depletion below the pycnocline (Zillén et al., 2008). Owing to the characteristic seafloor topography of the Baltic Sea, euxinic conditions are largely limited to a number of sub-basins (so-called “Deeps”) among which the Gotland Deep is the largest by area (Fig. 1B). The Gotland Deep has an aerial extent of ~4600 km^2 below the 150 m isobath and a maximum water depth of ~250 m (Seifert et al., 2001). The intensity and aerial extent of anoxia in the Baltic Sea have progressively increased since the industrial revolution (Zillén et al., 2008; Conley et al., 2009). This trend is generally attributed to large-scale changes in land use and eutrophication.

The water column redox structure of the Gotland Deep is affected by occasional inflow events of saline and well-oxygenated water from the North Sea. During such “Major Baltic Inflows” (MBI; Matthäus and Franck, 1992; Matthäus et al., 2008), North Sea water penetrates the Baltic Sea through the Danish Straits and, depending on the pre-existing density stratification, progressively propagates into the more distal Baltic Deeps (Fig. 1C) (Matthäus et al., 2008). After the Gotland Deep has been flushed with saline and well-oxygenated water, the deep water remains oxic for a period of several months before anoxia and eventually euxinia re-establishes (Matthäus et al., 2008). The occurrence, intensity and velocity of inflow events chiefly depend on the balance between the favoring effect of westerly winds and the impeding effect of freshwater runoff from the Baltic Sea drainage area (Schinke and Matthäus, 1998). In the long-term, both of these factors are controlled by the mean climate mode over the North Atlantic, i.e., the North Atlantic Oscillation (NAO). The NAO index is defined by the variability of the longitudinal pressure gradient across the North Atlantic, which exerts first-order control on the intensity of westerly winds and the rainfall pattern over Northern Europe (Hurrell, 1995; Hurrell and Van Loon, 1997). Through the late 1970s, MBIs occurred frequently, either as single events (e.g., 1960, 1965; Fig. 1D) or groups of events (e.g., 1931–1938, 1948–1956, 1968–1978; Fig. 1D) (Matthäus and Franck, 1992; Matthäus et al., 2008). Since then, only a few isolated events (chiefly 1993 and 2003) have been observed, which is attributed to a shift from negative to predominantly positive NAO conditions (Hanninen et al., 2000). It has been proposed that some of the recent NAO trend is

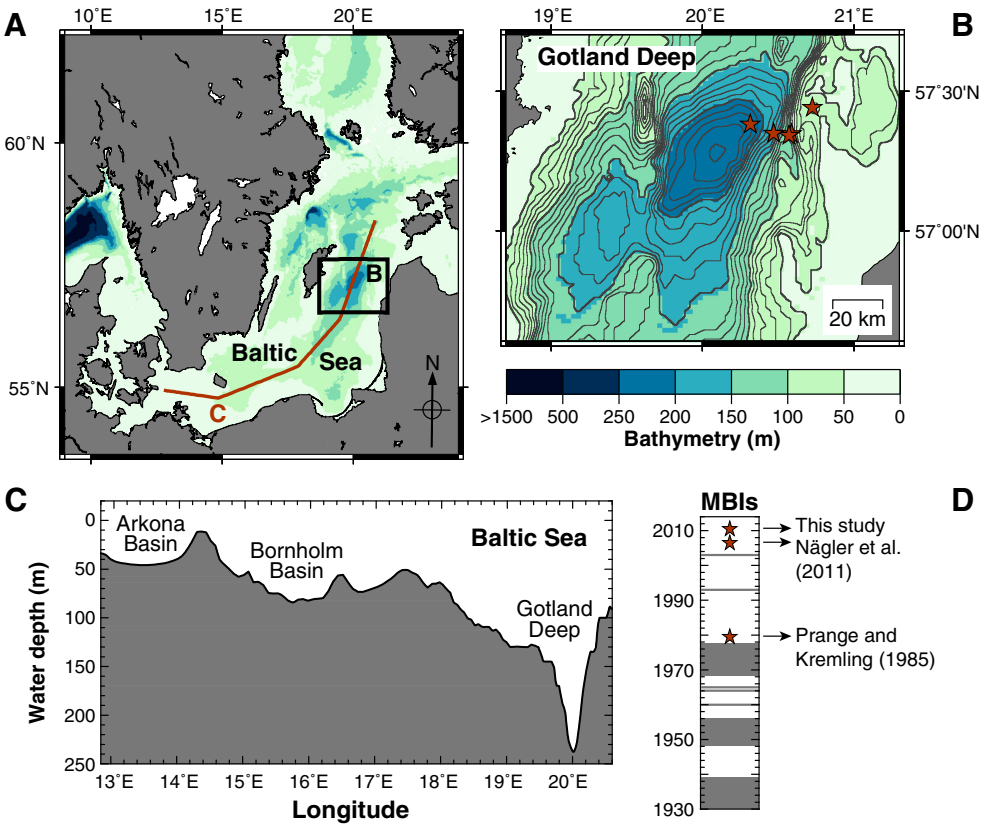

Fig. 1. (A) Bathymetric map of the Baltic Sea (bathymetric data from Seifert et al., 2001). (B) Close-up showing the Gotland Deep and the location of coring sites (stars). (C) Bathymetric cross section through the Baltic Sea from the Danish Straits to the Gotland Deep (see solid line in (A)). (D) Record of Major Baltic Inflows (MBI) from 1930 till present. Groups of events are depicted by gray areas and single events are depicted by gray lines. Stars in (D) represent the time of sampling campaigns in the Gotland Deep that are relevant to this study.

related to anthropogenic climate forcing (Visbeck et al., 2001). This relationship would link the deep water salinity and redox evolution in the Baltic Sea to global climate change.

3. Methods

Sediment and water samples were collected during Cruise AL355 of RV Alkor in May and June 2010. The water column was sampled using a CTD equipped with Niskin bottles. Short sediment cores were taken with a multiple coring device (MUC) equipped with PVC liners (inner diameter of 10 cm) (Table 1). Only sediment cores with an undisturbed sediment–water interface and at least 10 cm of bottom water overlying the sediment surface were accepted for pore water recovery. After core recovery, core liners were capped and transferred into a cooled lab container that was kept at ~6 °C. The bottom water was siphoned with a plastic tube and then filtered through cellulose acetate syringe filters. Pore water samples were obtained from parallel cores by two different methods. One core was sliced into 1 to 5 cm thick disks and the pore water was extracted with a sediment squeezer, which was operated with argon gas at pressures up to 2.5 bar. Upon squeezing, pore waters were filtered through 0.2 µm cellulose acetate membrane filters. The pore water samples obtained by this method were used for the analysis of dissolved chloride (Cl^-), sulfate (SO_4^{2-}) and total sulfide (TH_2S). A subsample of each sediment slice was stored in air-tight and pre-weighed polyethylene cups for determination of porosity as well as for acid digestions and elemental analysis after the cruise. The pore water of a second core was recovered with rhizons (obtained from Rhizosphere Research Products, Netherlands). To remove any oxygen prior to deployment, rhizons were preconditioned in an oxygen-free water bath. The pore water samples obtained by this technique were used for the analysis of redox-sensitive metals (Mn, Fe, Mo and U). Sub-aliquots for metal analysis were stored in acid-cleaned low-density polyethylene vials and acidified with concentrated HNO_3 (suprapur).

Analyses of dissolved oxygen (water column) and H_2S (water column, bottom and pore water) were performed onboard shortly after sample recovery. Oxygen concentrations were determined by Winkler titration and total H_2S_{aq} ($TH_2S = H_2S + HS^- + S^{2-}$) was analyzed photometrically by applying the methylene blue method (Grasshoff et al., 2002). Concentrations of Cl^- and SO_4^{2-} were measured at GEOMAR by ion chromatography (METROHM 761 Compact). Pore water salinity was calculated from Cl^- assuming a conservative Cl^- concentration of 560 mM at S = 35. Concentrations of Mn and Fe

Table 1
Geographical coordinates and water depth of the sampling stations. The stations are ordered according to increasing water depth and decreasing bottom water redox potential.

Station AL355	Gear	No.	Latitude N	Longitude E	Water depth (m)
Bottom water O_2 > 0 µM, H_2S = 0 µM:					
311	MUC	02	57°26.49′	20°43.49′	65
Bottom water O_2 = 0 µM, H_2S = 0 µM:					
308	MUC	01	57°20.88′	20°35.25′	94
366	MUC	11	57°20.52′	20°34.22′	111
Bottom water O_2 = 0 µM, H_2S > 0 µM:					
330	MUC	04	57°21.00′	20°28.13′	169
345	MUC	05	57°22.99′	20°18.98′	223

in pore water were analyzed at GEOMAR by inductively coupled plasma optical emission spectrometry (ICP-OES, VARIAN 720-ES). Samples with Mn or Fe concentrations below the detection limit of the ICP-OES method (~5 μM for Fe and ~1 μM for Mn) were analyzed by inductively coupled plasma mass spectrometry (ICP-MS) at Oregon State University (see below). The total carbon (TC), total organic carbon (TOC) and total sulfur (TS) contents of freeze-dried and ground sediment samples were determined at GEOMAR using a Carlo Erba Element Analyzer (NA1500). Carbon bound to carbonates was removed by adding 1 M HCl prior to TOC analysis and total inorganic carbon (TIC) was calculated by subtracting TOC from TC. A detailed description of the above procedures may be found on the following web page: http://www.geomar.de/en/research/fb2/fb2-mg/benthic-biogeochemistry/mg-analytik/.

All of the following chemical analyses were performed at Oregon State University. Pore water samples with low concentrations of Mn and Fe were analyzed by ICP-MS (THERMO X-Series 2). A collision cell was used to minimize polyatomic interferences. Calibration standards were prepared in metal-free seawater and cobalt was used as an internal standard for mass bias correction. The Fe concentration in common seawater standards (e.g., NASS-5; National Research Council Canada) is below the detection limit of our method. To check the reproducibility of the pore water Fe and Mn analyses, artificial pore water standards were prepared by spiking trace metal-clean seawater with an appropriate amount of Mn and Fe. Repeated analysis of samples and the artificial pore water standard (3 μM Mn and Fe) yielded a reproducibility of 1% for both Mn and Fe. Pore water Mo and U concentrations were determined by isotope dilution (ID) ICP-MS. The Mo and U concentrations obtained for the seawater standard NASS-5 (National Research Council Canada) were 94.4 ± 0.8 nM (n = 4) (certified Mo concentration: 100 ± 10 nM) and 11.6 ± 0.1 (information value for U concentration: 10.9 nM). Major and trace elements in sediments were determined after microwave-assisted digestion in an acid mix consisting of HF, HCl and HNO_3 (Muratli et al., 2012). Certified Reference Materials (SDO-1: Devonian Ohio Shale, USGS; PACS-2: Marine Sediment, National Research Council Canada), an in-house standard (RR9702A-42MC: Chilean margin sediment), sample duplicates and method blanks were run on a regular basis to monitor the reproducibility and accuracy of the digestion procedure. Concentrations of Al, Ca, Mn and Fe in digestion solutions were determined by ICP-OES (Teledyne Leeman Prodigy). Mo and U analyses were done by ICP-MS (THERMO X-Series 2) using rhodium as an internal standard. Isotope dilution was used to verify the Mo concentrations of external standards. The reproducibility and precision of the digestion method is summarized in Table 2.

To account for dilution with detrital material, solid phase concentrations of Mn, Fe, Mo and U are reported as metal to Al or metal to TOC ratios (10^2 wt.% wt.%$^{-1}$ for Mn, wt.% wt.%$^{-1}$ for Fe, 10^4 wt.% wt.%$^{-1}$ for Mo and U). Excess metal concentrations $(Me)_{XS}$ and metal enrichment factors (ME_{EF}) are both reported with respect to the detrital background and were calculated as follows (subscripts: T = total, detr = detrital):

$$(Me)_{XS} = (Me)_T - \left(\frac{Me}{Al}\right)_{detr} \cdot (Al)_T \quad (1)$$

$$Me_{EF} = \frac{\left(\frac{Me}{Al}\right)_T}{\left(\frac{Me}{Al}\right)_{detr}}. \quad (2)$$

The upper continental crust, as defined by McLennan (2001), was chosen as the detrital background ($(Mo/Al)_{detr} = 0.19$, $(U/Al)_{detr} = 0.35$). The Mo burial flux (F_{burial}, in nmol m^{-2} yr^{-1}) was calculated by multiplying the sediment mass accumulation rate (MAR, in g m^{-2} yr^{-1}) by $(Mo)_{XS}$ (in nmol g^{-1}).

Concentrations and activities of aqueous species, ionic strength and saturation indexes for amorphous iron monosulfide were calculated using the geochemical model PHREEQC by Parkhurst and Appelo (1999). Equilibrium constants and solubility products were taken from the built-in WATEQ4F database and water column pH data were taken from Ulfsbo et al. (2011). These authors measured a near-constant pH of 7.3 in the deep water of the Gotland Deep (i.e., below the halocline) over a period of one year during both euxinic and anoxic but non-sulfidic periods.

4. Results

During our sampling campaign in 2010, the salinity in the Gotland Deep water column was roughly constant in the upper 50 m (S ≈ 7) and transitioned below this to near-constant values below 150 m (S ≈ 12.5) (Fig. 2). Oxygen was present to roughly 100 m and dissolved sulfide was detected below 120 m (Fig. 2). The boundary between non-sulfidic and sulfidic waters is hereafter referred to as the chemocline. Thermodynamic equilibrium calculations using PHREEQC reveal that the threshold activity necessary for complete sulfidation of molybdate was reached below about 150 m water depth. The density stratification and redox structure found in this study are in good agreement with those reported in previous studies for euxinic periods in the Gotland Deep (Neretin et al., 2003; Dellwig et al., 2010; Ulfsbo et al., 2011; Meyer et al., 2012).

We present data from five cores that were retrieved along a depth transect between 65 and 223 m (Fig. 1B and Table 1). Three of these sediment cores were located above the chemocline and the remaining two sediment cores were located below the chemocline. Pore water data were obtained for the upper 15 cm for Cl^-, SO_4^{2-} and TH_2S and 9 cm for Mn, Fe, Mo and U (Fig. 3; see Electronic Supplement Table 1 for all pore water data). Pore water salinity generally increases with increasing water depth. The shallowest core (MUC02, 65 m) is the only one where SO_4^{2-} concentrations are not depleted. The remaining cores show downcore decreasing SO_4^{2-} concentrations. Concentrations of

Table 2
Accuracy of the digestion protocol. Measured values are given as mean ± SD.

	SDO-1[a]		PACS-2[b]		RR9702A-42MC[c]	
	This study (n = 8)	Certified	This study (n = 5)	Certified	This study (n = 13)	Previous studies
Al (wt.%)	6.24 ± 0.12	6.49 ± 0.12	6.32 ± 0.14	6.62 ± 0.32	8.24 ± 0.22	8.40 ± 0.20
Ca (wt.%)	0.74 ± 0.02	0.75 ± 0.03	1.99 ± 0.04	1.96 ± 0.18	2.69 ± 0.07	2.66 ± 0.04
Mn (μg g^{-1})	304 ± 8	325 ± 39	437 ± 9	440 ± 19	527 ± 14	530 ± 15
Fe (wt.%)	6.46 ± 0.14	6.53 ± 0.15	4.16 ± 0.10	4.09 ± 0.06	4.83 ± 0.13	4.80 ± 0.10
Mo (μg g^{-1}), ICP-MS	153 ± 4	134 ± 21	5.46 ± 0.13	5.43 ± 0.28	1.74 ± 0.09	1.90 ± 0.30
Mo (μg g^{-1}), ID ICP-MS	152 ± 4	134 ± 21	5.61 ± 0.14	5.43 ± 0.28	1.81 ± 0.09	1.90 ± 0.30
U (μg g^{-1}), ICP-MS	45.9 ± 1.0	48.5 ± 6.5	2.38 ± 0.04	3[d]	3.09 ± 0.14	3.3 ± 0.15

[a] Devonian Ohio Shale, USGS (Govindaraju, 1994).
[b] Marine Sediment (National Research Council, Canada).
[c] In-house standard, Chilean margin sediment, n > 100 (Muratli et al., 2012).
[d] Information value only.

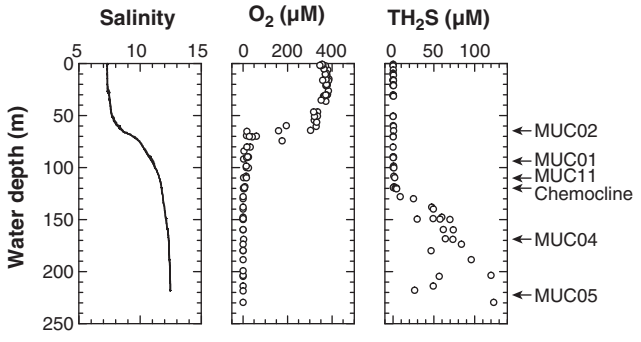

Fig. 2. Profiles of salinity, oxygen and TH_2S in the water column of the Gotland Deep during May and June 2010 (A. Noffke, unpublished data). The location of the chemocline and coring sites are depicted on the right-hand side.

TH_2S increase in the order MUC02 ($TH_2S \leq 15$ μM) < MUC01 < MUC04 < MUC11 ≈ MUC05 ($TH_2S \leq 838$ μM), i.e., there is no clear relationship between pore water H_2S and water depth. Pore water Mn shows a transient peak in cores above the chemocline and steadily increasing concentrations with depth in cores below the chemocline. Relatively high concentrations of dissolved Fe are observed in pore waters of the shallowest core (≤107 μM) whereas the deeper cores display dissolved Fe concentrations <3 μM. Above the chemocline and below a sediment depth of 1–3 cm, pore waters are depleted in Mo and U with respect to their conservative values. In the shallowest core Mn, Fe and Mo display increasing concentrations below 5 cm sediment depth. Below the chemocline, pore waters are generally less depleted in Mo and U and some samples are enriched in Mo and U with respect to salinity.

Sediments above the chemocline are depleted in Mn whereas sediments below the chemocline are generally enriched in Mn with

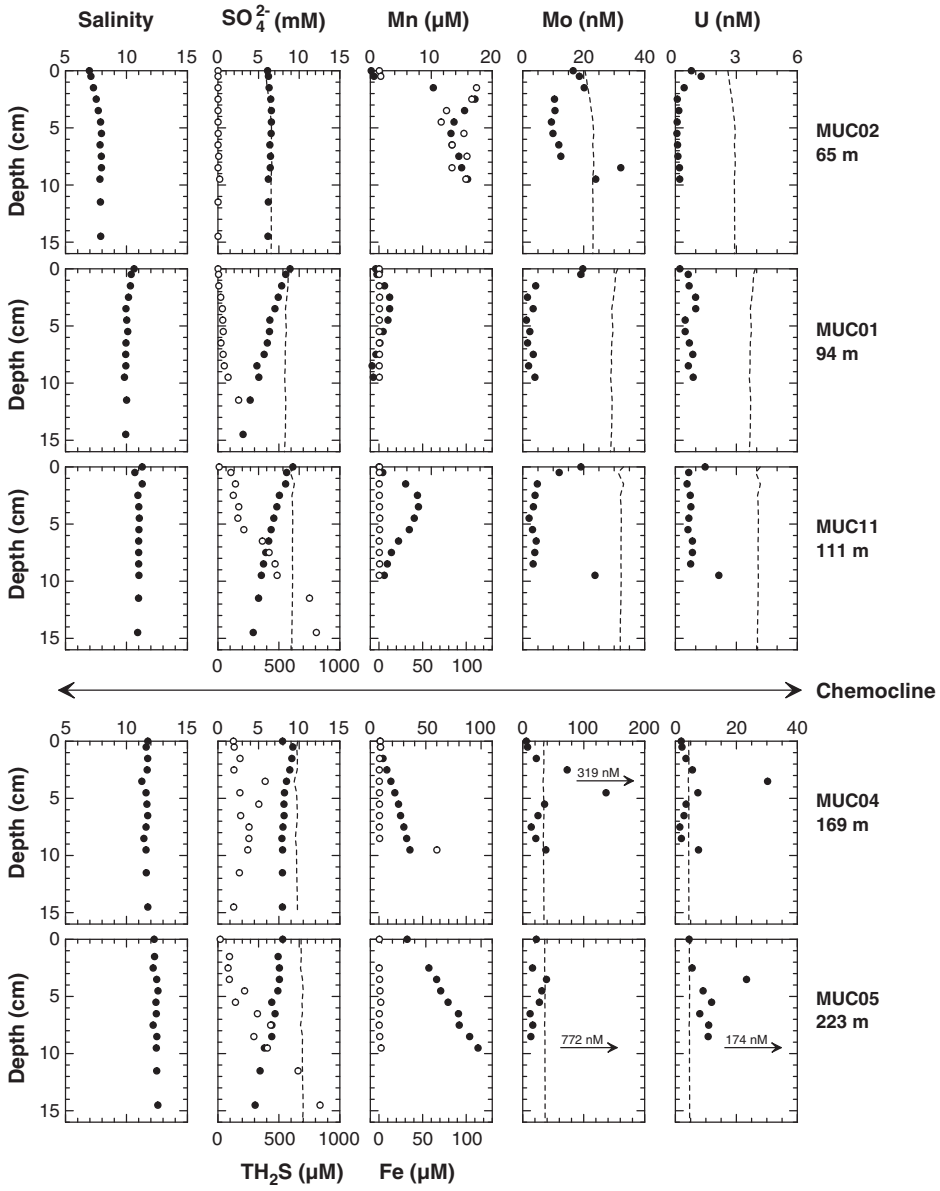

Fig. 3. Pore water profiles of salinity (calculated from Cl^-), SO_4^{2-} (black circles), TH_2S (open circles), Mn (black circles), Fe (open circles), Mo and U. The uppermost value of each profile (depth = 0 cm) indicates bottom water concentrations. Vertical dashed lines represent conservative SO_4^{2-}, Mo and U concentrations as calculated from Cl^-. The horizontal arrow between MUC11 and MUC04 indicates the location of the chemocline. The very high Mo and U concentration in sub-chemocline cores (3.5 cm in MUC04 and 9.5 cm in MUC05) are given as numerical values to avoid obscuring the shape of the pore water profile at lower concentrations. Note the differing concentration scales for Mn, Mo and U above and below the chemocline.

respect to the detrital background (Fig. 4; see Electronic Supplement Table 2 for all solid phase data). Cores below the chemocline display major and coincident peaks of Mn/Al (Mn ≤ 7.6 wt.%) and TIC. Ratios of Fe/Al (Fe ≤ 6.9 wt.%), Mo/Al (Mo ≤ 216 μg g^{-1}), U/Al (U ≤ 32.5 μg g^{-1}) and Mo/TOC generally increase with increasing water depth. Maxima of Fe/Al and TS occur at approximately the same sediment depth as the Mn/Al and TIC peaks. The downcore profiles of Mo/Al and U/Al are different from those of Fe/Al and TS but closely follow the depth distribution of TOC. Profiles of Mo/TOC resemble those of Mo/Al.

5. Discussion

5.1. Redox-controlled manganese and iron shuttle

The enrichments of Mn and Fe in sub-chemocline sediments of the Gotland Deep (MUC04 and MUC05) (Fig. 4) are consistent with a net transfer of detrital and diagenetically derived Mn and Fe into the euxinic basin, a so-called shuttle mechanism (e.g., Raiswell and Anderson, 2005; Lyons and Severmann, 2006; Fehr et al., 2008, 2010; Jilbert and Slomp, 2013). Sediments above the chemocline are generally depleted in Mn with respect to the detrital background, suggesting that shallower sediments are a net Mn source to the deeper basin. By contrast, the shallowest core at 65 m is the only one that is at least partly depleted in Fe and whose pore water Fe profile indicates a diffusive efflux into the water column (Fig. 3). The other cores from above the chemocline reveal pore water Fe concentrations near zero and Fe/Al ratios similar to or slightly higher than the detrital background. These observations indicate that the boundary between Fe sources and sinks is located at shallower water depths compared to that of Mn. The higher escape efficiency of Mn compared to Fe is typically observed in aquatic systems because of its higher solubility in sulfidic and slower oxidation kinetics in oxic water (e.g., Froelich et al., 1979; Canfield et al., 1993; Scholz and Neumann, 2007).

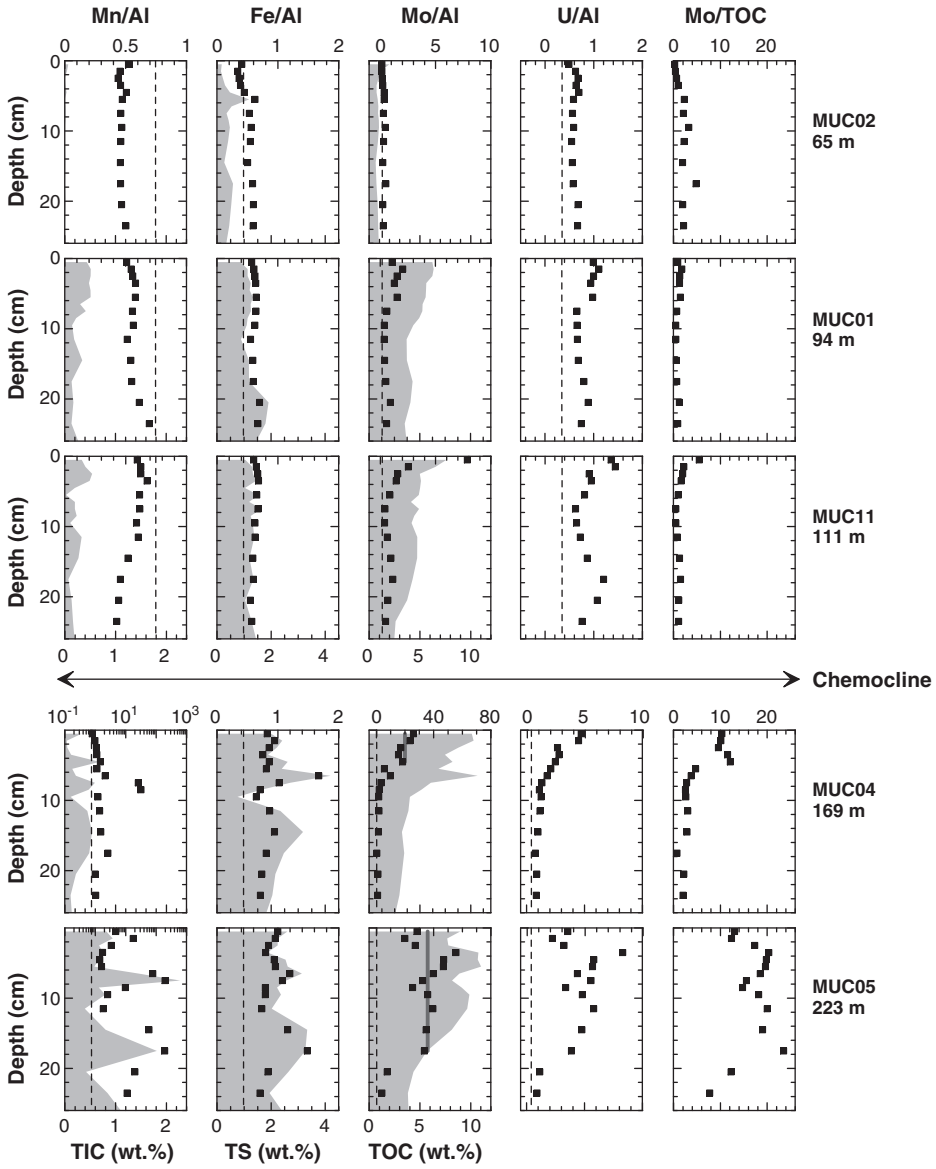

Fig. 4. Solid phase profiles of Mn/Al, TIC (shaded area), Fe/Al, TS (shaded area), Mo/Al, TOC (shaded area), U/Al and Mo/TOC. Vertical dashed lines represent average Mn/Al, Fe/Al and Mo/Al ratios of the upper continental crust ($(Mn/Al)_{detr}$ = 0.75, $(Fe/Al)_{detr}$ = 0.44, $(Mo/Al)_{detr}$ = 0.19, $(U/Al)_{detr}$ = 0.35; McLennan, 2001). The horizontal arrow between MUC11 and MUC04 indicates the location of the chemocline. Note differing concentration scales for Mn/Al (logarithmic for MUC04 and MUC05), Mo/Al and U/Al above and below the chemocline. Vertical lines in the Mo/Al diagrams of sub-chemocline cores depict the depth range and mean Mo/Al ratio used for the calculation of $(Mo)_{XS}$ and Mo burial fluxes (see Table 3).

Sediments below the chemocline are generally enriched in Mn and Fe. However, downcore variations in Mn/Al and Fe/Al (Fig. 4) suggest that the delivery of Mn and Fe to the basin floor is not temporally uniform. The pronounced peaks of Mn/Al and inorganic carbon are a well-known phenomenon in the Baltic Deeps and their occurrence has been attributed to inflow and oxygenation events (Suess, 1979; Huckriede and Meischner, 1996; Neumann et al., 1997). Most of the Mn that enters the Gotland Deep is reductively dissolved while transiting the euxinic water column (Neretin et al., 2003; Dellwig et al., 2010). This process allows dissolved Mn to accumulate in the deep water during stagnant periods. During (oxic) inflow events, much of this Mn is re-oxidized and deposited at the basin floor. As anoxia reestablishes, dissolved Mn and bicarbonate accumulate in the sediment pore water, thus promoting precipitation of Ca-rich rhodochrosite ($MnCO_3$) (Huckriede and Meischner, 1996; Sternbeck and Sohlenius, 1997; Neumann et al., 2002). The linear Mn–Ca relationship observed in sub-chemocline cores (Fig. 5) suggests that most of the conversion of Mn (oxyhydr)oxide to rhodochrosite takes place at or close to the sediment surface. However, the shallower two Mn peaks in sub-chemocline cores (8.5 cm in MUC04 and 7.5 cm in MUC05) plot above the general Mn–Ca relationship. This observation could indicate that a fraction of the Mn (oxyhydr)oxides does not form rhodochrosite at the sediment surface. Moreover, earlier studies have demonstrated that Ca-rich rhodochrosite is metastable and undergoes re-crystallization during burial (Jakobsen and Postma, 1989; Sternbeck and Sohlenius, 1997; Jilbert and Slomp, 2013). This notion is consistent with the linear pore water Mn gradient in sediments below the chemocline (Fig. 3). The deep-sourced Mn flux implied by this gradient could mask any shallower Mn dissolution.

Previous studies assigned Fe enrichments in sediments of the Gotland Deep to syngenetic pyrite formation in the euxinic water column (Boesen and Postma, 1988; Sternbeck and Sohlenius, 1997; Fehr et al., 2008, 2010). This scenario is supported by the general co-variation between Fe/Al and TS in sub-chemocline cores (Fig. 4). However, we suspect that syngenetic pyrite formation during euxinic periods is unlikely to be the only mode of Fe delivery to Gotland Deep sediments. Coincident excursions of Fe/Al and Mn/Al suggest that delivery of both elements is intensified during oxygenation events. Because Fe is poorly soluble in both oxic and sulfidic waters, the sediments will more effectively trap Fe relative to Mn and the difference between solid phase Fe maxima and minima can be less pronounced compared to that of Mn. Nonetheless, the solubility of Fe in sulfidic water is about three orders of magnitude higher than in oxic water (Saito et al., 2003), which is why dissolved Fe accumulates in the Gotland Deep water during euxinic periods (1–2 μM in 2010; Meyer et al., 2012; Pohl and Fernández-Otero, 2012). Oxidation and precipitation of this dissolved Fe pool during inflow events is a logical explanation for the coinciding Fe and Mn peaks in the sediments. In contrast to Mn, Fe does not form abundant sedimentary carbonates

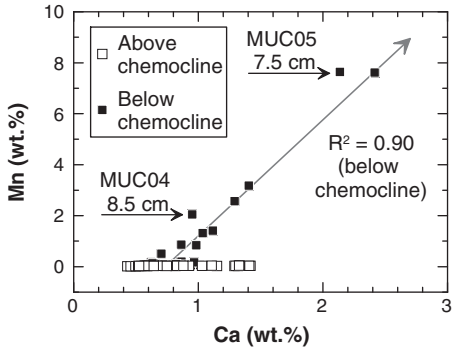

Fig. 5. Plot of Mn concentrations versus Ca concentrations for sediments above and below the chemocline.

but rather sulfide minerals in anoxic–sulfidic environments (Suess, 1979; Burdige, 1993; Sternbeck and Sohlenius, 1997). In agreement with this general observation, the coupling between Fe/Al and TS (Fig. 4) suggests that Fe sulfides represent the primary burial phase for Fe after re-dissolution of (oxyhydr)oxides. The Fe peaks at the deepest site (MUC05) are located at slightly shallower depth than the corresponding Mn peaks (Fig. 4). This observation could be explained by a shift in the ratio between marginal source to basin sink area after inflow and oxygenation events (Raiswell and Anderson, 2005; Fehr et al., 2010). Consistent with such a scenario, Jilbert and Slomp (2013) noted accelerated accumulation of authigenic phosphorous in the deepest part of the Baltic Deeps during times of spatially more limited anoxia throughout the Holocene. Repeated dissolution and re-precipitation of Fe(oxyhydr)oxides prior to burial and conversion to Fe sulfides may further contribute to the broadening and upward shift of the Fe peaks relative to the Mn peaks.

5.2. Age constraints from the manganese and carbon record

To obtain and approximate age model and sediment mass accumulation rate within the basin we utilize the vertical succession and previously defined timing of Mn- and TIC-rich layers in the deepest core (MUC05) (Neumann et al., 1997). These authors identified three major rhodochrosite layers in the topmost 20 cm of a sediment core from 243 m water depth in the Gotland Deep. ^{210}Pb and ^{137}Cs dating suggest that these layers are a result of the inflow periods of 1931–1939, 1948–1956 and 1968–1978 (Fig. 1D; Neumann et al., 1997). The Mn and TIC peaks at 6–8 cm in MUC05 likely correspond to the last one of these extended inflow periods. Because of compaction and the comparably low sample resolution below 10 cm sediment depth, we suspect that the rhodochrosite layers corresponding to the earlier two inflow periods (Fig. 1D) are merged in MUC05. As erosion and re-dissolution prior to final burial impede the preservation of rhodochrosite layers after single and short-lived inflow events (Heiser et al., 2001), the small Mn and TIC peaks close to the sediment surface of MUC05 (1.5 cm sediment depth) could be related to the inflow events of 1993 or 2003. Additional age information for MUC05 is obtained by comparing its TOC profile (Fig. 4) with those reported in earlier studies (Hille et al., 2006). Organic carbon accumulation in the Gotland Deep has increased from about 4 to 10 wt.% since 1900 (Hille et al., 2006). This TOC increase is located above 20 cm sediment depth in MUC05. Considering the high porosity (>0.9) and low dry bulk density (<0.5 g cm^{-3}; Leipe et al., 2011) of surface sediments in the Gotland Deep, the sediment MAR resulting from this age estimate is in good agreement with the average MAR reported for the Gotland Deep (129 ± 112 g m^{-2} yr^{-1} below 150 m water depth; Hille et al., 2006).

5.3. Controls on molybdenum accumulation

Given the well-established connection between the delivery of particulate Mn, Fe and Mo to marine sediments (Berrang and Grill, 1974; Shimmield and Price, 1986; Shaw et al., 1990; Morford et al., 2005; Scholz et al., 2011; Goldberg et al., 2012), it may be anticipated that the Mn and Fe shuttle operating in the Gotland Deep enhances the burial flux of Mo as well. Such interaction between Mn, Fe and Mo cycling has been demonstrated in other weakly restricted basins based on cross plots of Mo and U enrichment factors (e.g., Fig. 6; Algeo and Tribovillard, 2009). U removal from pore water is mediated by Fe- and sulfate-reducing bacteria through reduction of U(VI) to U(IV) and subsequent adsorption or precipitation of uraninite (UO_2) (Klinkhammer and Palmer, 1991; Lovley et al., 1991; Liger et al., 1999; Zheng et al., 2002; Suzuki et al., 2005). As sulfate reduction (and thus Mo removal as thiomolybdate) succeeds Fe reduction during early diagenesis, sedimentary $(Mo/U)_{XS}$ ratios increase with decreasing benthic redox potential (Fig. 6; Algeo and Tribovillard,

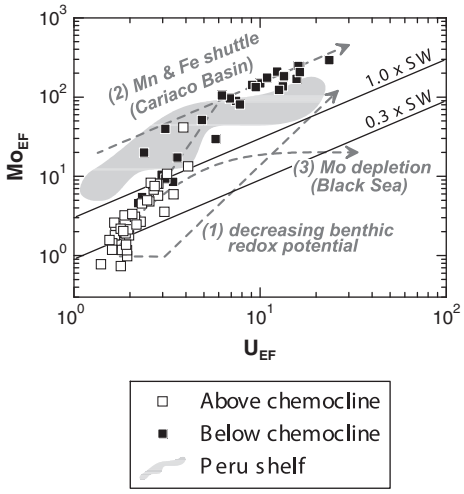

Fig. 6. Plot of Mo_{EF} versus U_{EF} for sediments above and below the chemocline. Note logarithmic scale of both axes. The solid lines depict the mass ratio of Mo/U in seawater (SW) (~3.2) times 1.0 and 0.3. The dashed gray lines are adopted from Algeo and Tribovillard (2009) and illustrate (1) increasing sedimentary $(Mo/U)_{XS}$ ratios with decreasing benthic redox potential; (2) sedimentary $(Mo/U)_{XS}$ ratios > seawater related to accelerated Mo accumulation associated with a Mn and Fe shuttle; (3) sedimentary $(Mo/U)_{XS}$ ratios < seawater related to Mo depletion in the water column of permanently euxinic basins. The shaded area depicts the range of $(Mo/U)_{XS}$ ratios of sediment on the Peruvian continental shelf (data from Scholz et al., 2011).

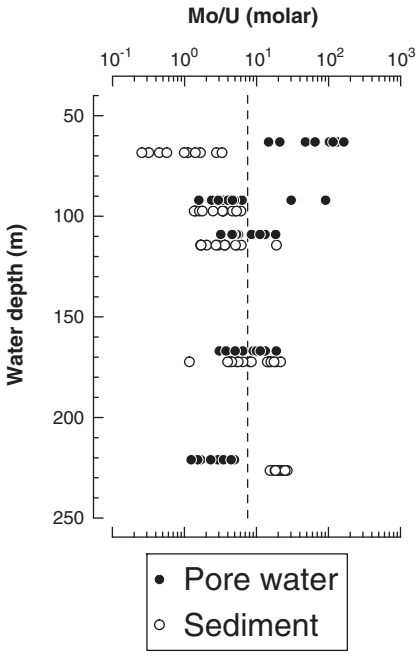

Fig. 7. Plot of molar Mo/U ratios in pore water and sediment versus water depth. Note logarithmic scale of x-axis. The vertical dashed line depicts the molar ratio of Mo/U in seawater (~7.5).

2009). Moreover, U has less affinity for adsorption to metal (oxyhydr) oxides compared to Mo (Klinkhammer and Palmer, 1991). Therefore, a high flux of Mn and Fe (oxyhydr)oxides across an oxic–anoxic interface in the water column (i.e., a Mn and Fe shuttle) may lead to a preferential accumulation of Mo relative to U ($(Mo/U)_{XS} > (Mo/U)_{seawater}$) (e.g., Cariaco Basin, Fig. 6; Algeo and Tribovillard, 2009). Finally, in permanently euxinic basins, where intense scavenging of thiomolybdate and sluggish deep water renewal have led to a preferential depletion of Mo over U in the water column (i.e., $(Mo/U)_{aq} < (Mo/U)_{seawater}$), sediments may be enriched in U relative to Mo ($(Mo/U)_{XS} < (Mo/U)_{seawater}$) (e.g., the Black Sea, Fig. 6; Algeo and Tribovillard, 2009). Consistent with the former two scenarios, pore water and sediment data in the Gotland Deep show an inverse pattern with decreasing $(Mo/U)_{porewater}$ and increasing $(Mo/U)_{XS}$ with increasing water depth (Fig. 7). Moreover, sub-chemocline sediments of the Gotland Deep plot on the trend defined by settings where a Mn and Fe shuttle has been identified (Fig. 6; Algeo and Tribovillard, 2009). This observation suggests that scavenging of Mo by Mn and Fe (oxyhydr)oxides is at least one major vector for Mo delivery to the sediment surface. As noted in Section 5.1, most of the Mn and Fe (oxyhydr)oxides arriving at the seafloor are converted to other authigenic phases during early diagenesis. The result of these phase changes and different reaction pathways during diagenesis means that both the pore fluid and solid phase Mo profiles will likely differ from those of Mn and Fe, particularly below the chemocline.

The three pore water profiles from above the chemocline exhibit Mo removal within the upper few cm, with apparent removal being shallower in the sediment column as the cores progress to greater water depth (Fig. 3). This pattern of removal generally follows that of TH_2S with almost complete Mo depletion in MUC01 (94 m) and MUC11 (111 m) being observed where TH_2S exceeds a few tens of μM (roughly corresponding to a $[H_2S]_{aq}$ of 11 μM). This observation is consistent with the model of Mo scavenging from sulfidic solutions after transformation of MoO_4^{2-} to MoS_4^{2-} (Helz et al., 1996; Erickson and Helz, 2000). In contrast, pore waters of the shallowest core do not reach the $[H_2S]_{aq}$ threshold ($TH_2S \approx 3$ μM at the Mo minimum) and Mo depletion is limited to values of about half the bottom water concentration (Fig. 3). One mechanistic rationale for this observation is that MoO_4^{2-} or intermediate thiomolybdate species dominate in the slightly sulfidic pore water of this core (Helz et al., 1996; Dahl et al., 2010). Oxythiomolybdates are thought to have a smaller affinity for reactive surfaces compared to MoS_4^{2-} (Dahl et al., 2010), which might explain the inefficient Mo removal from pore fluids. In addition, pore waters of the shallowest core display relatively high dissolved Mn and Fe concentrations and the Mo increase in pore water coincides with a slight increase in dissolved Mn and Fe. Therefore, release of Mo from a Mn- and Fe-rich sediment layer is another possible mechanism limiting Mo depletion in the pore water of this core.

The pore water of cores below the chemocline are the least depleted or even enriched in Mo in certain depth intervals, despite high TH_2S concentrations (Fig. 3) as well as high Mo/Al ratios (Fig. 4). This observation is consistent with an additional source of Mo, possibly associated with Mn and Fe (oxyhydr)oxides. Following prior work (Huckriede and Meischner, 1996; Sternbeck and Sohlenius, 1997; Neumann et al., 1997), we suspect that there is significant Mn as well as some Fe (see Section 5.1) supplied to Gotland Deep sediments during oxidation events. Mn- and Fe oxide-rich particles that precipitate at the chemocline of the Gotland Deep are indeed highly enriched in Mo (263 μg g^{-1}; Dellwig et al., 2010) whereas carbonate minerals are generally believed to not incorporate substantial amounts of Mo (≪1 μg g^{-1}; Voegelin et al., 2009). We therefore suspect that the conversion of Mn to rhodochrosite after an inflow event is initially accompanied by the transfer of Mo into solution. Under this scenario, a perhaps significant fraction of the Mo released from Mn (oxyhydr)oxides at the sediment surface is likely to diffuse into the overlying bottom water (see also Section 5.4). However, the isolated peaks in dissolved Mo in sub-chemocline cores (Fig. 3) suggest that another fraction of the shuttled Mo is initially buried and some of this Mo is also released into the pore water during early diagenesis. A portion of the Mo released at depth may derive from Fe and Mn (oxyhydr)oxides that have escaped shallow dissolution and transformation to rhodochrosite (Fig. 5), respectively. Moreover, some of the Mo released from Mn (oxyhydr)oxides at the sediment surface might be re-adsorbed by Fe (oxyhydr)oxides (e.g., Scholz et al., 2011; Goldberg et al., 2012) and later released into the pore water upon

conversion of Fe (oxyhydr)oxides to Fe sulfides through reaction with H_2S.

We also note that elevated pore water Mo concentrations in sub-chemocline cores coincide with elevated concentrations of dissolved U (Fig. 3). As U delivery with metal (oxyhydr)oxides is thought to be of minor importance (Klinkhammer and Palmer, 1991), additional explanations are necessary to explain their co-variation. Although both U and Mo show a trend towards higher pore water concentrations below the chemocline, the $(Mo/U)_{aq}$ ratio in pore water decreases from the shallower sites into the deep basin (Fig. 7). This observation implies greater mobility of U relative to Mo under the conditions prevailing at the deepest site (MUC05). Such mobility is consistent with prior work showing that in environments with fluctuating redox conditions, authigenic U is highly susceptible to re-mobilization (Zheng et al., 2002; Morford et al., 2009; Scholz et al., 2011) whereas Mo accumulation might be favored by the occasional occurrence of oxidizing conditions (Scholz et al., 2011; Dahl et al., 2013). The latter assumption is grounded on the experimental observation that zero-valent sulfur compounds (chiefly S_8), e.g., forming through incomplete re-oxidation of S(-II) (Rickard and Morse, 2005) at a mobile oxic–anoxic interface, favor the transformation of $Mo(VI)OS_3^{2-}$ to highly particle-reactive Mo(IV)-polysulfide complexes (Vorlicek et al., 2004; Dahl et al., 2013). Preferential delivery of Mo with Mn and Fe (oxyhydr)oxides and preferential remobilization of U are difficult to differentiate as both processes occur during inflow and oxygenation events. Scholz et al. (2011) reported a similar trend of gently increasing Mo and strongly increasing U concentrations in pore water on a sediment core transect across the Peruvian margin. The lowest pore water $(Mo/U)_{aq}$ ratios were observed at the shallowest sites where sediments are most sulfidic but also subject to occasional re-oxidation. Scholz et al. (2011) attributed this observation to enhanced Mo delivery by a Mn and Fe shuttle and preferential remobilization of U during occasional oxic events. A similar mechanism could be anticipated for sub-chemocline sediments of the Gotland Deep.

In general, either organic matter or metal sulfides are considered the final burial phases for Mo in anoxic marine sediments (e.g., Huerta-Diaz and Morse, 1992; Algeo and Lyons, 2006; Helz et al., 2011). The correlation between Mo/Al and Fe/Al or TS is poor ($R^2 = 0.001$ below the chemocline) suggesting that pyrite or other Fe sulfide minerals are of subordinate importance for Mo burial. In agreement with sediments from many other euxinic basins (Algeo and Lyons, 2006), however, Mo concentrations are well correlated with TOC (MUC04: $R^2 = 0.71$, $n = 15$; MUC05: $R^2 = 0.83$, $n = 15$). Organic carbon accumulation and preservation are generally more intense under anoxic or euxinic conditions. As a result, TOC concentrations are highest adjacent to the rhodochrosite layers. Much of the Mo bound to organic matter might have been scavenged as thiomolybdate in the water column during euxinic periods (Nägler et al., 2011). However, given the high Mo and H_2S concentrations in the pore water, ongoing sequestration of Mo by organic matter is likely to occur after deposition and during burial. We therefore assume that a significant portion of the Mo delivered by Mn and Fe (oxyhydr)oxides is ultimately buried in association with organic matter.

According to the above discussion, the burial flux of Mo is controlled by the following factors: (1) the mass of Mo scavenged by Mn and Fe (oxyhydr)oxides during inflow events; (2) the H_2S concentration in pore water and availability of appropriate organic compounds for the retention of Mo after release from Mn and Fe carrier phases; and (3) the mass of Mo scavenged as thiomolybdate during euxinic periods. The latter two factors have likely become more favorable for Mo accumulation since the late 19th century because of expanding anoxia in the Baltic Deeps (Hille et al., 2006; Zillén et al., 2008; Conley et al., 2009). The progressive shoaling of euxinia over the last century is reflected in the steady increase of Mo/Al and Mo/TOC ratios above 8 cm in the shallower sub-chemocline core (MUC04, 169 m water depth, Fig. 4). The mass of Mo shuttled by Mn and Fe (oxyhydr)oxides should depend on the balance between Mn and Fe accumulation in the deep water during euxinic periods and the frequency of inflow events for re-precipitation and Mo scavenging. In agreement with this hypothesis, Mo/Al and Mo/TOC ratios in the deepest core (MUC05, 223 m) are highest between 12 and 3.5 cm (Fig. 4), i.e., in the depth interval corresponding to the time span between the 1940s to the 1970s. The regular alternation of stagnation and inflow during this period (Fig. 1D) seems to have been most favorable for Mo accumulation in the deepest part of the Gotland Deep. Decreasing Mo/Al and Mo/TOC ratios above 3.5 cm might reflect the development of more permanent euxinia since the late 1970s. We also note that sediment profiles of U/Al display essentially the same pattern as Mo/Al below the chemocline. As U does not take part in the Mn and Fe shuttle, decreasing solid phase concentrations of U and Mo since the 1970s could also be attributed to a drawdown of these elements in the water column, i.e. the so-called "basin reservoir effect" (Algeo and Lyons, 2006).

5.4. Mechanisms driving the molybdenum inventory of the water column

In 2006, the Gotland Deep water column was depleted in Mo with respect to its conservative distribution ($(Mo)_{conserv} - (Mo)_{aq} \approx 8$ nM below ~80 m water depth; Nägler et al., 2011). Assuming that inflow of Mo-replete seawater is the primary source and burial in the sediment the primary sink for Mo, Emerson and Huested (1991) predicted the extent of Mo depletion in the water column of euxinic basins with the following mass balance equation:

$$(Mo)_{SS} = (Mo)_{conserv} - F(Mo)_{XS,burial} \cdot \frac{\tau_{salinity}}{z}. \quad (3)$$

In this equation $(Mo)_{ss}$ is the Mo concentration at steady state, $(Mo)_{conserv}$ is the conservative Mo concentration normalized to salinity, $F(Mo)_{XS,burial}$ is the Mo burial flux, $\tau_{salinity}$ is the residence time of conservative seawater constituents (equals the mean deep water age) and z is the average thickness of the anoxic water column. The average thickness of the anoxic water column in the Gotland Deep is about 90 m (taking the 150 m isobath as the boundary of the Gotland Deep; Table 3 and Fig. 1B,C). $\tau_{salinity}$ for the Baltic deep water is estimated to be ~20 yr (Reissmann et al., 2009). To account for decreasing sedimentary Mo concentrations with decreasing water depth (Fig. 4), we calculated an area-weighted burial flux that is based on the average MAR below 150 m water depth of Hille et al. (2006) and discrete Mo concentrations for the seafloor areas between 150 and 200 m and >200 m water depth (Table 3, Fig. 4). Based on these input values we calculate a $(Mo)_{ss}$ of 9.2 nM.

As an alternative to the budgetary approach of Emerson and Huested (1991), a thermodynamic model of Helz et al. (2011) predicts constant deep water Mo concentrations once equilibrium with respect to a nanoparticulate Fe–Mo–S mineral is attained (the proposed stoichiometry equals $Fe_5Mo_3S_{14}$). Prerequisite for the applicability of this model is oversaturation with respect to amorphous Fe monosulfide (Helz et al., 2011). Assuming oversaturation with respect to Fe monosulfide, which is consistent with the environmental state of the Gotland Deep water in 2010 ($S = 12.5$, $pH = 7.3$ (Ulfsbo et al., 2011), $(TH_2S)_{aq} = 50$ μM, $(Fe)_{aq} = 1.3$ μM (Meyer et al., 2012)), we predict a deep water Mo concentration ($(Mo)_{pred}$) of ~1.5 nM (based on the model of Helz et al., 2011). During the sampling campaign of Nägler et al. (2011), the Gotland Deep was less sulfidic than in 2010, which likely limited oversaturation with respect to Fe monosulfide to water depths below 200 m. The $(Mo)_{aq}$ measured at this depth was 34 nM (Nägler et al., 2011), i.e., the Mo concentrations predicted by the two models are very different and neither equals the observed $(Mo)_{aq}$.

The difference between the observed Mo concentration and the limiting Mo concentration calculated after Helz et al. (2011) may be

Table 3
Parameters and properties used for mass balance calculations. The basin geometry was computed from bathymetric data (Seifert et al., 2001) by the aid of the Generic Mapping Tool (GMT).

Parameter	Value
150–200 m water depth	
Seafloor area (m^2)	$3.61 \cdot 10^9$
$(Mo)_{conserv}$ (nM)[a]	41.6
$F(Mo)_{xs,burial}$ (nmol m^{-2} yr^{-1})[b]	$1.27 \cdot 10^5$
Below 200 m water depth	
Seafloor area (m^2)	$9.92 \cdot 10^8$
$(Mo)_{conserv}$ (nM)[a]	41.6
$F(Mo)_{xs,burial}$ (nmol m^{-2} yr^{-1})[c]	$2.14 \cdot 10^5$
Average thickness of water column, z (m)	18
Whole basin (defined by 150 m isobath)	
Seafloor area (m^2)	$4.60 \cdot 10^9$
$(Mo)_{conserv}$ (nM)[a]	41.6
$F(Mo)_{xs,burial}$ (nmol m^{-2} yr^{-1})	$1.47 \cdot 10^5$
Average thickness of anoxic water column, z (m)	90
$\tau_{salinity}$ (yr)[d]	20

[a] Conservative Mo concentration based on typical salinity after inflow events (Matthäus et al., 2008).
[b] Calculated from the mean $(Mo)_{XS}$ above 5 cm sediment depth of MUC04 (169 m water depth) and the mean MAR in the Gotland Deep (Hille et al., 2006).
[c] Calculated from mean $(Mo)_{XS}$ above 19 cm sediment depth of MUC05 (223 m water depth) and the mean MAR in the Gotland Deep.
[d] Reissmann et al. (2009).

explained by the short seawater residence time in the Gotland Deep. Relatively fast exchange of the deep water and associated oscillation between oxic and sulfidic conditions may prevent thermodynamic equilibrium with respect to nanoparticulate Fe–Mo–S. Consistent with this rationale, a similarly large offset between $(Mo)_{pred}$ and $(Mo)_{aq}$ has been reported for other weakly restricted euxinic systems, e.g. in the Cariaco Basin and Saanich Inlet (Helz et al., 2011). Similarly, some of the offset between the observed Mo concentration and the steady state Mo concentration (Eq. (3)) could be related to the relatively recent inflow event of 2003 (Fig. 1D). The majority of deep water renewal in the Gotland Deep takes place during inflow events rather than through continuous vertical exchange (without inflow events $\tau_{salinity}$ would be on the order of 100 yr; Feistel et al., 2006). As a result, most seawater constituents whose concentrations decrease during stagnant periods because of microbial metabolism or other biogeochemical processes experience a linear drawdown between inflow events (Matthäus et al., 2008). In the case of Mo, the mean slope or velocity of this drawdown is given by $((Mo)_{SS} - (Mo)_{conserv}) / \tau_{salinity}$ (in nmol yr^{-1}). According to this equation, a linear drop in the deep water Mo concentration by 8 nM (Nägler et al., 2011) requires a stagnant period of ~4.7 yr. This result would imply that the isolated inflow event of 2003 was accompanied by an almost complete exchange of the Gotland Deep water, which appears to be unlikely. Instead we propose that the Mo inventory of the deep water is buffered by two additional recharge mechanisms that are not considered in Eq. (3). As pointed out by Dellwig et al. (2010), the continuous cycle of Mn (oxyhydr)oxide precipitation at the chemocline and reductive dissolution in the euxinic water mass is likely to maintain a constant Mo flux into the deep water. Furthermore, our pore water and sediment results suggest that Mo removal and burial does not only take place during euxinic periods but also during inflow events. As mentioned earlier, much of the Mo scavenged during inflow events is likely to become recycled into the bottom water thus buffering its Mo inventory. Further evidence for Mo recycling in the aftermath of an inflow event is provided by water column Mo data from Prange and Kremling (1985). These data were obtained in 1979, i.e. shortly after the extended period of inflows from 1968 to 1978 (Fig. 1D). At this time, the Mo concentration in the Gotland Deep water was conservative (41.6 nM) up to 200 m water depth but as high as 46 nM below (Prange and Kremling, 1985). Using a modified version of Eq. (3), we can estimate the backflux of Mo that is required to achieve this concentration within the time elapsed since the last inflow event:

$$F(Mo)_{back} = \left((Mo)_{conserv} - (Mo)_{aq,1979}\right) \cdot \frac{z}{\tau_{1979-1978}}. \quad (4)$$

In this equation, z is the average thickness of the water column below 200 m water depth (~18 m; Table 3) and $\tau_{1979-1978}$ is the time span between the last inflow event in 1978 and the sampling campaign in 1979 (~1.5 yr). The resulting $F(Mo)_{back}$ of $-0.53 \cdot 10^5$ nmol m^{-2} yr^{-1} (the negative sign indicates an upward flux) is in good agreement with published benthic Mo fluxes from manganous or ferruginous sediments that were calculated based on pore water concentration gradients (e.g., $\geq -2.5 \cdot 10^5$ nmol m^{-2} yr^{-1} in the Santa Barbara Basin; Zheng et al., 2000; $\geq -2.0 \cdot 10^5$ nmol m^{-2} yr^{-1} on the Peruvian shelf; Scholz et al., 2011). Recycling of shuttled Mo after inflow events could be particularly important for buffering the Mo inventory of the deepest water layer where Mo scavenging during euxinic periods is likely to be most intense.

5.5. Further implications for the use of molybdenum as an ocean redox proxy

Published δ^{98}Mo data for sediments in the Gotland Deep range between +0.4 and +0.6‰ (Neubert et al., 2008). These isotope values differ from the modern seawater isotope composition ($\delta^{98}Mo = 2.3‰$), which is consistent with the idea that there is incomplete removal of a fractionated Mo pool from the water column. One likely mechanism contributing to the isotopic offset between sediment and seawater ($\Delta^{98}Mo_{seawater-sediment} \approx +1.8‰$) is the scavenging of intermediate thiomolybdate species during euxinic periods (e.g., Nägler et al., 2011). Nägler et al. (2011) hypothesized that occasional inflow of oxic seawater perturbs the transformation of $MoOS_3^{2-}$ to MoS_4^{2-}. As the progressive transformation of MoO_4^{2-} to MoS_4^{2-} is accompanied by isotope fractionation (Tossell, 2005), scavenging of intermediate thiomolybdate species should result in a greater isotopic offset between seawater and sediment than scavenging of MoS_4^{2-} alone (Nägler et al., 2011). Both previous (Dellwig et al., 2010) and our new findings on Mo cycling in the Gotland Deep suggest that a portion of the sedimentary Mo is shuttled by Mn and Fe (oxyhydr)oxides. The isotopically light Mo pool resulting from this transport mechanism is likely to contribute to the Mo isotopic offset between sediments and seawater (see also Nägler et al., 2011).

As observed in the Gotland Deep (Nägler et al., 2011), sediments of weakly restricted or intermittently euxinic basins often display an isotopic offset with respect to the Mo isotope composition of seawater (e.g., Cariaco Basin; Arnold et al., 2004). A common explanation for this offset is lower H_2S concentrations and thus less efficient conversion of MoO_4^{2-} to MoS_4^{2-} compared to the strongly and permanently sulfidic Black Sea (Neubert et al., 2008; Dahl et al., 2010). In addition, Dahl et al. (2010) pointed out that a short seawater residence time limits the progress of the MoO_4^{2-} to MoS_4^{2-} conversion and thus increases the isotopic offset between scavenged and dissolved Mo. Our work further emphasizes the role of Mn and Fe (oxyhydr)oxides in generating a light Mo isotope signature in euxinic systems with a short seawater residence time. Repeated inflow of oxic water or continuous mixing of oxic and anoxic water increases the frequency of Mn and Fe precipitation and re-dissolution (see sketch in Fig. 8A). The high Mo burial rates that are typically observed in weakly restricted euxinic basins with a short seawater residence time (i.e., Saanich Inlet, Cariaco Basin) have been assigned to this shuttle mechanism (Algeo and Lyons, 2006).

We further suggest that accelerated Mo burial in association with a Mn and Fe shuttle is not necessarily restricted to isolated basins, but may operate on open-marine continental margins as well, provided

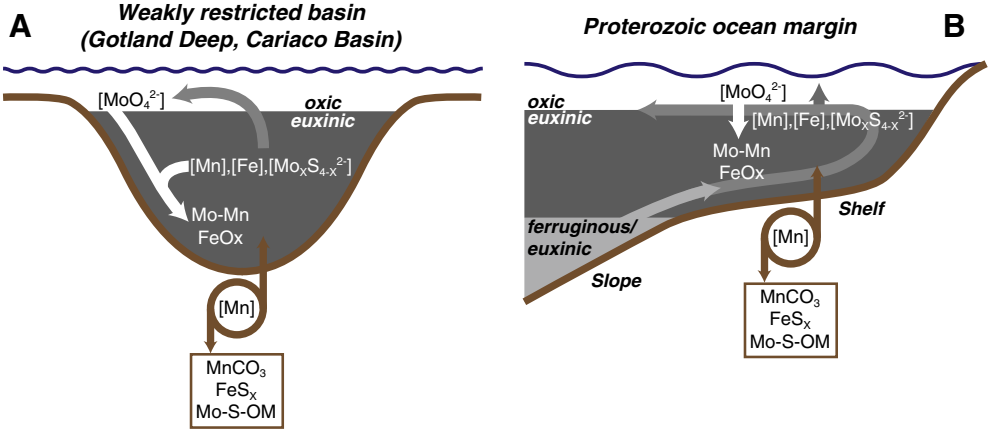

Fig. 8. Model for accelerated Mo accumulation associated with a Mn and Fe shuttle in (A) a weakly restricted basin with a short deep water residence time or regular inflow events (cf. Algeo and Tribovillard, 2009) and (B) at a euxinic continental margin in the Proterozoic (cf. Poulton and Canfield, 2011). Abbreviations are as follows: [] = dissolved species in the water column or pore water; Mo–MnFeOx = Mo absorbed to Mn and Fe (oxyhydr)oxides ($MoO_xS_{4-x}^{2-}$, $1 < x < 4$); $MnCO_3$ = Mn carbonates; FeS_X = Fe sulfides; Mo–S–OM = Mo associated with sulfur and organic matter. Note that scavenging of Mo by organic matter or Fe sulfides in the water column is likely to occur in both (A) and (B).

that an oxic–anoxic interface for Mn and Fe redox cycling is available. For instance, intense Mo burial and $(Mo/U)_{XS} > (Mo/U)_{seawater}$ (Fig. 6) in shelf sediments underlying the Peruvian oxygen minimum zone have been attributed to such a mechanism (Scholz et al., 2011). Furthermore, it is possible that such a shuttle operated at euxinic ocean margins in early Earth history. By analogy to the oxygen minimum zones of coastal upwelling areas in the modern ocean, a number of recent studies inferred localized euxinia underneath oxic surface waters for ocean margins in the late Archean (Reinhard et al., 2009; Kendall et al., 2010) and the Proterozoic (Poulton et al., 2010; Li et al., 2010; Poulton and Canfield, 2011). Euxinic water masses are generally enriched in Mn and Fe compared to oxic water masses (Saito et al., 2003) and it has been suggested that redox boundaries in the Proterozoic were subject to considerable fluctuation (Johnston et al., 2010; Poulton et al., 2010). These factors, along with the short seawater residence time at open-marine margins, likely favored the rapid redox cycling of Mn and Fe. Euxinic conditions in the water column overlying the continental shelf (Poulton et al., 2010; Li et al., 2010) should thus have promoted a Mn and Fe shuttle that efficiently transported Mo from the chemocline to the sediment (see sketch in Fig. 8B). By analogy to modern weakly restricted basins or continental margin environments (Siebert et al., 2006; Poulson Brucker et al., 2009), the Proterozoic Mn and Fe shuttle would have likely generated an offset in δ^{98}Mo between the sediment and contemporary seawater.

At the same time, the short seawater residence time likely limited the potential for Mo depletion within the local water column; for example, typical wind-driven upwelling rates on continental shelves are on the order of meters per day corresponding to seawater residence times ($\tau_{salinity}$) of tens of days (Bowden, 1977). Applying a $\tau_{salinity}$ of 50 days and an average oxygen minimum zone thickness of 150 m (e.g., Keeling et al., 2011) to Eq. (3) yields a $(Mo)_{SS}$ of 41.5 nM, which is analytically indistinguishable from $(Mo)_{conserv}$ (41.6 nM; Table 3). Importantly, the relative extent of Mo depletion at steady state is largely independent of $(Mo)_{conserv}$ and, within the limits defined by modern euxinic environments (Algeo and Lyons, 2006), of $F(Mo)_{XS,burial}$. This result implies that localized euxinic water bodies at ocean margins were unlikely depleted in Mo with respect to contemporary seawater or that in contrast to the deep Black Sea, residual Mo in the water column could likely escape precipitation along open-marine euxinic systems. Moreover, the short seawater residence time likely prevented the complete conversion of MoO_4^{2-} to MoS_4^{2-} (Dahl et al., 2010). The ultimate prerequisite for open-marine euxinic sediments to record the δ^{98}Mo of seawater thus seems to be widespread euxinia in the deep-ocean, which results in complete sulfidation of molybdate prior to upwelling on the continental shelf. However, the concept of persistent deep-ocean euxinia in the Proterozoic is increasingly superseded by the notion of euxinic intermediate waters sandwiched between ferruginous deep water and oxic surface water (Li et al., 2010; Poulton et al., 2010; Dahl et al., 2011; Poulton and Canfield, 2011). We suggest that this "oxygen minimum zone-type" redox-structure may not allow for a $\Delta^{98}Mo_{seawater-sediment}$ of zero. By contrast, the occurrence and intensity of the Mn and Fe shuttle at euxinic continental margins are independent of the redox state of the deep-ocean. Accordingly, continental margin sediment facies with a light Mo isotope signature (δ^{98}Mo < 2.3‰) and independent evidence for euxinia (e.g., from Fe proxies) does not necessarily reflect Mo depletion on a global scale, but could instead result from Mo transport via a Mn and Fe shuttle.

6. Conclusions

Euxinic sediments of the Gotland Deep in the Baltic Sea were investigated with the aim of characterizing geochemical processes that lead to Mo accumulation. Our data reveal that multiple mechanisms are likely contributing to Mo burial, including scavenging of thiomolybdate (or other Mo-sulfide-complexes) or Fe–Mo–S nanoparticles by organic matter during euxinic periods and adsorption of molybdate by Mn and Fe (oxyhydr)oxides during more oxic periods. The latter mechanism is primarily driven by inflow and oxygenation events during which dissolved Mn and Fe that has accumulated within the euxinic deep water is oxidized and deposited at the basin floor. This Mn and Fe shuttle is a common feature in weakly restricted basins. We suggest that Mo isotope fractionation associated with adsorption of Mo onto Mn and Fe (oxyhydr)oxides contributes to the Mo isotopic offset from seawater that is commonly observed in the sediments of these systems.

The occurrence of a Mn and Fe shuttle requires a water column redox boundary separating water masses with differing solubility of Mn and Fe as well as rapid turnover of water (corresponding to a short seawater residence time) to maintain intense redox cycling of Mn and Fe. These requirements are not only met in weakly restricted basins but also at the oxygen minimum zones of modern continental margins and, possibly, at sulfidic ocean margins during Earth history. A Mn and Fe shuttle, along with Mo isotope fractionation during adsorption, could thus contribute to the light Mo isotope composition recorded in Proterozoic black shales.

Supplementary data to this article can be found online at http://dx.doi.org/10.1016/j.chemgeo.2013.07.006.

Acknowledgments

Thanks are due to the officers and crew of RV Alkor, the chief scientist Olaf Pfannkuche and the shipboard scientific party for their support during ALK355. We also thank our colleagues Anke Bleyer, Maike Dibbern, Bettina Domeyer, Jesse Muratli, Regina Surberg and Andy Ungerer for manifold help in the labs at Kiel and Corvallis. Anna Noffke is acknowledged for providing salinity, oxygen and H_2S data for the water column. We greatly appreciate thoughtful comments by Tom Jilbert and one anonymous reviewer. Funding was provided by the 7th Framework Program of the European Union (HYPOX project, Grant Agreement No. 226213; Marie Curie IOF to FS, BICYCLE, Grant Agreement No. 300648). The US National Science Foundation (Grant No. 1029889) supported the participation of JM.

References

Algeo, T.J., Lyons, T.W., 2006. Mo-total organic carbon covariation in modern anoxic marine environments: implications for analysis of paleoredox and paleohydrographic conditions. Paleoceanography 21, PA1016. http://dx.doi.org/10.1029/2004PA001112.

Algeo, T.J., Tribovillard, N., 2009. Environmental analysis of paleoceanographic systems based on molybdenum–uranium covariation. Chemical Geology 268, 211–225.

Archer, C., Vance, D., 2008. The isotopic signature of the global riverine molybdenum flux and anoxia in the ancient oceans. Nature Geoscience 1, 597–600.

Arnold, G.L., Anbar, A.D., Barling, J., Lyons, T.W., 2004. Molybdenum isotope evidence for widespread anoxia in mid-proterozoic oceans. Science 304, 87–90.

Barling, J., Anbar, A.D., 2004. Molybdenum isotope fractionation during adsorption by manganese oxides. Earth and Planetary Science Letters 217, 315–329.

Barling, J., Arnold, G.L., Anbar, A.D., 2001. Natural mass-dependent variations in the isotopic composition of molybdenum. Earth and Planetary Science Letters 193, 447–457.

Berrang, P.G., Grill, E.V., 1974. The effect of manganese oxide scavenging on molybdenum in Saanich inlet, British Columbia. Marine Chemistry 2, 125–148.

Boesen, C., Postma, D., 1988. Pyrite formation in anoxic environments of the Baltic. American Journal of Science 288, 575–603.

Bostick, B.C., Fendorf, S., Helz, G.R., 2003. Differential adsorption of molybdate and tetrathiomolybdate on pyrite (FeS_2). Environmental Science and Technology 37, 285–291.

Bowden, K.F., 1977. Heat budget considerations in the study of upwelling. In: Angel, M. (Ed.), A Voyage of Discovery. Pergamon Press, Oxford, pp. 277–290.

Bruland, K.W., 1983. Trace elements in sea-water. In: Riley, J.P., Chester, R. (Eds.), Chemical Oceanography. Academic Press, London, pp. 157–220.

Burdige, D.J., 1993. The biogeochemistry of manganese and iron reduction in marine sediments. Earth-Science Reviews 35, 249–284.

Canfield, D.E., Thamdrup, B., Hansen, J.W., 1993. The anaerobic degradation of organic matter in Danish coastal sediments: iron reduction, manganese reduction, and sulfate reduction. Geochimica et Cosmochimica Acta 57, 3867–3883.

Cartapanis, O., Tachikawa, K., Bard, E., 2011. Northeastern Pacific oxygen minimum zone variability over the past 70 kyr: impact of biological production and oceanic ventilation. Paleoceanography 26, PA4208. http://dx.doi.org/10.1029/2011PA002126.

Conley, D.J., Björck, S., Bonsdorff, E., Carstensen, J., Destouni, G., Gustafsson, B.G., Hietanen, S., Kortekaas, M., Kuosa, H., Meier, H.E.M., Müller-Karulis, B., Nordberg, K., Norkko, A., Nürnberg, G., Pitkänen, H., Rabalais, N.N., Rosenberg, R., Savchuk, O.P., Slomp, C.P., Voss, M., Wulff, F., Zillén, L., 2009. Hypoxia-related processes in the Baltic Sea. Environmental Science and Technology 43, 3412–3420.

Dahl, T.W., Anbar, A.D., Gordon, G.W., Rosing, M.T., Frei, R., Canfield, D.E., 2010. The behavior of molybdenum and its isotopes across the chemocline and in the sediments of sulfidic Lake Cadagno, Switzerland. Geochimica et Cosmochimica Acta 74, 144–163.

Dahl, T.W., Canfield, D.E., Rosing, M.T., Frei, R.E., Gordon, G., Knoll, A., Anbar, A.D., 2011. Molybdenum evidence for expansive sulfidic water masses in 750 Ma oceans. Earth and Planetary Science Letters 311, 264–274.

Dahl, T.W., Chappaz, A., Fitts, J.P., Lyons, T.W., 2013. Molybdenum reduction in a sulfidic lake: evidence from X-ray absorption fine-structure spectroscopy and implications for the Mo paleoproxy. Geochimica et Cosmochimica Acta 103, 213–231.

Dellwig, O., Leipe, T., März, C., Glockzin, M., Pollehne, F., Schnetger, B., Yakushev, E.V., Böttcher, M.E., Brumsack, H.J., 2010. A new particulate Mn–Fe–P-shuttle at the redoxcline of anoxic basins. Geochimica et Cosmochimica Acta 74, 7100–7115.

Emerson, S.R., Huested, S.S., 1991. Ocean anoxia and the concentrations of molybdenum and vanadium in seawater. Marine Chemistry 34, 177–196.

Erickson, B.E., Helz, G.R., 2000. Molybdenum(VI) speciation in sulfidic waters: stability and lability of thiomolybdates. Geochimica et Cosmochimica Acta 64, 1149–1158.

Fehr, M.A., Andersson, P.S., Halenius, U., Mörth, C.M., 2008. Iron isotope variations in Holocene sediments of the Gotland Deep, Baltic Sea. Geochimica et Cosmochimica Acta 72, 807–826.

Fehr, M.A., Andersson, P.S., Hålenius, U., Gustafsson, Ö., Mörth, C.M., 2010. Iron enrichments and Fe isotopic compositions of surface sediments from the Gotland Deep, Baltic Sea. Chemical Geology 277, 310–322.

Feistel, R., Nausch, G., Hagen, E., 2006. Unusual Baltic inflow activity in 2002–2003 and varying deep-water properties. Oceanologia 48, 21–35.

Froelich, P.N., Klinkhammer, G.P., Bender, M.L., Luedtke, N.A., Heath, G.R., Cullen, D., Dauphin, P., Hammond, D., Hartmann, B., Maynard, V., 1979. Early oxidation of organic matter in pelagic sediments of the eastern equatorial Atlantic: suboxic diagenesis. Geochimica et Cosmochimica Acta 43, 1075–1090.

Goldberg, T., Archer, C., Vance, D., Poulton, S.W., 2009. Mo isotope fractionation during adsorption to Fe (oxyhydr)oxides. Geochimica et Cosmochimica Acta 73, 6502–6516.

Goldberg, T., Archer, C., Vance, D., Thamdrup, B., McAnena, A., Poulton, S.W., 2012. Controls on Mo isotope fractionations in a Mn-rich anoxic marine sediment, Gullmar Fjord, Sweden. Chemical Geology 296–297, 73–82.

Govindaraju, K., 1994. Compilation of working values and sample description of for 383 geostandards. Geostandards Newsletter 18, 1–158.

Grasshoff, K., Erhardt, M., Kremling, K., 2002. Methods of Seawater Analysis. Wiley VCH, Weinheim.

Hanninen, J., Vuorinen, I., Hjelt, P., 2000. Climatic factors in the Atlantic control the oceanographic and ecological changes in the Baltic Sea. Limnology and Oceanography 45, 703–710.

Heiser, U., Neumann, T., Scholten, J., Stüben, D., 2001. Recycling of manganese from anoxic sediments in stagnant basins by seawater inflow: a study of surface sediments from the Gotland Basin, Baltic Sea. Marine Geology 177, 151–166.

Helz, G.R., Miller, C.V., Charnoch, J.M., Mosselmans, J.F.W., Pattrick, R.A.D., Garner, C.D., Vaughan, D.J., 1996. Mechanism of molybdenum removal from the sea and its concentration in black shales: EXAFS evidence. Geochimica et Cosmochimica Acta 60, 3631–3642.

Helz, G.R., Bura-Nakić, E., Mikac, N., Ciglenečki, I., 2011. New model for molybdenum behavior in euxinic waters. Chemical Geology 284, 323–332.

Hille, S., Leipe, T., Seifert, T., 2006. Spatial variability of recent sedimentation rates in the Eastern Gotland Basin (Baltic Sea). Oceanologia 48, 297–317.

Huckriede, H., Meischner, D., 1996. Origin and environment of manganese-rich sediments within black-shale basins. Geochimica et Cosmochimica Acta 60, 1399–1413.

Huerta-Diaz, M.A., Morse, J.W., 1992. Pyritization of trace metals in anoxic marine sediments. Geochimica et Cosmochimica Acta 56, 2681–2702.

Hurrell, J.W., 1995. Decadal trends in the North Atlantic Oscillation: regional temperatures and precipitation. Science 269, 676–679.

Hurrell, J., Van Loon, H., 1997. Decadal variations in climate associated with the North Atlantic Oscillation. Climatic Change 36, 301–326.

Jakobsen, R., Postma, D., 1989. Formation and solid solution behavior of Ca-rhodochrosites in marine muds of the Baltic deeps. Geochimica et Cosmochimica Acta 53, 2639–2648.

Jilbert, T., Slomp, C.P., 2013. Iron and manganese shuttles control the formation of authigenic phosphorus minerals in the euxinic basins of the Baltic Sea. Geochimica et Cosmochimica Acta 107, 155–169.

Johnston, D.T., Poulton, S.W., Dehler, C., Porter, S., Husson, J., Canfield, D.E., Knoll, A.H., 2010. An emerging picture of Neoproterozoic ocean chemistry: insights from the Chuar Group, Grand Canyon, USA. Earth and Planetary Science Letters 290, 64–73.

Keeling, R.F., Körtzinger, A., Gruber, N., 2011. Ocean deoxygenation in a warming world. Annual Review of Marine Science 2, 199–229.

Kendall, B., Creaser, R.A., Gordon, G.W., Anbar, A.D., 2009. Re–Os and Mo isotope systematics of black shales from the Middle Proterozoic Velkerri and Wollogorang Formations, McArthur Basin, northern Australia. Geochimica et Cosmochimica Acta 73, 2534–2558.

Kendall, B., Reinhard, C.T., Lyons, T.W., Kaufmann, A.J., Poulton, S.W., Anbar, A.D., 2010. Pervasive oxygenation along late Archaean ocean margins. Nature Geoscience 3, 647–652.

Klinkhammer, G.P., Palmer, M.R., 1991. Uranium in the oceans — where it goes and why. Geochimica et Cosmochimica Acta 55, 1799–1806.

Leipe, T., Tauber, F., Vallius, H., Virtasalo, J., Uscinowicz, S., Kowalski, N., Hille, S., Lindgren, S., Myllyvirta, 2011. Particulate organic carbon (POC) in surface sediments of the Baltic Sea. Geo-Marine Letters 31, 175–188.

Li, C., Love, G.D., Lyons, T.W., Fike, D., Sessions, A.L., Chu, X., 2010. A stratified redox model for the Ediacaran Ocean. Science 328, 80–83.

Liger, E., Charlet, L., Van Cappellen, P., 1999. Surface catalysis of uranium(VI) reduction by iron(II). Geochimica et Cosmochimica Acta 63, 2939–2955.

Lovley, D.R., Phillips, E.J.P., Gorby, Y.A., Landa, E.R., 1991. Microbial reduction of uranium. Nature 350, 413–416.

Lyons, T.W., Severmann, S., 2006. A critical look at iron paleoredox proxies: new insights from modern euxinic marine basins. Geochimica et Cosmochimica Acta 70, 5698–5722.

Matthäus, W., Franck, H., 1992. Characteristics of major Baltic inflows — a statistical analysis. Continental Shelf Research 12, 1375–1400.

Matthäus, W., Nehring, D., Feistel, R., Nausch, G., Mohrholz, V., Lass, H.U., 2008. The inflow of highly saline water into the Baltic Sea. In: Feistel, R., Nausch, G., Wasmund, N. (Eds.), State and Evolution of the Baltic Sea, 1952–2005. A Detailed 50-year Survey of Meteorology and Climate, Physics, Chemistry, Biology, and Marine Environment. John Wiley & Sons, Hoboken, pp. 265–309.

McLennan, S.M., 2001. Relationships between the trace element composition of sedimentary rocks and upper continental crust. Geochemistry, Geophysics, Geosystems 2 (Paper number 2000GC000109).

McManus, J., Berelson, W.M., Severmann, S., Poulson, R.L., Hammond, D.E., Klinkhammer, G.P., Holm, C., 2006. Molybdenum and uranium geochemistry in continental margin sediments: paleoproxy potential. Geochimica et Cosmochimica Acta 70, 4643–4662.

Meyer, D., Prien, R.D., Dellwig, O., Connelly, D.P., Schulz-Bull, D.E., 2012. In situ determination of iron(II) in the anoxic zone of the central Baltic Sea using ferene as spectrophotometric reagent. Marine Chemistry 130–131, 21–27.

Morford, J.L., Emerson, S.R., Breckel, E.J., Kim, S.H., 2005. Diagenesis of oxyanions (V, U, Re, and Mo) in pore waters and sediments from a continental margin. Geochimica et Cosmochimica Acta 69, 5021–5032.

Morford, J.L., Martin, W.R., Carney, C.M., 2009. Uranium diagenesis in sediments underlying bottom waters with high oxygen content. Geochimica et Cosmochimica Acta 73, 2920–2937.
Muratli, J.M., McManus, J., Mix, A., Chase, Z., 2012. Dissolution of fluoride complexes following microwave-assisted hydrofluoric acid digestion of marine sediments. Talanta 89, 195–200.
Nägler, T.F., Neubert, N., Böttcher, M.E., Dellwig, O., Schnetger, B., 2011. Molybdenum isotope fractionation in pelagic euxinia: evidence from the modern Black and Baltic Seas. Chemical Geology 289, 1–11.
Neretin, L.N., Pohl, C., Jost, G., Leipe, T., Pollehne, F., 2003. Manganese cycling in the Gotland Deep, Baltic Sea. Marine Chemistry 82, 125–143.
Neubert, N., Nägler, T.F., Böttcher, M.E., 2008. Sulfidity controls molybdenum isotope fractionation into euxinic sediments: evidence from the modern Black Sea. Geology 36, 775–778.
Neumann, T., Christiansen, C., Clasen, S., Emeis, K.C., Kunzendorf, H., 1997. Geochemical records of salt-water inflows into the deep basins of the Baltic Sea. Continental Shelf Research 17, 95–115.
Neumann, T., Heiser, U., Leosson, M.A., Kersten, M., 2002. Early diagenetic processes during Mn-carbonate formation: evidence from the isotopic composition of authigenic Ca-rhodochrosites of the Baltic Sea. Geochimica et Cosmochimica Acta 66, 867–879.
Parkhurst, D.L., Appelo, C.A.J., 1999. User's guide to PHREEQC (version 2) — a computer program for speciation, batch-reaction, one-dimensional transport, and inverse geochemical calculations. U.S. Geological Survey Water-Resources Investigations Report 99-4259.
Pohl, C., Fernández-Otero, E., 2012. Iron distribution and speciation in oxic and anoxic waters of the Baltic Sea. Marine Chemistry 145–147, 1–15.
Poulson Brucker, R.L., McManus, J., Severmann, S., Berelson, W.M., 2009. Molybdenum behavior during early diagenesis: insights from Mo isotopes. Geochemistry, Geophysics, Geosystems 10, Q06010. http://dx.doi.org/10.1029/2008GC002180.
Poulson Brucker, R.L., McManus, J., Poulton, S.W., 2012. Molybdenum isotope fractionations observed under anoxic experimental conditions. Geochemical Journal 46, 201–209.
Poulton, S.W., Canfield, D.E., 2011. Ferruginous conditions: a dominant feature of the ocean through Earth's history. Elements 7, 107–112.
Poulton, S.W., Fralick, P.W., Canfield, D.E., 2010. Spatial variability in oceanic redox structure 1.8 billion years ago. Nature Geoscience 3, 486–490.
Prange, A., Kremling, K., 1985. Distribution of dissolved molybdenum, uranium and vanadium in Baltic Sea waters. Marine Chemistry 16, 259–274.
Raiswell, R., Anderson, T.F., 2005. Reactive iron enrichment in sediments deposited beneath euxinic bottom waters: constraints on supply by shelf recycling. Geological Society Special Publication 248, 179–194.
Reinhard, C.T., Raiswell, R., Scott, C., Anbar, A.D., Lyons, T.W., 2009. A Late Archean sulfidic sea stimulated by early oxidative weathering of the continents. Science 326, 713–716.
Reissmann, J.H., Burchard, H., Feistel, R., Hagen, E., Lass, H.U., Mohrholz, V., Nausch, G., Umlauf, L., Wieczorek, G., 2009. Vertical mixing in the Baltic Sea and consequences for eutrophication — a review. Progress in Oceanography 82, 47–80.
Rickard, D., Morse, J.W., 2005. Acid volatile sulfide (AVS). Marine Chemistry 97, 141–197.
Saito, M.A., Sigman, D.M., Morel, F.o.M.M., 2003. The bioinorganic chemistry of the ancient ocean: the co-evolution of cyanobacterial metal requirements and biogeochemical cycles at the Archean-Proterozoic boundary? Inorganica Chimica Acta 356, 308–318.
Schinke, H., Matthäus, W., 1998. On the causes of major Baltic inflows — an analysis of long time series. Continental Shelf Research 18, 67–97.
Scholz, F., Neumann, T., 2007. Trace element diagenesis in pyrite-rich sediments of the Achterwasser lagoon, SW Baltic Sea. Marine Chemistry 107, 516–532.
Scholz, F., Hensen, C., Noffke, A., Rohde, A., Liebetrau, V., Wallmann, K., 2011. Early diagenesis of redox-sensitive trace metals in the Peru upwelling area: response to ENSO-related oxygen fluctuations in the water column. Geochimica et Cosmochimica Acta 75, 7257–7276.
Scott, C., Lyons, C., Bekker, A., Shen, Y., Poulton, S.W., Chu, X., Anbar, A.D., 2008. Tracing the stepwise oxygenation of the Proterozoic ocean. Nature 452, 456–459.
Seifert, T., Tauber, F., Kayser, B., 2001. A High Resolution Spherical Grid Topography of the Baltic Sea, 2nd ed. Baltic Sea Science Congress, Stockholm, pp. 25–29 (November 2001, Poster #147).
Shaw, T.J., Gieskes, J.M., Jahnke, R.A., 1990. Early diagenesis in differing depositional environments: the response of transition metals in pore water. Geochimica et Cosmochimica Acta 54, 1233–1246.
Shimmield, G.B., Price, N.B., 1986. The behaviour of molybdenum and manganese during early sediment diagenesis — offshore Baja California, Mexico. Marine Chemistry 19, 261–280.
Siebert, C., Nägler, T.F., von Blanckenburg, F., Kramers, J.D., 2003. Molybdenum isotope records as a potential new proxy for paleoceanography. Earth and Planetary Science Letters 211, 159–171.
Siebert, C., McManus, J., Bice, A., Poulson, R., Berelson, W.M., 2006. Molybdenum isotope signatures in continental margin marine sediments. Earth and Planetary Science Letters 241, 723–733.
Sternbeck, J., Sohlenius, G., 1997. Authigenic sulfide and carbonate mineral formation in Holocene sediments of the Baltic Sea. Chemical Geology 135, 55–73.
Suess, E., 1979. Mineral phases formed in anoxic sediments by microbial decomposition of organic matter. Geochimica et Cosmochimica Acta 43, 339–352.
Suzuki, Y., Kelly, S.D., Kemner, K.M., Banfield, J.F., 2005. Direct microbial reduction and subsequent preservation of uranium in natural near-surface sediment. Applied and Environmental Microbiology 71, 1790–1797.
Tossell, J.A., 2005. Calculating the partitioning of the isotopes of Mo between oxidic and sulfidic species in aqueous solution. Geochimica et Cosmochimica Acta 69, 2981–2993.
Tribovillard, N., Riboulleau, A., Lyons, T.W., Baudin, F., 2004. Enhanced trapping of molybdenum by sulfurized marine organic matter of marine origin in Mesozoic limestones and shales. Chemical Geology 213, 385–401.
Ulfsbo, A., Hulth, S., Anderson, L.G., 2011. pH and biogeochemical processes in the Gotland Basin of the Baltic Sea. Marine Chemistry 127, 20–30.
Visbeck, M.H., Hurrell, J.W., Polvani, L., Cullen, H.M., 2001. The North Atlantic Oscillation: past, present, and future. Proceedings of the National Academy of Sciences of the United States of America 98, 12876–12877.
Voegelin, A.R., Nägler, T.F., Samankassou, E., Villa, I.M., 2009. Molybdenum isotopic composition of modern and Carboniferous carbonates. Chemical Geology 265, 488–498.
Vorlicek, T.P., Helz, G.R., 2002. Catalysis by mineral surfaces: implications for Mo geochemistry in anoxic environments. Geochimica et Cosmochimica Acta 66, 3679–3692.
Vorlicek, T.P., Kahn, M.D., Kasuya, Y., Helz, G.R., 2004. Capture of molybdenum in pyrite-forming sediments: role of ligand-induced reduction by polysulfides. Geochimica et Cosmochimica Acta 68, 547–556.
Wasylenki, L.E., Rolfe, B.A., Weeks, C.L., Spiro, T.G., Anbar, A.D., 2008. Experimental investigation of the effects of temperature and ionic strength on Mo isotope fractionation during adsorption to manganese oxides. Geochimica et Cosmochimica Acta 72, 5997–6005.
Zheng, Y., Anderson, R.F., van Geen, A., Kuwabara, J., 2000. Authigenic molybdenum formation in marine sediments: a link to pore water sulfide in the Santa Barbara Basin. Geochimica et Cosmochimica Acta 64, 4165–4178.
Zheng, Y., Anderson, R.F., Van Geen, A., Fleisher, M.Q., 2002. Remobilization of authigenic uranium in marine sediments by bioturbation. Geochimica et Cosmochimica Acta 66, 1759–1772.
Zillén, L., Conley, D.J., Andrén, T., Andrén, E., Björck, S., 2008. Past occurrences of hypoxia in the Baltic Sea and the role of climate variability, environmental change and human impact. Earth-Science Reviews 91, 77–92.

Available online at www.sciencedirect.com

ScienceDirect

Geochimica et Cosmochimica Acta 127 (2014) 368–380

Geochimica et Cosmochimica Acta

www.elsevier.com/locate/gca

Beyond the Black Sea paradigm: The sedimentary fingerprint of an open-marine iron shuttle

Florian Scholz [a,*], Silke Severmann [b], James McManus [a], Christian Hensen [c]

[a] College of Earth, Ocean, and Atmospheric Sciences, Oregon State University, 104 Ocean Admin. bldg., Corvallis, OR 97331-5503, USA
[b] Institute of Marine and Coastal Sciences, Rutgers University, New Brunswick, NJ 08901, USA
[c] GEOMAR Helmholtz Centre for Ocean Research Kiel, Wischhofstraße 1-3, D-24148 Kiel, Germany

Received 6 August 2013; accepted in revised form 26 November 2013; available online 8 December 2013

Abstract

We present iron (Fe) concentration and Fe isotope data for a sediment core transect across the Peru upwelling area, which hosts one of the ocean's most pronounced oxygen minimum zones (OMZs). The lateral progression of total Fe to aluminum ratios (Fe_T/Al) across the continental margin indicates that sediments within the OMZ are depleted in Fe whereas sediments below the OMZ are enriched in Fe relative to the lithogenic background. Rates of Fe loss within the OMZ, as inferred from Fe_T/Al ratios and sedimentation rates, are in agreement with benthic flux data that were calculated from pore water concentration gradients. The mass of Fe lost from sediments within the OMZ is within the same order of magnitude as the mass of Fe accumulating below the OMZ. Taken together, our data are in agreement with a shuttle scenario where Fe is reductively remobilized from sediments within the OMZ, laterally transported within the anoxic water column and re-precipitated within the more oxic water below the OMZ. Sediments within the OMZ have increased $^{56}Fe/^{54}Fe$ isotope ratios relative to the lithogenic background, which is consistent with the general notion of benthic release of dissolved Fe with a relatively low $^{56}Fe/^{54}Fe$ isotope ratio. The Fe isotope ratios increase across the margin and the highest values coincide with the greatest Fe enrichment in sediments below the OMZ. The apparent mismatch in isotope composition between the Fe that is released within the OMZ and Fe that is re-precipitated below the OMZ implies that only a fraction of the sediment-derived Fe is retained near-shore whereas another fraction is transported further offshore. We suggest that a similar open-marine shuttle is likely to operate along many ocean margins. The observed sedimentary fingerprint of the open-marine Fe shuttle differs from a related transport mechanism in isolated euxinic basins (e.g., the Black Sea) where the laterally supplied, reactive Fe is quantitatively captured within the basin sediments. We suggest that our findings are useful to identify OMZ-type Fe cycling in the geological record.

1. INTRODUCTION

The transport of bioavailable iron (Fe) from marginal sediments to the ocean interior is an important component of the marine Fe cycle with potential impact on marine productivity, global carbon cycling and climate (e.g., Poulton and Raiswell, 2002; De Baar and De Jong, 2001; Lohan and Bruland, 2008; Moore and Braucher, 2008; Raiswell and Canfield, 2012). The mechanism underlying this "Fe shuttle" involves remobilization of reactive Fe from reducing shelf and slope sediments, coupled to lateral transport through the water column, either as dissolved Fe complexes, as colloids, or as nanoparticles (De Baar and De Jong, 2001; Raiswell, 2011; Lam et al., 2012). Ideally, net offshore Fe transport should be traceable in open-marine sedimentary archives, e.g. as elevated total Fe to aluminum (Fe_T/Al) ratios or elevated highly reactive Fe to total Fe (Fe_{HR}/Fe_T) ratios (Poulton and Raiswell, 2002; Lyons and Severmann, 2006). However, most of our knowledge on the open-marine Fe shuttle is based on benthic flux data

* Corresponding author. Tel.: +1 541 737 5224.
E-mail address: fscholz@coas.oegonstate.edu (F. Scholz).

0016-7037/$ - see front matter © 2013 Elsevier Ltd. All rights reserved.
http://dx.doi.org/10.1016/j.gca.2013.11.041

as well as the distribution of Fe species within the water column (e.g., Landing and Bruland, 1987; Elrod et al., 2004; Lam and Bishop, 2008; Lohan and Bruland, 2008; Cullen et al., 2009). The alleged lack of shuttle-related Fe enrichments in modern continental slope or deep-sea sediments has been attributed to inefficient long-range transport and trapping of Fe in deep oxic basins as well as a large ratio between the basin sink and margin source area (Lyons and Severmann, 2006).

In contrast, sediments in isolated euxinic basins ($[O_2] = 0$ μM, $[H_2S] > 0$ μM in the bottom water) such as the Black Sea are generally enriched in reactive Fe that is delivered from the surrounding shelf areas (Canfield et al., 1996; Wijsman et al., 2001; Raiswell and Anderson, 2005; Lyons and Severmann, 2006). These shuttle-related Fe enrichments in euxinic basins have a characteristic isotope fingerprint. It has generally been demonstrated or inferred from sediment, pore water and water column data that reductive Fe dissolution within continental margin sediments produces a benthic Fe flux with low $^{56}Fe/^{54}Fe$ ratios relative to average continental crust (e.g., Bergquist and Boyle, 2006; Rouxel et al., 2008; Severmann et al., 2010; John et al., 2012). In euxinic basins, quantitative trapping of laterally supplied Fe through pyrite formation in the water column transfers the low $^{56}Fe/^{54}Fe$ ratios of the benthic efflux into the basin sediments thus giving rise to elevated Fe_T/Al ratios and light bulk Fe isotope compositions (i.e., low $\delta^{56}Fe_T$) compared to the source sediment on the shelf (Fehr et al., 2008, 2010; Severmann et al., 2008). Adopting this rationale, Fe_T/Al ratios above the lithogenic background as well as inverse correlations between Fe_T/Al and $\delta^{56}Fe_T$ are increasingly used to fingerprint the presence of a benthic Fe shuttle and, by inference, deep basin euxinia in the geological record (e.g., Duan et al., 2010; Owens et al., 2012).

Despite the general absence of euxinic conditions in the overlying water column, sediments on the open-marine continental margin off Peru (Fig. 1) feature Fe_T/Al ratios considerably higher than the regional lithogenic background (Scholz et al., 2011). Elevated Fe_T/Al ratios occur in a narrow band on the upper continental slope underlying a water column redox boundary (hereafter referred to as oxycline) that separates the eastern Pacific oxygen minimum zone (OMZ) from relatively well-oxygenated water masses below. In the present article, we establish a mass balance for reactive Fe and use Fe isotope systematics to evaluate if the Fe enrichment below the Peruvian OMZ could be related to a redox-controlled shuttle mechanism. We also compare the environmental conditions leading to Fe enrichments on the Peruvian margin and in euxinic basins and point out implications for the interpretation of Fe enrichments in the geological record.

2. STUDY AREA AND PRIOR WORK

Our study area is located off central Peru within the Humboldt Current system (Fig. 1). In this area, southerly alongshore winds driven by the Pacific Subtropical Anticyclone promote offshore Ekman transport within the Peru coastal current and upwelling of thermocline water from the poleward flowing Peru undercurrent (Brink et al., 1983; Strub et al., 1998). The water masses transported by the Peru undercurrent are derived from the Equatorial Undercurrent and are generally rich in nutrients but depleted in oxygen (Kessler, 2006). Upwelling of the nutrient-rich water off the Peru coast enables high primary productivity as well as high rates of subsurface and sedimentary organic matter degradation (Pennington et al., 2006). Poor ventilation and high oxygen demand within the water column lead to a perennial OMZ, which is located between <100 and ~700 m water depths (Fuenzalida et al., 2009).

Where the OMZ impinges the seafloor, nitrate, Fe and sulfate reduction dominate in the near-surface sediment package with a complete absence of an oxic layer (Bohlen et al., 2011). The combination of low bottom water oxygen and low sulfide concentrations within the shallow pore water creates a redox-environment where a large proportion of dissolved Fe(II) may escape oxide or sulfide precipitation and thus leaves the sediment package without being immobilized while transiting the benthic boundary (Noffke et al., 2012). Consequently, slope sediments within the permanent OMZ (~300–700 m water depth) are depleted in reactive Fe compounds (Suits and Arthur, 2000; Noffke et al., 2012) and the overlying water column is generally characterized by high concentrations of dissolved Fe(II) compared to more oxic continental margin water masses (Hong and Kester, 1985; Bruland et al., 2005).

Sedimentary Fe redox cycling on the Peruvian shelf (<100 to ~300 m water depth) is complicated by the occasional occurrence of oxygenation events that are most frequent and vigorous during El Niño events (Levin et al., 2002; Gutiérrez et al., 2008). When the bottom water is oxic, Fe (oxyhydr)oxides are deposited at the seafloor and the Fe(II) produced through Fe reduction in the sediment is re-oxidized and precipitated at the sediment surface. Upon recurrence of anoxia, some of the Fe that has accumulated during the oxic event is remobilized thus leading to an intense, yet transient Fe flux into the water column (Scholz et al., 2011; Noffke et al., 2012). For instance, 3 months after an oxic event in 2008, Noffke et al. (2012) observed a particularly high benthic Fe flux (i.e., an order of magnitude higher than in the permanent OMZ) at 78 m water depth. However, despite the episodically high benthic Fe flux, shelf sediments are characterized by higher concentrations of Fe_T and reactive Fe (Suits and Arthur, 2000; Scholz et al., 2011; Noffke et al., 2012) compared to the deeper slope sediments in the permanent OMZ. Based on this observation, Scholz et al. (2011) and Noffke et al. (2012) concluded that shallow shelf sediments have a largely balanced budget between Fe gain during oxic periods and Fe loss during anoxic periods. While pore waters within the OMZ were found to be non-sulfidic within the topmost 20 cm, pore waters on the shelf display measurable and increasing H_2S concentrations below 10 cm sediment depth (Scholz et al., 2011; Noffke et al., 2012). Moreover, shelf sediments are characterized by higher rates of sulfate reduction (Böning et al., 2004; Bohlen et al., 2011) as well as degrees of pyritization and pyrite concentrations (Suits and Arthur, 2000) compared to sediments within the

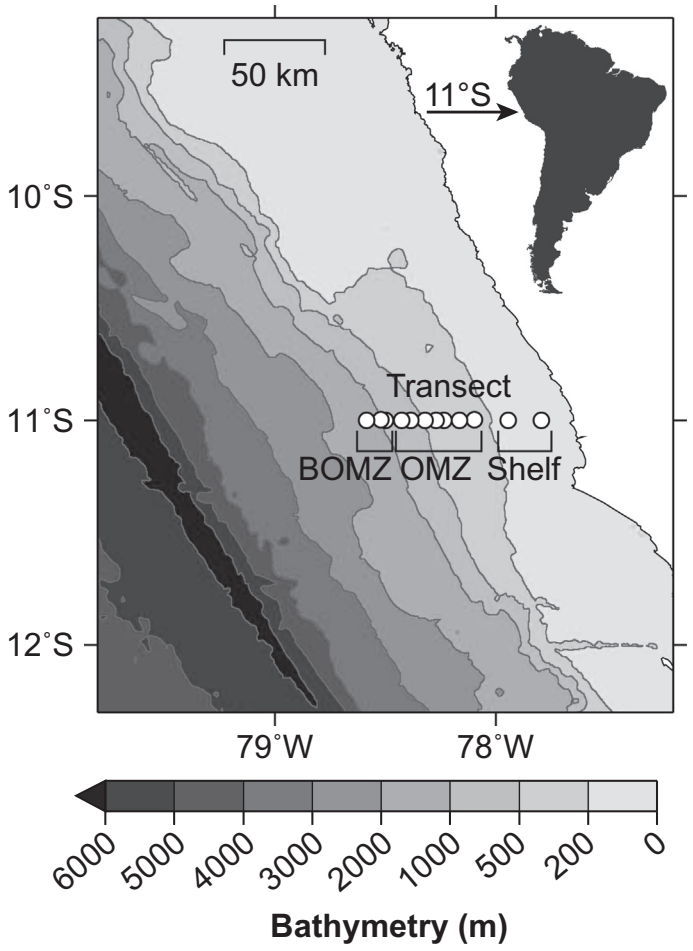

Fig. 1. Location map showing the Peruvian continental margin and the sediment core transect at 11°S (bathymetric data from GEBCO 2008 data base). The sediment cores are sub-grouped into cores from the shelf (Shelf01-Shelf02), cores from within the OMZ (OMZ01-OMZ07) and cores from below the OMZ (BOMZ01-BOMZ03).

permanent OMZ. The comparably efficient net retention of Fe in shelf sediments has therefore been attributed to a zrapid switch from oxic to sulfidic conditions in the surface sediment leading to a conversion of Fe (oxyhydr)oxides to Fe sulfides (Scholz et al., 2011).

3. MATERIAL AND METHODS

3.1. Sampling and chemical analyses

Sediment samples were collected during the RV Meteor cruises M77-1 and M77-2 in November and December 2008 using a multiple coring (MUC) device or a benthic lander (Biogeochemical Observatory – BIGO; Sommer et al., 2006). Water column oxygen concentrations were recorded by deploying a CTD rosette equipped with an oxygen sensor. Subsampling for sediments and pore waters was carried out at approximate seafloor temperatures. Details on the mode of pore water recovery and analysis may be found in Scholz et al. (2011).

For chemical and isotope analysis, 100 mg of freeze-dried and ground sediment sample were digested in a mix of concentrated HF, HNO_3 and $HClO_4$. The accuracy of this procedure was evaluated by including blanks and the reference standards SDO-1 (Devonian Ohio Shale, USGS; Govindaraju, 1994) and MESS-3 (Marine Sediment Reference Material, Canadian Research Council) as well as the in-house standard OMZ-1 into each digestion run. The analysis of Fe and Al in digestion solutions was carried out by inductively coupled plasma optical emission spectrometry (ICP-OES, VARIAN 720-ES). Average Fe and Al values of replicate digestions were within the recommended ranges and the relative standard deviations were $\leqslant 1\%$ ($n = 9$) for all three standards analyzed.

For isotope analyses, digestion solutions were purified following a standard anion exchange protocol (e.g., Beard and Johnson, 1999; Beard et al., 2003). In brief, a sample volume corresponding to 50 µg of Fe was evaporated, re-dissolved in 6 M HCl and loaded on Bio-Rad AG1X8 anion exchange resin. Following elution of the Fe with 0.5 M HCl, samples were evaporated and re-digested by adding a few drops of concentrated HNO_3. This latter step was done to dissolve any residual resin that might be present within the samples. Fe isotope analysis was performed on a multi collector inductively coupled plasma mass spectrometer at the Woods Hole Oceanographic Institution Plasma Laboratory

(Thermo Scientific, NEPTUNE) and the Department of Earth and Planetary Science at Rutgers University (Thermo Scientific NEPTUNE Plus) following the method of Arnold et al. (2004). Samples were introduced through an Apex desolvating nebulizer as 100–500 ppb Fe solutions. For correction of instrumental mass bias, an identical amount of elemental copper of known isotope composition was added to the purified sample solution. In addition, sample isotope ratios were normalized to the average of two standards (the pure metal Fe isotope reference material IRMM-014) measured before and after each second sample (standard-bracketing approach). Several geological standard reference materials of known isotope composition (SDO-1, SCo-2, BCR-2, MAG-1; all USGS) were measured routinely for each sample batch. Accuracy of the analysis was verified by measuring a solution of IRMM-014 that had been spiked with purified ^{54}Fe isotope spike to lower its isotope composition by 1‰ (see Arnold et al., 2004). Fe isotope ratios of $^{56/54}Fe$ are reported in per mil delta notation ($\delta^{56}Fe = ([^{56}Fe/^{54}Fe_{sample}]/[^{56}Fe/^{54}Fe_{standard}] - 1) \times 10^3$) relative to average igneous rock, which has an isotope composition of $\delta^{56}Fe = 0 \pm 0.05‰$ (Beard et al., 2003). The Fe isotope reference material IRMM-014 has a $\delta^{56}Fe$ of −0.09‰ on this scale. The average external precision for $\delta^{56}Fe$, which is based on full procedural replicates, is 0.09‰ (2 standard deviations, SD). Replicate analyses suggest that sediment heterogeneity was minimal and within the range of analytical uncertainty.

3.2. Mass balance and kinetic oxidation rate calculations

In this study, we focus on the bulk concentration and isotope composition of surface sediments (i.e., the uppermost 10–20 cm). To facilitate the identification of a net loss or gain of reactive Fe relative to the lithogenic or terrigenous Fe input, bulk Fe concentrations are presented as Fe_T to Al ratios (wt.%/wt.%) (e.g., Lyons et al., 2003; Lyons and Severmann, 2006). This approach is based on the assumption that the terrigenous supply to the sediment has a constant ratio of Fe to Al. Part of the terrigenous Fe and most of the Al reside in silicate minerals that are essentially unreactive during early diagenesis (Raiswell and Canfield, 1996). Another fraction of the terrigenous Fe, however (i.e., the reactive Fe), is potentially subject to reductive dissolution or transfer into sulfide minerals. If some of this terrigenous, reactive Fe is dissolved, lost from the sediment and transported to another location, the remaining sediment will display Fe_T/Al ratios below the lithogenic background. Conversely, sediments in the area of Fe re-precipitation will display Fe_T/Al ratios above the lithogenic background. An important prerequisite for this concept is that the flux of non-terrigenous, reactive (i.e., authigenic) Fe is high compared to the flux of terrigenous (i.e., lithogenic) Fe. In settings with high rates of continental erosion and runoff or frequent deposition of turbidities, a high flux of terrigenous Fe (and Al) may obscure depletion or enrichment of authigenic Fe (Lyons and Severmann, 2006). Moreover, although irrelevant to this study, Fe from hydrothermal sources may also lead to elevated sedimentary Fe_T/Al ratios (e.g., Dymond et al., 1973).

It is common practice to use the Fe_T/Al ratio (or, generally speaking, the metal/Al ratio) of the average upper continental crust or average shale as a reference line for the terrigenous metal supply (Tribovillard et al., 2006). However, if the geology of the hinterland and the elemental composition of the predominant rocks significantly deviate from average crust or shale, it is preferable to define a regional lithogenic background (Van der Weijden, 2002). Böning et al. (2004) compared the major element composition of Peru margin sediments with that of major rock types and concluded that andesite represents an appropriate lithogenic background for sediments on the Peruvian continental margin. We derived an average Fe_T/Al ratio for andesite rocks in the Andean Arc of 0.47 from the GEOROC data base of the Max-Planck Institute for Chemistry, Mainz, Germany (Sarbas and Nohl, 2009). Because of the high content of Fe-rich pyroxene in andesite rocks, this ratio is slightly higher than that of the average upper continental crust ($Fe_T/Al = 0.44$; McLennan, 2001). However, using the average continental crust Fe_T/Al in this study would not affect the overall conclusions presented.

Following the concept outlined above, sedimentary Fe_T/Al ratios and the lithogenic background ratio can be used to approximate the amount of Fe gained ($[Fe]_{XS}$, positive sign) or lost ($[Fe]_{XS}$, negative sign) relative to the lithogenic Fe pool (e.g., Brumsack, 2006; Tribovillard et al., 2006):

$$[Fe]_{XS} = [Fe]_T - \left(\frac{[Fe]}{[Al]}\right)_{lithogenic} \cdot [Al]_T. \quad (1)$$

Multiplying $[Fe]_{XS}$ with sediment mass accumulation rates (MAR, kg m^{-2} yr^{-1}; taken from Scholz et al., 2011) yields a gain (positive sign) or loss (negative sign) flux ($MAR[Fe]_{XS}$, in mmol m^{-2} yr^{-1}). By analogy to Eq. (1), the isotope composition of the Fe lost or gained relative to the lithogenic background ($\delta^{56}Fe_{XS}$) is given by the following equation (see also Fehr et al., 2010):

$$\delta^{56}Fe_{XS} = \frac{[Fe]_T \cdot \delta^{56}Fe_T - [Fe]_{lithogenic} \cdot \delta^{56}Fe_{lithogenic}}{[Fe]_{XS}} \quad (2)$$

The $\delta^{56}Fe$ for average igneous rock ($\delta^{56}Fe = 0 \pm 0.05‰$; Beard et al., 2003) was chosen for $\delta^{56}Fe_{lithogenic}$.

We note that $[Fe]_{XS}$ and $\delta^{56}Fe_{XS}$ calculated with Eqs. (1) and (2) are not directly comparable to operationally defined reactive Fe concentrations and isotope compositions that were obtained through treatment of sediments with hydrochloric acid or sodium dithionite (ideally yielding Fe (oxyhydr)oxides and Fe monosulfide) (Canfield, 1989; Raiswell et al., 1994) and nitric acid or chromous chloride (yielding pyrite) (Canfield et al., 1986; Huerta-Diaz and Morse, 1990), respectively. Deriving $[Fe]_{XS}$ from operationally defined reactive Fe concentrations requires normalization of the highly reactive Fe pool ($[Fe]_{HR}$, including Fe (oxyhydr)oxide, monosulfide and pyrite) to $[Fe]_T$ (Poulton and Raiswell, 2002). However, the uncertainty associated with the calculation of $\delta^{56}Fe_{XS}$ from multiple operationally defined Fe fractions likely exceeds the one associated with Eqs. (1) and (2).

Apparent first-order rate constants for Fe(II) oxidation and Fe(II) half-lives in bottom water ($t_{1/2}$ Fe(II)) were calculated according to Millero et al. (1987). The calculations

were performed over a hypothetical pH range from 7.5 to 7.7 (e.g., Feely et al., 2008) using CTD-derived temperature, salinity and oxygen data. The detection limit of the oxygen sensor (~1.5 μM) was adopted where the oxygen concentration in bottom water was below the detection limit (adopting $[O_2] = 0$ μM would yield an infinite half-life).

4. RESULTS

We present data for 12 multicores that were taken along a depth transect at 11°S (Fig. 1, Fig. 2A and Table 1). During the sampling campaign in 2008, the OMZ ($[O_2] \leqslant 0.5$ ml $L^{-1} \approx 22$ μM; after Levin et al., 2002) ranged from ~50 to 800 m water depth (Fig. 2A). Previous studies (Scholz et al., 2011; Noffke et al., 2012) demonstrated that metal cycling on the Peruvian shelf (Shelf01 and to a lesser extent Shelf02) is affected by occasional events of bottom water oxygenation. According to these earlier findings and the water column redox state observed during sampling, the sediment cores are sub-grouped into cores from the shelf (Shelf01–Shelf02), cores from within the OMZ (OMZ01–OMZ07) and cores from below the OMZ (BOMZ01–BOMZ03).

From the shelf through the OMZ Fe_T/Al ratios (Fig. 2B; see Table ES1 in the Electronic Supplement for all data) decrease with increasing water depth from values close to the lithogenic background (0.44–0.50 in Shelf01) to values ⩾0.33 in cores OMZ05 and OMZ06. Sediments below the OMZ generally display Fe_T/Al above the lithogenic background with the highest values being observed in BOMZ01 (⩽1.0). The increase in Fe_T/Al between OMZ07 and BOMZ01 coincides with an increase in bottom water oxygen concentrations from ~10 to 40 μM. Surficial $\delta^{56}Fe_T$ (uppermost 1–2 cm) for all cores and downcore data for selected cores (Shelf01, OMZ02 and BOMZ01) are plotted against longitude in Fig. 2C. Shelf sediments display $\delta^{56}Fe_T$ values close to zero and $\delta^{56}Fe_T$ gradually increases with water depth to reach highest values in BOMZ01 (0.42 ± 0.12‰), coinciding with maximum Fe_T/Al values. Downcore profiles of Fe_T/Al, dissolved Fe in pore water ($[Fe]_{PW}$) and $\delta^{56}Fe_T$ of Shelf01, OMZ02 and BOMZ01 are plotted in Fig. 3. The sediment depth of most intense Fe dissolution, as inferred from pore water Fe maxima, increases with increasing distance from shore. Fe_T/Al ratios in Shelf01 increase with depth while those of OMZ02 decrease with depth. $\delta^{56}Fe_T$ profiles of Shelf01 and OMZ02 show little downcore variability. Fe_T/Al and $\delta^{56}Fe_T$ profiles of BOMZ01 are characterized by a negative excursion at 3–4 cm sediment depth. This negative excursion coincides with a local maximum in $[Fe]_{PW}$.

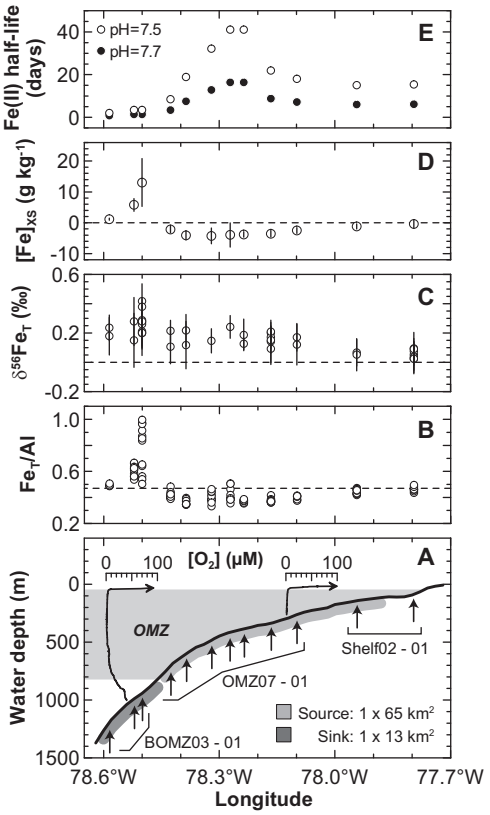

Fig. 2. Cross section of the Peruvian continental margin at 11°S showing: (A) bathymetry (bathymetric data from GEBCO 2008 data base), coring locations (vertical arrows) and water column oxygen profiles delineating the upper and lower oxycline. To fully resolve the oxygen gradient across the lower oxycline, the scales of the oxygen profiles are limited to 0–100 μM (oxygen concentrations in the surface ocean are of the order of 200 μM); (B) Downcore Fe_T/Al data for all cores; (C) Surface $\delta^{56}Fe_T \pm 2$ SD data for all cores (uppermost 1–2 cm) and downcore $\delta^{56}Fe_T \pm 2$ SD data for Shelf01, OMZ02 and BOMZ01; (D) Mean $[Fe]_{XS} \pm$ SD for all cores as calculated from Eq. (1) (Table 1); (E) The half-life of Fe(II) in the bottom water ($t_{1/2}$ Fe(II)) at each station for pH = 7.5–7.7. Dashed lines depict the regional lithogenic background ($Fe/Al = 0.47$, $\delta^{56}Fe = 0.0$‰). See Tables ES1 and ES2 in the Electronic Supplement for data and apparent first-order rate constants for Fe(II) oxidation.

5. DISCUSSION

5.1. Mass balance of reactive iron for the Peruvian continental margin

Sediments on an east–west transect across the Peruvian continental margin show a distinct pattern of Fe depletion and enrichment with respect to the regional lithogenic background (Fig. 2B): Lower Fe_T/Al ratios than the background are observed within the OMZ whereas considerably higher Fe_T/Al ratios than the background occur in slope sediments below the OMZ. The transition from Fe-depleted to Fe-enriched sediments coincides with the depth where the half-life of Fe(II) in bottom water drops from values of >40 days to near-constant values of ⩽3 days (valid for pH = 7.5; Fig. 2E). Dissolved oxygen is the primary control on the Fe(II) half-life across the OMZ (Lohan and Bruland, 2008). It is worth noting, however, that the abrupt decrease in Fe(II) half-life in the bottom water below the OMZ is likely to be even more pronounced due to the coupled effect of oxygen drawdown and increasing pCO_2 on pH (Feely et al., 2008) (compare pH = 7.5 and pH = 7.7 in Fig. 2E). The accordance between sedimentary Fe_T/Al and the half-life of dissolved Fe(II) in the overlying water column suggests that reactive Fe is reductively mobilized

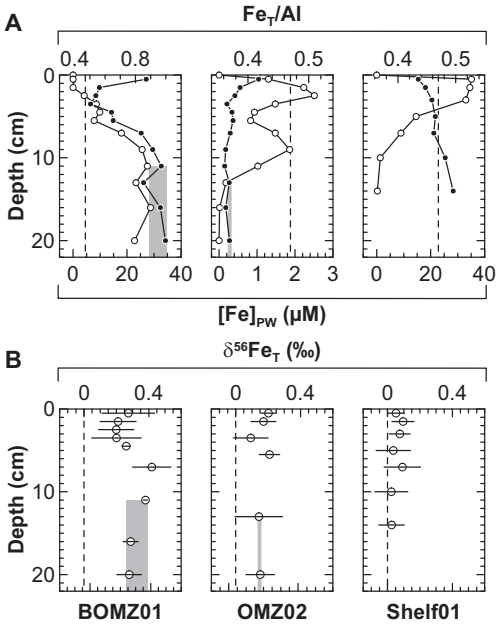

Fig. 3. Concentration-depth profiles for Shelf01, OMZ02 and BOMZ01 showing: (A) Dissolved Fe in pore water (PW) (open circles) and Fe_T/Al (closed circles) (Scholz et al., 2011); (B) $\delta^{56}Fe_T \pm 2$ SD. The shallowest sample in each pore water profile (depth = 0 cm) corresponds to the bottom water sample. Gray areas represent the mean $Fe_T/Al \pm 1$ SD and $\delta^{56}Fe_T \pm 1$ SD that were used in mass balance calculations. Black dashed lines depict the regional lithogenic background ($Fe/Al = 0.47$, $\delta^{56}Fe = 0.0‰$). See Table ES1 in the Electronic Supplement for data.

within the OMZ and re-oxidized and deposited on the continental slope below the OMZ. In the following we evaluate the plausibility of this scenario by establishing a mass balance of reactive Fe for our offshore transect.

Using our measured downcore average values of Fe_T/Al in Eq. (1), we calculate negative $[Fe]_{XS}$ concentrations within the OMZ and positive $[Fe]_{XS}$ concentrations below the OMZ (Fig. 2D). Negative $[Fe]_{XS}$ concentrations imply that reactive Fe has been lost from the sediment which is consistent with findings from Noffke et al. (2012) who demonstrated that sediments within the Peruvian OMZ have the lowest proportion of HCl leachable Fe (0.5 M HCl for 1 h) throughout the Peruvian margin (Noffke et al., 2012). Conversely, positive $[Fe]_{XS}$ concentrations imply a gain of reactive Fe relative to the lithogenic background. Previous studies have shown that sediments within the Peruvian OMZ lose dissolved Fe to the anoxic water column through Fe reduction during early diagenesis and transport across the sediment-bottom water interface (Noffke et al., 2012). We evaluate the capacity of this mechanism to deplete the sediment solid phase of reactive Fe by comparing benthic fluxes that were calculated from pore water profiles (Noffke et al., 2012) with the $MAR[Fe]_{XS}$ of selected cores (Table 1). Because of the generally coarse sample resolution of pore water profiles ($\geqslant$0.5–1.0 cm), benthic flux calculations are inherently associated with a high uncertainty (50% or more). Taking this uncertainty into account, the two independent estimates of Fe loss, $MAR[Fe]_{XS}$ and benthic flux, are in remarkable agreement suggesting that reductive dissolution and efflux across the benthic boundary is the principle mechanism of Fe loss from OMZ sediments. The increasing mismatch between benthic efflux and $MAR[Fe]_{XS}$ towards the lower boundary of the OMZ (Table 1) could be related to a recent shoaling of the lower oxycline (Scholz et al., 2011; Glock et al., 2013) which might have led to a temporary attenuation (OMZ06) or shut-down (OMZ07) of the Fe efflux. Sediments below the OMZ are characterized by a benthic flux of zero, which is consistent with addition and retention of solid phase Fe.

We note that in other areas where benthic Fe export has been detected or inferred, there is rarely a measurable deviation in Fe_T/Al from the lithogenic background (e.g., Black Sea shelf; Wijsman et al., 2001; Lyons and Severmann, 2006) and sediments are often not depleted in reactive Fe compounds (e.g., the Oregon/California margin; Severmann et al., 2010). This observation may be explained by the higher bottom water oxygen concentrations prevailing in those regions. The shorter Fe(II) half-life implied by higher oxygen concentrations impedes lateral Fe transport within the water column as most of the Fe is re-oxidized and -precipitated close to the source (Wijsman et al., 2001). By contrast, the comparably long half-life of Fe(II) in the bottom water of the Peruvian OMZ (~40 days; Fig. 2E) enables efficient lateral transport of sediment-derived Fe away from the source area. In addition, because of the regionally arid climate, lack of major fluvial inputs and high organic carbon burial rates, the terrigenous flux to sediments off central Peru is relatively small compared to other continental margin environments (e.g., upwelling areas off southern Chile, Oregon and California) (Muñoz et al., 2004; Severmann et al., 2010). The combination of a low terrigenous Fe supply, sustained Fe efflux and effective Fe transport within the bottom water may, therefore, produce conditions where loss of reactive Fe via benthic efflux leaves a resolvable imprint on the bulk sediments.

Following previous studies in euxinic basins (e.g., Raiswell and Anderson, 2005; Eckert et al., 2013), we test the shuttle hypothesis for the Peruvian margin by comparing area-weighted fluxes of $[Fe]_{XS}$ for sediments in the source and sink areas. These fluxes were calculated by multiplying the source and sink area along a 1 km-wide swath (source: 1×65 km^2, sink: 1×13 km^2; Fig. 2A) by the average $[Fe]_{XS}$ and MAR (Table 1) of sediment cores within the OMZ for the source flux ($-989 \pm 345 \times 10^3$ mol Fe yr^{-1}) and sediment cores below the OMZ for the sink flux ($791 \pm 709 \times 10^3$ mol Fe yr^{-1}) (the uncertainties were propagated from the SD of mean $[Fe]_{XS}$ in the source and sink areas). Despite the considerable uncertainty with this approach, we do note that the source and sink fluxes are generally in good agreement. This observation and the good match between benthic flux estimates (Noffke et al., 2012) and the calculated $MAR[Fe]_{XS}$ in the source area are consistent with a shuttle scenario where Fe is reductive remobilized from sediments within the OMZ and re-precipitated and deposited below the OMZ.

The lateral distribution of Fe_T/Al ratios in the sediment and Fe(II) half-lives in the bottom water also provide clues to how the down slope transport of Fe in the water column

Table 1
Geographical coordinates, water depth, bottom water (BW) temperature, salinity and oxygen concentration for all cores. Mass accumulation rates and fluxes of reactive Fe are given for selected cores. By definition, negative fluxes are directed out of the sediment.

Core	Code	Latitude S	Longitude W	Water depth (m)	BW temperature (°C)	BW salinity	BW $[O_2]$[a] (μM)	MAR[b] (kg m^{-2} yr^{-1})	Mean Fe_T/Al[b]	±SD	(*n*)	Mean $[Fe]_{XS}$ (g kg^{-1})	±SD	$MAR[Fe]_{XS}$ (mmol m^{-2} yr^{-1})	±SD	Diffusive Fe flux[c] (mmol m^{-2} yr^{-1})
Shelf																
BIGO-05	Shelf01	11°00.02′	77°47.72′	78	12.7	34.9	<LD		0.46	±0.02	(7)	−0.4	±1.4			
MUC29	Shelf02	11°00.00′	77°56.61′	145	12.8	34.8	<LD	0.28	0.45	±0.02	(12)	−1.2	±0.8	−6.0	±4.0	−6.6
Within OMZ																
BIGO-T	OMZ01	10°59.80′	78°05.91′	259	12.0	34.9	<LD		0.40	±0.01	(7)	−2.5	±0.9			
MUC19	OMZ02	11°00.01′	78°09.97′	319	11.1	34.9	<LD	0.08	0.37	±0.02	(12)	−3.5	±1.0	−5.0	±1.4	−3.3
MUC33	OMZ03	11°00.00′	78°14.19′	376	8.3	34.6	<LD		0.37	±0.01	(12)	−3.8	±0.9			
MUC43	OMZ04	11°00.01′	78°16.29′	410	8.3	34.6	<LD		0.42	±0.05	(11)	−3.9	±3.9			
MUC21	OMZ05	11°00.01′	78°19.24′	465	7.9	34.6	2.1		0.40	±0.04	(11)	−4.2	±2.5			
MUC39	OMZ06	11°00.00′	78°23.17′	487	7.2	34.6	4.2	0.18	0.36	±0.02	(9)	−4.1	±1.5	−13.1	±4.8	−4.3
MUC25	OMZ07	11°00.03′	78°25.60′	697	6.1	34.6	12.1	0.53	0.42	±0.02	(12)	−2.2	±1.1	−20.9	±10.4	0.0
Mean source (Shelf02–OMZ07)								0.27				−3.2	±1.1	−15.2	±5.3	
Below OMZ																
MUC15	BOMZ01	10°59.98′	78°30.02′	930	4.8	34.6	39.9		0.78	±0.18	(12)	13.0	±7.8			
MUC53	BOMZ02	10°59.99′	78°31.27′	1005	4.7	34.6	41.6	0.51	0.60	±0.04	(12)	5.8	±2.1	53.0	±19.2	0.0
MUC26	BOMZ03	11°00.01′	78°35.11′	1242	3.6	34.6	93.4		0.49	±0.01	(6)	1.2	±0.3			
Mean sink (BOMZ01–BOMZ03)								0.51				6.7	±5.9	60.9	±53.9	

[a] <LD = Below limit of detection (~1.5 μM).
[b] From Scholz et al. (2011).
[c] From Noffke et al. (2012).

may be mediated. Fe_T/Al ratios reach a maximum where Fe(II) half-lives rapidly decrease. This observation implies that Fe transport and re-precipitation, most likely as (oxy-hydr)oxides, take place in the near-bottom layer of the water column. Sediments on the Peruvian continental shelf and upper slope are located beneath the poleward-directed Peru Undercurrent (Strub et al., 1998; Kessler, 2006). By analogy to wind-induced friction at the sea surface, Ekman transport caused by bottom friction may deflect bottom currents in the offshore direction (MacCready and Rhines, 1993; Hill and Thomas, 1998). This mechanism, along with tidal currents, has been invoked to explain offshore and downslope transport of sediment-derived Fe off the coast of British Columbia (Cullen et al., 2009). The possibility of alongshore transport of Fe may also affect the sedimentary mass balance derived above. North of 10°30′S, the Fe concentrations in the subsurface water are on the order of tens of nM whereas further south Fe concentrations are typically below 0.1 nM (Bruland et al., 2005). The higher Fe concentration north of 10°30′S has been attributed to the greater shelf width in this area (see bathymetry in Fig. 1), which provides a greater interface between the undercurrent and Fe-releasing sediments (Bruland et al., 2005). Given the steep increase in water column dissolved Fe concentrations north of our study area, net alongshore supply of Fe within the undercurrent may contribute to the Fe enrichment observed in slope sediments at 11°S.

5.2. Isotope signature of the open-marine iron shuttle

The mass balance approach adopted in the previous section is useful for evaluating the general plausibility of a shuttle scenario. However, given the uncertainty of the underlying calculations, it does not allow us to evaluate whether all or only a fraction of the Fe mobilized within the OMZ is re-deposited below the OMZ. Moreover, the 2-D approach employed above neglects alongshore transport of sediment-derived Fe, which is likely to be important as most currents off Peru flow in an alongshore direction (Strub et al., 1998; Kessler, 2006). Previous studies have shown that reductive dissolution of Fe in marine sediments preferentially transfers dissolved Fe with low $\delta^{56}Fe$ into the water column, which has been proposed as an isotopic fingerprint for sediment-derived Fe in the open-ocean water column and basinal sediments, respectively (Severmann et al., 2006, 2010; Staubwasser et al., 2006; John et al., 2012). According to this rationale, we expect the distribution of $\delta^{56}Fe_T$ across the Peru margin to provide information about the balance between mobilization of Fe within the OMZ and re-deposition below the OMZ. Importantly, this concept should be unaffected by alongshore transport as most of the dissolved Fe in the water column of the Peruvian OMZ has a sedimentary origin (Bruland et al., 2005) and should thus have a similar isotope composition (i.e., $\delta^{56}Fe$ below the lithogenic background).

The $\delta^{56}Fe_T$ of sediments on the shelf falls close to the lithogenic background (Fig. 2C), which is consistent with its Fe_T/Al ratios (Fig. 2B) and the notion of a largely balanced budget between Fe gain during oxic periods and loss during anoxic periods (see Section 2; Scholz et al., 2011; Noffke et al., 2012). Furthermore, the good match between the Fe_T/Al and $\delta^{56}Fe_T$ of shelf sediments suggests that the andesite reference value is a reasonable representative for the lithogenic fraction of Peru margin sediments. Sediments within the OMZ display higher $\delta^{56}Fe_T$ values than the lithogenic background. This observation is anticipated based on the expectation that the benthic efflux has a low $\delta^{56}Fe$, thus leaving behind a high $\delta^{56}Fe$ residual Fe pool (Staubwasser et al., 2006; Severmann et al., 2010). If the low $\delta^{56}Fe$ Fe(II) mobilized from OMZ sediments was quantitatively re-precipitated on the continental slope, we would anticipate high Fe_T/Al ratios to be associated with low $\delta^{56}Fe_T$ values in the sediments. However, $\delta^{56}Fe_T$ is relatively uniform throughout the Peruvian slope and the highest Fe_T/Al ratios in BOMZ01 coincide with the highest $\delta^{56}Fe_T$ (Fig. 2B and C). This observation suggests that only a fraction of the exported Fe is re-deposited below the OMZ and that the overall shuttle mechanism preferentially removes the heavy Fe isotope.

The isotopic offset between Fe source and sink ($\Delta^{56}Fe_{sink-source}$) may be calculated using Eq. (2), i.e. by including $\delta^{56}Fe_T$ and $\delta^{56}Fe_{lithogenic}$ in the continental margin's Fe mass balance. This approach assumes that at sites where reactive Fe is lost from the sediments (i.e., within the OMZ), $\delta^{56}Fe_{XS}$ equals that of the sedimentary source ($\delta^{56}Fe_{source}$), whereas at sites where reactive Fe is added to the sediments (i.e., below the OMZ), $\delta^{56}Fe_{XS}$ equals that of the sedimentary sink ($\delta^{56}Fe_{sink}$). The $\delta^{56}Fe_{source}$ and $\delta^{56}Fe_{sink}$ calculated from Eq. (2) are corrected for dilution with lithogenic Fe and thus provide a more appropriate estimate of the shuttle-related Fe isotope fractionation than $\delta^{56}Fe_T$ values. The Fe_T/Al and $\delta^{56}Fe_T$ values adopted in Eq. (2) should reflect the net loss or gain of Fe at specific sites without any additional influence from vertical Fe transport within the sediment column. For instance, reductive dissolution of Fe in the subsurface coupled to upward diffusion and re-precipitation at the sediment surface may lead to an overestimation of the shuttle-related Fe enrichment. The effect of vertical re-arrangement of reactive Fe within the sediment column on $\delta^{56}Fe_T$ may be evaluated by examining the downcore profiles of Shelf01, OMZ02 and BOMZ01 (Fig. 3). The variable concentration-depth gradient of dissolved Fe ($[Fe]_{aq}$) across the sediment–bottom water interface ($d[Fe]_{aq}/dz$) demonstrates that in areas where the bottom water is anoxic, part of the dissolved Fe is lost through diffusion across the benthic boundary ($d[Fe]_{aq}/dz > 0$, Shelf01 and OMZ02). By contrast, in areas where the bottom water is oxic, upward diffusing Fe is mostly re-oxidized and precipitated at the sediment surface ($d[Fe]_{aq}/dz \approx 0$, BOMZ01). Another part of the Fe mobilized into the pore water diffuses downward and is precipitated as Fe sulfide. Solid phase profiles of OMZ02 and BOMZ02 reach constant values below the depth of Fe dissolution (see gray shaded areas in Fig. 3A and B). We suspect that these constant values (OMZ02: $Fe_T/Al = 0.37 \pm 0.02$, $\delta^{56}Fe_T = 0.15 \pm 0.01$; BOMZ01: $Fe_T/Al = 0.95 \pm 0.06$, $\delta^{56}Fe_T = 0.32 \pm 0.06$; uncertainty equals 1 SD of the mean) closely represent the sediments' isotope composition after early diagenesis which will eventually be archived in the sedimentary record. Employing these

Fe_T/Al and $\delta^{56}Fe_T$ values in Eq. (2) yields a $\delta^{56}Fe_{source}$ of $-0.53 \pm 0.15‰$ (OMZ02) and a $\delta^{56}Fe_{sink}$ of $+0.64 \pm 0.17‰$ (BOMZ01) (n.b., adopting downcore average values does not affect the following discussion). Our calculated $\delta^{56}Fe_{source}$ value is relatively high compared to benthic flux data that have been obtained through benthic lander incubations (-0.7 to $-4.0‰$; Severmann et al., 2010) or inferred from water column data ($-2.4‰$; John et al., 2012). Numerous previous studies concluded that Fe re-oxidation at the sediment surface preferentially removes the heavy Fe isotope thus shifting the $\delta^{56}Fe$ of the remaining efflux to lower values (Severmann et al., 2006; Staubwasser et al., 2006; Rouxel et al., 2008). Consequently, the relatively high $\delta^{56}Fe_{source}$ calculated for sediments in the Peruvian OMZ is consistent with minimal Fe re-oxidation and efficient long-term Fe loss, which have led to low concentrations of reactive Fe, $[Fe]_T$ and $[Fe]_{PW}$ in the sediment (see Section 5.1., Fig. 3 as well as Scholz et al., 2011 and Noffke et al., 2012).

Subtracting $\delta^{56}Fe_{source}$ from $\delta^{56}Fe_{sink}$ reveals a shuttle-related isotope fractionation factor $\Delta^{56}Fe_{sink-source}$ of $+1.2 \pm 0.2‰$. Multiple processes may contribute to this net fractionation factor. However, the lateral pattern of Fe(II) half-life in bottom water strongly suggests that oxidation of Fe(II) to Fe(III) and precipitation of Fe(oxyhydr)oxides or adsorption of Fe(II) onto suspended particulate matter are involved. The direction and magnitude of isotope fractionation during these latter processes is the subject of ongoing discussion. Fe isotope fractionation during Fe (oxyhydr)oxide precipitation has been described as a two-step process where an equilibrium fractionation of $\sim+3‰$ between $Fe(III)_{aq}$ and $Fe(II)_{aq}$ is followed by a $-1‰$ to $-2‰$ kinetic isotope fractionation during (oxyhydr)oxide precipitation (Anbar, 2004; Beard and Johnson, 2004; Johnson et al., 2004; Dauphas and Rouxel, 2006). Most experimental studies and field studies in a variety of freshwater and marine environments reported a net positive isotope fractionation factor $\Delta^{56}Fe_{FeOOH-Fe(II)aq}$ of $+0.6$ to $+1.8‰$ for the precipitation of Fe (oxyhydr)oxides or adsorption of Fe(II) onto Fe (oxyhydr)oxides (e.g., Bullen et al., 2001; Croal et al., 2004; Anbar, 2004; Ingri et al., 2006; Teutsch et al., 2005; Rouxel et al., 2008; Mikutta et al., 2009; Roy et al., 2012). By contrast, a negative $\Delta^{56}Fe_{FeOOH-Fe(II)aq}$ has been inferred from the isotopic offset between seawater (or brackish water) and water column particulate matter in the San Pedro Basin off California and the Baltic Sea (John et al., 2012; Staubwasser et al., 2013). Although the utility of our sediment data set to constrain isotope fractionation factors in the water column is limited, we note that the trend toward slightly heavier $\delta^{56}Fe_T$ below the Peruvian OMZ (Fig. 2C) (implying a $\delta^{56}Fe_{XS} > 0‰$) cannot be explained by a negative $\Delta^{56}Fe_{FeOOH-Fe(II)aq}$ but is consistent with the published range of positive $\Delta^{56}Fe_{FeOOH-Fe(II)aq}$. More importantly, the mismatch between the isotope composition of the source within the OMZ and that of the sink below the OMZ implies that only a fraction of the laterally supplied Fe is re-deposited near-shore. It is also possible that some of the Fe initially deposited below the OMZ is subsequently remobilized into the bottom water and transported further offshore, thus adding to the inefficient trapping of Fe near-shore. Transfer of pore water Fe across the oxic surface layer could be facilitated by bioirrigating fauna (Aller, 1980) that is abundant at the oxic portion of the Peruvian continental slope (Levin et al., 2002). A similar mechanism of biological or physical reworking is thought to mediate Fe export from ferruginous sediments on the oxic Black Sea shelf (Raiswell and Canfield, 2012). The transport of Fe within the bottom water and thus net loss of Fe from the sediment would be much less efficient than within the OMZ. However, the high isotope fractionation factor that is potentially associated with Fe loss under Fe-replete conditions (Severmann et al., 2010) could contribute to the relatively high $\delta^{56}Fe$ values of the sediment left behind.

5.3. The iron shuttle in open-marine oxygen minimum zones versus euxinic basins

According to previous as well as our new findings reactive Fe enrichments in both the Black Sea and the Peruvian margin are related to reductive remobilization as well as transport and re-precipitation within the water column. However, despite this common shuttle mechanism, the two systems display different trends between Fe_T/Al and $\delta^{56}Fe_T$. While the Fe shuttle in the Black Sea results in low $\delta^{56}Fe_{sink}$ values offshore (Fig. 4A), a slight tendency towards a relatively higher $\delta^{56}Fe_{sink}$ is observed on the Peruvian margin (Fig. 4B).

Raiswell and Anderson (2005) described the Fe shuttle in euxinic basins based on two characteristic parameters: the ratio between source area and basin sink area (S/B) and the ratio between the area-weighted source and sink fluxes (export efficiency, ε). This concept is useful here to point out mechanistic differences between the Fe shuttles in the isolated euxinic Black Sea and the open-marine OMZ off Peru (see also sketches in Fig. 4). Raiswell and Anderson (2005) derived $S/B = 0.37$ and $\varepsilon = 0.5$ for the Black Sea. According to our definition, the section of the Peru margin studies here has a $S/B = 65\ km/13\ km = 5.0$ (Fig. 2A) and the good match between benthic flux and $MAR[Fe]_{XS}$ within the OMZ (Table 1) implies a high export efficiency. The comparably efficient offshore export of sediment-derived Fe on the Peruvian margin is likely related to the low bottom water oxygen concentrations and, consequently, the long Fe(II) half-life (Fig. 2E) (Lohan and Bruland, 2008). By contrast, in the Black Sea much of the Fe export takes place from sediments beneath a relatively oxic water column. Therefore, sediment-derived Fe will likely undergo multiple cycles of re-oxidation, deposition and re-mobilization before a part of it reaches the deep basin (Wijsman et al., 2001). This repetitive redox-cycling is likely to limit the export efficiency but may contribute to the light $\delta^{56}Fe_{sink}$ compared to the Peruvian margin. The high S/B ratio of the Peruvian margin and the localized enrichment in reactive Fe (Fig. 2B and D) indicate that much of the sediment-derived Fe is (at least temporarily) deposited within a relatively confined area close to the lower oxycline. This focused removal may be related to the dramatically reduced Fe solubility upon transition from

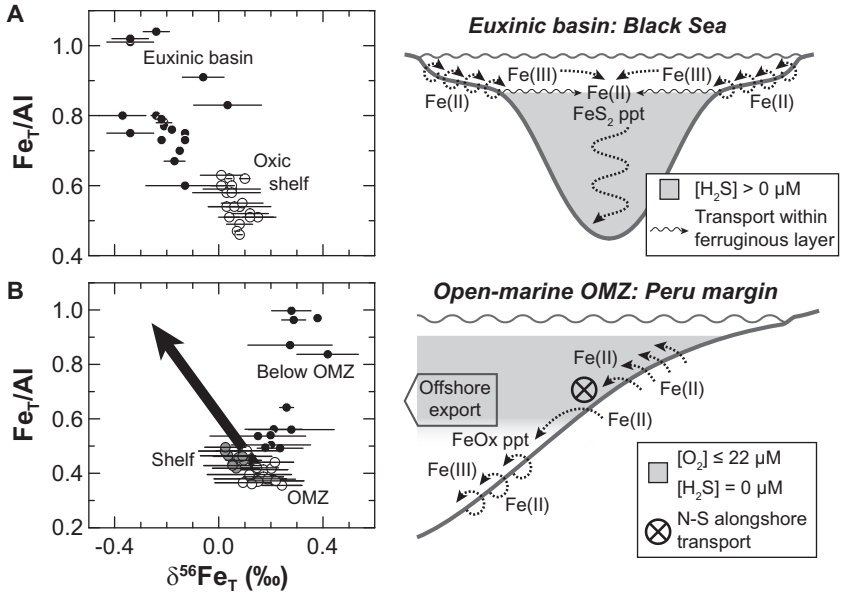

Fig. 4. Cross plots of Fe_T/Al versus $\delta^{56}Fe_T \pm 2$ SD for sediment cores from: (A) the Black Sea (data from Severmann et al., 2008); (B) the Peruvian continental margin. The black arrow in (B) illustrates a hypothetical situation where 100% of the Fe mobilized within the OMZ is re-deposited below the OMZ. The sketches on the right-hand side illustrate mechanistic differences between Fe shuttles in euxinic basins and open-marine OMZs (FeS_2 ppt = pyrite precipitation; FeOx ppt = Fe (oxyhydr)oxide precipitation). The gray shaded areas (see legend) refer to the redox state of the water column and do not provide information about the redox state of the sediments. See text for further explanation.

the anoxic to hypoxic bottom water within the OMZ to the oxic bottom water below the OMZ. By contrast, sulfidic water has a higher solubility for Fe compared to oxic water (e.g., Saito et al., 2003), which facilitates the spread of Fe within the euxinic deep water of the Black Sea. The ferruginous layer overlying the euxinic deep water provides another efficient avenue for long-range transport of Fe within the basin (Lewis and Landing, 1991; Lyons and Severmann, 2006; Eckert et al., 2013). Because of efficient long-range transport and the comparably simple redox-structure (i.e., basin-wide euxinia), the S/B ratio of euxinic basins is predefined by the basin geometry.

Differences in geometry and redox structure between the Peruvian margin and the Black Sea basin may also explain the differing Fe_T/Al versus $\delta^{56}Fe_T$ trend observed in the two environments (Fig. 4). Because of the Black Sea's restricted character and, consequently, the long seawater residence time compared to open-marine systems (cf., Scholz et al., 2013), all of the Fe that has entered the deep basin will ultimately be trapped in the sediment (trapping efficiency of 1.0). Such a simple two end member source-sink relationship necessarily results in a negative correlation between Fe_T/Al and $\delta^{56}Fe_T$ (Fig. 4A). The same trend would be observed on the Peruvian margin if all of the sediment-derived Fe were re-deposited and retained in the sediment (black arrow in Fig. 4B). However, slope sediments below the Peruvian OMZ are unlikely to represent an ultimate Fe sink. Our Fe isotope data imply that only part of the exported Fe is re-precipitated or retained and buried. The open-marine Fe shuttle in the Peruvian OMZ thus results in a rather complex situation where, depending on the relationship between source, sink and offshore flux, both positive and negative correlations between Fe_T/Al and $\delta^{56}Fe_T$ are possible.

6. SUMMARY AND IMPLICATIONS

Our findings reveal that sedimentary enrichments in reactive Fe are not limited to euxinic settings but may also occur in association with open-marine OMZs. Similar enrichments to those off Peru have been reported for other upwelling areas, e.g. in the Arabian Sea and off Mazatlan, Mexico (Van der Weijden et al., 1999; Nameroff et al., 2002). Differences in export and trapping efficiency between the Fe shuttles in open-marine OMZs and isolated euxinic basins are related to the differing redox-state of the bottom water in the Fe source (hypoxic or anoxic versus oxic) and sink (oxic versus euxinic) areas. However, differences in circulation pattern, geometry and redox structure likely play an important role as well. Alongshore undercurrents that are typical for eastern-boundary upwelling areas (e.g., Mittelstaedt, 1983; Hill and Thomas, 1998; Kessler, 2006; Cullen et al., 2009) may complicate the mass balance between source and sink areas. Moreover, the "sandwich-type" redox structure (oxic–anoxic/hypoxic–oxic) typical for OMZs precludes the formation of an ultimate Fe sink thus complicating the Fe_T/Al-$\delta^{56}Fe_T$ relationship. On the Peruvian margin, partial re-deposition or retention of the sediment-derived Fe impedes the formation of an isotopically light Fe sink. This observation demonstrates that shuttle-related Fe enrichments do not necessarily result in low $\delta^{56}Fe$ values in the (near-shore) sink.

The shuttle mechanism observed in this study is likely to operate along many ocean margins, regardless whether sedimentary Fe enrichments are detectable or not. Off Peru, the focused accumulation of sediment-derived Fe is favored by the abrupt drop in Fe solubility at the transition from anoxic (or hypoxic) to oxic water masses at the lower oxycline.

If this water column redox boundary was less pronounced or absent, the re-precipitation of sediment-derived Fe would be less focused and the resulting Fe enrichment more widespread and thus difficult to detect.

There is growing evidence for the occurrence of OMZ-type redox structures in Earth history (Brumsack, 2006; Meyer and Kump, 2008) although sometimes with a contrasting chemistry compared to contemporary OMZs. For instance, sulfidic "OMZs" sandwiched between ferruginous deep water and slightly oxic surface water have been proposed for the late Archean (Reinhard et al., 2009) and the Proterozoic (Poulton et al., 2010; Li et al., 2010; Poulton and Canfield, 2011). The simple source-sink relationship observed in the Black Sea is unlikely to be a universally applicably model for Fe and Fe isotope cycling in such systems. Instead, we propose that some of the mechanisms identified in this study, i.e., those related to geometry, redox structure and circulation pattern, may have operated at these open-marine euxinic margins as well. Taking these factors into account, an "atypical" Fe_T/Al–$\delta^{56}Fe_T$ relationship may help to identify an open-marine Fe shuttle in the geological record.

ACKNOWLEDGEMENTS

We thank the officers and crew of RV Meteor as well as the involved lab technicians for their support during sampling and analyses. Funding was provided by the German Research Foundation (Sonderforschungsbereich 754, "Climate-Biogeochemistry Interactions in the Tropical Ocean"), the US National Science Foundation (Grant #1029889 to J.M. and #1029739 to S.S.) and the 7th Framework Program of the European Union (Marie Curie IOF to F.S., Project #300648, BICYCLE). Constructive comments by anonymous referees as well as the editorial handling by Clark Johnson are gratefully acknowledged. Most of all, we would like to thank Rob Raiswell for his fair and encouraging reviews.

APPENDIX A. SUPPLEMENTARY DATA

Supplementary data associated with this article can be found, in the online version, at http://dx.doi.org/10.1016/j.gca.2013.11.041.

REFERENCES

Aller R. C. (1980) Quantifying solute distributions in the bioturbated zone of marine sediments by defining an average microenvironment. *Geochim. Cosmochim. Acta* **44**, 1955–1965.

Anbar A. D. (2004) Iron stable isotopes: beyond biosignatures. *Earth Planet. Sci. Lett.* **217**, 223–236.

Arnold G. L., Weyer S. and Anbar A. D. (2004) Fe isotope variations in natural materials measured using high mass resolution multiple collector ICPMS. *Anal. Chem.* **76**, 322–327.

Beard B. L. and Johnson C. M. (1999) High precision iron isotope measurements of terrestrial and lunar materials. *Geochim. Cosmochim. Acta* **63**, 1653–1660.

Beard B. L. and Johnson C. M. (2004) Fe isotope variations in the modern and ancient Earth and other planetary bodies. In *Geochemistry of Non-Traditional Stable Isotopes* (eds. C. M. Johnson, B. L. Beard and F. Albarède). Mineralogical Society of America, pp. 319–357.

Beard B. L., Johnson C. M., Skulan J. L., Nealson K. H., Sun H. and Cox L. (2003) Application of Fe isotopes to tracing the geochemical and biochemical cycling of Fe. *Chem. Geol.* **195**, 87–117.

Bergquist B. A. and Boyle E. A. (2006) Iron isotopes in the Amazon River system: weathering and transport signatures. *Earth Planet. Sci. Lett.* **248**, 54–68.

Bohlen L., Dale A. W., Sommer S., Mosch T., Hensen C., Noffke A., Scholz F. and Wallmann K. (2011) Benthic nitrogen cycling traversing the Peruvian oxygen minimum zone. *Geochim. Cosmochim. Acta* **75**, 6094–6111.

Böning P., Brumsack H. J., Böttcher M. E., Schnetger B., Kriete C., Kallmeyer J. and Borchers S. L. (2004) Geochemistry of Peruvian near-surface sediments. *Geochim. Cosmochim. Acta* **68**, 4429–4451.

Brink K. H., Halpern D., Huyer A. and Smith R. L. (1983) The physical environment of the Peruvian upwelling system. *Progr. Oceanogr.* **12**, 285–305.

Bruland K. W., Rue E. L., Smith G. J. and DiTullio G. R. (2005) Iron, macronutrients and diatom blooms in the Peru upwelling regime: Brown and blue waters of Peru. *Mar. Chem.* **93**, 81–103.

Brumsack H. J. (2006) The trace metal content of recent organic carbon-rich sediments: implications for Cretaceous black shale formation. *Palaeogeogr. Palaeoclimatol. Palaeoecol.* **232**, 344–361.

Bullen T. D., White A. F., Childs C. W., Vivit D. V. and Schulz M. S. (2001) Demonstration of significant abiotic iron isotope fractionation in nature. *Geology* **29**, 699–702.

Canfield D. E. (1989) Reactive iron in marine sediments. *Geochim. Cosmochim. Acta* **53**, 619–632.

Canfield D. E., Raiswell R., Westrich J. T., Reaves C. M. and Berner R. A. (1986) The use of chromium reduction in the analysis of reduced inorganic sulfur in sediments and shales. *Chem. Geol.* **54**, 149–155.

Canfield D. E., Lyons T. W. and Raiswell R. (1996) A model for iron deposition to euxinic Black Sea sediments. *Am. J. Sci.* **296**, 818–834.

Croal L. R., Johnson C. M., Beard B. L. and Newman D. K. (2004) Iron isotope fractionation by Fe(II)-oxidizing photoautotrophic bacteria. *Geochim. Cosmochim. Acta* **68**, 1227–1242.

Cullen J. T., Chong M. and Ianson D. (2009) British Columbian continental shelf as a source of dissolved iron to the subarctic northeast Pacific Ocean. *Global Biogeochem. Cy.* **23**, GB4012. http://dx.doi.org/10.1029/2008GB003326.

Dauphas N. and Rouxel O. (2006) Mass spectrometry and natural variations of iron isotopes. *Mass Spectrom. Rev.* **25**, 515–550.

De Baar H. J. W. and De Jong J. T. M. (2001) Distributions, sources and sinks of iron in seawater. In *Biogeochemistry of Iron in Seawater* (eds. D. Turner and K. A. Hunter). John Wiley & Sons, Chichester, pp. 123–253.

Duan Y., Severmann S., Anbar A. D., Lyons T. W., Gordon G. W. and Sageman B. B. (2010) Isotopic evidence for Fe cycling and repartitioning in ancient oxygen-deficient settings: examples from black shales of the mid-to-late Devonian Appalachian basin. *Earth Planet. Sci. Lett.* **290**, 244–253.

Dymond J., Corliss J. B., Heath G. R., Field C. W., Dasch E. J. and Veeh H. H. (1973) Origin of metalliferous sediments from the Pacific Ocean. *Geol. Soc. Am. Bull.* **84**, 3355–3372.

Eckert S., Brumsack H.-J., Severmann S., Schnetger B., März C. and Fröllje H. (2013) Establishment of euxinic conditions in the Holocene Black Sea. *Geology* **41**, 431–434.

Elrod V. A., Berelson W. M., Coale K. H. and Johnson K. S. (2004) The flux of iron from continental shelf sediments: a missing source for global budgets. *Geophys. Res. Lett.* **31**. http://dx.doi.org/10.1029/2004GL020216.

Feely R. A., Sabine C. L., Hernandez-Ayon J. M., Ianson D. and Hales B. (2008) Evidence for upwelling of corrosive "acidified" water onto the continental shelf. *Science* **320**, 1490–1492.

Fehr M. A., Andersson P. S., Hålenius U. and Mörth C. M. (2008) Iron isotope variations in Holocene sediments of the Gotland Deep, Baltic Sea. *Geochim. Cosmochim. Acta* **72**, 807–826.

Fehr M. A., Andersson P. S., Hålenius U., Gustafsson Ö. and Mörth C. M. (2010) Iron enrichments and Fe isotopic compositions of surface sediments from the Gotland Deep, Baltic Sea. *Chem. Geol.* **277**, 310–322.

Fuenzalida R., Schneider W., Garcés-Vargas J., Bravo L. and Lange C. (2009) Vertical and horizontal extension of the oxygen minimum zone in the eastern South Pacific Ocean. *Deep Sea Res. Pt. II* **56**, 992–1003.

Glock N., Eisenhauer A., Liebetrau V., Wiedenbeck M., Hensen C. and Nehrke G. (2013) EMP and SIMS studies on Mn/Ca and Fe/Ca systematics in benthic foraminifera from the Peruvian OMZ: a contribution to the identification of potential redox proxies and the impact of cleaning protocols. *Biogeosciences* **9**, 341–359.

Govindaraju K. (1994) Compilation of working values and sample description for 383 geostandards. *Geostandard Newslett.* **18**, 1–158.

Gutiérrez D., Enríquez E., Purca S., Quipúzcoa L., Marquina R., Flores G. and Graco M. (2008) Oxygenation episodes on the continental shelf of central Peru: remote forcing and benthic ecosystem response. *Progr. Oceanogr.* **79**, 177–189.

Hill E. A., Hickey B. M., Shillington F. A., Strub P. T., Brink K. H., Barton E. D. and Thomas A. C. (1998) Eastern ocean boundaries coastal segment. In *The Sea* (eds. A. R. Robinson and K. H. Brink). John Wiley & Sons, New York, pp. 29–67.

Hong H. and Kester D. R. (1985) Redox state of iron in the offshore waters of Peru. *Limnol. Oceanogr.* **31**, 512–524.

Huerta-Diaz M. A. and Morse J. W. (1990) A quantitative method for determination of trace metal concentrations in sedimentary pyrite. *Mar. Chem.* **29**, 119–144.

Ingri J., Malinovsky D., Rodushkin I., Baxter D. C., Widerlund A., Andersson P., Gustafsson Ö., Forsling W. and Öhlander B. (2006) Iron isotope fractionation in river colloidal matter. *Earth Planet. Sci. Lett.* **245**, 792–798.

John S. G., Mendez J., Moffett J. and Adkins J. (2012) The flux of iron and iron isotopes from San Pedro Basin sediments. *Geochim. Cosmochim. Acta* **93**, 14–29.

Johnson C. M., Beard B. L., Roden E. E., Newman D. K. and Nealson K. H. (2004) Isotopic constraints on biogeochemical cycling of Fe. In *Geochemistry of Non-Traditional Stable Isotopes* (eds. C. M. Johnson, B. L. Beard and F. Albarède). Mineralogical Society of America, pp. 359–508.

Kessler W. S. (2006) The circulation of the eastern tropical Pacific: a review. *Progr. Oceanogr.* **69**, 181–217.

Lam P. J. and Bishop J. K. B. (2008) The continental margin is a key source of iron to the HNLC North Pacific Ocean. *Geophys. Res. Lett.* **35**, L07608.

Lam P. J., Ohnemus D. C. and Marcus M. A. (2012) The speciation of marine particulate iron adjacent to active and passive continental margins. *Geochim. Cosmochim. Acta* **80**, 108–124.

Landing W. M. and Bruland K. W. (1987) The contrasting biogeochemistry of iron and manganese in the Pacific Ocean. *Geochim. Cosmochim. Acta* **51**, 29–43.

Levin L., Gutiérrez D., Rathburn A., Neira C., Sellanes J., Muñoz P., Gallardo V. and Salamanca M. (2002) Benthic processes on the Peru margin: a transect across the oxygen minimum zone during the 1997–98 El Niño. *Prog. Oceanogr.* **53**, 1–27.

Lewis B. L. and Landing W. M. (1991) The biogeochemistry of manganese and iron in the Black Sea. *Deep Sea Res.* **38** (Supplement 2), S773–S803.

Li C., Love G. D., Lyons T. W., Fike D. A., Sessions A. L. and Chu X. (2010) A stratified redox model for the Ediacaran ocean. *Science* **328**, 80–83.

Lohan M. C. and Bruland K. W. (2008) Elevated Fe(II) and dissolved Fe in hypoxic shelf waters off Oregon and Washington: an enhanced source of iron to coastal upwelling regimes. *Environ. Sci. Technol.* **42**, 6462–6468.

Lyons T. W. and Severmann S. (2006) A critical look at iron paleoredox proxies: new insights from modern euxinic marine basins. *Geochim. Cosmochim. Acta* **70**, 5698–5722.

Lyons T. W., Werne J. P., Hollander D. J. and Murray R. W. (2003) Contrasting sulfur geochemistry and Fe/Al and Mo/Al ratios across the last oxic-to-anoxic transition in the Cariaco Basin, Venezuela. *Chem. Geol.* **195**, 131–157.

MacCready P. and Rhines P. B. (1993) Slippery bottom boundary layers on a slope. *J. Phys. Oceanogr.* **23**, 5–22.

McLennan S. M. (2001) Relationships between the trace element composition of sedimentary rocks and upper continental crust. *Geochem. Geophys. Geosyst.* **2**, Paper number 2000GC000109.

Meyer K. M. and Kump L. R. (2008) Oceanic euxinia in earth history: causes and consequences. *Annu. Rev. Earth Planet. Sci.* **36**, 251–288.

Mikutta C., Wiederhold J. G., Cirpka O. A., Hofstetter T. B., Bourdon B. and Gunten U. V. (2009) Iron isotope fractionation and atom exchange during sorption of ferrous iron to mineral surfaces. *Geochim. Cosmochim. Acta* **73**, 1795–1812.

Millero F. J., Sotolongo S. and Izaguirre M. (1987) The oxidation kinetics of Fe(II) in seawater. *Geochim. Cosmochim. Acta* **51**, 793–801.

Mittelstaedt E. (1983) The upwelling area off Northwest Africa – a description of phenomena related to coastal upwelling. *Prog. Oceanogr.* **12**, 307–331.

Moore J. K. and Braucher O. (2008) Sedimentary and mineral dust sources of dissolved iron to the world ocean. *Biogeosciences* **5**, 631–656.

Muñoz P., Lange C. B., Gutierrez D., Hebbeln D., Salamanca M. A., Dezileau L., Reyss J. L. and Benninger L. K. (2004) Recent sedimentation and mass accumulation rates based on Pb-210 along the Peru-Chile continental margin. *Deep Sea Res. Pt. II* **51**, 2523–2541.

Nameroff T. J., Balistrieri L. S. and Murray J. W. (2002) Suboxic trace metal geochemistry in the Eastern Tropical North Pacific. *Geochim. Cosmochim. Acta* **66**, 1139–1158.

Noffke A., Hensen C., Sommer S., Scholz F., Bohlen L., Mosch T., Graco M. and Wallmann K. (2012) Benthic iron and phosphorus fluxes across the Peruvian oxygen minimum zone. *Limnol. Oceanogr.* **57**, 851–867.

Owens J. D., Lyons T. W., Li X., Macleod K. G., Gordon G., Kuypers M. M. M., Anbar A., Kuhnt W. and Severmann S. (2012) Iron isotope and trace metal records of iron cycling in the proto-North Atlantic during the Cenomanian-Turonian oceanic anoxic event (OAE-2). *Paleoceanography* **27**, PA3223. http://dx.doi.org/10.1029/2012PA002328.

Pennington J. T., Mahoney K. L., Kuwahara V. S., Kolber D. D., Calienes R. and Chavez F. P. (2006) Primary production in the eastern tropical Pacific: a review. *Prog. Oceanogr.* **69**, 285–317.

Poulton S. W. and Canfield D. E. (2011) Ferruginous conditions: a dominant feature of the ocean through Earth's history. *Elements* **7**, 107–112.

Poulton S. W. and Raiswell R. (2002) The low-temperature geochemical cycle of iron: from continental fluxes to marine sediment deposition. *Am. J. Sci.* **302**, 774–805.

Poulton S. W., Fralick P. W. and Canfield D. E. (2010) Spatial variability in oceanic redox structure 1.8 billion years ago. *Nat. Geosci.* **3**, 486–490.

Raiswell R. (2011) Iron transport from the continents to the open ocean: the Aging-rejuvenation cycle. *Elements* **7**, 101–106.

Raiswell R. and Anderson T. F. (2005) Reactive iron enrichment in sediments deposited beneath euxinic bottom waters: constraints on supply by shelf recycling. *Geol. Soc. London Spec. Publ.* **248**, 179–194.

Raiswell R. and Canfield D. E. (1996) Rates of reaction between silicate iron and dissolved sulfide in Peru Margin sediments. *Geochim. Cosmochim. Acta* **60**, 2777–2787.

Raiswell R. and Canfield D. E. (2012) The iron biogeochemical cycle past and present. *Geochem. Perspect.* **1**, 1–220.

Raiswell R., Canfield D. E. and Berner R. A. (1994) A comparison of iron extraction methods for the determination of degree of pyritisation and the recognition of iron-limited pyrite formation. *Chem. Geol.* **111**, 101–110.

Reinhard C. T., Raiswell R., Scott C., Anbar A. D. and Lyons T. W. (2009) A late Archean sulfidic sea stimulated by early oxidative weathering of the continents. *Science* **326**, 713–716.

Rouxel O., Sholkovitz E., Charette M. and Edwards K. J. (2008) Iron isotope fractionation in subterranean estuaries. *Geochim. Cosmochim. Acta* **72**, 3413–3430.

Roy M., Rouxel O., Martin J. B. and Cable J. E. (2012) Iron isotope fractionation in a sulfide-bearing subterranean estuary and its potential influence on oceanic Fe isotope flux. *Chem. Geol.* **300–301**, 133–142.

Saito M. A., Sigman D. M. and Morel F. M. M. (2003) The bioinorganic chemistry of the ancient ocean: the co-evolution of cyanobacterial metal requirements and biogeochemical cycles at the Archean-Proterozoic boundary? *Inorg. Chim. Acta* **356**, 308–318.

Sarbas B. and Nohl U. (2009) The GEOROC database – a decade of "online geochemistry". *Geochim. Cosmochim. Acta* **73**, A1158.

Scholz F., Hensen C., Noffke A., Rohde A., Liebetrau V. and Wallmann K. (2011) Early diagenesis of redox-sensitive trace metals in the Peru upwelling area – response to ENSO-related oxygen fluctuations in the water column. *Geochim. Cosmochim. Acta* **75**, 7257–7276.

Scholz F., McManus J. and Sommer S. (2013) The manganese and iron shuttle in a modern euxinic basin and implications for molybdenum cycling at euxinic ocean margins. *Chem. Geol.* **355**, 56–68.

Severmann S., Johnson C. M., Beard B. L. and McManus J. (2006) The effect of early diagenesis on the Fe isotope compositions of porewaters and authigenic minerals in continental margin sediments. *Geochim. Cosmochim. Acta* **70**, 2006–2022.

Severmann S., Lyons T. W., Anbar A., McManus J. and Gordon G. (2008) Modern iron isotope perspective on the benthic iron shuttle and the redox evolution of ancient oceans. *Geology* **36**, 487–490.

Severmann S., McManus J., Berelson W. M. and Hammond D. E. (2010) The continental shelf benthic iron flux and its isotope composition. *Geochim. Cosmochim. Acta* **74**, 3984–4004.

Sommer S., Pfannkuche O., Linke P., Luff R., Greinert J., Drews M., Gubsch S., Pieper M., Poser M. and Viergutz T. (2006) Efficiency of the benthic filter: biological control of the emission of dissolved methane from sediments containing shallow gas hydrates at Hydrate Ridge. *Global Biogeochem. Cy.* **20**, GB2019. http://dx.doi.org/10.1029/2004GB002389.

Staubwasser M., von Blanckenburg F. and Schoenberg R. (2006) Iron isotopes in the early marine diagenetic iron cycle. *Geology* **34**, 629–632.

Staubwasser M., Schoenberg R., von Blanckenburg F., Krüger S. and Pohl C. (2013) Isotope fractionation between dissolved and suspended particulate Fe in the oxic and anoxic water column of the Baltic Sea. *Biogeosciences* **10**, 233–245.

Strub P. T., Mesías J. M., Montecino V., Rutllant J. and Salinas S. (1998) Coastal ocean circulation off Western South America. In *The Sea* (eds. A. R. Robinson and K. H. Brink). John Wiley & Sons, New York, pp. 273–313.

Suits N. S. and Arthur M. A. (2000) Sulfur diagenesis and partitioning in Holocene Peru shelf and upper slope sediments. *Chem. Geol.* **163**, 219–234.

Teutsch N., Von Gunten U., Porcelli D., Cirpka O. A. and Halliday A. N. (2005) Adsorption as a cause for iron isotope fractionation in reduced groundwater. *Geochim. Cosmochim. Acta* **69**, 4175–4185.

Tribovillard N., Algeo T. J., Lyons T. W. and Riboulleau A. (2006) Trace metals as paleoredox and paleoproductivity proxies: an update. *Chem. Geol.* **232**, 12–32.

Van der Weijden C. H. (2002) Pitfalls of normalization of marine geochemical data using a common divisor. *Mar. Geol.* **184**, 167–187.

Van der Weijden C. H., Reichart G. J. and Visser H. J. (1999) Enhanced preservation of organic matter in sediments deposited within the oxygen minimum zone in the northeastern Arabian Sea. *Deep Sea Res. Pt. I* **46**, 807–830.

Wijsman J. W. M., Middelburg J. J. and Heip C. H. R. (2001) Reactive iron in Black Sea sediments: implications for iron cycling. *Mar. Geol.* **172**, 167–180.

Associate editor: Clark M. Johnson

Chemical Geology 389 (2014) 48–59

Contents lists available at ScienceDirect

Chemical Geology

journal homepage: www.elsevier.com/locate/chemgeo

On the isotope composition of reactive iron in marine sediments: Redox shuttle versus early diagenesis

Florian Scholz [a,*], Silke Severmann [b], James McManus [a,c], Anna Noffke [d], Ulrike Lomnitz [d], Christian Hensen [d]

[a] College of Earth, Ocean, and Atmospheric Sciences, Oregon State University, 104 Ocean Admin. Bldg., Corvallis, OR 97331-5503, USA
[b] Institute of Marine and Coastal Sciences, Rutgers University, New Brunswick, NJ 08901, USA
[c] Department of Geosciences, University of Akron, Akron, OH 44325–4101, USA
[d] GEOMAR Helmholtz Centre for Ocean Research Kiel, Wischhofstraße 1-3, 24148 Kiel, Germany

ARTICLE INFO

Article history:
Received 19 February 2014
Received in revised form 1 September 2014
Accepted 6 September 2014
Available online 28 September 2014

Editor: Michael E. Böttcher

Keywords:
Reactive iron
Iron isotopes
Shuttle
Diagenesis
Authigenic minerals
Paleo-redox

ABSTRACT

The isotope composition of reactive iron (Fe) in marine sediments and sedimentary rocks is a promising tool for identifying Fe sources and sinks across ocean basins. In addition to cross-basinal Fe redistribution, which can modify Fe isotope signatures, Fe minerals also undergo diagenetic redistribution during burial. The isotope fractionation associated with this redistribution does not affect the bulk isotope composition, but complicates the identification of mineral-specific isotope signatures. Here, we present new Fe isotope data for Peru margin sediments and revisit previously published data for sediments from the California margin to unravel the impact of early diagenesis on Fe isotope compositions of individual Fe pools.

Sediments from oxic California margin sites are dominated by terrigenous Fe supply with Fe release from sediments having a negligible influence on the solid phase Fe isotope composition. The highly reactive Fe pool (sum of Fe bound to (oxyhydr)oxide, carbonate, monosulfide and pyrite) of these sediments has a light isotope composition relative to the bulk crust, which is consistent with earlier studies showing that continental weathering shifts the isotope composition of Fe (oxyhydr)oxides to lighter values. Ferruginous sediments within the Peruvian oxygen minimum zone are depleted in Fe relative to the lithogenic background, which we attribute to extensive Fe release to the water column. The remaining highly reactive Fe pool has a heavier isotope composition compared to California margin sediments. This observation is in agreement with the general notion of an isotopically light benthic Fe efflux. Most of the reactive Fe delivered and retained in the sediment is transferred into authigenic mineral phases within the topmost 10 to 20 cm of the sediments. We observe a first-order relationship between the extent of pyritization of Fe monosulfide and the isotope composition of authigenic pyrite. With increasing pyritization, the isotope composition of authigenic pyrite approaches the isotope composition of the highly reactive Fe pool. We argue that the isotope composition of authigenic pyrite or other Fe minerals that may undergo pyritization may only be used to trace water column sources or sinks if the extent of pyritization is separately evaluated and either close to 100% or 0%. Alternatively, one may calculate the isotope composition of the highly reactive Fe pool, thereby avoiding isotope effects due to internal diagenetic redistribution. In depositional settings with high Fe but low sulfide concentrations, source and sink signatures in the isotope composition of the highly reactive Fe pool may be compromised by sequestration of Fe within authigenic silicate minerals. Authigenic silicate minerals appear to be an important burial phase for reactive Fe below the Peruvian oxygen minimum zone.

1. Introduction

1.1. Scientific rationale

An increasing number of studies use the concentration and speciation of reactive iron (Fe) within marine sediments or sedimentary rocks to infer past processes related to Fe biogeochemical cycling and the ocean's redox structure (e.g., Raiswell and Canfield, 1998; Poulton et al., 2004, 2010; Canfield et al., 2008; Poulton and Canfield, 2011; März et al., 2012). Reactive Fe is defined as the fraction of Fe in marine sediments (chiefly Fe (oxyhydr)oxides) which readily reacts (or has already undergone reaction) with hydrogen sulfide to form Fe sulfide minerals such as Fe monosulfide (FeS) and eventually pyrite (FeS_2) (Berner, 1970, 1984; Canfield, 1989). To assess these operationally defined species, various sequential extraction techniques have been developed and applied to bulk sediments and rocks (Canfield, 1989; Huerta-Diaz and Morse, 1990; Kostka and Luther, 1994; Raiswell et al., 1994; Poulton and Canfield, 2005). Reactive Fe is typically calculated

* Corresponding author at: GEOMAR Helmholtz Centre for Ocean Research Kiel, Wischhofstraße 1-3, 24148 Kiel, Germany. Tel.: +49 431 600 2114.
E-mail address: fscholz@geomar.de (F. Scholz).

http://dx.doi.org/10.1016/j.chemgeo.2014.09.009
0009-2541/

as the sum of Fe extracted by dithionite (or equivalent) and Fe present as pyrite (Raiswell and Canfield, 1998, 2012; Raiswell and Anderson, 2005; Lyons and Severmann, 2006). An alternative approach to sequential extractions uses total Fe to aluminum ratios (Fe_T/Al) to assess reactive Fe enrichments (Lyons et al., 2003; Lyons and Severmann, 2006). The advantage of this latter approach is that elevated Fe_T/Al (over lithogenic background) is preserved even when some of the reactive Fe has been transferred to the silicate fraction through diagenetic or metamorphic processes, i.e., it is independent of the specific reactive phases (Lyons and Severmann, 2006).

Generally speaking, enrichments of reactive Fe occur when Fe is transferred from an area of high Fe solubility (e.g., with reducing but non-sulfidic conditions) to an area of low Fe solubility (e.g., with oxic or sulfidic conditions). If this transfer operates on the scale of ocean basins it is typically referred to as a redox shuttle. Prominent examples of areas where a redox shuttle has been observed are anoxic and sulfidic (i.e., euxinic) basins (e.g., the Black Sea and Baltic Sea Deeps), where Fe is mobilized from reducing shelf sediments and scavenged from the euxinic water column through syngenetic pyrite formation (Canfield et al., 1996; Wijsman et al., 2001; Anderson and Raiswell, 2004; Lyons and Severmann, 2006; Dellwig et al., 2010; Fehr et al., 2010; Scholz et al., 2013). This euxinic Fe shuttle is identified in sedimentary records by a high proportion of reactive Fe to total Fe (or high Fe_T/Al) coupled to a high proportion of pyrite in the reactive Fe pool (i.e., a high extent of pyritization) (Raiswell et al., 1988; Raiswell and Anderson, 2005; Lyons and Severmann, 2006; Raiswell and Canfield, 2012). In contrast to euxinic settings, a high ratio of reactive Fe to total Fe coupled to a low extent of pyritization has been attributed to ferruginous settings, i.e., those with abundant dissolved Fe but no hydrogen sulfide (H_2S) in the water column. This kind of environment is limited to isolated lakes today (e.g., Lake Matano, Indonesia; Crowe et al., 2008) but was likely dominant in the ocean during the Archean and much of the Proterozoic (Canfield et al., 2008; Poulton et al., 2010; Poulton and Canfield, 2011). Findings from a recent study (Scholz et al., 2014) suggest that shuttle-related Fe enrichments may also occur in association with contemporary oxygen minimum zones (OMZs). Scholz et al. (2014) reported elevated Fe_T/Al ratios in sediments underneath the lower boundary of the Peruvian OMZ and attributed this observation to a net lateral transfer of Fe from reducing sediments within the OMZ.

In addition to sequential extraction techniques, Fe isotope systematics have been suggested as a potentially powerful tool for constraining Fe transport across basinal redox gradients. Fe that is mobilized through reductive dissolution has a low $\delta^{56}Fe$ relative to lithogenic Fe (Bergquist and Boyle, 2006; Rouxel et al., 2008; Severmann et al., 2010; John et al., 2012). Depending on the efficiency of the Fe trapping mechanism within the basin and the extent of isotope fractionation during re-precipitation, the sediment-derived Fe may be traceable within the sedimentary bulk Fe pool (i.e., $\delta^{56}Fe_T \neq \delta^{56}Fe_{lithogenic}$) (Scholz et al., 2014). A highly efficient sink is characteristic of isolated euxinic basins where the mobilized Fe is quantitatively trapped within basin sediments (Fehr et al., 2008, 2010; Severmann et al., 2008). In many open-marine settings, however, the trapping efficiency and proportion of shuttle-derived Fe in the sediment are small and deviations in $\delta^{56}Fe_T$ from $\delta^{56}Fe_{lithogenic}$ cannot be resolved analytically (Scholz et al., 2014). Analyzing the isotope composition of specific authigenic Fe mineral phases, which are part of the reactive Fe pool, could be an appropriate solution to identifying primary signatures. However, interpreting the isotope composition of authigenic Fe minerals is complicated by early diagenetic processes such as, e.g., reductive dissolution of Fe (oxyhydr)oxides, partial loss of dissolved Fe across the sediment-bottom water interface and re-precipitation of Fe as carbonate, monosulfide and pyrite (e.g., Berner, 1970; Canfield, 1989, 1993; Haese et al., 1997; Pakhomova et al., 2007). Unless all of the trapped reactive Fe is transferred into one single mineral phase prior to burial, these processes are likely to result in a variable isotopic offset among different authigenic Fe fractions (Severmann et al., 2006; Staubwasser et al., 2006). Extracting information on water column Fe cycling from the isotope composition of individual authigenic Fe pools therefore requires a more complete understanding of Fe isotope fractionation during early diagenesis. Here we continue the discussion on how and under what circumstances an open-marine Fe shuttle may be tracked in sedimentary archives (cf. Scholz et al., 2014). Specifically, we evaluate how a shuttle-related isotopic fingerprint in the reactive Fe pool may be distinguished from fractionation effects inherited during early diagenesis. Our findings provide useful constraints on the interpretation of Fe isotope variability in reactive Fe minerals in the geological record.

1.2. Prior work and open questions

This study is based on samples that were taken on a sediment core transect across the Peru upwelling area at 11°S (Figs. 1 and 2A). Previous work on benthic Fe fluxes as well as bulk Fe concentrations (Fig. 2B) and isotope data (Fig. 3A) for the same sediment cores (Noffke et al., 2012; Scholz et al., 2014) suggests that terrigenous reactive Fe undergoes a redox-dependent lateral relocation across the Peruvian continental margin. The findings of these previous studies will be briefly summarized in the following paragraphs, followed by an outline of the major goals of the present study.

The physical environment and general biogeochemistry of the Peruvian continental margin have been discussed extensively within the literature (Brink et al., 1983; Reimers and Suess, 1983; Strub et al., 1998; Levin et al., 2002; Böning et al., 2004). Briefly, off the Peru coast upwelling of oxygen-depleted and nutrient-rich water leads to a near-complete oxygen drawdown in the water column overlying the upper slope and shelf. The OMZ ($[O_2] \leq 0.5$ ml $L^{-1} \approx 22$ μM; definition after Levin et al., 2002) resulting from this mechanism extends from less than 100 m to roughly 700 m water depth (Fuenzalida et al., 2009). Where the OMZ comes into contact with the seafloor, Fe reducing conditions prevail close to the sediment–bottom water interface. Because of the high mobility of Fe under anoxic but non-sulfidic conditions, Fe dissolved in pore water may escape into the water column without being immobilized while transiting the sediment-bottom water interface (Noffke et al., 2012). Sediments within the permanent OMZ (~300–700 m water depth) are characterized by Fe_T/Al below the regional lithogenic background (Fig. 2B), which has been attributed to long-term Fe loss to the water column inferred from benthic flux data (Scholz et al., 2011). Sediments underneath the lower boundary of the OMZ display Fe_T/Al above the lithogenic background (Fig. 2B) indicating that they are enriched in Fe relative to the lithogenic background

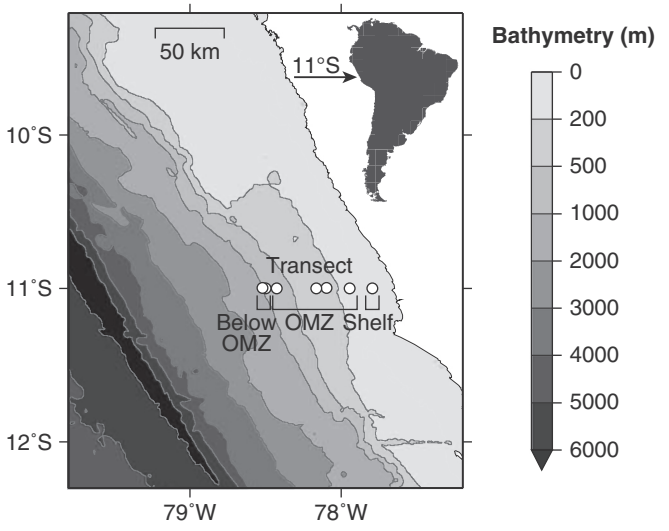

Fig. 1. Location map showing the sediment core transect (bathymetric data from GEBCO). The transect is subdivided into three domains corresponding to sediment cores from the shelf, from within the OMZ and from below the OMZ.

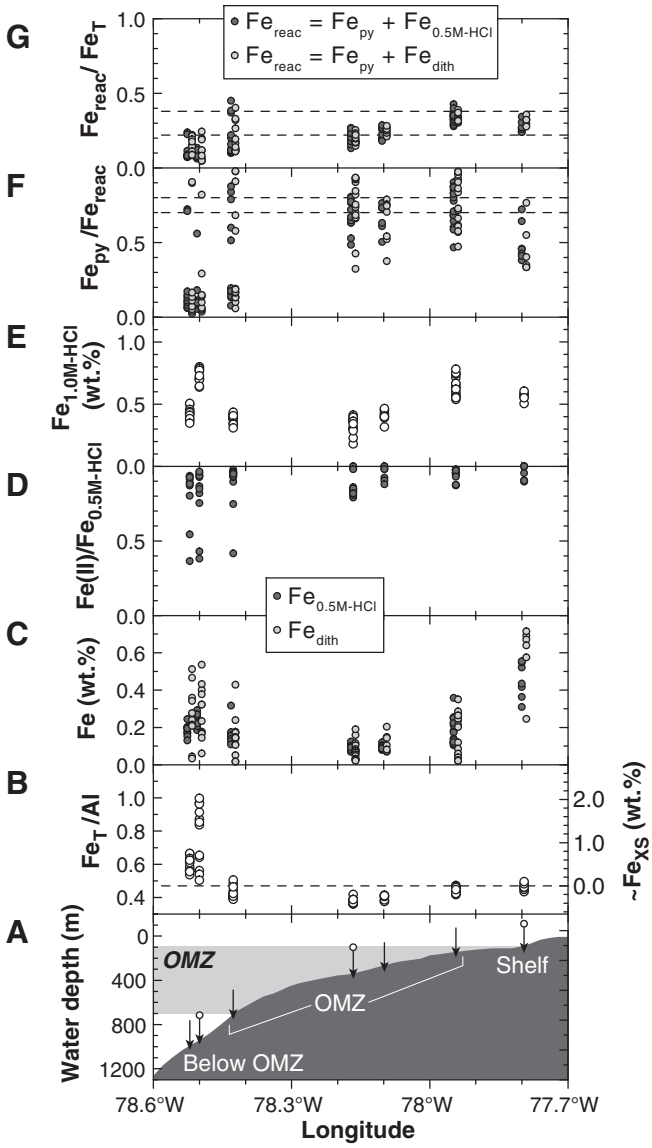

Fig. 2. Lateral distribution of sedimentary Fe species across the Peruvian continental margin: (A) bathymetry, OMZ extension and coring locations (see also Fig. 1; arrows with circles depict sediment cores for which Fe isotope data were collected); (B) Fe_T/Al ratios and Fe_{XS} (data from Scholz et al., 2014), dashed line is the lithogenic background ($(Fe/Al)_{lithogenic}$); (C) $Fe_{0.5M\text{-}HCl}$ and Fe_{dith}; (D) Fe(II)/$Fe_{0.5M\text{-}HCl}$; (E) $Fe_{1.0M\text{-}HCl}$; (F) Fe_{py}/Fe_{reac} (Fe_{reac} based on $Fe_{0.5M\text{-}HCl}$ and Fe_{dith}), dashed lines depict the transition area between non-euxinic and euxinic sediments (Poulton and Canfield, 2011); (G) Fe_{reac}/Fe_T (Fe_{reac} based on $Fe_{0.5M\text{-}HCl}$ and Fe_{dith}), dashed lines depict the transition area between oxic and anoxic sediments (Poulton and Canfield, 2011). Note that the boundaries in (F) and (G) (dashed lines) were defined based on a differing extraction scheme with additional steps for the recovery of magnetite and Fe carbonates (see text for further explanation).

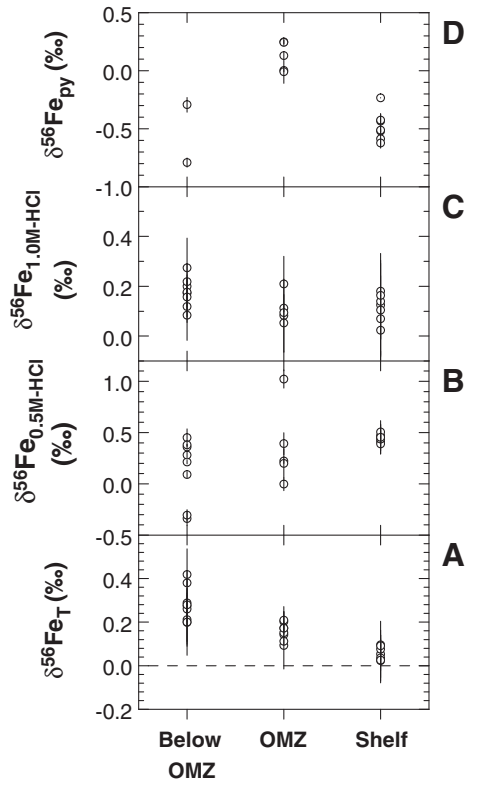

Fig. 3. Fe isotope composition for samples from selected sites on the shelf, within the OMZ and below the OMZ (see Fig. 2A for location): (A) $\delta^{56}Fe_T$, dashed line is the lithogenic background ($\delta^{56}Fe_{lithogenic}$) (Beard et al., 2003); (B) $\delta^{56}Fe_{0.5M\text{-}HCl}$; (C) $\delta^{56}Fe_{1.0M\text{-}HCl}$; (D) $\delta^{56}Fe_{py}$.

(Scholz et al., 2011). The coincidence between the transition from Fe-depleted to Fe-enriched sediments and the rise in bottom water oxygen suggests that Fe mobilized from OMZ sediments is transported within the anoxic bottom water and re-oxidized within more oxic water below the OMZ. This shuttle scenario is supported by flux calculations showing that the mass of Fe lost from sediments within the OMZ is roughly equal to the mass of excess Fe accumulating below the OMZ (Scholz et al., 2014).

Sediments within the OMZ have an increased $\delta^{56}Fe_T$ relative to the lithogenic background (Fig. 3A) (Scholz et al., 2014), which is consistent with the loss of isotopically light Fe (Rouxel et al., 2008; Severmann et al., 2010; John et al., 2012). The isotope composition of Fe sink sediments below the OMZ is slightly heavier than that of source sediments within the OMZ (Fig. 3A) (Scholz et al., 2014). The apparent mismatch in isotope composition between Fe source and sink has been attributed to partial (as opposed to quantitative) re-precipitation or retention of the sediment-derived Fe as well as offshore transport of the remaining Fe (Scholz et al., 2014). Partial removal or retention of Fe with a relatively heavy isotope composition below the OMZ is consistent with findings from a number of laboratory and field studies which have reported a positive Fe isotope fractionation factor for the precipitation of Fe(oxyhydr)oxides from dissolved Fe(II) (e.g., Bullen et al., 2001; Croal et al., 2004; Severmann et al., 2004; Rouxel et al., 2008; Busigny et al., 2014). It should be noted, however, that negative isotopic offsets between water column particulate matter and residual dissolved Fe have also been inferred (John et al., 2012; Staubwasser et al., 2013). Shallow shelf sediments display Fe_T/Al and $\delta^{56}Fe$ close to the lithogenic background (Figs. 2B and 3A), despite low bottom water oxygen concentrations. The comparably weak signal of Fe loss in shelf sediments may be related to higher sedimentation rates (Reimers and Suess, 1983) or a more efficient mechanism of Fe retention. Comparably efficient net retention of the terrestrially derived Fe has been attributed to occasional events of bottom water oxygenation as well as comparably shallow H_2S accumulation and thus Fe fixation as Fe sulfide (Scholz et al., 2011; Noffke et al., 2012).

In the present study, we applied a sequential extraction scheme to evaluate (1) if the abundance and isotope composition of reactive Fe phases are consistent with a shuttle-related signal in the bulk Fe pool, (2) how a shuttle-derived signal is modified during the conversion of Fe (oxyhydr)oxides into Fe sulfides and other authigenic mineral phases and (3) the utility of the Peruvian OMZ as an analog site for Fe biogeochemical cycling in anoxic open-marine environments in the past.

2. Methods

2.1. Sequential extraction

The sediment cores used in this study were collected during the M77-1 and M77-2 cruises of RV Meteor in November and December

2008 using a multiple coring device (MUC) or a benthic lander (Biogeochemical Observatory, BIGO) (Scholz et al., 2011). The subsampling of the cores was performed at approximate seafloor temperature in an argon-flushed glove bag. After centrifuging and recovery of the pore water, sediment samples were stored frozen and under an argon atmosphere until further treatment after the cruise. Seven sediment cores between 85 and 1005 m water depth were selected for sequential extractions (Table 1). Information on the lithology of the sediment cores as well as pore water profiles for major redox species have been published in previous studies (Bohlen et al., 2011; Scholz et al., 2011; Mosch et al., 2012; Noffke et al., 2012) (see also Table 1).

Our sequential leaching protocol comprises four steps. The extraction efficiency of each step was calibrated against pure mineral phases in previous studies.

1. Easily HCl-extractable Fe ($Fe_{0.5M\text{-}HCl}$): Add 20 ml 0.5 M HCl to 0.5 g of wet sediment, shake for 1 h, centrifuge, decant and analyze total Fe and ferrous Fe(II) photometrically using Ferrozine with and without hydroxylamine hydrochloride, respectively (Stookey, 1970). The total Fe concentration in the extraction solution was additionally analyzed by inductively coupled optical emission spectrometry (ICP OES, VARIAN 720-ES). This fraction comprises Fe bound to amorphous Fe (oxyhydr)oxides, carbonates, Fe monosulfide and, possibly, some silicate minerals (Kostka and Luther, 1994).
2. Recalcitrant HCl-extractable Fe ($Fe_{1.0M\text{-}HCl}$): Add 15 ml 1.0 M HCl to residue from previous extraction step, shake for 23 h, centrifuge, decant, wash with 10 ml deionized water, centrifuge, decant and analyze the combined solution by ICP-OES. In principle, this step extracts the same minerals as step 1 (Huerta-Diaz and Morse, 1990; Raiswell et al., 1994) but the longer extraction time results in greater Fe recovery from silicate minerals (Kostka and Luther, 1994).
3. Silicate Fe (Fe_{sil}): Add 10 ml 10 M HF to residue from previous extraction step, shake for 1 h, centrifuge, decant, add 10 ml 10 M HF, shake for 16 h, add 2 g boric acid to dissolved fluoride minerals that may have precipitated, shake for 8 h, centrifuge decant, wash with 10 ml boiling deionized water, centrifuge, decant and analyze the combined solution by ICP-OES. This step dissolves all the silicate minerals remaining after step 2 (Huerta-Diaz and Morse, 1990).
4. Pyrite Fe (Fe_{py}): Add 10 ml concentrated HNO_3 to residue from previous extraction step, shake for 2 h, filter through a cellulose filter to separate the solution from low-density organic aggregates (Scholz and Neumann, 2007), wash with 10 ml deionized water, filter again and analyze the combined solution by ICP-OES. This fraction comprises Fe bound to pyrite (Huerta-Diaz and Morse, 1990).

The extraction steps applied in this study have been applied in previous studies on the isotope composition of reactive Fe in marine sediments and terrestrial soils (e.g., Severmann et al., 2006; Wiederhold et al., 2007). We chose to apply this scheme to ensure comparability with published isotope data, although alternative schemes for the recovery of reactive Fe phases are more selective (e.g., Poulton and Canfield, 2005). We also opted for the HCl-based extraction of non-pyritized reactive Fe because proton-promoted (as opposed to ligand-controlled or reductive) dissolution of Fe (oxyhydr)oxides does not appear to be accompanied by isotope fractionation, even if the extraction is incomplete (Wiederhold et al., 2006). A notable disadvantage of the HCl-based extraction is that it does not dissolve crystalline Fe (oxyhydr) oxides such as goethite and hematite, although these are considered reactive on early diagenetic time scales (Canfield et al., 1992). To evaluate the amount of crystalline Fe (oxyhydr)oxides, we carried out a separate extraction with sodium dithionite (buffered to pH 4.8 using acetic acid and sodium citrate) (Kostka and Luther, 1994; Raiswell et al., 1994), which yields all Fe (oxyhydr)oxides including goethite and hematite (Fe_{dith}). For conversion from wet wt.% into dry wt.%, the water content of a separate sediment aliquot was determined through weighing before and after freeze drying. We monitored the long-term precision of the extraction protocol by including an in-house standard into each extraction run. This in-house standard consists of a homogenized mixture of sediments from the Peruvian continental margin at 11°S. We calculate an average precision of 8% relative standard deviation (RSD) for $Fe_{0.5M\text{-}HCl}$, 21% RSD for $Fe_{1.0M\text{-}HCl}$, 4% RSD for Fe_{sil} and 2% for Fe_{py}. The overall precision of the four step protocol is thus 23% RSD and only samples where the total recovery is within this error range are reported in the following sections. The average recovery (± 1 SD) for these samples was 97 $\pm$ 12%. The average precision of Fe_{dith} was found to be 10% RSD. Total Al, Fe and potassium (K) concentrations were determined by ICP-OES after complete sediment dissolution using HCl, HNO_3 and HF (Scholz et al., 2011).

2.2. Iron isotope analyses

Samples from three sediment cores were selected for isotope analysis. The leach and digestion solutions were transferred into an HCl matrix and purified following a standard anion exchange protocol (e.g., Beard et al., 2003; Arnold et al., 2004). In brief, a sample aliquot corresponding to 50 μg of Fe was evaporated, re-dissolved in 6 M HCl and loaded on Bio-Rad AG1X8 anion exchange resin. The sample matrix was removed and Fe was purified with two 3 ml 6 M HCl rinses. Following elution of the Fe with 0.5 M HCl, samples were evaporated and re-digested by adding a few drops of concentrated HNO_3. This latter step was done to dissolve any residual resin that might be present within the samples. Fe isotope analysis was performed in medium-resolution on a multi collector inductively coupled plasma mass spectrometer at the Woods Hole Oceanographic Institution Plasma Laboratory (Thermo Scientific, NEPTUNE) and the Department of Earth and Planetary Science at Rutgers University (Thermo Scientific NEPTUNE Plus) following the method of Arnold et al. (2004). Depending on the individual session, samples were introduced as 100–500 ppb Fe solutions through an Apex desolvating nebulizer. The on-peak background was 10^2, 10^3 and 10^5 times smaller than the signal measured for ^{57}Fe, ^{54}Fe and ^{56}Fe, respectively and did not change through the course of the run. For correction of instrumental mass bias, a copper solution of the same concentration and known isotope composition (NIST-976 copper isotope standard) was added to the purified sample solution. In addition, sample isotope

Table 1
Location and biogeochemical context of sediment cores.

Station and gear	Domain of the transect	Latitude S	Longitude W	Water depth (m)	Bottom water oxygen (μM)[a]	Pore water redox state[b]	Mean organic carbon (wt.%)[b]
568 BIGO-05	Shelf	11°00.02′	77°47.72′	85	<LD	Ferruginous to sulfidic	3.2
470 MUC29	OMZ (upper boundary)	11°00.00′	77°56.61′	145	<LD	Ferruginous to sulfidic	7.3
016 BIGO-T	OMZ	10°59.80′	78°05.91′	259	<LD	Ferruginous to sulfidic	13.8
449 MUC19	OMZ	11°00.01′	78°09.97′	319	<LD	Ferruginous to sulfidic	14.3
459 MUC25	OMZ (lower boundary)	11°00.03′	78°25.60′	697	12.1	Oxic to ferruginous	6.3
445 MUC15	Below OMZ	10°59.98′	78°30.02′	930	39.9	Oxic to ferruginous	4.4
549 MUC53	Below OMZ	10°59.99′	78°31.27′	1005	41.6	Oxic to ferruginous	3.8

[a] LD = limit of detection (~1.5 μM).
[b] After Scholz et al. (2011).

Table 2
Concentration (dry wt.%) and Fe isotope (relative to average igneous rock) data for operationally defined Fe fractions and the bulk sediment. The uncertainty represents the two-fold standard deviation (SD) of the mean of n measurements. Fe_T and Al concentrations as well as $\delta^{56}Fe_T$ data were taken from Scholz et al. (2011, 2014).

Station and gear	Sediment depth (cm)	$Fe_{0.5M\text{-}HCl}$ (wt.%)	Fe(II)/ $Fe_{0.5M\text{-}HCl}$	$\delta^{56}Fe_{0.5M\text{-}HCl}$ (wt.%)	2 SD	n	$Fe_{1.0M\text{-}HCl}$ (wt.%)	$\delta^{56}Fe_{1.0M\text{-}HCl}$ (wt.%)	2 SD	n	Fe_{dith} (wt.%)	Fe_{sil} (wt.%)	Fe_{PY} (wt.%)	$\delta^{56}Fe_{py}$ (‰)	2 SD	n	Fe_T (wt.%)	K (wt.%)	Al (wt.%)	$\delta^{56}Fe_T$ (‰)	2 SD	n
Shelf																						
568 BIGO-05	0–1	0.36	0.90	0.41	0.02	2	0.51	0.02	0.10	1	n.d.	1.37	0.31	−0.52	0.03	3	2.79	1.60	6.41	0.05	0.05	5
	1–2	0.42	0.91	0.46	0.06	3	0.56	0.18	0.06	2	0.69	1.46	0.35	−0.51	0.01	2	3.18	1.73	7.11	0.10	0.07	4
	2–4	0.52	1.00	0.47	0.11	5	0.59	0.12	0.21	4	0.72	1.50	0.38	−0.43	0.06	2	3.42	1.77	7.45	0.08	0.06	4
	4–6	0.55	1.00	0.39	0.10	5	0.57	0.14	0.15	4	0.67	1.45	0.34	−0.59	0.08	2	3.40	1.75	7.32	0.04	0.11	5
	6–8	0.55	0.95	0.51	0.08	5	0.56	0.10	0.20	5	0.57	1.44	0.39	−0.62	0.03	2	3.46	1.79	7.48	0.09	0.11	4
	8–12	0.44	0.90	0.44	0.11	4	0.60	0.16	0.00	2	0.64	1.78	0.78	−0.42	0.05	2	3.98	1.93	8.26	0.02	0.10	5
	12–16	0.31	1.00	0.46	0.16	4	0.55	0.07	0.08	4	0.25	1.35	0.80	−0.23	0.00	2	3.25	1.61	6.55	0.03	0.08	3
OMZ																						
470 MUC29	0–1	d.r.	d.r.				d.r.				0.28	d.r.	d.r.				1.65	1.28	3.93			
	1–2	0.18	0.98				0.58				0.24	1.20	0.39				2.05	1.34	4.78			
	2–3	0.25	0.95				0.72				0.29	0.92	0.38				2.13	1.38	4.91			
	3–4	0.22	0.96				0.60				0.24	1.13	0.47				2.11	1.34	4.90			
	4–5	0.21	0.97				0.56				0.25	1.00	0.38				2.07	1.31	4.83			
	5–6	0.26	0.98				0.56				0.26	0.92	0.36				2.01	1.29	4.65			
	6–8	0.36	0.98				0.54				0.35	0.72	0.31				1.93	1.21	4.09			
	8–10	0.25	0.96				0.66				0.21	0.93	0.54				2.47	1.36	5.33			
	10–12	0.22	0.97				0.63				0.20	0.91	0.54				2.36	1.32	5.07			
	12–14	0.17	0.96				0.64				0.12	0.89	0.62				2.33	1.33	5.07			
	14–18	0.14	0.94				0.67				0.06	0.97	0.69				2.24	1.30	4.95			
	18–22	0.12	0.95				0.62				0.06	0.92	0.69				2.22	1.25	4.87			
	22–26	0.13	0.95				0.56				0.09	0.81	0.54				1.97	1.20	4.52			
	26–30	0.12	0.97				0.55				0.06	0.73	0.56				1.59	1.02	3.68			
	30–35	0.12	0.87				0.74				0.04	1.14	0.81				2.61	1.48	6.26			
	35–40	0.10	0.93				0.74				0.03	1.11	0.97				2.68	1.40	5.81			
	40–45	0.11	0.87				0.75				0.02	1.10	0.80				2.59	1.51	6.10			
	45–50	0.12	0.88				0.78				0.02	1.08	0.82				2.69	1.44	6.01			
016 BIGO–T	0–1	0.12	0.92				0.32				0.20	0.64	0.12				1.20	0.93	2.90			
	1–2	0.10	0.91				0.42				0.15	0.79	0.16				1.40	1.09	3.70			
	2–3	0.10	0.88				0.45				0.14	0.87	0.17				1.48	1.15	3.95			
	3–6	0.09	0.98				0.47				0.10	0.80	0.25				1.50	1.11	3.88			
	6–9	0.08	1.00				0.40				0.07	0.64	0.26				1.31	0.95	3.21			
	9–12	0.08	1.00				0.39				0.07	0.57	0.23				1.16	0.88	2.85			
	12–15	0.09	0.98				0.40				0.08	0.63	0.24				1.14	0.86	2.78			
449 MUC19	0–1	0.08	0.86	1.02	0.09	4	0.18	0.21	0.11	6	0.16	0.45	0.08				0.93	0.88	2.23	0.20	0.05	5
	1–2	d.r.	d.r.				d.r.				0.19	d.r.	d.r.				1.08	0.93	2.79	0.17	0.08	5
	2–3	d.r.	d.r.				d.r.				0.12	d.r.	d.r.				1.09	0.98	2.87			
	3–4	0.07	0.79	0.39	0.11	3	0.23	0.08	0.15	3	0.10	0.47	0.08				1.11	1.02	3.04	0.09	0.11	5
	4–5	0.09	0.84				0.31				0.08	0.58	0.15				1.42	1.15	3.79			
	5–6	0.10	0.85	0.22	0.02	4	0.36	0.05	0.11	3	0.08	0.67	0.20	0.00	0.01	2	1.54	1.19	4.10	0.21	0.06	3
	6–8	0.09	0.84				0.30				0.08	0.55	0.15				1.53	1.20	4.13			
	8–10	d.r.	d.r.				d.r.				0.08	d.r.	d.r.				1.42	1.14	3.90			
	10–12	0.09	0.83				0.30				0.06	0.54	0.17				1.34	1.07	3.71			
	12–14	0.09	0.84	0.00	0.06	4	0.29	0.11	0.14	3	0.07	0.52	0.16	−0.01	0.10	2	1.37	1.06	3.72	0.14	0.15	4
	14–18	0.11	0.81				0.36				0.07	0.69	0.20				1.53	1.21	4.22			
	18–22	0.12	0.82	0.20	0.14	4	0.41	0.09	0.16	2	0.06	0.73	0.25	0.13	0.03	2	1.81	1.33	4.89	0.15	0.09	3
	22–26	0.10	0.85				0.40				0.05	0.69	0.26				1.79	1.32	4.76			
	26–30	0.09	0.82				0.38				0.03	0.68	0.31	0.25	0.01	2	1.75	1.25	4.51	0.17	0.08	4
	30–35	0.09	1.00				0.36				0.03	0.68	0.36	0.25	0.03	2	1.77	1.29	4.61	0.11	0.09	5
	35–40	0.09	0.99				0.40				0.03	0.73	0.37				1.72	1.30	4.61			
	40–45	0.08	1.00				0.36				0.02	0.67	0.33				1.73	1.33	4.71			
	45–50	0.09	0.98				0.34				0.02	0.60	0.32				1.54	1.15	3.99			
459 MUC25	0–1	0.32	0.42				0.42				0.43	0.93	0.03				1.72	1.08	3.55			
	1–2	0.17	0.75				0.40				0.24	0.87	0.03				1.61	1.12	3.65			
	2–3	0.13	0.90				0.39				0.18	0.79	0.03				1.58	1.14	3.70			
	3–4	0.13	0.94				0.41				0.17	0.82	0.03				1.58	1.18	3.78			
	4–5	0.16	0.94				0.42				0.17	0.86	0.03				1.59	1.18	3.81			
	5–6	0.14	0.98				0.39				0.15	0.87	0.03				1.53	1.17	3.84			
	6–8	0.13	0.95				0.38				0.14	0.83	0.03				1.55	1.18	3.87			
	8–10	0.14	0.96				0.40				0.14	0.86	0.03				1.54	1.16	3.85			
	10–12	0.16	0.96				0.39				0.14	0.87	0.03				1.60	1.24	4.03			
	12–14	0.16	0.96				0.44				0.11	0.90	0.23				1.77	1.38	4.56			
	14–18	0.14	0.93				0.41				0.11	0.88	0.15				1.79	1.36	4.39			
	18–22	0.14	0.95				0.35				0.05	0.77	0.52				1.78	1.30	4.20			
	22–26	0.13	0.93				0.34				0.02	0.77	0.67				2.07	1.29	4.09			
	26–30	0.11	0.95				0.31				0.02	0.71	0.77				1.95	1.32	4.21			
Below OMZ																						
445 MUC15	0–1	0.26	0.38	−0.34	0.07	4	0.64	0.12	0.04	2	0.40	2.23	0.02				3.64	1.70	4.17	0.27	0.16	5
	1–2	0.28	0.43	−0.31	0.06	3	0.71	0.08	0.10	5	0.54	1.29	0.03				2.33	1.32	4.14	0.21	0.11	3
	2–3	0.23	0.75	0.21	0.02	2	0.80	0.27	0.12	3	0.43	1.86	0.02				2.29	1.35	4.24	0.20	0.11	3
	3–4	0.21	0.82	0.36	0.02	2	0.77	0.17	0.12	2	0.38	1.41	0.02				2.10	1.30	4.16	0.20	0.15	3

Table 2 *(continued)*

Station and gear	Sediment depth (cm)	$Fe_{0.5M\text{-}HCl}$ (wt.%)	Fe(II)/$Fe_{0.5M\text{-}HCl}$	$\delta^{56}Fe_{0.5M\text{-}HCl}$ (wt.%)	2 SD	n	$Fe_{1.0M\text{-}HCl}$ (wt.%)	$\delta^{56}Fe_{1.0M\text{-}HCl}$ (wt.%)	2 SD	n	Fe_{dith} (wt.%)	Fe_{sil} (wt.%)	Fe_{PY} (wt.%)	$\delta^{56}Fe_{py}$ (‰)	2 SD	n	Fe_T (wt.%)	K (wt.%)	Al (wt.%)	$\delta^{56}Fe_T$ (‰)	2 SD	n
	4–5	d.r.	d.r.				d.r.				0.32	d.r.	d.r.				2.75	1.56	4.29	0.26	0.03	2
	5–6	0.19	0.93				0.70				0.32	2.09	0.02				2.86	1.54	4.38			
	6–8	0.21	0.94	0.45	0.09	2	0.70	0.20	0.03	2	0.23	2.49	0.03				3.70	1.84	4.42	0.42	0.12	3
	8–10	0.26	0.96				0.79				0.18	3.08	0.03				4.09	2.04	4.48			
	10–12	0.29	0.94	0.38	0.00	2	0.79	0.18	0.06	3	0.17	3.45	0.03				4.22	2.10	4.35	0.38	0.01	2
	12–14	0.27	0.96				0.77				0.17	2.89	0.03				3.76	1.88	4.41			
	14–18	0.27	0.87	0.28	0.03	2	0.73	0.22	0.03	2	0.14	3.08	0.06	−0.79	0.04	2	4.20	1.98	4.35	0.29	0.05	3
	18–21	0.22	0.85	0.09	0.03	2	0.64	0.16	0.05	2	0.06	2.66	0.28	−0.29	0.06	2	4.17	1.95	4.18	0.28	0.08	2
549 MUC53	0–1	0.20	0.36				0.37				0.51	1.17	0.01				2.36	1.37	4.21			
	1–2	0.25	0.54				0.50				0.47	1.82	0.02				2.26	1.32	4.22			
	2–3	0.20	0.80				0.51				0.36	1.93	0.02				2.46	1.40	4.35			
	3–4	0.18	0.89				0.46				0.34	1.64	0.02				2.50	1.40	4.29			
	4–6	d.r.	d.r.				d.r.				0.27	d.r.	d.r.				2.73	1.50	4.40			
	5–6	0.17	0.93				0.43				0.28	1.67	0.02				2.66	1.49	4.37			
	6–8	0.20	0.91				0.44				0.24	2.02	0.03				3.00	1.62	4.54			
	8–10	0.19	0.94				0.43				0.22	1.88	0.03				2.96	1.59	4.45			
	10–14	0.20	0.93				0.41				0.21	1.72	0.04				2.84	1.56	4.47			
	14–18	d.r.	d.r.				d.r.				0.19	d.r.	d.r.				2.82	1.56	4.52			
	18–23	0.15	0.87				0.38				0.05	1.20	0.40				2.34	1.40	4.17			
	23–28	0.13	0.88				0.35				0.03	1.05	0.32				2.00	1.28	3.61			

n.d.: Not determined (not enough material left).
d.r.: Dissatisfying recovery (recovery is worse than the propagated uncertainty of the sequential extraction protocol).

ratios were normalized to the average of two bracketing standards (the pure metal Fe isotope reference material IRMM-014) measured before and after each second sample. Several geological standard reference materials of known isotope composition (shale SDO-1, shale SCo-2, basalt BCR-2, marine sediment MAG-1; all USGS) were measured routinely for each sample batch. The accuracy of the analysis was monitored by measuring a solution of IRMM-014 that had been spiked with purified ^{54}Fe isotope spike to lower its isotope composition by 1‰ (see Arnold et al., 2004). Fe isotope ratios are reported in per mil delta notation ($\delta^{56}Fe = ([^{56}Fe/^{54}Fe_{sample}] / [^{56}Fe/^{54}Fe_{standard}] - 1) \times 10^3$) relative to average igneous rock, which has an isotope composition of $\delta^{56}Fe = 0 \pm 0.05$‰ (Beard et al., 2003). The Fe isotope reference standard IRMM-014 has a $\delta^{56}Fe$ of −0.09‰ on this scale. The average external precision for $\delta^{56}Fe$, which is based on full procedural replicates, is 0.08‰ (2 standard deviations, SD).

3. Results

The results of the sediment extraction are presented as a function of longitude and water depth (Fig. 2; see Table 2 for all concentration and isotope data). Previously published Fe_T/Al and excess Fe (Fe_{XS}) are shown for comparison (Scholz et al., 2011, 2014). Fe_{XS} was calculated from the Fe/Al of the lithogenic background: $Fe_{XS} = Fe_T - (Fe/Al)_{lithogenic} \times Al_T$. Negative Fe_{XS} indicates Fe depletion relative to the lithogenic background (i.e., $Fe_T/Al < (Fe/Al)_{lithogenic}$; within OMZ) whereas positive Fe_{XS} indicates Fe enrichment relative to the lithogenic background (i.e., $Fe_T/Al > (Fe/Al)_{lithogenic}$; below OMZ). Andesite in the Andean arc was chosen as the regional lithogenic background ($Fe_T/Al = 0.47$; Böning et al., 2004; Scholz et al., 2011, 2014). Examples for cumulative downcore profiles of sequentially leached Fe fractions as well as pore water Fe profiles are shown for one sediment core from within the OMZ, below the OMZ and the shelf (Fig. 4).

Sediments within the OMZ are characterized by lower $Fe_{0.5M\text{-}HCl}$, $Fe_{1.0M\text{-}HCl}$ and Fe_{dith} compared to sediments on the upper shelf and those below the OMZ (Figs. 2C,E and 4). A single maximum below the OMZ characterizes the lateral distribution of Fe_T/Al (and Fe_{XS}) (Fig. 2B). By contrast, $Fe_{0.5M\text{-}HCl}$, $Fe_{1.0M\text{-}HCl}$ and Fe_{dith} are elevated both below the OMZ and at the upper boundary of the OMZ and on the shelf, respectively (Fig. 2C,E). A substantial fraction of $Fe_{0.5M\text{-}HCl}$ at the lower boundary of the OMZ and below the OMZ consists of ferric Fe ($Fe(II)/Fe_{0.5M\text{-}HCl} \approx 0.4$ at the sediment surface) (Fig. 2D). By contrast, within the OMZ, $Fe_{0.5M\text{-}HCl}$ consists almost exclusively of ferrous Fe ($Fe(II)/Fe_{0.5M\text{-}HCl} \geq 0.8$). Fe_{dith} decreases to values near zero (Fig. 2C) and $Fe(II)/Fe_{0.5M\text{-}HCl}$ increases to values close to 1.0 (Fig. 2D) at most of the sites. These observations are consistent with a near-complete conversion of Fe (oxyhydr)oxides into Fe sulfides within the recovered depth interval.

The co-variation trend between $Fe_{0.5M\text{-}HCl}$ and Fe_{dith} (Fig. 5) provides information about the differing extraction efficiency for Fe minerals of the two methods. If $Fe_{0.5M\text{-}HCl}$ and Fe_{dith} consisted of the same Fe phases, the results would be linearly correlated and plot on a 1:1 line. Indeed, Fe concentrations in $Fe_{0.5M\text{-}HCl}$ and Fe_{dith} are reasonably well correlated ($R^2 = 0.72$) (Fig. 5). However, a number of samples from the shelf and below the OMZ display higher Fe concentrations in Fe_{dith}. This mismatch between the two extraction procedures may be related to the presence of crystalline Fe (oxyhydr)oxides (hematite and goethite) which are generally not recovered by cold HCl (Raiswell et al., 1994). The correlation between Fe_{dith} and $Fe_{0.5M\text{-}HCl}$ has a positive x-intercept, i.e., samples with zero Fe_{dith} have low but measurable Fe concentrations in $Fe_{0.5M\text{-}HCl}$. This residual Fe pool could be recovered from silicate minerals, Fe monosulfides or Fe carbonates, which are poorly extracted from wet sediments by sodium dithionite (Canfield, 1989; Raiswell et al., 1994).

Fe_{py} generally increases with increasing sediment depth (Table 2 and Fig. 4). To illustrate the extent to which reactive Fe has been converted to pyrite, we calculated the ratio between Fe_{py} and the sum of Fe that is highly reactive towards dissolved sulfide (i.e., including Fe bound to Fe (oxyhydr)oxides, carbonates, monosulfide and pyrite). This pool of highly reactive Fe (Fe_{reac}) is defined here as the sum of either $Fe_{0.5M\text{-}HCl}$ or Fe_{dith} and Fe_{py}. Fe_{py}/Fe_{reac} is closely related to the degree of pyritization (DOP) introduced by Berner (1970). We avoid the term degree of pyritization, however, as it was originally defined based on reactive Fe obtained through extraction with boiling 12 M HCl. Fe_{py}/Fe_{reac} generally increases with sediment depth (Table 2) and

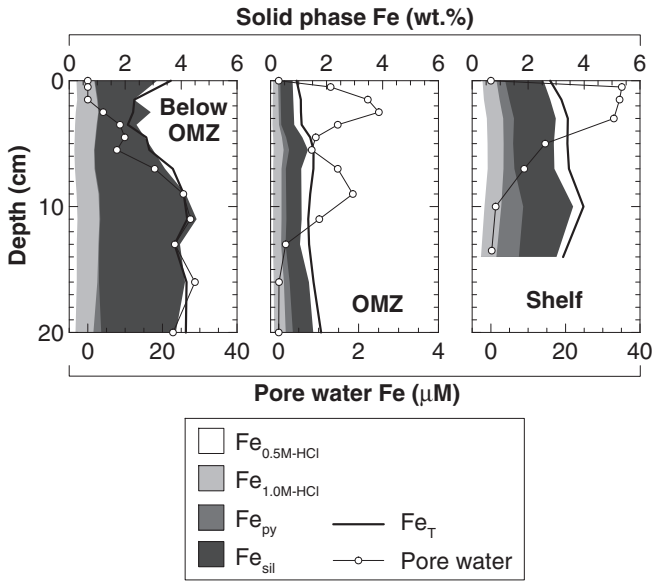

Fig. 4. Downcore distribution of $Fe_{0.5M\text{-}HCl}$, $Fe_{1.0M\text{-}HCl}$, Fe_{py}, Fe_{sil}, Fe_T and pore water Fe for selected sites on the shelf, within the OMZ and below the OMZ (see Fig. 2A for location). The shallowest sample in each pore water profile (depth = 0 cm) corresponds to the bottom water sample (dissolved Fe data from Scholz et al., 2014).

reaches values between 0.7 and 1.0, depending on whether the ratios are calculated based on $Fe_{0.5M\text{-}HCl}$ or Fe_{dith} (Fig. 2F).

Fe isotope data were collected for one sediment core from within the OMZ, one from below the OMZ and one from the shelf (Fig. 3, see Fig. 2A for locations). $\delta^{56}Fe_{0.5M\text{-}HCl}$ and $\delta^{56}Fe_{py}$ range from −0.34 to +1.02‰ (Fig. 3B) and −0.79 to +0.25‰ (Fig. 3D), respectively. The heaviest $\delta^{56}Fe$ values in $Fe_{0.5M\text{-}HCl}$ and Fe_{py} are observed within the OMZ. $\delta^{56}Fe_{1.0M\text{-}HCl}$ ranges from +0.02 to +0.27‰ (Fig. 3C). Similar to $\delta^{56}Fe_T$, which ranges from +0.02 to +0.42‰ (Fig. 3A), downcore average $\delta^{56}Fe$ values of $Fe_{1.0M\text{-}HCl}$ show a slight increase with increasing water depth. The heaviest $\delta^{56}Fe$ values in $Fe_{1.0M\text{-}HCl}$ and Fe_T are observed below the OMZ.

4. Discussion

4.1. Isotope composition of highly reactive iron: terrigenous supply versus offshore export

Sediments within the OMZ are depleted in $Fe_{0.5M\text{-}HCl}$ and Fe_{dith} (Fig. 2C), which is consistent with low Fe_T/Al (or negative Fe_{XS}) in the bulk sediment. Scholz et al. (2014) attributed Fe depletion in sediments within the Peruvian OMZ to a steady loss of reactive Fe from the sediment and lateral transport within the bottom water or the water column. Given that reductive Fe dissolution in the sediment is known to preferentially mobilize the light Fe isotope (e.g., Rouxel et al., 2008; Severmann et al., 2010; John et al., 2012), the reactive Fe left behind in Fe-depleted sediments should be enriched in the heavy Fe isotope. To evaluate this hypothesis, we compare $\delta^{56}Fe_{0.5M\text{-}HCl}$ data from the Peruvian margin with previously published Fe isotope data for sediments from off California (Severmann et al., 2006). The data are plotted on a mixing diagram of Fe(II)/$Fe_{0.5M\text{-}HCl}$ versus $\delta^{56}Fe_{0.5M\text{-}HCl}$ (Fig. 6A), which was used by Severmann et al. (2006) to derive end members for ferrous and ferric Fe phases in $Fe_{0.5M\text{-}HCl}$. Fe isotope data for $Fe_{0.5M\text{-}HCl}$ in Peru margin sediments are consistent with the previously identified mixing trend between ferrous and ferric Fe but plot at the upper end or beyond the range of $\delta^{56}Fe_{0.5M\text{-}HCl}$ defined by California margin sediments. This shift to higher $\delta^{56}Fe$ values is consistent with $\delta^{56}Fe_T$ values above the average crust (Fig. 3A) and the notion of a net offshore export of isotopically light Fe (Scholz et al., 2014).

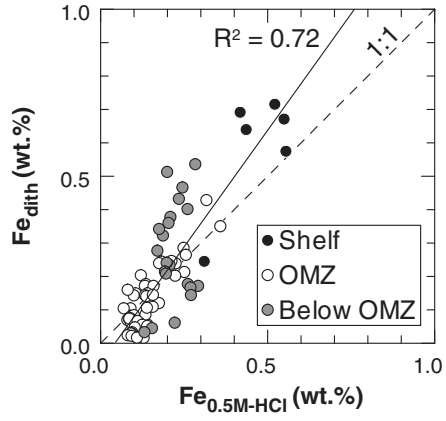

Fig. 5. Cross plot of Fe_{dith} versus $Fe_{0.5M\text{-}HCl}$. The solid black line represents the linear regression through all data (n = 87). The dashed line represents a line through origin with a slope of unity.

Although constraining a net loss of reactive Fe to the water column from the isotope composition of sedimentary $Fe_{0.5M\text{-}HCl}$ may work under certain circumstances, it is questionable if a significant portion of (isotopically fractionated) $Fe_{0.5M\text{-}HCl}$ has already been converted to pyrite. A more rigorous estimate of the isotope composition of the highly reactive Fe pool is therefore achieved by combining $\delta^{56}Fe_{0.5M\text{-}HCl}$ with Fe_{py} in a mass balance equation:

$$\delta^{56}Fe_{reac} = \left(Fe_{0.5M\text{-}HCl} \cdot \delta^{56}Fe_{0.5M\text{-}HCl} + Fe_{py} \cdot \delta^{56}Fe_{py}\right) / Fe_{reac}. \quad (1)$$

Analogous to Fig. 6A, $\delta^{56}Fe_{reac}$ is plotted against the proportion of Fe(II) in the highly reactive Fe pool ($Fe(II)_{reac}/Fe_{reac}$; Fig. 6B). Consistent with the notion of a more efficient net offshore Fe export (with a $\delta^{56}Fe$ < zero), Peru margin sediments have a significantly higher $\delta^{56}Fe_{reac}$ than California margin sediments. Although previous studies demonstrated or inferred Fe release from California margin sediments (Elrod et al., 2004; Severmann et al., 2010; John et al., 2012), we argue that several factors are likely to limit the net Fe loss compared to the Peruvian margin. One of the two sediment cores investigated by Severmann et al. (2006) was retrieved from the Monterey Canyon where the bottom water is well oxygenated ($[O_2]$ > 100 μM). Under such conditions, most of the Fe mobilized in the sediment is re-precipitated at the sediment surface or on-site within the bottom water (Pakhomova et al., 2007; Severmann et al., 2010). Accordingly, benthic flux data reported for sites with oxic bottom water in the Monterey Bay are 2 to 3 orders of magnitude smaller than those measured within the Peruvian OMZ (Elrod et al., 2004; Severmann et al., 2010; Noffke et al., 2012). The other sediment core was retrieved from the Santa Barbara basin, a silled depression within the California Borderland. The bottom water here is oxygen-depleted ($[O_2]$ = ~10 μM; Zheng et al., 2000) and indeed Fe release into the bottom water has been inferred from water column Fe profiles (John et al., 2012). However, sediment mass accumulation rates in the Santa Barbara Basin exceed those of the Peruvian margin by 2 to 3 orders of magnitude (Zheng et al., 2000; Scholz et al., 2011). Therefore, even a high benthic efflux is unlikely to result in a resolvable imprint on the sediments' Fe_{reac}/Fe_T. Moreover, the basin's restricted character and the sharp oxygen gradient across the sill (Zheng et al., 2000) likely limit offshore Fe export from the Santa Barbara Basin. Consistent with this rationale, the Santa Barbara Basin and Monterey Canyon sites have an indistinguishable Fe_{reac}/Fe_T, i.e., 0.15 ± 0.03 (n = 9) compared to 0.12 ± 0.01 (n = 12), respectively.

The majority of the reactive Fe in continental margin sediments is derived from terrigenous sources (Poulton and Raiswell, 2002). Assuming that there is negligible loss of Fe via reductive dissolution and sediment-water exchange, the sedimentary $\delta^{56}Fe_{reac}$ may thus be used to derive an estimate of the isotope composition of the terrigenous

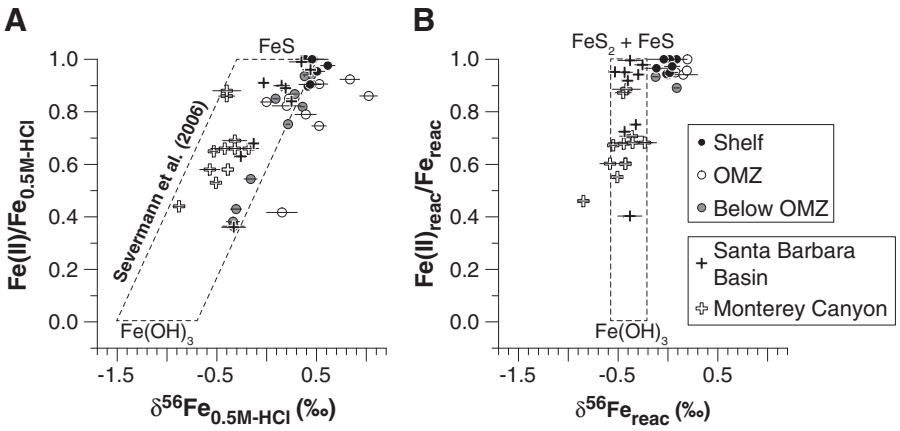

Fig. 6. Cross plots of (A) $Fe(II)/Fe_{0.5M\text{-}HCl}$ versus $\delta^{56}Fe_{0.5M\text{-}HCl}$ and (B) $Fe(II)_{reac}/Fe_{reac}$ versus $\delta^{56}Fe_{reac}$ (Fe_{reac} based on $Fe_{0.5M\text{-}HCl}$). The delimited areas (dashed line) illustrate the data range observed for sediment samples from Monterey Canyon and the Santa Barbara Basin off California (Severmann et al., 2006) as well as the end member values inferred for ferrous and ferric Fe by Severmann et al. (2006)(A) and in the present study (B).

reactive Fe. The California margin sites display average $\delta^{56}Fe_{reac}$ of -0.46 ± 0.16‰ (1 SD, n = 12, Monterey Canyon) and -0.35 ± 0.08‰ (1 SD, n = 9, Santa Barbara Basin) whereas the $\delta^{56}Fe_{reac}$ of Peru margin sediments is as high as +0.20‰ (Fig. 6B). Considering that the Monterey Canyon Site is likely to be least affected by reductive remobilization and loss of isotopically light Fe, we tentatively infer that the terrigenous particulate reactive Fe supply has a negative $\delta^{56}Fe$. One might argue that the terrigenous Fe supply should have a $\delta^{56}Fe$ of zero (i.e., similar to average igneous rock; Beard et al., 2003). However, Fe isotope studies in the context of silicate weathering and soil formation have revealed that the notion of the terrigenous Fe supply having a $\delta^{56}Fe$ of zero is only valid for the bulk Fe pool and only if it contains both the weathered mineral phases and the weathering residue (or if the terrigenous material has not undergone any weathering yet). Leaching of Fe from primary silicate minerals preferentially mobilizes the light Fe isotope, which is why pedogenic Fe (oxyhydr)oxides are isotopically lighter than the weathering residue (Brantley et al., 2004; Fantle and DePaolo, 2004; Wiederhold et al., 2007; Kiczka et al., 2010, 2011). We suspect that the Fe isotope composition of the terrigenous particulate reactive Fe may vary depending on the balance between weathering intensity and soil denudation. However, combined Fe isotope and X-ray absorption spectroscopy work on a chronosequence in a glacier forefield suggests that the kinetic isotope effect associated with silicate weathering is not a transient phenomenon but can persist over significant reaction advance (Kiczka et al., 2011).

4.2. Iron isotope fractionation during early diagenesis

Most of the Fe (oxyhydr)oxides that are retained on the shelf or within the OMZ and accumulate below the OMZ are reductively dissolved and transferred into other authigenic mineral phases during early diagenesis (Fig. 2C–E). Pyrite is a major burial phase for highly reactive Fe on the Peruvian margin (Fig. 2F), which is consistent with bacterial sulfate reduction being the dominant organic matter degradation pathway (Bohlen et al., 2011). Variable circumstances for pyrite formation across the Peruvian margin will be discussed in Section 4.2.1, followed by an evaluation of how these circumstances affect the isotope composition of authigenic pyrite in Section 4.2.2. The burial phase for reactive Fe in less reducing sediments below the OMZ will be evaluated in Section 4.2.3.

4.2.1. Iron- versus organic matter-limited pyrite formation on the Peruvian margin

At the H_2S concentrations typical for marine sediments, Fe monosulfide precipitates faster than pyrite. Therefore, pyrite does not form directly but through reaction of Fe monosulfide precursors with H_2S or polysulfide (S_n^{2-}) (Berner, 1970; Schoonen and Barnes, 1991; Rickard and Luther, 1997, 2007; Rickard and Morse, 2005). The amount of pyrite formed in a specific marine environment is limited by the availability of reactive Fe minerals and organic matter, the latter of which controls the production rate of H_2S through bacterial sulfate reduction (Berner et al., 1970, 1984). We use a cross plot of Fe_{py} versus total sulfur (TS) (Fig. 7) to differentiate between Fe- and organic matter-limited pyrite formation across the Peru continental margin. Progressive pyritization is indicated by the arrow, which represents the Fe to sulfur stoichiometry in pyrite (1:2). Shallow sediments below the OMZ (<15 cm sediment depth) have negligible Fe_{py} (samples with $Fe_{py} \approx 0$ wt.% and TS > 0.2 wt.% in Fig. 7), although plenty of $Fe_{0.5M\text{-}HCl}$ in the form of both Fe (oxyhydr)oxide and Fe monosulfide is available (Fig. 2C,D). This observation indicates that not enough H_2S is available for the conversion of FeS to pyrite or, in other words, that pyrite formation is limited by the availability of H_2S and organic matter, respectively. Deeper sediment samples from below the OMZ (>15 cm sediment depth) as well as sediment cores from the lower boundary of the OMZ (MUC25; see Table 1 and Fig. 2A) and from the shelf plot on the pyritization trend (Fig. 7). Most $Fe_{0.5M\text{-}HCl}$ is eventually converted to pyrite in these cores (as indicated by Fe_{py}/Fe_{reac} approaching 1.0; Fig. 2F) suggesting that pyrite formation is limited by the availability of reactive Fe. Sediments from within the OMZ plot mostly below the pyrite stoichiometry line in Fig. 7. Since Fe_{py}/Fe_{reac} approaches 1.0 in these cores, Fe monosulfide is unlikely to represent the primary host phase for non-pyritized sulfur. Earlier studies have demonstrated that most of the non-pyritized sulfur in sediments of the Peruvian OMZ is present as sulfidized organic matter (Suits and Arthur, 2000). Organic sulfur compounds typically form in anoxic settings where ample H_2S but relatively

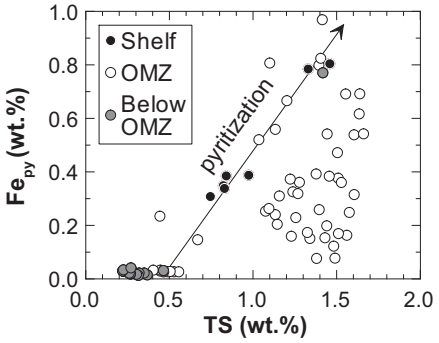

Fig. 7. Cross plot of Fe_{py} versus total sulfur (TS) (TS data from Scholz et al., 2011). The arrow represents the Fe to sulfur stoichiometry in pyrite (1:2). Note that no TS data are available for several samples with high Fe_{py} from below the OMZ.

little reactive Fe is available (Berner et al., 1985; Sinninghe Damsté et al., 1989; Sinninghe Damsté and De Leeuw, 1990). The abundance of sulfidized organic matter is thus indicative of highly Fe-limited pyrite formation. The shortage of reactive Fe within OMZ sediments has been attributed to extensive Fe release to the water column, which is in line with the relatively heavy $\delta^{56}Fe_T$ (Fig. 3A) and $\delta^{56}Fe_{reac}$ (Fig. 6B).

It should be noted that Suits and Arthur (2000) rejected a direct relationship between Fe-depletion and the presence of organic sulfur in sediments of the Peru OMZ, because they did not find an inverse correlation between organic sulfur and the highly reactive Fe pool (defined as the sum of non-pyritized reactive Fe extracted with boiling 12 M HCl and Fe_{py}). We suggest that the lack of such an inverse relationship could also be related to the use of boiling HCl for the extraction of non-pyritized reactive Fe. Boiling HCl recovers considerably more Fe from silicate minerals compared to cold HCl (e.g., 25–40% more in sediments of the Long Island Sound, the Mississippi Delta and the Gulf of California; Raiswell et al., 1994). As silicate-bound Fe is not reactive towards sulfide on early diagenetic time scales (Canfield et al., 1992; Raiswell et al., 1994; Raiswell and Canfield, 1996), the boiling HCl method overestimates the amount of Fe that is available for pyritization during early diagenesis. Our extraction results indicate that Fe_{py}/Fe_{reac} reach 0.8–1.0 in the uppermost 10 to 20 cm of the sediment for both $Fe_{0.5M\text{-}HCl}$ and Fe_{dith}; for comparison Suits and Arthur (2000) reported degrees of pyritization ≤0.65. The accumulation of organic sulfur likely intensifies once most of the Fe that is available for pyritization has been converted to pyrite. A linear relationship between highly reactive Fe and organic sulfur is not to be expected under such circumstances.

4.2.2. Iron isotope fractionation within the (oxyhydr)oxide-monosulfide-pyrite system

The differing availability of reactive Fe and hydrogen sulfide across the Peruvian margin may provide insights into the factors controlling the isotope composition of authigenic pyrite. In a previous study, Severmann et al. (2006) evaluated Fe isotope fractionation within the Fe (oxyhydr)oxide–monosulfide–pyrite system using a cross plot Fe(II)/$Fe_{0.5M\text{-}HCl}$ versus $\delta^{56}Fe_{0.5M\text{-}HCl}$ (Fig. 6A). Through extrapolation of the mixing trend in Fig. 6A to Fe(II)/$Fe_{0.5M\text{-}HCl}$ = 0.0, Severmann et al. (2006) inferred a δ^{56}Fe as low as −1.5‰ for pure Fe (oxyhydr)oxides. They further argued that such a low δ^{56}Fe in Fe (oxyhydr)oxides is in conflict with the general notion of ferrous Fe phases being isotopically lighter than ferric Fe phases (e.g., Beard and Johnson, 2004; Johnson et al., 2004) and suggested that the low δ^{56}Fe could be caused by extensive Fe cycling in an open system (Severmann et al., 2006).

Following the reasoning in Section 4.1, we argue that deriving end member values for the isotope composition of Fe (oxyhydr)oxides and Fe monosulfide from $\delta^{56}Fe_{0.5M\text{-}HCl}$ alone may be compromised by isotope fractionation associated with the transfer of Fe from Fe monosulfide to pyrite (e.g., Guilbaud et al., 2011; Syverson et al., 2013). To include this latter process in our considerations, we calculated the isotope composition of the highly reactive Fe pool $\delta^{56}Fe_{reac}$ (Eq. (1); see Section 4.1), which is plotted against $Fe(II)_{reac}/Fe_{reac}$ (fraction of ferrous Fe, including pyrite, in the highly reactive Fe pool) in Fig. 6B. The wide range of values observed in Fig. 6A shrinks to a narrower range between the proposed ferrous and ferric Fe end members in Fig. 6B (except for one sample: 0.5 cm sediment depth at the Monterey Canyon Site). This observation suggests that the proposed mixing trend between ferrous and ferric $Fe_{0.5M\text{-}HCl}$ in Fig. 6A is not caused by isotope fractionation between FeS and Fe (oxyhydr)oxides or Fe cycling in an open system; rather it is caused by the preferential transfer of the light Fe isotope from $Fe_{0.5M\text{-}HCl}$, or more specifically FeS, to pyrite.

We further explore Fe isotope fractionation during conversion of FeS to pyrite by plotting the isotope composition of $Fe_{0.5M\text{-}HCl}$ and Fe_{py} as a function of the extent to which $Fe_{0.5M\text{-}HCl}$ has been converted to pyrite (Fe_{py}/Fe_{reac}) (Fig. 8). Most of the $Fe_{0.5M\text{-}HCl}$ in the Peru margin samples shown in Fig. 8 consists of Fe(II) (≥85%; Fig. 2D and Table 2). $Fe_{0.5M\text{-}HCl}$ should thus essentially represent FeS. Due to the low solubility of pyrite under reducing conditions, the conversion of FeS to pyrite is effectively a unidirectional process (Rickard and Luther, 2007). One would therefore expect the data to follow a Rayleigh distillation trend (dashed lines in Fig. 8). Most of the samples, however, seem to be more accurately described by a closed system equilibrium model with an isotope fractionation factor between Fe monosulfide and pyrite $\Delta^{56}Fe_{FeS\text{-}py}$ of ≤+1‰ (solid lines in Fig. 8). A similar linear relationship between the isotope composition of Fe monosulfide and pyrite and the extent of pyritization has been found in laboratory experiments at elevated temperature (Guilbaud et al., 2011). These authors attributed the apparent equilibrium trend to a continuous equilibration between aquatic and solid FeS as well as a kinetic isotope effect during pyrite precipitation. We cannot evaluate if such an ongoing equilibration is possible under the low-temperature conditions prevailing in continental margin sediments. In addition, the isotope composition of the FeS pool may be buffered through ongoing dissolution and sulfidation of crystalline Fe (oxyhydr)oxides. This partial replenishment of the FeS pool is indicated by the downcore decrease in Fe_{dith} which exceeds $Fe_{0.5M\text{-}HCl}$ at the sediment surface but almost disappears at greater depth (Fig. 2C and Table 2).

Guilbaud et al. (2011) reported an average isotope fractionation factor $\Delta^{56}Fe_{FeS\text{-}py}$ of +2.2 ± 0.7‰ which is about twice as high as the maximum value observed in our study. The kinetic isotope effect during the conversion of FeS to pyrite likely depends on the rate of pyrite precipitation, which in turn is a function of the availability of Fe monosulfide, hydrogen sulfide and polysulfide as well as pH (Rickard and Morse, 2005; Rickard and Luther, 2007). The lower fractionation factor observed in Peru margin sediments may thus be explained by lower reactant concentrations and a higher pH compared to the experimental conditions used by Guilbaud et al. (2011). The isotopic offset between FeS and pyrite seems to decrease at higher levels of pyritization (Fe_{py}/Fe_{reac} > 0.5; Fig. 8). This observation may be related to a lower rate of pyrite precipitation and thus a smaller kinetic isotope effect under conditions where most of the FeS has already been consumed. Consistent with this rationale, sediments within the OMZ, where pyrite formation is strongly Fe-limited (see Section 4.2.1) display almost no isotopic offset between FeS and pyrite.

4.2.3. Iron diagenesis in sediments below the oxygen minimum zone

Cumulative downcore profiles for the operationally defined Fe fractions (Fig. 4) reveal that much of the difference in the bulk Fe content

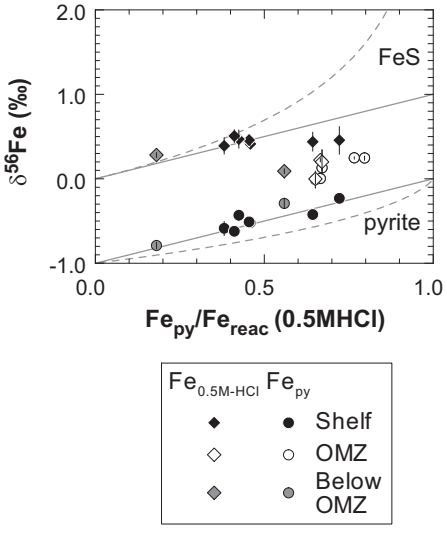

Fig. 8. Plot of $\delta^{56}Fe_{0.5M\text{-}HCl}$ and $\delta^{56}Fe_{py}$ versus Fe_{py}/Fe_{reac} (Fe_{reac} based on $Fe_{0.5M\text{-}HCl}$). The gray lines represent closed system equilibrium (solid line) and Rayleigh distillation (dashed lines) models with a $\Delta^{56}Fe_{FeS\text{-}py}$ of +1‰. Note that for two samples from within the OMZ $\delta^{56}Fe_{py}$ but no $\delta^{56}Fe_{0.5M\text{-}HCl}$ data are available.

(or the Fe_T/Al) between sediments within the OMZ and below the OMZ is related to differences in Fe_{sil} and $Fe_{1.0M\text{-}HCl}$ rather than $Fe_{0.5M\text{-}HCl}$ or Fe_{py} (Fig. 4). As pointed out in the Methods and Results sections, cold HCl has a poor recovery for crystalline Fe (oxyhydr)oxides such as goethite and hematite. Some of the excess Fe in the silicate Fe fraction below the OMZ is likely to represent crystalline Fe (oxyhydr)oxides, especially at the sediment surface where Fe_{dith} exceeds $Fe_{0.5M\text{-}HCl}$ by up to a factor of 2 (Figs. 2C and 4). Deeper in the sediment, however, even the sum of Fe_{dith}, $Fe_{0.5M\text{-}HCl}$ and Fe_{py} cannot account for the Fe_{XS} (up to 2 wt.%; Fig. 2B) that was calculated by Scholz et al. (2014) based on Fe_T/Al and the lithogenic background. Much of the Fe enrichment below the OMZ is therefore likely to be related to the presence of Fe-rich silicate minerals with a relatively heavy Fe isotope composition.

One possible explanation for the accumulation of isotopically heavy silicate Fe below the OMZ could be downslope transport of sediments that are enriched in residual, unreactive Fe from within the OMZ. However, sediments within the OMZ have Fe_T/Al below the lithogenic background (Fig. 2B). Therefore, if downslope transport of sediments from within the OMZ is the reason for the bulk Fe isotope trend, sediments below the OMZ would have lower rather than higher Fe_T/Al than the lithogenic background. An alternative explanation is that some of the Fe supplied by the redox shuttle is incorporated into authigenic silicate minerals during early diagenesis (Michalopoulos and Aller, 1995, 2004; Taylor and Macquaker, 2011). Previous studies reported or inferred the presence of glauconite in sediments below the Peruvian OMZ (Suits and Arthur, 2000; Böning et al., 2004). For instance, Suits and Arthur (2000) found Fe concentrations up to 18 wt.% in sediments below the lower boundary of the Peruvian OMZ at 13.5°S and most of this Fe was present as glauconite. Glauconite is an authigenic clay mineral that contains both Fe(II) and Fe(III). Fe(II) and also magnesium replace trivalent Al in the octahedral layers, which is why alkali metal ions (mostly K) are taken up in the exchangeable interlayers to redress the crystal lattice's charge balance (McRae, 1972; Harder, 1980; Odin and Matter, 1981). In accordance with the mineralogical characteristics of glauconite, Fe-enrichments related to authigenic glauconite formation should thus be identifiable in a plot of K versus Fe_T/Al (Fig. 9). Indeed, most Fe-rich samples below the OMZ plot on a linear trend corresponding to Al exchange with Fe and K. We further note that when plotting K/Al instead of K concentrations (see insert diagram in Fig. 9) high K samples on the shelf are no longer apparent whereas the Fe–K correlation below the OMZ persists. This observation is supportive of an authigenic host phase for Fe below the OMZ.

The formation of authigenic clay minerals during early diagenesis is a slow process compared to sulfidation of Fe (oyhydr)oxides or precipitation of FeS from dissolved Fe(II) (order of years versus less than an hour to a few days; Raiswell et al., 1994; Rickard and Morse, 2005; Michalopoulos and Aller, 1995, 2004). We therefore suggest that glauconite formation below the OMZ is favored by high pore water Fe concentrations related to a combination of enhanced Fe supply by the redox shuttle and slow Fe removal because of low sulfide concentrations (Taylor and Macquaker, 2011). For comparison, because of the long-term Fe loss and greater sulfide availability, pore waters and sediments within the OMZ have low Fe concentrations and the majority of the Fe is present as Fe(II) (Figs. 2 and 4). These conditions are unfavorable for glauconite formation. This inference, as well as the close match between the downcore profiles of Fe_{sil} and pore water Fe (Fig. 4), indicates that authigenic glauconite is formed in-situ below the OMZ rather than supplied through downslope transport.

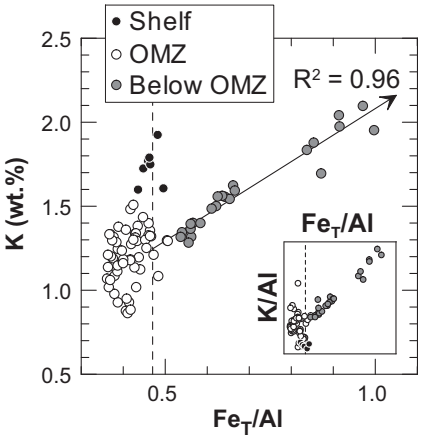

Fig. 9. Cross plot of K versus Fe_T/Al and K/Al versus Fe_T/Al (inset). The vertical dashed line depicts $(Fe/Al)_{lithogenic}$. Samples from below the OMZ plot on a linear trend (solid arrow, n = 24) corresponding to Al exchange with Fe and K.

Mass balance considerations suggest that glauconite has relatively heavy isotope compositions compared to other reactive Fe pools. We did not measure the isotope composition of Fe_{sil} directly. We note, however, that $\delta^{56}Fe_{1.0M\text{-}HCl}$ displays a similar trend towards higher values below the OMZ as $\delta^{56}Fe_T$ (Fig. 3C). $Fe_{1.0M\text{-}HCl}$ likely contains a high proportion of Fe from silicate minerals (see Methods section and Kostka and Luther, 1994), which supports the notion of authigenic silicate minerals being isotopically heavy. Moreover, Rouxel et al. (2003) reported heavy isotope compositions for celadonite in hydrothermally altered crustal rocks, which provides further support for our hypothesis. Analogous to glauconite, celadonite is an Fe- (in both valence states) and K-rich phyllosilicate mineral that forms through interaction of basalt with seawater at low temperature (Alt, 1986). Rouxel et al. (2003) suggested that secondary clay minerals preferentially incorporate the heavy Fe isotope, possibly due to an equilibrium effect between isotopically light dissolved Fe(II) and isotopically heavy Fe(III) in the secondary clay.

5. Summary and implications for the paleo-record

Our findings provide further refinements for interpreting Fe isotope variability in reactive Fe minerals within the geological record. Provided that the source rocks in the continental hinterland have undergone physical and chemical weathering, the terrigenous particulate reactive Fe supplied to continental margin sediments likely has a slightly lighter isotope composition than the bulk crust. Reductive dissolution in the marine sediments and loss of reduced Fe to the water column drive the isotope composition of the remaining reactive Fe to heavier values. Most of the terrigenous and non-terrigenous (i.e., shuttle-derived) reactive Fe is transferred to authigenic Fe minerals during early diagenesis. We observe a first-order relationship between the extent of pyritization of FeS and the isotope composition of authigenic pyrite. The associated isotope fractionation factor $\Delta^{56}Fe_{FeS\text{-}py}$ decreases with increasing extent of pyritization, which we attribute to a lower rate of pyrite precipitation under Fe-limited conditions. With increasing extent of pyritization, the isotope composition of the authigenic pyrite approaches the isotope composition of the highly reactive Fe pool. We suggest that attempts to gain information on water column Fe cycling (e.g., a redox shuttle) in the past from the isotope composition of isolated authigenic Fe phases may be prone to misinterpretation as the water column Fe isotopic fingerprint cannot be distinguished from fractionation effects during partial pyritization. This drawback could be overcome by calculating the isotope composition of the highly reactive Fe pool (including Fe (oxyhydr)oxides, carbonates, monosulfide and pyrite; Eq. (1) and Fig. 6B), which should be unaffected by isotope fractionation during early diagenesis. However, in some cases, identifying water column Fe cycling from the isotope composition of the highly reactive Fe pool may be further complicated by the formation of authigenic silicate minerals. The formation of Fe-rich authigenic silicate minerals is favored under conditions where plenty of reactive Fe but little sulfide is available. Provided that a shuttle-related Fe depletion or enrichment is significant enough to produce a measurable offset in $\delta^{56}Fe_T$ from $\delta^{56}Fe_{lithogenic}$ water column source or sink signals are best evaluated

from bulk Fe isotope data as these are not affected by early diagenetic processes (NB: defining $(Fe/Al)_{lithogenic}$ and $\delta^{56}Fe_{lithogenic}$ may be challenging in many cases, which would complicate even this approach).

Finally, we further evaluate the Peruvian margin's utility as an analog site for Fe biogeochemical cycling in anoxic open-marine environments in the past. A number of studies have shown that anoxic depositional settings are typically characterized by highly reactive Fe to total Fe ratios above 0.22–0.38 (Poulton et al., 2004, 2010; Canfield et al., 2008; Poulton and Canfield, 2011). Ferruginous and euxinic settings can be distinguished based on the extent of pyritization with values exceeding 0.70–0.80 indicating euxinia (Poulton et al., 2004, 2010; Canfield et al., 2008; Poulton and Canfield, 2011). The extraction protocol designed for this proxy suite (Fe_{HR}/Fe_T and Fe_{py}/Fe_{HR}, where Fe_{HR} refers to highly reactive Fe) includes not only a dithionite leach for the extraction of Fe (oxyhydr)oxides but also additional steps for the recovery of magnetite and Fe carbonates (Poulton and Canfield, 2005). Small amounts of these minerals could be present in Peru margin sediments, which is why Fe_{HR} as defined by Poulton and Canfield (2011) and Fe_{reac} used in this study (Fig. 2F and G) are not comparable in the strictest sense. Despite this obvious shortcoming, our sequential extraction data may still provide some insights into the commonalities and disparities of modern and ancient anoxic continental margin settings.

A number of samples from the OMZ boundaries and the shelf fall in the transitional area between oxic and anoxic settings (Fig. 2F and G). We suggest that these sites represent a transitional environment, where sedimentary sulfide concentrations are high enough to transform most of the reactive Fe into pyrite (Fig. 2F), but where the overall flux of reactive Fe is not sufficient to generate the more extreme enrichments that are typical for truly euxinic or ferruginous settings (Poulton and Canfield, 2011). Samples from below the OMZ plot in the range of fully oxic settings, despite highly elevated Fe_T/Al (Fig. 2B). Our results indicate that much of the excess Fe below the OMZ is sequestered by authigenic glauconite that is not accounted for in Fe_{reac}/Fe_T (in fact, the increase in Fe_T in the denominator additionally masks any enrichment in Fe_{reac}). Interestingly, a similar combination of elevated Fe_T/Al and low Fe_{HR}/Fe_T has been reported for Paleo-Proterozoic shales (Virginia Formation, Minnesota, USA) that were likely deposited in a ferruginous upper-slope setting and below the lower boundary of a localized euxinic water mass that impinges on the shelf (Poulton et al., 2010). The overall continental margin setting proposed by Poulton et al. (2010) corresponds to a "sulfidic OMZ" maintained through upwelling and high productivity in the relatively sulfur-poor and Fe-rich Proterozoic ocean (Poulton and Canfield, 2011). Although none of the Peruvian margin samples plot in the fully anoxic range, the above observations imply a number of broad similarities between the redox structure and lateral pattern of Fe enrichment on the Peruvian and Proterozoic ocean margin. An important disparity between Fe enrichments on the Peruvian margin and those on the Proterozoic ocean margin studied by Poulton et al. (2010) is related to the Fe origin. Excess Fe in sediments of the Proterozoic ocean margin was likely derived through upwelling of (mostly hydrothermal) Fe from the deep ocean rather than through release of Fe from reducing sediments within the OMZ (hence the absence of Fe-depleted OMZ sediments on the Proterozoic ocean margin). However, in both environments sedimentary Fe enrichments seem to be generated through transport of Fe between ocean regions with contrasting Fe solubility. We therefore suggest that contemporary OMZs represent a relevant analog for studying Fe redox cycling in ancient oceans.

Acknowledgments

We would like to thank the captain and crew of RV Meteor as well as the GEOMAR technician team for excellent support during ship-board operations and laboratory analyses. Funding for this study was provided by the 7th Framework Program of the European Union (Marie Curie IOF to F.S., Project #300648, BICYCLE), the German Research Foundation (Sonderforschungsbereich 754, "Climate-Biogeochemistry Interactions in the Tropical Ocean") and the US National Science Foundation (Grant #1029739 to S.S. and #1029889 to J.M.). Helpful comments by two anonymous reviewers as well as the editorial handling by M. E. Böttcher are gratefully acknowledged.

References

Anderson, T.F., Raiswell, R., 2004. Sources and mechanisms for the enrichment of highly reactive iron in euxinic Black Sea sediments. Am. J. Sci. 304, 203–233.
Alt, J.C., Honnorez, J., Laverne, C., Emmermann, R., 1986. Hydrothermal alteration of a 1 km section through the upper oceanic crust, Deep Sea Drilling Project Hole 504B: mineralogy, chemistry, and evolution of seawater-basalt interactions. J. Geophys. Res. 91, 309–335.
Arnold, G.L., Weyer, S., Anbar, A.D., 2004. Fe isotope variations in natural materials measured using high mass resolution multiple collector ICPMS. Anal. Chem. 76, 322–327.
Beard, B.L., Johnson, C.M., 2004. Fe isotope variations in the modern and ancient Earth and other planetary bodies. In: Johnson, C.M., Beard, B.L., Albarède, F. (Eds.), Geochemistry of Non-traditional Stable Isotopes. Mineralogical Society of America, pp. 319–357.
Beard, B.L., Johnson, C.M., Skulan, J.L., Nealson, K.H., Cox, L., Sun, H., 2003. Application of Fe isotopes to tracing the geochemical and biological cycling of Fe. Chem. Geol. 195, 87–117.
Bergquist, B.A., Boyle, E.A., 2006. Iron isotopes in the Amazon River system: weathering and transport signatures. Earth Planet. Sci. Lett. 248, 54–68.
Berner, R.A., 1970. Sedimentary pyrite formation. Am. J. Sci. 268, 1–23.
Berner, R.A., 1984. Sedimentary pyrite formation: an update. Geochim. Cosmochim. Acta 48, 605–615.
Berner, R.A., Leeuw, J.W.D., Spiro, B., Murchison, D.G., Eglinton, G., 1985. Sulphate reduction, organic matter decomposition and pyrite formation [and Discussion]. Philos. Trans. R. Soc. Lond. A Math. Phys. Sci. 315, 25–38.
Bohlen, L., Dale, A.W., Sommer, S., Mosch, T., Hensen, C., Noffke, A., Scholz, F., Wallmann, K., 2011. Benthic nitrogen cycling traversing the Peruvian oxygen minimum zone. Geochim. Cosmochim. Acta 75, 6094–6111.
Böning, P., Brumsack, H.J., Böttcher, M.E., Schnetger, B., Kriete, C., Kallmeyer, J., Borchers, S.L., 2004. Geochemistry of Peruvian near-surface sediments. Geochim. Cosmochim. Acta 68, 4429–4451.
Brantley, S.L., Liermann, L.J., Guynn, R.L., Anbar, A., Icopini, G.A., Barling, J., 2004. Fe isotopic fractionation during mineral dissolution with and without bacteria. Geochim. Cosmochim. Acta 68, 3189–3204.
Brink, K.H., Halpern, D., Huyer, A., Smith, R.L., 1983. The physical environment of the Peruvian upwelling system. Prog. Oceanogr. 12, 285–305.
Bullen, T.D., White, A.F., Childs, C.W., Vivit, D.V., Schulz, M.S., 2001. Demonstration of significant abiotic iron isotope fractionation in nature. Geology 29, 699–702.
Busigny, V., Planvsky, N.J., Jézéqel, D., Crowe, S., Louvat, P., Moureau, J., Viollier, E., Lyons, T.W., 2014. Iron isotopes in an Archean ocean analogue. Geochim. Cosmochim. Acta 133, 443–462.
Canfield, D.E., 1989. Reactive iron in marine sediments. Geochim. Cosmochim. Acta 53, 619–632.
Canfield, D.E., Raiswell, R., Bottrell, S.H., 1992. The reactivity of sedimentary iron minerals toward sulfide. Am. J. Sci. 292, 659–683.
Canfield, D.E., Thamdrup, B., Hansen, J.W., 1993. The anaerobic degradation of organic matter in Danish coastal sediments: iron reduction, manganese reduction, and sulfate reduction. Geochim. Cosmochim. Acta 57, 3867–3883.
Canfield, D.E., Lyons, T.W., Raiswell, R., 1996. A model for iron deposition to euxinic Black Sea sediments. Am. J. Sci. 296, 818–834.
Canfield, D.E., Poulton, S.W., Knoll, A.H., Narbonne, G.M., Ross, G., Goldberg, T., Strauss, H., 2008. Ferruginous conditions dominated later Neoproterozoic deep-water chemistry. Science 321, 949–952.
Croal, L.R., Johnson, C.M., Beard, B.L., Newman, D.K., 2004. Iron isotope fractionation by Fe(II)-oxidizing photoautotrophic bacteria. Geochim. Cosmochim. Acta 68, 1227–1242.
Crowe, S.A., Jones, C., Katsev, S., Magen, C., O'Neill, A.H., Sturm, A., Canfield, D.E., Haffner, G.D., Mucci, A., Sundby, B., Fowle, D.A., 2008. Photoferrotrophs thrive in an Archean Ocean analogue. Proc. Natl. Acad. Sci. 105, 15938–15943.
Dellwig, O., Leipe, T., März, C., Glockzin, M., Pollehne, F., Schnetger, B., Yakushev, E.V., Böttcher, M.E., Brumsack, H.J., 2010. A new particulate Mn–Fe–P-shuttle at the redoxcline of anoxic basins. Geochim. Cosmochim. Acta 74, 7100–7115.
Elrod, V.A., Berelson, W.M., Coale, K.H., Johnson, K.S., 2004. The flux of iron from continental shelf sediments: a missing source for global budgets. Geophys. Res. Lett. 31, L12307. http://dx.doi.org/10.1029/2004GL020216.
Fantle, M.S., DePaolo, D.J., 2004. Iron isotopic fractionation during continental weathering. Earth Planet. Sci. Lett. 228, 547–562.
Fehr, M.A., Andersson, P.S., Hålenius, U., Mörth, C.-M., 2008. Iron isotope variations in Holocene sediments of the Gotland Deep, Baltic Sea. Geochim. Cosmochim. Acta 72, 807–826.
Fehr, M.A., Andersson, P.S., Hålenius, U., Gustafsson, Ö., Mörth, C.M., 2010. Iron enrichments and Fe isotopic compositions of surface sediments from the Gotland Deep, Baltic Sea. Chem. Geol. 277, 310–322.
Fuenzalida, R., Schneider, W., Garcés-Vargas, J., Bravo, L., Lange, C., 2009. Vertical and horizontal extension of the oxygen minimum zone in the eastern South Pacific Ocean. Deep-Sea Res. II Top. Stud. Oceanogr. 56, 992–1003.
Guilbaud, R., Butler, I.B., Ellam, R.M., 2011. Abiotic pyrite formation produces a large Fe isotope fractionation. Science 332, 1548–1551.

Haese, R.R., Wallmann, K., Dahmke, A., Kretzmann, U., Müller, P.J., Schulz, H.D., 1997. Iron species determination to investigate early diagenetic reactivity in marine sediments. Geochim. Cosmochim. Acta 61, 63–72.
Harder, H., 1980. Syntheses of glauconite at surface temperatures. Clays Clay Miner. 28, 217–222.
Huerta-Diaz, M.A., Morse, J.W., 1990. A quantitative method for determination of trace metal concentrations in sedimentary pyrite. Mar. Chem. 29, 119–144.
John, S.G., Mendez, J., Moffett, J., Adkins, J., 2012. The flux of iron and iron isotopes from San Pedro Basin sediments. Geochim. Cosmochim. Acta 93, 14–29.
Johnson, C.M., Beard, B.L., Roden, E.E., Newman, D.K., Nealson, K.H., 2004. Isotopic constraints on biogeochemical cycling of Fe. In: Johnson, C.M., Beard, B.L., Albarède, F. (Eds.), Geochemistry of Non-traditional Stable Isotopes. Mineralogical Society of America, pp. 359–508.
Kiczka, M., Wiederhold, J.G., Frommer, J., Kraemer, S.M., Bourdon, B., Kretzschmar, R., 2010. Iron isotope fractionation during proton- and ligand-promoted dissolution of primary phyllosilicates. Geochim. Cosmochim. Acta 74, 3112–3128.
Kiczka, M., Wiederhold, J.G., Frommer, J., Voegelin, A., Kraemer, S.M., Bourdon, B., Kretzschmar, R., 2011. Iron speciation and isotope fractionation during silicate weathering and soil formation in an alpine glacier forefield chronosequence. Geochim. Cosmochim. Acta 75, 5559–5573.
Kostka, J.E., Luther, G.W., 1994. Partitioning and speciation of solid-phase iron in salt-marsh sediments. Geochim. Cosmochim. Acta 58, 1701–1710.
Levin, L., Gutiérrez, D., Rathburn, A., Neira, C., Sellanes, J., Muñoz, P., Gallardo, V., Salamanca, M., 2002. Benthic processes on the Peru margin: a transect across the oxygen minimum zone during the 1997–98 El Niño. Prog. Oceanogr. 53, 1–27.
Lyons, T.W., Severmann, S., 2006. A critical look at iron paleoredox proxies: new insights from modern euxinic marine basins. Geochim. Cosmochim. Acta 70, 5698–5722.
Lyons, T.W., Werne, J.P., Hollander, D.J., Murray, R.W., 2003. Contrasting sulfur geochemistry and Fe/Al and Mo/Al ratios across the last oxic-to-anoxic transition in the Cariaco Basin, Venezuela. Chem. Geol. 195, 131–157.
März, C., Poulton, S.W., Brumsack, H.J., Wagner, T., 2012. Climate-controlled variability of iron deposition in the Central Arctic Ocean (southern Mendeleev Ridge) over the last 130,000 years. Chem. Geol. 330–331, 116–126.
McRae, S.G., 1972. Glauconite. Earth Sci. Rev. 8, 397–440.
Michalopoulos, P., Aller, R.C., 1995. Rapid clay mineral formation in Amazon Delta sediments: reverse weathering and oceanic elemental cycles. Science 1995, 614–617.
Michalopoulos, P., Aller, R.C., 2004. Early diagenesis of biogenic silica in the Amazon delta: alteration, authigenic clay formation, and storage. Geochim. Cosmochim. Acta 68, 1061–1085.
Mosch, T., Sommer, S., Dengler, M., Noffke, A., Bohlen, L., Pfannkuche, O., Liebetrau, V., Wallmann, K., 2012. Factors influencing the distribution of epibenthic megafauna across the Peruvian oxygen minimum zone. Deep-Sea Res. I Oceanogr. Res. Pap. 68, 123–135.
Noffke, A., Hensen, C., Sommer, S., Scholz, F., Bohlen, L., Mosch, T., Graco, M., Wallmann, K., 2012. Benthic iron and phosphorus fluxes across the Peruvian oxygen minimum zone. Limnol. Oceanogr. 57, 851–867.
Odin, G.S., Matter, A., 1981. De glauconiarum origine. Sedimentology 28, 611–641.
Pakhomova, S.V., Hall, P.O.J., Kononets, M.Y., Rozanov, A.G., Tengberg, A., Vershinin, A.V., 2007. Fluxes of iron and manganese across the sediment-water interface under various redox conditions. Mar. Chem. 107, 319–331.
Poulton, S.W., Canfield, D.E., 2005. Development of a sequential extraction procedure for iron: implications for iron partitioning in continentally derived particulates. Chem. Geol. 214, 209–221.
Poulton, S.W., Canfield, D.E., 2011. Ferruginous conditions: a dominant feature of the ocean through Earth's history. Elements 7, 107–112.
Poulton, S.W., Raiswell, R., 2002. The low-temperature geochemical cycle of iron: from continental fluxes to marine sediment deposition. Am. J. Sci. 302, 774–805.
Poulton, S.W., Fralick, P.W., Canfield, D.E., 2004. The transition to a sulphidic ocean ~1.84 billion years ago. Nature 431, 173–177.
Poulton, S.W., Fralick, P.W., Canfield, D.E., 2010. Spatial variability in oceanic redox structure 1.8 billion years ago. Nat. Geosci. 3, 486–490.
Raiswell, R., Canfield, D.E., 1996. Rates of reaction between silicate iron and dissolved sulfide in Peru Margin sediments. Geochim. Cosmochim. Acta 60, 2777–2787.
Raiswell, R., Canfield, D.E., 1998. Sources of iron for pyrite formation in marine sediments. Am. J. Sci. 298, 219–245.
Raiswell, R., Canfield, D.E., 2012. The iron biogeochemical cycle past and present. Geochem. Perspect. 1, 1–220.
Raiswell, R., Anderson, T.F., 2005. Reactive iron enrichment in sediments deposited beneath euxinic bottom waters: constraints on supply by shelf recycling. Geol. Soc. Lond. Spec. Publ. 248, 179–194.
Raiswell, R., Buckley, F., Berner, R.A., Anderson, T.F., 1988. Degree of pyritization of iron as a paleoenvironmental indicator of bottom-water oxygenation. J. Sediment. Res. 58, 812–819.
Raiswell, R., Canfield, D.E., Berner, R.A., 1994. A comparison of iron extraction methods for the determination of degree of pyritisation and the recognition of iron-limited pyrite formation. Chem. Geol. 111, 101–110.
Reimers, C.E., Suess, E., 1983. Spatial and temporal patterns of organic matter accumulation on the Peru continental margin. In: Suess, E., Thiede, J. (Eds.), Coastal Upwelling: Part B. Sedimentary Record of Ancient Coastal Upwelling. Plenum Press, New York, pp. 311–346.
Rickard, D., Luther, G.W., 1997. Kinetics of pyrite formation by the H_2S oxidation of iron (II) monosulfide in aqueous solutions between 25 and 125 °C: the mechanism. Geochim. Cosmochim. Acta 61, 135–147.
Rickard, D., Luther, G.W., 2007. Chemistry of iron sulfides. Chem. Rev. 107, 514–562.
Rickard, D., Morse, J.W., 2005. Acid volatile sulfide (AVS). Mar. Chem. 97, 141–197.
Rouxel, O., Dobbek, N., Ludden, J., Fouquet, Y., 2003. Iron isotope fractionation during oceanic crust alteration. Chem. Geol. 202, 155–182.
Rouxel, O., Sholkovitz, E., Charette, M., Edwards, K.J., 2008. Iron isotope fractionation in subterranean estuaries. Geochim. Cosmochim. Acta 72, 3413–3430.
Scholz, F., Neumann, T., 2007. Trace element diagenesis in pyrite-rich sediments of the Achterwasser lagoon, SW Baltic Sea. Mar. Chem. 107, 516–532.
Scholz, F., Hensen, C., Noffke, A., Rohde, A., Liebetrau, V., Wallmann, K., 2011. Early diagenesis of redox-sensitive trace metals in the Peru upwelling area: response to ENSO-related oxygen fluctuations in the water column. Geochim. Cosmochim. Acta 75, 7257–7276.
Scholz, F., McManus, J., Sommer, S., 2013. The manganese and iron shuttle in a modern euxinic basin and implications for molybdenum cycling at euxinic ocean margins. Chem. Geol. 355, 56–68.
Scholz, F., Severmann, S., McManus, J., Hensen, C., 2014. Beyond the Black Sea paradigm: the sedimentary fingerprint of an open-marine iron shuttle. Geochim. Cosmochim. Acta 127, 368–380.
Schoonen, M.A.A., Barnes, H.L., 1991. Reactions forming pyrite and marcasite from solution: II. Via FeS precursors below 100 °C. Geochim. Cosmochim. Acta 55, 1505–1514.
Severmann, S., Johnson, C.M., Beard, B.L., German, C.R., Edmonds, H.N., Chiba, H., Green, D. R.H., 2004. The effect of plume processes on the Fe isotope composition of hydrothermally derived Fe in the deep ocean as inferred from the Rainbow vent site, Mid-Atlantic Ridge, 36° 14′ N. Earth Planet. Sci. Lett. 225, 63–76.
Severmann, S., Johnson, C.M., Beard, B.L., McManus, J., 2006. The effect of early diagenesis on the Fe isotope compositions of porewaters and authigenic minerals in continental margin sediments. Geochim. Cosmochim. Acta 70, 2006–2022.
Severmann, S., Lyons, T.W., Anbar, A., McManus, J., Gordon, G., 2008. Modern iron isotope perspective on the benthic iron shuttle and the redox evolution of ancient oceans. Geology 36, 487–490.
Severmann, S., McManus, J., Berelson, W.M., Hammond, D.E., 2010. The continental shelf benthic iron flux and its isotope composition. Geochim. Cosmochim. Acta 74, 3984–4004.
Sinninghe Damsté, J.S., De Leeuw, J.W., 1990. Analysis, structure and geochemical significance of organically-bound sulphur in the geosphere: state of the art and future research. Org. Geochem. 16, 1077–1101.
Sinninghe Damsté, J.S., Rijpstra, W.I.C., De Leeuw, J.W., Schenck, P.A., 1989. The occurrence and identification of series of organic sulphur compounds in oils and sediment extracts: II. Their presence in samples from hypersaline and non-hypersaline palaeoenvironments and possible application as source, palaeoenvironmental and maturity indicators. Geochim. Cosmochim. Acta 53, 1323–1341.
Staubwasser, M., von Blanckenburg, F., Schoenberg, R., 2006. Iron isotopes in the early marine diagenetic iron cycle. Geology 34, 629–632.
Staubwasser, M., Schoenberg, M., von Blanckenburg, F., Krüger, S., Pohl, C., 2013. Isotope fractionation between dissolved and suspended particulate Fe in the oxic and anoxic water column of the Baltic Sea. Biogeosciences 10, 233–245.
Stookey, L.L., 1970. Ferrozine — a new spectrophotometric reagent for iron. Anal. Chem. 42, 779–781.
Strub, P.T., Mesías, J.M., Montecino, V., Rutllant, J., Salinas, S., 1998. Coastal ocean circulation off Western South America. In: Robinson, A.R., Brink, K.H. (Eds.), The Sea. John Wiley & Sons, New York, pp. 273–313.
Suits, N.S., Arthur, M.A., 2000. Sulfur diagenesis and partitioning in Holocene Peru shelf and upper slope sediments. Chem. Geol. 163, 219–234.
Syverson, D.D., Borrok, D.M., Seyfried, W.E., 2013. Experimental determination of equilibrium Fe isotopic fractionation between pyrite and dissolved Fe under hydrothermal conditions. Geochim. Cosmochim. Acta 122, 170–183.
Taylor, K.G., Macquaker, J.H.S., 2011. Iron minerals in marine sediments record chemical environments. Elements 7, 113–118.
Wiederhold, J.G., Kraemer, S.M., Teutsch, N., Borer, P.M., Halliday, A.N., Kretzschmar, R., 2006. Iron isotope fractionation during proton-promoted, ligand-controlled, and reductive dissolution of goethite. Environ. Sci. Technol. 40, 3787–3793.
Wiederhold, J.G., Teutsch, N., Kraemer, S.M., Halliday, A.N., Kretzschmar, R., 2007. Iron isotope fractionation in oxic soils by mineral weathering and podzolization. Geochim. Cosmochim. Acta 71, 5821–5833.
Wijsman, J.W.M., Middelburg, J.J., Heip, C.H.R., 2001. Reactive iron in Black Sea sediments: implications for iron cycling. Mar. Geol. 172, 167–180.
Zheng, Y., Anderson, R.F., van Geen, A., Kuwabara, J., 2000. Authigenic molybdenum formation in marine sediments: a link to pore water sulfide in the Santa Barbara Basin. Geochim. Cosmochim. Acta 64, 4165–4178.

nature geoscience

LETTERS

PUBLISHED ONLINE: 18 MAY 2014 | DOI: 10.1038/NGEO2162

The impact of ocean deoxygenation on iron release from continental margin sediments

Florian Scholz[1,2*], James McManus[3], Alan C. Mix[1], Christian Hensen[2] and Ralph R. Schneider[4]

In the oceans' high-nitrate–low-chlorophyll regions, such as the Peru/Humboldt Current system and the adjacent eastern equatorial Pacific[1], primary productivity is limited by the micronutrient iron. Within the Peruvian upwelling area, bioavailable iron is released from the reducing continental margin sediments[2]. The magnitude of this seafloor source could change with fluctuations in the extension or intensity of the oxygen minimum zones[3,4]. Here we show that measurements of molybdenum, uranium and iron concentrations can be used as a proxy for sedimentary iron release, and use this proxy to assess iron release from the sea floor beneath the Peru upwelling system during the past 140,000 years. We observe a coupling between levels of denitrification, as indicated by nitrogen isotopes, trace metal proxies for oxygenation, and sedimentary iron concentrations. Specifically, periods with poor upper ocean oxygenation are characterized by more efficient iron retention in the sediment and a diminished iron supply to the water column. We attribute efficient iron retention under more reducing conditions to widespread sulphidic conditions in the surface sediment and concomitant precipitation of iron sulphides. We argue that iron release from continental margin sediments is most effective in a narrow redox window where neither oxygen nor sulphide is present. We therefore suggest that future deoxygenation in the Peru upwelling area would be unlikely to result in increased iron availability, whereas in weaker oxygen minimum zones partial deoxygenation may enhance the iron supply.

Changes in iron (Fe) supply from continental margin sediments are suggested to affect primary productivity and carbon export in high-nitrate–low-chlorophyll (HNLC) regions on a variety of timescales[5–7], but the magnitude and driving factors of past changes in seafloor Fe supply remain poorly constrained. The mobility and residence time of Fe in sea water is greatest in the absence of oxygen and hydrogen sulphide[8]. Accordingly, seafloor Fe supply should be most efficient in oxygen-depleted ocean regions where Fe-reducing (that is, ferruginous) but not sulphidic conditions prevail close to the sediment/bottom water interface (Fig. 1a).

Evaluating the export efficiency of bioavailable Fe from marine sediments in the past requires a combination of palaeo-redox proxies. We use sedimentary 'excess' (XS) concentrations (Methods) of Fe, molybdenum (Mo) and uranium (U) to reconstruct palaeo-Fe export and to locate the palaeo-position of the ferruginous and sulphidic zones relative to the sediment surface (Fig. 1a). Negative Fe_{XS} relative to the lithogenic background implies that lithogenic Fe has been reductively dissolved and lost from the sediment[9]. Mo and U have a negligible lithogenic background but accumulate in the sediment under reducing conditions. Fe- and sulphate-reducing bacteria mediate U reduction and fixation[10] whereas Mo fixation requires the availability of hydrogen sulphide[11]. As Fe reduction precedes sulphate reduction in the natural sequence of respiration processes, U begins to accumulate under slightly less reducing conditions compared with Mo and sedimentary $(Mo/U)_{XS}$ increases from slightly reducing to ferruginous to sulphidic settings[10,12]. Importantly, $(Mo/U)_{XS}$ is unaffected by changes in grain size or sedimentation rate, as both Mo and U reside in the same fine-grained fraction of the sediment.

We calibrate our proxy suite relative to bottom water oxygen concentrations and the redox state of surface sediments on a transect across the Peruvian margin at 11° S (Fig. 1b)[9,12]. Shelf sediments underlying the present-day upwelling system ($\sim$ <200 m water depth) exhibit $(Mo/U)_{XS}$ greater than the seawater ratio ($(Mo/U)_{SW} \approx 3$) and Fe_{XS} close to zero, which is consistent with bottom water anoxia and sulphidic conditions close to the sediment surface[12,13]. Although shelf sediments are a source of iron to the upwelling water[2,12], the sedimentary fingerprint suggests that there is little net transport of iron away from the shelf. Slope sediments between $\sim$300 and 600 m are characterized by $(Mo/U)_{XS}$ less than $(Mo/U)_{SW}$ and negative Fe_{XS}. This situation is consistent with slightly higher bottom water oxygen concentrations, ferruginous conditions at the sediment surface[12] and overall more favourable conditions for Fe export[9]. However, sediments on the slope are beyond the reach of the upwelling cell[14] and the Fe released is thus unlikely to support primary productivity in the surface ocean. Instead, most of the Fe exported from this area is transported downslope and re-precipitated at the transition to more oxic waters below the oxygen minimum zone (OMZ; $(Mo/U)_{XS} << (Mo/U)_{SW}$, $Fe_{XS} >$ zero)[9]. According to the present-day pattern of benthic redox conditions on the Peruvian margin, changes in the depth distribution of ferruginous and sulphidic conditions relative to the depth of the upwelling cell could have led to more or less favourable conditions for Fe supply to the surface ocean in the past.

We constrain past variability in Fe export from Peru margin sediments using data from piston core M77/2-024-5 (11° 05.01′ S, 78° 00.91′ W). M77/2-024-5 was retrieved from 210 m water depth, beneath the poleward-flowing Peru–Chile Undercurrent (PCUC) and within the Peruvian OMZ (Figs 1b,c and 2a). The sea floor at this site is within reach of the upwelling cell today[14] and probably was so during times of lower sea level. Wind-driven surface currents transport the upwelled water to the northwest into the eastern equatorial Pacific HNLC region (Fig. 2b). The Holocene age model of M77/2-024-5 is based on six radiocarbon dates (Fig. 3). Previous palaeoceanographic work off Peru has revealed that shifts

[1]College of Earth, Ocean, and Atmospheric Sciences, Oregon State University, 104 CEOAS Administration Building, Corvallis, Oregon 97331-5503, USA, [2]GEOMAR Helmholtz Centre for Ocean Research Kiel, Wischhofstraße 1–3, 24148 Kiel, Germany, [3]Department of Geoscience, University of Akron, Akron, Ohio 44325, USA, [4]Institute of Geosciences, Kiel University, Ludewig-Meyn Straße 10, 24118 Kiel, Germany. *e-mail: fscholz@coas.oregonstate.edu

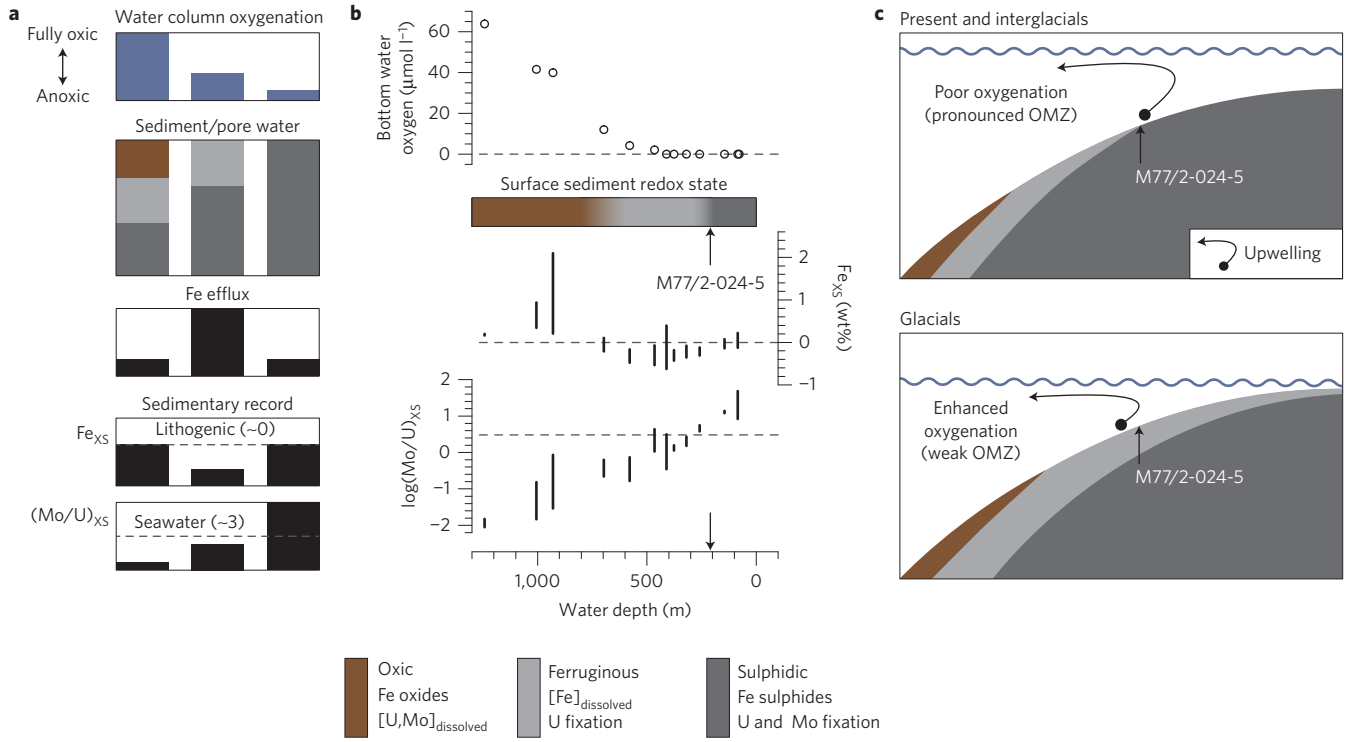

Figure 1 | Relationship between water column oxygenation and iron release from continental margin sediments. a, Representation of how seafloor Fe release and associated palaeo-proxies change as a function of water column oxygenation. **b**, Calibration of palaeo-proxies for seafloor Fe export relative to bottom-water oxygen concentrations and the redox state of surface sediments on an east–west transect across the Peruvian margin at 11° S. Vertical bars encompass the range of Fe_{XS} and $(Mo/U)_{XS}$ observed in the uppermost 10 cm of the sediment[9,12]. To avoid asymmetry effects, all element abundance ratios are presented as log ratios in this article. **c**, Schematic illustration of how the lateral pattern of redox conditions in surface sediments and the centre of seafloor Fe export shift as a function of water column oxygenation. OMZ, oxygen minimum zone.

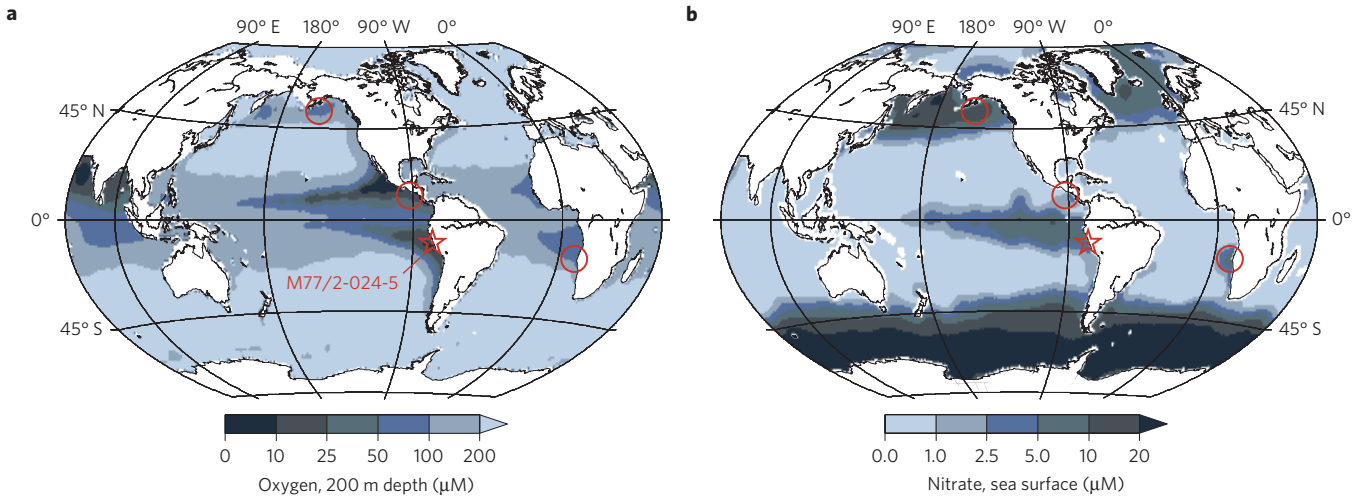

Figure 2 | Study area and biogeochemical context. a,**b**, Piston core M77/2-024-5 is located within the centre of the Peruvian OMZ (**a**) and at the southern end of the eastern equatorial Pacific HNLC region (**b**). Red circles depict other upwelling areas where an OMZ and a Fe-limited HNLC region (from ref. 1) overlap (oxygen and nitrate data from NOAA World Ocean Atlas).

in the strength and position of the PCUC as well as changes in organic matter preservation lead to coarser sediment grain sizes and lower organic carbon concentrations during times of cooler temperatures and lower sea level[15]. Following this rationale, the pre-Holocene age model was established by correlating the grain size and organic carbon records of M77/2-024-5 with the global benthic $\delta^{18}O$ record[16] (Fig. 3). Zirconium to rubidium ratios (Zr/Rb) from X-ray fluorescence (XRF) core scanning are used as a high-resolution grain size indicator. Coarser grain size and stronger bottom currents are identified by a higher proportion of Zr-rich sand over Rb-rich clay. The organic carbon record is complemented with high-resolution bromine (Br) to titanium (Ti) ratios from XRF core scanning[17]. With the exception of a hiatus at 423 cm (~50 to 20 kyr BP), piston core M77/2-024-5 covers the past 140 kyr. The good match between the bulk nitrogen isotope ($\delta^{15}N$) records of M77/2-024-5 and piston core CD38-02 from the Nazca Ridge[18]

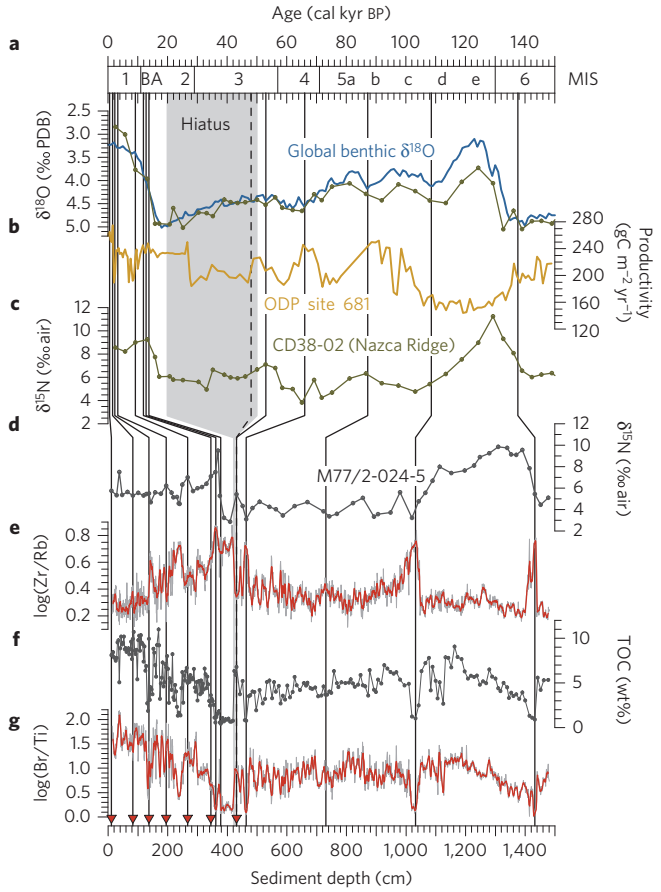

Figure 3 | Age model. a–c, Global benthic foraminiferal $\delta^{18}O$ stack[16], benthic $\delta^{18}O$ and bulk $\delta^{15}N$ of CD38-02 on the Nazca Ridge (~16° S)[18] and palaeo-productivity based on diatoms at ODP Site 681 (~11° S; ref. 25) plotted against age (MIS, Marine Isotope Stage; BA, Bølling–Ållerød). **d–g**, Bulk $\delta^{15}N$, Zr/Rb (red lines in XRF core scanning records represent ~5 cm running mean), total organic carbon (TOC) and Br/Ti of M77/2-024-5 (~11° S) plotted against sediment depth. Red triangles depict sample depths of radiocarbon dates. The oldest radiocarbon date (dashed line) is a minimum age and was not further considered in the age model. The grey-shaded area depicts the age range of a hiatus at 423 cm. See Supplementary Information for location map and more details on the age model.

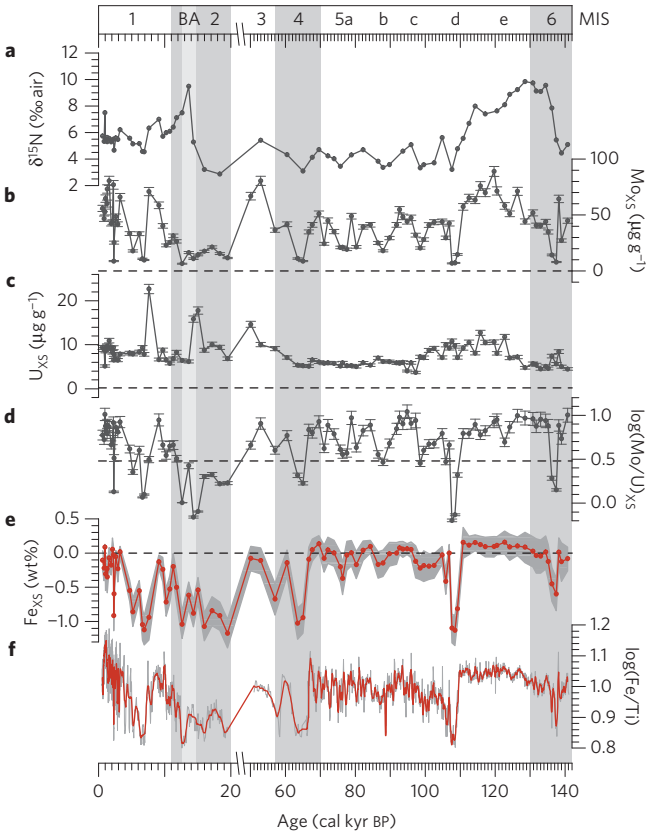

Figure 4 | Redox proxies. a–f, $\delta^{15}N$ (**a**), Mo_{XS} (**b**), U_{XS} (**c**), $(Mo/U)_{XS}$ (dashed line represents sea water) (**d**), Fe_{XS} (**e**) and Fe/Ti (**f**) of M77/2-024-5 plotted against age. Excess concentrations were calculated relative to the lithogenic background (dashed lines). Error bars were propagated from the external analytical uncertainty (error bars of $\delta^{15}N$ are smaller than symbols). The grey-shaded area behind Fe_{XS} represents the range defined by two lithogenic background values (Methods) and the external analytical uncertainty. The excellent agreement between Fe_{XS} and the high-resolution Fe/Ti record from XRF core scanning implies that our interpretations are not aliased by sampling resolution.

(~16° S, 2,525 m water depth) supports the accuracy of the age model (Fig. 3 and see Supplementary Information for more details on the age model).

Sedimentary $\delta^{15}N$ is an established palaeo-proxy for fixed nitrogen-loss from the water column under oxygen-deficient conditions and has been used in conjunction with redox-sensitive metals (for example, Mo and U) to reconstruct water column and bottom water oxygenation in the past[18–22]. The $\delta^{15}N$, Mo_{XS} and U_{XS} records of M77/2-024-5 (Fig. 4) show a number of similarities with records from other OMZs of the world ocean[18–22]: coincident $\delta^{15}N$, Mo_{XS} and U_{XS} maxima during Marine Isotope Stage (MIS) 5e, 3 and from the last deglaciation through the early Holocene (Bølling–Ållerød—lower MIS 1) indicate poorer oxygenation whereas minima during MIS 6, 4 and the last glacial (MIS 2 before Bølling–Ållerød) are indicative of enhanced oxygenation. Subordinate differences in timing among the proxies, mainly during the last deglaciation, may be attributed to differing oxygenation thresholds for fixed nitrogen-loss in the water column and Mo and U fixation in the sediment. Moreover, the $\delta^{15}N$ record may be influenced by changes in nitrogen fixation and relative nitrate utilization as well[18]. The global synchronicity of oxygenation trends in OMZs has generally been assigned to climate-controlled changes in oxygen supply to the global thermocline[19,20,22]. OMZs are laterally fed with intermediate water that is formed through subduction of cold and relatively saline water at high latitudes[23]. Lower sea surface temperatures under glacial conditions increased the oxygen solubility in source waters and stronger winds as well as enhanced sea ice formation may have increased the rate of intermediate water formation[19,22,24]. On the Peruvian margin, oxygen-depleted water is supplied by the PCUC. The general coincidence of lower $\delta^{15}N$, Mo_{XS} and U_{XS} with coarser grain size in M77/2-024-5 (Figs 3 and 4) is thus consistent with a stronger and better ventilated PCUC during glacial intervals[15]. Changes in respiration or productivity along the flow path of the intermediate water may have also contributed to the long-term trend in oxygenation[20]. We note, however, that primary productivity off Peru was lower during MIS 5e and 3 and higher during MIS 6, 4 and the last glacial (Fig. 3)[25]. This observation argues against a link between local productivity and water column oxygenation.

The downcore variability of oxygenation proxies is generally matched by high-amplitude changes in $(Mo/U)_{XS}$ and Fe_{XS} (Fig. 4). We interpret this observation as a close coupling among water column and bottom water oxygenation and seafloor Fe export on the Peruvian margin (other potential influences on Fe_{XS} are evaluated in the Supplementary Information). The accumulation of up to 90 μg g^{-1} Mo_{XS} during intervals of poor oxygenation

(Fig. 4) required strongly sulphidic conditions in the near-surface sediment[10,11]. Under such conditions, most of the reducible Fe is retained as Fe sulphide[8], which is consistent with Fe_{XS} close to zero and a low sedimentary Fe export flux, respectively. During intervals of enhanced oxygenation, Mo_{XS} drops to values near zero whereas U_{XS} decreases more gently. The associated decrease in $(Mo/U)_{XS}$ implies a shift from sulphidic to ferruginous conditions in the shallow sediment (Fig. 1a,b) along with an increase in Fe mobility. Consistent with this inference, sediments that accumulated during intervals of enhanced oxygenation are depleted in Fe by up to 1.2 wt.%. Comparison of the Fe_{XS} and $(Mo/U)_{XS}$ values that are typical for intervals of enhanced bottom water oxygenation with near-surface sediment data today (Fig. 1b) suggests an increase in oxygen concentration by ~5–10 μmol l^{-1} during glacials at the site of M77/2-024-5. This change in oxygenation shifted or extended the centre of most intense seafloor Fe export, which today is located at ~300–600 m water depth (Fig. 1b), into the upwelling cell (Fig. 1c). In addition to this redox-related mechanism, enhanced resuspension of particulate Fe by the stronger and shallower PCUC may have further increased the flux of Fe to the surface ocean. Other workers argued that lower sea level and reduced shelf areas during glacials implied a lower Fe flux from continental margin sediments[6]. Our study indicates the opposite, at least for the Peruvian margin. As a result of the slightly more oxygenated bottom water, sediment redox conditions underneath the upwelling cell were less sulphidic and thus more conducive to Fe export compared with the present-day. The enhanced sedimentary Fe supply during glacials probably relieved Fe limitation in the surface ocean to some extent and may have contributed to enhanced glacial productivity off Peru (Fig. 3)[25] and downstream in the equatorial Pacific HNLC region[26].

Our findings confirm that, in contrast to the common assumption[27,28], Fe release from continental margin sediments is not necessarily a first-order function of the organic carbon rain rate or decreasing sediment redox potential. Instead, Fe export peaks in a narrow 'redox window' where neither oxygen nor sulphide is present in the shallow sediment. Accordingly, the Fe flux from sediments in oxygen-deficient ocean regions is unlikely to respond uniformly to global oxygenation changes. As a result of the decreased oxygen solubility and increased stratification in a warmer ocean, OMZs are expected to expand in the coming decades[4]. A trend towards greater oxygen deficiency in the pronounced OMZs of the north- and southeastern equatorial Pacific (that is, off Mexico and Peru; Fig. 2) will probably be accompanied by a further expansion of sulphidic conditions. This scenario is supported by a recent study[29] that recorded the largest hydrogen sulphide plume ever reported for oceanic waters in the water column overlying the Peruvian shelf in 2009. An expansion of sulphidic conditions in the sediment and bottom water will lead to more efficient Fe retention as Fe sulphide. We therefore predict that ocean deoxygenation is likely to increase rather than decrease the extent of Fe limitation in these regions. A different scenario may be anticipated for other upwelling areas where HNLC, but less oxygen-deficient, conditions prevail, for example, the southeast Atlantic and subarctic Pacific (Fig. 2). In these areas, a shift from slightly oxic to ferruginous conditions in the shelf sediments would enhance Fe release, potentially easing Fe limitation and increasing net carbon fixation in the upper ocean.

Methods

Piston core M77/2-024-5 was retrieved during the M77/2 cruise of Research Vessel *Meteor* in December 2008. XRF core scanning was carried out on the split core surface of the archive core half using an Avaatech XRF core scanner at Kiel University. XRF measurements were taken every 0.5 cm (0–466 cm) or 1 cm (466–1,492 cm) with a generator setting of 10 kV for Fe and Ti and 20 kV for Br, Rb and Zr. Samples for radiocarbon, organic matter and nitrogen isotope analysis as well as sediment digestions were taken from the working half of the core. Bulk organic matter radiocarbon measurements were realized at the AMS facility of the Leibniz-Laboratory for Radiometric Dating and Isotope Research at Kiel University. Total organic carbon was analysed at GEOMAR using a Carlo Erba element analyser (NA1500) with a reproducibility of about 1% relative standard deviation (RSD). Before analysis, carbonate minerals were removed by leaching the sediment with 1 M HCl. Bulk nitrogen isotope ratios were determined at Oregon State University using a Carlo Erba element analyser (NA1500) coupled to a DeltaPlusXL isotope ratio mass spectrometer. The standard deviation of sample and standard replicates in delta notation relative to air was approximately 0.2‰. Major and trace metals were analysed after microwave-assisted (CEM MARS-5) acid digestion (HCl, HNO_3 and HF) by inductively coupled plasma optical emission spectrometry (Al, Ti and Fe) (Teledyne Leeman Prodigy) and inductively coupled plasma mass spectrometry (Mo and U; THERMO X-Series 2) at Oregon State University. The reproducibility of the whole procedure, as revealed from sample and standard replicates, was ~2% RSD for Al, Ti and Fe and ~5% RSD for Mo and U. Accuracy for certified reference material SDO-1 and an in-house standard is shown in Supplementary Table 1.

Metal (Me) concentrations are presented as excess (XS) concentrations; that is, the assumed lithogenic source component was subtracted from the total (T) element concentrations: $Me_{XS} = Me_T - (Me/Al)_{lithogenic} \times Al_T$ (ref. 10). Positive Me_{XS} depict enrichment of an element with respect to the lithogenic background whereas negative Me_{XS} depict depletion with respect to the lithogenic background. The average composition of the upper continental crust[30] was chosen as the lithogenic background for Mo and U ($Mo/Al = 0.19 \times 10^{-4}$, $U/Al = 0.35 \times 10^{-4}$). Fe_{XS} was calculated relative to the upper continental crust ($Fe/Al = 0.44$) and the average composition of andesite in the Andean Arc ($Fe/Al = 0.47$), the predominant rock type in the Peruvian hinterland[9,12,13]. As a result of the low X-ray yields for light-weight elements, XRF count rates for Fe and Br are normalized to Ti instead of Al. Al and Ti are linearly correlated throughout the data set ($r = 0.98$, $p < 0.001$), which is why Ti and Al can be used interchangeably without introducing errors related to changes in provenance, productivity or grain size (Supplementary Information).

Received 27 November 2013; accepted 9 April 2014; published online 18 May 2014

References

1. Moore, C. M. *et al.* Processes and patterns of oceanic nutrient limitation. *Nature Geosci.* **6,** 701–710 (2013).
2. Bruland, K. W., Rue, E. L., Smith, G. J. & DiTullio, G. R. Iron, macronutrients and diatom blooms in the Peru upwelling regime: Brown and blue waters of Peru. *Mar. Chem.* **93,** 81–103 (2005).
3. Capone, D. G. & Hutchins, D. A. Microbial biogeochemistry of coastal upwelling regimes in a changing ocean. *Nature Geosci.* **6,** 711–717 (2013).
4. Keeling, R. F., Körtzinger, A. & Gruber, N. Ocean deoxygenation in a warming world. *Ann. Rev. Mar. Sci.* **2,** 199–229 (2011).
5. Mix, A. C. *et al.* Rapid climate oscillations in the Northeast Pacific during the last deglaciation reflect northern and southern hemisphere sources. *Geoph. Monogr. Ser.* **112,** 127–148 (1999).
6. Johnson, K. S., Chavez, F. P. & Friederich, G. E. Continental-shelf sediment as a primary source of iron for coastal phytoplankton. *Nature* **398,** 697–700 (1999).
7. Lam, P. J. *et al.* Wintertime phytoplankton bloom in the subarctic Pacific supported by continental margin iron. *Glob. Biogeochem. Cycle* **20,** GB1006 (2006).
8. Raiswell, R. & Canfield, D. E. The iron biogeochemical cycle past and present. *Geochem. Perspect.* **1,** 1–220 (2012).
9. Scholz, F., Severmann, S., McManus, J. & Hensen, C. Beyond the Black Sea paradigm: The isotopic fingerprint of an open-marine iron shuttle. *Geochim. Cosmochim. Acta* **127,** 368–380 (2014).
10. Tribovillard, N., Algeo, T. J., Lyons, T. & Riboulleau, A. Trace metals as paleoredox and paleoproductivity proxies: An update. *Chem. Geol.* **232,** 12–32 (2006).
11. Helz, G. R. *et al.* Mechanism of molybdenum removal from the sea and its concentration in black shales: EXAFS evidence. *Geochim. Cosmochim. Acta* **60,** 3631–3642 (1996).
12. Scholz, F. *et al.* Early diagenesis of redox-sensitive trace metals in the Peru upwelling area: Response to ENSO-related oxygen fluctuations in the water column. *Geochim. Cosmochim. Acta* **75,** 7257–7276 (2011).
13. Böning, P. *et al.* Geochemistry of Peruvian near-surface sediments. *Geochim. Cosmochim. Acta* **68,** 4429–4451 (2004).
14. Brink, K. H., Halpern, D., Huyer, A. & Smith, R. L. The physical environment of the Peruvian upwelling system. *Prog. Oceanogr.* **12,** 285–305 (1983).
15. Heinze, P-M. & Wefer, G. The history of coastal upwelling off Peru (11° S, ODP leg 112, Site 680B) over the past 650,000 years. *Geol. Soc. Spec.* **64,** 451–462 (1992).
16. Lisiecki, L. E. & Raymo, M. E. A Pliocene–Pleistocene stack of 57 globally distributed benthic $\delta^{18}O$ records. *Paleoceanography* **20,** PA1003 (2005).

17. Ziegler, M., Jilbert, T., de Lange, G. J., Lourens, L. J. & Reichart, G. J. Bromine counts from XRF scanning as an estimate of the marine organic carbon content of sediment cores. *Geochem. Geophys. Geosyst.* **9,** Q05009 (2008).
18. Ganeshram, R. S., Pedersen, T. F., Calvert, S. E., McNeill, G. W. & Fontugne, M. R. Glacial–interglacial variability in denitrification in the world's oceans: Causes and consequences. *Paleoceanography* **15,** 361–376 (2000).
19. Galbraith, E. D., Kienast, M., Pedersen, T. F. & Calvert, S. E. Glacial–interglacial modulation of the marine nitrogen cycle by high-latitude O_2 supply to the global thermocline. *Paleoceanography* **19,** PA4007 (2004).
20. Jaccard, S. L. & Galbraith, E. D. Large climate-driven changes of oceanic oxygen concentrations during the last deglaciation. *Nature Geosci.* **5,** 151–156 (2012).
21. Nameroff, T. J., Calvert, S. E. & Murray, J. W. Glacial–interglacial variability in the eastern tropical North Pacific oxygen minimum zone recorded by redox-sensitive trace metals. *Paleoceanography* **24,** PA1010 (2004).
22. Muratli, J. M., Chase, Z., Mix, A. C. & McManus, J. Increased glacial-age ventilation of the Chilean margin by antarctic intermediate water. *Nature Geosci.* **3,** 23–26 (2010).
23. Sarmiento, J. L., Gruber, N., Brzezinski, M. A. & Dunne, J. P. High-latitude controls of thermocline nutrients and low latitude biological productivity. *Nature* **427,** 56–60 (2004).
24. Meissner, K. J., Galbraith, E. D. & Völker, C. Denitrification under glacial and interglacial conditions: A physical approach. *Paleoceanography* **20,** PA3001 (2005).
25. Schrader, H. Peruvian coastal primary palaeo-productivity during the last 200,000 years. *Geol. Soc. Spec.* **64,** 391–410 (1992).
26. Murray, R. W., Leinen, M. & Knowlton, C. W. Links between iron input and opal deposition in the Pleistocene equatorial Pacific Ocean. *Nature Geosci.* **5,** 270–274 (2012).
27. Elrod, V. A., Berelson, W. M., Coale, K. H. & Johnson, K. S. The flux of iron from continental margin sediments: A missing source for global budgets. *Geophys. Res. Lett.* **31,** L12307 (2004).
28. Moore, J. K. & Braucher, O. Sedimentary and mineral dust sources of dissolved iron to the world ocean. *Biogeosciences* **5,** 631–656 (2008).
29. Schunck, H. *et al.* Giant hydrogen sulfide plume in the oxygen minimum zone off Peru supports chemolithoautotrophy. *PLoS ONE* **8,** e68661 (2013).
30. McLennan, S. M. Relationships between the trace element composition of sedimentary rocks and upper continental crust. *Geochem. Geophys. Geosyst.* **2,** 1021 (2001).

Acknowledgements

Financial support for this study was provided by the 7th Framework Program of the European Union (Marie Curie IOF to F.S., BICYCLE, Project No. 300648) and the German Research Foundation through Collaborative Research Centre 754 'Climate-Biogeochemistry Interactions in the Tropical Ocean' (www.sfb754.de/en). The US National Science Foundation supported J.M. (Grant No. 1029889) and A.C.M. (Grant No. 1131834). We thank A. Bleyer, B. Domeyer, J. McKay and A. Ungerer for assistance in the laboratory and A. Schmittner for insightful comments on the manuscript.

Author contributions

F.S., J.M., A.C.M. and C.H. designed the study; F.S. carried out the laboratory work; R.R.S. guided the coring campaign and contributed radiocarbon dates; F.S. wrote the manuscript with contributions from all co-authors.

Additional information

Supplementary information is available in the online version of the paper. Reprints and permissions information is available online at www.nature.com/reprints. Correspondence and requests for materials should be addressed to F.S.

Competing financial interests

The authors declare no competing financial interests.

nature geoscience

SUPPLEMENTARY INFORMATION

DOI: 10.1038/NGEO2162

The impact of ocean deoxygenation on iron release from continental margin sediments

Florian Scholz*, James McManus, Alan C. Mix, Christian Hensen and Ralph R. Schneider

*Author to whom correspondence should be addressed, e-mail: fscholz@coas.oregonstate.edu

Radiocarbon dating and age model

The age model for the sediment section from 0 to 345 cm is based on six radiocarbon dates. As foraminifera or other calcareous remains are scarce, radiocarbon measurements were carried out on organic matter[1,2]. Prior to analysis samples were pre-treated according to the common acid-alkali-acid extraction protocol[3]. This procedure yields the alkali residue fraction and the humic acid fraction, both of which were subjected to radiocarbon measurements at the AMS facility of the Leibniz-Laboratory for Radiometric Dating and Isotope Research at Kiel University. Any terrigenous carbon that is present in the sample is typically recovered in the alkali residue which is why the radiocarbon date of the humic acid fraction (always the younger one) was used for the age model (Supplementary Table 2). Radiocarbon dates were calibrated using CALIB version 6.1.0 (ref. 4). In addition to the global ocean reservoir age correction of about 400 years that is subtracted by CALIB, we included an additional regional reservoir age correction of 400 years[1,2,5]. The ^{14}C concentration of the sample at 431 cm was smaller than the 2 SD uncertainty of the radiocarbon measurement. The resulting age is thus likely to be a minimum age and was not explicitly included in the age model. Previous paleoceanographic studies on the Peruvian margin have demonstrated that shifts in the strength and position of the undercurrent as well as differences in organic matter preservation lead to coarser grain sizes and lower organic carbon concentrations during times of cooler temperatures and lower sea level[6,7]. Following this rationale, tie points for the age model below 345 cm were selected by correlating maxima in grain size (as inferred from zirconium to rubidium ratios) and minima in organic carbon with the global benthic $\delta^{18}O$ stack by Lisiecki and Raymo (ref. 8). The final age versus depth model is shown in Supplementary Figure 2. The close match between the $\delta^{15}N$ records of M77/2-024-5 and CD38-02 from the Nazca Ridge[9] (Supplementary Figure 3) are supportive of the assumptions used in deriving the age model. Furthermore, the age model of M77/2-024-5 is in general agreement with those of ODP Sites 680 (11°03.90'S, 78°04.67'W, ~253 m water depth[6]), 1228 (11°03.85'S, 78°04.67'W, ~273 m water depth[5,10]), 681 (10°58.57'S, 77°57.46'W, ~150 m water depth[11]) and 1229 (10°58.60'S, 77°57.46'W, ~150 m water depth[10]) which are located within a distance of ~7 km and ~13 km from M77/2-024-5. An erosional unconformity, covering parts of Marine Isotope Stage (MIS) 2 and 3 (~50 – 20 kyr BP), was identified at 423 cm. The sediments corresponding to this time interval were likely eroded during the time of lowest sea level at the Last Glacial Maximum (cp. ODP Sites 1228 and 1229; ref. 10).

Redox-related versus other influences on the concentration of iron relative to aluminum and titanium

Most of the aluminum (Al), titanium (Ti) and iron (Fe) in continental margin sediments is supplied from terrigenous sources through river runoff or aeolian transport. While Al and Ti behave largely conservative during early diagenesis, a fraction of the terrigenous Fe (the reactive Fe pool, chiefly Fe (oxyhydr)oxides) may be subject

DOI: 10.1038/NGEO2162

to reductive dissolution and diffusive or advective transport across the sediment-bottom water interface. If the Fe lost from the sediment is transported elsewhere within the water column, the sediment left behind will be depleted in reactive Fe relative to Al or Ti[12,13]. Provided that the amount of Fe lost is sufficiently high compared to the overall terrigenous Fe, Al and Ti supply, Fe depletion may be illustrated by comparing its Fe/Al or Fe/Ti with the lithogenic background ratios or by calculating Fe_{XS} ($Fe_{XS} = Fe_T - (Fe/Al)_{lithogenic} \times Al_T$)[14]. Most of the Al and unreactive Fe in continental margin sediments reside in alumosilicate minerals, whereas Ti is often contained in heavy minerals such as rutile. Given their common occurrence, it is generally preferable to normalize Fe to Al rather than Ti and to calculate Fe_{XS} relative to $(Fe/Al)_{lithogenic}$. However, because of the insufficient x-ray yield for Al, the Fe data from XRF core scanning were normalized to Ti instead of Al. A prerequisite for the comparability of Al-based Fe_{XS} and Fe/Ti is that any downcore variability in Ti/Al, e.g., due to changes in sediment provenance[15], biological productivity[16] or grain size[17], is negligible relative to the redox-related variability in Fe_{XS} or Fe/Ti. Consistent with this prerequisite, Ti and Al are linearly correlated and Ti/Al ranges close to the ratio of the average upper continental crust[18] (Supplementary Figure 4). Moreover, Fe-depleted samples show a similar relative offset from Al and Ti in both data sets (Supplementary Figure 4). Importantly, if current-related grain size effects (rather than redox-controlled Fe release) were an important reason for the observed downcore variability in Fe_{XS}, Fe-depleted samples would be also depleted in Al relative to Ti, as grain size effects are known to enrich Ti relative to both Fe and Al[17].

Supplementary Table 1 | Accuracy of the sediment digestion protocol. Measured values are given as mean ± SD.

	SDO-1[19]		RR9702A-42MC[20]	
	This study (n = 9)	Certified	This study (n = 6)	Previous studies
Al (wt.%)	6.20 ± 0.17	6.49 ± 0.12	8.32 ± 0.14	8.18 ± 0.11
Ti (μg g^{-1})	404 ± 11	426 ± 19	488 ± 9	490 ± 19
Fe (wt.%)	6.39 ± 0.17	6.53 ± 0.15	4.86 ± 0.08	4.73 ± 0.07
Mo (μg g^{-1})	152 ± 5	134 ± 21	2.03 ± 0.11	1.83 ± 0.07
U (μg g^{-1})	45.0 ± 2.5	48.5 ± 6.5	3.41 ± 0.05	3.31 ± 0.22

Supplementary Table 2 | Radiocarbon ages. Calibration data from ref. 21.

	Alkali residue fraction			Humic acid fraction			
Depth (cm)	^{14}C age ± SD (yr BP)	Cal age (1 SD range) (yr BP)	Relative area under distribution	^{14}C age ± SD (yr BP)	Cal age (1 SD range) (yr BP)	Relative area under distribution	Cal age used (1 SD range)[b] (yr BP)
11	1525 ± 20	966 - 1089	1.00	1325 ± 20	871 - 929	1.00	471 - 529
83	2580 ± 25	2210 - 2220	0.08	2320 ± 25	1892 - 1972	1.00	1492 - 1572
		2225 - 2235	0.08				
		2240 - 2312	0.84				
137	3085 ± 25	2800 - 2893	1.00	2855 ± 30	2580 - 2700	1.00	2180 - 2700
195	4020 ± 30	3980 - 4077	1.00	3725 ± 25	3602 - 3688	1.00	3202 - 3288
267	8905 ± 40	9524 - 9652	1.00	8780 ± 35	9417 - 9482	1.00	9017 - 9082
345	11080 ± 45	12569 - 12647	1.00	10780 ± 50	12109 - 12153	0.21	11709 - 11924
					12159 - 12324	0.79	
431	47650[a]			43995 ± 1580[a]	45462 - 48442	1.00	45062 - 48042

[a]Minimum age.

[b]Age used includes an additional reservoir age correction of 400 yr[1,2,5].

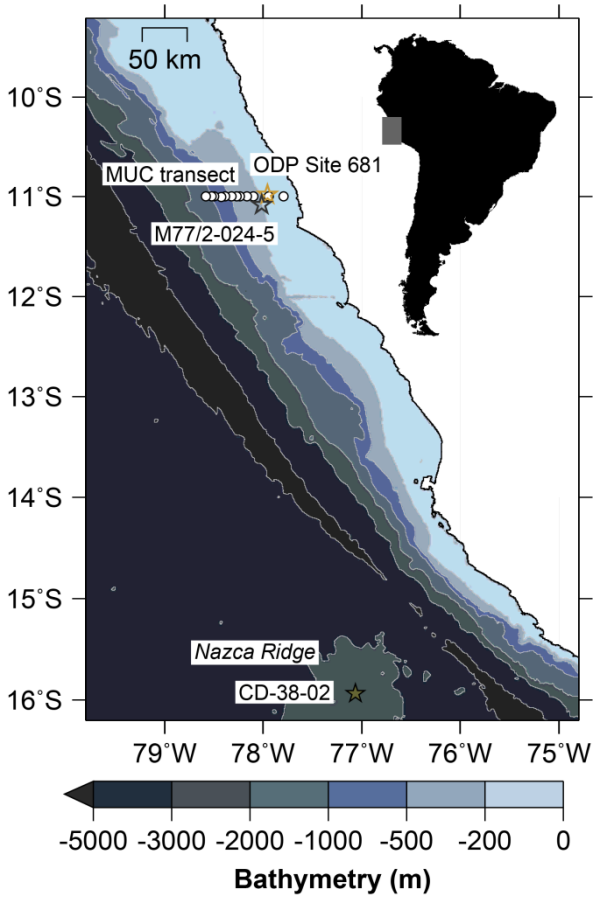

Supplementary Figure 1 | Bathymetric map of the Peruvian continental margin. Stars depict the location of M77/2-024-5, CD38-02 (ref. 9) and ODP Site 861 (ref. 10). Black circles depict the location of short sediment cores (multicores, MUCs) that are used for proxy calibration.

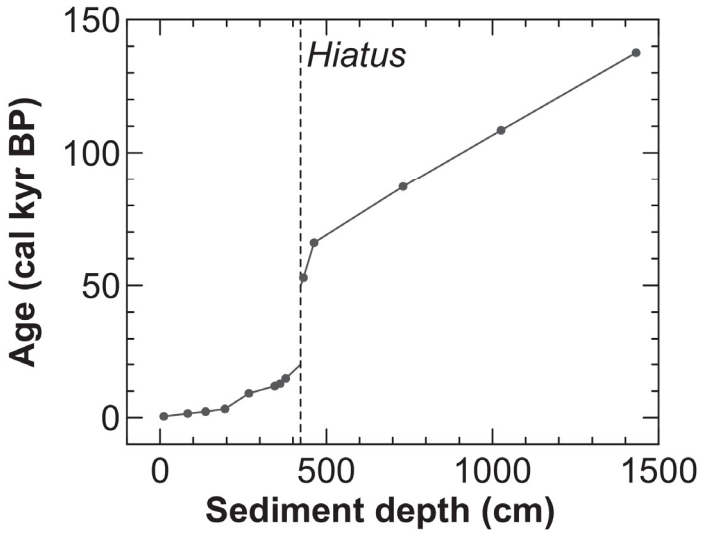

Supplementary Figure 2 | Age versus depth model for piston core M77/2-024-5.

DOI: 10.1038/NGEO2162

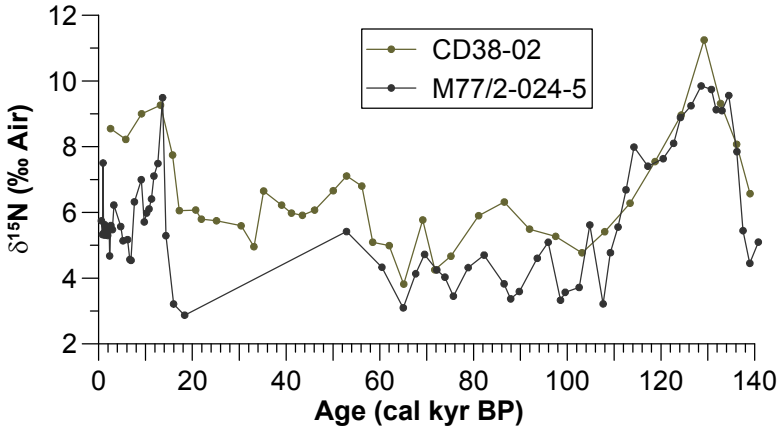

Supplementary Figure 3 | $\delta^{15}N$ records of M77/2-024-5 and CD38-02 (ref. 9). The original age model of CD38-02 is based on oxygen isotope stratigraphy (Figure 3).

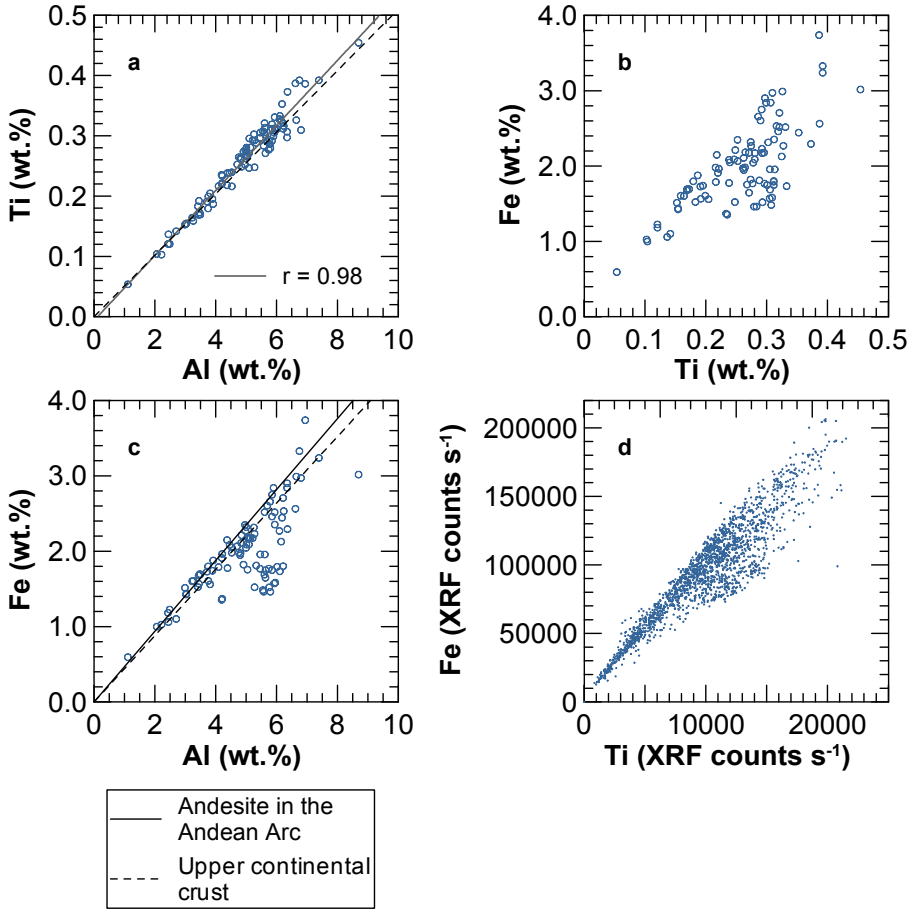

Supplementary Figure 4 | Comparison of Fe, Al and Ti data from sediment digestion and XRF core scanning. **a,** Ti versus Al (digestion). **b**, Fe versus Ti (digestion). **c**, Fe versus Al (digestion). **d**, Fe versus Ti (XRF scanning).

References

1. Rein, B. et al. El Nino variability off Peru during the last 20,000 years. *Paleoceanography* **20**, PA4003 (2005).
2. Rein, B., Lückge, A. & Sirocko F. A major Holocene ENSO anomaly during the Medieval period. *Geophys. Res. Lett.* **31**, L17211 (2004).
3. Grootes, P. M., Nadeau, M.-J. & Rieck, A. ^{14}C-AMS at the Leibniz-Labor: radiometric dating and isotope research. *Nucl. Instrum. Meth. B* **223-224**, 55-61 (2004).
4. Stuiver, M. & and Reimer, P. J. Extended ^{14}C data base and revised CALIB 3.0 ^{14}C age calibration program. *Radiocarbon* **35**, 215-230 (2006).
5. Agnihotri, R., Altabet, M. A. & Herbert, T. D. Influence of marine denitrification on atmospheric N_2O variability during the Holocene. *Geophys. Res. Lett.* **33**, L13704 (2006).
6. Wefer, G., Heinze, P. & Suess, E. Stratigraphy and sedimentation rates from oxygen isotope composition, organic carbon content, and grain size distribution at the Peru upwelling region: Holes 680B and 686B. *Proc. Ocean Drill. Program, Sci. Res.* **112**, 355-367 (1990).
7. Heinze, P.-M. & Wefer, G. The history of coastal upwelling off Peru (11°S, ODP leg 112, Site 680B) over the past 650000 years. *Geol. Soc. Sp.* **64**, 451-462 (1992).
8. Lisiecki, L. E. & Raymo, M. E. A Pliocene-Pleistocene stack of 57 globally distributed benthic δ^{18}O records. *Paleoceanography* **20**, PA1003 (2005).
9. Ganeshram, R. S., Pedersen, T. F., Calvert, S. E., McNeill, G. W. & Fontugne, M. R. Glacial-interglacial variability in denitrification in the World's Oceans: Causes and consequences. *Paleoceanography* **15**, 361-376 (2000).
10. Skilbeck, C.G. & Fink, D. Data report: radiocarbon dating and sedimentation rates for Holocene–upper Pleistocene sediments, eastern equatorial Pacific and Peru continental margin. *Proc. ODP, Sci. Results* **201**, 1–15 (2006).
11. Schrader, H. Peruvian coastal primary palaeo-productivity during the last 200.000 years. *Geol. Soc. Sp.* **64**, 391-410 (1992).
12. Lyons, T. W. & Severmann, S. A critical look at iron paleoredox proxies: New insights from modern euxinic marine basins. *Geochim. Cosmochim. Acta* **70**, 5698-5722 (2006).
13. Scholz, F., Severmann, S., McManus, J. & Hensen, C. Beyond the Black Sea paradigm: The isotopic fingerprint of an open-marine iron shuttle. Geochim. Cosmochim. Acta 127, 368-380 (2014).
14. Tribovillard, N., Algeo, T. J., Lyons, T. & Riboulleau, A. Trace metals as paleoredox and paleoproductivity proxies: An update. *Chem. Geol.* **232**, 12-32 (2006).
15. de Lange, G. J., Jarvis, I. & Kuijpers, A. Geochemical characteristics and provenance of late Quaternary sediments from the Madeira Abyssal Plain, N Atlantic. *Geol. Soc. Spec. Pub.* **31**, 147-165 (1987).
16. Murray, R. W. & Leinen, M. Scavenged excess aluminum and its relationship to bulk titanium in biogenic sediment from the central equatorial Pacific Ocean. *Geochim. Cosmochim. Acta* **60**, 3869-3878 (1996).
17. Schnetger, B., Brumsack, H. J., Schale, H., Hinrichs, J. & Dittert, L. Geochemical characteristics of deep-sea sediments from the Arabian Sea: a high-resolution study. *Deep-Sea Res. Pt. II* **47**, 2735-2768 (2000).
18. McLennan, S. M. Relationships between the trace element composition of sedimentary rocks and upper continental crust. *Geochem. Geophys. Geosyst.* **2**, Paper number 2000GC000109 (2001).
19. Govindaraju, K. Compilation of working values and sample description of 383 geostandards. *Geostandards Newslett.* **18**, 1-158 (1994).
20. Muratli, M., McManus, J., Mix, A. C. & Chase, Z. Dissolution of fluoride complexes following microwave-assisted hydrofluoric acid digestion of marine sediments. *Talanta* **89**, 195-200 (2012).
21. Reimer, P. J. et al. INTCAL09 and MARINE09 radiocarbon age calibration curves, 0-50000 years CAL BP. *Radiocarbon* **51**, 1111-1150 (2009).

AGU PUBLICATIONS

Global Biogeochemical Cycles

RESEARCH ARTICLE
10.1002/2014GB005017

Key Points:
- Global dissolved iron flux from margin sediments of 109 ± 55 Gmol yr^{-1}
- Benthic dissolved iron flux has been underestimated in the marine iron cycle
- Iron scavenging rates in water column probably higher than currently presumed

Supporting Information:
- Text S1, Figure S1, and Tables S1–S5

Correspondence to:
A. W. Dale,
adale@geomar.de

Citation:
Dale, A. W., L. Nickelsen, F. Scholz, C. Hensen, A. Oschlies, and K. Wallmann (2015), A revised global estimate of dissolved iron fluxes from marine sediments, *Global Biogeochem. Cycles*, *29*, doi:10.1002/2014GB005017.

Received 15 OCT 2014
Accepted 2 APR 2015
Accepted article online 7 APR 2015

A revised global estimate of dissolved iron fluxes from marine sediments

A. W. Dale[1], L. Nickelsen[1], F. Scholz[1], C. Hensen[1], A. Oschlies[1], and K. Wallmann[1]

[1]GEOMAR Helmholtz Centre for Ocean Research Kiel, Kiel, Germany

Abstract Literature data on benthic dissolved iron (DFe) fluxes (μmol m^{-2} d^{-1}), bottom water oxygen concentrations (O_{2BW}, μM), and sedimentary carbon oxidation rates (C_{OX}, mmol m^{-2} d^{-1}) from water depths ranging from 80 to 3700 m were assembled. The data were analyzed with a diagenetic iron model to derive an empirical function for predicting benthic DFe fluxes: DFe flux $= \gamma \cdot \tanh\left(\frac{C_{OX}}{O_{2BW}}\right)$ where γ (= 170 μmol m^{-2} d^{-1}) is the maximum flux for sediments at steady state located away from river mouths. This simple function unifies previous observations that C_{OX} and O_{2BW} are important controls on DFe fluxes. Upscaling predicts a global DFe flux from continental margin sediments of 109 ± 55 Gmol yr^{-1}, of which 72 Gmol yr^{-1} is contributed by the shelf (<200 m) and 37 Gmol yr^{-1} by slope sediments (200–2000 m). The predicted deep-sea flux (>2000 m) of 41 ± 21 Gmol yr^{-1} is unsupported by empirical data. Previous estimates of benthic DFe fluxes derived using global iron models are far lower (approximately 10–30 Gmol yr^{-1}). This can be attributed to (i) inadequate treatment of the role of oxygen on benthic DFe fluxes and (ii) improper consideration of continental shelf processes due to coarse spatial resolution. Globally averaged DFe concentrations in surface waters simulated with the intermediate-complexity University of Victoria Earth System Climate Model were a factor of 2 higher with the new function. We conclude that (i) the DFe flux from marginal sediments has been underestimated in the marine iron cycle and (ii) iron scavenging in the water column is more intense than currently presumed.

1. Introduction

Iron (Fe) is a regulating micronutrient for phytoplankton productivity and the efficiency of the biological pump over large areas of the ocean [*Martin and Fitzwater*, 1988; *Martin*, 1990; *Moore and Doney*, 2007; *Boyd and Ellwood*, 2010]. Natural iron fertilization by enhanced dust inputs is believed to have contributed to lower CO_2 levels during the Last Glacial Maximum [*Martin*, 1990; *Sigman and Boyle*, 2000]. Understandably, therefore, global circulation models with a focus on Fe have often considered dissolution from dust to be the major external source of dissolved iron to the surface ocean [*Archer and Johnson*, 2000; *Aumont et al.*, 2003; *Parekh et al.*, 2004]. The atmospheric, dissolvable iron input is around 10 Gmol yr^{-1} or less, yet is highly uncertain due to the poorly constrained solubility of particulate iron [*Jickells et al.*, 2005; *Luo et al.*, 2008; *Mahowald et al.*, 2005; *Galbraith et al.*, 2010; *Misumi et al.*, 2014; *Nickelsen et al.*, 2015].

More recently, continental margin sediments have been shown to be important sources of dissolved iron (DFe) to the coastal ocean and beyond [*Elrod et al.*, 2004; *Lohan and Bruland*, 2008; *Cullen et al.*, 2009; *Severmann et al.*, 2010; *Jeandel et al.*, 2011; *John et al.*, 2012; *Conway and John*, 2014]. Most global iron models now include an explicit sediment source of DFe, albeit with very different parameterizations. For instance, benthic DFe fluxes have been described using a fixed or maximum flux at the seafloor [*Moore et al.*, 2004; *Aumont and Bopp*, 2006; *Misumi et al.*, 2014]. Others used the empirical relationship between DFe flux and benthic carbon oxidation rates (C_{OX}) proposed by *Elrod et al.* [2004] [*Moore and Braucher*, 2008; *Palastanga et al.*, 2013]. In recognition that DFe fluxes from marine sediments are enhanced under oxygen-deficient bottom waters [*McManus et al.*, 1997; *Lohan and Bruland*, 2008; *Severmann et al.*, 2010], some workers opted for an oxygen "switch" [*Galbraith et al.*, 2010; *Nickelsen et al.*, 2015]. Here, all particulate iron that falls to the seafloor is returned to the water column as DFe if bottom water oxygen concentration (O_{2BW}) falls below a predefined threshold. Given the lack of consensus of how benthic iron should be described in models, the magnitude of this source is only vaguely constrained at 8–32 Gmol yr^{-1} [*Jickells et al.*, 2005; *Galbraith et al.*, 2010; *Misumi et al.*, 2014; *Nickelsen et al.*, 2015; *Tagliabue et al.*, 2014]. This uncertainty is very likely propagated to the parameterization of the DFe source/sink terms in the water column, which themselves are very poorly understood [*Nickelsen et al.*, 2015]. Thus, there is a real need to better constrain DFe sources and sinks in the ocean.

Table 1. Literature Data on Benthic DFe Fluxes

Region	Water Depth[a] (m)	O_2 (μM)	C_{OX} (mmol m^{-2} d^{-1})	DFe Flux (μmol m^{-2} d^{-1})	Remarks
Californian margin and Borderland Basins[b]	100–3700	8–138	0.3–7.3	0.02–48	Highest fluxes with shallow oxygen penetration depths
Monterey Bay (California)[c]	100	101–185	6.9–14.7	1.3–10.8	Interannual and intraannual variability at a single station
Oregon-California shelf and Californian Borderland Basins[d]	90–900	3–153	2–23	12–568	High fluxes for Eel River mouth and San Pedro and Santa Monica Basins, temporal variability
Peruvian margin[e]	95–400	< d.l	2.4–7.7	11–888	Highest flux measured for an open margin setting

[a]Depth range where the data were collected.
[b]*McManus et al.* [1997]: Total dissolved iron determined by chemiluminescence. Positive fluxes only (= out of sediment). Negative fluxes are <0.5 μmol m^{-2} d^{-1} and ignored in this study. C_{OX} was determined from ΣCO_2 fluxes corrected for carbonate dissolution.
[c]*Berelson et al.* [2003]: Total dissolved iron determined by flow injection analysis with chemiluminescence detection. C_{OX} was determined from ΣCO_2 fluxes corrected for carbonate dissolution.
[d]*Severmann et al.* [2010]: Total dissolved iron determined by inductively coupled plasma mass spectrometry. DFe fluxes of 421 to 568 μmol m^{-2} d^{-1} were reported for the San Pedro and Santa Monica Basins compared to only 13–18 μmol m^{-2} d^{-1} measured previously at the same sites (reported by *Elrod et al.* [2004]). C_{OX} was determined from ΣCO_2 fluxes without correction for carbonate dissolution.
[e]*Noffke et al.* [2012]: Total dissolved iron determined by inductively coupled plasma mass spectrometry. C_{OX} was determined as the HCO_3^- flux from pore water total alkalinity gradients and showed very good agreement with numerical modeling results [*Bohlen et al.*, 2011].

While there is little disagreement that both O_{2BW} and C_{OX} are important factors for predicting DFe fluxes, a unifying paradigm has so far not been proposed in a quantitative and empirical fashion. The oxygen threshold used by *Galbraith et al.* [2010] and *Nickelsen et al.* [2015] is an advance in the right direction, but the threshold concentration is somewhat arbitrary and not well justified empirically. In this study, we reanalyze the available literature data at sites where benthic DFe fluxes, O_{2BW}, and C_{OX} have been reported. Our prime objective is to derive a simple algorithm to predict DFe fluxes from marine sediments at the global scale based on O_{2BW} and C_{OX} as the two key controlling variables. We then analyze the impact of this source on DFe distributions in ocean surface waters by coupling the algorithm to the intermediate-complexity University of Victoria Earth System Climate Model (UVic ESCM). We find that the sedimentary DFe source may be several times higher than current estimates suggest, implying that scavenging in the water column is currently too weak in global iron models and that the residence time of iron in the ocean is shorter than assumed previously.

2. Data Acquisition and Evaluation

Benthic iron fluxes were compiled from the literature along with reported O_{2BW} and C_{OX} (Table 1). In these studies, the water samples for iron analysis were filtered (0.45 μm), acidified, and analyzed for the total dissolved fraction using various analytical methodologies (see Table 1). Only fluxes measured using non-invasive benthic chambers were considered. DFe fluxes derived from pore water gradients often do not correlate with in situ fluxes due to processes at the sediment-water interface operating over spatial scales smaller than the typical centimeter-scale sampling resolution [e.g., *Homoky et al.*, 2012]. Furthermore, enhanced DFe flux to the bottom water by flushing of animal burrows (bioirrigation) is also not captured by pore water gradients. We note, however, that benthic DFe fluxes determined using chambers may also suffer from artifacts due to oxidative losses and scavenging onto particles [e.g., *Severmann et al.*, 2010]. In this study, we make no attempt to reevaluate the published data with regards to these aspects and the reported benthic DFe fluxes are used.

Almost all data where DFe fluxes, O_{2BW}, and C_{OX} have been measured simultaneously originate from the Californian shelf and slope [*McManus et al.*, 1997; *Berelson et al.*, 2003; *Severmann et al.*, 2010]. These data cover a wide range of C_{OX} and O_{2BW} from severely hypoxic (~3 μM) to normal oxic (>63 μM) conditions. DFe fluxes range from <0.1 μmol m^{-2} d^{-1} on the slope to 568 μmol m^{-2} d^{-1} in the San Pedro Basin. High fluxes of 332 μmol m^{-2} d^{-1} were also measured on the Oregon margin close to river mouths [*Severmann et al.*, 2010]. Absent from the Californian data are DFe fluxes under anoxic conditions. In situ fluxes are available for anoxic areas of the Baltic and Black Seas [*Friedrich et al.*, 2002; *Pakhomova et al.*, 2007]. Yet these are not included in our database because supporting C_{OX} data are unfortunately lacking. We therefore supplemented the database with fluxes from the Peruvian oxygen minimum zone where bottom waters on the shelf and upper slope are predominantly anoxic [*Noffke et al.*, 2012]. The highest DFe flux in

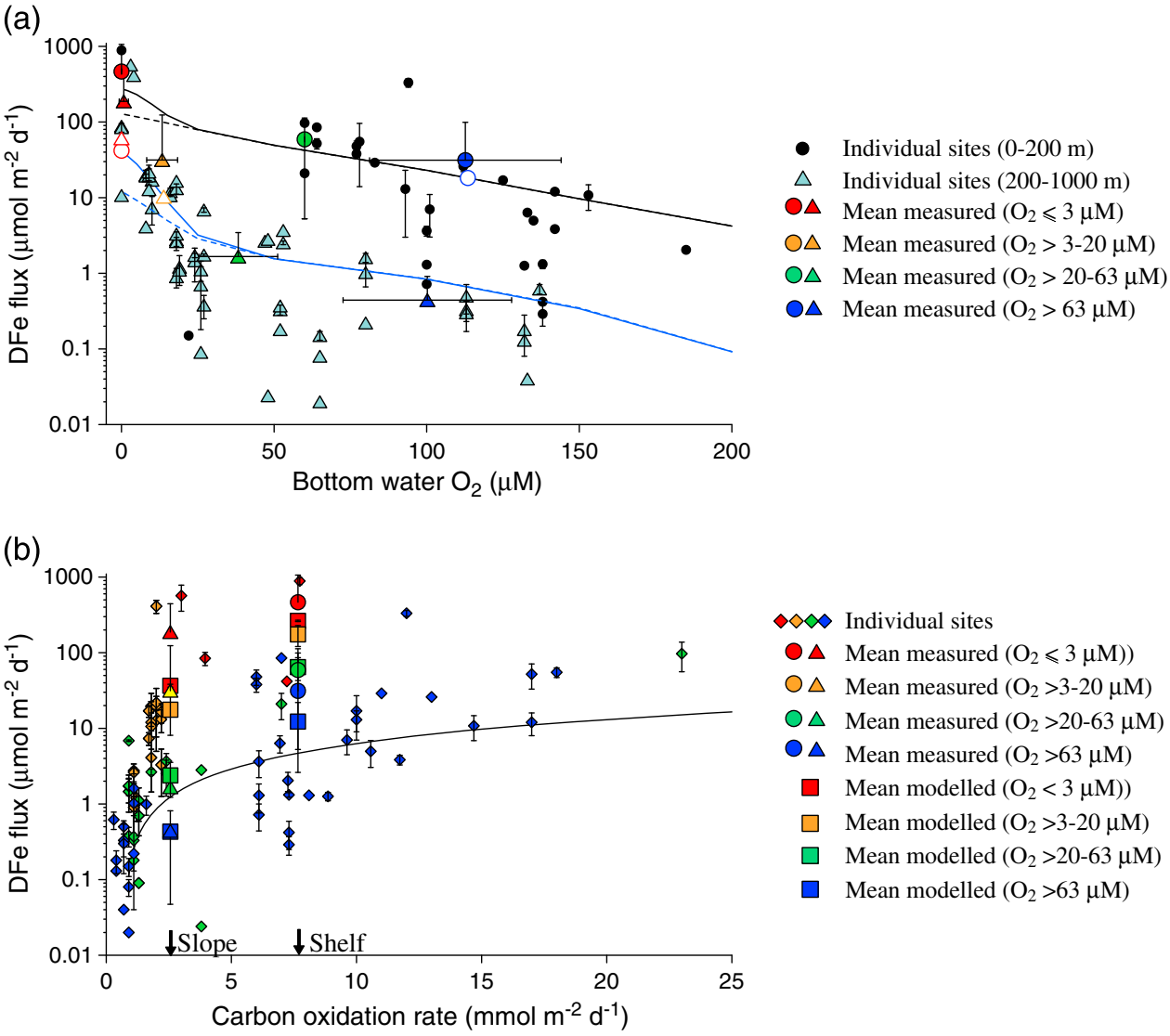

Figure 1. (a) Measured DFe fluxes versus bottom water O_2. Black circles and light blue triangles correspond to individual sites with $C_{OX} > 4$ (≈ shelf) and <4 mmol m^{-2} d^{-1} (≈ slope), respectively. The larger colored symbols are the mean DFe fluxes and O_2 concentrations within each binned range of O_2 (error bars are standard deviations), where circles and triangles denote shelf and slope, respectively. The large white symbols with colored outlines show the binned data without the four fluxes >300 µmol m^{-2} d^{-1} (San Pedro Basin, Santa Monica Basin, Eel River shelf, and Peruvian shelf). The black and blue curves are modeled fluxes for the shelf and slope, respectively; solid curves = standard model and dashed lines = standard model with no decrease in faunal activity at low O_{2BW}. (b) Measured DFe fluxes versus C_{OX} color coded according to O_{2BW} (diamonds). The large circles (shelf) and triangles (slope) are the measured binned data from Figure 1a plotted for the shelf and slope values of C_{OX} (indicated on the *x* axis). The mean modeled fluxes for each O_{2BW} interval are the corresponding colored squares. The curve is the regression of *Elrod et al.* [2004]: DFe = 0.68 × C_{OX} − 0.5, based on data published by *McManus et al.* [1997] and *Berelson et al.* [2003]. Error bars for the individual sites in Figures 1a and 1b are taken from the literature where reported (Table 1). Error bars on C_{OX} are not shown for clarity.

our database was measured here (888 µmol m^{-2} d^{-1}). In this study, we define anoxia as O_2 concentrations below the detection limit of the Winkler titration, approximately 3 µM.

The final database includes 81 data points where DFe flux, O_{2BW}, and C_{OX} data have been reported for the same site. DFe fluxes and C_{OX} were taken as the reported mean values plus error (where given) determined from multiple chambers during the same deployment. Hence, the actual number of individual DFe fluxes is much greater than 81. In total, 25 fluxes are from shelf settings (≤200 m), 40 are from the slope (>200–2000 m), and 16 are from deeper waters down to 3700 m. The deep sea is thus underrepresented in the database compared to the continental margin.

At first glance, defining any relationship between DFe flux, O_{2BW}, and C_{OX} seems like an impossible task (Figure 1). DFe fluxes scatter over many orders of magnitude for any given O_{2BW} or C_{OX}. The apparent dependence of DFe flux on O_{2BW}, as observed in the data set of *Severmann et al.* [2010], is much more tenuous when data from all studies are considered collectively. The linear relationship between DFe flux (in $\mu mol\,m^{-2}\,d^{-1}$) and C_{OX} (in $mmol\,m^{-2}\,d^{-1}$) proposed by *Elrod et al.* [2004] does seem to broadly apply ($DFe = 0.68 \times C_{OX} - 0.5$), although DFe fluxes $>10\,\mu mol\,m^{-2}\,d^{-1}$ for low C_{OX} are not well represented by that model (Figure 1b).

In order to understand the scatter in these plots, we first organized the individual fluxes into two groups depending on whether the C_{OX} was above or below $4\,mmol\,C\,m^{-2}\,d^{-1}$. This definition is not arbitrary; it represents the C_{OX} at the shelf break (approximately 200 m) where a sharp gradient change in total benthic O_2 uptake occurs [*Andersson et al.*, 2004]. Above this depth (i.e., on the shelf), C_{OX} increases to $>20\,mmol\,m^{-2}\,d^{-1}$, whereas on the slope it declines much more gradually to approximately $1\,mmol\,m^{-2}\,d^{-1}$ or less at 3000 m [*Burdige*, 2007]. Although we recognize that C_{OX} does not strictly correlate with water depth, the overall relationship is clear enough [see *Burdige*, 2007] that we can collectively term the sites above and below the C_{OX} threshold as shelf and slope, respectively.

In a second step, the DFe fluxes were binned into discrete O_{2BW} intervals: anoxic ($O_{2BW} \leq 3\,\mu M$), severely hypoxic ($>3\,\mu M < O_{2BW} \leq 20\,\mu M$), weakly hypoxic ($>20\,\mu M < O_{2BW} \leq 63\,\mu M$), and normal oxic ($O_{2BW} > 63\,\mu M$). Two of these boundaries were chosen based on strict (i.e., anoxia, that is, below detection limit) or more consensual definitions (i.e., hypoxia = $O_2 < \sim 63\,\mu M$). The $20\,\mu M$ boundary is somewhat subjective. We chose this value because *Elrod et al.* [2004] noted that their DFe-C_{OX} correlation did not capture iron fluxes at sites with O_{2BW} concentrations below this value. It may well be that this concentration represents a tipping point beyond which large changes in DFe flux occur due to alterations in respiration pathways and/or faunal regime shifts [*Levin and Gage*, 1998]. We will revisit this idea later.

Following these criteria, the data broadly show that DFe flux correlates inversely with increasing O_{2BW} and decreasing C_{OX}. High DFe fluxes on the shelf (circles in Figure 1a) are clearly distinguishable from the much lower fluxes on the slope (triangles). For the slope setting, low DFe fluxes of 1.3 and $0.4\,\mu mol\,m^{-2}\,d^{-1}$ are found for the weakly hypoxic and oxic intervals, respectively, whereas a pronounced increase to 36 and $188\,\mu mol\,m^{-2}\,d^{-1}$ is associated with the severely hypoxic and anoxic intervals (respectively). A very similar trend emerges for the shelf with a high-end flux of $465\,\mu mol\,m^{-2}\,d^{-1}$ in anoxic shelf settings. However, there is a large uncertainty associated with these numbers due to (i) few data available for anoxic and hypoxic sites on the shelf and (ii) bias toward the high fluxes measured in the San Pedro and Santa Monica Basins and on the Peru and Eel River shelves. Excluding these four points with DFe fluxes $>300\,\mu mol\,m^{-2}\,d^{-1}$ considerably reduces the binned values for anoxic and severely hypoxic waters (open symbols in Figure 1a). Furthermore, it is also not clear if the high fluxes on the shelf truly reflect higher C_{OX} or whether this simply reflects the fact that most organic matter is deposited on the shelf along with iron-rich terrestrial material. Consequently, in the following section we use a diagenetic model to identify the factors regulating benthic iron fluxes and provide a mechanistic understanding of the emerging trends in Figure 1.

3. Benthic Iron Model

A vertically resolved 1-D reaction-transport model was used to simulate the coupled C, N, Fe, Mn, and S cycles in the upper 30 cm of sediments. Our aim is to calculate benthic DFe fluxes in representative shelf (0–200 m) and upper slope (200–1000 m) environments for the observed range of O_{2BW} (1–200 μM) and compare these to the measured data in Figure 1. Water depths of 100 m and 600 m (respectively) were chosen based on conventional hypsometric intervals [*Menard and Smith*, 1966]. In the model, solids are transported dynamically by sediment accumulation and by bioturbation in the upper mixed surface layer where metazoans mainly reside. Solutes are also affected by molecular diffusion and bioirrigation, the latter describing the nonlocal exchange of seawater with pore water by burrowing fauna. The model is described fully in the supporting information. It is based on previous empirical diagenetic models, and for greater transparency we have formulated the biogeochemical reactions and parameters in line with these studies [e.g., *Van Cappellen and Wang*, 1996; *Wang and Van Cappellen*, 1996; *Berg et al.*, 2003; *Dale et al.*, 2009, 2013].

Table 2. Key Model Parameters Used in the Simulation of the Shelf and Slope Sediments[a]

	Shelf	Slope	Source
Representative water depth (m)[b]	100	600	*Menard and Smith* [1966]
Temperature of the bottom water (°C)	10	8	*Thullner et al.* [2009]
Sediment accumulation rate, ω_{acc} (cm kyr^{-1})	100	16	*Burwicz et al.* [2011]
POC rain rate, F_{POC} (mmol m^{-2} d^{-1})[c]	9.4	3	*Burdige* [2007]
Total iron oxide (Fe_T) rain rate, F_{FeT} (μmol m^{-2} d^{-1})[d]	1840	290	This study
Dissolved oxygen concentration in seawater, O_{2BW} (μM)[e]	Variable	Variable	This study
Dissolved ferrous iron concentration in seawater	0	0	This study
Rate constant for aerobic Fe^{2+} oxidation, k_{13} (M^{-1} yr)[f]	5×10^{-8}	5×10^{-8}	Various
Bioturbation coefficient at surface, $D_b(0)$ (cm^2 yr^{-1})[g]	$28\cdot f$	$18\cdot f$	*Middelburg et al.* [1997]
Bioturbation halving depth, z_{bt} (cm^2 yr^{-1})	3	3	*Teal et al.* [2008]
Bioirrigation coefficient at surface, $\alpha(0)$ (yr^{-1})[g,h]	$465\cdot f$	$114\cdot f$	*Meile and Van Cappellen* [2003]
Bioirrigation attenuation coefficient, z_{bio} (cm)[i]	2	0.75	This study
Average lifetime of the reactive POC components, a (yr)[j]	3×10^{-4}	3×10^{-4}	*Boudreau et al.* [2008]
Shape of gamma distribution for POC mineralization, υ (−)[j]	0.125	0.125	*Boudreau et al.* [2008]

[a]The complete model is described in the supporting information.
[b]The mid-depth of the shelf (0–200 m) and upper slope (200–1000 m) according to *Menard and Smith* [1966].
[c]Table 4 in *Burdige* [2007], based on his compilation of benthic carbon oxidation rates.
[d]Fluxes of total particulate iron oxide (Fe_T) to the sediment were based on the Fe content in average sedimentary rock (~5%) [*Garrels and Mackenzie*, 1971] which is similar to Fe content in red clays [*Glasby*, 2006]. The total Fe flux was calculated using the equation $0.05\cdot\omega_{acc}\cdot(1-\varphi(L))\cdot\rho_s/A_W$ where $\varphi(L)$ is the porosity of compacted sediment (0.7), ρ_s is the dry sediment density (2.5 g cm^{-3}), and A_W is the standard atomic weight of iron (55.8 g mol^{-1}). Fifty percent of this flux is unreactive [*Poulton and Raiswell*, 2002], and the other 50% is divided equally among Fe_{HR}, Fe_{MR}, and Fe_{PR} (see text).
[e]Values tested in the model are 1, 2, 5, 10, 15, 25, 50, 100, and 200 μM.
[f]*Van Cappellen and Wang* [1996], *Wang and Van Cappellen* [1996], *Berg et al.* [2003], and others. See supporting information for reaction stoichiometry and kinetics.
[g]A dimensionless factor that scales the bioturbation and bioirrigation coefficients to O_{2BW} (μM) is *f*. It is equal to $0.5+0.5\cdot\mathrm{erf}((O_{2BW}-a)/b)$, where erf is the error function and *a* (20 μM) and *b* (12 μM) are constants that define the steepness of decline of *f* with decreasing O_{2BW}.
[h]*Meile and Van Cappellen* [2003] calculated the average bioirrigation coefficient in surface sediments ($\overline{\alpha}$, year^{-1}) based on total sediment oxygen uptake and bottom water O_2. As a first approximation, sediment oxygen uptake was assumed to be equal to F_{POC}. $\alpha(0)$ was calculated from $\overline{\alpha}$ following *Thullner et al.* [2009] for a bottom water O_2 concentration of 120 μM which is representative of shelf and slope environments. Irrigation of Fe^{2+} was scaled to 20% of that for the other solutes due to its high affinity for oxidation on burrow walls.
[i]The depth of the sediment affected by irrigation on the shelf was adjusted to coincide with the depth of the bioturbation zone (approximately 7 cm).
[j]A full description of POC degradation kinetics is given in the supporting information.

The parameterization of key transport processes, boundary conditions, and kinetic parameters was achieved using global empirical relationships where possible (Table 2). The sedimentation rate and surface bioturbation coefficient were calculated on the basis of water depth [*Burwicz et al.*, 2011; *Middelburg et al.*, 1997]. Similarly, *Burdige* [2007] compiled a database of sediment C_{OX} for the same water depth intervals as used here. As a first approximation, this was assumed to be equal to the total rain rate of particulate organic carbon (POC) to the seafloor since less than 10% of organic matter reaching the ocean floor is ultimately preserved in marine sediments [*Hedges and Keil*, 1995]. Bioirrigation coefficients were calculated following the procedure of *Meile and Van Cappellen* [2003]. In line with other models, irrigation of Fe^{2+} was lowered relative to other solutes due to its high affinity to oxidation on burrow walls [*Berg et al.*, 2003; *Dale et al.*, 2013]. Fluxes of total iron oxides were defined according to the bulk sedimentation rate (Table 2).

Due to the general scarcity of data from sediments underlying oxygen-deficient waters, these global relationships apply to normal oxic conditions. Yet the bioirrigation and bioturbation coefficients cannot be treated as constant parameters in the simulations due to the dependency of metazoans on oxygen. Faunal activity levels under low O_2 are not well documented, but the rate and intensity of bioturbation and irrigation are probably lower [*Diaz and Rosenberg*, 1995; *Middelburg and Levin*, 2009]. The bioirrigation and bioturbation coefficients were thus multiplied by a factor (*f*) that mimics the reduction in faunal activity at low O_{2BW} (Table 2). Specifically, the maximum bioirrigation and bioturbation rates are reduced by 50% when O_{2BW} is at the level where shifts in faunal community structure occur (approximately 20 μM) [*Levin and Gage*, 1998]. Bioirrigation and bioturbation rates are depressed even further at lower O_{2BW}, in line with field observations [*Dale et al.*, 2013]. The model sensitivity to constant animal mixing rates for all O_{2BW} levels is shown below.

Continuum kinetics for describing POC degradation is a key aspect of the model [*Middelburg*, 1989; *Boudreau and Ruddick*, 1991]. This approach captures the temporal evolution of organic matter reactivity, as opposed to multi-G models that predefine a fixed first-order decay constant of one or more carbon fractions [*Westrich and Berner*, 1984]. However, continuum models cannot be readily applied to bioturbated sediments due to random mixing of particles of different ages by animals [*Boudreau and Ruddick*, 1991]. Thus, we developed a procedure for approximating the continuum model in bioturbated sediments by defining multiple (14) carbon pools based on the initial distribution of carbon reactivity (see supporting information). This distribution is defined by two parameters: the average lifetime of the reactive components, a (yr), and the distribution of POC reactivity, υ $(-)$ (Table 2). Low υ values indicate that organic matter is dominated by refractory components, whereas higher values correspond to a more even distribution of reactive types. Similarly, organic matter characterized by low a will be rapidly degraded below the sediment-water interface, whereas a high a implies less reactive material that is more likely to be buried to deeper sediments. While we can expect some regional differences in these parameters, we used values corresponding to fresh organic matter to shelf and slope settings [*Boudreau et al*., 2008]. This is a reasonable, but not entirely robust, assumption given relatively rapid particulate sinking rates in the water column [*Kriest and Oschlies*, 2008].

A comprehensive iron cycle is included. The reactivity of particulate iron (oxyhydr)oxides (hereafter Fe oxides) was defined according to the widely employed classification based on wet chemical extraction methods [*Canfield et al*., 1992; *Raiswell and Canfield*, 1998; *Poulton et al*., 2004]. Reactive Fe oxides can be broadly defined as highly reactive (Fe_{HR}), moderately reactive (Fe_{MR}), or poorly reactive (Fe_{PR}). Fe_{HR} has a half-life of <1 yr and represents iron contained within amorphous and reactive crystalline oxides (ferrihydrite, goethite, lepidocrocite, and hematite), pyrite, and acid volatile sulfides, plus a small fraction of iron in reactive silicates [*Canfield et al*., 1992; *Raiswell and Canfield*, 1998]. Fe_{PR} has a half-life of at least 10^5 years and represents iron released from a wide range of reactive silicates and magnetite. Fe_{MR} comprises all the iron with a reactivity intermediate between Fe_{HR} and Fe_{PR} (i.e., magnetite and reactive silicates) with a half-life of 10^2 years. An additional terrigenous detrital iron fraction, representing Fe bound within silicate minerals (Fe_U), is essentially unreactive on early diagenetic time scales and constitutes about half of all sedimentary iron underlying oxic waters [*Poulton and Raiswell*, 2002]. The model simulates all four of these fractions, defined chemically as $Fe(OH)_3$.

The Fe cycle involves a number of oxidation-reduction pathways (see supporting information). These include authigenic precipitation of Fe_{HR} via aerobic and anaerobic oxidation of ferrous iron; processes that constitute an efficient geochemical barrier against DFe release from the sediment [*McManus et al*., 1997; *Berg et al*., 2003]. Reactive Fe oxides can be reduced by dissolved sulfide according to the reaction kinetics proposed by *Poulton et al*. [2004]. Fe_{HR} is also consumed by dissimilatory iron reduction (DIR), whereas the other phases are too crystalline (unreactive) to be of benefit to iron-reducing bacteria [*Weber et al*., 2006]. Nonreductive dissolution of iron has also been proposed to be a dominant source of benthic iron on continental margins that display low rates of reductive Fe dissolution [*Radic et al*., 2011; *Jeandel et al*., 2011; *Homoky et al*., 2013; *Conway and John*, 2014]. However, this process has not been described mechanistically and is not considered in our model at this point in time. Fe_{HR} further undergoes aging into more crystalline Fe_{MR} [*Cornell and Schwertmann*, 1996]. The iron module also includes iron monosulfide (FeS) and pyrite (FeS_2) precipitation, the latter via the H_2S pathway (Berzelius reaction) and by reaction with elemental sulfur, S^0 (Bunsen reaction) [*Rickard and Luther*, 2007]. FeS and FeS_2 can be oxidized aerobically, whereas S^0 can disproportionate to sulfate and sulfide.

The model was coded and solved using the method of lines with MATHEMATICA 7.0 assuming a diffusive boundary layer of 0.04 cm thickness at the sediment-water interface [*Boudreau*, 1996]. Further details on the model solution can be found in the supporting information.

4. Model Results

The model reproduces the trend of higher DFe fluxes with decreasing O_{2BW} (Figure 1a) and increasing C_{OX} (Figure 1b). The absolute magnitude of the modeled fluxes for the shelf and slope settings depends on the water depths chosen to represent these environments, meaning that the fluxes are not as rigidly defined as implied in the plots. The modeled DFe fluxes for each O_{2BW} interval in the anoxic and severely hypoxic intervals are underestimated. Yet with the exception of the anoxic shelf, removing the four fluxes

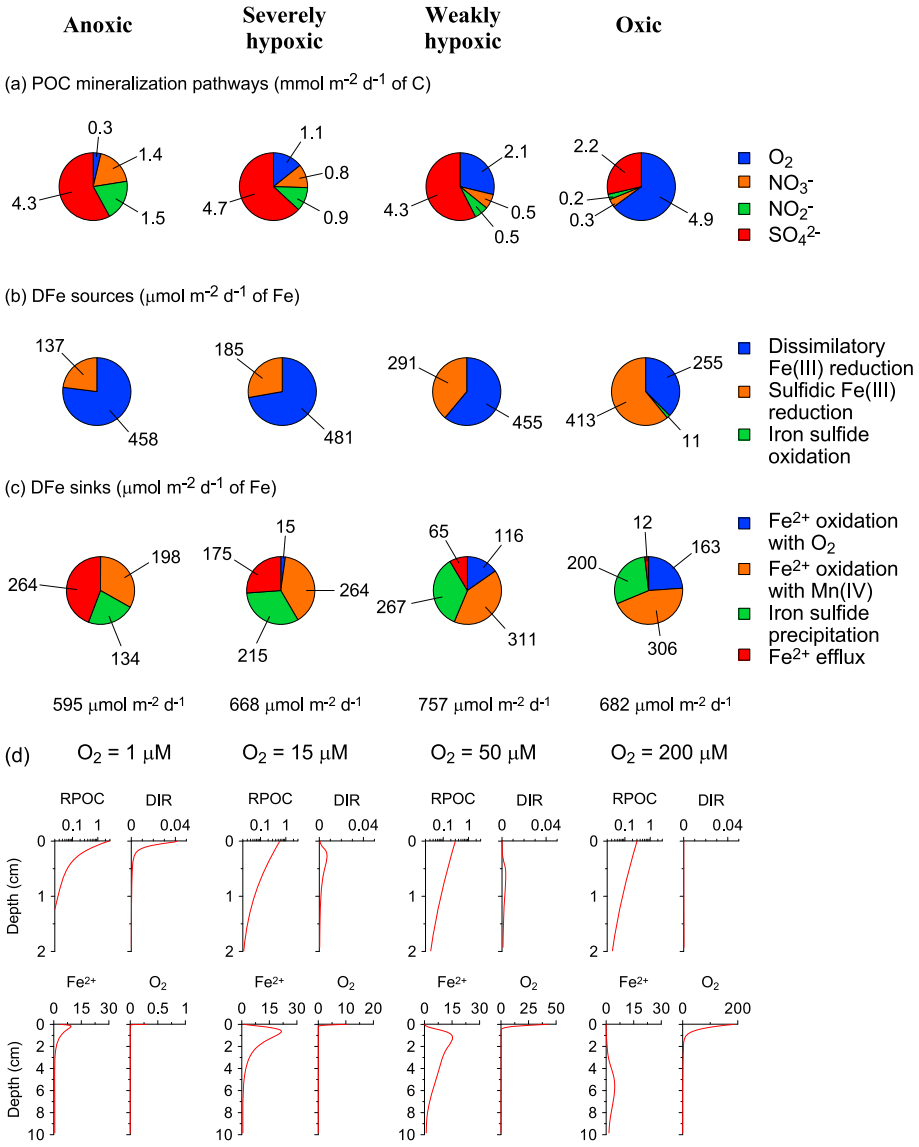

Figure 2. Simulated rates for the shelf environment for each oxygen regime are indicated at the top of the figure (Figures 2a–2c). (a) POC mineralization pathways. Fe and Mn oxide reduction rates are <0.1 mmol m^{-2} d^{-1} and not indicated. (b) DFe sources. Iron sulfide oxidation is negligible and only shown for the oxic setting. (c) DFe sinks. Oxidation by NO_3^- and irrigation are negligible and not shown. Aerobic oxidation of ferrous iron in the anoxic setting is zero and also not shown. The total sum of sinks (= sum of sources) is shown underneath the lower pie charts. (d) Sediment depth profiles of POC mineralization rate (RPOC) and dissimilatory iron reduction (DIR) in mmol cm^{-3} yr^{-1} of C and dissolved ferrous iron and oxygen concentration in μM for representative O_{2BW} in each interval (note different depth scales). Total fluxes on the slope are lower, but the pathways are qualitatively similar.

>300 μmol m^{-2} d^{-1} improves the agreement with the model (open symbols, Figure 1a). The anoxic shelf flux is tenuous because only two data points are available here.

As O_{2BW} increases, a larger fraction of POC is respired by O_2 at the expense of other electron acceptors, principally sulfate (Figure 2a). DIR accounts for less than 2% of POC respiration under all O_{2BW} conditions on the shelf and less than 0.2% on the slope. Nonetheless, DIR constitutes the largest source of DFe for anoxic and hypoxic settings (Figure 2b). At higher O_{2BW}, reduction of iron oxides by sulfide becomes more important. This finding is counterintuitive because sulfidic reduction is expected to be less pronounced as O_{2BW} increases. It can be explained by the increase in bioturbation which mixes labile iron oxide below the surface sediment where POC mineralization rates are highest (Figure 2d). This results in a less pronounced

Table 3. Input Parameters and Boundary Conditions Used in the Standard Model and for the Sensitivity Analysis[a]

	Standard Model	Sensitivity Analysis
Representative water depth (m)	350	350
Sediment accumulation rate, ω_{acc} (cm kyr^{-1})	60	60
POC rain rate, F_{POC} (mmol m^{-2} d^{-1})	6.2	0.5–15[b]
Total iron oxide (Fe_T) rain rate, F_{FeT} (μmol m^{-2} d^{-1})	1110	1110
Dissolved oxygen concentration in seawater, O_{2BW} (μM)	120	1–200[c]
Bioturbation coefficient at surface, $D_b(0)$ (cm^2 yr^{-1})	$23 \cdot f$	$23 \cdot f$
Bioirrigation coefficient at surface, $\alpha(0)$ (year^{-1})	$290 \cdot f$	$290 \cdot f$
Bioirrigation attenuation coefficient, z_{bio} (cm)	1.4	1.4

[a]Model parameters that are unchanged from Table 2 are not listed.
[b]Values tested (in mmol m^{-2} d^{-1}) are 0.5, 1, 2, 4, 6, 8, 10, 12, 14, and 16, which are equivalent to C_{OX} of 0.4, 0.8, 1.7, 3.3, 5.0, 6.6, 8.3, 9.9, 11.6, and 13.2.
[c]Values tested are 1, 2, 5, 10, 15, 25, 50, 100, and 200 μM.

DIR peak and a greater likelihood that iron oxide is instead reduced by sulfide deeper down. In these subsurface horizons, iron undergoes repeated redox cycling (Figures 2b and 2c) whereby DFe is oxidized to Fe(III), mainly by Mn(IV), and then regenerated when the authigenic iron oxide is again reduced by sulfide or organic matter [e.g., *Wang and Van Cappellen*, 1996]. This tends to increase the apparent total rate of iron sources (or sinks), from 595 μmol m^{-2} d^{-1} under anoxia to 757 μmol m^{-2} d^{-1} under weakly hypoxic conditions, even though the total flux of particulate iron to the sediment is the same in all cases.

Under near-anoxic conditions, almost half of all DFe is lost to the water column (Figure 2c). A sink switching effect takes place with higher O_{2BW}, whereby DFe oxidation increases at the expense of benthic DFe loss, thereby leading to greater retention of DFe. DFe fluxes fall sharply when bottom waters transition from severe to weak hypoxia, which is reflected in the field observations by the increase in DFe fluxes when $O_{2BW} < 20$ μM (Figure 1). This concentration may represent a tipping point, beyond which sediments become highly efficient at retaining the iron deposited on the sediment surface. In this regard, it is noteworthy that the boundary between surface sediments that are enriched and depleted in Fe in the Peruvian oxygen minimum zone is located exactly where bottom oxygen concentrations rise above 20 μM [*Scholz et al*., 2014a].

The impact of O_{2BW} on DFe fluxes is illustrated more graphically by the DFe pore water concentrations in Figure 2d. Under very low O_{2BW}, the DFe concentration gradient at the sediment-water interface is extremely sharp, which drives a large flux across the diffusive boundary layer. In this case, O_2 barely penetrates the sediment and acts as a poor geochemical barrier to DFe flux [*McManus et al*., 1997]. Under weakly hypoxic conditions, O_{2BW} penetrates deeper leading to a more efficient oxidative sink for DFe. The resulting DFe concentration gradient in the uppermost millimeters is markedly shallower and the flux to the bottom water much smaller. Finally, under normal oxic conditions, the DFe peak is spatially separated from the surface by several centimeters and only a very weak DFe flux is predicted.

We propose that the DFe flux tipping point is related to sediment ventilation by burrowing animals. The impact of irrigation in our model is demonstrated by the dashed curves in Figure 1a which show that DFe fluxes are much lower on the shelf and slope if faunal activity is unaffected by low O_{2BW}. This conflicts with *Elrod et al*. [2004], who suggested that DFe fluxes were enhanced by bioirrigation in Monterey Bay sediments ($O_{2BW} > 100$ μM). Yet the importance of bioirrigation in mitigating DFe fluxes is supported by previous observations. First, mesocosm experiments showed that burrowing fauna increase iron retention due to rapid immobilization of DFe as particulate iron oxide phases on burrow walls [*Lewandowski et al*., 2007]. These results have been reproduced using bioirrigation models that employ empirically derived rate constants for aerobic DFe oxidation [*Meile et al*., 2005]. Second, bottom water DFe concentrations in the later stages of sediment incubations increase quasi-exponentially concomitant with dissolved oxygen depletion [*Severmann et al*., 2010]. This has been attributed to the loss of the surface oxidized layer on the walls of animal burrows as well as a reduced rate of DFe oxidation in oxygen-depleted chamber waters. More generally, DFe fluxes are low in sediments bearing a surface oxidized layer [*McManus et al*., 1997]. Clearly, then, in addition to C_{OX}, DFe fluxes show a strong dependence on O_{2BW}, especially for concentrations below 20 μM. In the following section, we derive a function based on both these variables to predict DFe fluxes from sediments.

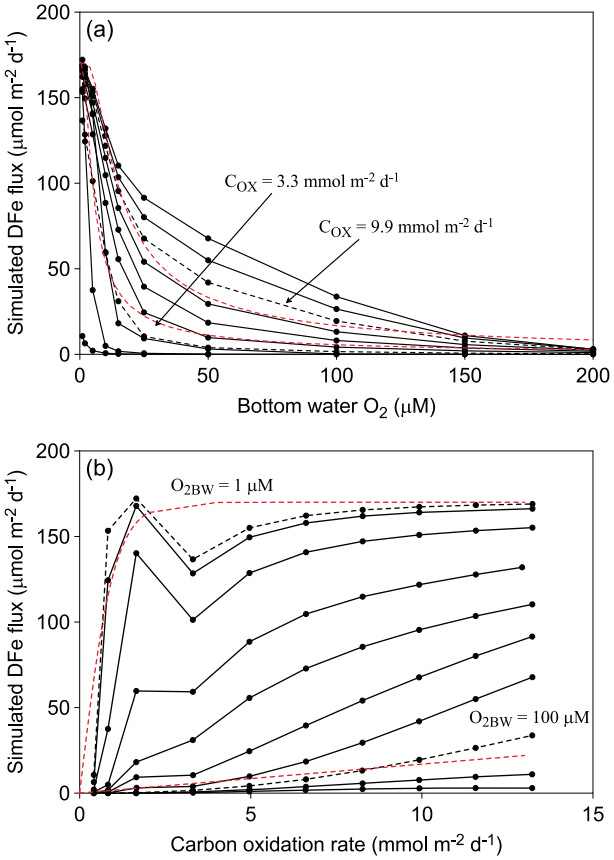

Figure 3. Simulated DFe fluxes from the standardized numerical model versus (a) bottom water oxygen concentration and (b) carbon oxidation rate. In Figure 3a, the results for a C_{OX} of 9.9 and 3.3 mmol m^{-2} d^{-1} are shown as dashed curves and compared to the predicted fluxes from the new function (equation (1)) in adjacent red dashed curves. In Figure 3b, the results for O_{2BW} of 1 and 100 μM are compared to the new function. All other black curves correspond to the O_{2BW} and C_{OX} intervals listed in Table 3.

5. Derivation of a Predictive Function for Benthic Iron Fluxes

An empirical function for predicting benthic DFe fluxes from C_{OX} and O_{2BW} was derived using a more detailed sensitivity analysis. This was based on a standardized model defined by the average parameter values of the shelf and slope settings (Table 3). A series of model runs was executed where organic matter rain rate and O_{2BW} were varied between 0.5–16 mmol m^{-2} d^{-1} and 1–200 μM, respectively. The corresponding C_{OX} for these rain rates is 0.4–13.2 mmol m^{-2} d^{-1}. These ranges are characteristic of the sites in Table 1 and much of the seafloor in general. Although rain rate and O_{2BW} were the only two model aspects to be varied directly, the bioturbation and bioirrigation coefficients were dependent on O_{2BW}, as described previously. This avoids anomalous scenarios, such as high bioirrigation at sites with low benthic respiration.

The dependence of DFe flux on O_{2BW} for constant values of C_{OX} is shown in Figure 3a. DFe flux increases with decreasing O_{2BW} for all C_{OX}, with a tipping point centered at around 20 μM, as observed previously. Furthermore, sediments release more iron as C_{OX} increases due to higher rates of aerobic carbon respiration at the expense of DFe oxidation. Benthic DFe flux also responds strongly to small increases in C_{OX} when O_{2BW} is below approximately 10 μM (Figure 3b). The pronounced peak in DFe centered at C_{OX} = 2 mmol m^{-2} d^{-1} originates from high DIR rates close to the sediment surface (cf. Figure 2d). The subsequent dip in DFe flux when C_{OX} ~ 4 mmol m^{-2} d^{-1} signifies sequestration of iron into sulfide minerals as sulfate reduction rates increase. DFe fluxes then gradually increase again with higher C_{OX} as in Figure 3a. These results demonstrate that C_{OX} is itself an important factor to consider for predicting DFe fluxes, in addition to the total flux of labile particulate iron (see below).

The sensitivity analysis supports observations that C_{OX} acts on DFe flux in an opposite way to O_{2BW} [*Elrod et al.*, 2004; *Severmann et al.*, 2010]. Hence, we derived a predictive function for DFe fluxes (in μmol m^{-2} d^{-1}) to reflect this behavior:

$$\text{DFe flux} = \gamma \cdot \tanh\left(\frac{C_{OX}}{O_{2BW}}\right) \quad (1)$$

where C_{OX} is in mmol m^{-2} d^{-1} and O_{2BW} is in μM. The maximum flux that can escape the sediment for a given Fe content and reactivity is γ. In our simulations, this is predicted to be 170 μmol m^{-2} d^{-1}.

The function is an example of a 0-D vertically integrated sediment model following the criteria of *Soetaert et al.* [2000]. Although the function is unable to simulate the local minimum of the DFe flux at low O_{2BW}, it broadly reproduces the hyperbolic trends in the sensitivity analysis results (dashed red curves, Figure 3). A comparison of the new function with each paired C_{OX} and O_{2BW} point on these curves shows that it

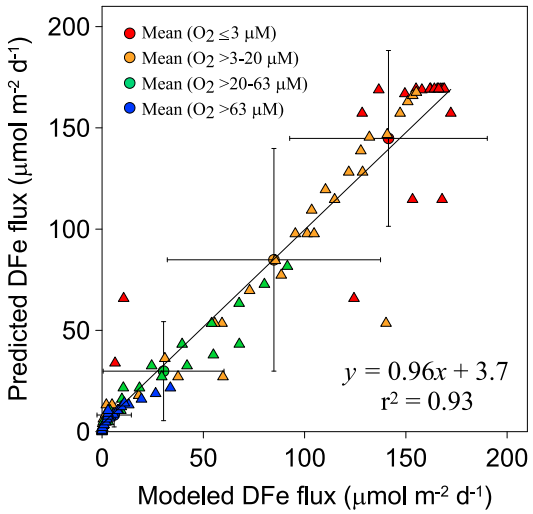

Figure 4. Comparison of the DFe fluxes simulated using the standardized numerical model for each paired O_{2BW}-C_{OX} data (black circles in Figure 3) and the DFe fluxes predicted using equation (1), color coded according to O_{2BW} (triangles). The large circles represent the mean flux ± standard deviation in each O_{2BW} interval. The straight line is the linear regression curve (equation indicated).

explains 93% of the variance in the modeled rates, with a standard error of the slope of 0.027 µmol m^{-2} d^{-1} (Figure 4). C_{OX} and O_{2BW} alone each explain less than 20%. More complex functions did not improve the fit significantly.

The extreme DFe fluxes observed on the Peruvian shelf, Californian Borderland Basins, and the Eel River mouth are not captured by the new function. One factor to consider may simply be that sediments display a wide range of reactive iron content. In our simulations we used a Fe_{HR}/Fe_T of 0.17, which is within the range of 0.08–0.40 for continental margin sediments [*Raiswell and Canfield*, 1998]. Rivers tend to deposit large amounts of terrigenous inorganic material on the shelf which may be more enriched in Fe_{HR} compared to the global average [*Poulton and Raiswell*, 2002]. We tested the sensitivity of DFe fluxes to the Fe_{HR} content by repeating the model simulations for the shelf site with 1 and 100 µM O_{2BW}. In these simulations, the total iron flux was held constant but the fluxes of Fe_{HR} and Fe_U were varied. The results show a quasi-linear dependence of benthic DFe fluxes on the Fe_{HR}/Fe_T ratio with a steeper response when O_{2BW} is in the normal oxic range compared to the anoxic range (Figure 5). The model predicts that the observed variability in Fe_{HR}/Fe_T for the Fe_T flux used in the simulations can result in DFe fluxes that vary by an order of magnitude. This supports the idea that high DFe fluxes on the Eel River shelf are driven by a higher-than-average Fe_{HR} content [*Severmann et al.*, 2010] and, possibly, seasonal variability too [*Severmann et al.*, 2010; *Berelson et al.*, 2003; *Pakhomova et al.*, 2007]. Similarly, low DFe fluxes were calculated from pore water profiles in sediments with a low Fe_{HR} content on the South African margin [*Homoky et al.*, 2013]. Clearly, though, the total Fe_{HR} flux is the controlling factor on DFe flux rather than Fe_{HR}/Fe_T, the latter of which is likely to be determined by the weathering regime rather than the overall flux of terrigenous material.

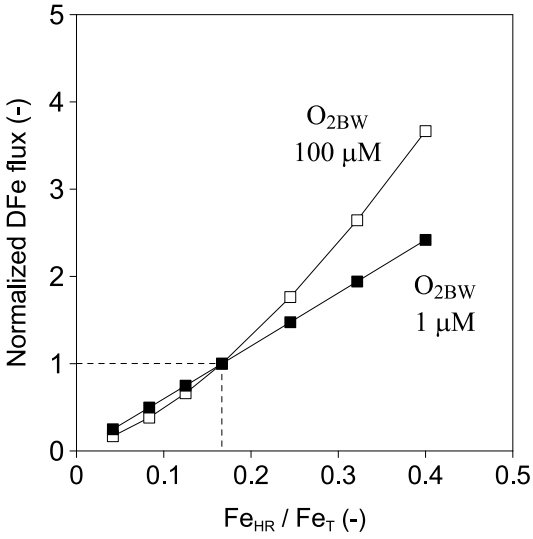

Figure 5. Sensitivity of modeled benthic DFe fluxes in shelf sediments to the Fe_{HR}/Fe_T ratio in particulate iron oxide deposited on the seafloor [*Raiswell and Canfield*, 1998]. Results are shown for low (1 µM) and high (100 µM) O_{2BW}. DFe fluxes are normalized to the modeled shelf fluxes in Figure 1a for O_{2BW} = 1 and 100 µM, indicated by the dashed lines.

By contrast, terrigenous Fe supply to the California Borderland Basins and the shallow Peruvian shelf is very low. Extremely high benthic DFe fluxes in these regions may be caused by the transient occurrence of oxidizing conditions in the bottom water and the focused discharge of DFe after the recurrence of anoxia [*Scholz et al.*, 2011; *Noffke et al.*, 2012]. The idea is that during oxic periods, a thin oxidized layer develops on the sediment surface which favors the precipitation of Fe oxides and mitigates DFe flux to the bottom water. Deposition of particulate Fe oxides from the water column would also be enhanced under these conditions. A resurgence of anoxic conditions favors reductive dissolution of the accumulated oxides, leading to pulsed release of DFe to the bottom water. Moreover, iron fluxes in

Table 4. Dissolved Iron Fluxes From Marine Sediments Calculated Using Equation (1)

	Area[a] (10^{12} m^2)	Mean C_{OX}[b] (mmol m^{-2} d^{-1})	Mean DFe Flux[c] (μmol m^{-2} d^{-1})	Total DFe Flux[d] (Gmol yr^{-1})	Total DFe Flux[e] [*Elrod et al.*, 2004] (Gmol yr^{-1})
			Continental Margin		
Shelf (0–200 m)	27.12	9.4	7.3	72.2 ± 36.1	63.3
Upper slope (>200–1000 m)	16.01	3.0	3.5	20.5 ± 10.3	11.9
Lower slope (>1000–2000 m)	15.84	1.5	2.9	16.6 ± 8.4	5.9
Total margin[f]	58.98 (0.38)	5.5	5.1 (35)	109 ± 55 (5)	81
			Deep Sea		
>2000 m	302.5	0.4	0.37	41 ± 21	30
			Global Ocean		
Σ				150 ± 75	111

[a] *Menard and Smith* [1966].
[b] *Burdige* [2007].
[c] Using the gridded O_{2BW} and bathymetry in combination with equation (1).
[d] Integrated over the corresponding ocean area. The uncertainties (±) are calculated based on the uncertainty in Fe_{HR} and Fe_T content. Standard deviations in Fe_{HR} and Fe_T are reported for a mean marine sediment by *Poulton and Raiswell* [2002, Table 7]. Using standard error propagation rules, the relative error in the Fe_{HR}/Fe_T ratio using their data is 50%, which is taken as the error in DFe flux.
[e] The flux calculated assuming the regression provided by *Elrod et al.* [2004] in Figure 1. For consistency with *Elrod et al.* [2004], we used a flux ratio of 0.68 μmol DFe/mmol carbon oxidized in this calculation, ignoring the intercept DFe flux of 0.5 μmol m^{-2} d^{-1} in their linear regression equation.
[f] Values in parenthesis correspond to sediments underlying oxygen-deficient bottom waters (<20 μM).

such temporally anoxic and occasionally euxinic settings such as the Peruvian shelf may be largely influenced by additional controls such as the availability of sulfide in the pore water and bottom water and benthic boundary layer [*Scholz et al.*, 2014b]. These factors cannot be constrained with our benthic model, as we assume a bottom water sulfide concentration of zero in all model runs. More generally, the magnitude of the terrigenous Fe_{HR} flux and/or focused deposition of Fe oxides due to seasonal or other transient effects might play a more important role in generating the observed variability in benthic DFe fluxes than implied by the model.

6. A Revised Estimate for Global Benthic Iron Flux

Our new estimate of the global benthic DFe flux is based on spatially resolved bathymetry, O_{2BW}, and C_{OX} data. Maps of bathymetry and O_{2BW} on a 1° × 1° resolution were taken from *Bohlen et al.* [2012] based on data from the World Ocean Atlas [*Garcia et al.*, 2006]. Gridded C_{OX} data are unavailable, and instead, we used average C_{OX} for several hypsometric intervals [*Burdige*, 2007]. Upscaling using the new function (equation (1)) predicts a global DFe flux of 150 ± 75 Gmol yr^{-1} (Table 4), of which 109 ± 55 Gmol yr^{-1} is contributed by continental margin sediments and 41 ± 21 Gmol yr^{-1} by the deep sea (>2000 m). The uncertainties are calculated assuming that variability in Fe_{HR}/Fe_T and Fe_T content contributes to the largest error in the model predictions (see Table 4). This is equivalent to 50% for margin and deep-sea sediments. However, it is obvious from the scatter in Figure 1 that there are other sources of variability in DFe fluxes. This is not surprising given the physical and biogeochemical heterogeneity of continental margin sediments, implying that the calculated uncertainty is a conservative estimate [*Liu et al.*, 2010].

Note that the average DFe flux from deep-sea sediments is very low (0.37 μmol m^{-2} d^{-1}) yet globally significant by virtue of the vast expanse of the ocean basins. Nonetheless, this flux is speculative because very few flux measurements have been made in the ocean basins. Sequestration of DFe in deep-sea sediments may be more efficient than predicted, especially if other DFe removal pathways currently ignored in the model are significant, such as precipitation of authigenic carbonates, phosphates, or silicates. Consequently, the data currently only support a global DFe flux of 109 Gmol yr^{-1}, but it may be higher, especially if nonreductive iron dissolution contributes significantly to the global Fe budget [*Homoky et al.*, 2013; *Conway and John*, 2014]. In fact, the Biogeochemical Elemental Cycling ocean model that is tuned to pelagic DFe distribution does consider a very low DFe flux from the lower slope and deep basins [*Moore and Braucher*, 2008].

Taking the lower global DFe flux of 109 Gmol yr^{-1}, our model suggests that two thirds (72 Gmol yr^{-1}) is contributed by shelf sediments (Table 4). This is similar to 89 Gmol yr^{-1} derived by *Elrod et al.* [2004]

assuming a mean C_{OX} of 12 mmol m^{-2} d^{-1}. Our lower shelf C_{OX} (9.4 mmol m^{-2} d^{-1}) is derived from a well-constrained empirical relationship between C_{OX} and water depth [*Burdige*, 2007]. Using Burdige's C_{OX} would decrease Elrod et al.'s shelf estimate by around one third. Importantly, however, we find that continental slope sediments are also major sources of iron to ocean bottom waters (37.1 Gmol yr^{-1}). The implication is that sedimentary DFe release has been grossly underestimated in the marine Fe budget [*Jickells et al.*, 2005; *Boyd and Ellwood*, 2010].

Our derived global flux is 3 to 14 times higher than most previous estimates (see section 1). The average DFe flux from continental margins (5.1 μmol m^{-2} d^{-1}; Table 4) is also 3 to 5 times higher than the maximum benthic DFe flux of 1–2 μmol m^{-2} d^{-1} imposed as a seafloor boundary condition in some global iron models [e.g., *Moore et al.*, 2004; *Aumont and Bopp*, 2006]. One reason for the lower flux estimates from the global approaches may be an underestimation of organic carbon rain rates [*Moore and Braucher*, 2008]. It would be interesting to compare carbon export fluxes from these models, but this datum is unfortunately seldom reported. A more important consideration is that carbon rain rates and tracer distributions are generally poorly resolved over shelf sediments in global models, meaning that the shelf DFe flux (72.2 Gmol yr^{-1}), equivalent to two thirds of the global sedimentary DFe release, is not properly accounted for. Instead, the models are tuned to the lower DFe fluxes from slope sediments. However, a fraction of the iron released from shelf sediments is not retained in coastal waters but exported offshore in both dissolved and particulate form [*Johnson et al.*, 1999; *Lam et al.*, 2006; *Lohan and Bruland*, 2008; *de Jong et al.*, 2012]. Too little export of coastal iron to the ocean basins may lead to a too strong dependence of surface iron concentrations on atmospheric iron deposition, thus influencing model sensitivity toward this source [*Moore and Braucher*, 2008; *Tagliabue et al.*, 2014].

An additional factor to consider that has been highlighted in this study is the role of bottom water oxygen concentration. Comparison of our DFe fluxes with those predicted by *Elrod et al.* [2004] using the same C_{OX} provides a broad overview of the effect of O_{2BW}. Most notably, we find that our DFe fluxes on the continental slope are 2–3 times higher than predicted by Elrod et al.'s function (Table 4). This is partly because oxygen-deficient waters of the eastern boundary upwelling systems tend to impinge on the seafloor at these depths [*Helly and Levin*, 2004]. Sediments underlying bottom waters below the 20 μM threshold are flux hot spots, releasing DFe at an average rate of 35 μmol m^{-2} d^{-1}. They account for 4% of total DFe flux on the margin despite covering $<$1% of the seafloor. Yet it should be noted that the relatively coarse 1° × 1° resolution does not accurately capture shallow marginal sediments. Taking a more sophisticated approach, *Helly and Levin* [2004] estimated that around 1.4×10^{12} m^2 of sediments are in contact with bottom water $<$22 μM, which is equivalent to 3% by area of the shelf and upper slope (0–1000 m). Our DFe flux from oxygen-deficient regions is, therefore, likely to be a minimum estimate and may be up to a factor of 3 higher.

7. Impact of Benthic Iron Release on Oceanic Dissolved Iron Distributions

The ability of our simple function to predict DFe fluxes is encouraging because it can easily be implemented in global biogeochemical models. Most models routinely simulate dissolved oxygen and organic carbon rain rates to the seafloor ($\approx C_{OX}$). Thus, it provides a straightforward tool to test how the spatial distribution of DFe in the ocean is impacted by benthic iron release.

We tested the impact of our predictive function on global iron distributions in the ocean using the University of Victoria Earth System Climate Model (UVic ESCM). This model includes a coupled physical biogeochemical ocean component with a dynamic iron cycle [*Nickelsen et al.*, 2015]. Like other global models, shelf processes are not adequately described due to the coarse spatial resolution. The model has two iron pools, dissolved and particulate, and is similar to other global iron models [e.g., *Moore and Braucher*, 2008; *Tagliabue et al.*, 2014]. Scavenging of iron from the water column by organic particles is tuned to provide a good correlation between observed and modeled surface ocean DFe distributions. The model does not include scavenging by resuspended inorganic particles. Sedimentary iron release is proportional to carbon oxidation rate (i.e., Elrod et al.'s function), and the model further uses a simple oxygen-dependent switch threshold of 5 μM. If bottom water O_2 falls below this value, all iron deposited on the seafloor is released back to the water column. Benthic DFe fluxes predicted by the UVic ESCM model are shown in Figure 6a, and tuning of scavenging rates leads to a good fit to observed surface DFe concentrations (Figure 6b). The global benthic DFe flux predicted by the model in this configuration is 19 Gmol yr^{-1} [*Nickelsen et al.*, 2015].

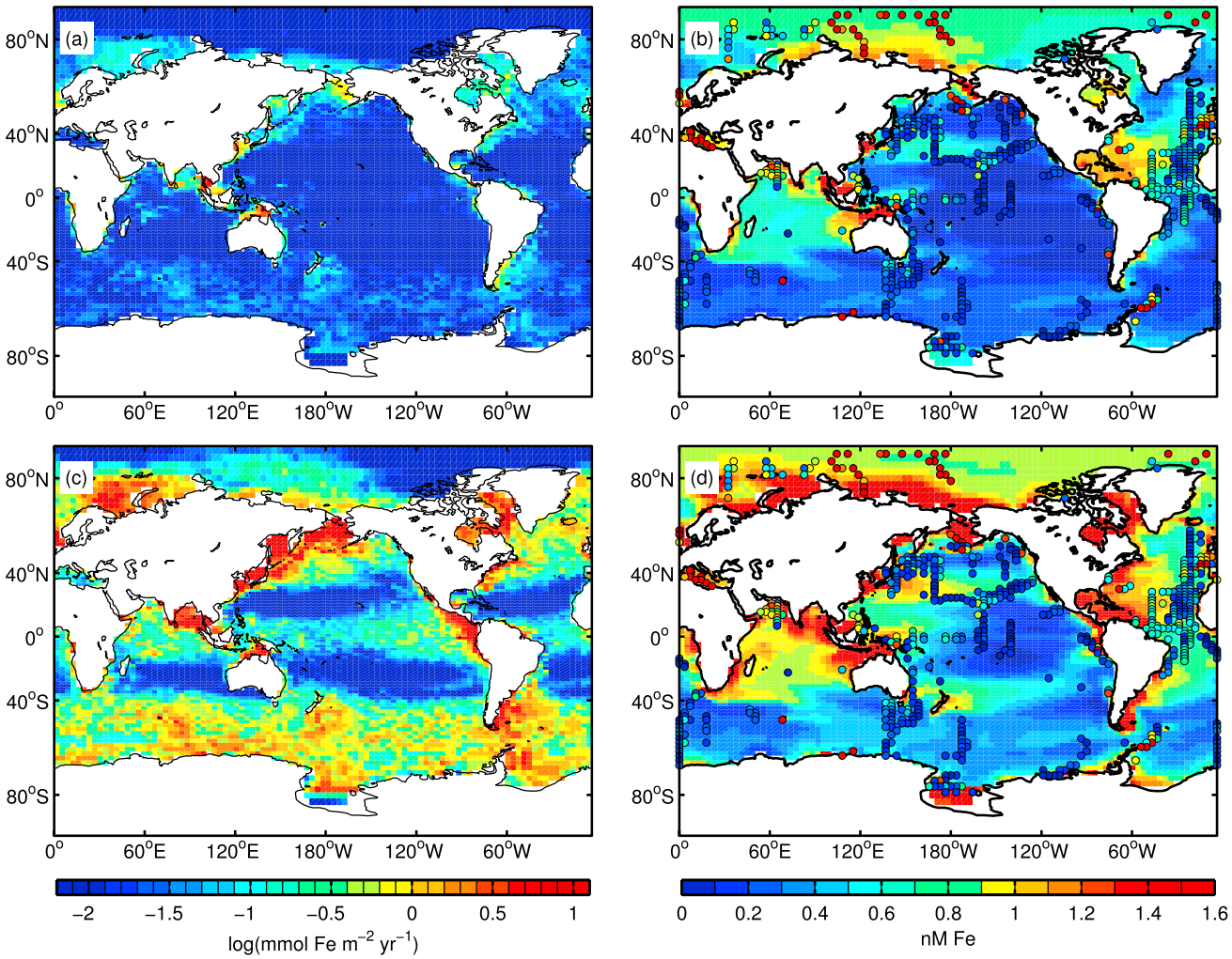

Figure 6. (a) Benthic DFe fluxes (mmol m^{-2} yr^{-1}, log scale) and (b) surface ocean DFe distributions (nM) using the UVic ESCM model [from *Nickelsen et al.*, 2015]. The results show the best model fit to observations (colored circles) [*Tagliabue et al.*, 2012]. (c and d) The model results where the new function for benthic DFe flux (equation (1)) is used to parameterize the benthic DFe flux, with all other model parameters held constant.

Benthic DFe fluxes increase strongly in the northern and eastern tropical Pacific, the Southern Ocean, and the North Atlantic when the model is executed using our function with all other parameters held constant (Figure 6c). The global DFe flux from sediments increases to 333 Gmol yr^{-1}, which is a factor of 2–3 higher than the predicted flux from the gridded data (Table 4). The elevated iron flux is caused by a positive feedback with POC rain rate to the seafloor driven by benthic Fe fertilization. Benthic DFe fluxes are thus enhanced in the new function configuration in otherwise iron-limited areas. Although scavenging depletes a fraction of the DFe released from the sediments, surface iron concentrations generally show a poorer agreement with the observations (Figure 6d). DFe concentrations are also elevated in deep waters (>3000 m) by around 0.3 nM compared to observations (not shown). This model configuration would require much higher scavenging rates in order to bring the model predictions back in line with the observations. They would need to be 4 times higher to reduce the globally averaged surface iron concentration from 0.83 nM to 0.48 nM, similar to previous "best fit" values of 0.41 nM (Figure 6b).

The sensitivity of surface ocean DFe to benthic iron release suggests that the poorly constrained scavenging rates are currently too low in the state-of-the-art global iron models. DFe removal into organic/inorganic particulates or colloids very likely prevents a large fraction of sedimentary iron reaching the surface ocean in a bioavailable form [*Honeyman et al.*, 1988; *Homoky et al.*, 2012; *John et al.*, 2012]. However, the model cannot currently resolve whether iron scavenging occurs close to the sediments or higher up in the water

column. In reality, scavenging by inorganic particles is likely to be exacerbated in intermediate and bottom nepheloid layers on continental margins [*Jahnke et al*., 1990; *Inthorn et al*., 2006]. In agreement with this, lateral relocation of sediment-derived Fe on the Peruvian margin appears to take place in colloids or nanoparticulates near the seafloor [*Scholz et al*., 2011]. A fraction of iron scavenged within these layers may be exported offshore to distant Fe-limited regions, redeposited on the seafloor or upwelled into surface waters [*Johnson et al*., 1999; *Lam et al*., 2006]. Particle settling of inorganically bound iron in addition to colloidal aggregation and pumping [*Honeyman and Santschi*, 1991] may be an important yet overlooked component of the marine Fe budget. It is worth noting that organically bound iron exported from the surface ocean to the sediments would support $<5\%$ of the measured DFe flux from the continental margins, given the C_{OX} rate in Table 4 and a molar Fe/C_{org} ratio of 20 μmol/mol [*Wu and Boyle*, 2002; *Moore and Braucher*, 2008].

We thus propose that there exists a rapid removal of benthic-derived DFe into colloidal or inorganic phases close to the seafloor in particle-rich water layers. This serves as a barrier for sedimentary DFe reaching the surface mixed layer. Given that our benthic DFe fluxes are several fold higher than those presently used in global iron models tuned to DFe distributions, the fraction of bioavailable iron that arrives at the sunlit ocean is probably much smaller than the fraction that is scavenged. Diagenetic alteration and dissolution of iron particles and aggregates following deposition on the sediment allows DFe to be returned to the water column and rescavenged. We believe that this cycle could be an important vector for transporting iron offshore away from the margins. Future studies should try to quantify these sources and sinks with the aim to improve the conceptual iron cycle in Earth system models.

8. Conclusions

The main objective of this study was to develop a simple, mathematical tool for predicting the flux of dissolved iron (DFe) from marine sediments and to better quantify its contribution to the global iron cycle. We derived an empirical function that unifies the role of bottom water oxygen concentration (O_{2BW}) and organic carbon oxidation rate in sediments (C_{OX}) as key controls on benthic DFe flux. The new function predicts a global DFe flux that is around 5 times higher than the previous estimates derived using global models. This can be attributed to (i) inadequate treatment of the role of O_2 on benthic DFe fluxes in global models and (ii) poorly resolved biogeochemical dynamics on the shelf (for the sake of computational efficiency) where two thirds of the global sedimentary DFe release occurs.

When the new function is applied to the state-of-the-art intermediate-complexity Earth system climate model UVic ESCM [*Nickelsen et al*., 2015], simulated surface water DFe concentrations are increased significantly over most of the ocean. This leads us to conclude that iron scavenging rates, mainly as inorganic particulates and colloidal aggregates close to the seafloor, must also be far higher than assumed previously. Otherwise, a strong positive feedback becomes established between primary productivity (hence C_{OX}) and DFe flux. The enhanced benthic DFe source may not have critical consequences for the current generation of ocean models if they correctly simulate the net flux of sediment iron that reaches the surface. However, the excess benthic iron that is scavenged close to the seabed is likely to be poorly represented. This could have important implications for the marine Fe budget as well as for simulating long-range transport of iron to Fe-limited regions. Once the significance of this "dark" Fe cycle has been evaluated and parameterized more carefully, it would be interesting to test whether simulated atmospheric CO_2 concentrations during the Last Glacial Maximum are greatly diminished in global model simulations that employ our new benthic Fe input function [e.g., *Parekh et al*., 2006].

Acknowledgments
We thank the editorial team and two anonymous reviewers for their thoughtful comments. This work is a contribution of the Sonderforschungsbereich 754 "Climate-Biogeochemistry Interactions in the Tropical Ocean" (www.sfb754.de) financially supported by the Deutsche Forschungsgemeinschaft (DFG). The Seventh Framework Program of the European Union supported the participation of F.S. (Marie Curie IOF 300648, BICYCLE). All field data used in this manuscript have been published previously and are directly obtainable from the literature cited in Table 1.

References

Andersson, J. H., J. W. M. Wijsman, P. M. J. Herman, J. J. Middelburg, K. Soetaert, and C. Heip (2004), Respiration patterns in the deep ocean, *Geophys. Res. Lett.*, *31*, L03304, doi:10.1029/2003GL018756.

Archer, D. E., and K. Johnson (2000), A model of the iron cycle in the ocean, *Global Biogeochem. Cycles*, *14*, 269–279, doi:10.1029/1999GB900053.

Aumont, O., and L. Bopp (2006), Globalizing results from ocean in situ iron fertilization studies, *Global Biogeochem. Cycles*, *20*, GB2017, doi:10.1029/2005GB002591.

Aumont, O., E. Maier-Reimer, S. Blain, and P. Monfray (2003), An ecosystem model of the global ocean including Fe, Si, P colimitations, *Global Biogeochem. Cycles*, *17*(2), 1060, doi:10.1029/2001GB001745.

Berelson, W. M., J. McManus, K. Coale, K. Johnson, D. Burdige, T. Kilgore, D. Colodner, F. Chavez, R. Kudela, and H. Boucher (2003), A time series of benthic flux measurements from Monterey Bay, CA, *Cont. Shelf Res.*, *23*, 457–481.

Berg, P., S. Rysgaard, and B. Thamdrup (2003), Dynamic modeling of early diagenesis and nutrient cycling. A case study in an Arctic marine sediment, *Am. J. Sci.*, *303*, 905–955.
Bohlen, L., A. W. Dale, S. Sommer, T. Mosch, C. Hensen, A. Noffke, F. Scholz, and K. Wallmann (2011), Benthic nitrogen cycling traversing the Peruvian oxygen minimum zone, *Geochim. Cosmochim. Acta*, *75*, 6094–6111.
Bohlen, L., A. W. Dale, and K. Wallmann (2012), Simple transfer functions for calculating benthic fixed nitrogen losses and C:N:P regeneration ratios in global biogeochemical models, *Global Biogeochem. Cycles*, *26*, GB3029, doi:10.1029/2011GB004198.
Boudreau, B. P. (1996), A method-of-lines code for carbon and nutrient diagenesis in aquatic sediments, *Comput. Geosci.*, *22*, 479–496.
Boudreau, B. P., and B. R. Ruddick (1991), On a reactive continuum representation of organic matter diagenesis, *Am. J. Sci.*, *291*, 507–538.
Boudreau, B. P., C. Arnosti, B. B. Jørgensen, and D. E. Canfield (2008), Comment on "Physical model for the decay and preservation of marine organic carbon", *Science*, *319*, 1616–1617.
Boyd, P. W., and M. J. Ellwood (2010), The biogeochemical cycle of iron in the ocean, *Nat. Geosci.*, *3*, 675–682.
Burdige, D. J. (2007), Preservation of organic matter in marine sediments: Controls, mechanisms, and an imbalance in sediment organic carbon budgets?, *Chem. Rev.*, *107*, 467–485.
Burwicz, E. B., L. H. Rüpke, and K. Wallmann (2011), Estimation of the global amount of submarine gas hydrates formed via microbial methane formation based on numerical reaction-transport modeling and a novel parameterization of Holocene sedimentation, *Geochim. Cosmochim. Acta*, *75*, 4562–4576.
Canfield, D. E., R. Raiswell, and S. Bottrell (1992), The reactivity of sedimentary iron minerals toward sulfide, *Am. J. Sci.*, *292*, 659–683.
Conway, T. M., and S. G. John (2014), Quantification of dissolved iron sources to the North Atlantic Ocean, *Nature*, *511*, 212–215.
Cornell, R. M., and U. Schwertmann (1996), *The Iron Oxides: Structure, Properties, Reactions, Occurrences and Uses*, 703 pp., Wiley-VCH, Darmstadt, Germany.
Cullen, J. T., M. Chong, and D. Ianson (2009), British Columbian continental shelf as a source of dissolved iron to the subarctic northeast Pacific Ocean, *Global Biogeochem. Cycles*, *23*, GB4012, doi:10.1029/2008GB003326.
Dale, A. W., V. Brüchert, M. Alperin, and P. Regnier (2009), An integrated sulfur isotope model for Namibian shelf sediments, *Geochim. Cosmochim. Acta*, *73*, 1924–1944.
Dale, A. W., V. J. Bertics, T. Treude, S. Sommer, and K. Wallmann (2013), Modeling benthic–pelagic nutrient exchange processes and pore water distributions in a seasonally hypoxic sediment: Evidence for massive phosphate release by *Beggiatoa*?, *Biogeosciences*, *10*, 629–651, doi:10.5194/bg-10-629-2013.
de Jong, J., V. Schoemann, D. Lannuzel, P. Croot, H. de Baar, and J. -L. Tison (2012), Natural iron fertilization of the Atlantic sector of the Southern Ocean by continental shelf sources of the Antarctic Peninsula, *J. Geophys. Res.*, *117*, G01029, doi:10.1029/2011JG001679.
Diaz, R. J., and R. Rosenberg (1995), Marine benthic hypoxia—Review of ecological effects and behavioral responses on macrofauna, *Oceanogr. Mar. Biol.*, *33*, 245–303.
Elrod, V. A., W. M. Berelson, K. H. Coale, and K. S. Johnson (2004), The flux of iron from continental shelf sediments: A missing source for global budgets, *Geophys. Res. Lett.*, *31*, L12307, doi:10.1029/2004GL020216.
Friedrich, J., C. Dinkel, G. Friedl, N. Pimenov, J. Wijsman, M. T. Gomoiu, A. Cociasu, L. Popa, and B. Wehrli (2002), Benthic nutrient cycling and diagenetic pathways in the North-western Black Sea, *Estuarine Coastal Shelf Sci.*, *54*, 369–383.
Galbraith, E. D., A. Gnanadesikan, J. P. Dunne, and M. R. Hiscock (2010), Regional impacts of iron-light colimitation in a global biogeochemical model, *Biogeosciences*, *7*, 1043–1064.
Garcia, H. E., R. A. Locarnini, T. P. Boyer, and J. I. Antonov (2006), *World Ocean Atlas 2005, Volume 3: Dissolved Oxygen, Apparent Oxygen Utilization, and Oxygen Saturation*, *NOAA Atlas NESDIS*, vol. 63, edited by S. Levitus, 342 pp., NOAA, Silver Spring, Md.
Garrels, R. M., and F. T. Mackenzie (1971), *Evolution of Sedimentary Rocks*, 397 pp., Norton, New York.
Glasby, G. P. (2006), Manganese: Predominant role of nodules and crusts, in *Marine Geochemistry*, 2nd ed., edited by H. D. Schulz and M. Zabel, pp. 391–427, Springer, Berlin.
Hedges, J. I., and R. G. Keil (1995), Sedimentary organic matter preservation: An assessment and speculative synthesis, *Mar. Chem.*, *49*, 81–115.
Helly, J. J., and L. A. Levin (2004), Global distribution of naturally occurring marine hypoxia on continental margins, *Deep Sea Res., Part I*, *51*, 1159–1168.
Homoky, W. B., S. Severmann, J. McManus, W. M. Berelson, T. E. Riedel, P. J. Statham, and R. A. Mills (2012), Dissolved oxygen and suspended particles regulate the benthic flux of iron from continental margins, *Mar. Chem.*, *134–135*, 59–70.
Homoky, W. B., S. G. John, T. M. Conway, and R. A. Mills (2013), Distinct iron isotopic signatures and supply from marine sediment dissolution, *Nat. Commun.*, *4*, 2143, doi:10.1038/ncomms3143.
Honeyman, B. D., and P. H. Santschi (1991), Coupling adsorption and particle aggregation: Laboratory studies of "colloidal pumping" using ^{59}Fe-labeled hematite, *Environ. Sci. Technol.*, *25*, 1739–1747.
Honeyman, B. D., L. S. Balistrieri, and J. W. Murray (1988), Oceanic trace metal scavenging: The importance of particle concentration, *Deep Sea Res.*, *35*, 227–246.
Inthorn, M., T. Wagner, G. Scheeder, and M. Zabel (2006), Lateral transport controls distribution, quality, and burial of organic matter along continental slopes in high-productivity areas, *Geology*, *34*, 205–208.
Jahnke, R. A., C. E. Reimers, and D. B. Craven (1990), Intensification of recycling of organic matter at the sea floor near ocean margins, *Nature*, *348*, 50–54.
Jeandel, C., B. Peucker-Ehrenbrink, M. T. Jones, C. R. Pearce, E. H. Oelkers, Y. Godderis, F. Lacan, O. Aumont, and T. Arsouze (2011), Ocean margins: The missing term in oceanic element budgets?, *Eos Trans. AGU*, *26*, 217–224, doi:10.1029/2011EO260001.
Jickells, T. D., et al. (2005), Global iron connections between desert dust, ocean biogeochemistry, and climate, *Science*, *308*, 67–71.
John, S. G., J. Mendez, J. Moffett, and J. Adkins (2012), The flux of iron and iron isotopes from San Pedro Basin sediments, *Geochim. Cosmochim. Acta*, *93*, 14–29.
Johnson, K. S., F. P. Chavez, and G. E. Friederich (1999), Continental-shelf sediment as a primary source of iron for coastal phytoplankton, *Nature*, *398*, 697–700.
Kriest, I., and A. Oschlies (2008), On the treatment of particulate organic matter sinking in large-scale models of marine biogeochemical cycles, *Biogeosciences*, *5*, 55–72.
Lam, P. J., J. K. B. Bishop, C. C. Henning, M. A. Marcus, G. A. Waychunas, and I. Y. Fung (2006), Wintertime phytoplankton bloom in the subarctic Pacific supported by continental margin iron, *Global Biogeochem. Cycles*, *20*, GB1006, doi:10.1029/2005GB002557.
Levin, L. A., and J. D. Gage (1998), Relationships between oxygen, organic matter and the diversity of bathyal macrofauna, *Deep Sea Res., Part II*, *45*, 129–163.
Lewandowski, J., C. Laskov, and M. Hupfer (2007), The relationship between *Chironomus plumosus* burrows and the spatial distribution of pore-water phosphate, iron and ammonium in lake sediments, *Freshwater Biol.*, *52*, 331–343.

Liu, K.-K., L. Atkinson, R. Quiñones, and L. Talaue-McManus (2010), *Carbon and Nutrient Fluxes in Continental Margins: A Global Synthesis*, 741 pp., Springer, Berlin.
Lohan, M. C., and K. W. Bruland (2008), Elevated Fe(II) and dissolved Fe in hypoxic shelf waters off Oregon and Washington: An enhanced source of iron to coastal upwelling regimes, *Environ. Sci. Technol.*, *42*, 6462–6468.
Luo, C., N. Mahowald, T. Bond, P. Y. Chuang, P. Artaxo, R. Siefert, Y. Chen, and J. Schauer (2008), Combustion iron distribution and deposition, *Global Biogeochem. Cycles*, *22*, GB1012, doi:10.1029/2007GB002964.
Mahowald, N. M., A. R. Baker, G. Bergametti, N. Brooks, R. A. Duce, T. D. Jickells, N. Kubilay, J. Prospero, and I. Tegen (2005), Atmospheric global dust cycle and iron inputs to the ocean, *Global Biogeochem. Cycles*, *19*, GB4025, doi:10.1029/2004GB002402.
Martin, J. H. (1990), Glacial-interglacial CO_2 change: The iron hypothesis, *Paleoceanography*, *5*, 1–13, doi:10.1029/PA005i001p00001.
Martin, J. H., and S. E. Fitzwater (1988), Iron deficiency limits phytoplankton growth in the north-east Pacific subarctic, *Nature*, *331*, 341–343.
McManus, J., W. M. Berelson, K. H. Coale, K. S. Johnson, and T. E. Kilgore (1997), Phosphorus regeneration in continental margin sediments, *Geochim. Cosmochim. Acta*, *61*, 2891–2907.
Meile, C., and P. Van Cappellen (2003), Global estimates of enhanced solute transport in marine sediments, *Limnol. Oceanogr.*, *48*, 777–786.
Meile, C., P. Berg, P. Van Cappellen, and K. Tuncay (2005), Solute-specific pore water irrigation: Implications for chemical cycling in early diagenesis, *J. Mar. Res.*, *64*, 601–621.
Menard, H. W., and S. M. Smith (1966), Hypsometry of ocean basin provinces, *J. Geophys. Res.*, *71*, 4305–4325, doi:10.1029/JZ071i018p04305.
Middelburg, J. J. (1989), A simple rate model for organic matter decomposition in marine sediments, *Geochim. Cosmochim. Acta*, *53*, 1577–1581.
Middelburg, J. J., and L. A. Levin (2009), Coastal hypoxia and sediment biogeochemistry, *Biogeosciences*, *6*, 1273–1293.
Middelburg, J. J., K. Soetaert, and P. M. J. Herman (1997), Empirical relationships for use in global diagenetic models, *Deep Sea Res., Part I*, *44*, 327–344.
Misumi, K., K. Lindsay, J. K. Moore, S. C. Doney, F. O. Bryan, D. Tsumune, and Y. Yoshida (2014), The iron budget in ocean surface waters in the 20th and 21st centuries: Projections by the Community Earth System Model version 1, *Biogeosciences*, *11*, 33–55.
Moore, J. K., and O. Braucher (2008), Sedimentary and mineral dust sources of dissolved iron to the world ocean, *Biogeosciences*, *5*, 631–656.
Moore, J. K., and S. C. Doney (2007), Iron availability limits the ocean nitrogen inventory stabilizing feedbacks between marine denitrification and nitrogen fixation, *Global Biogeochem. Cycles*, *21*, GB2001, doi:10.1029/2006GB002762.
Moore, J. K., S. C. Doney, and K. Lindsay (2004), Upper ocean ecosystem dynamics and iron cycling in a global three-dimensional model, *Global Biogeochem. Cycles*, *18*, GB4028, doi:10.1029/2004GB002220.
Nickelsen, L., D. Keller, and A. Oschlies (2015), Including a dynamic marine iron cycle in the University of Victoria Earth System Climate Model, *Geosci. Model Dev.*, *8*, 1357–1381, doi:10.5194/gmd-8-1357-2015.
Noffke, A., C. Hensen, S. Sommer, F. Scholz, L. Bohlen, T. Mosch, M. Graco, and K. Wallmann (2012), Benthic iron and phosphorus fluxes across the Peruvian oxygen minimum zone, *Limnol. Oceanogr.*, *57*, 851–867.
Pakhomova, S. V., P. O. J. Hall, M. Y. Kononets, A. G. Rozanov, A. Tengberg, and A. V. Vershinin (2007), Fluxes of iron and manganese across the sediment-water interface under various redox conditions, *Mar. Chem.*, *107*, 319–331.
Palastanga, V., C. P. Slomp, and C. Heinze (2013), Glacial-interglacial variability in ocean oxygen and phosphorus in a global biogeochemical model, *Biogeosciences*, *10*, 945–958.
Parekh, P., M. J. Follows, and E. Boyle (2004), Modeling the global ocean iron cycle, *Global Biogeochem. Cycles*, *18*, GB1002, doi:10.1029/2003GB002061.
Parekh, P., M. J. Follows, S. Dutkiewicz, and T. Ito (2006), Physical and biological regulation of the soft tissue carbon pump, *Paleoceanography*, *21*, PA3001, doi:10.1029/2005PA001258.
Poulton, S. W., and R. Raiswell (2002), The low-temperature geochemical cycle of iron: From continental fluxes to marine sediment deposition, *Am. J. Sci.*, *302*, 774–805.
Poulton, S. W., M. D. Krom, and R. Raiswell (2004), A revised scheme for the reactivity of iron (oxyhydr)oxide minerals towards dissolved sulfide, *Geochim. Cosmochim. Acta*, *68*, 3703–3715.
Radic, A., F. Lacan, and J. W. Murray (2011), Iron isotopes in the seawater of the equatorial Pacific Ocean: New constraints for the oceanic iron cycle, *Earth Planet. Sci. Lett.*, *306*, 1–10.
Raiswell, R., and D. E. Canfield (1998), Sources of iron for pyrite formation in marine sediments, *Am. J. Sci.*, *298*, 219–245.
Rickard, D., and G. W. Luther III (2007), Chemistry of iron sulfides, *Chem. Rev.*, *107*, 514–562.
Scholz, F., C. Hensen, A. Noffke, A. Rohde, V. Liebetrau, and K. Wallmann (2011), Early diagenesis of redox-sensitive trace metals in the Peru upwelling area—Response to ENSO-related oxygen fluctuations in the water column, *Geochim. Cosmochim. Acta*, *75*, 7257–7276.
Scholz, F., S. Severmann, J. McManus, and C. Hensen (2014a), Beyond the Black Sea paradigm: The sedimentary fingerprint of an open-marine iron shuttle, *Geochim. Cosmochim. Acta*, *127*, 368–380.
Scholz, F., J. McManus, A. C. Mix, C. Hensen, and R. Schneider (2014b), The impact of ocean deoxygenation on iron release from continental margin sediments, *Nat. Geosci.*, *7*, 433–437.
Severmann, S., J. McManus, W. M. Berelson, and D. E. Hammond (2010), The continental shelf benthic iron flux and its isotope composition, *Geochim. Cosmochim. Acta*, *74*, 3984–4004.
Sigman, D. M., and E. A. Boyle (2000), Glacial/interglacial variations in atmospheric carbon dioxide, *Nature*, *407*, 859–869.
Soetaert, K., J. J. Middelburg, P. M. J. Herman, and K. Buis (2000), On the coupling of benthic and pelagic biogeochemical models, *Earth Sci. Rev.*, *51*, 173–201.
Tagliabue, A., T. Mtshali, O. Aumont, A. R. Bowie, M. B. Klunder, A. N. Roychoudhury, and S. Swart (2012), A global compilation of dissolved iron measurements: Focus on distributions and processes in the Southern Ocean, *Biogeosciences*, *9*, 2333–2349, doi:10.5194/bg-9-2333-2012.
Tagliabue, A., O. Aumont, and L. Bopp (2014), The impact of different external sources of iron on the global carbon cycle, *Geophys. Res. Lett.*, *41*, 920–926, doi:10.1002/2013GL059059.
Teal, L. R., M. T. Bulling, E. R. Parker, and M. Solan (2008), Global patterns of bioturbation intensity and mixed depth of marine soft sediments, *Aquat. Biol.*, *2*, 207–218.
Thullner, M., A. W. Dale, and P. Regnier (2009), Global-scale quantification of mineralization pathways in marine sediments: A reaction-transport modeling approach, *Geochem. Geophys. Geosyst.*, *10*, Q10012, doi:10.1029/2009GC002484.
Van Cappellen, P., and Y. Wang (1996), Cycling of iron and manganese in surface sediments: A general theory for the coupled transport and reaction of carbon, oxygen, nitrogen, sulfur, iron, and manganese, *Am. J. Sci.*, *296*, 197–243.
Wang, Y., and P. Van Cappellen (1996), A multicomponent reactive transport model of early diagenesis: Application to redox cycling in coastal marine sediments, *Geochim. Cosmochim. Acta*, *60*, 2993–3014.

Weber, K. A., L. A. Achenbach, and J. D. Coates (2006), Microorganisms pumping iron: Anaerobic microbial iron oxidation and reduction, *Nat. Rev. Microbiol.*, *4*, 752–764.

Westrich, J. T., and R. A. Berner (1984), The role of sedimentary organic matter in bacterial sulfate reduction: The G-model tested, *Limnol. Oceanogr.*, *29*, 236–249.

Wu, J., and E. Boyle (2002), Implications for the processes controlling dissolved Fe distribution in the ocean, *Global Biogeochem. Cycles*, *16*(4), 1086, doi:10.1029/2001GB001453.

Global Biogeochemical Cycles

Supporting Information for

A revised global estimate of dissolved iron fluxes from marine sediments

A. W. Dale, L. Nickelsen, F. Scholz, C. Hensen, A. Oschlies, K. Wallmann

GEOMAR Helmholtz Centre for Ocean Research Kiel, Kiel, Germany

Contents of this file

Introduction

This Supplement describes the numerical model used to simulate the biogeochemical dynamics in marine sediments.

Text S1.

A numerical reaction-transport model for quantifying benthic fluxes

This text describes the numerical model used to simulate the biogeochemical dynamics in marine sediments. Section 1.1 describes the basic model architecture including the transport processes; Section 1.2 describes the biogeochemical reaction network; Section 1.3 presents the POC degradation kinetics; Section 1.4 presents details on the boundary conditions and model solution. The model has been published several times previously for specific steady and non-steady state applications (Dale et al., 2010; 2011; 2012; 2013).

1.1. Numerical framework

A vertically-resolved 1-D reaction-transport model (RTM) was used to simulate the distribution of the chemical species listed in Table S1 in the upper 30 cm of sediment.

The model includes the most important transport pathways of solid particles and interstitial fluids in sedimentary environments and simultaneously accounts for production and consumption of chemical species by biogeochemical reactions. Mathematically, these processes can be summarized as the following mass-conservation equations (Berner, 1980; Boudreau, 1997):

$$\varphi \frac{\partial C_a(z,t)}{\partial t} = \frac{\partial}{\partial z}\left(\varphi D \frac{\partial C_a(z,t)}{\partial z}\right) - \frac{\partial \varphi v_a C_a(z,t)}{\partial z} + \alpha\varphi\left(C_a(0,t) - \mathrm{C_a}(z,t)\right) + \Sigma\varphi R(z,t) \qquad (1a)$$

$$(1-\varphi)\frac{\partial \mathrm{C_s}(z,t)}{\partial t} = \frac{\partial}{\partial z}\left((1-\varphi) D_b \frac{\partial C_s(z,t)}{\partial z}\right) - \frac{\partial (1-\varphi) v_s C_s(z,t)}{\partial z} + \Sigma(1-\varphi)R(z,t) \qquad (1b)$$

where $C_a(z,t)$ and $C_s(z,t)$ are the concentrations of solutes in mmol cm^{-3} (of pore water) and particulate species in weight percent of dry sediment (%), respectively, z (cm) denotes depth in the sediment, t (yr) is time, φ is porosity, v_a (cm yr^{-1}) and v_s (cm yr^{-1}) are the burial velocities of porewater and solids, respectively, D (cm^2 yr^{-1}) is the sedimentary molecular diffusion coefficient, D_b (cm^2 yr^{-1}) is the bioturbation coefficient representing sediment mixing by animals, α (y^{-1}) is the bioirrigation coefficient for solutes and $C_a(0,t)$ is the solute concentration at the sediment-water interface. ΣR is the sum of the rate of change of concentration due to biogeochemical reactions. Constitutive equations describing the depth dependency of φ, D, v_s, v_a, D_b, and α are provided in Table S2. Corresponding model parameters are listed in Table S3 and Table 2 in the main text.

Porosity describes the volume of porewater relative to the volume of total sediment. Similarly, the solid components of the sediment occupy a volume fraction equal to 1-φ. Porosity generally decreases with depth in the sediment due to steady state compaction (Berner, 1980). The function for porosity used in the model is based on the widely observed exponential decrease with sediment depth (Berner, 1980).

Molecular diffusion coefficients for solutes in seawater, D_W (cm^2 y^{-1}), were calculated using data provided by Boudreau (1997) and Schulz (2000) for the relevant temperature and salinity. In situ diffusion coefficients of each dissolved species, D, were further corrected for tortuosity (Boudreau, 1997). This phenomenon accounts for the longer path length for solutes to diffuse around particles in sediments.

Relative to the sea floor, both solids and solutes are advected downwards due to accumulation of new sediment at the surface. However, as a result of compaction, pore fluids are expelled upwards relative to the sediment particles. Equations for the burial velocity of solutes and solids (Table S2) were taken from Berner (1980).

Bioturbation, the stirring of the sediment by animals, is assumed not to affect porosity gradients (i.e. intraphase mixing; Boudreau, 1986). Bioturbation was formulated as a diffusive process where the mixing rate at the sediment surface is defined by the coefficient $D_b(0)$ (cm^2 yr^{-1}). With increasing sediment depth, bioturbation becomes less intense, reflecting the overall decrease in metazoan abundance. This change in bioturbation intensity with sediment is described using a Gaussian-type function, where the parameter z_{bt} (cm) is the bioturbation halving depth (Boudreau, 1996).

Burrowing macrofauna that build and live inside tube-like structures ventilate their burrows by pumping seawater through and around their bodies. This process, termed bioirrigation, leads to a rapid exchange of porewater and seawater and reduced concentration gradients of solutes between the sediment and overlying water column (Aller and Aller, 1998). Bioirrigation, like bioturbation, tends to be highest on the continental margins where food availability is higher (Glud et al., 1994; Meile and van Cappellen, 2003). Bioirrigation was described as a non-local 1-D mixing process whose rate depends on the difference in solute concentration between the water column and sediment (Table S2). Irrigation intensity at the sediment surface is defined by the parameter $\alpha(0)$ (yr^{-1}). Irrigation decreases with sediment depth following a simple exponential function with an attenuation coefficient, z_{bio} (cm) (Martin and Banta, 1992).

1.2. Biogeochemical reactions

The set of coupled biogeochemical reactions included in the model (Table S4) is similar to those published previously (e.g. Dhakar and Burdige, 1996; Van Cappellen and Wang, 1996; Berg et al., 2003). In this study, 12 solutes and 13 solid species were considered (Table S1). The cycling of chemical elements is ultimately driven by the mineralization of organic matter (OM) by microorganisms using specific electron acceptors (e.g. O_2, NO_2^-, NO_3^-, Mn^{IV}, Fe^{III}, SO_4^{2-}). OM is chemically defined as $CN_{rNC}P_{rPC}$ with a carbon oxidation state of zero and where r_{NC} and r_{PC} are the (Redfield) atomic ratios of particulate organic nitrogen and phosphorus to carbon in this material. Electron acceptors are mainly delivered to the sediment from the overlying water column but may also, with the exception of O_2 in the absence of benthic photosynthesis, be produced in situ by re-oxidation of their reduced forms. The order in which the electron acceptors are consumed broadly reflects the Gibbs energy yield per mole of carbon respired (Froelich et al., 1979). Accordingly, OM is first mineralized by aerobic respiration, followed by denitrification, manganese oxide reduction, iron oxide reduction, sulfate reduction and methanogenesis (Table S5). This sequence is maintained in the model through the use of dimensionless limitation terms based on the availability of electron acceptors (e.g. Berner, 1980; Boudreau, 1997). In contrast to the previous models listed above, ours includes nitrite as an additional electron acceptor. This step was taken since it provides a more realistic description of the N cycle (Bohlen et al., 2011). OM degradation kinetics is described separately in the following section.

The metabolic (dissolved) end products of OM degradation are free to be exported from the sediment or take part in secondary redox reactions. These reactions largely follow Van Cappellen and Wang (1996), Berg et al. (2003) and Dale et al. (2009). In keeping with common practice, the rates of these processes are generally described as first- or second-order rates expressions (Table S5). Kinetic constants were also taken from those studies (Table S3). Main differences between our model and previous versions mainly relate to N and Fe cycling. Firstly, our model considers a more complete N cycle, including dissimilatory nitrate reduction to ammonium (DNRA, R_8) and anaerobic ammonium oxidation (anammox, R_9). DNRA mainly occurs in sediments underlying near-anoxic bottom water (e.g. Otte et al., 1999). In this study, we set this reaction to zero in the standard shelf and slope model simulations since these regions comprise much less than 1 % of the continental margin area (Bohlen et al., 2012). Nitrate

can be produced and consumed by several reactions including denitrification (R_2, R_3) and nitrification (R_{10}, R_{11}) and anammox. Nitrate can also be denitrified by reaction with ferrous iron (R_{14}) (Dhakar and Burdige, 1996). Kinetic constants for the N cycle were mainly taken the empirical model study of Bohlen et al. (2011).

The reactivity of iron (oxyhydr)oxides (hereafter Fe oxides) was defined according to the widely-employed classification based on wet chemical extraction methods (Canfield et al., 1992; Raiswell and Canfield, 1998; Poulton et al., 2004). These studies have shown that reactive Fe oxides can be broadly defined as being highly reactive (Fe_{HR}), moderately reactive (Fe_{MR}) or poorly reactive (Fe_{PR}). Fe_{HR} has a half-life of < 1 yr and represents iron contained within amorphous and reactive crystalline oxides (ferrihydrite, goethite, lepidocrocite and hematite), pyrite and acid volatile sulfides, plus a small fraction of iron in reactive silicates (Canfield et al., 1992; Raiswell and Canfield, 1998). Fe_{PR} has a half-life of at least 10^5 yr and represents iron released from a wide range of reactive silicates and magnetite. Fe_{MR} comprises all the iron with a reactivity intermediate between Fe_{HR} and Fe_{PR} (i.e. magnetite and reactive silicates) with a half life of 10^2 yr. An additional detrital iron fraction, representing Fe bound within sheet silicates (Fe_U), is essentially unreactive on early diagenetic time scales and constitutes about half of all sedimentary iron underlying oxic waters (Poulton and Raiswell, 2002). The model simulates all four of these fractions, defined chemically as $Fe(OH)_3$. Similarly, two pools of manganese oxide were considered: Mn_{HR} and Mn_{MR} (Berg et al., 2003).

Particulate Fe was added to the sediment by deposition from the water column. Fe_{HR} can be also produced authigenically via the aerobic oxidation of ferrous iron that diffuses into the surface oxidized zone from the underlying anaerobic layers. This process is the most efficient geochemical barrier to ferrous iron release from the sediment (McManus et al., 1997; Berg et al., 2003). The rate was parameterized using a linear dependency on Fe^{2+} and O_2 concentrations (Millero et al., 1987). We also allow oxidation of Fe^{2+} to occur using Mn(IV) and, as mentioned, NO_3^-, as the electron acceptor. All fractions (except Fe_U) can be reduced by porewater sulfide according to the reaction kinetics proposed by Poulton et al. (2004), leading to production of dissolved ferrous iron and particulate elemental sulfur, S^0. The rate of iron reduction is linearly dependent on the iron concentration and shows a square root dependence on sulfide concentration (Table S5). The rate constants for these reactions were defined based on the half-lives listed above assuming a 1 mM sulfide concentration (see also Poulton et al. (2004)). This equates to rate constants which are broadly definable as 100, 0.1 and 0.0003 $L^{0.5}$ $mol^{-0.5}$ yr^{-1} for Fe_{HR}, Fe_{MR} and Fe_{PR}, respectively. Previous approaches considered only the total iron concentration with a single bulk reactivity (Van Cappellen and Wang, 1996; Berg et al., 2003). Fe_{HR} has an additional sink due to dissimilatory iron reduction (DIR), whereas the other phases are too crystalline (unreactive) to be of benefit to iron reducing bacteria (Weber, et al., 2006). Fe_{HR} also slowly undergoes preservation or ageing into more crystallization phases such as goethite and hematite (Lijklema, 1980; Cornell and Schwertmann, 1996). This is conceptualized in the model by transformation to Fe_{MR}. In a study on the Arctic shelf, the ageing half-life of Fe_{HR} was calculated to be 0.7 years (Berg et al., 2003). We use the same proportionality constant in our model, whilst noting that the ageing process is one of least well-constrained aspects of our model. Ageing of Mn_{HR} to Mn_{MR} is treated analogously. The iron module also includes iron mono-sulfide precipitation (R_{19}) and pyrite precipitation (R_{20}, R_{21}). The latter can occur via the H_2S

pathway (Berzelius reaction) or by reaction with S^0 (Bunsen reaction) (Rickard and Luther, 2007). Finally, molecular hydrogen produced by pyritization can be oxidized by all electron acceptors (EA), producing electron donors (ED, R_{22}). Including a sink for H_2 conserves electrons in the sediment (Meysman and Middelburg, 2005).

Iron carbonate (siderite) was not considered in the model since siderite precipitation is inhibited by low levels of sulfide (Haese, 2000). However, the precipitation of siderite is strongly dependent on the Eh-pH conditions, and co-precipitation of siderite and pyrite may occur simultaneously in micro-environments within the sediment matrix (Bell et al., 1987). Since our model does not resolve pH explicitly, and considering that siderite appears to be quantitatively unimportant in near-surface sediments in both marginal (Rajendran et al., 1992) and deep sea sediments environments (Ellwood et al., 1988), we have chosen to ignore siderite dynamics in the model.

1.3. Organic carbon degradation

1.3.1. Background

Mineralization of OM is arguably the most important process to parameterize correctly since the rate and depth at which it takes place will determine the proportion in which the electron acceptors are consumed and the rate at which reducing equivalents are produced. For instance, highly reactive OM with half life of days to weeks will tend to be respired by oxygen and nitrate in the upper oxidized layer. The consumption of electron acceptors will, therefore, be largely controlled by the amount and reactivity of organic matter at any given depth in the sediment, which is in turn controlled by the rate of sediment burial and mixing. A realistic simulation of the redox structure of the sediment thus requires sound definition of the degradation kinetics.

OM can be envisaged as a complex mixture of high molecular weight compounds. Because these compounds cannot be taken up by microbes directly, extracellular hydrolysis and fermentation is required to produce smaller, monomeric molecules such as sugars, amino acids and hydrogen (Megonigal et al., 2004). These steps are normally considered to determine the rate at which OM decay takes place (Arnosti, 2004) although thermodynamic limitations may also be important (LaRowe and Van Cappellen, 2011). Most model applications typically assume that bulk organic matter is present in discrete pools (often referred to as '*G'* fractions), each characterized by its own reactivity or first-order rate constant, *k*, with units of inverse time (e.g. Jørgensen, 1978; Westrich and Berner, 1984). In many cases, OM degradation has been described quantitatively using 1 to 3 reactive fractions (i.e. 'multi-*G*' model, reviewed by Regnier et al. (2011) and Arndt et al., 2013)). However, the degradation of OM in the upper few mm where reaction rates are highest are often poorly described due to a lack of sufficiently resolved data to constrain the highly reactive fractions.

An alternative approach to the multi-*G* model is based on the reactive continuum theory of OM degradation kinetics (Boudreau and Ruddick, 1991). Here, OM (hereafter POC to make carbon the point of reference) is assumed to be composed of an infinite number of fractions each with its own *k*. The apparent reactivity of POC is defined by the changing composition of the mass with time. Assuming first-order decay of each fraction,

the bulk POC sample is initially (at t = 0) distributed over k according to the Gamma distribution (Boudreau and Ruddick, 1991):

$$g(k,0) = \frac{g_0 \cdot k^{\nu-1} \cdot e^{-a \cdot k}}{\Gamma(\nu)} \tag{2}$$

where $g(k,0)$ is a probability density function (PDF) which determines the concentration of G described by a decay constant k at time zero, or more precisely the G concentration having a reactivity between k and k + dk where dk is an infinitesimal increment in k. In Eq. (2), Γ is the Gamma function, a (yr) is the average live time of the more reactive components of the mixture, and υ is a dimensionless parameter determining the shape of the distribution near k = 0. Low values of υ indicate that the bulk organic matter is dominated by refractory components clustered near k = 0, whereas higher values correspond to a more even distribution of reactive types. Similarly, organic matter characterized by low a will be rapidly degraded and vice-versa.

The Gamma function satisfies the following relation:

$$\Gamma(\nu) = \int_0^\infty x^{\nu-1} \cdot e^{-x} dx \tag{3}$$

while g_0 is defined as (Boudreau and Ruddick, 1991):

$$g_0 = G(0) \cdot a^{\nu} \tag{4}$$

where $G(0)$ is the initial total concentration POC at t = 0. In a closed system (i.e. a non-mixed sediment), the initial Gamma distribution corresponds to a very simple $G(t)$ function (Boudreau and Ruddick, 1991):

$$G(t) = \frac{g_0}{(a+t)^{\nu}} = G(0) \cdot \left(\frac{a}{a+t} \right)^{\nu} \tag{5}$$

where $G(0)$ is the initial concentration of total POC and $G(t)$ defines the decrease of total POC over time (t). The POC degradation rate is defined as differential of $G(t)$ over time:

$$\frac{dG(t)}{dt} = -\frac{\nu \cdot g_0}{(a+t)^{\nu+1}} = -\frac{\nu \cdot G(0) \cdot a^{\nu}}{(a+t)^{\nu+1}} = -\nu \cdot (a+t)^{-1} \cdot G(t) \tag{6}$$

1.3.2. Approximation of reactive continuum model using multi-G kinetics

Reactive continuum-type models are useful to describe the down-core change in organic matter reactivity below the bioturbated zone but are very difficult to apply for bioturbated surface sediments since the age and reactivity of organic matter within the bioturbated zone are only poorly constrained (Boudreau and Ruddick, 1991; Meile and Van Cappellen, 2005; Middelburg, 1989; Rothman and Forney, 2007). Ages of reactive

tracers within the bioturbated zone depend not only on burial velocity and bioturbation rate but also on the reactivity of the tracer (Meile and Van Cappellen, 2005). So far, POC ages in bioturbated sediments have only been determined assuming simple first-order degradation kinetics (Meile and Van Cappellen, 2005). POC ages determined using reactive continuum models are virtually unknown. Furthermore, reactive POC fractions may be preferentially taken up and displaced by benthic macro-fauna within the bioturbated layer (Smith et al., 1993).

We used a multi-*G* model to simulate the continuum model in bioturbated sediments where POC was represented by a finite number of different fractions each having their own first-order decay constant, *k*. The multi-G model was constructed applying the Gamma distribution. For $a > 0$ and $k > 0$:

$$f(k,0) = \frac{a^{\nu} \cdot k^{\nu-1} \cdot e^{-a \cdot k}}{\Gamma(\nu)} \tag{7}$$

where $f(k,0)$ is a PDF which determines the fraction of POC having a reactivity of k at time zero. The corresponding cumulative distribution function (CDF) is defined as:

$$F(k,0) = \frac{\Gamma(\nu,0,a \cdot k)}{\Gamma(\nu)} = \frac{\int_0^{a \cdot k} x^{\nu-1} \cdot e^{-x} dx}{\int_0^{\infty} x^{\nu-1} \cdot e^{-x} dx} \tag{8}$$

where $F(k,0)$ gives the fraction of total POC having a reactivity $\leq k$ at $t = 0$. A 14-G model was constructed by separating POC into 14 different species. The fraction of total POC having the kinetic constant $k_i = 10^{-i+1/2}$ yr^{-1} for given values of a and υ was calculated as:

$$F_i(k_i,0) = \frac{\Gamma(\nu,0,a \cdot k_{i+1}) - \Gamma(\nu,0,a \cdot k_i)}{\Gamma(\nu)} = \frac{\int_0^{a \cdot k_{i+1}} x^{\nu-1} \cdot e^{-x} dx - \int_0^{a \cdot k_i} x^{\nu-1} \cdot e^{-x} dx}{\int_0^{\infty} x^{\nu-1} \cdot e^{-x} dx} \tag{9}$$

for i = -10 to +1.

The low-reactivity fraction with a kinetic constant $k \leq 10^{-10}$ yr^{-1} was calculated from the CDF as:

$$F_i(10^{-10},0) = \int_0^{a \cdot 10^{-10}} x^{\nu-1} \cdot e^{-x} dx \tag{10}$$

The high reactivity fraction with a kinetic constant $k \geq 100$ yr^{-1} was calculated as:

$$F_i(100,0) = \frac{\int_0^{a \cdot \infty} x^{\nu-1} \cdot e^{-x} dx - \int_0^{a \cdot 100} x^{\nu-1} \cdot e^{-x} dx}{\int_0^{\infty} x^{\nu-1} \cdot e^{-x} dx} \tag{11}$$

Values of a (3×10^{-4} yr^{-1}) and υ (0.125) were calculated by Boudreau et al. (2008) using data from an experiment where fresh phytoplankton was degraded over a 2 yr period (Westrich and Berner, 1984). The POC fractions and kinetic constants that define these Gamma distribution values are:

POC_1:	$k_1 = 1\times10^{-10}$ yr^{-1},	$F_1 = 0.021746$
POC_2:	$k_2 = 3.16\times10^{-10}$ yr^{-1},	$F_2 = 0.00725275$
POC_3:	$k_3 = 3.16\times10^{-9}$ yr^{-1},	$F_3 = 0.0096717$
POC_4:	$k_4 = 3.16\times10^{-8}$ yr^{-1},	$F_4 = 0.0128974$
POC_5:	$k_5 = 3.16\times10^{-7}$ yr^{-1},	$F_5 = 0.017199$
POC_6:	$k_6 = 3.16\times10^{-6}$ yr^{-1},	$F_6 = 0.0229352$
POC_7:	$k_7 = 3.16\times10^{-5}$ yr^{-1},	$F_7 = 0.0305846$
POC_8:	$k_8 = 3.16\times10^{-4}$ yr^{-1},	$F_8 = 0.0407852$
POC_9:	$k_9 = 3.16\times10^{-3}$ yr^{-1},	$F_9 = 0.0543879$
POC_{10}:	$k_{10} = 0.0316$ yr^{-1},	$F_{10} = 0.0725265$
POC_{11}:	$k_{11} = 0.316$ yr^{-1},	$F_{11} = 0.0967046$
POC_{12}:	$k_{12} = 3.16$ yr^{-1},	$F_{12} = 0.12881$
POC_{13}:	$k_{13} = 31.6$ yr^{-1},	$F_{13} = 0.169822$
POC_{14}:	$k_{14} = 100$ yr^{-1},	$F_{14} = 0.314677$

where the fractions F_i add up to unity.

The multi-G model was tested in a batch set-up to compare the model performance with the analytical solution of the continuum model for the phytoplankton degradation experiment. The following system of initial conditions and ordinary differential equations defines the multi-G model in a batch set-up (no transport):

$$\sum_{i=1}^{14}\left(\mathrm{POC}_i(0) = F_i \cdot \mathrm{POC}_\mathrm{T}(0)\right) \qquad \sum_{i=1}^{14}\left(\frac{d\,\mathrm{POC}_i}{dt} = -k_i \cdot \mathrm{POC}_i\right) \qquad (12)$$

The analytical solution results as:

$$\mathrm{POC}_\mathrm{T} = \sum_{i=1}^{14}\left(F_i \cdot \mathrm{POC}_\mathrm{T}(0) \cdot e^{-k_i \cdot t}\right) \qquad (13)$$

where POC_T is the total POC concentration. This solution was tested against the analytical solution of the continuum model:

$$\mathrm{POC}_\mathrm{T} = \mathrm{POC}_\mathrm{T}(0) \cdot \left(\frac{a}{a+t}\right)^{\upsilon} \qquad (14)$$

with $a = 3\times10^{-4}$ yr^{-1}, $\upsilon = 0.125$, and $POC_T(0) = 13.3$ wt-%. Figure S1 shows that the results of the multi-G model (blue line) are consistent with the continuum model (red line). Only at $t < 0.05$ yr, a significant deviation occurs since the multi-G model does not resolve changes in reactivity for $k > 20$ yr^{-1}. The multi-G model based on 14 discrete

fractions is, however, a good approximation of the continuum model for the time period relevant for most bioturbated sediments (0.05 – 10 000 yr).

The 14-*G* model was implemented into the differential equation (Eq. 1) after defining values of a and υ. We used the above values of a and υ applicable to fresh phytoplankton in the simulations.

1.4. Model boundary conditions and solution

Robin type (constant flux) conditions were used for the solid species at the upper boundary (see Table S1 and Table 2 in main text). For solutes, a diffusive boundary layer of 0.04 cm thickness was assumed and implemented as described by Boudreau (1996). Dirichlet type (fixed concentration) boundary conditions were used for solutes in seawater, corresponding to mean oceanic values. At the lower boundary, all species were prescribed with a zero flux (Neumann) boundary condition. To solve the model, the continuous spatial derivatives in Eq. (1) were replaced with finite differences considering an unevenly spaced grid of 100 layers (Boudreau, 1997). The resulting set of ordinary differential equations was solved using the NDSolve algorithm in MATHEMATICA 7.0 using the method of lines (Boudreau, 1996). A high spatial resolution of 0.03 cm was used at the surface to minimize numerical errors in the layers where reaction rates are highest. At the base of the sediment, the grid thickness increased to 1.9 cm. A centered finite difference scheme was used for dissolved species and solid species within the bioturbated zone. An upward scheme was applied for the transport of solids below this depth to avoid numerical instabilities (Boudreau, 1996). The model was run using a long simulation time (10^4 yr) until steady-state conditions were achieved. Mass conservation for each species was checked by comparing depth-integrated reaction rates with fluxes across the model boundaries.

References

Aller, R. C., Aller, J. Y. (1998) The effect of biogenic irrigation intensity and solute exchange on diagenetic reaction rates in marine sediments. *J. Mar. Res.,* 56, 905-936.

Arndt, S., Jørgensen, B. B., LaRowe, D. E., Middelburg, J. J., Pancost, R. D., Regnier, P. (2013) Quantifying the degradation of organic matter in marine sediments: A review and synthesis. *Earth-Sci. Rev.*, 123, 53-86.

Arnosti, C. (2004) Speed bumps and barricades in the carbon cycle: substrate structural effects on carbon cycling. *Mar. Chem.*, 92, 263-273.

Bell, P. E., Mills, A. L., Herman, J. S. (1987) Biogeochemical conditions favoring magnetite formation during anaerobic iron reduction. *App. Environ. Microbiol.,* 53, 2610-2616.

Berg, P., Rysgaard, S., Thamdrup, B. (2003) Dynamic modeling of early diagenesis and nutrient cycling. A case study in an Arctic marine sediment. *Am. J. Sci.,* 303, 905-955.

Berner, R. A. (1980) Early Diagenesis: A Theoretical Approach, Princeton University Press, Princeton, 241 pp.

Bohlen, L., Dale, A. W., Sommer, S., Mosch, T., Hensen, C., Noffke, A., Scholz, F., Wallmann, K. (2011) Benthic nitrogen cycling traversing the Peruvian oxygen minimum zone. *Geochim. Cosmochim. Acta,* 75, 6094-6111.

Bohlen, L., Dale, A. W., Wallmann, K. (2012) Simple transfer functions for calculating benthic fixed nitrogen losses and C:N:P regeneration ratios in global biogeochemical models. *Glob. Biogeochem. Cy.*, 26, GB3029, doi:10.1029/2011GB004198.

Boudreau, B. P. (1986) Mathematics of tracer mixing in sediments; I, Spatially-dependent, diffusive mixing. *Am. J. Sci.*, 286, 161-198.

Boudreau, B. P. (1996) A method-of-lines code for carbon and nutrient diagenesis in aquatic sediments. *Comput. Geosci.*, 22, 479-496.

Boudreau, B. P. (1997) Diagenetic Models and Their Implementation: Modelling Transport and Reactions in Aquatic Sediments, Springer-Verlag, Berlin, 414 pp.

Boudreau, B. P., Ruddick, B. R. (1991) On a reactive continuum representation of organic matter diagenesis. *Am. J. Sci.*, 291, 507-538.

Canfield, D. E., Raiswell, R., Bottrell, S. (1992) The reactivity of sedimentary iron minerals toward sulfide. *Am. J. Sci.*, 292, 659-683.

Cornell, R. M., Schwertmann, U. (1996) The Iron Oxides: Structure, Properties, Reactions, Occurrences and Uses, Wiley-VCH, Darmstadt, Germany, 703 pp.

Dale, A. W., Brüchert, V., Alperin, M., Regnier, P. (2009) An integrated sulfur isotope model for Namibian shelf sediments. *Geochim. Cosmochim. Acta*, 73, 1924-1944.

Dale, A. W., Sommer, S., Haeckel, M., Wallmann, K., Linke, P., Wegener, G., Pfannkuche, O. (2010) Pathways and regulation of carbon, sulfur and energy transfer in marine sediments overlying methane gas hydrates on the Opouawe Bank (New Zealand). *Geochim. Cosmochim. Acta*, 74, 5763-5784.

Dale, A. W., Sommer, S., Bohlen, L., Treude, T., Bertics, V. J., Bange, H. W., Pfannkuche, O., Schorp, T., Mattsdotter, M., Wallmann, K. (2011) Rates and regulation of nitrogen cycling in seasonally hypoxic sediments during winter (Boknis Eck, SW Baltic Sea): sensitivity to environmental variables. *Estuar. Coast. Shelf Sci.*, 95, 14-28.

Dale, A. W., Meyers, S. R., Aguilera, D. R., Arndt, S., Wallmann, K. (2012) Controls on carbon and molybdenum accumulation rates in Cretaceous marine sediments from the Cenomanian-Turonian interval including Oceanic Anoxic Event 2. *Chem. Geol*., 324-325, doi:10.1016/j.chemgeo.2011.10.004.

Dale, A. W., Bertics, V. J., Treude, T., Sommer, S., Wallmann, K. (2013) Modeling benthic–pelagic nutrient exchange processes and porewater distributions in a seasonally hypoxic sediment: evidence for massive phosphate release by *Beggiatoa*? *Biogeosciences*, 10, 629-651, doi:10.5194/bg-10-629-2013.

Dhakar, S. P., Burdige, D. J. (1996) A coupled, non-linear, steady-state model for early diagenetic processes in pelagic sediments. *Am. J. Sci.*, 296, 296-330.

Ellwood, B. B., Chrzanowski, T. H., Frantisek Hrouda, F., Long, G. J., Buhl, M. L. (1988) Siderite formation in anoxic deep-sea sediments: A synergetic bacteria controlled process with improtant implications in paleomagnetism. *Geology*, 16, 980-982.

Froelich, P. N., Klinkhammer, G. P., Bender, M. L., Luedtke, N. A., Heath, G. R., Cullen, D., Dauphin, P. (1979) Early oxidation of organic matter in pelagic sediments of the eastern equatorial Atlantic: suboxic diagenesis. *Geochim. Cosmochim. Acta*, 43, 1075-1090.

Glasby, G. P. (2006) Manganese: Predominant role of nodules and crusts, in Marine Geochemistry 2nd edition, edited by H. D. Schulz and M. Zabel, pp 391-427, Springer-Verlag, Berlin.

Glud, R. N., Gundersen, J. K., Jorgensen, B. B., Revsbech, N. P., Schulz, H. D. (1994) Diffusive and total oxygen uptake of deep-sea sediments in the eastern South Atlantic Ocean: in situ and laboratory measurements. *Deep-Sea Res.,* II 41, 1767-1788.

Haese, R. R. (2000) The reactivity of iron, in Marine Geochemistry, edited by H. D. Schulz and M. Zabel, pp 233-261, Springer-Verlag, Berlin.

Jørgensen, B. B. (1978) A comparison of methods for the quantification of bacterial sulfate reduction in coastal marine sediments. II Calculation from mathematical models. *Geomicrobiol. J.*, 1, 29-47.

LaRowe, D. E., Van Cappellen, P. (2011) Degradation of natural organic matter: A thermodynamic analysis. *Geochim. Cosmochim. Acta* 75, 2030-2042.

Lijklema, L. (1980) Interaction of orthophosphate with iron(III) and aluminum hydroxides. *Environ. Sci. Technol.,* 14, 537-541. 1980.

Linke, P., Wallmann, K., Suess, E., Hensen, C., Rehder, G. (2005) In situ benthic fluxes from an intermittently active mud volcano at the Costa Rica convergent margin. *Earth Planet. Sci. Lett.* 235, 79-95.

Martin, W. R., Banta, G. T. (1992) The measurement of sediment irrigation rates: A comparison of the Br- tracer and 222Rn/226Ra disequilibrium techniques. *J. Mar. Res.*, 50, 125-154.

McManus, J., Berelson, W. M., Coale, K. H., Johnson, K. S., Kilgore, T. E. (1997) Phosphorus regeneration in continental margin sediments. *Geochim. Cosmochim. Acta,* 61, 2891-2907.

Megonigal, J.P., M.E. Hines, and P.T. Visscher. (2004) Anaerobic metabolism: Linkages to trace gases and aerobic processes, Biogeochemistry, edited by W. H. Schlesinger, pp 317-424, Elsevier-Pergamon, Oxford, UK.

Meile, C., Van Cappellen, P. (2003) Global estimates of enhanced solute transport in marine sediments. *Limnol. Oceanogr.*, 48, 777-786.

Meile, C., Van Cappellen, P. (2005) Particle age distributions and O_2 exposure times: Timescales in bioturbated sediments. *Glob. Biogeochem. Cy.,* 19, GB3013, doi:10.1029/2004GB002371.

Meile, C., Berg, P., Van Cappellen, P., Tuncay, K. (2005) Solute-specific pore water irrigation: Implications for chemical cycling in early diagenesis. *J. Mar. Res.,* 64, 601-621.

Meysman, F. J. R., Middelburg, J. J. (2005) Acid-volatile sulfide (AVS) — A comment. *Mar. Chem.,* 97, 202-212.

Middelburg, J. J. (1989) A simple rate model for organic matter decomposition in marine sediments. *Geochim. Cosmochim. Acta,* 53, 1577-1581.

Millero, F. J., Sotolongo, S., Izaguirre, M. (1987) The oxidation kinetics of Fe(II) in seawater. *Geochim. Cosmochim. Acta,* 51, 793-801.

Otte, S., Kuenen, J. G., Nielsen, L. P., Paerl, H. W., Zopfi, J., Schulz, H. N., Teske, A., Strotmann, B., Gallardo, V. A., Jørgensen, B. B. (1999) Nitrogen, carbon, and sulfur metabolism in natural Thioploca samples. *App. Environ. Microbiol.,* 65, 3148-3157.

Raiswell, R., Canfield, D. E. (1998) Sources of iron for pyrite formation in marine sediments. *Am. J. Sci.,* 298, 219-245.

Poulton, S. W., Raiswell, R. (2002) The low-temperature geochemical cycle of iron: From continental fluxes to marine sediment deposition. *Am. J. Sci.,* 302, 774-805.

Poulton, S. W., Krom, M. D., Raiswell, R. (2004) A revised scheme for the reactivity of iron (oxyhydr)oxide minerals towards dissolved sulfide. *Geochim. Cosmochim. Acta,* 68, 3703-3715.

Rajendran, A., Dileep Kumar, M., Bakker, J. F. (1992) Control of manganese and iron in Skagerrak sediments (northeastern North Sea). *Chem. Geol.,* 98, 111-129.

Redfield, A. C., Ketchum, B. H., Richards, F. A. (1963). The influence of organisms on the composition of seawater, in The Sea, edited by M. N. Hill, pp 26-77, Interscience, New York.

Regnier, P., Dale, A. W., Arndt, S., LaRowe, D. E., Mogollón, J. M., Van Cappellen, P. (2011) Quantitative analysis of anaerobic oxidation of methane (AOM) in marine sediments: A modelling perspective. *Earth-Sci. Rev.,* 106, 105-130.

Rickard, D., Luther III, G. W. (2007) Chemistry of iron sulfides. *Chem. Rev.,* 107, 514-562.

Rothman, D. H., Forney, D. C. (2007) Physical model for the decay and preservation of marine organic carbon. *Science,* 316, 1325-1328.

Schulz, H. D. (2000) Conceptual models and computer models, in Marine Geochemistry, edited by H. D. Schulz and M. Zabel, pp 417-442, Springer-Verlag, Berlin.

Smith, C. R., Pope, R. H., DeMaster, D. J., Magaard, L. (1993) Age-dependent mixing of deep-sea sediments. *Geochim. Cosmochim. Acta,* 57, 1473-1488.

Van Cappellen, P., Wang, Y. (1996) Cycling of iron and manganese in surface sediments: a general theory for the coupled transport and reaction of carbon, oxygen, nitrogen, sulfur, iron, and manganese. *Am. J. Sci.,* 296, 197-243.

Weber, K. A., Achenbach, L. A., Coates, J. D. (2006) Microorganisms pumping iron: anaerobic microbial iron oxidation and reduction. *Nat. Rev. Microbiol.,* 4, 752-764.

Westrich, J. T., Berner, R. A. (1984). The role of sedimentary organic matter in bacterial sulfate reduction: the G-model tested. *Limnol. Oceanogr.,* 29, 236-249.

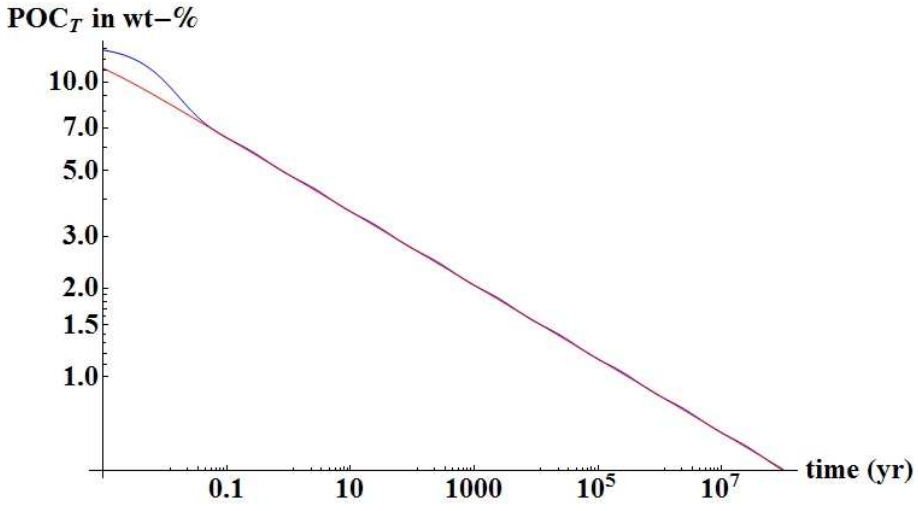

Figure S1. Comparison of analytical solutions of the 14-G model (blue line) and the continuum model (red line).

Variable	Value [a]
Solutes	
Oxygen (C_{O2}) [b]	Variable (see main text)
Nitrate (C_{NO3})	35×10^{-6}
Nitrite (C_{NO2})	0
Sulfate (C_{SO4})	28×10^{-3}
Ferrous iron (C_{Fe})	0
Manganese (C_{Mn})	0
Ammonium (C_{NH4})	1×10^{-6}
Total phosphate (C_{PO4})	2×10^{-6}
Total inorganic carbon (C_{TCO2})	2×10^{-3}
Total sulfide (C_{H2S})	0
Methane (C_{CH4})	0
Hydrogen (C_{H2})	0
Solids	
Organic carbon (F_{POC})	Variable (see main text)
Organic nitrogen (F_{POC})	$F_{POC}\cdot r_{NC}$
Organic phosphorus (F_{POP})	$F_{POC}\cdot r_{PC}$
Adsorbed ammonium (F_{NH4ads})	0
Total Fe oxide (F_{FeT})	Variable (see main text)
Highly reactive Fe oxide (F_{FeHR})	$F_{FeT} \times {}^{1}/_{6}$
Moderately reactive Fe oxide (F_{FeMR})	$F_{FeT} \times {}^{1}/_{6}$
Poorly reactive Fe oxide (F_{FePR})	$F_{FeT} \times {}^{1}/_{6}$
Unreactive Fe oxide (F_{FeU})	$F_{FeT} \times {}^{1}/_{2}$
Total Mn oxide (F_{MnT})	Variable [c]
Highly reactive Mn oxide (F_{MnHR})	$F_{MnT} \times {}^{1}/_{2}$
Moderately reactive Mn oxide (F_{MnMR})	$F_{MnT} \times {}^{1}/_{2}$
Elemental sulfur (F_{S})	0
Iron mono-sulfide (F_{FeS})	0
Pyrite (F_{FeS2})	0

[a] Zero flux (Neumann) conditions were prescribed for all variables at the lower boundary.
[b] Abbreviated to O_{2BW} in the main text.
[c] The flux of total manganese oxide was defined according to the bulk sedimentation rate assuming a 0.5 % Mn content (Glasby, 2006) in an analogous manner as described for Fe oxides in Table 2 (main text). This gives total fluxes of 187 and 30 μmol m^{-2} d^{-1} for shelf and slope settings, respectively, which are divided equally among Mn_{HR} and Mn_{MR}.

Table S1. Chemical species included in the model with corresponding boundary conditions at the sediment-water interface. Fixed seawater concentrations are defined for solutes (in mmol cm^{-3}) and constant fluxes to the seafloor for solids (in mmol cm^{-2} yr^{-1}).

Parameter	Equation
Porosity	$\varphi(z) = \varphi(L) + \left(\varphi(0) - \varphi(L)\right) \cdot \exp\left(-\frac{z}{z_{por}}\right)$
Diffusion coefficients	$D(z) = \frac{D_W}{1 - \ln(\varphi(z)^2)}$
Burial velocity of solids	$v_s(z) = \frac{\left(1 - \varphi(L)\right) \cdot \omega_{acc}}{\left(1 - \varphi(z)\right)}$
Burial velocity of solutes	$v_a(z) = \frac{\varphi(L) \cdot \omega_{acc}}{\varphi(z)}$
Bioturbation	$D_b(z) = D_b(0) \cdot \exp\left(-\frac{z^2}{2 \cdot {z_{bt}}^2}\right)$
Bioirrigation	$\alpha(z) = \alpha(0) \cdot \gamma \cdot \exp\left(-\frac{z}{z_{bio}}\right)$

Table S2. Depth–dependent constitutive equations used in the biogeochemical model.

Parameter	Description	Value	Unit	Source
L	Length of simulated sediment column	30	cm	1
S	Bottom water salinity	35	1	1
z_{dbl}	Diffusive boundary layer thickness	0.04	cm	2
ρ_s	Dry sediment density	2.5	g cm^{-3}	3
$\varphi(0)$	Porosity at 0 cm	0.9	1	1
$\varphi(L)$	Porosity at L cm	0.7	1	1
z_{por}	Porosity attenuation length	10	cm	1
z_{bt}	Bioturbation halving depth	3	cm	4
γ	Irrigation scaling coefficient for Fe^{2+}	0.2	1	5,9
γ	Irrigation scaling coefficient for other solutes	1	1	5
k_8	Rate constant for anaerobic oxidation of H_2S (DNRA)	0	M^{-1} yr^{-1}	1
k_9	Rate constant for anammox	1×10^8	M^{-1} yr^{-1}	6
k_{10}	Rate constant for aerobic oxidation of NH_4^+	1×10^7	M^{-1} yr^{-1}	6
k_{11}	Rate constant for aerobic oxidation of NO_2^-	1×10^7	M^{-1} yr^{-1}	6
k_{12}	Rate constant for aerobic oxidation of Mn^{2+}	5×10^6	M^{-1} yr^{-1}	3
k_{13}	Rate constant for aerobic oxidation of Fe^{2+}	5×10^8	M^{-1} yr^{-1}	3
k_{14}	Rate constant for anaerobic oxidation of Fe^{2+}	1×10^5	M^{-1} yr^{-1}	8
k_{15}	Rate constant for aerobic oxidation of H_2S	1×10^5	M^{-1} yr^{-1}	3
k_{16}	Rate constant for aerobic oxidation of FeS	1×10^5	M^{-1} yr^{-1}	3
k_{17}	Rate constant for aerobic oxidation of FeS_2	1×10^3	M^{-1} yr^{-1}	9
k_{18}	Rate constant for anaerobic oxidation of CH_4	1×10^5	yr^{-1}	10
k_{19}	Rate constant for FeS precipitation	1×10^6	M^{-1} yr^{-1}	9
k_{20}	Rate constant for FeS_2 precipitation	1×10^5	M^{-1} yr^{-1}	10
k_{21}	Rate constant for FeS_2 precipitation	1×10^5	M^{-1} yr^{-1}	10
k_{22}	Rate constant for H_2 oxidation	1×10^6	M^{-1} yr^{-1}	1
k_{23}	Rate constant for S^0 disproportionation	1	yr^{-1}	9
k_{24}	Rate constant for Mn_{HR} / Mn_{MR} reduction by Fe^{2+}	1×10^7 / 1×10^5	M^{-1} yr^{-1}	11
k_{25}	Rate constant for Mn_{HR} / Mn_{MR} reduction by H_2S	1×10^5 / 1×10^3	M^{-1} yr^{-1}	11
k_{26}	Rate constant for Fe_{HR} / Fe_{MR} / Fe_{PR} / Fe_U reduction by H_2S	100 / 0.1 / 3×10^{-4} / 0	$M^{-0.5}$ yr^{-1}	12
k_{27}	Rate constant for Mn_{HR} ageing to Mn_{MR}	1.7	yr^{-1}	9
k_{28}	Rate constant for Fe_{HR} ageing to Fe_{MR}	0.7	yr^{-1}	9
K_{O2}	Half–saturation constant for O_2 for OM degradation	1	µM	3
K_{NO3}	Half–saturation constant for NO_3^- for OM degradation	10	µM	3
K_{NO2}	Half–saturation constant for NO_2^- for OM degradation	10	µM	6
K_{Mn}	Half–saturation constant for Mn_{HR} for OM degradation	0.1	wt–%	3
K_{Fe}	Half–saturation constant for Fe_{HR} for OM degradation	0.6	wt–%	3
K_{SO4}	Half–saturation constant for SO_4^{2-} for OM degradation	0.5	mM	3
r_{PC}	Atomic P-C ratio in deposited organic matter	1/106	mol P (mol C)$^{-1}$	13
r_{NC}	Atomic N-C ratio in deposited organic matter	16/106	mol P (mol C)$^{-1}$	13
a	Average lifetime of the reactive POC components	3×10^{-4}	yr	14
υ	Shape of gamma distribution for POC mineralization	0.125	1	14

Parameter values were based on the following sources: 1. This study. 2. Linke et al. (2005). 3. Van Cappellen and Wang (1996). 4. Boudreau (1997). 5. Meile et al. (2005), Dale et al (2013). 6. Bohlen et al. (2011). 7. Dale et al. (2012). 8. Dhakar and Burdige (1996). 9. Berg et al. (2003). 10. Dale et al. (2009). 11. Ref. 3 gives values of 10^6 and 10^4 for k_{24} and k_{25}, respectively, which correspond to the bulk mineral reactivity. Values for the HR and MR fractions arbitrarily increased and decreased from these values by a factor of 10, respectively. 12. Canfield et al. (1992) and Poulton et al. (2004). 13. Redfield et al. (1963). 14. Boudreau et al. (2008)

Table S3. Fixed model parameters. Variable parameters for shelf and slope settings are listed in Table 2 in the main text.

Rate	Stoichiometry	Footnote
	Organic matter mineralization reactions	a
R_1	$CN_{rNC}P_{rPC} + O_2 \rightarrow TCO_2 + r_{NC}NH_4^+ + r_{PC}PO_4^{3-}$	
R_2	$CN_{rNC}P_{rPC} + 2NO_3^- \rightarrow 2NO_2^- + TCO_2 + r_{NC}NH_4^+ + r_{PC}PO_4^{3-}$	
R_3	$CN_{rNC}P_{rPC} + 1.33NO_2^- \rightarrow 0.66N_2 + TCO_2 + r_{NC}NH_4^+ + r_{PC}PO_4^{3-}$	
R_4	$CN_{rNC}P_{rPC} + 2Mn_j \rightarrow 2Mn^{2+} + TCO_2 + r_{NC}NH_4^+ + r_{PC}PO_4^{3-}$	b
R_5	$CN_{rNC}P_{rPC} + 4Fe_j \rightarrow 4Fe^{2+} + TCO_2 + r_{NC}NH_4^+$	b
R_6	$CN_{rNC}P_{rPC} + 0.5SO_4^{2-} \rightarrow 0.5H_2S + TCO_2 + r_{NC}NH_4^+ + r_{PC}PO_4^{3-}$	
R_7	$CN_{rNC}P_{rPC} \rightarrow 0.5CH_4 + 0.5TCO_2 + r_{NC}NH_4^+ + r_{PC}PO_4^{3-}$	
	Secondary redox reactions	a
R_8	$H_2S + NO_3^-{}_{bac} \rightarrow SO_4^{2-} + NH_4^+$	
R_9	$NH_4^+ + NO_2^- \rightarrow N_2$	
R_{10}	$NH_4^+ + 1.5O_2 \rightarrow NO_2^-$	
R_{11}	$NO_2^- + 0.5O_2 \rightarrow NO_3^-$	
R_{12}	$Mn^{2+} + 0.5O_2 \rightarrow Mn_j$	b
R_{13}	$Fe^{2+} + 0.25O_2 \rightarrow Fe_j$	b
R_{14}	$Fe^{2+} + 0.2NO_3^- \rightarrow Fe_j + 0.1N_2$	b
R_{15}	$H_2S + 2O_2 \rightarrow SO_4^{2-}$	
R_{16}	$FeS + 2O_2 \rightarrow Fe^{2+} + SO_4^{2-}$	
R_{17}	$FeS_2 + 3.5O_2 \rightarrow Fe^{2+} + 2SO_4^{2-}$	
R_{18}	$CH_4 + SO_4^{2-} \rightarrow H_2S$	
R_{19}	$Fe^{2+} + H_2S \rightarrow FeS$	
R_{20}	$FeS + H_2S \rightarrow FeS + H_2$	
R_{21}	$FeS + S^0 \rightarrow FeS_2$	
R_{22}	$H_2 + EA \rightarrow ED$	c
R_{23}	$S^0 \rightarrow 0.25SO_4^{2-} + 0.75H_2S$	
R_{24}	$Mn_j + 2Fe^{2+} \rightarrow 2Fe_{HR} + Mn^{2+}$	d
R_{25}	$Mn_j + H_2S \rightarrow S^0 + Mn^{2+}$	d
R_{26}	$Fe_j + 0.5H_2S \rightarrow S^0 + Fe^{2+}$	e
R_{27}	$Mn_{HR} \rightarrow Mn_{MR}$	
R_{28}	$Fe_{HR} \rightarrow Fe_{MR}$	

[a] For clarity, H_2O is omitted from the reactions and they are not proton balanced. Particulate iron (Fe_j) and manganese oxides (Mn_j) are chemically defined as $Fe(OH)_3$ and MnO_2, respectively.
[b] For j = HR.
[c] Oxidation of H_2 is permitted by all electron acceptors, EA (O_2, NO_3^-, NO_2^-, Mn_{HR}, Fe_{HR} and SO_4^{2-}), leading to the formation of electron donors, ED (N_2, Mn^{2+}, Fe^{2+} and H_2S).
[d] For j = HR, MR.
[e] For j = HR, MR and PR.

Table S4. Reactions considered in the biogeochemical model.

Rate	Rate expression [a]	Unit [b]
R_1	$\sum_{i=1}^{14} k_i \cdot \mathrm{POC}_i \cdot f_{K-\mathrm{O_2}}$	mmol C cm^{-3} yr^{-1}
R_2	$\sum_{i=1}^{14} k_i \cdot \mathrm{POC}_i \cdot \prod_{i=\mathrm{O_2,NO_2}}(1 - f_{K-i})$	mmol C cm^{-3} yr^{-1}
R_3	$\sum_{i=1}^{14} k_i \cdot \mathrm{POC}_i \cdot \prod_{i=\mathrm{O_2}}(1 - f_{K-i})$	mmol C cm^{-3} yr^{-1}
R_4	$\sum_{i=1}^{14} k_i \cdot \mathrm{POC}_i \cdot \prod_{i=\mathrm{O_2,NO_2,NO_3}}(1 - f_{K-i})$	mmol C cm^{-3} yr^{-1}
R_5	$\sum_{i=1}^{14} k_i \cdot \mathrm{POC}_i \cdot \prod_{i=\mathrm{O_2,NO_2,NO_3,Mn_{HR}}}(1 - f_{K-i})$	mmol C cm^{-3} yr^{-1}
R_6	$\sum_{i=1}^{14} k_i \cdot \mathrm{POC}_i \cdot \prod_{i=\mathrm{O_2,NO_2,NO_3,Mn_{HR},Fe_{HR}}}(1 - f_{K-i})$	mmol C cm^{-3} yr^{-1}
R_7	$\sum_{i=1}^{14} k_i \cdot \mathrm{POC}_i \cdot \prod_{i=\mathrm{O_2,NO_2,NO_3,Mn_{HR},Fe_{HR},SO_4}}(1 - f_{K-i})$	mmol C cm^{-3} yr^{-1}
R_8	$k_8 \cdot \mathrm{NO_3^-}_{\mathrm{bac}} \cdot \mathrm{H_2S}$	mmol N cm^{-3} yr^{-1}
R_9	$k_9 \cdot \mathrm{NO_2^-} \cdot \mathrm{NH_4^+}$	mmol N_2 cm^{-3} yr^{-1}
R_{10}	$k_{10} \cdot \mathrm{O_2} \cdot \mathrm{NH_4^+}$	mmol N cm^{-3} yr^{-1}
R_{11}	$k_{11} \cdot \mathrm{O_2} \cdot \mathrm{NO_2^-}$	mmol N cm^{-3} yr^{-1}
R_{12}	$k_{12} \cdot \mathrm{O_2} \cdot \mathrm{Mn^{2+}}$	mmol Mn cm^{-3} yr^{-1}
R_{13}	$k_{13} \cdot \mathrm{O_2} \cdot \mathrm{Fe^{2+}}$	mmol Fe cm^{-3} yr^{-1}
R_{14}	$k_{14} \cdot \mathrm{NO_3^-} \cdot \mathrm{Fe^{2+}}$	mmol Fe cm^{-3} yr^{-1}
R_{15}	$k_{15} \cdot \mathrm{O_2} \cdot \mathrm{H_2S}$	mmol S cm^{-3} yr^{-1}
R_{16}	$k_{16} \cdot \mathrm{O_2} \cdot \mathrm{FeS}$	mmol Fe cm^{-3} yr^{-1}
R_{17}	$k_{17} \cdot \mathrm{O_2} \cdot \mathrm{FeS_2}$	mmol Fe cm^{-3} yr^{-1}
R_{18}	$k_{18} \cdot \mathrm{CH_4} \cdot \mathrm{f_{SO4}}$	mmol C cm^{-3} yr^{-1}
R_{19}	$k_{19} \cdot \mathrm{Fe^{2+}} \cdot \mathrm{H_2S}$	mmol Fe cm^{-3} yr^{-1}
R_{20}	$k_{20} \cdot \mathrm{FeS} \cdot \mathrm{H_2S}$	mmol Fe cm^{-3} yr^{-1}
R_{21}	$k_{21} \cdot \mathrm{FeS} \cdot \mathrm{S^0}$	mmol Fe cm^{-3} yr^{-1}
R_{22}	$k_{22} \cdot \mathrm{H_2} \cdot \mathrm{EA}$	mmol EA cm^{-3} yr^{-1}
R_{23}	$k_{23} \cdot \mathrm{S^0}$	mmol S cm^{-3} yr^{-1}
R_{24}	$k_{24\text{-}j} \cdot \mathrm{Mn_j} \cdot \mathrm{Fe^{2+}}$	mmol Mn cm^{-3} yr^{-1}
R_{25}	$k_{25\text{-}j} \cdot \mathrm{Mn_j} \cdot \mathrm{H_2S}$	mmol Mn cm^{-3} yr^{-1}
R_{26}	$k_{26\text{-}j} \cdot \mathrm{Fe_j} \cdot \mathrm{H_2S^{0.5}}$	mmol Fe cm^{-3} yr^{-1}
R_{27}	$k_{27} \cdot \mathrm{Mn_{HR}}$	mmol Mn cm^{-3} yr^{-1}
R_{28}	$k_{286} \cdot \mathrm{Fe_{HR}}$	mmol Fe cm^{-3} yr^{-1}

[a] Kinetic limiting terms: $f_{K-i} = \frac{[i]}{[i]+K_i}$, where K_i is the half–saturation constant for species *i*.

[b] Refers to cm^{-3} of pore fluid. The factor $f = \frac{100\ \% \cdot \mathrm{A_W} \cdot \varphi(z)}{\frac{10^3 \mathrm{mmol}}{\mathrm{mol}} \cdot \rho_s \cdot (1-\varphi(z))}$ converts between wt % and mmol cm^{-3}, where $\mathrm{A_W}$ (g mol^{-1}) is the standard atomic weight of the element in question and ρ_s (2.5 g cm^{-3}) is the dry sediment density.

Table S5. Rate expressions and units.

Earth and Planetary Science Letters 454 (2016) 272–281

Contents lists available at ScienceDirect

Earth and Planetary Science Letters

www.elsevier.com/locate/epsl

Nitrate-dependent iron oxidation limits iron transport in anoxic ocean regions

Florian Scholz [a,*], Carolin R. Löscher [a,1], Annika Fiskal [a], Stefan Sommer [a], Christian Hensen [a], Ulrike Lomnitz [a], Kathrin Wuttig [a,b], Jörg Göttlicher [c], Elke Kossel [a], Ralph Steininger [c], Donald E. Canfield [d]

[a] GEOMAR Helmholtz Centre for Ocean Research Kiel, Wischhofstraße 1-3, 24148 Kiel, Germany
[b] Antarctic Climate and Ecosystems Cooperative Research Centre (ACE CRC), University of Tasmania, Private Bag 80, Hobart Tasmania 7001, Australia
[c] Institute for Photon Science and Synchrotron Radiation, Karlsruhe Institute of Technology, 76344 Eggenstein-Leopoldshafen, Germany
[d] Nordic Center for Earth Evolution (NordCEE), Institute of Biology, University of Southern Denmark, 5230 Odense, Denmark

ARTICLE INFO

Article history:
Received 15 July 2016
Received in revised form 9 September 2016
Accepted 13 September 2016
Available online 3 October 2016
Editor: D. Vance

Keywords:
iron (II) oxidation
nitrate reduction
oxygen minimum zone
anoxic marine sediment
X-ray absorption spectroscopy

ABSTRACT

Iron is an essential element for life on Earth and limits primary production in large parts of the ocean. Oxygen-free continental margin sediments represent an important source of bioavailable iron to the ocean, yet little of the iron released from the seabed reaches the productive sea surface. Even in the anoxic water of oxygen minimum zones, where iron solubility should be enhanced, most of the iron is rapidly re-precipitated. To constrain the mechanism(s) of iron removal in anoxic ocean regions we explored the sediment and water in the oxygen minimum zone off Peru. During our sampling campaign the water column featured two distinct redox boundaries separating oxic from nitrate-reducing (i.e., nitrogenous) water and nitrogenous from weakly sulfidic water. The sulfidic water mass in contact with the shelf sediment contained elevated iron concentrations >300 nM. At the boundary between sulfidic and nitrogenous conditions, iron concentrations dropped sharply to <20 nM coincident with a maximum in particulate iron concentration. Within the iron gradient, we found an increased expression of the key functional marker gene for nitrate reduction (*narG*). Part of this upregulation was related to the activity of known iron-oxidizing bacteria. Collectively, our data suggest that iron oxidation and removal is induced by nitrate-reducing microbes, either enzymatically through anaerobic iron oxidation or by providing nitrite for an abiotic reaction. Given the important role that iron plays in nitrogen fixation, photosynthesis and respiration, nitrate-dependent iron oxidation likely represents a key-link between the marine biogeochemical cycles of nitrogen, oxygen and carbon.

1. Introduction

Metabolic processes that regulate carbon fixation in the surface ocean and export into the ocean interior (nitrogen fixation, photosynthesis and respiration) require bioavailable iron (Fe). In many ocean regions, the Fe supply is insufficient relative to the supply of the macronutrients nitrogen and phosphorous. Therefore, Fe availability is regarded one of the key-limiting factors for primary and export production in the ocean (Falkowski, 1997; Moore and Doney, 2007; Boyd and Ellwood, 2010). Traditionally, Fe supplied by atmospheric dust was considered the main source of bioavailable Fe to the ocean (Jickells et al., 2005). More recently, however, sedimentary processes have been highlighted as important in mobilizing and transferring Fe into the water column (Lam and Bishop, 2008; Lohan and Bruland, 2008; Severmann et al., 2010; Homoky et al., 2013; Scholz et al., 2014a; Dale et al., 2015). The highest sedimentary Fe fluxes have been recorded in oxygen-deficient ocean regions (oxygen minimum zones, OMZs) where reductive dissolution of ferric Fe (oxyhydr)oxide minerals, either by Fe-reducing bacteria or through reaction with hydrogen sulfide (H_2S), liberates dissolved ferrous Fe (Fe^{2+}) into the sediment pore water (Severmann et al., 2010; Noffke et al., 2012). Due to the absence of oxygen within the surface sediment, the mobilized Fe escapes re-oxidation and -precipitation as Fe (oxyhydr)oxide and may therefore diffuse across the sediment-water interface.

Whether sediment-derived Fe can support nitrogen fixation and primary production in the surface ocean critically depends on

* Corresponding author.
E-mail address: fscholz@geomar.de (F. Scholz).
[1] Present address: Nordic Center for Earth Evolution (NordCEE), Institute of Biology, University of Southern Denmark, 5230 Odense, Denmark.

http://dx.doi.org/10.1016/j.epsl.2016.09.025
0012-821X/

the extent of re-precipitation and demobilization during transport within the water column. The distribution of dissolved Fe concentrations in the water column overlying continental margin sediments suggests that most of the Fe discharged from the seabed is rapidly re-precipitated and thus prevented from reaching the surface ocean and becoming transported offshore (Lohan and Bruland, 2008; Bruland et al., 2005; Vedamati et al., 2014). According to current thinking, sediment-derived ferrous Fe is demobilized through re-oxidation with oxygen (O_2) to ferric Fe (Fe^{3+}) and precipitation of nanoparticulate or colloidal Fe (oxyhydr)oxides, followed by aggregation or scavenging by larger particles (Lohan and Bruland, 2008; Boyd and Ellwood, 2010). A small fraction of the sediment-derived Fe remains in solution as ferric Fe through complexation with organic ligands (Kondo and Moffett, 2015; Noble et al., 2012) or in suspension as colloids or nanoparticles (Raiswell and Canfield, 2012). This Fe fraction can be transported over longer distances within oxygenated seawater.

Fe oxidation with oxygen, either abiotically or microbially induced, is a viable explanation for rapid Fe removal in ocean regions where at least trace amounts of oxygen are present in the water column. However, this process cannot explain Fe removal from effectively anoxic waters columns such as the OMZs off Chile and Peru. Previous studies have reported total dissolved Fe (dFe) concentrations >100 nM (sum of dissolved Fe^{2+} and Fe^{3+}, with Fe^{2+} being dominant) in near-bottom waters overlying the Peruvian shelf (Hong and Kester, 1986; Bruland et al., 2005; Vedamati et al., 2014). Despite anoxia (<10 nM O_2) (Thamdrup et al., 2012) and pervasive sedimentary Fe release in this area of the Peru OMZ (Noffke et al., 2012; Scholz et al., 2014b), dFe concentrations in the water column rapidly decline offshore to a level that is typical for well-oxygenated, near-shore seawater (<5 nM dFe). As the zone of dFe removal is located well below the photic zone (e.g., <10 m in the water column overlying the Peruvian shelf), phototrophic Fe^{2+} oxidation (Widdel et al., 1993) can also be excluded as a mechanism of Fe removal.

It has recently been hypothesized that in the nitrate-containing OMZs of the contemporary ocean ferrous Fe is oxidized anaerobically with nitrate (Raiswell and Canfield, 2012). Anaerobic Fe oxidation with nitrate (NO_3^-) results in the production of nitrite (NO_2^-), nitrogenous gases (N_2O or N_2) or ammonium (NH_4^+) (Straub et al., 1996; Weber et al., 2006a; Carlson et al., 2013) and, depending on pH and ambient water chemistry, a variety of authigenic Fe minerals (Kappler et al., 2005; Miot et al, 2009; Pantke et al., 2012), e.g.:

$$2Fe^{2+} + NO_3^- + 5H_2O \rightarrow 2Fe(OH)_3 + NO_2^- + 4H^+ \quad (1)$$

$$6Fe^{2+} + 2NO_2^- + 14H_2O \rightarrow 6Fe(OH)_3 + N_2 + 10H^+ \quad (2)$$

If nitrite is present, e.g., from heterotrophic nitrate reduction, Fe oxidation with nitrite (Equation (2)) has also been shown to take place abiotically at circum-neutral pH, especially when reactive Fe (oxyhydr)oxide mineral surfaces are available to catalyze the reaction (Picardal, 2012; Klueglein and Kappler, 2013). Microbial and partly abiotic mechanisms by which ferrous Fe is oxidized with nitrate as the terminal electron acceptor are hereafter summarized under the term "nitrate-dependent Fe oxidation" (Carlson et al., 2013; Picardal, 2012; Klueglein and Kappler, 2013).

Nitrate-dependent Fe oxidation has been demonstrated in laboratory cultures (Straub et al., 1996) and in a variety of marine and freshwater sediments (Edwards et al., 2003; Weber et al., 2006b; Laufer et al., 2016). By contrast, direct evidence for nitrate-dependent Fe oxidation in the water column of the ocean is missing. Particularly in OMZs, nitrate-dependent Fe oxidation could represent a key-process in biogeochemical cycling. For instance, sediments underneath the Peru OMZ release high amounts of Fe into the anoxic water column (Noffke et al., 2012; Vedamati et al., 2014), yet primary production in the eastern equatorial Pacific high-nitrate-low-chlorophyll (HNLC) region off Peru has been shown to be Fe-limited (Hutchins et al., 2002). Moreover, much of the Fe released from Peru margin sediments is not transported offshore within the OMZ but re-deposited and buried close to its source (Scholz et al., 2014b). Nitrate-dependent Fe oxidation within the anoxic water column could be a meaningful explanation for both of these puzzling observations.

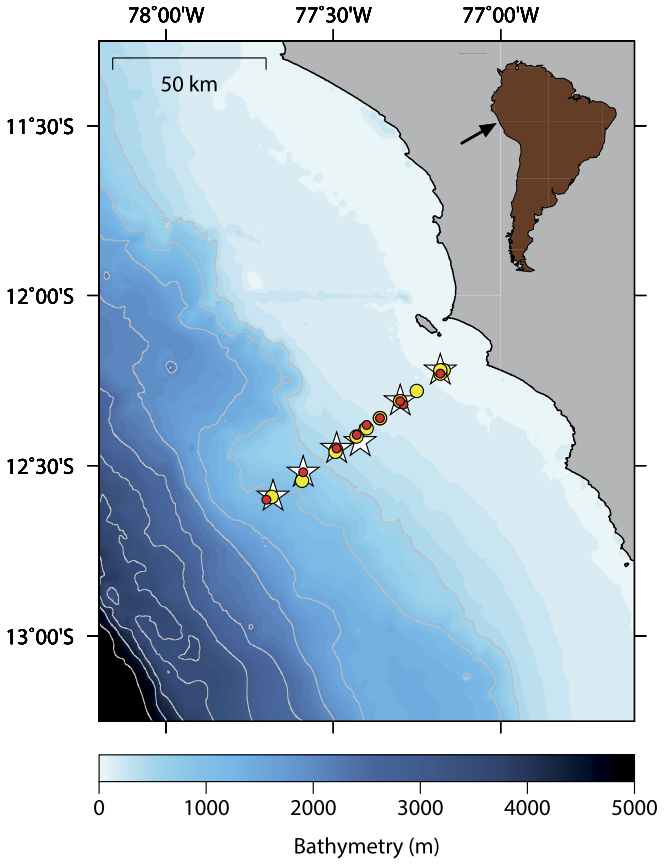

Fig. 1. Bathymetric map of the Peruvian continental margin (bathymetric data were taken from GEBCO). GO-FLO stations are depicted by red dots, CTD stations by yellow dots and MUC stations by white stars. The location of the study area off South America is indicated on the upper right side. The coordinates of all sampling stations are contained in the Electronic Supplement. (For interpretation of the references to color in this figure legend, the reader is referred to the web version of this article.)

Here, we report geochemical and metagenomic data for sediment, water and suspended particulate matter samples from the Peruvian continental margin. Collectively, these data provide evidence that nitrate-dependent Fe oxidation is an active process in OMZ waters, limiting the transport of sediment-derived Fe. Implications for nutrient cycling and redox dynamics in the ocean are discussed.

2. Methods

2.1. Sampling

Samples for this study were collected during the M92 cruise of research vessel Meteor in January 2013 (Fig. 1). Water samples for dissolved and particulate Fe analyses were collected using an array of six PTFE-coated 8 l GO-FLO bottles (General Oceanics) individually mounted on a Kevlar wire. Upon recovery the GO-FLO bottles were transferred to a laboratory and pressurized with nitrogen gas (0.2 bar). The water was filtered in-line through polyethersulfone filters (0.2 µm pore size, 47 mm diameter) (PALL Corporation) in a laminar flow bench. Prior to filtration the filters were cleaned

repeatedly with 1 M HCl and rinsed with deionized water. The filtered seawater was collected in acid-cleaned LDPE bottles and acidified with sub-boiled distilled HCl to pH <2. The filters were transferred to acid-cleaned Petri dishes and stored at −20 °C until further treatment in shore-based laboratories. Water and particulate matter samples for dissolved nutrient and metagenomic analyses were collected with a Seabird CTD rosette system. Up to 2 l of seawater were filtered through polyethersulfone filters (0.2 µm pore size, 47 mm) (Millipore). The filters were frozen and stored at −80 °C until nucleic acid extraction. Sediment and bottom water samples were retrieved with a multiple corer (MUC). Sediment subsampling was realized in an argon-filled glove bag. The pore water was separated from the sediment by centrifuging and filtered through cellulose acetate syringe filters (0.2 µm pore size).

2.2. Analysis of water samples

Dissolved total Fe concentrations were determined at GEOMAR (Kiel, Germany) by graphite furnace atomic absorption spectroscopy (Perkin Elmer 4100 ZL) after pre-concentration following a dithiocarbamate-freon extraction procedure (Danielsson et al., 1987). The accuracy and precision of the whole procedure were evaluated by including the seawater standard NASS-5 on a regular basis (measured value: 4.09 ± 0.49 nM, $n = 8$; certified value: 3.70 ± 0.63 nM) (Canadian Research Council). Concentrations of NO_3^- and NO_2^- were measured onboard using a QuAAtro AutoAnalyzer (SEAL Analytical) with a reproducibility of ±0.1 µM. Hydrogen sulfide concentrations ($\Sigma H_2S = H_2S + HS^- + S^{2-}$) were determined photometrically by applying the methylene blue method (Grasshoff et al., 1999). Reported O_2 concentrations were measured with the oxygen optode attached to the seabird CTD rosette system. The sensor was calibrated by titration according to Winkler with a theoretical detection limit of ∼2 µM O_2. However, comparison with highly oxygen-sensitive STOX sensors in previous studies revealed that the actual detection limit of the optode is of the order of less than 100 nM (Thamdrup et al., 2012). Bottom water and pore water Fe^{2+} concentrations were determined photometrically using the Ferrozine reagent (Stookey, 1970). The flux of Fe^{2+} across the sediment-bottom water interface was calculated according to Fick's 1st Law from the concentration difference between bottom water and uppermost pore water sample (0–0.5 cm) (see Electronic Supplement for details).

2.3. Analysis of particulate matter and sediment samples

To characterize the distribution and speciation of particulate Fe, X-ray fluorescence (XRF) and X-ray absorption spectroscopy analyses (XAS) were carried out at the SUL-X beamline at the Synchrotron Radiation Facility ANKA, Karlsruhe Institute of Technology. An exactly defined subsection (1/8) was cut from selected filters with a ceramic scalpel and a custom-built PTFE intake device with guiding grooves. Freeze-dried and disaggregated sediments were embedded in epoxy resin and ground down to a thickness of ∼100 µm. The filter subsections and sediment thin sections were attached to sample holders using adhesive or Kapton tape and installed in the vacuum chamber of the beamline. To minimize oxidation artifacts and mineral aging effects, the filters were unfrozen and subsampled on-site at the beamline shortly before the start of the X-ray experiments.

To gain an overview about the Fe distribution on the filters and thin sections, XRF maps of 1000 × 1000 µm^2 (26 × 26 pixels) were collected at an excitation energy of 9.5 keV. Visual inspection under the microscope revealed a fairly even distribution of particulate matter on the filters. Therefore, XRF mappings were conducted at random locations on the filter. For the XRF mapping of sediments, clusters of grains were located under the microscope. Because of highly variable Fe concentrations across the sample set, XRF maps were recorded at different distances between sample surface and fluorescence detector. For the recalculation of XRF counts to a common semi-quantitative concentration scale, a transfer function was derived by conducting a set of XRF measurements with variable detector distance on a single Fe-rich spot. The sum XRF spectra of individual maps were fit and background corrected using the open source program PyMCA (Solé et al., 2007). Examples for XRF Fe maps for suspended particulate matter and surface sediments are shown in Supplementary Fig. S1.

Following the XRF mapping (1 to 4 maps per sample), X-ray absorption near-edge structure (XANES) spectra across the Fe K-edge (7,010–7,575 eV) were recorded at selected spots with elevated Fe concentrations and within the matrix in between. The step sizes ranged from 0.3 eV across the absorption edge (7,090–7,0130 eV) up to 5 eV in the pre- and post-edge interval. A spectrum of elemental Fe was collected simultaneously with each sample spectrum for energy calibration. The mineralogy of the Fe on the analyzed spots was determined by fitting XANES reference spectra of pure Fe minerals to the sample spectra (linear combination fitting) (see Supplementary Fig. S1 for examples) using the software IFFEFIT (Ravel and Newville, 2005). Reference spectra for the following minerals were collected (Supplementary Fig. S2): ferryhydrite ($Fe_2O_3 \cdot 0.5H_2O$), goethite (α-FeO(OH)), hematite (α-Fe_2O_3), akaganeite (FeO(OH,Cl)), schwertmannite ($Fe_8O_8(OH)_6(SO_4) \cdot nH_2O$), magnetite ($Fe_3O_4$), glauconite (mixed ferrous/ferric clay mineral in marine sediments), smectite (pedogenic clay mineral), pyrite (FeS_2), pyrrhotite (FeS), vivianite ($Fe_3(PO_4)_2 \cdot 8H_2O$), siderite ($FeCO_3$), olivine ((Mg,Fe) SiO_4), pyroxene ((FeMg)(Si,Al)$_2O_6$), biotite $K(Mg,Fe)_3AlSi_3O_{10}(F,OH)_2$. All of the sample spectra could be fit with variable combinations of Fe (oxyhydr)oxide (ferrihydrite, goethite and hematite), primary silicate (olivine, biotite, pyroxene) and sulfide (pyrite) minerals, regardless of the Fe concentration. In a number of cases, the fits could be further improved by including the reference spectra of the mixed ferrous-ferric clay minerals glauconite and smectite. However, the significance of these fitting results are ambiguous as the spectra of glauconite and smectite themselves could be fit with a combination of Fe (oxyhydr)oxide and primary silicate minerals. We therefore decided not to report fitting results with mixed ferrous-ferric clay minerals. In addition to the linear combination fitting, the average oxidation state (fraction of ferric Fe, Fe(III)/ΣFe) of sample spots and reference compounds was determined from the centroid position of the pre-edge peak (Wilke et al., 2001; Lam and Bishop, 2008). Consistent with their theoretical stoichiometry, the Fe(III)/ΣFe of reference compounds was found to be either close to zero or one (except for the mixed ferrous-ferric compounds glauconite, smectite and magnetite). The Fe(III)/ΣFe of sample spots determined from the centroid position of the pre-edge peak were in good agreement with those obtained by summing up the fractions of individual ferrous and ferric minerals (see Supplementary Fig. S3).

To determine the concentration of Fe and Al in the solid phase, particulate matter samples were digested following the sampling and sample-handling protocols for GEOTRACES cruises (http://www.geotraces.org/science/intercalibration/222-sampling-and-sample-handling-protocols-for-geotraces-cruises). The filters were cut into halves with a ceramic scalpel and placed against the walls of acid-cleaned PTFE vials. An acid mixture consisting of 1 ml concentrated HNO_3 (sub-boiled distilled), 0.4 ml concentrated HF (Suprapur) and 0.6 ml deionized water was added. The capped PTFE vials were placed on a hotplate at 130 °C for refluxing. After 4 hours the digestion solution was evaporated to near dryness and 100 µl of HNO_3 was added to re-dissolve fluorides which may have precipitated during the digestion. The solution was then evaporated again to near dryness, re-dissolved in 3 ml 5% HNO_3

and heated to 60 °C for 4 hours. Finally, the digestion solutions were transferred to acid-cleaned HDPE vials and analyzed at GEOMAR by inductively coupled plasma optical emission spectrometry (ICP-OES, VARIAN 720-ES). Concentrations of Fe and Al in sediment samples were also measured by ICP-OES following total digestion in HNO_3 (sub-boiled distilled), HF (Suprapur) and $HClO_4$ (p.a.). For quality control, certified reference material MESS-3 (marine sediment, Canadian Research Council) and method blanks were included in the digestion and analysis procedures. The recovery for Fe and Al was $95 \pm 2.7\%$ relative to the certified values of MESS-3 (Fe: 4.34 ± 0.11 wt.%, Al: 8.59 ± 0.23 wt.%). Particulate Fe and Al concentrations in water samples were calculated by dividing the Fe and Al concentration per filter by the amount of seawater filtered (0.4–6 l). An additional correction factor (divided by 7/8) was applied for filters where a subsection had been removed for XRF and XANES analyses.

2.4. Metagenomic analysis

To characterize the composition and activity of the nitrate-reducing microbial community, we performed metagenomic analyses of the filtered material in near-bottom waters. DNA and RNA were purified using the Qiagen All prep DNA/RNA Kit (Qiagen) according to the manufacturer protocol. Potential DNA contaminations were removed from the RNA by a DNase treatment (DNaseI, Life Technologies) and the purity was checked using RNA-template controls in functional gene qPCRs (see below). cDNA libraries were generated using the Superscript II reverse transcription Kit (Life technologies, Carlsbad, Ca, USA).

To first assess the microbial diversity in near-bottom waters, a 16S rDNA amplicon sequencing was performed as a commercially available service (GATC, Konstanz, Germany) on a MiSeq Instrument using MiSeq reagent kit with V3 chemistry (Illumina). Primers 27F (AGAGTTTGATCCTGGCTCAG) and 534R (ATTACCGCGGCTGCT) were used to amplify the V1–V3 regions of 16S rDNA. The sequence processing was performed as described previously (Löscher et al., 2015) using a Mothur-based pipeline. In short, sequences were screened and contigs containing ambiguous bases, homopolymers longer than 8 bases or a length greater than 507 were deleted from the dataset followed by a de-replication step. Sequences were aligned against the SILVA database release 102. The alignment was optimized by removing sequences not aligning in the correct region. Redundant sequences were again removed, followed by a screening for chimeric sequences using the implemented software UCHIME. Classification of the remaining sequences was done using a modified version of the Greengenes database with a bootstrap threshold of 80%. Sequences were then filtered for archaea, chloroplasts and mitochondria which were removed from the data set. A sample by operational taxonomic unit (OTU) table was generated (97% sequence similarity) resulting in 13,383 OTUs. This OTU table was used for subsequent analysis. Accessory metagenomes were sequenced using Illumina NextSeq V2 chemistry. Sequences were analyzed using the MG-RAST pipeline (Meyer et al., 2008). OTUs were classified using the NCBI database option. The amplicon sequences were deposited to the NCBI sequence read archive (SRP072293). Metagenomes were deposited at NCBI, Bioproject PRJNA280942.

The phylogenetic identity of potential Fe-oxidizing organisms was determined by comparing the 16S rDNA dataset to the collection of potential Fe oxidizers and reducers (Altermann, 2014). Identical sequences from our amplicon dataset (>97% identity) were collected into a subset of potential Fe cycling organisms. Sequences were Blast searched against the SILVA database and a phylogenetic neighbor joining tree based on ClustalW alignment was constructed in Mega 6.0 (Tamura et al., 2013).

To quantify potential key organisms, i.e., nitrate or nitrite reducing microbes, functional marker genes for nitrate and nitrite reduction (*narG* and *nirS*) were used in a qPCR system, as described in Lam et al. (2009). The qPCR was applied on DNA and cDNA samples using 12.5 µl SYBRGreen (Life technologies), 1 µl of each primer (10 µM), 1 µl BSA (20 mg ml^{-1}; Fermentas), 2.5 µl H_2O and 5 µl template DNA or cDNA. Quantification was performed against a standard dilution series of plasmids containing the target gene (10^7–10^1 genes; *narG* from *E. coli* DH5a, *nirS* from *Paracoccus denitrificans*). All samples and standards were run in duplicates on an ABI7500 qPCR machine (Life technologies) as described in Lam et al. (2009). Non-template controls containing water instead of nucleic acids were run in parallel on the same plate. No amplification was detectable after 40 cycles thus setting the theoretical detection limit of the assays to 1 copy.

To further determine the identity of actively nitrate reducing organisms from samples with strongest upregulation, a *narG* clone library was constructed (TopoTA cloning kit for sequencing, Life Technologies). Sequencing was carried out at the Institute for Clinical Molecular Biology, Kiel, Germany. 120 sequences were generated. Sequences were Blast searched against the NCBI and FunGene databases. Sequences not matching the FunGene seed assembly were removed from the dataset. The remaining sequences were de-replicated and ClustalW aligned. A neighbor joining tree was generated using Mega 6.0 (Tamura et al., 2013). The sequences were submitted to GenBank (accession numbers: KU899867–KU899990).

3. Results and discussion

3.1. Environmental setting of the Peru oxygen minimum zone

The persistent upwelling of oxygen-depleted and nutrient-rich intermediate water, and the resulting intense primary production and respiration keep the core of the Peruvian OMZ anoxic most of the time ($O_2 < 10$ nM at ~100–300 m water depth and ~10–20°S) (Thamdrup et al., 2012). Consequently, biogeochemical cycling in the water column is dominated by reductive processes within the nitrogen cycle, i.e., denitrification and anammox (anaerobic ammonium oxidation). Long-lasting periods of nitrogenous conditions within the Peru OMZ are occasionally interrupted by oxygenation events related to the propagation of coastal trapped waves (Gutiérrez et al., 2008) or by the injection of hydrogen sulfide from anoxic-sulfidic shelf sediments (Schunck et al., 2013).

During cruise M92 in January 2013, the water column overlying the Peruvian shelf at 12°S was relatively stagnant. Due to the restricted water mass exchange, the water column at the shallowest station (70 m depth to bottom) was not only depleted in oxygen (Fig. 2A, Fig. 3A) but also in both nitrate and nitrite (Fig. 2B, C, Fig. 3B). Under these conditions, hydrogen sulfide could escape from the sediment into the water column (Sommer et al., 2014, 2016). Consequently, the anoxic water mass overlying the shallow shelf was weakly sulfidic ($\leq$13 µM ΣH_2S) and characterized by high dFe concentrations up to 317 nM in near-bottom waters (Fig. 2D, Fig. 3C). In accordance with the water column redox state, and following previous studies (Bruland et al., 2005; Vedamati et al., 2014), we assume that this dFe was mostly Fe^{2+}. The dFe concentrations declined steeply in upward direction, and reached values below 10 nM in the shallowest sample which was taken in a water depth of 14 m (Fig. 3C). Moving laterally offshore, dFe concentrations in near-bottom waters declined gradually (Fig. 4A). At the 145 m station, where nitrate and nitrite reappeared, dFe concentrations declined to <20 nM. At the 407 m station, where trace amounts of oxygen (few hundred nM) were detected in the near-bottom water, dFe concentrations declined to ~2 nM. The Fe^{2+} flux across the sediment-water interface was

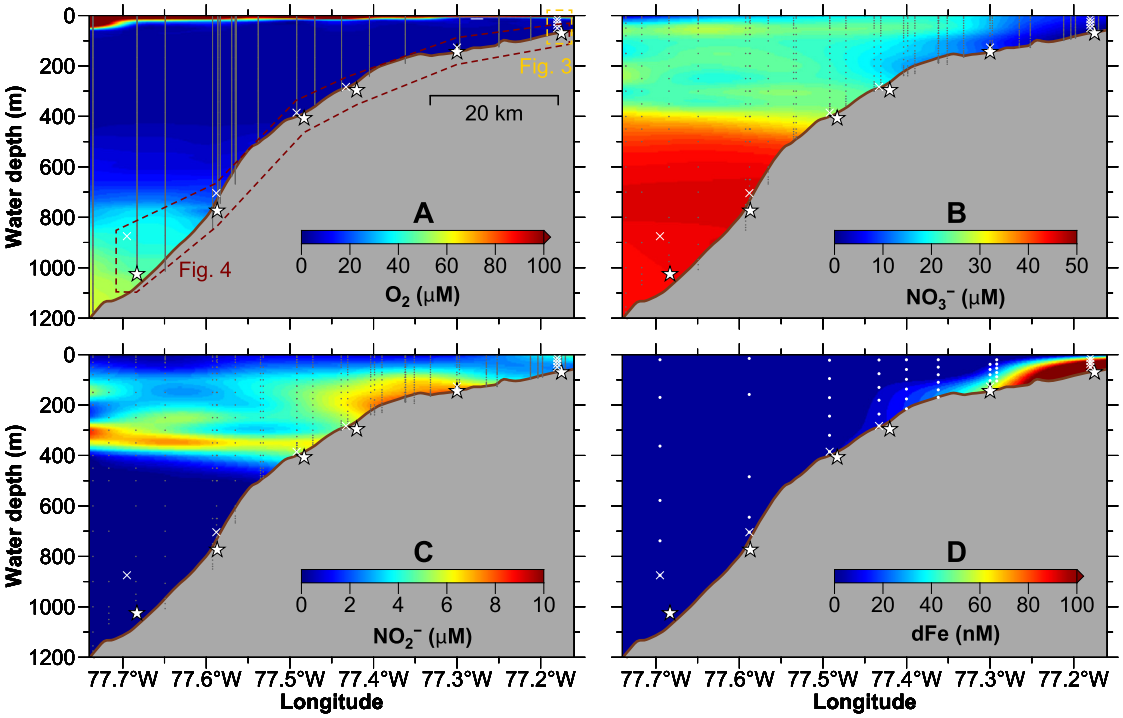

Fig. 2. Lateral distribution of dissolved constituents in the water column of the Peru OMZ. (A) O_2, (B) NO_3^-, (C) NO_2^-, (D) dFe. The approximate bathymetry along the transect was taken from GEBCO. The white and gray dots depict the location of sensor measurements (discrete oxygen measurements at high-resolution appear as a continuous line) (A), CTD rosette bottles (N species) (B, C) and GO-FLO bottles (dFe) (D). White crosses depict particulate matter samples for which XRF and XANES data are available. White stars depict the location of sediment cores. The samples covered by Figs. 3 and 4 are indicated in (A). The data shown in this figure are contained in the Electronic Supplement (dFe) or are available at https://www.pangaea.de/.

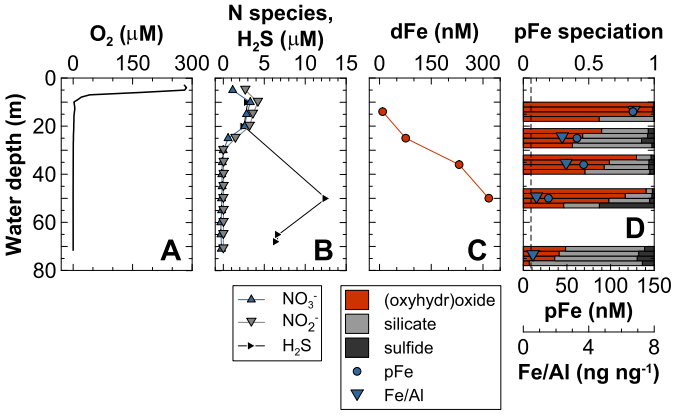

Fig. 3. Chemical and mineralogical data for the shelf station: (A) O_2, (B) NO_3^-, NO_2^- and H_2S, (C) dFe, (D) pFe, particulate Fe speciation and particulate Fe/Al in water samples and surface sediments (lowermost sample). The H_2S concentrations were measured on samples from a different CTD which was taken 10 days later and 1.3 km apart. The vertical dashed line in (D) depicts the regional lithogenic background (andesite in the Andean arc) (Scholz et al., 2014b). The depiction of particulate Fe speciation is based on four spots with elevated Fe concentration on the XRF maps (see Supplementary Fig. S1). Individual Fe minerals are grouped to Fe (oxyhydr)oxides, Fe silicates and Fe sulfides. The data shown in this figure are contained in the Electronic Supplement.

nearly identical at the 70 m and 145 m stations (Fig. 4D). Therefore, a change in Fe source from the sediment is unlikely to account for the one order of magnitude decrease in dFe in the near-bottom water between these two stations. A physical boundary preventing mixing of the Fe-rich and Fe-depleted water masses can also be excluded as no abrupt change in temperature or salinity is discernable between the two stations (Supplementary Fig. S4). We therefore argue that oxidative removal of sediment-derived Fe^{2+} in the water column was responsible for the decline in dFe between the 70 m and 145 m stations.

3.2. Mechanism of iron oxidation in the water column

To further constrain the mechanism of Fe removal in the anoxic water column of the Peru OMZ, we characterized particulate Fe speciation by XANES analysis and determined total particulate Fe (pFe) and aluminum (Al) concentrations. The sedimentary and particulate Fe speciation reported in Figs. 3 and 4 represent spots with elevated Fe concentration recorded on XRF maps of sediment grains and filtered particulate matter. To illustrate in-situ precipitation of Fe in the water column, pFe concentrations are also reported as ratios of pFe to particulate Al (Fe/Al) and compared to the Fe/Al of the regional lithogenic background (dashed lines) (Scholz et al., 2014b) and of the underlying sediments. Oxidative precipitation of Fe minerals from dissolved Fe^{2+} in the water column and an accumulation of the re-oxidized Fe in the sediment decouple Fe from Al thus generating particulate Fe/Al above the lithogenic background. In contrast, maxima in pFe associated with Fe/Al similar to the lithogenic background indicate the presence of terrigenous particulate matter in the water column, either supplied from land or by re-suspension of bottom sediments.

The particularly high dFe concentrations in the near-bottom water sample at the 70 m shelf station is accompanied by a Fe/Al close to the lithogenic background (Fig. 3D). This observation indicates that sediment-derived dFe was efficiently transported within the anoxic and weakly sulfidic waters overlying the shelf sediment at the time of sampling. With the exception of one Fe sulfide-rich spot on the analyzed particles, Fe (oxyhydr)oxide and silicate minerals are the dominant particulate Fe species throughout the OMZ (Fig. 3D). The weakly sulfidic water overlying the shelf sediment was highly undersaturated with respect to Fe monosulfide, the Fe sulfide mineral which would first precipitate under the prevailing conditions (Rickard, 2006). We therefore suspect that particulate sulfide minerals in the water column were derived from sediment re-suspension rather than in-situ precipitation.

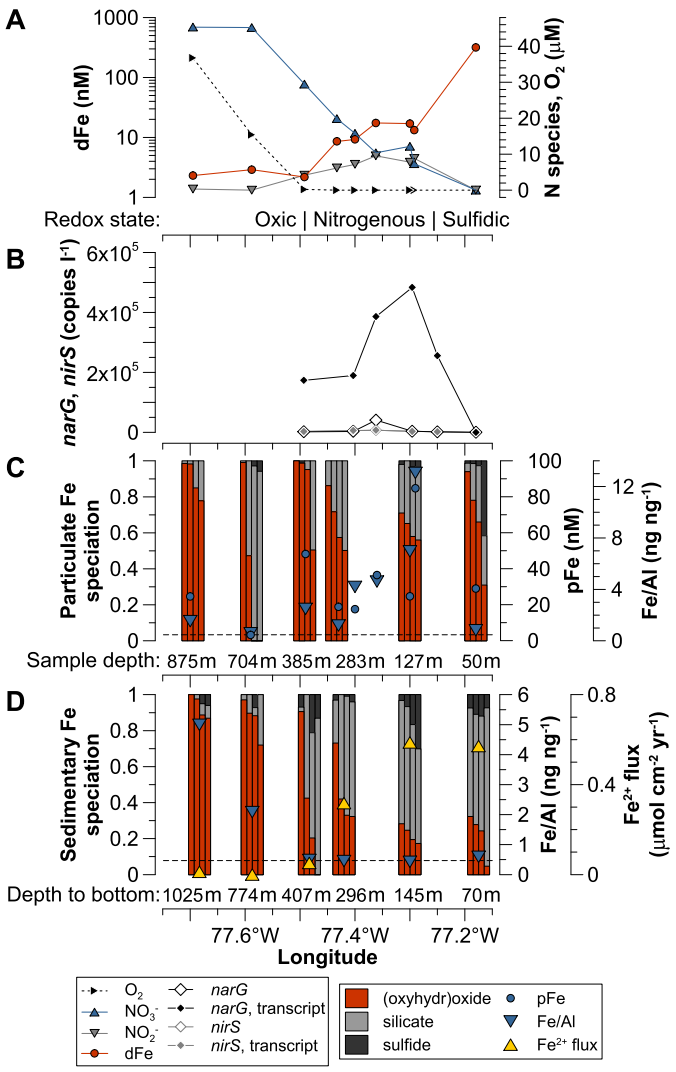

Fig. 4. Chemical, mineralogical and metagenomic data for the bottom transect: (A) dissolved O_2, NO_3^-, NO_2^- and dFe concentrations in near-bottom water (note logarithmic scale for dFe), (B) gene and transcript abundance of *narG* coding for nitrate reductase and *nirS* coding for nitrite reductase in near-bottom water, (C) particulate Fe speciation (see Fig. 3 for details) and Fe/Al in near-bottom water (lowermost GO-FLO bottle at each station), (D) particulate Fe speciation and Fe/Al in surface sediments, Fe^{2+} flux across the sediment-water interface (see Supplementary Fig. S5 for pore water concentration profiles of Fe^{2+}). The horizontal dashed line in (C) and (D) depicts the Fe/Al of the regional lithogenic background (andesite in the Andean arc) (Scholz et al., 2014b). The depths to bottom of the GO-FLO stations and sampling depths of samples for which Fe speciation data are available (dissolved and particulate concentration data but no speciation data are available for the 144 m, 195 m and 244 m stations) as well as the redox zonation in near-bottom waters are indicated above the x-axes. The data shown in this figure are contained in the Electronic Supplement.

The Fe/Al increases vertically into shallower water, and the lowest dFe concentrations in the shallowest sample coincides with the highest Fe/Al and a predominance of Fe (oxyhydr)oxides in the particulate matter (Fig. 3D). This vertical pattern is consistent with upward transport of sediment-derived dFe across the water column redox boundary followed by oxidative precipitation and downward sinking of particulate Fe (oxyhydr)oxides. The transitions from weakly sulfidic to nitrogenous to oxygenated waters in moving from the sediment towards the sea surface are in near proximity to one other (<10 m). It is therefore not possible at the given sampling resolution to discern if the upward-transported dFe is oxidized with nitrate or oxygen as the terminal electron acceptor. In contrast, in moving offshore, the transitions from weakly sulfidic to nitrogenous to oxic bottom waters are located several kilometers from each other (Fig. 4A). The sharp drop in dFe and pronounced maximum in particulate Fe/Al at the 145 m station (Fig. 4C) clearly coincides with the transition from sulfidic to nitrogenous conditions in near-bottom waters. This observation is in line with nitrate-dependent Fe oxidation. A similar succession of redox transitions and dFe concentrations has been reported for the anoxic water column of the Black Sea (Lewis and Landing, 1991). These authors found a dFe maximum of 300 nM within the weakly sulfidic zone (180 m water depth) and a steep decline towards dFe concentrations of the order of 20 nM across the sulfidic-nitrogenous transition, the latter of which was located several tens of meters deeper than the nitrogenous-oxic transition. Even though Lewis and Landing (1991) did not provide an explanation for this observation, their data is consistent with nitrate-dependent Fe oxidation.

We note that high Fe/Al at the 145 m station are not accompanied by a net increase in the fraction of Fe (oxyhydr)oxide minerals in the particulate matter (Fig. 4C). This observation may be related to the formation of mixed ferrous-ferric minerals such as green rust, which are known to precipitate during nitrate-dependent Fe oxidation (Pantke et al., 2012). Moreover, nitrate-dependent Fe oxidation is likely to generate finely dispersed Fe (oxyhydr)oxide minerals that are attached to bacteria (Kappler et al., 2005; Pantke et al., 2012) rather than Fe-rich particles that are readily detected on XRF maps of filtered particulate matter.

Even though the dFe concentration drops sharply between the 70 m and 145 m stations (Fig. 4A), the Fe/Al of surface sediments in this area is equal to or slightly lower than the lithogenic background (Fig. 4D). Thus, the sediments in the nitrogenous zone of the OMZ do not represent a net sink for sedimentary Fe supplied laterally from the shelf, despite nitrate-dependent Fe oxidation in the overlying water column. Instead, sedimentary Fe/Al increases first in oxygenated bottom waters where O_2 concentrations increase above a few µM (774 m and 1025 m stations). This transition is also accompanied by a considerable increase in the fraction of Fe (oxyhydr)oxides in the sediment (Fig. 4D). These observations are consistent with findings from earlier studies off the coast of Peru (Scholz et al., 2014b) which concluded that most of the sediment-derived Fe ultimately accumulates in sediments below the boundary between nitrogenous and oxygenated bottom waters. The transition from Fe/Al below or equal to the lithogenic background to elevated Fe/Al coincides with the depth where the sedimentary Fe efflux drops to zero (Fig. 4D). This pattern suggests that nitrate-dependent Fe oxidation is not efficient enough to prevent pore water Fe from leaking into the nitrogenous water column. Therefore, sediment-derived Fe is continuously released, oxidized, sedimented, reduced and re-released until it is ultimately circulated into the oxygenated waters below the OMZ. In this area with oxygenated bottom waters, both oxygen and nitrate penetrate into the sediment thus inducing a switch from Fe efflux to Fe accumulation. In agreement with this scenario, particulate Fe/Al in the water column decreases from maximum values in the near-bottom water at the sulfidic-nitrogenous transition to values around the lithogenic background in oxygenated waters below the OMZ (Figs. 4C and 5).

To quantitatively substantiate this nitrate-dependent 'iron shuttle' (Scholz et al., 2014b), we combine the sedimentary Fe^{2+} flux (F_{sed}) with the dFe concentration in near-bottom water samples to compute an apparent first order rate constant for Fe removal (k_{ppt}) and to approximate a half-life of dFe ($t_{1/2}$) in the anoxic and nitrogenous water column (Table 1):

$$\frac{d[dFe]}{dt} = F_{sed} - k_{ppt}\,[dFe] = 0 \qquad (3)$$

Table 1
Half-life for dFe removal within the nitrogenous OMZ off Peru.

Station/depth to bottom (m)	Fe^{2+} flux (F_{sed}) (mol m^{-2} yr^{-1})	dFe (mol m^{-3})	k_{ppt} (yr^{-1})	$t_{1/2}$ (Fe) (h)
145 m	5.87E−03	1.70E−05	3.46E+02	17.6
296 m	3.17E−03	8.58E−06	3.70E+02	16.4

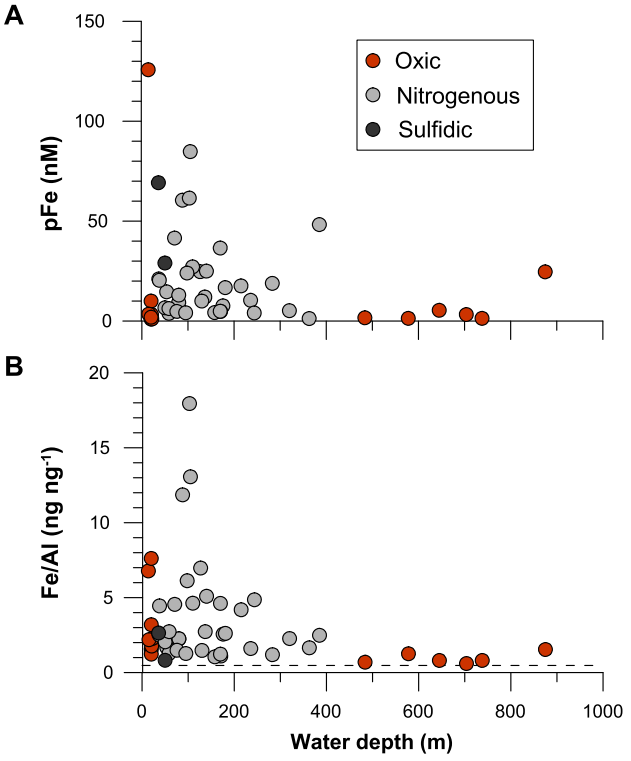

Fig. 5. Particulate Fe data in the water column: (A) pFe and (B) Fe/Al in the water column versus water depth for all GO-FLO stations. Samples are subdivided according to their redox state (oxic, nitrogenous and sulfidic). The horizontal dashed line in (B) depicts the Fe/Al of the regional lithogenic background (andesite in the Andean arc) (Scholz et al., 2014b). The data shown in this figure are contained in the Electronic Supplement.

Equation (3) assumes that sedimentary Fe release is the only source of dFe to the bottom water and oxidative precipitation, as determined by k_{ppt}, is the only sink. In the anoxic and nitrogenous OMZ, k_{ppt} likely depends on the nitrate and/or nitrite concentration and pH (see Equations (1) and (2)) whereas at the boundary to oxygenated waters, the O_2 concentration becomes increasingly important (Millero et al., 1987). A notable uncertainty associated with our calculations is related to the distance between the near-bottom water samples and the seafloor (~10–20 m at the nitrogenous stations). The Fe concentration in the actual bottom water in contact with the sediment is likely to be higher thus implying a lower k_{ppt} and longer $t_{1/2}$. Despite this uncertainty, we can use Equation (3) to approximate the efficiency of Fe removal through nitrate-dependent Fe oxidation and to compare the result with $t_{1/2}$ values for Fe oxidation with oxygen (Millero et al., 1987). Adopting the sedimentary dFe fluxes and dFe concentrations at the nitrogenous stations (145 m and 296 m) in Equation (3) yields a fairly consistent $t_{1/2}$ around 17 hours (Table 1). Typical zonal current velocities within the Peruvian OMZ range in the order of a 5 cm s^{-1} (Sommer et al., 2014). Combining this value with a dFe half-life of 17 hours yields a transport distance of ~20 km over which a typical background concentration of 2 nM dFe is reached. Indeed, this transport distance is great enough to allow much of the Fe to become transferred into the oxic Fe sink area at the 774 m and 1025 m stations but not great enough to transport the dFe into the open ocean. For comparison, Fe oxidation with oxygen with a half-life of 17 hours requires an O_2 concentration of 5 µM (Millero et al., 1987) (assuming a pH of 7.6 which is typical for OMZ waters Feely et al., 2008 and a temperature of 12 °C). This calculation reveals that without nitrate-dependent Fe oxidation (i.e., if dFe removal was induced by oxidation with oxygen alone) the anoxic OMZ would represent a much more efficient transport avenue for sediment-derived Fe, particularly in an offshore direction where O_2 concentrations remain below 5 µM for several hundred kilometers (Thomsen et al., 2016).

3.3. Microbial ecology of iron oxidation

To investigate the microbial potential for nitrate-dependent Fe oxidation within the nitrogenous OMZ, we performed a high-throughput 16S rDNA based phylogenetic analysis of the bacterial community in the near-bottom water. The sequences obtained were compared to the genome dataset of previously identified Fe-oxidizing microbes (Altermann, 2014). We detected 18 bacterial clades matching described Fe oxidizers (Fig. 6). Among those, the majority (11 individual clades) are described to oxidize Fe with nitrate as terminal electron acceptor (Weber et al., 2006a). This observation corroborates the microbial potential for nitrate-dependent Fe oxidation in the Peru OMZ.

Microbial Fe oxidation may be coupled to the reduction of nitrate or nitrite (Carlson et al., 2013) catalyzed by nitrate or nitrite reductase enzymes (Lack et al., 2002). To quantify the potential for microbial Fe oxidation with nitrate or nitrite, we determined the abundance and expression of key genes for nitrate and nitrite reduction (*narG* and *nirS*, respectively) both of which potentially involve Fe oxidation. We observed an enhanced gene expression of *narG*, as indicated by an increased transcript versus gene abundance, between the 70 m and 296 m stations (Fig. 4B). By contrast, expression of *nirS* was comparably low. Along with an accumulation of nitrite in the bottom water at the same stations, this observation indicates that nitrate reduction to nitrite is the dominant nitrogen turnover process, whereas further reduction of nitrite to dinitrogen gas is not apparent from our molecular data. Upregulation of *narG* co-occurred with the removal of dFe from the near-bottom water (Fig. 4A), which could indicate that Fe oxidation is coupled to nitrate reduction (Equation (1)). We identified the most abundant phylogenetic groups involved in nitrate reduction, possibly mediating Fe oxidation, by sequencing *narG* transcripts from samples with the highest upregulation. A total of 120 *narG* clones were generated, and clones related to a known Fe oxidizing microbe (*Marinobacter aquaeoli*) accounted for 22% of the sequences (Fig. 7). In addition to the *Marinobacter* clade, several clades of γ-Proteobacteria, *Deferribacteres*, *Sphaerobacteraceae* and *Acethothermia* were detected. Like most other nitrate-dependent Fe-oxidizing bacteria, *Marinobacter aquaeoli* is mixotrophic, i.e., requires an additional carbon source to mediate Fe oxidation (Weber et al., 2006a). However, in the high productivity waters of the Peru upwelling, organic matter availability is unlikely to restrict Fe oxidation by mixotrophic microbes.

As an alternative to microbial Fe oxidation with nitrate, the lack of an upregulation of *nirS* and the accumulation of nitrite in the zone Fe removal could indicate that ferrous Fe is oxidized abiotically with nitrite (Equation (2); Picardal, 2012;

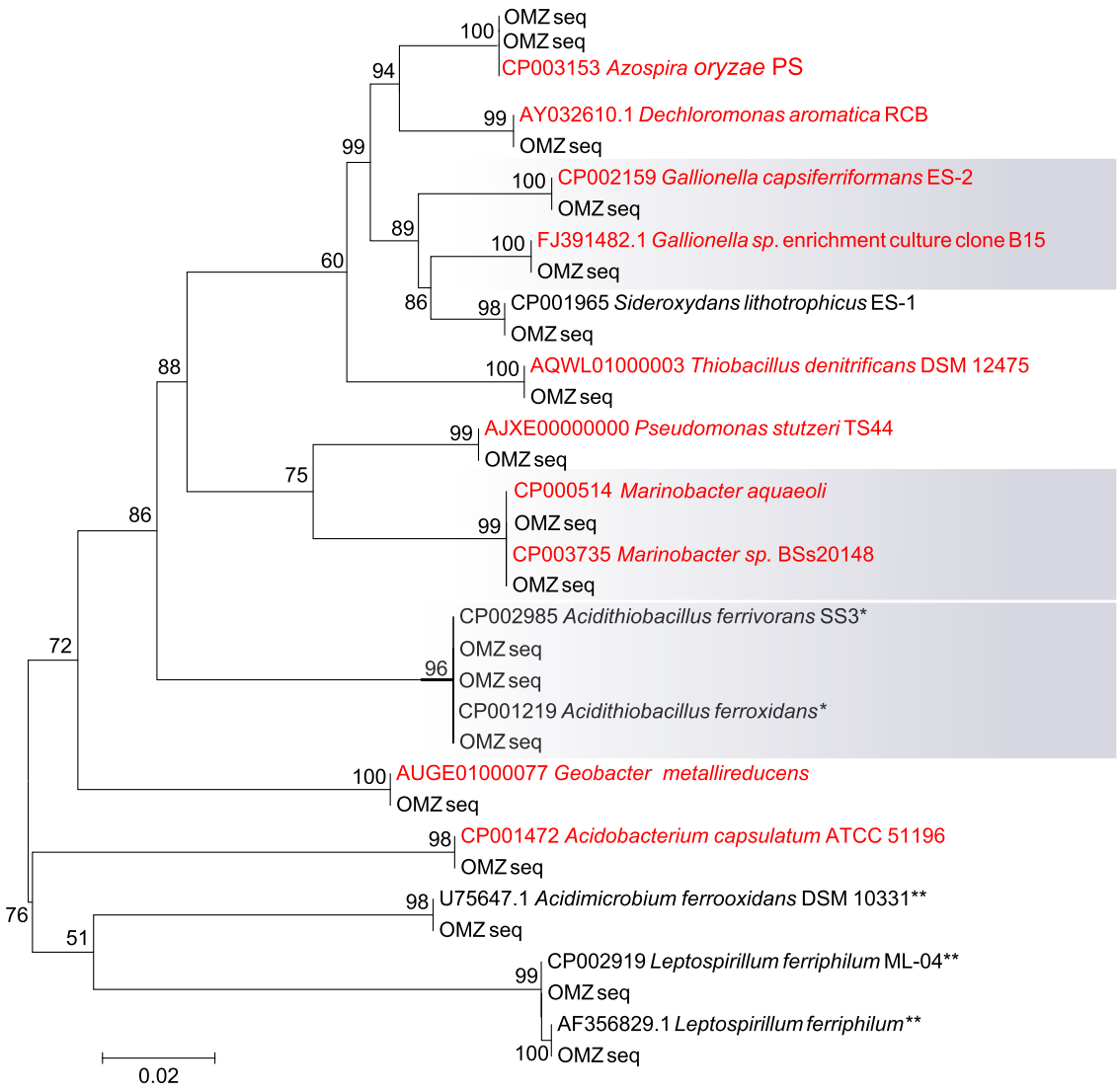

Fig. 6. Diversity of Fe oxidizing microbes in the Peru OMZ. Microbial phyla were identified from a comparison to the Fe oxidizer genome dataset of Altermann (2014). Nitrate reducers (red color), sulfate reducers (*) and acidophiles (**) were identified. Microbes also capable of aerobic Fe oxidation are shaded in blue. OMZ sequences were retrieved from the PRJNA280942 datasets based on a ClustalW alignment followed by neighbor joining analysis. The percentage of replicate trees in which the associated taxa clustered together in the bootstrap test (1000 replicates) is shown next to the branches. (For interpretation of the references to color in this figure legend, the reader is referred to the web version of this article.)

Klueglein and Kappler, 2013). This abiotic reaction is favored by the presence of Fe (oxyhydr)oxide minerals which are abundant throughout the nitrogenous OMZ (Fig. 4C). We cannot unambiguously identify whether Fe oxidation is mediated enzymatically by nitrate-reducing microbes or takes place abiotically through reaction with nitrite based on our metagenomic data. However, since the nitrite accumulating in the Peru OMZ is chiefly produced by heterotrophic bacteria (Lam et al., 2009), the overall mechanism of Fe removal is induced by the activity of denitrifying microbes in either case.

4. Conclusions and implications

Our findings provide strong evidence that in anoxic nitrogenous water columns, sediment-derived Fe^{2+} is oxidized with nitrate as terminal electron acceptor. The particular environmental conditions encountered on the Peruvian continental margin during this study, i.e., a water column redox boundary separating anoxic and weakly sulfidic from anoxic nitrogenous waters, enabled us to identify a distinct biogeochemical imprint of this process. Earlier studies on nitrate-dependent Fe oxidation concluded based on experimental results and theoretical considerations that nitrate and dissolved ferrous Fe should not co-occur at circum-neutral pH in natural environments (Straub et al., 2004; Raiswell and Canfield, 2012). Consistent with this notion, our findings demonstrate the presence and activity of bacterial groups which can mediate Fe oxidation with nitrate in the Peru OMZ. In addition, our data are consistent with an abiotic process whereby Fe is oxidized abiotically with nitrite. However, if this latter process was dominant, it should theoretically prevent the ferrous Fe maxima which have been observed in the secondary nitrite maximum in the offshore reaches of the Peruvian and Arabian OMZs (Moffett et al., 2007; Vedamati et al., 2014). We therefore conclude that microbial Fe oxidation with nitrate is more likely the mechanism of Fe removal.

OMZs are key regions for the global ocean's nitrogen inventory as they accommodate reductive nitrogen loss in the water column through denitrification and anammox (Gruber, 2008). Our results imply that not only the inventory of the macronutrient nitrogen but also the availability of the micronutrient Fe is affected by reductive processes within the nitrogen cycle. Accordingly, the transition from nitrogenous to Fe-rich and weakly sulfidic conditions in anoxic water columns represents an efficient barrier preventing

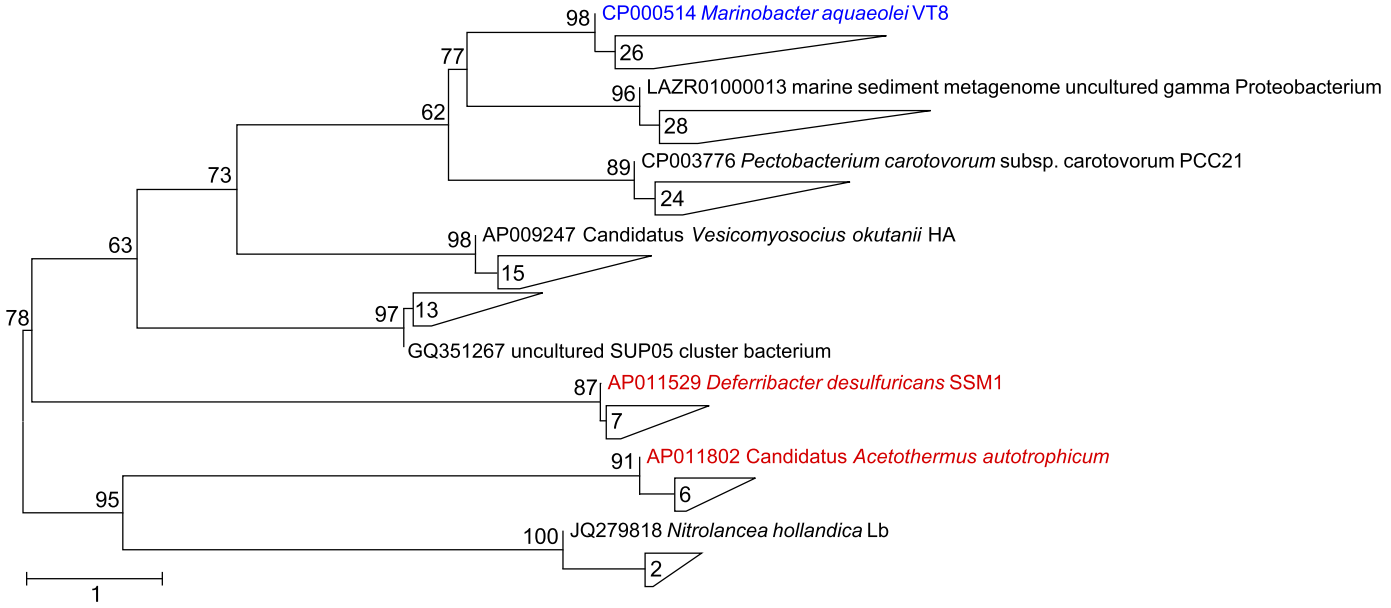

Fig. 7. Neighbor joining tree of *narG* genes from cDNA clone libraries (120 clones). Numbers in triangles denote the abundance of sequences in the library. Fe oxidizers are indicated in blue and iron reducers are indicated in red. Bootstrap values ($n = 1000$) are given as % next to the branches. (For interpretation of the references to color in this figure legend, the reader is referred to the web version of this article.)

mobile Fe generated through dissimilatory or abiotic Fe reduction to reach Fe-limited ecosystems at the sea surface and in the open ocean.

Reductive nitrogen loss within OMZs represents an important negative feedback for primary production, respiratory oxygen consumption and thus further OMZ intensification and expansion. Modeling studies have suggested that this negative feedback mechanism could be overcome if the nitrogen inventory at the sea surface was continuously replenished by nitrogen fixation (Canfield, 2006). In most ocean regions, nitrogen-fixation is limited by Fe availability (Falkowski, 1997). Nitrate-dependent Fe oxidation separates Fe-limited phytoplankton communities in the surface ocean from the Fe source in anoxic continental margin sediments. We therefore suggest that nitrate-dependent Fe oxidation exerts a balancing effect on the ocean's nitrogen inventory and redox dynamics.

Acknowledgements

We wish to thank the government of Peru for granting access to their territorial waters as well as the crew of RV Meteor for supporting our research at sea. We are grateful for the technical and analytical assistance provided by A. Bleyer, A. Petersen, B. Domeyer, E. Breitbarth, N. Martogli, D. Nitschkowsky, T. Reusch, R. Surberg, S. Steigenberger, P. Streu and V. Thoennissen. We also acknowledge the Synchrotron Light Source ANKA for provision of instruments at their beamlines as well as Max Wilke for providing insights into XANES pre-edge data treatment procedures. This study was supported by the 7th Framework Program of the European Union (Marie Curie IOF to FS, Project #300648, BICYCLE), the German Research Foundation (Sonderforschungsbereich 754, "Climate-Biogeochemistry Interactions in the Tropical Ocean"; Cluster of Excellence "The Future Ocean"; Emmy Noether Nachwuchsforschergruppe ICONOX to FS), the German Federal Ministry for Education and Research (SOPRAN, FKZ03F0662A) and the European Union Framework Program Horizon 2020 (Marie Curie IEF to CRL, Project #704272, NITROX). Constructive comments by three reviewers as well as the editorial handling by Derek Vance are gratefully acknowledged.

Appendix A. Supplementary material

Supplementary material related to this article can be found online at http://dx.doi.org/10.1016/j.epsl.2016.09.025.

References

Altermann, E., 2014. Invited commentary: lubricating the rusty wheel, new insights into iron oxidising bacteria through comparative genomics. Front. Microbiol. 5, 1–4.

Boyd, P.W., Ellwood, M.J., 2010. The biogeochemical cycle of iron in the ocean. Nat. Geosci. 3, 675–682.

Bruland, K.W., Rue, E.L., Smith, G.J., DiTullio, G.R., 2005. Iron, macronutrients and diatom blooms in the Peru upwelling regime: brown and blue waters of Peru. Mar. Chem. 93, 81–103.

Canfield, D.E., 2006. Models of oxic respiration, denitrification and sulfate reduction in zones of coastal upwelling. Geochim. Cosmochim. Acta 70, 5753–5765.

Carlson, H.K., Clark, I.C., Blazewicz, S.J., Iavarone, A.T., Coates, J.D., 2013. Fe(II) oxidation is an innate capability of nitrate-reducing bacteria that involves abiotic and biotic reactions. J. Bacteriol. 195, 3260–3268.

Dale, A.W., Nickelsen, L., Scholz, F., Hensen, C., Oschlies, A., Wallmann, K., 2015. A revised global estimate of dissolved iron fluxes from marine sediments. Glob. Biogeochem. Cycles. http://dx.doi.org/10.1002/2014GB005017.

Danielsson, L.-G., Magnusson, B., Westerlund, S., 1987. An improved metal extraction procedure for the determination of trace metals in sea water by atomic absorption spectrometry with electrothermal atomization. Anal. Chim. Acta 98, 47–57.

Edwards, K.J., Rogers, D.R., Wirsen, C.O., McCollom, T.M., 2003. Isolation and characterization of novel psychrophilic, neutrophilic, Fe-oxidizing, chemolithoautotrophic alpha- and gamma-proteobacteria from the deep sea. Appl. Environ. Microbiol. 69, 2906–2913.

Falkowski, P.G., 1997. Evolution of the nitrogen cycle and its influence on the biological sequestration of CO_2 in the ocean. Nature 387, 272–275.

Feely, R.A., Sabine, C.L., Hernandez-Ayon, J.M., Ianson, D., Hales, B., 2008. Evidence for upwelling of corrosive "acidified" water onto the continental shelf. Science 320, 1490–1492.

Grasshoff, M., Erhardt, M., Kremling, K., 1999. Methods of Seawater Analysis. Wiley-VCH, Weinheim.

Gruber, N., 2008. The marine nitrogen cycle: overview and challenges. In: Capone, D.G., Bronk, D.A., Mulholland, M.R., Carpenter, E.J. (Eds.), Nitrogen in the Marine Environment. Academic Press, San Diego, pp. 1–50.

Gutiérrez, D., Gutiérrez, D., Enriquez, E., Purca, S., Quipúzcoa, L., Marquina, R., Flores, G., Graco, M., 2008. Oxygenation episodes on the continental shelf of central Peru: remote forcing and benthic ecosystem response. Prog. Oceanogr. 79, 177–189.

Homoky, W.B., John, S.G., Conway, T.M., Mills, R.A., 2013. Distinct iron isotopic signatures and supply from marine sediment dissolution. Nat. Commun. 4. http://dx.doi.org/10.1038/ncomms3143.

Hong, H., Kester, D.R., 1986. Redox state of iron in the offshore waters of Peru. Limnol. Oceanogr. 31, 512–524.
Hutchins, D.A., Hare, C.E., Weaver, R.S., Zhang, Y., Firme, G.F., DiTullio, G.R., Alm, M.B., Riseman, S.F., Maucher, J.M., Geesey, M.E., Trick, C.G., Smith, G.J., Rue, E.L., Conn, J., Bruland, K.W., 2002. Phytoplankton iron limitation in the Humboldt Current and Peru upwelling. Limnol. Oceanogr. 47, 997–1011.
Jickells, T.D., An, Z.S., Andersen, K.K., Baker, A.R., Bergametti, G., Brooks, N., Cao, J.J., Boyd, P.W., Duce, R.A., Hunter, K.A., Kawahata, H., Kubilay, N., laRoche, J., Liss, P.S., Mahowald, N., Prospero, J.M., Ridgwell, A.J., Tegen, I., Torres, R., 2005. Global iron connections between desert dust, ocean biogeochemistry, and climate. Science 308, 67–71.
Kappler, A., Schink, B., Newman, D.K., 2005. Fe(III) mineral formation and cell encrustation by the nitrate-dependent Fe(II)-oxidizer strain BoFeN1. Geobiology 3, 235–245.
Klueglein, N., Kappler, A., 2013. Abiotic oxidation of Fe(II) by reactive nitrogen species in cultures of the nitrate-reducing Fe(II) oxidizer Acidovorax sp. BoFeN1 – questioning the existence of enzymatic Fe(II) oxidation. Geobiology 11, 180–190.
Kondo, Y., Moffett, J.W., 2015. Iron redox cycling and subsurface offshore transport in the eastern tropical South Pacific oxygen minimum zone. Mar. Chem. 168, 95–103.
Lack, J.G., Chaudhuri, S.K., Chakraborty, R., Achenbach, L.A., Coates, J.D., 2002. Anaerobic biooxidation of Fe(II) by Dechlorosoma suillum. Microb. Ecol. 43, 424–431.
Lam, P.J., Bishop, J.K.B., 2008. The continental margin is a key source of iron to the HNLC North Pacific Ocean. Geophys. Res. Lett. 35, L07608.
Lam, P., Lavik, G., Jensen, M.M., van de Vossenberg, J., Schmid, M., Woebken, D., Gutiérrez, D., Amann, R., Jette, M.S.M., Kuypers, M.M.M., 2009. Revising the nitrogen cycle in the Peruvian oxygen minimum zone. Proc. Natl. Acad. Sci. 106, 4752–4757.
Laufer, K., Nordhoff, M., Røy, H., Schmidt, C., Behrens, S., Jørgensen, B.B., Kappler, A., 2016. Co-existence of microaerophilic, nitrate-reducing and phototrophic Fe(II)-oxidizers and Fe(III)-reducers in coastal marine sediment. Appl. Environ. Microbiol. 82, 1433–1447.
Lewis, B.L., Landing, W.M., 1991. The biogeochemistry of manganese and iron in the Black Sea. Deep-Sea Res. 38 (Supplement 2), S773–S803.
Lohan, M.C., Bruland, K.W., 2008. Elevated Fe(II) and dissolved Fe in hypoxic shelf waters off Oregon and Washington: an enhanced source of iron to coastal upwelling regimes. Environ. Sci. Technol. 42, 6462–6468.
Löscher, C.R., Fischer, M.A., Neulinger, S.C., Fiedler, B., Philippi, M., Schütte, F., Singh, A., Hauss, H., Karstensen, J., Körtzinger, A., Künzel, S., Schmitz, R.A., 2015. Hidden biosphere in an oxygen-deficient Atlantic open ocean eddy reveals future implications of ocean deoxygenation on primary production in the eastern tropical North Atlantic. Biogeosciences 12, 7467–7482.
Meyer, F., Paarmann, D., D'Souza, M., Olson, R., Glass, E.M., Kubal, M., Paczian, T., Rodriguez, A., Stevens, R., Wilke, A., Wilkening, J., Edwards, R.A., 2008. The metagenomics RAST server – a public resource for the automatic phylogenetic and functional analysis of metagenomes. BMC Bioinform. 9. http://dx.doi.org/10.1186/1471-2105-9-386.
Millero, F.J., Sotolongo, S., Izaguirre, M., 1987. The oxidation kinetics of Fe(II) in seawater. Geochim. Cosmochim. Acta 51, 793–801.
Miot, J., Benzerara, K., Morin, G., Kappler, A., Bernard, S., Obst, M., Férard, C., Skouri-Panet, F., Guigner, J.-M., Posth, N., Galvez, M., Brown Jr., G.E., Guyot, F., 2009. Iron biomineralization by anaerobic neutrophilic iron-oxidizing bacteria. Geochim. Cosmochim. Acta 73, 696–711.
Moffett, J.W., Goepfert, T.J., Naqvi, S.W.A., 2007. Reduced iron associated with secondary nitrite maxima in the Arabian Sea. Deep-Sea Res. 54, 1341–1349.
Moore, J.K., Doney, S.C., 2007. Iron availability limits the ocean nitrogen inventory stabilizing feedbacks between marine denitrification and nitrogen fixation. Glob. Biogeochem. Cycles 21, GB2001. http://dx.doi.org/10.1029/2006GB002762.
Noble, A.E., Lamborg, C.H., Ohnemus, D.C., Lam, P.J., Goepfert, T.J., Measures, C.I., Frame, C.H., Casciotti, K.L., DiTullio, G.R., Jennings, J., Saito, M.A., 2012. Basin-scale inputs of cobalt, iron, and manganese from the Benguela-Angola front to the South Atlantic Ocean. Limnol. Oceanogr. 57, 989–1010.
Noffke, A., Hensen, C., Sommer, S., Scholz, F., Bohlen, L., Mosch, T., Graco, M., Wallmann, K., 2012. Benthic iron and phosphorus fluxes across the Peruvian oxygen minimum zone. Limnol. Oceanogr. 57, 851–867.
Pantke, C., Obst, M., Benzerara, K., Morin, G., Ona-Nguema, G., Dippon, U., Kappler, A., 2012. Green rust formation during Fe(II) oxidation by the nitrate-reducing Acidovorax sp. strain BoFeN1. Environ. Sci. Technol. 46, 1439–1446.
Picardal, F., 2012. Abiotic and microbial interactions during anaerobic transformations of Fe(II) and NOx. Front. Microbiol. 3. http://dx.doi.org/10.3389/fmicb.2012.00112.
Raiswell, R., Canfield, D.E., 2012. The iron biogeochemical cycle past and present. Geochem. Perspect. 1, 1–220.
Ravel, B., Newville, M., 2005. ATHENA, ARTEMIS, HEPHAESTUS: data analysis for X-ray absorption spectroscopy using IFEFFIT. J. Synchrotron Radiat. 12, 537–541.
Rickard, D., 2006. The solubility of FeS. Geochim. Cosmochim. Acta 70, 5779–5789.
Scholz, F., McManus, J., Mix, A.C., Hensen, C., Schneider, R.R., 2014a. The impact of ocean deoxygenation on iron release from continental margin sediments. Nat. Geosci. 7, 433–437.
Scholz, F., Severmann, S., McManus, J., Hensen, C., 2014b. Beyond the Black Sea paradigm: the sedimentary fingerprint of an open-marine iron shuttle. Geochim. Cosmochim. Acta 127, 368–380.
Schunck, H., Lavik, G., Desai, D.K., Großkopf, T., Kalvelage, T., Löscher, C.R., Paulmier, A., Contreras, S., Siegel, H., Holtappels, M., Rosenstiel, P., Schilhabel, M.B., Graco, M., Schmitz, R.A., Kuypers, M.M.M., LaRoche, J., 2013. Giant hydrogen sulfide plume in the oxygen minimum zone off Peru supports chemolithoautotrophy. PLoS ONE 8, e68661. http://dx.doi.org/10.1371/journal.pone.0068661.
Severmann, S., McManus, J., Berelson, W.M., Hammond, D.E., 2010. The continental shelf benthic iron flux and its isotope composition. Geochim. Cosmochim. Acta 74, 3984–4004.
Solé, V.A., Papillon, E., Cotte, M., Walter, P., Susini, J., 2007. A multiplatform code for the analysis of energy-dispersive X-ray fluorescence spectra. Spectrochim. Acta B 62, 63–68.
Sommer, S., Dengler, M., Treude, T., 2014. Benthic element cycling, fluxes and transport of solutes across the benthic boundary layer in the Peruvian oxygen minimum zone, (SFB 754) – Cruise No. M92 – January 05–February 03, 2013 – Callao (Peru) – Callao (Peru). METEOR-Berichte M92. http://dx.doi.org/10.2312/cr_m92. 55 pp., DFG-Senatskommission für Ozeanographie.
Sommer, S., Gier, J., Treude, T., Lomnitz, U., Dengler, M., Cardich, J., Dale, A.W., 2016. Depletion of oxygen, nitrate and nitrite in the Peruvian oxygen minimum zone cause an imbalance of benthic nitrogen fluxes. Deep-Sea Res. 112, 113–122.
Stookey, L.L., 1970. Ferrozine – a new spectrophotometric reagent for iron. Anal. Chem. 42, 779–781.
Straub, K.L., Benz, M., Schink, B., Widdel, F., 1996. Anaerobic, nitrate-dependent microbial oxidation of ferrous iron. Appl. Environ. Microbiol. 62, 1458–1460.
Straub, K.L., Schönhuber, W.A., Buchholz-Cleven, B.E.E., Schink, B., 2004. Diversity of ferrous iron-oxidizing, nitrate-reducing bacteria and their involvement in oxygen-independent iron cycling. Geomicrobiol. J. 21, 371–378.
Tamura, K., Stecher, G., Peterson, D., Filipski, A., Kumar, S., 2013. MEGA6: molecular evolutionary genetics analysis version 6.0. Mol. Biol. Evol. 30, 2725–2729.
Thamdrup, B., Dalsgaard, T., Revsbech, N.P., 2012. Widespread functional anoxia in the oxygen minimum zone of the Eastern South Pacific. Deep-Sea Res. 65, 36–45.
Thomsen, S., Kanzow, T., Krahmann, G., Greatbatch, R.J., Dengler, M., Lavik, G., 2016. The formation of a subsurface anticyclonic eddy in the Peru–Chile undercurrent and its impact on the near-coastal salinity, oxygen, and nutrient distributions. J. Geophys. Res., Oceans 121, 476–501.
Vedamati, J., Goepfert, T., Moffett, J.W., 2014. Iron speciation in the eastern tropical South Pacific oxygen minimum zone off Peru. Limnol. Oceanogr. 59, 1945–1957.
Weber, K.A., Achenbach, L.A., Coates, J.D., 2006a. Microorganisms pumping iron: anaerobic microbial iron oxidation and reduction. Nat. Rev. Microbiol. 4, 752–764.
Weber, K.A., Urrutia, M.M., Churchill, P.F., Kukkadapu, R.K., Roden, E.E., 2006b. Anaerobic redox cycling of iron by freshwater sediment microorganisms. Environ. Microbiol. 8, 100–113.
Widdel, F., Schnell, S., Heising, S., Ehrenreich, A., Assmus, B., Schink, B., 1993. Ferrous iron oxidation by anoxygenic phototrophic bacteria. Nature 362, 834–836.
Wilke, M., Farges, F., Petit, P.-E., Brown, G.E., Martin, F., 2001. Oxidation state and coordination of Fe in minerals: an Fe K-XANES spectroscopic study. Am. Mineral. 86, 714–730.

Available online at www.sciencedirect.com

ScienceDirect

Geochimica et Cosmochimica Acta 213 (2017) 400–417

Geochimica et Cosmochimica Acta

www.elsevier.com/locate/gca

Intense molybdenum accumulation in sediments underneath a nitrogenous water column and implications for the reconstruction of paleo-redox conditions based on molybdenum isotopes

Florian Scholz *, Christopher Siebert, Andrew W. Dale, Martin Frank

GEOMAR Helmholtz Centre for Ocean Research Kiel, Wischhofstraße 1-3, 24148 Kiel, Germany

Received 26 January 2017; accepted in revised form 29 June 2017; Available online 11 July 2017

Abstract

The concentration and isotope composition of molybdenum (Mo) in sediments and sedimentary rocks are widely used proxies for anoxic conditions in the water column of paleo-marine systems. While the mechanisms leading to Mo fixation in modern restricted basins with anoxic and sulfidic (euxinic) conditions are reasonably well constrained, few studies have focused on Mo cycling in the context of open-marine anoxia. Here we present Mo data for water column particulate matter, modern surface sediments and a paleo-record covering the last 140,000 years from the Peruvian continental margin. Mo concentrations in late Holocene and Eemian (penultimate interglacial) shelf sediments off Peru range from ~70 to 100 μg g^{-1}, an extent of Mo enrichment that is thought to be indicative of (and limited to) euxinic systems. To investigate if this putative anomaly could be related to the occasional occurrence of sulfidic conditions in the water column overlying the Peruvian shelf, we compared trace metal (Mo, vanadium, uranium) enrichments in particulate matter from oxic, nitrate-reducing (nitrogenous) and sulfidic water masses. Coincident enrichments of iron (Fe) (oxyhydr)oxides and Mo in the nitrogenous water column as well as co-variation of dissolved Fe and Mo in the sediment pore water suggest that Mo is delivered to the sediment surface by Fe (oxyhydr)oxides. Most of these precipitate in the anoxic-nitrogenous water column due to oxidation of sediment-derived dissolved Fe with nitrate as a terminal electron acceptor. Upon reductive dissolution in the surface sediment, a fraction of the Fe and Mo is re-precipitated through interaction with pore water sulfide. The Fe- and nitrate-dependent mechanism of Mo accumulation proposed here is supported by the sedimentary Mo isotope composition, which is consistent with Mo adsorption onto Fe (oxyhydr)oxides. Trace metal co-variation patterns as well as Mo and nitrogen isotope systematics suggest that the same mechanism of Mo delivery caused the 'anomalously' high interglacial Mo accumulation rates in the paleo-record. Our findings suggest that Fe- and nitrate-dependent Mo shuttling under nitrogenous conditions needs to be considered a possible reason for sedimentary Mo enrichments during past periods of widespread anoxia in the open ocean.

Keywords: Paleo-redox; Molybdenum isotopes; Early diagenesis; Oxygen minimum zone; Anoxic marine sediment

1. INTRODUCTION

1.1. Scientific rationale

The Peruvian continental margin and associated oxygen minimum zone (OMZ) represent one of the most extreme

* Corresponding author.
E-mail address: fscholz@geomar.de (F. Scholz).

http://dx.doi.org/10.1016/j.gca.2017.06.048
0016-7037/

open-marine redox environments in the contemporary ocean. Oxygen concentrations in the core of the Peruvian OMZ (~100–300 m water depth, 10–20 °S) remain below the detection limit of state-of the art micro-sensors most of the time (<10 nM O_2) (Thamdrup et al., 2012). Moreover, stagnation events, during which hydrogen sulfide (H_2S) is released from the sediment into the water column, have been reported in recent studies (Schunck et al., 2013; Sommer et al., 2016). As a consequence of these unique characteristics, the Peruvian margin is an excellent locality to calibrate paleo-redox proxies in the context of open-marine anoxia.

It could be argued that restricted anoxic basins such as the Black Sea and Baltic Sea Deeps represent more appropriate analogues for extreme anoxia in Earth history than upwelling regions like the Peruvian margin. This notion is largely based on chemical arguments such as the more persistent occurrence of sulfidic conditions and higher H_2S concentrations in the water column of these systems compared to modern open ocean settings (Richards, 1965). However, the enclosed bathymetry, restricted estuarine circulation pattern and long seawater residence time in silled basins limit the comparability to open-marine systems in the geological past (e.g., Emerson and Huested, 1991; Algeo and Lyons, 2006; Scholz et al., 2013, 2014a). This is particularly true for paleo-systems characterized by complex lateral and vertical redox-structures, as suggested for several key periods and events in Earth history (e.g., Poulton et al., 2010; Hammarlund et al., 2012; Westermann et al., 2014; Goldberg et al., 2016), rather than uniform and basin-wide anoxia.

Here, we investigate the behavior of molybdenum (Mo) in the water column and sediments of the Peruvian continental margin. The main purpose of this study is to gain a mechanistic understanding of the factors controlling the concentration and isotope composition of Mo in sediments that accumulate in an open-marine anoxic environment. We also evaluate the likelihood that similar mechanisms operated during past periods of widespread anoxia in the open ocean.

1.2. The molybdenum proxy

Sedimentary Mo concentrations and isotope compositions are (along with iron (Fe) speciation) the most commonly used proxies for the identification of anoxic and sulfidic (i.e., euxinic) conditions in the water column of ancient marine systems. Molybdenum has a long residence time (~440,000 years) (Miller et al., 2011) in oxygenated seawater and thus a uniform concentration (~110 nM at a salinity of 35) throughout the global ocean (Bruland, 1983). In the presence of dissolved H_2S, molybdate (MoO_4^{2-}), the stable Mo species in oxygenated seawater, is converted to sulfur-containing Mo complexes (e.g., thiomolybdate ($Mo^{VI}O_xS_{4-x}^{2-}$, $1 < x < 4$) or Mo polysulfide ($Mo^{IV}O(S_4)S^{2-}$) (Helz et al., 1996; Erickson and Helz, 2000; Vorlicek et al., 2004; Dahl et al., 2013a). Thiomolybdate or Mo polysulfide (hereafter referred to as Mo-S species) are particle reactive and show a strong affinity to Fe sulfide minerals and sulfur-rich organic matter (Huerta-Diaz and Morse, 1992; Zheng et al., 2000; Vorlicek and Helz, 2002; Vorlicek et al., 2004; Tribovillard et al., 2004; Helz et al., 2011). This leads to an efficient mechanism of Mo fixation under sulfidic conditions. Therefore, marine systems in which H_2S is present in the shallow sediment or bottom waters are typically characterized by sedimentary Mo enrichments. In general, the extent of Mo enrichment increases from environments where H_2S is only present in the sediment pore water to environments where H_2S accumulates in the water column. Based on this observation, previous studies have proposed that sedimentary Mo concentrations >25 μg g^{-1} are indicative of at least intermittently euxinic conditions (Scott and Lyons, 2012; Dahl et al., 2013b). In some cases, sedimentary Mo enrichments in euxinic settings can be masked by dilution with detrital material (Scott and Lyons, 2012). Moreover, sustained periods of Mo fixation in euxinic basins with a long seawater residence time can lead to a drawdown of the Mo inventory in the water column (Algeo, 2004; Algeo and Lyons, 2006) thus impeding significant Mo enrichment (i.e., ≫25 μg g^{-1}) in the sediment.

The relatively heavy Mo isotope composition of modern seawater ($\delta^{98}Mo = 2.3‰$) has been attributed to the balance between the terrigenous input flux supplied via weathering and continental runoff (average $\delta^{98}Mo$ of +0.7‰) (Archer and Vance, 2008) and an isotopically light sink associated with Mo adsorption onto manganese (Mn) (oxy-

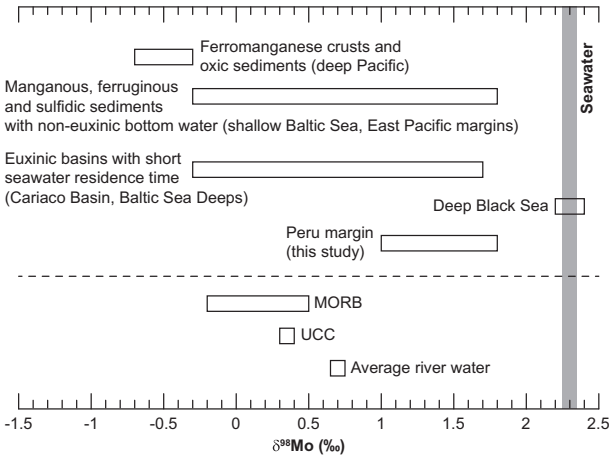

Fig. 1. Schematic overview of the range of Mo isotope values at different type localities in the contemporary ocean: Ferromanganese crusts and oxic sediments in the deep-sea (Barling et al., 2001; Poulson et al., 2006; Poulson Brucker et al., 2009); manganous, ferruginous and sulfidic sediments at continental margins (Poulson et al., 2006; Poulson Brucker et al., 2009; Goldberg et al., 2012)); euxinic basins with a short seawater residence time (~≤100 years; Baltic Sea Deeps, Cariaco Basin) (Arnold et al., 2004; Noordmann et al., 2015); euxinic basin with a long seawater residence time (hundreds to thousands of years; Black Sea) (Barling et al., 2001; Arnold et al., 2004). The range of isotope values observed in the present study as well as the Mo isotope compositions of Mid-ocean ridge basalt (MORB) (Freymuth et al., 2015), upper continental crust (UCC) (Voegelin et al., 2014) and average river water (Archer and Vance, 2008) are shown for comparison.

hydr)oxides in oxic deep-sea sediments (Barling et al., 2001; Siebert et al., 2003) (Fig. 1). Early in the history of Mo isotope geochemical research, it was discovered that sediments in the euxinic Black Sea have a Mo isotope composition similar to oxic seawater (Barling et al., 2001; Arnold et al., 2004) (Fig. 1). Based on the assumption that sediments underneath euxinic waters generally record the Mo isotope composition of contemporary seawater, it was argued that if large parts of the ocean remained euxinic for a prolonged period of time (theoretically implying near-quantitative Mo removal with no apparent isotope fractionation) the isotope composition of seawater would reach a new steady state value that lies closer to the δ^{98}Mo of the Mo input flux from rivers. Following this concept, black shales with a δ^{98}Mo below contemporary seawater and Black Sea sediments (below the chemocline) combined with independent evidence for euxinic conditions (e.g., from Fe speciation) have been interpreted as a quantitative indicator for more expanded euxinia during the corresponding intervals in Earth history (e.g., Arnold et al., 2004; Wille et al., 2008; Kendall et al., 2009; Dahl et al., 2011; Goldberg et al., 2016).

It is important to note, however, that the Black Sea is the only large euxinic basin investigated to date where the sedimentary Mo isotope signature reflects the δ^{98}Mo of contemporary seawater. In all other large euxinic basins investigated so far, δ^{98}Mo values span the entire range between the isotopically light oxic sink and modern seawater (see Fig. 1 and compilation in Goldberg et al. (2016)) thus implying partial removal of a fractionated Mo pool. In fact, the sedimentary Mo isotope values reported for most euxinic settings are similar to those observed in settings where H_2S is only present in the sediment pore water (Fig. 1). Such sulfidic continental margin sediments represent another important sink in the global ocean's Mo mass balance (McManus et al., 2006; Poulson Brucker et al., 2009).

Essentially two different mechanisms have been invoked to explain the Mo isotopic offset between sediments and seawater in both euxinic and non-euxinic settings: The first explanation is related to an incomplete conversion of molybdate to thiomolybdate species followed by partial removal of the latter (Neubert et al., 2008; Dahl et al., 2010; Nägler et al., 2011). The change in aqueous Mo speciation is expected to be accompanied by isotope fractionation (Tossell, 2005) and should thus impart an isotopic offset in the solid phase if one of the species is preferentially removed. The conversion of molybdate to thiomolybdate is a function of the H_2S concentration (Helz et al., 1996), which is why incomplete conversion in many euxinic settings could be the result of lower H_2S concentrations than those prevailing in the Black Sea.

The second explanation is related to the deposition of a particulate phase where Mo is adsorbed to the surfaces of metal (oxyhydr)oxides (McManus et al., 2002; Poulson Brucker et al., 2009; Goldberg et al., 2012). Experimental studies have demonstrated that the light Mo isotopes preferentially adsorb to the surfaces of Mn and Fe (oxyhydr) oxide minerals. The extent of isotope fractionation decreases from Mn ($\Delta^{98}Mo_{seawater\text{-}adsorbed} = +2.8‰$) (Siebert et al., 2003; Barling and Anbar, 2004; Wasylenki et al., 2008) to Fe minerals ($\Delta^{98}Mo_{seawater\text{-}adsorbed} = +0.8 - +2.2‰$) and with decreasing crystallinity of the Fe (oxyhydr)oxides: hematite ($\Delta^{98}Mo_{seawater\text{-}adsorbed} = +2.19 \pm 0.54‰$) > goethite ($\Delta^{98}Mo_{seawater\text{-}adsorbed} = +1.40 \pm 0.48‰$) > ferrihydrite ($\Delta^{98}Mo_{seawater\text{-}adsorbed} = +1.11 \pm 0.15‰$) (Goldberg et al., 2009). Release of Mo from Mn and/or Fe (oxyhydr)oxides followed by interaction with pore water sulfide and precipitation of an authigenic Mo phase would thus also produce a lighter Mo isotope value than seawater.

Even though the fundamental processes contributing to Mo isotope fractionation in marine sedimentary environments have been identified, the detailed pathway of Mo transfer from the water column into the sedimentary paleo-record is still poorly constrained. One reason for this knowledge gap is that, in most cases, either shallow sediments or paleo-records (mostly in deep time) are investigated but not both at the same site. Therefore, it is difficult to link the findings of regional process studies to paleo-signals and paleo-environmental conditions. Moreover, few Mo data for water column particulate matter are available. To overcome this situation, we present here Mo concentration data for water column particulate matter, shallow sediments and pore waters as well as a late Quaternary paleo-record. In addition, Mo isotope data for the shallow sediments and paleo-record are reported. All samples were taken in close proximity to each other on the Peruvian continental margin.

2. STUDY AREA AND SAMPLES

Wind-driven upwelling of nutrient-rich intermediate water off Peru results in high primary and export production. Due to low oxygen concentrations in the upwelling water masses and intense respiration of the downward sinking organic matter, the Peruvian upwelling system is characterized by a pronounced OMZ with essentially anoxic conditions between 100 and 300 m water depth (Fig. 2A) (Thamdrup et al., 2012). A permanent nitrate deficit and the presence of a secondary nitrite maximum in the oxygen minimum zone indicate that denitrification and anammox (anaerobic ammonium oxidation) are the dominant biogeochemical processes in the water column (Fig. 2B and C) (Lam et al., 2009; Dalsgaard et al., 2012). Denitrification, Fe reduction and bacterial sulfate reduction dominate organic matter respiration in the underlying surface sediments (Bohlen et al., 2011). Due to the absence of oxygen in the bottom water, dissolved ferrous Fe generated in the sediment diffuses across the sediment-water interface (Noffke et al., 2012) thus leading to elevated Fe concentrations in the water column (Bruland et al., 2005; Vedamati et al., 2014). A recent study using the same water column particulate matter samples as the present study has demonstrated that long distance transport of dissolved Fe in the anoxic water column is likely limited by Fe oxidation with nitrate as a terminal electron acceptor (Scholz et al., 2016).

Long-lasting periods of nitrate-reducing (i.e., nitrogenous) conditions in the water column are occasionally interrupted by oxygenation events, which are related to the

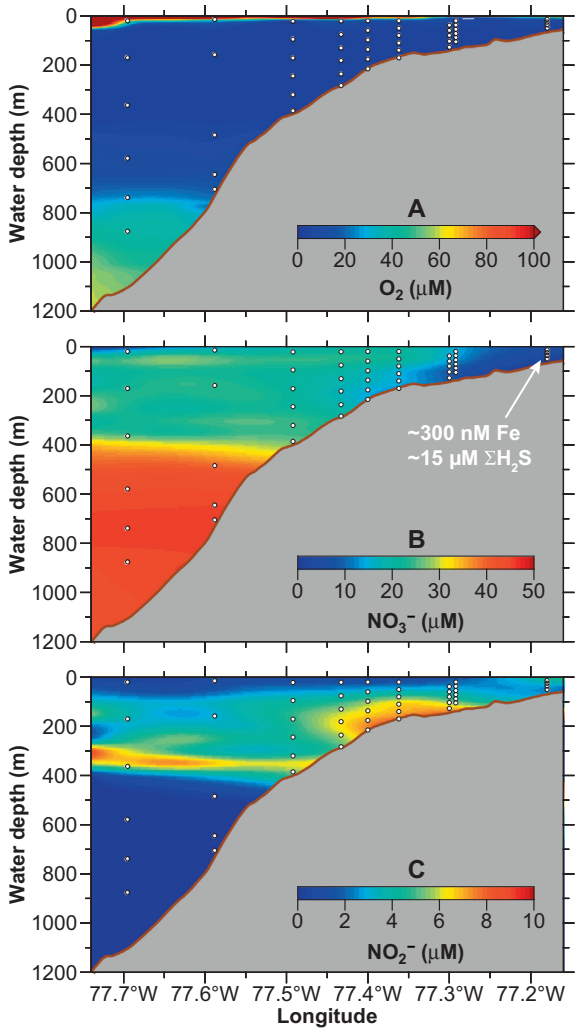

Fig. 2. Water column redox conditions across the Peruvian continental margin at 12 °S (see Fig. 3 for location map) during research cruise M92 in January 2013 (data from Scholz et al., 2016): (A) O_2, (B) nitrate (NO_3^-), (C) nitrite (NO_2^-). The nitrate- and nitrite-depleted water mass overlying the shelf was characterized by elevated dissolved Fe and H_2S concentrations (see arrow in (B)). Circles depict the location of particulate matter samples that were taken during the cruise.

passage of coastal trapped waves (Gutiérrez et al., 2008). Such transient oxygenation is most intense during El Niño events (e.g., >20 µM O_2 in bottom waters below 200 m water depth) (Levin et al., 2002). Sulfidic events, the opposite redox extreme in the water column overlying the Peruvian shelf, occur during times of water column stagnation. Upon complete consumption of nitrate and nitrite in the bottom water, H_2S is released from the sediment into the water column (Schunck et al., 2013; Dale et al., 2016). Paleoceanographic studies have demonstrated that the OMZ off Peru and Chile was better ventilated during the last glacial maximum. By contrast, interglacials (Holocene and Eemian (MIS5e)) were characterized by more reducing conditions with more intense denitrification (Ganeshram et al., 2000; Muratli et al., 2010; Scholz et al., 2014b; Salvatteci et al., 2015).

Samples for this study were collected during three cruises of research vessel Meteor in November and December 2008 (cruises M77-1 and M77-2) and in January 2013 (M92) (Table 1). Water column particulate matter samples were collected during cruise M92 along a zonal section at 12 °S (Fig. 3). During M92, the water column overlying the shallow shelf was characterized by weakly sulfidic conditions ($\Sigma H_2S = H_2S + HS^- + S^{2-} = \sim 15$ µM) and high dissolved Fe concentrations (dissolved Fe = ~300 nM) (Fig. 2B) (Scholz et al., 2016). Shallow sediment cores were collected on a transect at 11 °S during cruises M77-1 and M77-2 (Fig. 3). No hydrogen sulfide was detected in the water column during these cruises. The piston core from which the paleo-record investigated in this study was derived (piston core M77-2-024-5) was retrieved at ~11° at 210 m water depth, i.e., close to the shorter sediment cores MUC29 and BIGO-T (Table 1, Fig. 3). The age model of M77-2-024-5 was established by a combination of radiocarbon dating on organic matter and stratigraphic correlation with other records (see Scholz et al., 2014b for details). With the exception of a hiatus at 423 cm core depth (~50,000–20,000 yr BP), the age model of M77-2-024-5 covers the last 140,000 yrs. Some of the data used in this article were published previously (trace metal concentrations in sediments (Scholz et al., 2011, 2014b), pore water concentration data (Scholz et al., 2011), Fe speciation data (Scholz et al., 2014c)). All Mo isotope data as well as the trace metal concentration data for suspended particulate matter samples are new to this study.

3. METHODS

3.1. Sampling

Water column particulate matter samples were collected using an array of six PTFE-coated 8 L GO-FLO bottles (General Oceanics) individually mounted on a Kevlar wire. Upon recovery, the GO-FLO bottles were transferred to a laboratory and pressurized with nitrogen gas. The water was filtered through polyethersulfone filters (0.2 µm pore size, 47 mm) (PALL Corporation) in a laminar flow bench. Prior to use the filters had been leached with 1 M HCl and rinsed with deionized water. The filters were transferred to acid-cleaned Petri dishes and stored at −20 °C until further treatment after the cruise. Shallow sediments (uppermost 15–30 cm) were collected using a multiple corer (MUC) or benthic landers (Biogeochemical Observatory, BIGO). Subsampling of the sediment cores was done in an argon-filled glove bag as described in detail in Scholz et al. (2011). The pore water was separated from the solid phase by centrifuging and filtered in a second glove bag through cellulose acetate membrane filters (0.2 µm pore size). The pore water aliquots for trace metal analyses were acidified using concentrated HNO_3 (purified by sub-boiling distillation) and stored in acid-cleaned HDPE vials. The residual sediment in centrifuge tubes was frozen and stored for solid phase analyses after the cruise. Sediment core M77-2-024-5 was retrieved with a piston corer and sediment samples were collected with cut syringes at the GEOMAR core repository.

Table 1
Geographical coordinates and water depth of all sampling stations.

Cruise	Station	Code	Longitude W	Latitude S	Water depth (m)	Bottom water oxygen[a, b] (μM)
Water column						
M92	72	GO-FLO05	12°13.5′	77°10.8′	74	
M92	212	GO-FLO11	12°18.9′	77°17.5′	144	
M92	60	GO-FLO04	12°18.7′	77°18.0′	145	
M92	278	GO-FLO12	12°21.5′	77°21.7′	195	
M92	31	GO-FLO03	12°23.0′	77°24.0′	244	
M92	112	GO-FLO07	12°24.8′	77°26.0′	298	
M92	135	GO-FLO09	12°27.2′	77°29.5′	407	
M92	102	GO-FLO06	12°31.3′	77°35.3′	774	
M92	126	GO-FLO08	12°35.9′	77°41.7′	1022	
Sediment cores						
M77-1	568	BIGO05	11°00.0′	77°47.7′	85	<LD
M77-1	470	MUC29	11°00.0′	77°56.6′	145	<LD
M77-2	016	BIGO-T	10°59.8′	78°05.9′	259	<LD
M77-1	449	MUC19	11°00.0′	78°10.0′	319	<LD
M77-1	459	MUC25	11°00.0′	78°25.6′	697	12.1
Paleo-record						
M77-2		M77-2-024-5	11°05.0′	78°00.91′	210	

LD: Limit of detection.
[a] Shallow sediment cores only.
[b] Bottom waters on the Peruvian shelf can be oxic or sulfidic (Scholz et al., 2011, 2016).

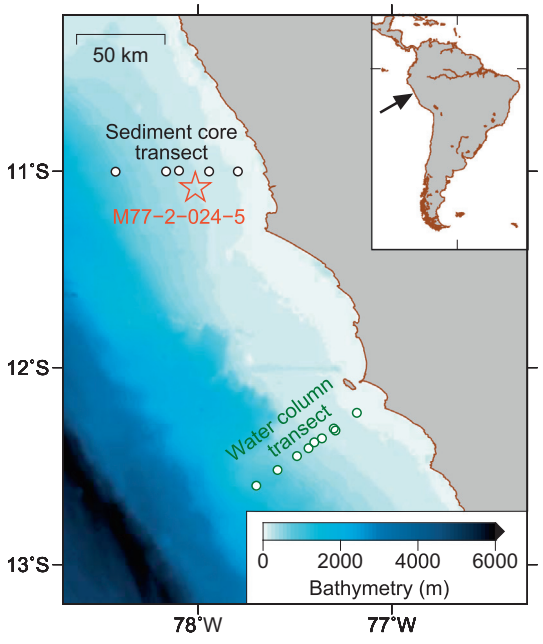

Fig. 3. Bathymetric map of the Peruvian continental margin showing the location of all GO-FLO (water column particulate matter) and sediment core stations.

3.2. Chemical analyses

Suspended particulate matter on filters was digested following the sampling and sample-handling protocols for GEOTRACES cruises (Cutter et al., 2014). In brief, filters were cut into halves, placed into PTFE vials and the particles were digested through refluxing of HNO_3 and HF on a hot plate. After repeated evaporation of the solution and re-dissolution with concentrated HNO_3, the residue was re-dissolved in 5 M HNO_3 and stored for further analysis. Sediment samples from MUCs and BIGOs were digested on a hotplate with an acid mix consisting of HNO_3, HF and $HClO_4$. Sediment samples from M77-2-024-5 were digested with a CEM MARS-5 microwave system in an acid mix consisting of HCl, HNO_3 and HF (Muratli et al., 2012). Major element (Fe, aluminum (Al), Mn) concentrations were analyzed by inductively coupled plasma optical emission spectrometry (ICP-OES) and trace element (vanadium (V), Mo, uranium (U)) concentrations were analyzed by inductively coupled plasma mass spectrometry (ICP-MS) (see Scholz et al. (2011, 2014b, 2016) for details). For quality control, blanks, sample duplicates and the certified reference materials SDO-1 (Devonian Ohio Shale, USGS) and MESS-3 (Marine Sediment, Canadian Research Council) as well as several in-house standards were included in the whole digestion and analysis procedure. Measured concentrations for certified reference materials were always within the certified ranges, except for Mo in MESS-3 following the digestion protocol for suspended particulate matter where the recovery was consistently about 20% too low. The digestion procedure for particulate matter is relatively gentle compared to the more aggressive protocols for sediment samples (lower acid concentrations and shorter digestion period) and residual sediment grains, presumably representing refractory minerals, were present after the digestion of MESS-3. Therefore, we attribute the incomplete recovery to the relatively low and crustal-like

Mo concentration in MESS-3 (2.78 ± 0.07 μg g^{-1}; 2-fold enrichment over average upper continental crust). By contrast, particulate matter from the Peruvian margin is strongly enriched in Mo compared to crustal material (10^1–10^4-fold enrichment over average upper continental crust) and suspended particulate matter samples did not reveal residual material after the digestion. We therefore consider the Mo concentrations obtained for particulate matter samples as reliable and unaffected by the incomplete recovery for MESS-3. Dissolved concentrations of Mo in pore water were also analyzed by ICP-MS. The accuracy and precision of these analyses was monitored by repeatedly analyzing certified reference material CASS-5 (Nearshore Seawater, Canadian Research Council) (recommended value: 102 nM; measured value (mean ± standard deviation, SD): 95.4 ± 1.5, n = 87).

To separate the authigenic from the lithogenic Mo fraction in the solid phase, trace metal concentrations are expressed as excess concentrations (Eq. (1)) or enrichment factors (Eq. (2)) relative to the trace metal (TM) to Al ratio of the regional lithogenic background (Brumsack, 2006; Tribovillard et al., 2006):

$$TM_{XS} = TM_{sample} - \frac{TM_{background}}{Al_{background}} \cdot Al_{sample} \quad (1)$$

$$TM_{EF} = \frac{\left(\frac{TM_{sample}}{Al_{sample}}\right)}{\left(\frac{TM_{background}}{Al_{background}}\right)} \quad (2)$$

Andesite in the Andean Arc was chosen as the regional lithogenic background (Fe/Al = 0.47, Mn/Al = $1.23 \cdot 10^{-2}$, V/Al = $1.39 \cdot 10^{-3}$, Mo/Al = $0.26 \cdot 10^{-4}$, U/Al = $0.37 \cdot 10^{-4}$) (Böning et al., 2004; Scholz et al., 2011).

3.3. Isotope analyses

Analysis of Mo isotopes in this study was performed at GEOMAR on a Nu Instruments multi collector ICP-MS with a DSN-100 Desolvation Nebulizer System utilizing a double isotope tracer (^{100}Mo, ^{97}Mo) for correction of instrumental and possible laboratory mass fractionation (Siebert et al., 2001). All samples were spiked with the tracer before chemical separation of Mo from the sample matrix. Chemical separation was performed in 0.5 M HCl on 2 mL of Biorad AG50W-X8 cation resin to remove Fe, followed by separation from the remaining matrix in 4 M HCl on 1 mL Biorad AG1-X8 anion exchange resin and elution in 2 M HNO_3. Total procedural blanks were <1 ng of Mo.

During measurements 50 ng of Mo was analyzed resulting in an ion beam intensity of approximately 120 V ppm^{-1} (excluding double spike signal) using 10^{11} Ω resistors. Each measurement is the average of 4 blocks of 10 measurement cycles with 10 s signal integration time each. Mass 99 was monitored for possible isobaric interferences of ruthenium. Samples were scanned for Fe before measurements to exclude possible Fe-argide interferences.

All Mo isotopic variations are presented in delta notation as the deviation of the ^{98}Mo/^{95}Mo ratio in parts per thousand (‰) relative to a standard:

$$\delta^{98}Mo = \left(\frac{\left(\frac{^{98}Mo}{^{95}Mo}\right)_{sample}}{\left(\frac{^{98}Mo}{^{95}Mo}\right)_{standard}} - 1 \right) \cdot 1000 \quad (3)$$

Isotope values in this study are presented relative to Alfa Aesar Mo plasma standard solution, Specpure #38791 (lot no. 011895D). This standard is offset from international interlaboratory reference material NIST SRM 3134 by a δ^{98}Mo value of -0.15 ± 0.03‰ (2 SD) (Greber et al., 2012; Nägler et al., 2014). Nägler et al. (2014) suggested open-ocean seawater with a homogenous δ^{98}Mo of +2.34 ± 0.10‰ (relative to NIST SRM 3134) as a secondary reference standard for Mo isotope measurement. Repeated analysis of IAPSO seawater standard in this study yielded a δ^{98}Mo of $+2.25 \pm 0.09$‰ (2 SD; $n = 4$), which is within analytical uncertainty of the internationally agreed seawater reference value. For information purposes, Mo isotope data are given relative to both the in-house standard and NIST SRM 3134 in Supplementary Tables S2 and S4.

USGS rock standard reference material SDO-1 (black shale) was processed through column chemistry and measured with each sample run. The long-term external reproducibility of SDO-1 is 0.09‰ (2 SD, average δ^{98}Mo is +0.99‰). Therefore, a uniform analytical error of ±0.1‰ is plotted in the figures. With the exception of a few samples from sediment core M77-2-024-5 (see Supplementary Table S4) sample duplicates are generally within this error range. The long-term external reproducibility of the Specpure standard solution is 0.07‰ (2 SD).

Analogous to Eq. (1) and assuming two-component-mixing of crustal Mo and authigenic Mo phases (Mo_{XS}), the isotope composition of Mo_{XS} is calculated according to the following mass balance equation:

$$\delta^{98}Mo_{XS} = \frac{\left(\delta^{98}Mo_{sample} - \left(1 - \frac{Mo_{XS}}{Mo_{sample}}\right) \cdot \delta^{98}Mo_{crust}\right)}{\left(\frac{Mo_{XS}}{Mo_{sample}}\right)} \quad (4)$$

Published estimates for the Phanerozoic average upper continental crust range from +0.3‰ to +0.4‰ (e.g., Malinovsky et al., 2007 Voegelin et al., 2014). In agreement with this range and following Goldberg et al. (2012) we chose to adopt +0.3‰ for $\delta^{98}Mo_{crust}$. Lithogenic contributions to the sedimentary Mo isotope signal observed in this study are generally low (<1% within the OMZ to 36% below the OMZ) so that using slightly higher or lower $\delta^{98}Mo_{crust}$ values would not affect the data interpretation.

4. RESULTS

4.1. Water column

Particulate metal concentrations in the water column are presented as a function of water depth and redox state (Fig. 4). Oxic samples are from the surface ocean and below the OMZ, nitrogenous samples were taken within the OMZ and sulfidic samples were taken at the shallowest station within the sulfidic plume overlying the shelf sediments (Fig. 2).

Enrichment factors of Mo in suspended particulate matter are reported together with enrichment factors of other

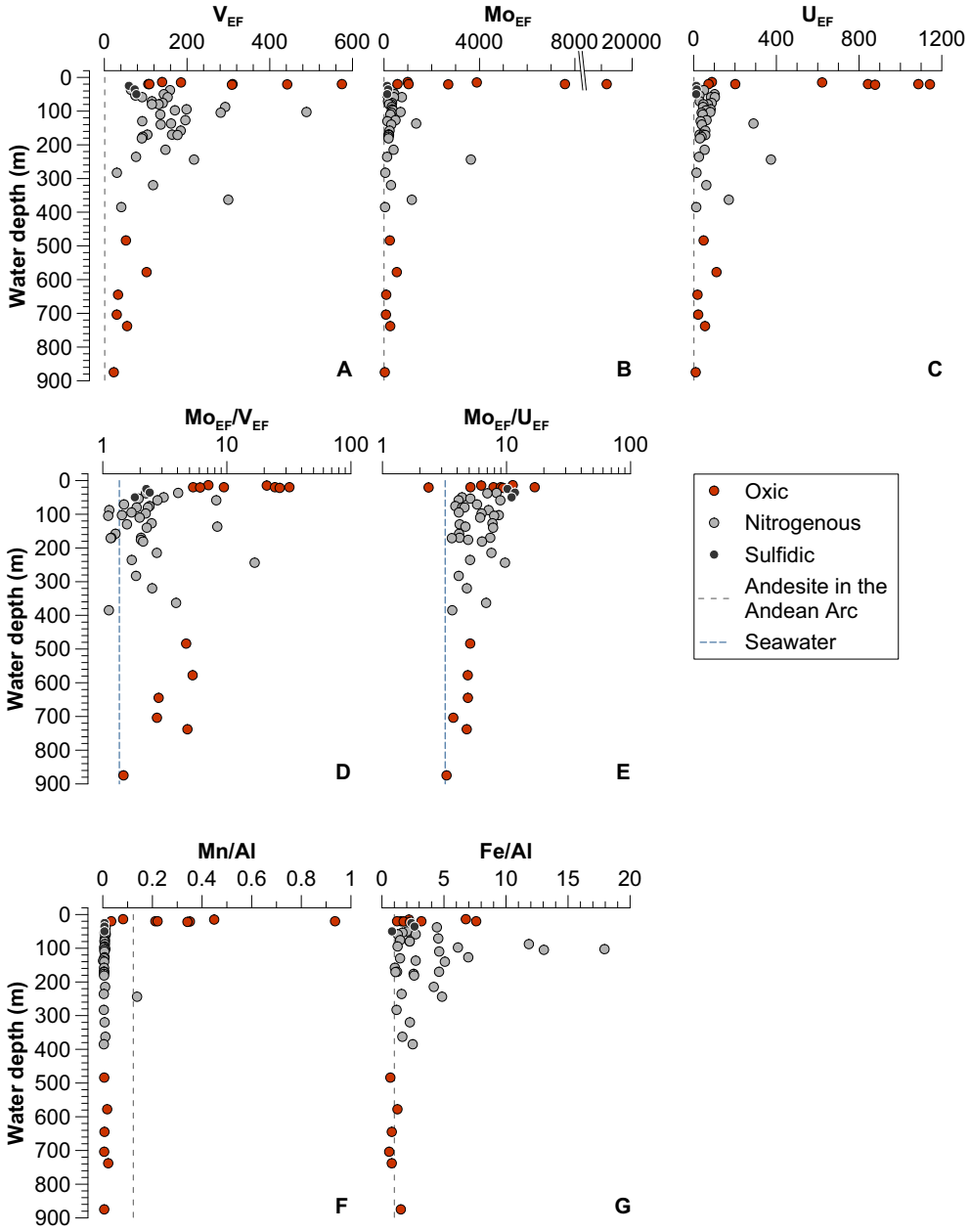

Fig. 4. Distribution of particulate metals in the water column: (A) V_{EF}, (B) Mo_{EF}, (C) U_{EF}, (D) Mo_{EF}/V_{EF}, (E) Mo_{EF}/U_{EF}, (F) Mn/Al, (G) Fe/Al). Samples are plotted against water depth and subdivided according to their redox state in oxic, nitrogenous and sulfidic. Vertical dashed lines depict the regional lithogenic background (andesite in the Andean Arc) or seawater (dissolved) Mo/V and Mo/U). The data shown in this figure are contained in Supplementary Table S1.

metals that are known to be enriched in anoxic marine sediments. Trace metal enrichment factors decrease in the following order: oxic samples from the surface ocean > nitrogenous samples > sulfidic samples = oxic samples from below the OMZ (Fig. 4A–C). Enrichment factor ratios (Mo_{EF}/V_{EF}, Mo_{EF}/U_{EF}) are greater than one and exceed the seawater ratios in most samples (Fig. 4D and E). This observation indicates that Mo has the strongest affinity for suspended particulate matter among the trace metals investigated.

Particulate Mn and Fe concentrations are reported as Mn to Al and Fe to Al ratios which are compared to the Mn/Al and Fe/Al of the regional lithogenic background. In contrast to Mn and Fe, Al is not involved in redox-driven mineral dissolution or precipitation processes. Mn/Al and Fe/Al above or below the regional lithogenic background are thus indicative of in-situ precipitation or dissolution of Mn and Fe minerals. Suspended particulate matter in the well-oxygenated zone at the sea surface is enriched in Mn relative to the regional litho-

genic background (Fig. 4F). In contrast, sulfidic and nitrogenous samples as well as oxic samples from below the OMZ are Mn-depleted. Analogous to Mn, oxic samples from the surface ocean are enriched in Fe (Fig. 4G). However, nitrogenous samples from within the OMZ are characterized by even more pronounced Fe enrichments. Sulfidic samples and oxic samples from below the OMZ are characterized by Fe/Al similar to the lithogenic background.

4.2. Shallow sediment core transect

The highest Mo_{XS} concentrations ($\leq 100\ \mu g\ g^{-1}$) are observed in sediments between ~100 and ~400 m water depth (Fig. 5A) where bottom waters are nitrogenous most of the time. Sediments on the shallow shelf (<100 m water depth), where bottom waters can be oxic or sulfidic, and sediments below the OMZ (>500 m water depth) are characterized by lower Mo_{XS} concentrations. Enrichment factor ratios (Mo_{EF}/V_{EF}, Mo_{EF}/U_{EF}) increase with decreasing water depth and reach the highest values at 145 m water depth (Fig. 5B and C) where they are broadly consistent with the enrichment factor ratios of particulate matter in the overlying water column (Fig. 4F and G).

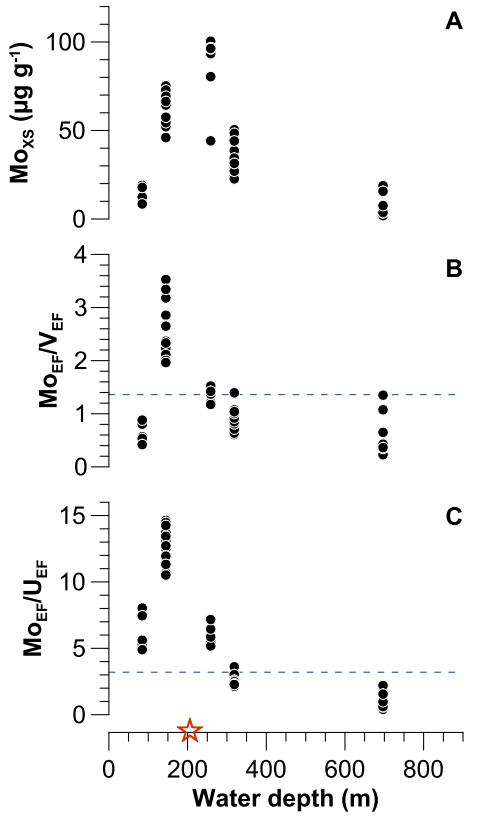

Fig. 5. Distribution of trace metals in shallow sediments: (A) Mo_{XS}, (B) Mo_{EF}/V_{EF}, (C) Mo_{EF}/U_{EF}. Horizontal dashed lines depict the dissolved Mo/V and Mo/U of seawater. The star above the x-axis depicts the water depth of M77-2-024-5. The data shown in this figure are contained in Supplementary Table S2.

4.3. Solid phase and pore water molybdenum profiles in shallow sediments

The downcore distribution of pore water Mo, Mo_{XS} and $\delta^{98}Mo_{XS}$ is compared to the distribution of dissolved Fe and H_2S as well as solid phase Fe speciation for selected cores (Fig. 6, Table 1). The cores shown in Fig. 6 were chosen because they cover the transition from Fe-rich (ferruginous) to sulfidic pore water (the two other cores listed in Table 1 and plotted in Fig. 5 are shorter).

All three cores display elevated dissolved Mo concentrations in the topmost pore water sample compared to seawater and bottom water. This pore water concentration pattern indicates a flux of Mo from the sediment into the bottom water. In the shallower two cores with nitrogenous bottom water (145 m and 319 m water depth), the increase in pore water Mo coincides with increasing concentrations of dissolved Fe (Fig. 6A and B). Below a maximum at or close to the sediment surface, pore water Mo concentrations decrease and the lowest concentrations are observed at the depth where H_2S accumulates in the pore water. Higher dissolved Mo concentrations persist to greater sediment depth than dissolved Fe concentrations. The transition from Mo-enriched and ferruginous pore water to Mo-depleted and sulfidic pore water is accompanied by decreasing Fe (oxyhydr)oxide and increasing pyrite concentrations (Fig. 6A and B). The sediments are characterized by significant Mo enrichments throughout the cored depth interval ($Mo_{XS} > 20\ \mu g\ g^{-1}$) and $\delta^{98}Mo_{XS}$ values fall into a relatively narrow range between +1.25‰ and +1.52‰.

At the deepest site (697 m water depth), where weakly oxic bottom waters prevail both dissolved (Mo < 1100 nM) and solid phase ($Mo_{XS} < 20\ \mu g\ g^{-1}$) Mo concentrations increase towards the base of the core, coincident with decreasing Fe (oxyhydr)oxide and increasing pyrite concentrations (Fig. 6C). No H_2S was detected in this core. The $\delta^{98}Mo_{XS}$ consistently decrease from +1.55‰ at the sediment surface to +1.04‰ at the lower end of the core.

4.4. Paleo-record

The trace metal and Mo isotope variability in core M77-2-024-5 is compared with previously published nitrogen isotope data for the same record (Fig. 7). Reduction of nitrate to nitrite in the water column coupled to reduction of nitrite to N_2 by denitrification and anammox leaves the remaining nitrate enriched in ^{15}N. If the enriched nitrate is incorporated into phytoplankton biomass and subsequently preserved in the sediments a paleoceanographic record is created (Altabet et al., 2002). High $\delta^{15}N$ signatures during the late Holocene, the last deglaciation (BA) and the Eemian (Marine MIS5e), thus indicate more intense water column denitrification and anammox. In contrast, lower $\delta^{15}N$ values during MIS2 (last glacial), MIS3 and MIS5a through MIS5d indicate less intense denitrification and anammox (Fig. 7A). The temporal variability of Mo_{XS} is largely synchronous with the $\delta^{15}N$ record, i.e., higher Mo_{XS} is observed during the Holocene, MIS3 and MIS5e (Mo_{XS} up to 88 $\mu g\ g^{-1}$) whereas lower Mo_{XS} is observed during MIS2, MIS4 and MIS5a though MIS5d (Mo_{XS} as low as

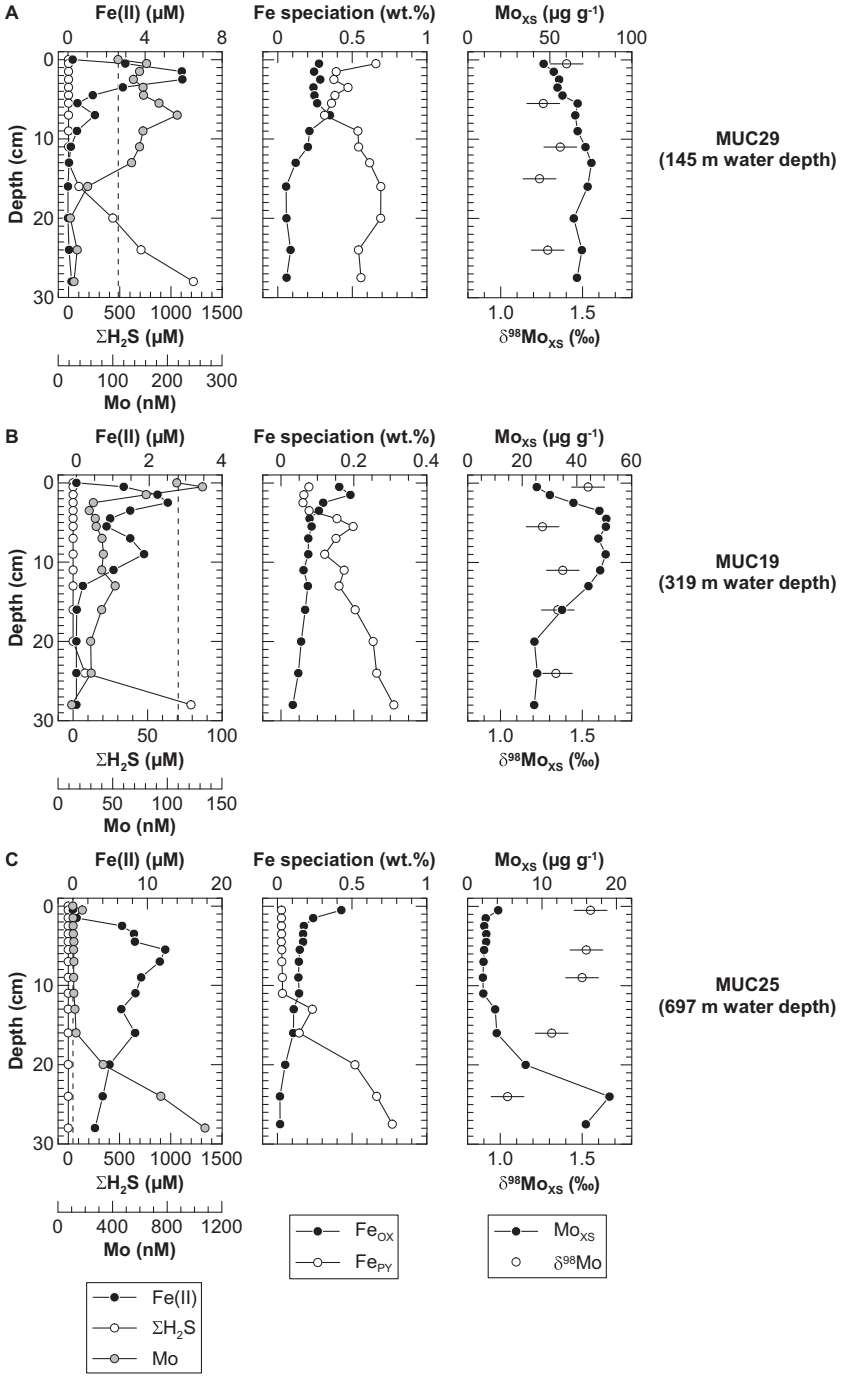

Fig. 6. Downcore profiles for (A) shelf sediments with predominantly nitrogenous bottom water, (B) slope sediments with nitrogenous bottom water, (C) slope sediments with weakly oxic bottom water: (left column) dissolved Fe, hydrogen sulfide and Mo in pore water (vertical dashed lines indicate seawater Mo concentration) (data from Scholz et al. (2011)): (central column) Fe (oxyhydr)oxide minerals (Fe_{OX}) leached with sodium dithionite and pyrite Fe (Fe_{PY}) leached with HNO_3 after removal of the remaining Fe phases with HCl and HF (data from Scholz et al. (2014c), see there for methodological details); (right column) Mo_{XS} and $\delta^{98}Mo_{XS}$. Note the different scales of the x-axes in (A), (B) and (C). The data shown in this figure are contained in the Supplementary Tables S2 and S3.

6 μg g^{-1}) (Fig. 7B). The $\delta^{98}Mo_{XS}$ values range from +1.07‰ to +1.95‰ and do not significantly correlate with Mo_{XS} (Fig. 7C). The records of Mo_{EF}/V_{EF} and Mo_{EF}/U_{EF} display systematic variations that are synchronous with Mo_{XS}. The higher Mo_{EF}/V_{EF} and Mo_{EF}/U_{EF} values are also consistent with the composition of particulate matter from the nitrogenous water column and surface sediments at the same water depth.

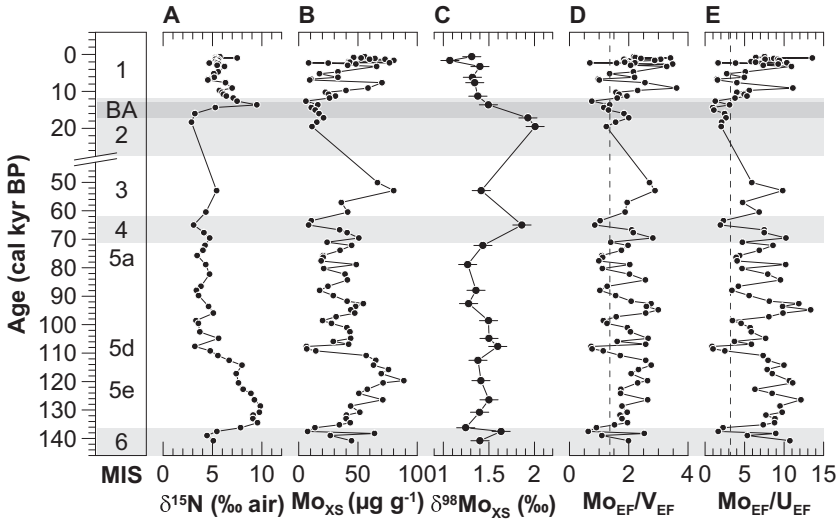

Fig. 7. Paleo-records of (A) $\delta^{15}N$, (B) Mo_{XS}, (C) $\delta^{98}Mo_{XS}$, (D) Mo_{EF}/V_{EF}, (E) Mo_{EF}/U_{EF} (MIS: Marine Isotope Stage; BA: Bølling Ållerød). Vertical dashed lines in (D) and (E) depict the dissolved Mo/V and Mo/U of seawater. The data shown in this figure are contained in Supplementary Table S4.

5. DISCUSSION

Sedimentary Mo_{XS} concentrations on the Peruvian shelf and through much of the paleo-record (Figs. 5A and 6B) by far exceed the threshold value for euxinic conditions of 25 µg g^{-1} (Scott and Lyons, 2012; Dahl et al., 2013b). Dissolved nitrogen species in the water column (Fig. 2B and C) as well as the nitrogen isotope record (Fig. 7A) indicate nitrogenous conditions at the same time. In general, H_2S does not accumulate in the water column unless nitrate and nitrite are quantitatively consumed, thus implying low or negligible enrichment of organic nitrogen in ^{15}N due to denitrification and anammox. Therefore, the presence of nitrate/nitrite in the water column along with the nitrogen isotope record presents a situation that is clearly inconsistent with euxinic conditions.

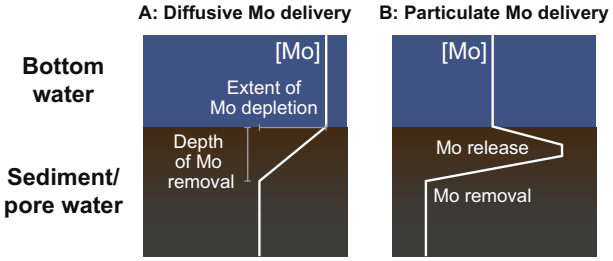

Fig. 8. Generalized representation of pore water Mo profiles being consistent with different mechanisms of Mo accumulation: (A) Accumulation through diffusion from the bottom water to the depth of Mo removal (extent of Mo depletion refers to the concentration difference between bottom water and the depth of Mo removal); (B) Mo release from a solid carrier phase followed by upward diffusion across the sediment water interface and downward diffusion to the depth of Mo removal. The solid phase Mo mass accumulation rate in (B) is higher because of the steeper concentration-depth gradient above the depth of Mo removal.

The Mo isotope data in the paleo-record presented here cover a $\delta^{98}Mo_{XS}$ range of almost 1‰ with the heaviest values being close to the Mo isotope composition of contemporary seawater. Surprisingly, the highest $\delta^{98}Mo_{XS}$ values are observed during intervals with low Mo_{XS} and $\delta^{15}N$ (MIS2 and MIS4), i.e., during intervals with presumably less reducing conditions.

These observations raise key-questions for the use and interpretation of Mo concentrations and Mo isotopes as paleo-redox proxies in open ocean settings, which will be discussed in detail below:

(1) What is the mechanism of intense Mo delivery and accumulation at the Peruvian continental margin?
(2) How do Mo isotopes in the sediment respond to this mechanism?
(3) How relevant are the underlying processes for the interpretation of Mo concentrations and isotope ratios in the paleo-record?

5.1. Diffusive versus particulate molybdenum delivery

Previous studies have argued that Mo accumulation in sediments of productive upwelling regions is mediated through diffusion of Mo from the bottom water into the sulfidic zone of the sediment (Böning et al., 2004; Brumsack, 2006). The pore water profiles discussed in this study reveal an upward concentration gradient across the sediment-water interface (Fig. 6, left column), which is inconsistent with sedimentary Mo accumulation through diffusion. However, pore water profiles underlie a strong temporal variability and can only provide snapshot evidence for the mechanisms driving Mo accumulation. Therefore, a more general evaluation of diffusion-driven Mo mass accumulation rates is required to assess whether diffusion from bottom waters can explain the high Mo concentrations observed in Peru margin sediments.

According to Fick's First Law, the accumulation rate of an element (Mo in the present case) through molecular diffusion at steady state depends on the ratio between the extent of element depletion and the depth over which element removal takes place (Fig. 8A). In addition, sediment diffusion is also affected by porosity and ambient temperature via the diffusion coefficient. We calculated diffusive fluxes of Mo into the sediment (hence Mo mass accumulation rates) for three end member scenarios of porosity and ambient temperature (Fig. 9). The three scenarios cover the full range of porosities and temperatures that may have prevailed at the coring location of M77-2-024-5 over the time span covered by the paleo-record. If Mo accumulated through diffusion, the time-integrated Mo mass accumulation rate would have to be consistent with the concentration-depth gradients implied by these scenarios.

The actual Mo_{XS} mass accumulation rates during the late Holocene, last glacial and Eemian were estimated by multiplying sedimentation rates, dry bulk densities and Mo_{XS} during the corresponding intervals (Table 2). Plotting these mass accumulation rates as continuous lines in Fig. 9 reveals that the high Mo_{XS} concentrations in sediments of the late Holocene and Eemian require complete Mo-depletion at very shallow depth (<0.1–2 cm). Such a shallow Mo depletion is not only inconsistent with the pore water profiles presented here (Fig. 6) but, to our best knowledge, with any pore water Mo profile in organic matter-rich sediments published to date (e.g., Zheng et al., 2000; Morford et al., 2005; Scholz et al., 2013). We therefore conclude that diffusion alone is an unrealistic mechanism of Mo accumulation in these sediments. Instead, a particulate Mo source forming in the water column has to be invoked to explain the extremely high Mo_{XS} concentrations in Peru margin sediments.

5.2. Molybdenum cycling in the water column

Considering the repeated detection of H_2S plumes during recent research cruises to the Peruvian margin (Schunck et al., 2013; Sommer et al., 2016), it could be argued that interactions between Mo and H_2S in the water column are responsible for high Mo concentrations in shelf sediments (e.g., Dahl et al., 2013b). According to the traditional model, Mo removal from sulfidic waters requires the conversion of molybdate to thiomolybdate, which is possible at an aqueous H_2S ($\neq \Sigma H_2S$) concentration of $\geq$11 μM (Erickson and Helz, 2000). In a more recent study, Helz et al. (2011) pointed out that Mo might be removed from sulfidic waters as a nanoparticulate Fe-Mo-S mineral, which requires oversaturation with respect to amorphous Fe monosulfide. Concentrations of ΣH_2S in recently sampled sulfidic plumes overlying the Peruvian shelf did not exceed 15 μM (Schunck et al., 2013; Scholz et al., 2016) and, considering the typical pH range of seawater, the majority of this H_2S was likely present as HS^-. Moreover, these weakly sulfidic waters were highly undersaturated with respect to Fe monosulfide (Scholz et al., 2016). From a thermodynamic point of view, water column Mo scavenging as aqueous Mo-S species or Fe-Mo-S nanoparticle is unlikely to take place under these conditions. Consistent with this notion, suspended particulate matter in sulfidic samples is least enriched in Mo compared to oxic and nitrogenous samples (Fig. 4B).

As an alternative to scavenging as Mo-S species or nanoparticulate Fe-Mo-S, Mo may be delivered to the sediment surface in association with Mn and Fe (oxyhydr)oxide minerals. Such a Mn and Fe shuttle mechanism has been postulated in an earlier study (Scholz et al., 2011) based on Mo-U covariation in the sediments (Algeo and Tribovillard, 2009). To evaluate the viability and elucidate the detailed mechanism of this supply pathway, we compare the distribution of particulate Mo with the distribution of other trace metals that are known to have some affinity for adsorption to metal (oxyhydr)oxides (i.e., V and U) (e.g., Chan and Riley, 1966; Wehrli and Stumm, 1989; Waite et al., 1994; Wang et al., 2012) as well as the distribution of particulate Mn and Fe carrier phases. All investigated trace metals show particulate enrichments in oxic

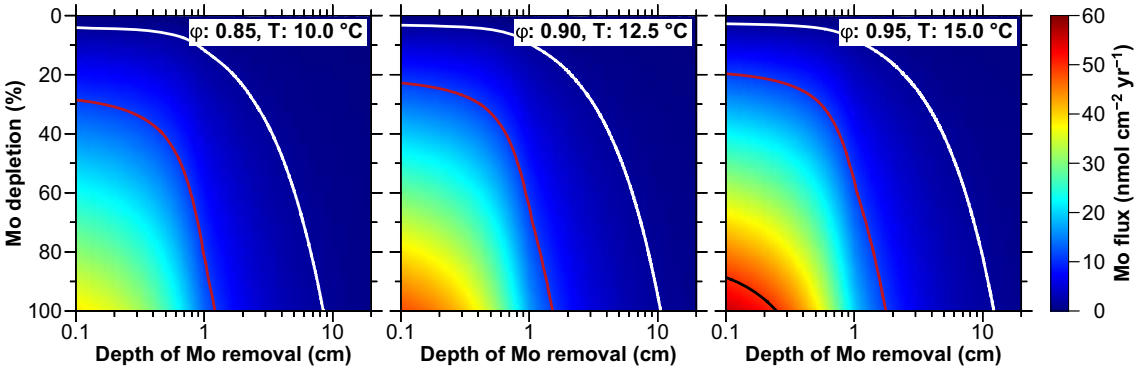

Fig. 9. Interpolated Mo mass accumulation rates calculated according to Fick's 1st Law as a function of the extent of Mo depletion (y-axis; 0% equals 110 nM) and the depth of Mo removal (x-axis; note log scale). The three panels represent three different scenarios of porosity and ambient temperature covering the range of values that may have prevailed in shelf sediments off Peru during the time span covered by the samples presented in this article. See Scholz et al. (2011) for details on the calculation. Solid lines depict the Mo mass accumulation rates observed during the late Holocene (black, only visible in the scenario with the highest temperature and porosity) last glacial (white) and the penultimate interglacial (red) (see also Table 2). (For interpretation of the references to colour in this figure legend, the reader is referred to the web version of this article.)

Table 2
Mo mass accumulation rates (MAR) during different time intervals in M77-2-024-5.

Time interval	Depth interval (cm)	Sedimentation rate[a] (cm yr^{-1})	Dry bulk density[b] (g cm^{-3})	Mass accumulation rate (MAR) (g cm^{-2} yr^{-1})	Mo_{XS} (μg g^{-1})	SD (μg g^{-1})	Mo_{XS}-MAR (nmol cm^{-2} yr^{-1})	SD (nmol cm^{-2} yr^{-1})
Late Holocene	0–200	0.0679	1.35	9.17E−02	52.2	19.3	49.9	18.44
Last glacial	400–420	0.0085	1.35	1.15E−02	13.2	2.9	1.6	0.34
Eemian (MIS5e)	1100–1400	0.0138	1.35	1.86E−02	57.3	16.3	11.1	3.17

[a] Mean sedimentation rate during the interval from Scholz et al. (2014b).
[b] Dry bulk density of sediments from the same time interval at ODP Site 680 which is located at a similar water depth and in close vicinity to M77-2-024-5 (Shipboard Scientific Party, 1988).

surface waters (Fig. 4A–C), coincident with a pronounced maximum in particulate Mn/Al (Fig. 4F). This observation indicates that Mo is scavenged by Mn (oxyhydr)oxides in the surface ocean. Adsorption of Mo to organic matter (Wasylenki et al., 2007) could also be important in the productive surface waters of the Peruvian upwelling.

Manganese to Al ratios drop abruptly below the oxycline and, in contrast to Mo, particles within the nitrogenous zone are depleted in Mn relative to the regional lithogenic background. A similar trend of Mn depletion has been observed in other water column studies on the Peruvian margin (Hawco et al., 2016) and surface sediments are also strongly depleted in Mn relative to the lithogenic background (Böning et al., 2004; Scholz et al., 2011). According to these previous studies, most of the particulate Mn (oxyhydr)oxides present at the sea surface are reductively dissolved during sinking through the oxygen-depleted water mass. Consequently, any trace metals scavenged in the surface ocean by Mn (oxyhydr)oxides will not reach the sediment surface and particulate trace metal enrichments in the nitrogenous zone must be associated with another carrier phase.

Nitrogenous samples are characterized by elevated Fe/Al compared to both most of the oxic samples and the lithogenic background. Recently published X-ray absorption spectroscopy and other geochemical as well as metagenomic data for the same sample material suggest that these particulate Fe enrichments are formed through re-oxidation of sediment-derived dissolved Fe^{2+} with nitrate as terminal electron acceptor (Scholz et al., 2016). Nitrate-dependent Fe oxidation is relatively inefficient in demobilizing dissolved Fe compared to Fe oxidation in well-oxygenated surface sediments and bottom waters. Therefore, pore water Fe^{2+} can escape the sediment and be oxidized in the water column. We suggest that Fe is continually cycled between the sediments and overlying water through oxidation, deposition and dissolution until a fraction of it is retained and buried in the sediment. Repeated precipitation of Fe-rich particles in the water column by nitrate-dependent Fe oxidation and re-dissolution in the sediment provides an efficient transport mechanism for particle-reactive trace metals to the sediment surface. In agreement with this hypothesis, surface sediments in the nitrogenous OMZ display Mo_{EF}/V_{EF} and Mo_{EF}/U_{EF} similar to the particulate matter in the overlying water column (Fig. 5).

Further support for Mo deposition with Fe (oxyhydr) oxides is provided by the Mo isotope composition of the surface sediments. The average $\delta^{98}Mo_{XS} \pm 1$ SD observed in shallow sediment cores is $+1.35 \pm 0.13$‰, which is in good agreement with the experimentally derived isotope composition of seawater Mo adsorbed to the Fe (oxyhydr)oxide minerals ferrihydrite ($\delta^{98}Mo = +1.2 \pm 0.15$) and goethite ($\delta^{98}Mo = +0.9 \pm 0.48$) (at pH 7.7; a smaller isotopic offset from seawater is to be expected at lower pH) (Goldberg et al., 2009). Both minerals have been shown to be abundant in the particulate matter in the nitrogenous zone of the Peruvian OMZ (Scholz et al., 2016). Other minerals that could play an important role in delivering Mo to the sediment surface in the nitrogenous

OMZ are mixed ferrous-ferric Fe minerals such as green rust (Heller et al., 2017). This type of mineral is known to form by anoxic Fe oxidation (Kappler and Newman, 2004; Pantke et al., 2012) and has a high adsorption capacity for particle-reactive trace metals (Zegeye et al., 2012). However, the isotopic effect associated with Mo adsorption to green rust has yet to be determined.

5.3. Early diagenesis of molybdenum

Pore water profiles of both dissolved Fe and Mo for the two shallow sediment cores from the nitrogenous OMZ display an increase from the bottom water into the surface sediment (Fig. 6a and b, left column). This observation is consistent with the scenario outlined in Fig. 8B, that is, Mo liberation upon reductive dissolution of Fe (oxyhydr) oxide minerals driving an upward-directed diffusive Fe and Mo flux across the sediment-bottom water interface. Below the dissolved Fe and Mo maxima, pore water Fe and Mo profiles are decoupled with near-complete Mo depletion occurring at greater sediment depth than Fe depletion. Fe removal is controlled by H_2S production through bacterial sulfate reduction. Since any H_2S produced immediately reacts with dissolved Fe in pore water and reactive Fe (oxyhydr)oxide minerals, H_2S does not accumulate in the pore water until the highly reactive Fe has been completely converted to sulfide minerals (Canfield et al., 1992). Efficient Mo removal from pore water as Mo-S-species requires the accumulation of H_2S in the pore water (Helz et al., 1996). Therefore, near-quantitative Mo scavenging from pore water occurs at greater sediment depth than Fe removal. However, even in the uppermost cm of the sediment, where no H_2S was detectable, Mo_{XS} concentrations range from 20 to 50 μg g^{-1} (Fig. 6A and B, right column). Mo accumulation at this shallow depth could be related to co-precipitation with Fe monosulfide minerals or pyrite (Zheng et al., 2000), which are both present at this depth (Fig. 6A, central column and Fig. 2C and D in Scholz et al., 2014c), or to precipitation as nanoparticulate Fe-Mo-S (Helz et al., 2011). The importance of pyrite as a host phase for Mo in Peru margin sediments is highlighted by the coincident increase of Mo_{XS} and pyrite concentrations despite the absence of dissolved H_2S in sediments below the OMZ (Fig. 6C).

All surface sediment samples display a negative correlation between $\delta^{98}Mo_{XS}$ and Mo_{XS} concentration (Fig. 6, right column, Fig. 10A). Part of this shift towards lighter Mo isotope compositions with depth and increasing Mo content may be related to the isotope fractionation associated with the conversion of molybdate to thiomolybdate species (Tossell, 2005) at the transition from ferruginous to sulfidic conditions in pore water. Alternatively or in addition, the isotopic shift may be related to the progressive scavenging of isotopically light dissolved Mo in pore water originating from the dissolution of Fe (oxyhydr)oxide minerals (the light Mo isotope composition was originally acquired during adsorption in the water column).

Sediments associated with nitrogenous bottom waters (Fig. 6A and B) and sediments with weakly oxic bottom waters (Fig. 6C) plot on separate correlation trends, with the latter being characterized by lighter $\delta^{98}Mo_{XS}$ at lower Mo_{XS} concentrations (Fig. 10A). Given that sediments and pore waters from all sites are uniformly depleted in Mn (Scholz et al., 2011), Mo delivery with Mn (oxyhydr) oxides is an unlikely explanation for the light Mo isotope composition of sediments at the site with weakly oxic bottom water. However, these sediments at the lower boundary of the OMZ are characterized by a higher content of crystalline Fe (oxyhydr)oxides (i.e., goethite and hematite) (Scholz et al., 2014c) and a higher concentration of Fe (oxyhydr)oxide minerals in general (Fig. 6C, central column). As Mo adsorbed to crystalline Fe (oxyhydr)oxides has a relatively light isotope composition (Goldberg et al., 2009), the differing slope of the correlation trends in Fig. 10A could be assigned to the difference in concentration and mineralogy of Fe (oxyhydr)oxide minerals.

To evaluate the fate of Mo and reactive Fe upon transition from ferruginous to sulfidic conditions during early diagenesis, we examine the Mo isotope composition as a function of the extent to which reactive Fe has been converted to pyrite (extent of pyritization, $Fe_{PY}/(Fe_{OX} + Fe_{PY})$) (Fig. 11A). In this diagram, the separate correlation trends between sediments with nitrogenous

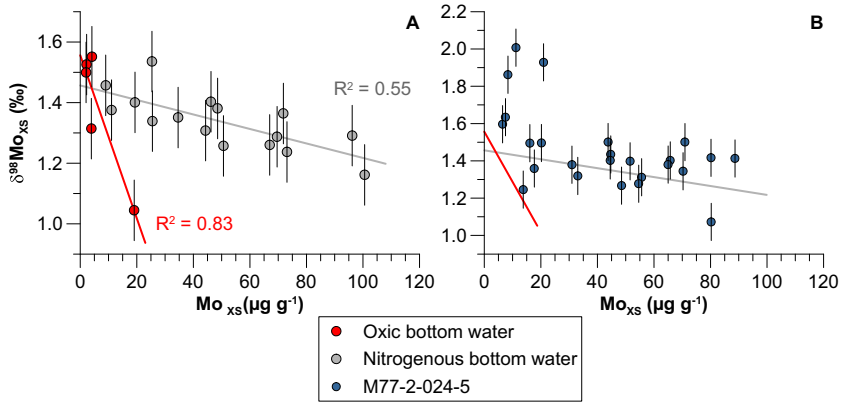

Fig. 10. Plot of $\delta^{98}Mo_{XS}$ versus Mo_{XS} for (A) shallow sediment core samples and (B) samples from the paleo-record (M77-2-024-5). The correlation trends displayed by sediments with nitrogenous and oxic bottom waters in (A) are also plotted in (B) for comparison.

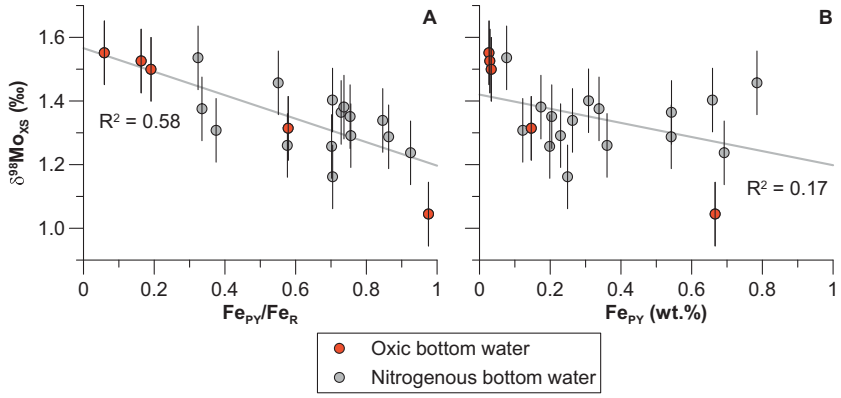

Fig. 11. Plot of (A) $\delta^{98}Mo_{XS}$ versus the extent to which Fe (oxyhydr)oxides have been converted to pyrite ($Fe_{PY}/(Fe_{OX} + Fe_{PY})$ and (B) $\delta^{98}Mo_{XS}$ versus pyrite concentration (Fe_{PY}) for shallow sediment core samples.

and oxic bottom water in Fig. 10A form one unique correlation. For comparison, no such correlation exists between $\delta^{98}Mo_{XS}$ and pyrite concentration (Fig. 11B). This observation indicates that not only the isotope composition of the Mo source (different Fe (oxyhydr)oxide minerals) and sink (presumably pyrite) phases but also the actual process of pyrite formation is important for the $\delta^{98}Mo_{XS}$ recorded in the geological record. Future work on the Mo isotope composition of sedimentary Fe pools combined with transport-reaction modeling may help to fully constrain the mechanisms driving Mo isotope fractionation during early sediment diagenesis.

5.4. Reconstruction of molybdenum cycling over the last 140,000 years

In the paleo-record, the highest Mo_{XS} concentrations coincide with high $\delta^{15}N$ values during the Eemian and late Holocene (Fig. 7A and B). Previous studies have demonstrated that these periods were (and still are in case of the late Holocene) characterized by strong oxygen-depletion in the bottom water and intense water column denitrification (Ganeshram et al., 2000; Scholz et al., 2014b; Salvatteci et al., 2015). Such conditions are conducive to sedimentary Fe release and re-precipitation of Fe (oxyhydr)oxide minerals in the nitrogenous water column through nitrate-dependent Fe oxidation (Scholz et al., 2014a, 2016). Taking into account our new findings on Mo cycling in the present-day water column and surface sediments, this nitrate-dependent Fe shuttle for Mo is likely responsible for the high Mo mass accumulation rates observed during the Eemian and late Holocene. This interpretation is supported by trace metal co-variation patterns revealing that the highest Mo_{XS} concentrations are accompanied by Mo_{EF}/V_{EF} and Mo_{EF}/U_{EF} higher than seawater (Fig. 7D and E) and are thus similar to those of suspended particulate matter and modern surface sediments in the nitrogenous OMZ (Figs. 4D, E and 5B, C).

Most of the $\delta^{98}Mo_{XS}$ signatures in core M77-2-024-5 are relatively uniform (Fig. 7C) and plot on the nitrogenous and weakly oxic correlation trends defined by modern surface sediments (compare Fig. 10A and B). A similar suite of processes, i.e., Mo delivery with variable Fe (oxyhydr)oxide minerals, liberation into the pore water upon Fe reduction and re-precipitation with Fe sulfide minerals, has likely contributed to the Mo isotope composition of these sediments. However, there are a few samples with relatively high $\delta^{98}Mo_{XS}$ values ($\delta^{98}Mo_{XS}$ up to +1.95‰), which are isotopically heavier than any Mo isotope composition associated with metal oxides observed to date. Adsorption of seawater Mo is thus unlikely to be the reason for the sedimentary Mo isotope composition of these samples. All processes known to fractionate Mo isotopes in the marine environment produce lighter $\delta^{98}Mo$ values in the solid phase relative to the dissolved phase (Siebert et al., 2003; Barling and Anbar, 2004; Tossell, 2005; Wasylenki et al., 2008; Goldberg et al., 2009). Therefore, essentially unaltered seawater ($\delta^{98}Mo = +2.3‰$) is the only conceivable Mo source that can explain the relatively heavy $\delta^{98}Mo_{XS}$ values observed in certain intervals of M77-2-024-5.

Samples with the heaviest $\delta^{98}Mo_{XS}$ values correspond to sediments that were deposited during the glacial intervals MIS2 and MIS4 (Fig. 7C). These intervals are characterized by low $\delta^{15}N$ values, low Mo_{XS} as well as Mo_{EF}/V_{EF} and Mo_{EF}/U_{EF} lower than seawater (Fig. 7). This combination of proxy signals indicates less reducing conditions with little or no water column denitrification and, therefore, a lack of accelerated Mo delivery due to repeated dissolution of Fe (oxyhydr)oxide minerals in the sediment and nitrate-dependent re-oxidation of dissolved Fe in the water column. Samples with a high $\delta^{98}Mo_{XS}$ are characterized by low total Fe to Al (Fe_T/Al) ratios compared to the regional lithogenic background (Fig. 12), which is indicative of a diminished delivery or net retention of reactive Fe minerals (Raiswell and Canfield, 2012) on the Peruvian continental margin under glacial conditions (Scholz et al., 2014b). Under conditions where little reactive Fe is present in the sediments and, by inference, little Mo is released from Fe (oxyhydr)oxide minerals into the pore water, a direct concentration-depth gradient from the bottom water into the sediment can ensue. Such a scenario of diffusive Mo delivery (Fig. 8A) is generally consistent with the low Mo mass accumulation rates during glacial intervals, which can be explained with a reasonable depth of Mo depletion of 5–10 cm (Fig. 9) (see, e.g., Zheng et al. (2000) and Scholz et al. (2013) for comparable pore water profiles).

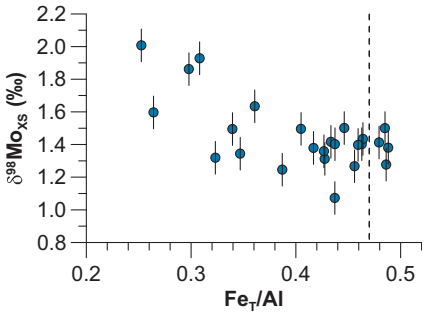

Fig. 12. Plot of $\delta^{98}Mo_{XS}$ versus Fe_T/Al for samples from the paleo-record (M77-2-024-5). The vertical dashed line depicts the Fe_T/Al of the regional lithogenic background.

Moreover, glacial sediments in core M77-2-024–5 display moderately high organic carbon (~0.9 wt.%) and total sulfur (~0.8 wt.%) concentrations (see Supplementary Table S4) indicating that hydrogen sulfide production was high enough to enable Mo fixation under sulfidic conditions at some depth below the sediment-water interface. In diffusion-dominated sedimentary systems, the expressed isotope fractionation factor decreases with the diffusive length-scale between the bottom water source and the depth of Mo fixation in the sediment (Clark and Johnson, 2008). Therefore, Mo fixation within the sediment coupled to a direct diffusive Mo flux from the bottom water is a viable explanation for the relatively heavy, seawater-like $\delta^{98}Mo_{XS}$ observed during glacial intervals.

6. SUMMARY AND IMPLICATIONS FOR THE USE OF MOLYBDENUM ISOTOPES AS A PALEO-REDOX PROXY

Sediments in the Peruvian OMZ are strongly enriched in Mo with interglacial Mo_{XS} concentrations being similar to those observed in restricted basins with sulfidic conditions in the water column. The water column of the Peruvian margin occasionally experiences sulfidic events. However, the water column particulate matter sampled in a sulfidic plume is depleted rather than enriched in Mo relative to oxic or anoxic-nitrogenous samples. Therefore, Mo scavenging under sulfidic conditions is ruled out as a major mechanism of Mo delivery to the sediment surface. Likewise, the mass accumulation rates observed during periods of peak Mo accumulation are too high as to be explained by diffusion of dissolved Mo from the bottom water into the sulfidic zone of the sediments.

Mn- and Fe-rich particles at the sea surface as well as Fe-rich particles in the OMZ are characterized by pronounced Mo enrichments. Mn (oxyhydr)oxides are efficiently dissolved during gravitational sinking through the anoxic water column. In contrast, Fe (oxyhydr)oxide-rich particles are preserved and the majority of Fe-rich particles form in the anoxic water column itself due to re-oxidation of sediment-derived dissolved Fe with nitrate as the terminal electron acceptor. Repeated recycling of reactive Fe between the sediment and the nitrogenous water column provides an efficient shuttle for particulate Mo to the sediment surface.

Some of the Mo that is released from Fe (oxyhydr)oxide minerals in the surface sediment is recycled into the bottom water by diffusion. The remaining Mo is co-precipitated with Fe sulfide minerals thus leading to high Mo burial rates. The Mo isotope composition of surface sediments and most samples from the paleo-record are consistent with Mo delivery adsorbed to Fe (oxyhydr)oxides and conversion to authigenic Mo-S phases during early diagenesis. A few samples from the paleo-record are characterized by exceptionally heavy isotope values close to the Mo isotope composition of modern seawater. Coeval proxy signals for reduced Mo delivery with Fe (oxyhydr)oxide minerals suggest that these heavy Mo isotope values can be explained by diffusion of bottom water Mo into a sulfidic reaction zone deeper in the sediment.

Our scenario of particulate Mo delivery and fixation in sulfidic sediments of the Peruvian OMZ is broadly consistent with the so-called particulate shuttle that has been proposed to explain high Mo mass accumulation rates in restricted euxinic basins with a short seawater residence time (Algeo and Tribovillard, 2009). These authors introduced sedimentary Mo_{EF}/U_{EF} greater than seawater as the diagnostic proxy signal for this mode of Mo cycling. Peru margin sediments are characterized by similar Mo_{EF}/U_{EF} as sediments from the euxinic Cariaco Basin and the Baltic Sea Deeps (see Figs. 5C and 7E as well as plots of Mo_{EF} versus U_{EF} in Scholz et al. (2011, 2013)). However, unlike implied by the original proxy rationale, the Peruvian continental margin is neither restricted nor euxinic and the generation of Fe- and Mo-rich particles is related to reductive processes in the nitrogen cycle rather than interactions with sulfide below or oxygen above the chemocline. We argue that a particulate shuttle for Mo is likely to operate in any anoxic marine environment with short seawater residence time, ranging from nitrogenous to euxinic. Importantly, as long as the reactive Fe present is repeatedly recycled between sediments and water column, accelerated delivery of Mo with Fe (oxyhydr)oxides does not require that the supply of reactive Fe is elevated overall (e.g., as indicated by elevated Fe_T/Al or highly reactive Fe over total Fe, Fe_{HR}/Fe_T) (Fig. 12).

Our findings demonstrate that a particulate shuttle for Mo generates a sedimentary Mo isotope value intermediate between seawater and riverine Mo input. Similar isotope values have been found in other anoxic, marine systems regardless if these are euxinic or not (Fig. 1) (e.g., Arnold et al., 2004; Poulson et al., 2006; Poulson Brucker et al., 2009). Any paleo-approach attempting to identify a globally reduced Mo inventory from a shift to lighter Mo isotope values in Black Shales needs to assess if particulate Mo delivery with Fe (or Mn) (oxyhydr)oxides can be ruled out. Otherwise, the Mo isotope fractionation associated with this shuttle needs to be taken into account in mass balance calculations.

ACKNOWLEDGEMENTS

We are grateful to the government of Peru for granting access to their territorial waters as well as to the crew of RV Meteor for supporting our research at sea. Thanks are due to A. Bleyer, A. Fis-

kal, B. Domeyer, E. Breitbarth, D. Nitschkowsky, R. Surberg and S. Steigenberger for technical and analytical assistance. Constructive comments by two anonymous reviewers and the associate editor Silke Severmann helped to improve the manuscript. This study was supported by the German Research Foundation through Sonderforschungsbereich 754 ("Climate-Biogeochemistry Interactions in the Tropical Ocean") and the Emmy Noether Nachwuchsforschergruppe ICONOX ("Iron Cycling in Marine Sediments and the Oxygen and Nutrient Balance of the Ocean") to FS.

APPENDIX A. SUPPLEMENTARY MATERIAL

Supplementary data associated with this article can be found, in the online version, at http://dx.doi.org/10.1016/j.gca.2017.06.048.

REFERENCES

Algeo T. J. (2004) Can marine anoxic events draw down the trace element inventory of seawater? *Geology* **32**, 1057–1060.

Algeo T. J. and Lyons T. W. (2006) Mo-total organic carbon covariation in modern anoxic marine environments: implications for analysis of paleoredox and paleohydrographic conditions. *Paleoceanography* **21**, PA1016.

Algeo T. J. and Tribovillard N. (2009) Environmental analysis of paleoceanographic systems based on molybdenum-uranium covariation. *Chem. Geol.* **268**, 211–225.

Altabet M. A., Higginson M. J. and Murray D. W. (2002) The effect of millennial-scale changes in Arabian Sea denitrification on atmospheric CO_2. *Nature* **415**, 159–162.

Archer C. and Vance D. (2008) The isotopic signature of the global riverine molybdenum flux and anoxia in the ancient oceans. *Nat. Geosci.* **1**, 597–600.

Arnold G. L., Anbar A. D., Barling J. and Lyons T. W. (2004) Molybdenum isotope evidence for widespread anoxia in mid-proterozoic oceans. *Science* **304**, 87–90.

Barling J. and Anbar A. D. (2004) Molybdenum isotope fractionation during adsorption by manganese oxides. *Earth Planet. Sci. Lett.* **217**, 315–329.

Barling J., Arnold G. L. and Anbar A. D. (2001) Natural mass-dependent variations in the isotopic composition of molybdenum. *Earth Planet. Sci. Lett.* **193**, 447–457.

Bohlen L., Dale A. W., Sommer S., Mosch T., Hensen C., Noffke A., Scholz F. and Wallmann K. (2011) Benthic nitrogen cycling traversing the Peruvian oxygen minimum zone. *Geochim. Cosmochim. Acta* **75**, 6094–6111.

Böning P., Brumsack H. J., Böttcher M. E., Schnetger B., Kriete C., Kallmeyer J. and Borchers S. L. (2004) Geochemistry of Peruvian near-surface sediments. *Geochim. Cosmochim. Acta* **68**, 4429–4451.

Bruland K. W. (1983) Trace elements in seawater. In *Chemical Oceanography* (eds. J. P. Riley and R. Chester). Academic Press, New York, pp. 157–221.

Bruland K. W., Rue E. L., Smith G. J. and DiTullio G. R. (2005) Iron, macronutrients and diatom blooms in the Peru upwelling regime: brown and blue waters of Peru. *Mar. Chem.* **93**, 81–103.

Brumsack H.-J. (2006) The trace metal content of recent organic carbon-rich sediments: implications for Cretaceous black shale formation. *Palaeogeogr. Palaeoclimatol. Palaeoecol.* **232**, 344–361.

Canfield D. E., Raiswell R. and Bottrell S. H. (1992) The reactivity of sedimentary iron minerals toward sulfide. *Am. J. Sci.* **292**, 659–683.

Chan K. M. and Riley J. P. (1966) The determination of vanadium in sea and natural waters, biological materials and silicate sediments and rocks. *Anal. Chim. Acta* **34**, 337–345.

Clark S. K. and Johnson T. M. (2008) Effective isotopic fractionation factors for solute removal by reactive sediments: a laboratory microcosm and slurry study. *Environ. Sci. Technol.* **42**, 7850–7855.

Cutter, G., Andersson, P., Codispoti, L., Croot, P., Francois, R., Lohan, M., Obata, H., Rutgers van der Loeff, M., 2014. Sampling and Sample-handling Protocols for GEOTRACES Cruises. <www.geotraces.org/images/stories/documents/intercalibration/Cookbook.pdf>.

Dahl T. W., Anbar A. D., Gordon G. W., Rosing M. T., Frei R. and Canfield D. E. (2010) The behavior of molybdenum and its isotopes across the chemocline and in the sediments of sulfidic Lake Cadagno, Switzerland. *Geochim. Cosmochim. Acta* **74**, 144–163.

Dahl T. W., Canfield D. E., Rosing M. T., Frei R. E., Gordon G. W., Knoll A. H. and Anbar A. D. (2011) Molybdenum evidence for expansive sulfidic water masses in ~750 Ma oceans. *Earth Planet. Sci. Lett.* **311**, 264–274.

Dahl T. W., Chappaz A., Fitts J. P. and Lyons T. W. (2013a) Molybdenum reduction in a sulfidic lake: Evidence from X-ray absorption fine-structure spectroscopy and implications for the Mo paleoproxy. *Geochim. Cosmochim. Acta* **103**, 213–231.

Dahl T. W., Ruhl M., Hammarlund E. U., Canfield D. E., Rosing M. T. and Bjerrum C. J. (2013b) Tracing euxinia by molybdenum concentrations in sediments using handheld X-ray fluorescence spectroscopy (HHXRF). *Chem. Geol.* **360–361**, 241–251.

Dale A. W., Sommer S., Lomnitz U., Bourbonnais A. and Wallmann K. (2016) Biological nitrate transport in sediments on the Peruvian margin mitigates benthic sulfide emissions and drives pelagic N loss during stagnation events. *Deep Sea Res. Part I* **112**, 123–136.

Dalsgaard T., Thamdrup B., Farías L. and Revsbech N. P. (2012) Anammox and denitrification in the oxygen minimum zone of the eastern South Pacific. *Limnol. Oceanogr.* **57**, 1331–1346.

Emerson S. R. and Huested S. S. (1991) Ocean Anoxia and the concentrations of molybdenum and vanadium in seawater. *Mar. Chem.* **34**, 177–196.

Erickson B. E. and Helz G. R. (2000) Molybdenum(VI) speciation in sulfidic waters: Stability and lability of thiomolybdates. *Geochim. Cosmochim. Acta* **64**, 1149–1158.

Freymuth H., Vils F., Willbold M., Taylor R. N. and Elliott T. (2015) Molybdenum mobility and isotopic fractionation during subduction at the Mariana arc. *Earth Planet. Sci. Lett.* **432**, 176–186.

Ganeshram R. S., Pedersen T. F., Calvert S. E., McNeill G. W. and Fontugne M. R. (2000) Glacial-interglacial variability in denitrification in the World's Oceans: causes and consequences. *Paleoceanography* **15**, 361–376.

Goldberg T., Archer C., Vance D. and Poulton S. W. (2009) Mo isotope fractionation during adsorption to Fe (oxyhydr)oxides. *Geochim. Cosmochim. Acta* **73**, 6502–6516.

Goldberg T., Archer C., Vance D., Thamdrup B., McAnena A. and Poulton S. W. (2012) Controls on Mo isotope fractionations in a Mn-rich anoxic marine sediment, Gullmar Fjord, Sweden. *Chem. Geol.* **296–297**, 73–82.

Goldberg T., Poulton S. W., Wagner T., Kolonic S. F. and Rehkämper M. (2016) Molybdenum drawdown during Cretaceous Oceanic Anoxic Event 2. *Earth Planet. Sci. Lett.* **440**, 81–91.

Greber N. D., Siebert C., Nägler T. F. and Pettke T. (2012) $\Delta^{98}/^{95}$Mo values and Molybdenum Concentration Data for

NIST SRM 610, 612 and 3134: towards a Common Protocol for Reporting Mo Data. *Geostand. Geoanal. Res.* **36**, 291–300.

Gutiérrez D., Enríquez E., Purca S., Quipúzcoa L., Marquina R., Flores G. and Graco M. (2008) Oxygenation episodes on the continental shelf of central Peru: remote forcing and benthic ecosystem response. *Prog. Oceanogr.* **79**, 177–189.

Hammarlund E. U., Dahl T. W., Harper D. A. T., Bond D. P. G., Nielsen A. T., Bjerrum C. J., Schovsbo N. H., Schönlaub H. P., Zalasiewicz J. A. and Canfield D. E. (2012) A sulfidic driver for the end-Ordovician mass extinction. *Earth Planet. Sci. Lett.* **331–332**, 128–139.

Hawco N. J., Ohnemus D. C., Resing J. A., Twining B. S. and Saito M. A. (2016) A dissolved cobalt plume in the oxygen minimum zone of the eastern tropical South Pacific. *Biogeosciences* **13**, 5697–5717.

Heller M. I., Lam P. J., Moffett J. W., Till C. P., Lee J.-M., Toner B. M. and Marcus M. A. (2017) Accumulation of Fe oxyhydroxides in the Peruvian oxygen deficient zone implies non-oxygen dependent Fe oxidation. *Geochim. Cosmochim. Acta* **211**, 174–193.

Helz G. R., Miller C. V., Charnock J. M., Mosselmans J. F. W., Pattrick R. A. D., Garner C. D. and Vaughan D. J. (1996) Mechanism of molybdenum removal from the sea and its concentration in black shales: EXAFS evidence. *Geochim. Cosmochim. Acta* **60**, 3631–3642.

Helz G. R., Bura-Nakic E., Mikac N. and Ciglenecki I. (2011) New model for molybdenum behavior in euxinic waters. *Chem. Geol.* **284**, 323–332.

Huerta-Diaz M. A. and Morse J. W. (1992) Pyritization of trace metals in anoxic marine sediments. *Geochim. Cosmochim. Acta* **56**, 2681–2702.

Kappler A. and Newman D. K. (2004) Formation of Fe(III)-minerals by Fe(II)-oxidizing photoautotrophic bacteria. *Geochim. Cosmochim. Acta* **68**, 1217–1226.

Kendall B., Creaser R. A., Gordon G. W. and Anbar A. D. (2009) Re-Os and Mo isotope systematics of black shales from the Middle Proterozoic Velkerri and Wollogorang Formations, McArthur Basin, northern Australia. *Geochim. Cosmochim. Acta* **73**, 2534–2558.

Lam P., Lavik G., Jensen M. M., van de Vossenberg J., Schmid M., Woebken D., Gutiérrez D., Amann R., Jetten M. S. M. and Kuypers M. M. M. (2009) Revising the nitrogen cycle in the Peruvian oxygen minimum zone. *Proc. Natl. Acad. Sci.* **106**, 4752–4757.

Levin L., Gutiérrez D., Rathburn A., Neira C., Sellanes J., Muñoz P., Gallardo V. and Salamanca M. (2002) Benthic processes on the Peru margin: a transect across the oxygen minimum zone during the 1997–98 El Niño. *Prog. Oceanogr.* **53**, 1–27.

Malinovsky D., Hammarlund D., Ilyashuk B., Martinsson O. and Gelting J. (2007) Variations in the isotopic composition of molybdenum in freshwater lake systems. *Chem. Geol.* **236**, 181–198.

McManus J., Nägler T. F., Siebert C., Wheat C. G. and Hammond D. E. C. (2002) Oceanic molybdenum isotope fractionation: Diagenesis and hydrothermal ridge-flank alteration. *Geochem. Geophys. Geosyst.* **3**, 1–9.

McManus J., Berelson W. M., Severmann S., Poulson R. L., Hammond D. E., Klinkhammer G. P. and Holm C. (2006) Molybdenum and uranium geochemistry in continental margin sediments: Paleoproxy potential. *Geochim. Cosmochim. Acta* **70**, 4643–4662.

Miller C. A., Peucker-Ehrenbrink B., Walker B. D. and Marcantonio F. (2011) Re-assessing the surface cycling of molybdenum and rhenium. *Geochim. Cosmochim. Acta* **75**, 7146–7179.

Morford J. L., Emerson S. R., Breckel E. J. and Kim S. H. (2005) Diagenesis of oxyanions (V, U, Re, and Mo) in pore waters and sediments from a continental margin. *Geochim. Cosmochim. Acta* **69**, 5021–5032.

Muratli J. M., Chase Z., Mix A. C. and McManus J. (2010) Increased glacial-age ventilation of the Chilean margin by Antarctic Intermediate Water. *Nat. Geosci.* **3**, 23–26.

Muratli J. M., McManus J., Mix A. and Chase Z. (2012) Dissolution of fluoride complexes following microwave-assisted hydrofluoric acid digestion of marine sediments. *Talanta* **89**, 195–200.

Nägler T. F., Neubert N., Böttcher M. E., Dellwig O. and Schnetger B. (2011) Molybdenum isotope fractionation in pelagic euxinia: Evidence from the modern Black and Baltic Seas. *Chem. Geol.* **289**, 1–11.

Nägler T. F., Anbar A. D., Archer C., Goldberg T., Gordon G. W., Greber N. D., Siebert C., Sohrin Y. and Vance D. (2014) Proposal for an International Molybdenum Isotope Measurement Standard and Data Representation. *Geostand. Geoanal. Res.* **38**, 149–151.

Neubert N., Nägler T. F. and Böttcher M. E. (2008) Sulfidity controls molybdenum isotope fractionation into euxinic sediments: evidence from the modern Black Sea. *Geology* **36**, 775–778.

Noffke A., Hensen C., Sommer S., Scholz F., Bohlen L., Mosch T., Graco M. and Wallmann K. (2012) Benthic iron and phosphorus fluxes across the Peruvian oxygen minimum zone. *Limnol. Oceanogr.* **57**, 851–867.

Noordmann J., Weyer S., Montoya-Pino C., Dellwig O., Neubert N., Eckert S., Paetzel M. and Böttcher M. E. (2015) Uranium and molybdenum isotope systematics in modern euxinic basins: case studies from the central Baltic Sea and the Kyllaren fjord (Norway). *Chem. Geol.* **396**, 182–195.

Pantke C., Obst M., Benzerara K., Morin G., Ona-Nguema G., Dippon U. and Kappler A. (2012) Green rust formation during Fe(II) oxidation by the nitrate-reducing Acidovorax sp. strain BoFeN1. *Environ. Sci. Technol.* **46**, 1439–1446.

Poulson R. L., Siebert C., McManus J. and Berelson W. M. (2006) Authigenic molybdenum isotope signatures in marine sediments. *Geology* **34**, 617–620.

Poulson Brucker R. L., McManus J., Severmann S. and Berelson W. M. (2009) Molybdenum behavior during early diagenesis: Insights from Mo isotopes. *Geochem. Geophys. Geosyst.* **10**.

Poulton S. W., Fralick P. W. and Canfield D. E. (2010) Spatial variability in oceanic redox structure 1.8 billion years ago. *Nat. Geosci.* **3**, 486–490.

Raiswell R. and Canfield D. E. (2012) The iron biogeochemical cycle past and present. *Geochem. Perspect.* **1**, 1–220.

Richards F. A. (1965) Anoxic basins and fjords. In *Chemical Oceanography* (eds. J. P. Riley and G. Skirrow). Academic Press, New York, pp. 611–643.

Salvatteci R., Gutierrez D., Sifeddine A., Ortlieb L., Druffel E., Boussafir M. and Schneider R. (2015) Centennial to millennial-scale changes in oxygenation and productivity in the Eastern Tropical South Pacific during the last 25,000 years. *Quatern. Sci. Rev.* **131**(Part A), 102–117.

Scholz F., Hensen C., Noffke A., Rohde A., Liebetrau V. and Wallmann K. (2011) Early diagenesis of redox-sensitive trace metals in the Peru upwelling area: response to ENSO-related oxygen fluctuations in the water column. *Geochim. Cosmochim. Acta* **75**, 7257–7276.

Scholz F., McManus J. and Sommer S. (2013) The manganese and iron shuttle in a modern euxinic basin and implications for molybdenum cycling at euxinic ocean margins. *Chem. Geol.* **355**, 56–68.

Scholz F., Severmann S., McManus J. and Hensen C. (2014a) Beyond the Black Sea paradigm: the sedimentary fingerprint of

an open-marine iron shuttle. *Geochim. Cosmochim. Acta* **127**, 368–380.

Scholz F., McManus J., Mix A. C., Hensen C. and Schneider R. R. (2014b) The impact of ocean deoxygenation on iron release from continental margin sediments. *Nat. Geosci.* **7**, 433–437.

Scholz F., Severmann S., McManus J., Noffke A., Lomnitz U. and Hensen C. (2014c) On the isotope composition of reactive iron in marine sediments: Redox shuttle versus early diagenesis. *Chem. Geol.* **389**, 48–59.

Scholz F., Löscher C. R., Fiskal A., Sommer S., Hensen C., Lomnitz U., Wuttig K., Göttlicher J., Kossel E., Steininger R. and Canfield D. E. (2016) Nitrate-dependent iron oxidation limits iron transport in anoxic ocean regions. *Earth Planet. Sci. Lett.* **454**, 272–281.

Schunck H., Lavik G., Desai D. K., Grosskopf T., Kalvelage T., Loescher C. R., Paulmier A., Contreras S., Siegel H., Holtappels M., Rosenstiel P., Schilhabel M. B., Graco M., Schmitz R. A., Kuypers M. M. M. and LaRoche J. (2013) Giant hydrogen sulfide plume in the oxygen minimum zone off Peru supports chemolithoautotrophy. *PLoS ONE* **8**.

Scott C. and Lyons T. W. (2012) Contrasting molybdenum cycling and isotopic properties in euxinic versus non-euxinic sediments and sedimentary rocks: Refining the paleoproxies. *Chem. Geol.* **324–325**, 19–27.

Siebert C., Nägler T. F. and Kramers J. D. C. (2001) Determination of molybdenum isotope fractionation by double-spike multicollector inductively coupled plasma mass spectrometry. *Geochem. Geophys. Geosyst.* **2**. http://dx.doi.org/10.1029/2000GC000124.

Siebert C., Nägler T. F., von Blanckenburg F. and Kramers J. D. (2003) Molybdenum isotope records as a potential new proxy for paleoceanography. *Earth Planet. Sci. Lett.* **211**, 159–171.

Sommer S., Gier J., Treude T., Lomnitz U., Dengler M., Cardich J. and Dale A. W. (2016) Depletion of oxygen, nitrate and nitrite in the Peruvian oxygen minimum zone cause an imbalance of benthic nitrogen fluxes. *Deep Sea Res. Part I* **112**, 113–122.

Thamdrup B., Dalsgaard T. and Revsbech N. P. (2012) Widespread functional anoxia in the oxygen minimum zone of the Eastern South Pacific. *Deep Sea Res. Part I* **65**, 36–45.

Tossell J. A. (2005) Calculating the partitioning of the isotopes of Mo between oxidic and sulfidic species in aqueous solution. *Geochim. Cosmochim. Acta* **69**, 2981–2993.

Tribovillard N., Riboulleau A., Lyons T. and Baudin F. (2004) Enhanced trapping of molybdenum by sulfurized marine organic matter of marine origin in Mesozoic limestones and shales. *Chem. Geol.* **213**, 385–401.

Tribovillard N., Algeo T. J., Lyons T. W. and Riboulleau A. (2006) Trace metals as paleoredox and paleoproductivity proxies: An update. *Chem. Geol.* **232**, 12–32.

Vedamati J., Goepfert T. and Moffett J. W. (2014) Iron speciation in the eastern tropical South Pacific oxygen minimum zone off Peru. *Limnol. Oceanogr.* **59**, 1945–1957.

Voegelin A. R., Pettke T., Greber N. D., von Niederhäusern B. and Nägler T. F. (2014) Magma differentiation fractionates Mo isotope ratios: Evidence from the Kos Plateau Tuff (Aegean Arc). *Lithos* **190–191**, 440–448.

Vorlicek T. P. and Helz G. R. (2002) Catalysis by mineral surfaces: Implications for Mo geochemistry in anoxic environments. *Geochim. Cosmochim. Acta* **66**, 3679–3692.

Vorlicek T. P., Kahn M. D., Kasuya Y. and Helz G. R. (2004) Capture of molybdenum in pyrite-forming sediments: Role of ligand-induced reduction by polysulfides. *Geochim. Cosmochim. Acta* **68**, 547–556.

Waite T. D., Davis J. A., Payne T. E., Waychunas G. A. and Xu N. (1994) Uranium(VI) adsorption to ferrihydrite: application of a surface complexation model. *Geochim. Cosmochim. Acta* **58**, 5465–5478.

Wang Z., Lee S.-W., Catalano J. G., Lezama-Pacheco J. S., Bargar J. R., Tebo B. M. and Giammar D. E. (2012) Adsorption of uranium(VI) to manganese oxides: X-ray absorption spectroscopy and surface complexation modeling. *Environ. Sci. Technol.* **47**, 850–858.

Wasylenki L. E., Anbar A. D., Liermann L. J., Mathur R., Gordon G. W. and Brantley S. L. (2007) Isotope fractionation during microbial metal uptake measured by MC-ICP-MS. *J. Anal. At. Spectrom.* **22**, 905–910.

Wasylenki L. E., Rolfe B. A., Weeks C. L., Spiro T. G. and Anbar A. D. (2008) Experimental investigation of the effects of temperature and ionic strength on Mo isotope fractionation during adsorption to manganese oxides. *Geochim. Cosmochim. Acta* **72**, 5997–6005.

Wehrli B. and Stumm W. (1989) Vanadyl in natural waters: adsorption and hydrolysis promote oxygenation. *Geochim. Cosmochim. Acta* **53**, 69–77.

Westermann S., Vance D., Cameron V., Archer C. and Robinson S. A. (2014) Heterogeneous oxygenation states in the Atlantic and Tethys oceans during Oceanic Anoxic Event 2. *Earth Planet. Sci. Lett.* **404**, 178–189.

Wille M., Nägler T. F., Lehmann B., Schroder S. and Kramers J. D. (2008) Hydrogen sulphide release to surface waters at the Precambrian/Cambrian boundary. *Nature* **453**, 767–769.

Zegeye A., Bonneville S., Benning L. G., Sturm A., Fowle D. A., Jones C., Canfield D. E., Ruby C., MacLean L. C., Nomosatryo S., Crowe S. A. and Poulton S. W. (2012) Green rust formation controls nutrient availability in a ferruginous water column. *Geology* **40**, 599–602.

Zheng Y., Anderson R. F., van Geen A. and Kuwabara J. (2000) Authigenic molybdenum formation in marine sediments: a link to pore water sulfide in the Santa Barbara Basin. *Geochim. Cosmochim. Acta* **64**, 4165–4178.

Associate Editor: Silke Severmann